

11 00 11 11

TR-220-1039
DECEMBER 1971

SHUTTLE ASCENT AND SHOCK IMPINGEMENT AERODYNAMIC HEATING STUDIES

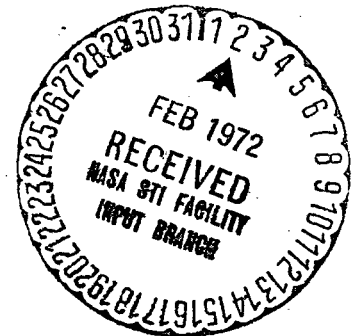
FINAL REPORT

**CASE FILE
COPY**

Prepared for:

**NATIONAL AERONAUTICS AND SPACE ADMINISTRATION
GEORGE C. MARSHALL SPACE FLIGHT CENTER
Aero-Astroynamics Laboratory**

Under Contract NAS8-26268



NORTHROP SERVICES, INC.

P. O. BOX 1484
HUNTSVILLE, ALABAMA 35807
TELEPHONE (205)837 0580

SHUTTLE ASCENT AND SHOCK IMPINGEMENT AERODYNAMIC HEATING STUDIES

FINAL REPORT

December 1971

by

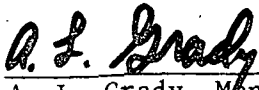
W. D. Lanning
F. T. Hung

PREPARED FOR:

**NATIONAL AERONAUTICS AND SPACE ADMINISTRATION
GEORGE C. MARSHALL SPACE FLIGHT CENTER
AERO-ASTRODYNAMICS LABORATORY**

Under Contract NAS8-26268

REVIEWED AND APPROVED BY:



A. L. Grady, Manager
Advanced Engineering Analysis

**NORTHROP SERVICES, INC.
HUNTSVILLE, ALABAMA**

FOREWORD

This report presents the results of the work performed by Northrop Services, Inc. and its subcontractors under contract NAS8-26268. Technical coordination was provided by Messrs. J. A. Forney and J. D. Warmbrod of the Aerothermodynamics Branch, Aerophysics Division, Aero-Astroynamics Laboratory, George C. Marshall Space Flight Center.

ABSTRACT

The collection and analysis of aerodynamic heating data obtained from shock impingement experimental investigations have been completed. The data were categorized into four interference areas; fin leading edge, wing/fuselage fin/plate corners, and space shuttle configurations. The effects of shock impingement were found to increase the heating rates 10-40 times the undisturbed values.

A test program was completed at NASA/Langley Research Center to investigate the magnitudes and surface patterns of the mated shock interference flowfield. A 0.0065 scale thin-skin model of the MDAC 256-20 space shuttle booster mated with a Stycast model of the MDAC Internal tank orbiter was tested in the 20-inch M=6 tunnel, the 31-inch M=10 tunnel, and the 48-inch Unitary Plan Tunnel. The gap region of the ascent configuration was the principal area of interest where both thermocouple and phase-change paint data were obtained. The results of a brief study of possible errors in data reduction methods were summarized.

Results are presented of a study of the pressure and heat transfer distributions on the leeward surface of a 75-degree sweep slab delta wing. Mach numbers of 15 and 20 at Reynolds numbers per meter of 1.8×10^7 and 8.7×10^6 , respectively, were investigated. The maximum angle-of-attack was 25 degrees using nitrogen as the test gas. Based on the experimental results, the dominant flowfield characteristics for the leeward surface flowfield over a blunt delta wing were postulated.

The effects of surface roughness on boundary layer transition and aerodynamic heating were investigated. A comprehensive literature survey was completed. A finite difference computer program of the Spalding-Patankar boundary layer method was modified to treat the flow over a sinusoidal wall. The application indicated that a parametric study was feasible using the computer program.

A review of the base thermal environment of the Saturn S-II stage was compiled as a section of a design handbook to be used in shuttle studies. The model and flight tests were studied, summarized, and compared with prediction methods.

TABLE OF CONTENTS

<u>Section</u>	<u>Title</u>	<u>Page</u>
	FOREWORD	ii
	ABSTRACT	iii
	LIST OF ILLUSTRATIONS.	v
	NOMENCLATURE	vi
I	INTRODUCTION	1-1
II	SHOCK INTERFERENCE HEATING	2-1
	2.1 SHOCK IMPINGEMENT TO WING OR CANARD LEADING EDGES	2-1
	2.2 ANALYSES OF GAP REGION.	2-9
	2.3 INTERFERENCE AT FIN/PLATE CORNERS	2-11
	2.4 SHOCK INTERFERENCE HEATING TO SPACE SHUTTLE CONFIGURATIONS.	2-13
III	SHUTTLE ASCENT AND SHOCK IMPINGEMENT AERODYNAMIC HEATING TESTS	3-1
IV	DELTA WING LEEWARD SURFACE FLOWFIELD	4-1
V	EFFECTS OF ROUGHNESS ON COMPRESSIBLE FLOWS	5-1
VI	BASE HEATING REVIEW	6-1
VII	MODIFICATIONS TO THE NASA/LEWIS COMPRESSIBLE LAMINAR AND TURBULENT BOUNDARY LAYER COMPUTER PROGRAM.	7-1
VIII	CONCLUSIONS AND RECOMMENDATIONS	8-1
IX	REFERENCES	9-1
	Appendix A SHOCK INTERFERENCE	A
	Appendix B HEATING TESTS	B
	Appendix C LEEWARD SURFACE FLOWFIELD	C
	Appendix D EFFECTS OF ROUGHNESS ON COMPRESSIBLE FLOWS	D
	Appendix E SATURN S-II BASE ENVIRONMENT REVIEW	E
	Appendix F BOUNDARY LAYER PROGRAM	F

LIST OF ILLUSTRATIONS

<u>Figure No.</u>	<u>Title</u>	<u>Page</u>
2-1	SPACE SHUTTLE SHOCK INTERFERENCE	2-2
2-2	SHOCK/SHOCK INTERACTION ON STRAIGHT WING	2-4
2-3	SHOCK/SHOCK INTERACTION ON WING WITH INTERMEDIATE SWEEP ANGLE	2-5
2-4	SHOCK/SHOCK INTERACTION ON HIGHLY SWEEP WING	2-6
2-5	SHOCK INTERFERENCE HEATING DATA ON HIGHLY SWEEP CYLINDER	2-8
2-6	SHOCK/BOUNDARY-LAYER INTERACTION HEATING CORRELATION (REF. 4)	2-10
2-7	SHOCK INTERFERENCE HEATING DATA ON WING WITH INTERMEDIATE SWEEP ANGLE	2-10
2-8	FIN-PLATE MODEL FOR INTERFERENCE HEATING TEST	2-12
2-9	MDC SPACE SHUTTLE SHOCK INTERFERENCE	2-14
2-10	HEAT TRANSFER CURVES GENERATED BY SEMI-INFINITE SOLID METHOD	2-16
2-11	BOOSTER UPPER SURFACE CENTERLINE INTERFERENCE HEATING DUE TO PRESENCE OF ORBITER	2-17
2-12	SHOCK INTERFERENCE HEATING NEAR BOOSTER CANARD/ FUSELAGE JUNCTURE ($h_{\text{IMPINGEMENT}}/h_{\text{UNDISTURBED}}$)	2-18
2-13	OVERALL SHOCK WAVE INTERFERENCE DIAGRAM ON BOOSTER	2-20
2-14	SHOCK INTERFERENCE HEATING AREAS ON GDC DELTA WING BOOSTER	2-22

NOMENCLATURE

<u>Symbol</u>	<u>Definition</u>
M	Mach Number
P	Pressure
h	Heat Transfer Coefficient, Enthalpy
R_N	Reynolds Number
r	Nose Radius
α	Flat Plate Angle-of-Attack
δ	Fin Deflection Angle
θ	Deflection Angle
Λ	Sweep Angle
ρ	Density
	Ratio of Specific Heats

<u>Subscript</u>	<u>Definition</u>
pk	Peak Value
o	Undisturbed Value

Section I

INTRODUCTION

Northrop and its subcontractors have been actively participating in the preliminary design studies of the Space Shuttle vehicles. Preliminary design of hypersonic aircraft and lifting spacecraft is accomplished through an evaluation of each design component and augmented by evaluating the influence of every other component in the system. The flight environment, particularly the thermal environment, must carefully be analyzed if the design parameters are to be put in the proper perspective. In order to establish reliable shuttle design heating methods germane to optimizing the thermal protection system, Northrop has systematically analyzed potential aerodynamic heating problems that may be encountered during the flight of the Space Shuttle. This report summarizes the results of these aerothermodynamic studies.

The primary objective in performing these aerothermodynamic studies was to analyze the ascent and shock-impingement flowfield test data which was collected and categorized during an intensified literature search. The results of this study would yield useful flowfield properties, particularly the location and severity of shock impingement areas, which should provide design specifications for a thin-skin model of the Shuttle booster and a phase-change coating model of the Shuttle orbiter. During the test data analysis, the correlation techniques developed during the literature survey will be applied to the shuttle wind tunnel data.

The literature survey yielded experimental data on simple geometric combinations, such as fins, wedges, cylinders, and flat plates, and on shuttle orbiter and booster configurations. These data showed that with shock impingement, the heating rates can be 30-40 times the undisturbed value. The data were correlated for each model geometry as a function of Mach number, Reynolds number, shock strength, sweep angle, etc. This study was performed by Dr. F. Hung and reported in Section II.

In Section III, REMTECH, Inc. summarizes the experimental test program performed at Langley Research Center using an MDAC Space Shuttle launch

configuration. The purpose of these tests were to obtain both thermocouple and phase-change paint data on the ascent configuration. The gap region between the orbiter and booster was of primary concern during this shock impingement test program.

The leeward surface flowfield of a delta wing model in simulated reentry flow is reported in Section IV. This experimental program was performed by W. D. Lanning at the von Karman Institute's Longshot facility in Belgium. The objective of this experimental program was to obtain heat transfer and pressure data as a function of angle-of-attack and Mach number. The leeward surface is of particular importance in minimizing the thermal protection system because it is subjected to high heating rates. These high temperatures are the result of vortical flowfield interactions. This vortex phenomenon is not well understood and the experimental data obtained in this study will contribute to a better understanding of the problem.

The surface of the Shuttle may be rough due to the joints of the refurbished thermal protection system. Consequently, the effects of roughness on the aerodynamic environment must be known. Auburn University, under the project leadership of Dr. K. Pell, reports on the effects of roughness on compressible flows in Section V. This task included the collection of experimental data from the open literature and the application of Spalding-Patankar boundary layer methods for predicting the effects of roughness on boundary layer transition and heat transfer.

A review of the Saturn S-II base thermal environment which summarizes the base heating experiences is presented in Section VI. REMTECH, Inc. compiled this summary which will become a portion of a handbook to be used as a design guide on the Space Shuttle. This review includes a general description of the stage and the J-2 engine characteristics, the model test program results, flight data, and a comparison of model and flight results.

The modifications to the NASA/Lewis compressible laminar and turbulent boundary layer computer program are described in Section VII by W. W. Youngblood. Northrop determined the program's usefulness in the overall definition of the NASA Space Shuttle thermal environment. The program is capable of analyzing

both laminar and turbulent boundary layers in arbitrary pressure gradients. Two sample problems were calculated by the computer program and compared to experimental data.

Section VIII summarizes the accomplishments of this project and makes recommendations for future work to be initiated in the area of interference heating.

Section II

SHOCK INTERFERENCE HEATING

The design of space shuttle systems for operation at supersonic and hypersonic speeds requires the understanding of aerodynamic heating generated through shock wave interfering flow fields in order to determine an optimum thermal protection system.

For a typical shuttle configuration, such as shown in Figure 2-1, a bow shock generating from the booster nose impinges on and interacts with the bow shock on the wing or canard area (A). Near the wing or canard root, the wing or canard bow shock will also interact with the boundary layer on the fuselage/wing junction as shown in area (B) in Figure 2-1. For mated configuration, the booster and the orbiter bow shock waves also interact with each other in area (C).

Both experimental and analytical studies indicate that the shock wave interference results in severe heating on the shuttle surfaces. Test data show that with shock impingement, the heating rates can be as high as 30-40 times the values with no shock impingement. An example of the severe heating due to shock interference was given by the NASA X-15 test flights. During one flight, the ventral fin, which supported a ram-jet test model, was burned completely through in several places where shock impingement occurred. This indicates that reliable methods have to be developed to estimate or minimize the shock interfering heating rates involved in the shuttle flights.

2.1 SHOCK IMPINGEMENT TO WING OR CANARD LEADING EDGES

For the shock/shock interaction on a wing leading edge, the flowfield in the shock interference region has been analyzed by Edney (ref. 1). Depending on the wing sweep angle, the shock/shock interaction on the wing will result in one of the following interactions which acting on the wing surface and causing high heating rates:

- Supersonic jet impingement (for low sweep angle)
- Shock wave/boundary layer interaction (for intermediate sweep angle)
- No shock impingement (for high sweep angle).

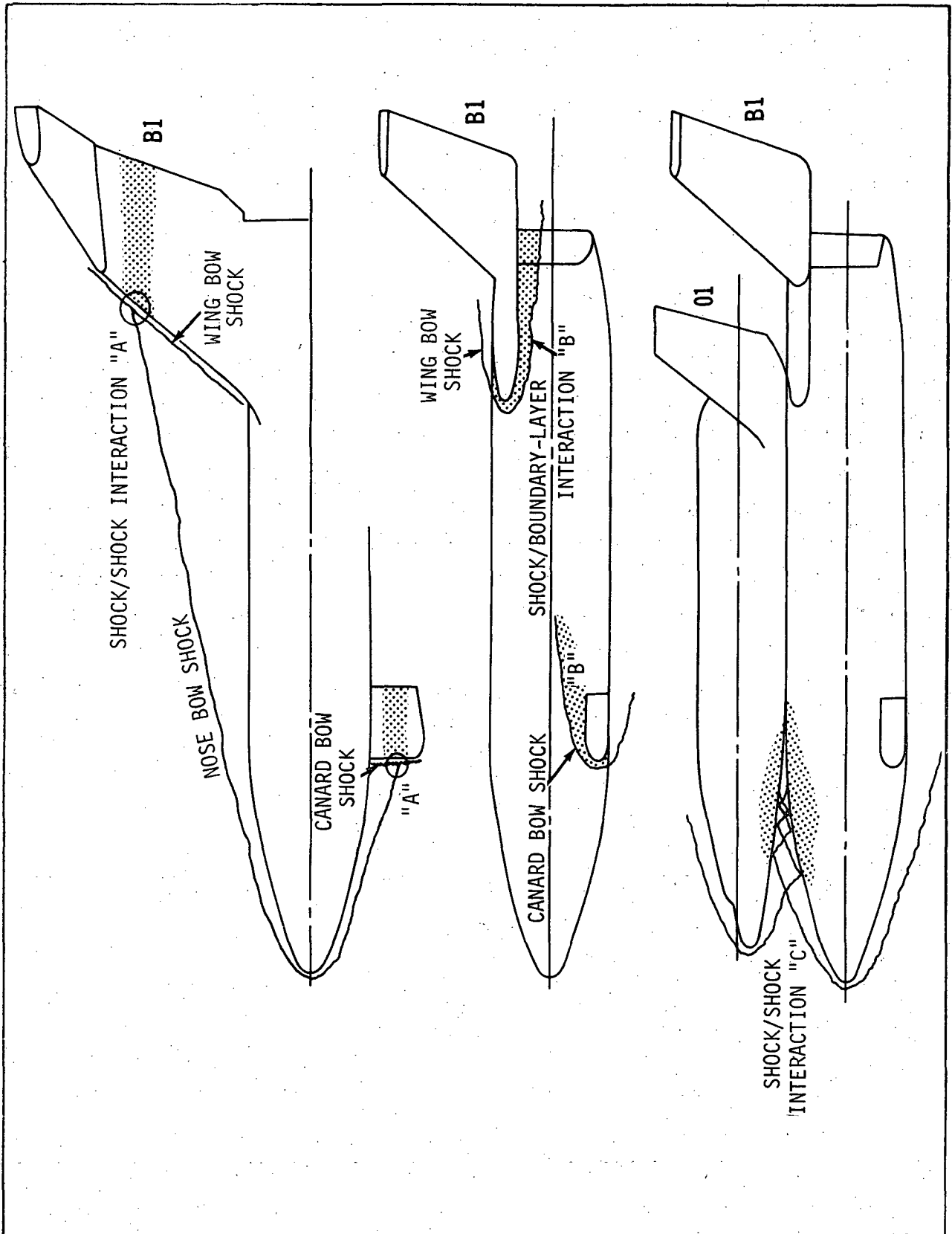


Figure 2-1. SPACE SHUTTLE SHOCK INTERFERENCE

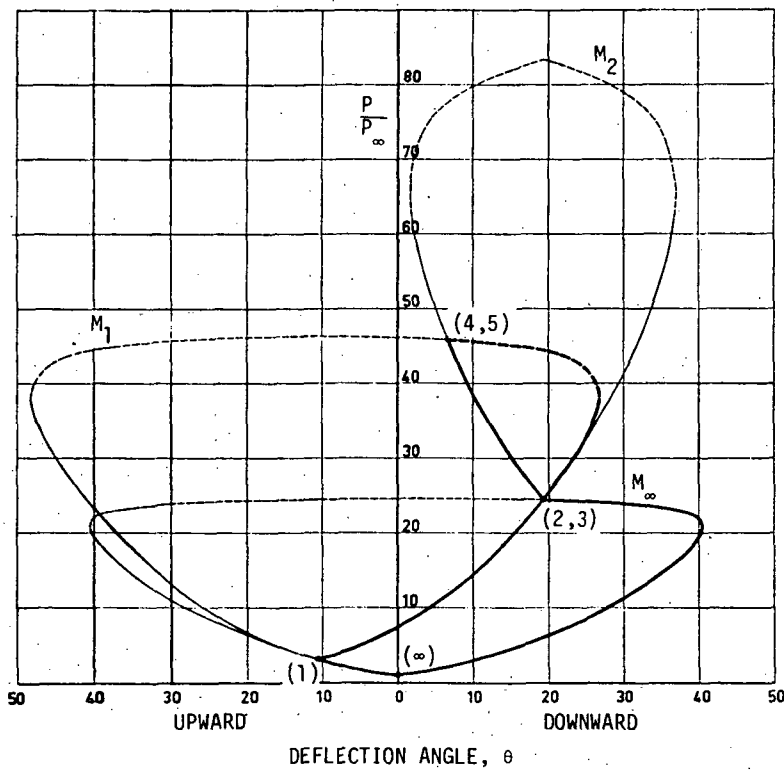
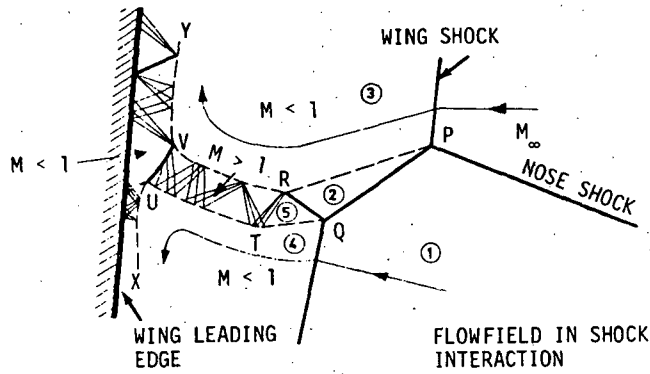
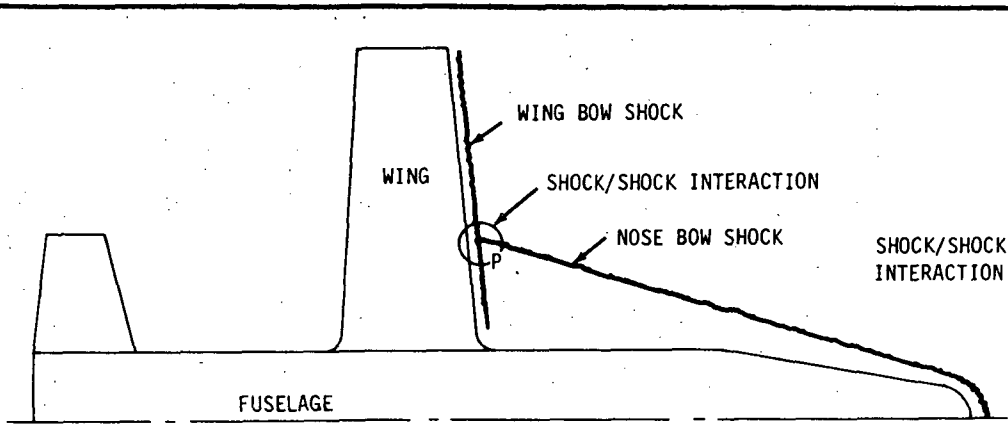
The supersonic jet impinging on the wing surface causes very high and localized heating rates. The shock wave/boundary layer interaction also causes high heating rates which depend on the state of the boundary layer (laminar or turbulent), the strength of the shock wave and the flow separation in the interference region. For the highly swept wing, no shock wave impinges on the wing surface and consequently no highly localized heating. For this case, the heating rates can be calculated using the swept-cylinder technique (ref. 2) based on local flow conditions.

Methods to estimate the shock interfering heating rates can be analytical or experimental or the combination of both. An analytical approach is necessary in order to have a better insight of the basic physical problems involved in the shock wave interference. However, it is also realized that an analytical approach is very limited due to the complexity of the problem. This indicates that existing experimental data have to be used in order to have a reliable interference heating estimation. In this study, a literature search on existing experimental data have been made. Sixteen references (refs. 3 through 18) dealing with wing leading edges and 12 references (refs. 6, 7, 11 through 14, and 19 through 24) dealing with wing/fuselage and canard/fuselage junctures have been compiled and analyzed. The test conditions of the compiled experimental data can be summarized as below:

- Model geometries: flat plate, cylinder, hemisphere, fin with hemicylindrical leading edge, corner, etc.
- Mach number range: 2.7 to 19
- Reynolds number (per foot) range: 3.0×10^4 to 4.8×10^7
- Shock generator deflection angle: 0 to 60 degrees
- Wing sweep angle: 0 to 75 degrees.

A summary of the existing leading edge shock interference heating test data is given in Appendix A-1.

The analytical approach was also made to predict the interference heating on the leading edges. For typical shuttle configurations as shown in Figures 2-2, 2-3, and 2-4, a bow shock generating from the shuttle nose impinges on and interacts with the bow shock on the wings. As discussed earlier, depending on the wing sweep angle, the shock/shock interaction results in one of the following



SHOCK POLAR DIAGRAM

Figure 2-2. SHOCK/SHOCK INTERACTION ON STRAIGHT WING

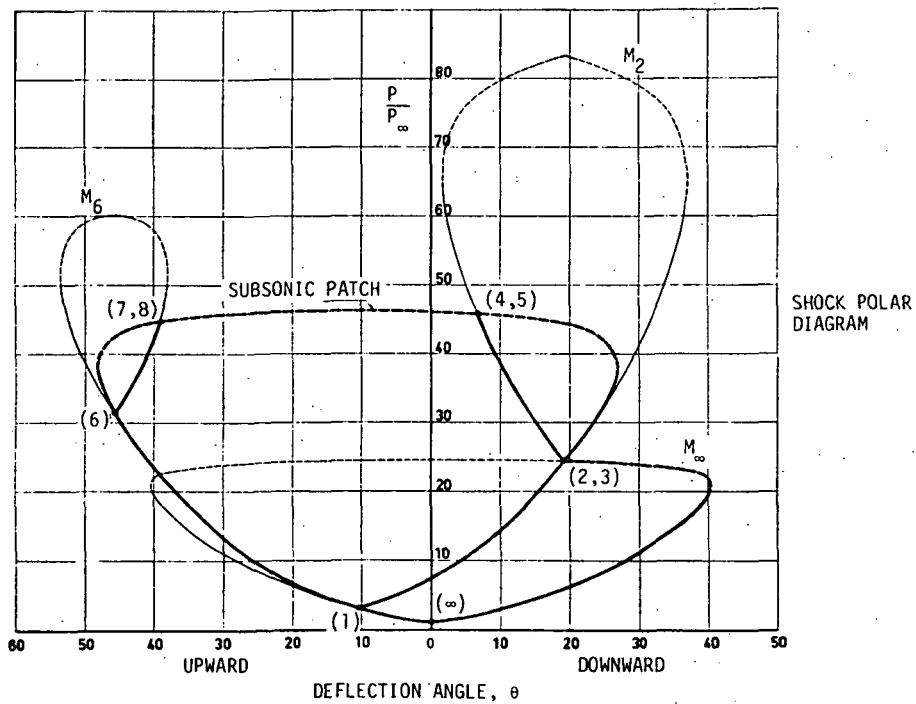
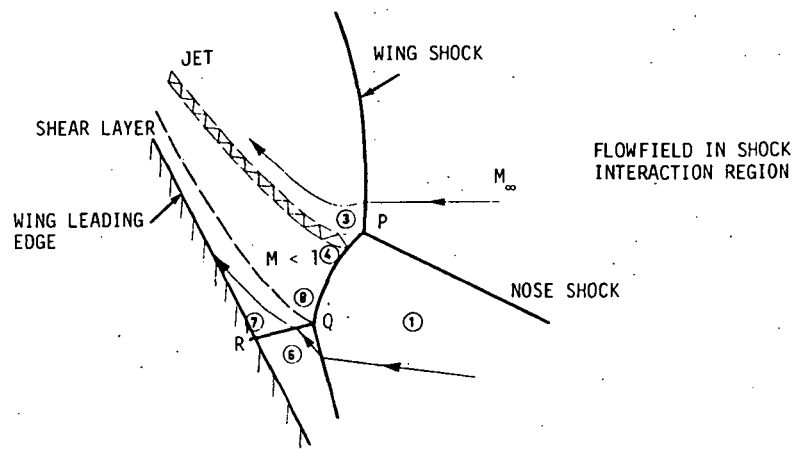
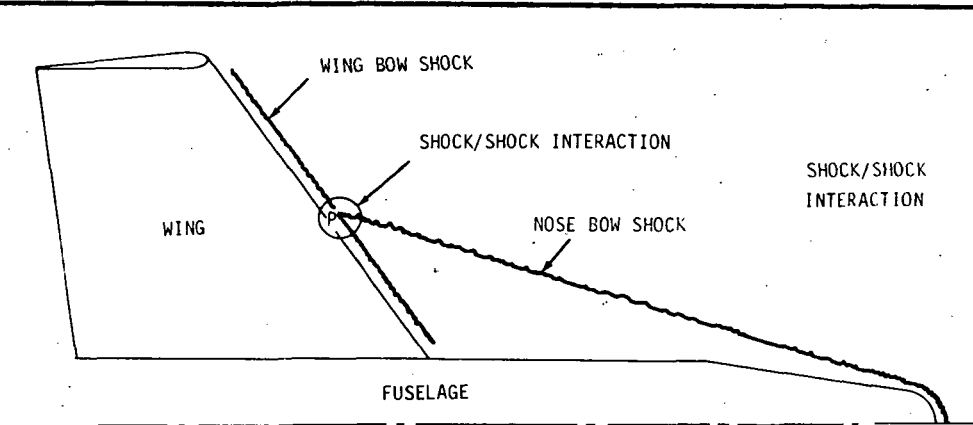


Figure 2-3. SHOCK/SHOCK INTERACTION ON WING WITH INTERMEDIATE SWEEP ANGLE

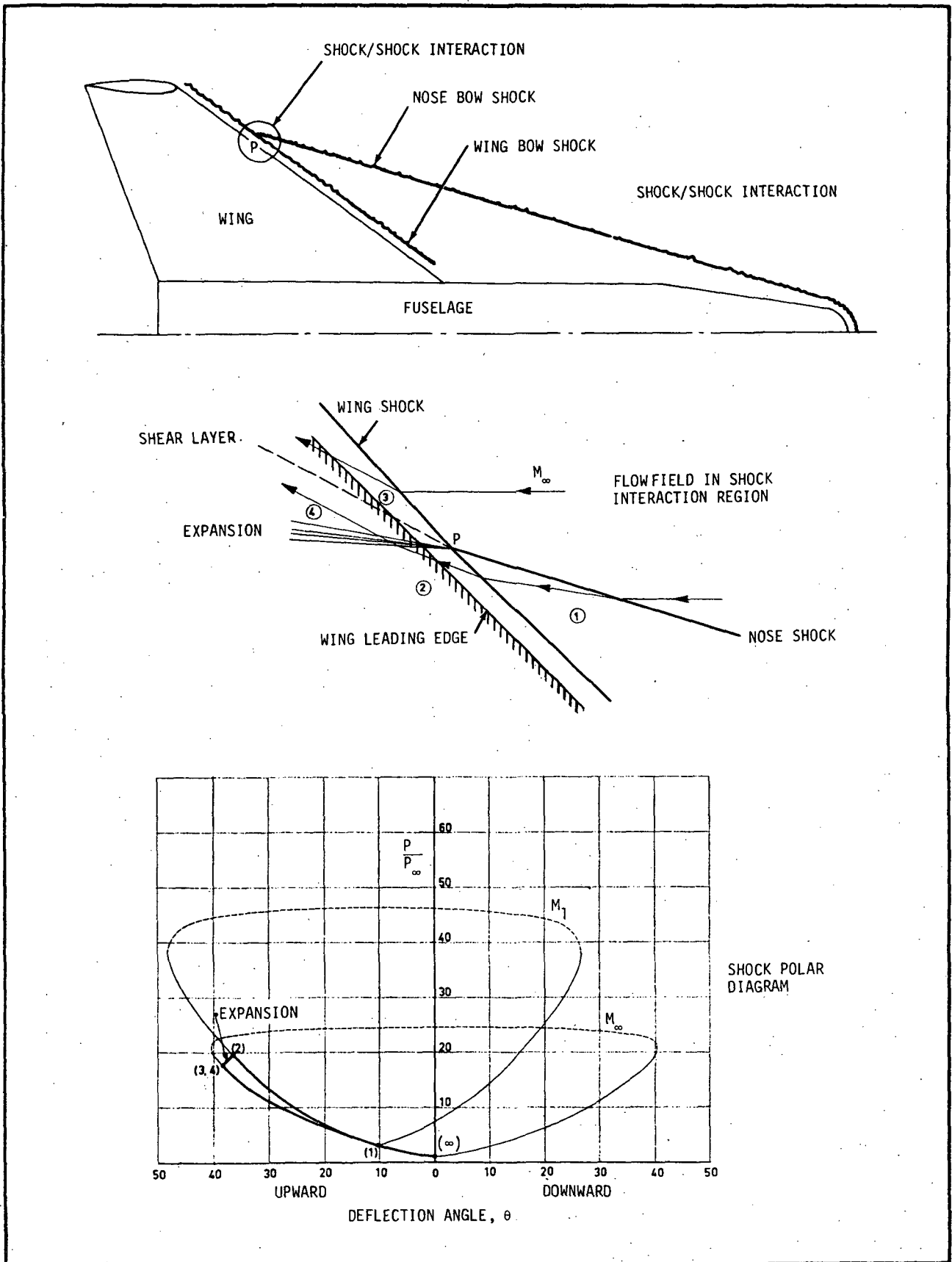


Figure 2-4. SHOCK/SHOCK INTERACTION ON HIGHLY SWEEP WING

mechanisms which act on the wing surface and cause high heating rates:

- Supersonic jet impingement on wing surface (for straight wing or wing with low sweep angle - Figure 2-2)
- Shock impingement on wing boundary layer (for intermediate sweep angle - Figure 2-3).
- No jet or shock impingement - high heating rate due to change of flow-field (for high sweep angle - Figure 2-4).

The three heating mechanisms listed above create completely different heating rates on the wing leading edges. For the cases of wings with high or intermediate sweep angles, analytical methods have been developed to predict the interference heating rates. Results were compared with existing test data with good agreement. For the case of straight wing or wings with a small sweep angle, the complex flowfield makes it more difficult to develop an analytical prediction method. Details of each of the heating prediction methods are discussed below.

2.1.1 Wings With High Sweep Angle

The flowfield in the shock interference region can be solved by using a shock polar diagram as shown in Figure 2-4 which indicates that the interaction between the wing shock and the nose shock does not result in jet or shock impingement on the wing surface. Consequently, the swept cylinder heating methods developed by Beckwith and Gallagher (ref. 2) can be used to calculate the heating rates on the wing leading edges. It should be noted that the flow conditions after the nose shock (condition (1) in Figure 2-4) should be used as free-stream conditions for the swept-cylinder heating calculation.

Although 16 references dealing with wing leading edge interference heating have been compiled, only four provide useful test data on highly swept wings (refs. 8, 9, 10, and 16). These data were compared with the predicted values. Figure 2-5 shows a typical comparison which indicates that the predicted values match fairly well with the test data.

It should be noted that two-dimensional wedges were used as shock generators in all the collected references as shown in Figure 2-5.

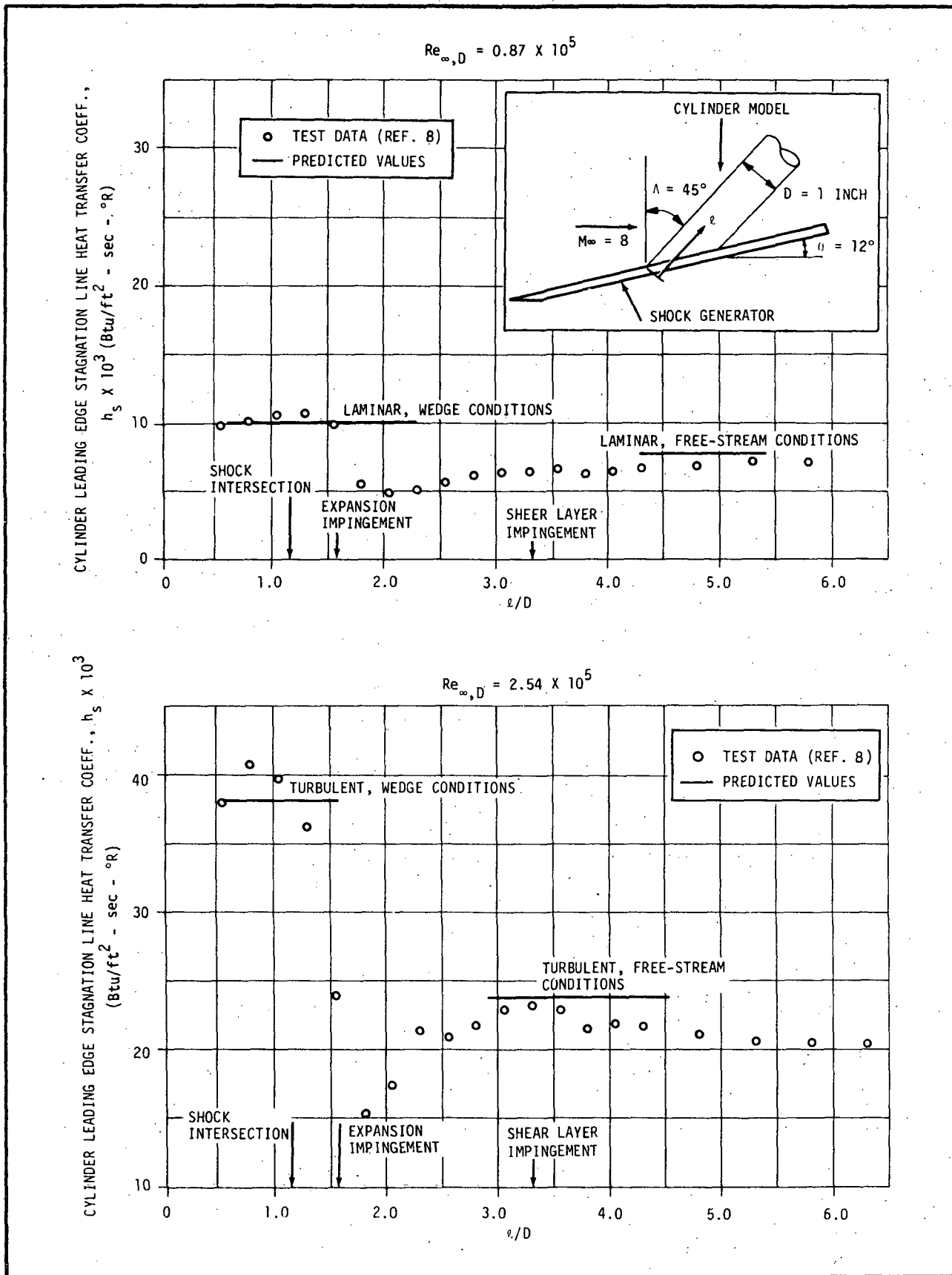


Figure 2-5. SHOCK INTERFERENCE HEATING DATA ON HIGHLY SWEEPED CYLINDER

2.1.2 Wings With Intermediate Sweep Angle

As shown in Figure 2-3, the shock/shock interaction on wing with intermediate sweep angle results in a shock wave (QR) impinging on the wing leading edge and interacting with the wing boundary layer. The magnitude of heating rates due to shock/boundary-layer interaction depends on the impinging shock strength and the state of the boundary layer. Shock impingement may cause boundary layer separation. Transition may also occur if the boundary layer was originally laminar. Both transition and separation can cause high heating rates.

It is realized that an analytical approach to predict shock/boundary-layer interaction heating is very limited due to the complexity of the problem. However, based on the test results for both laminar and turbulent flows, empirical equations have been derived by Sayano (ref. 3), Sayano and Bausch (ref. 4), Levin and Fabish (ref. 25), Neumann (ref. 6), and Gulbran, et al. (ref. 7) to correlate the peak heating rates with the pressure ratios across the impinging shock waves. The correlation equation in reference 4 was used in this study as shown in Figure 2-6. Thus the peak heat transfer coefficient can easily be calculated once the pressure ratio across the impinging shock (P_7/P_6) is obtained from the shock polar diagram as shown in Figure 2-3.

The predicted heating values were compared with existing test data with fairly good agreement. A typical comparison is shown in Figure 2-7 with test data from reference 16.

2.1.3 Straight Wing (or Wing with Small Sweep Angle)

Interference heating prediction on straight wings is more difficult due to both the complex flowfield and the poor and scarce test data available at the present time. It is realized that the thin supersonic jet creates very sharp heat transfer peak at the impingement point. This indicates that heat transfer measurements along the wing leading edges might have missed these peaks since in almost all the tests the thermocouple spacings were quite large. More reliable measurements are needed before any data correlation can be derived.

2.2 ANALYSIS OF GAP REGION

During the preliminary design of Space Shuttle launch configuration, it became apparent that the effects of shock impingement would be a primary

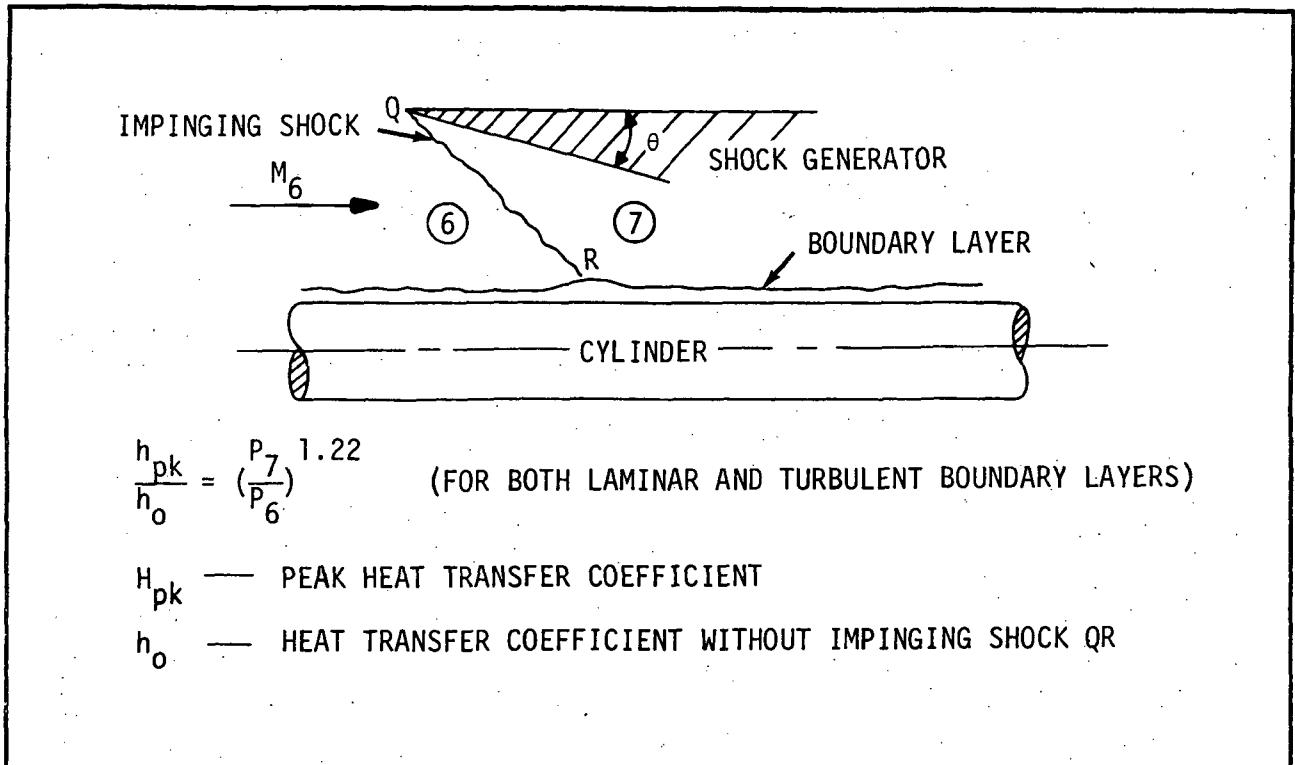


Figure 2-6. SHOCK/BOUNDARY-LAYER INTERACTION HEATING CORRELATION (Ref. 4)

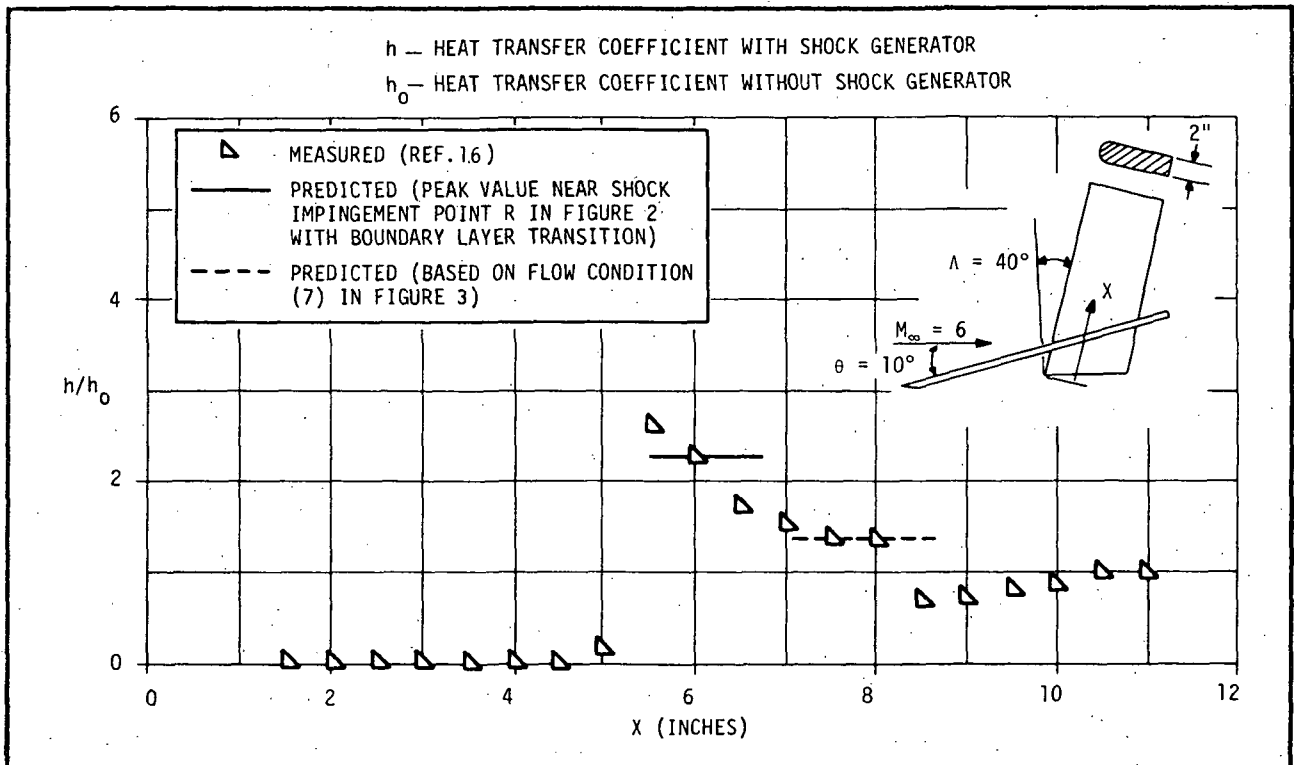


Figure 2-7. SHOCK INTERFERENCE HEATING DATA ON WING WITH INTERMEDIATE SWEEP ANGLE

consideration in the design of the thermal protection systems for both the orbiter and booster. It is a well known fact that high heating rates occur in the vicinity of the "point" where a shock wave impinges. The magnitude of the heating rates is closely related to the strength and impingement angle of the shock wave. The gap interference region between the orbiter and booster is further complicated by the reflection of the shocks between the two vehicles. This study described in reference 26 was initiated to determine the location and strength of the impinging shocks in the gap region in the mated ascent configuration.

An analytical solution of the gap flowfield was undertaken. Due to the extreme complexity of the shock interaction phenomena, the study was limited to the plane of symmetry which permitted a quasi-two-dimensional flow analysis. The governing equations of motion were formulated and subjected to various techniques in an attempt to analytically solve the flowfield. No successful solution was obtained, but the governing equations were developed which are thought suitable for a method of characteristic solution.

An alternate approach based on the data was the concept of obtaining the shock strength and number of shock reflections from schlieren photographs. A computer program was developed and compared favorably to experimental data. Reference 26 is included in Appendix A-2 which describes the analytical formulation of the gap flowfield and a listing of the computer program to calculate the flowfield properties based on experimental input values.

2.3 INTERFERENCE AT FIN/PLATE CORNERS

Interference heating data for simple geometry fin-flat plate models (Figure 2-8) tested in wind tunnels were compiled (refs. 6, 7, 11 through 14, and 19 through 24) and analyzed in order to predict interference heating on the space shuttle booster fuselage due to the pressure of booster wings or canards. The swept shock wave generating from the wing or canard interacts with the fuselage boundary layer and causes boundary layer separation and/or transition which in turn causes high heating rates on the fuselage surface.

- M_∞ = FREE-STREAM MACH NUMBER
- R_N = FREE-STREAM REYNOLDS NUMBER
- α = FLAT PLATE ANGLE-OF-ATTACK
- D = FIN LEADING EDGE DIAMETER
($D = 0$ FOR WEDGE WITH SHARP L.E.)
- δ = FIN DEFLECTION ANGLE
- Λ = FIN SWEEP ANGLE
- ϕ = FIN CANT ANGLE
- t = BOUNDARY LAYER THICKNESS

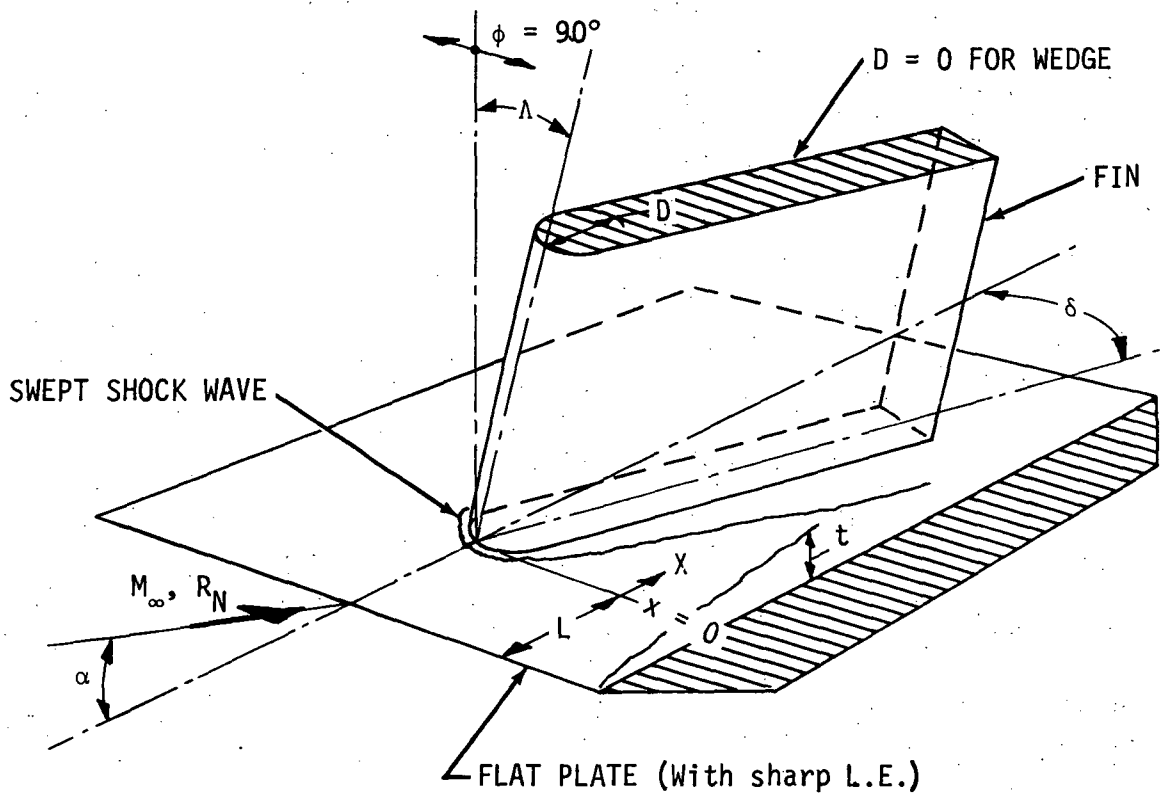


Figure 2-8. FIN-PLATE MODEL FOR INTERFERENCE HEATING TEST

The thermocouple measured heating data, presented as the ratio of interference heat transfer coefficients to the undisturbed values h_i/h_u , have been correlated with the following flow conditions and model configurations (Figure 2-8):

- Fin deflection angle, δ
- Fin sweep angle, Λ
- Flat plate angle-of-attack, α
- Fin leading edge diameter, D
- Fin cant angle, ϕ
- Free-stream Mach number, M_∞
- Free-stream Reynolds number, R_N
- Boundary layer state
- Fin location on flat plate, L
- Thermocouple location on flat plate, X
- Boundary layer thickness, t .

The correlations derived in this study are applicable to the booster fuselage interference heating prediction in the presence of wings and canards. Details of this study are given in Northrop Technical Report TR-794-921A which is included as Appendix A-3.

2.4 SHOCK INTERFERENCE HEATING TO SPACE SHUTTLE CONFIGURATIONS

Both the MDC and the GDC Phase B Space Shuttle Model test data were collected and analyzed in this study. All of the existing thermocouple and phase change paint data were used in the shock interference heating analysis.

2.4.1 MDC Phase B Booster Model Test

By using the phase change coating test data of reference 27, the shock interference effects were derived and presented as the ratios of the shock interference heat transfer coefficients to the undisturbed values, h_i/h_u . The shock interference heating involved in the shuttle flight is shown in Figure 2-9. The areas at the booster (B1) canard/fuselage juncture and between the booster (B1) and the orbiter (O1) fuselages were considered in this study. Detailed study results are given in Appendix A-4.

In this study, a portion of the movie films taken during the MDC Phase B shuttle heating tests (ref. 27) were borrowed from Martin Marietta Corporation

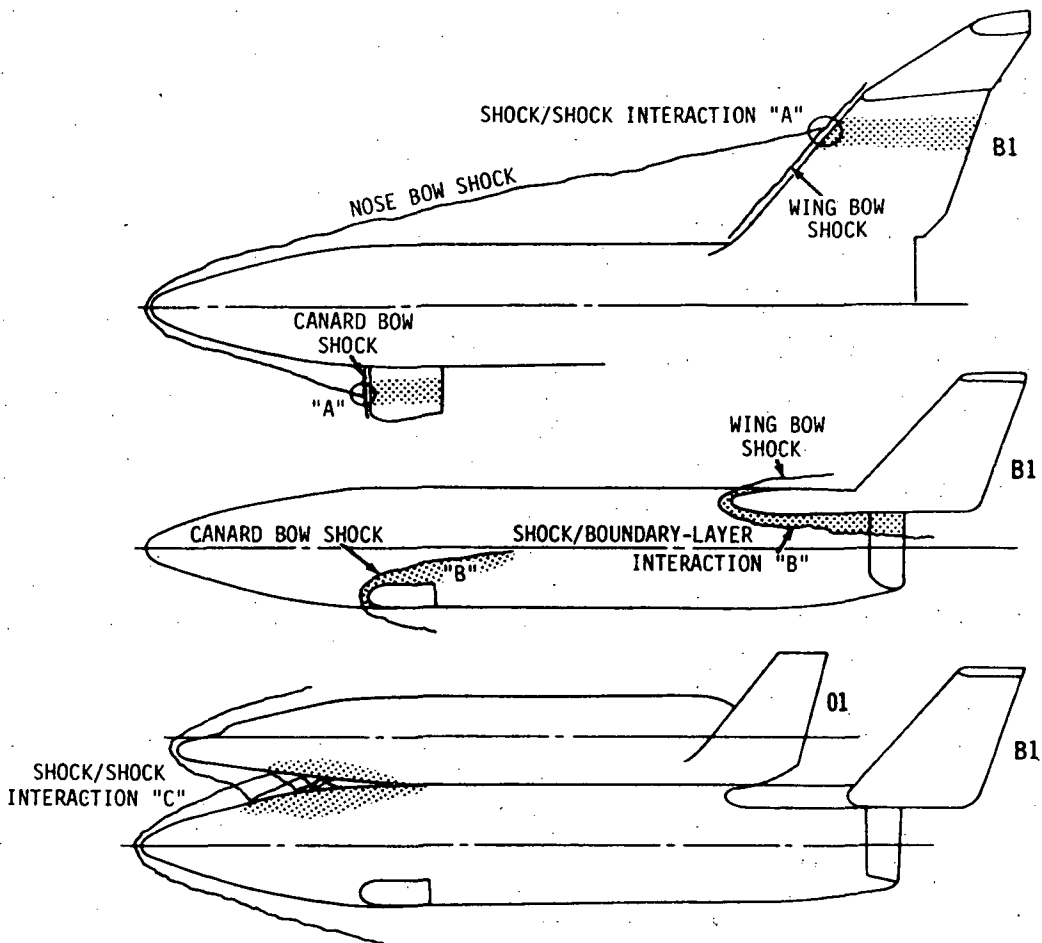


Figure 2-9. MDC SPACE SHUTTLE SHOCK INTERFERENCE

for further analysis. It is believed that a better estimate of peak interference heat values was obtained from this review.

As indicated in reference 27, for most of the runs, the eighth movie frame (time = 0.8 sec for the 10 frames/sec movie taken during the tests) was used by Martin Marietta to deduce the first isotherm (or constant $h/h_{r=1}$, line). Examination of the films shows that in most shock interference regions the paint phase change occurs before 0.8 sec. This indicates that some of the peak interference heating data which are available in the movie films were not deduced and not presented in reference 27.

In the present study, the $h/h_{r=1}$, versus time curves for typical runs were generated as shown in Figure 2-10 and peak heating values in the interference regions were deduced as shown in Figures 2-11 and 2-12 which indicate that the peak heating values are 3 to 4 times higher than the peak values reported in reference 27.

It should be noted that heating data accuracy decreases when phase change occurs too early in a test (i.e., when time is less than 0.4 sec). This is due to the disturbance created when the model is pushed into the wind tunnel and also due to the difficulty involved in determining the initial time (time = 0). It is suggested that paints with higher phase change temperature should be used in future paint tests in order to have better interference heating data. Also, all movie films taken during the paint tests should be reexamined in order to provide more realistic peak interference heating data.

MDC Phase B baseline (B1) booster interference heating during ascent and reentry flights has been analyzed qualitatively based on paint test data contained in reference 27. Typically, the test conditions were as listed below.

- Free-stream Mach number, $M_\infty \approx 6$ and 8
- Free-stream Reynolds number, $R_N \approx 0.5 \times 10^6$, 1×10^6 and 5×10^6 /ft
- Booster angle-of-attack, $\alpha = -5, 0, 15, 30, 45$ and 60 degrees
- Booster model scale : 0.00325

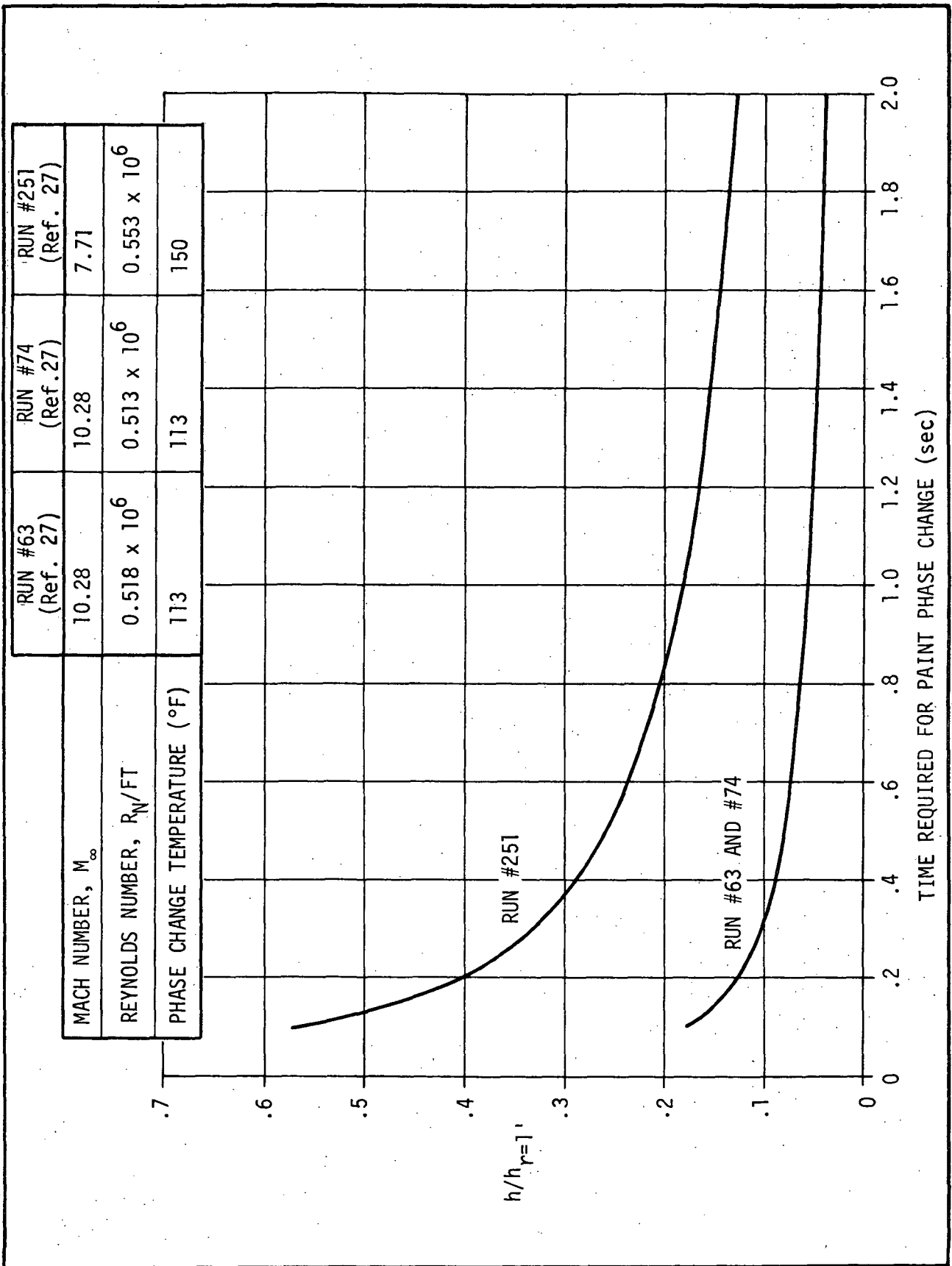


Figure 2-10. HEAT TRANSFER CURVES GENERATED BY SEMI-INFINITE SOLID METHOD

RUN NO. 74 (Ref. 27)

$\alpha = 0^\circ$

$M_\infty = 10.28$

$R_N = 513,000/\text{FT}$

○ FROM REFERENCE 27

△ FROM THIS STUDY

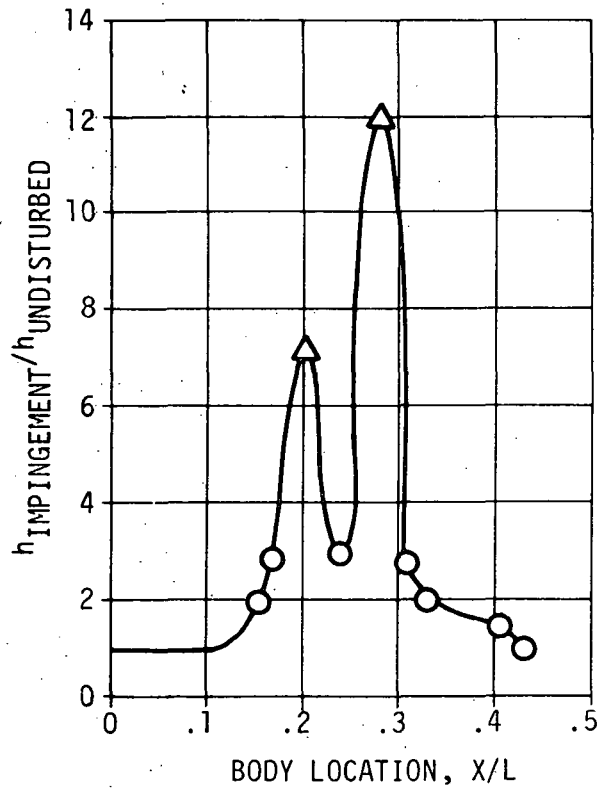


Figure 2-11. BOOSTER UPPER SURFACE CENTERLINE INTERFERENCE HEATING DUE TO THE PRESENCE OF ORBITER

RUN NO. 63 (Ref. 27)

$\alpha = 0^\circ$

$M_\infty = 10.28$

$R_N = 518,000/FT$

● FROM REFERENCE 27

▲ FROM THIS STUDY

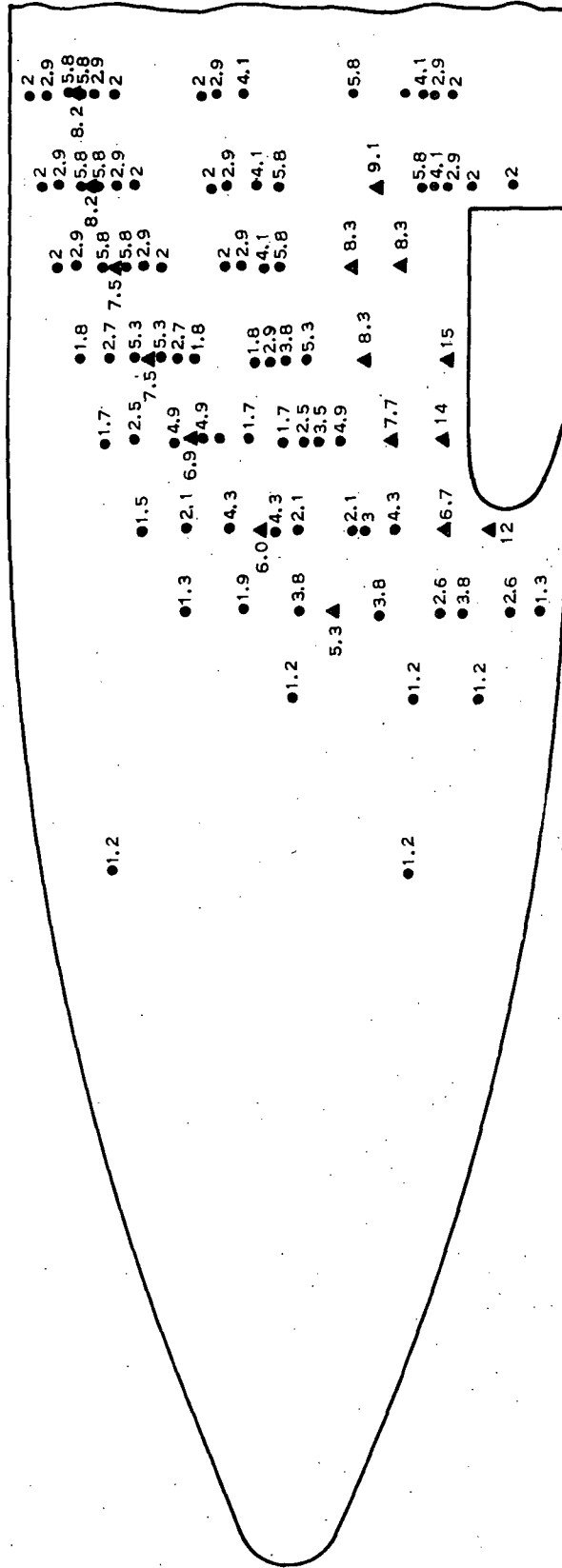


Figure 2-12. SHOCK INTERFERENCE HEATING NEAR BOOSTER CANARD/FUSELAGE JUNCTURE
($h_{IMPINGEMENT}/h_{UNDISTURBED}$)

As just discussed, the interference heating data in reference 27 can be analyzed only in a qualitative manner since peak interference heating data are not available at the present time. Study of both schlieren photographs, and the test data indicates that, depending on the angle-of-attack, the booster will experience interference heating in nine regions during ascent and reentry flights as shown in Figure 2-13:

- Area (A) - Fuselage heating due to canard shock
- Area (B) - Fuselage heating due to wing shock
- Area (C) - Wing heating due to canard or fuselage shock
- Area (D) - Wing tip heating due to fin shock
- Area (E) - Fin root heating due to wing shock
- Area (F) - Fin heating due to canard shock
- Area (G) - Fin outboard surface heating due to wing tip flow separation
- Area (H) - Canard heating due to fuselage nose shock
- Area (I) - Fuselage heating due to orbiter fuselage.

The results of this study can be used as a guideline to locate possible interference heating areas on the booster. Appendix A-5 addresses itself to the details of this study.

2.4.2 GDC Booster

Shock interference heating on the General Dynamics, Phase B, Delta Wing Booster has been analyzed and correlated with Mach number and angle-of-attack. This study is based on the thermocouple and paint test results contained in references 28 - 33 which cover a wide range of Mach number, Reynolds number, and angle-of-attack. Mated orbiter-booster models were used to study the interference heating on the booster fuselage due to orbiter-generated shock waves during ascent flight.

It should be noted that even though a large amount of heating data has been taken during the tests, the shock interference heating data available at the present time are somewhat limited. For the case of thermocouple measurements, the thermocouple spacings on the booster models were not close enough to measure the localized peak heating values. For the paint tests, the quality of the measurements was affected by the difficulty involved in photographing the paint phase change history at some booster surface areas. In other tests

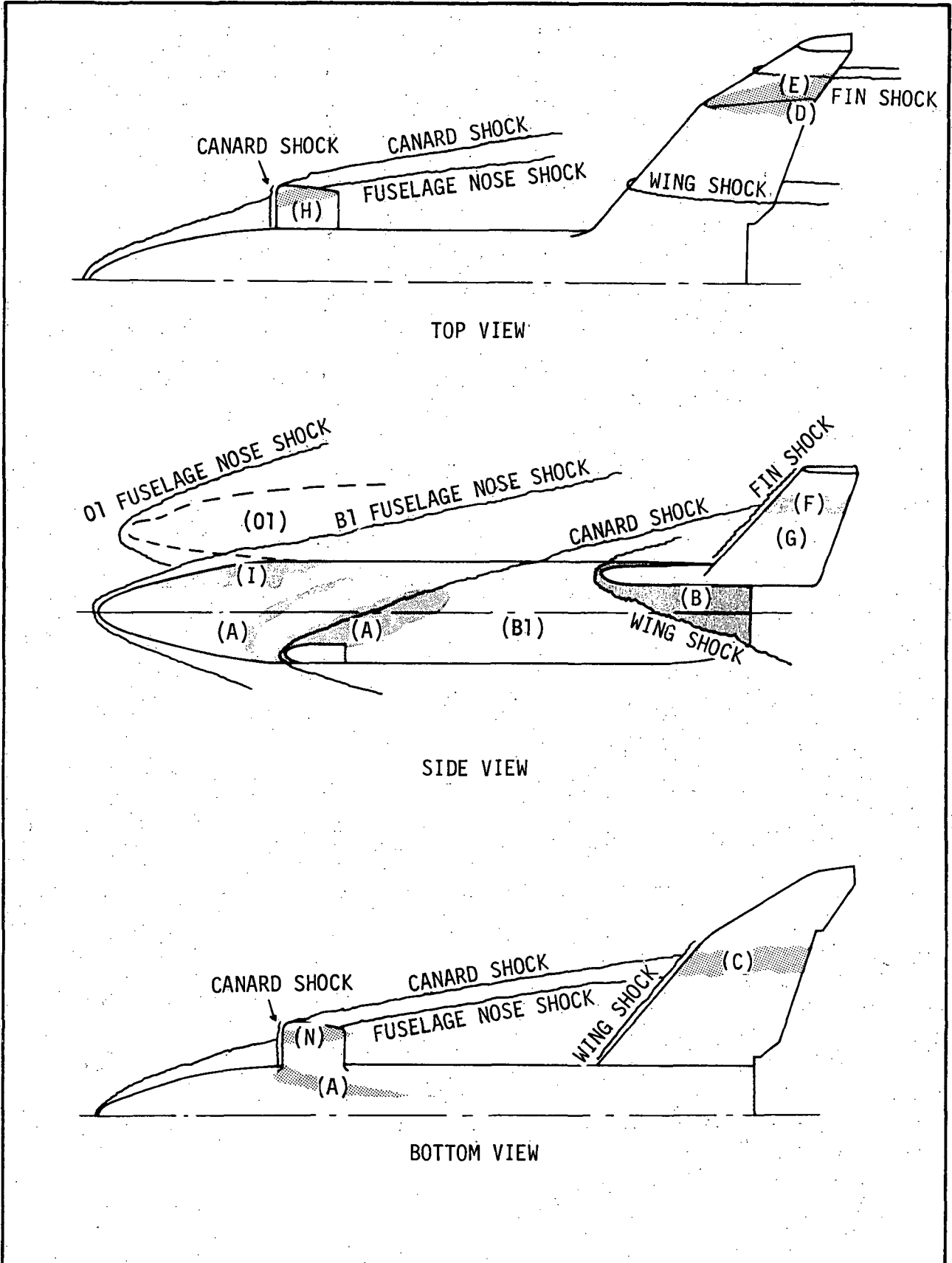


Figure 2-13 . OVERALL SHOCK WAVE INTERFERENCE DIAGRAM ON BOOSTER

the paints employed had extremely low phase change temperatures. As a consequence, some test data were lost since the movie films showed phase change on the very first frame. The preceding considerations deem it probable that some interference heating peaks were missed in both the paint and the thermocouple measurements.

In this study, the interference heating data are presented in the form of h_i/h_u , the ratio of interference heat transfer coefficient to the undisturbed value. The effects of Mach number and booster angle-of-attack on h_i/h_u were also analyzed and correlated. The Reynolds number effect could not be determined quantitatively due to the quality and limited amount of data. The different interference heating areas on the booster (during ascent and reentry flights) are shown in Figure 2-14 and study details are given in Appendix A-6.

It should be noted that improved correlations can be developed when more and better heating data become available.

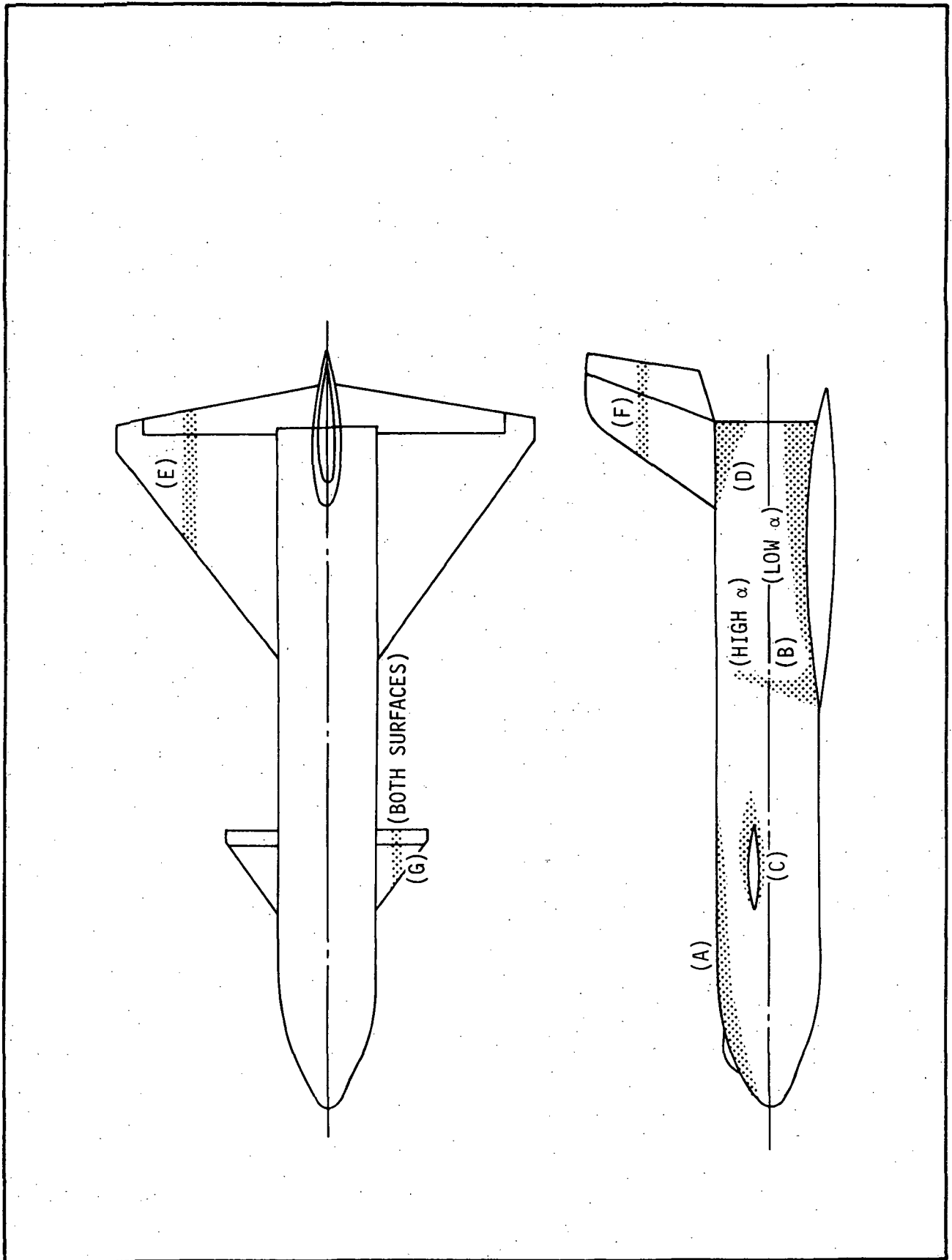


Figure 2-14. SHOCK INTERFERENCE HEATING AREAS ON GDC DELTA WING BOOSTER

Section III

SHUTTLE ASCENT AND SHOCK IMPINGEMENT AERODYNAMIC HEATING TESTS

At the conclusion of the literature survey described in Section II, an experimental program was planned to investigate interference heating to a mated configuration of the space shuttle vehicle. The plan was to compare and apply the data and correlations obtained from the literature survey in the analysis of the test data. But due to wind tunnel scheduling delays, the experimental program was delayed several times preventing either the inclusion or analysis of the test data in this report. At this time the data are being published in a SADSAC (System for Analysis of Static Aerothermodynamic Criteria) report and REMTECH, Inc. will perform an analysis of the data.

The test program was planned and conducted for ascent heating tests on a 0.0065 scale thin skin model of the MDAC 256-20 space shuttle booster mated with a Stycast model of the MDAC Internal Tank Orbiter. The booster model was provided by NASA/MSFC and Northrop purchased three orbiter models from Lockheed Missiles and Space Company/Huntsville Research and Engineering Center. Reference 34 reports on the test work and the report is included as Appendix B. The report includes a review of the test facility characteristics and test data reduction methods, the model design and fabrication procedures, the test plans, and on-site observations made during the testing.

The tests were performed in three facilities at NASA-Langley Research Center: the 20-inch M=6 tunnel, the 31-inch M=10 tunnel, and the 48-inch Unitary Plan Tunnel. Both thermocouple and phase change paint data were obtained in addition to schlieren photographs and some oil-flow results. The general performance of the models and the test programs were satisfactory and successful.

Section IV

DELTA WING LEEWARD SURFACE FLOWFIELD

Identification and interpretation of the significant flowfield characteristics of complex configurations such as the Space Shuttle are extremely difficult without quantitative knowledge of the phenomena. With adequate experimental data a realistic assessment of the phenomenon can be obtained which can result in either an empirical or analytical formulation of the problem. But unfortunately, there is a dearth of experimental data on the leeward surface flowfield properties inhibiting a quantitative description of the flowfield phenomena.

The need for experimental data on leeward surface flowfield properties, especially for conditions approximating hypersonic flight, was obvious and Northrop responded accordingly. An experimental program was originated to obtain hypersonic flowfield properties on the leeward surface of a blunt delta wing. This test program was completed at the von Karman Institute's piston-driven wind tunnel at nominal Mach numbers of 15 and 20 at Reynolds numbers per meter of 1.8×10^7 and 8.7×10^6 respectively.

The experimental program is thoroughly discussed in reference 35 and is included as Appendix C. The results of the investigation revealed the location and magnitude of the maximum pressure force and heat transfer rates. The effects of Mach number and angle-of-attack were assessed. The similarities and differences between sharp and blunt leading-edge delta wings were discussed. The most important result of this study was a qualified interpretation of the principal aspects of the lee-side flowfield. This description should prove invaluable by providing a basic understanding of the flowfield phenomena during the formulation of an analytical description of the flowfield.

Section V

EFFECTS OF ROUGHNESS ON COMPRESSIBLE FLOWS

Surface roughness on the Space Shuttle will probably result from the surface discontinuities which result from assembling and fabrication of the surface panels of the vehicles. Preliminary designs suggest that the Shuttle Orbiter will have a refurbishable ablative thermal protection system. The ability to predict inflight aerodynamic heating for minimizing the weight of the thermal protection system is dependent upon knowing the properties of the flowfield and the nature of the boundary layer. The boundary layer state, which may be laminar, transitional, or turbulent, depends on the flowfield properties but to a higher degree of sensitivity on the body surface condition.

No simple theory exists for predicting the effects of surface roughness on boundary layer transition and heat transfer. The Reynolds number at which transition occurs on a hydraulically smooth surface is already a controversial parameter without introducing the effects of roughness. The parameters affecting boundary layer transition on a rough surface are the shape, distribution, and height of the roughness as well as free-stream velocity, turbulence, and heat transfer. After transition the heat transfer rates are usually increased by increasing the height of the roughness. The complexity of these problems was such that they merited further study.

This study was subcontracted to Auburn University and Appendix D contains the final report (ref. 36). The effects of roughness on compressible flows was restricted to the case of two-dimensional roughness created by sinusoidal walls. A literature survey was compiled which revealed that little experimental data were available, especially at low supersonic Mach numbers. No practical correlation was available which was not excessively restrictive. In an attempt to develop a useful correlation, a version of a Spalding-Patankar boundary layer computer program was modified and applied to the problem. The results were compared to the data found in the literature survey which indicated that the Spalding-Patankar method was amendable for predicting the effects of roughness. These recommendations are outlined in Appendix D.

Section VI

BASE HEATING REVIEW

A review of previous base thermal environment prediction techniques is being prepared for MSFC to serve as background information for future predictions on the Space Shuttle. Because of past experience of REMTECH personnel with the Saturn S-II thermal environment prediction, a request was made to summarize the S-II prediction experience as a part of the space shuttle thermal environment studies. Appendix E presents the results of this review (ref. 37) in a format which was requested to facilitate inclusion of the work in the overall review document.

The S-II review was prepared by reviewing and summarizing the S-II configuration and engine characteristics and the base prediction methods. The model and flight tests were studied and summarized, and the predicted environment and flight data were evaluated in an attempt to present a comparison of the results which could be used in evaluating the effectiveness of the prediction techniques. Additional work under this contract in support of aerodynamic heating experiments is reported in REMTECH Report RTR 003-1.

Section VII

MODIFICATIONS TO THE NASA/LEWIS COMPRESSIBLE LAMINAR AND TURBULENT BOUNDARY LAYER COMPUTER PROGRAM

This computer program was originated by the NASA/Lewis Research Center to study some real boundary-layer effects under known conditions of pressure gradient in the prediction of turbomachinery performance. The program designated BLAYER is capable of analyzing two-dimensional laminar and turbulent boundary layers with arbitrary pressure gradients. Laminar separation and reattachment and boundary layer transition can be predicted. These boundary layer characteristics are typical of many aerodynamic problems and Northrop placed the program into operation with the intentions of applying it to Space Shuttle vehicles. As the debugging process progressed, it was necessary to make several modifications and changes as found in reference 38 which is conveniently included in Appendix F. Some of the modifications were the result of extending the program to be applicable to high supersonic or hypersonic flows. Two of the most important changes were the boundary layer transition criteria and the addition of an axisymmetric option. The application of the axisymmetric version for use in conjunction with the methodology for axisymmetric analogy to three-dimensional flow was the primary motive for modifying the program. The program was tested on several configurations; NACA airfoil, cooled flat plate, cone-cylinder-flare body, and a cone. The results were compared to experimental data and the comparisons were favorable, but it was concluded that the program must be exhaustively tested over all Mach number ranges before the applicability of the program can be established. A list of recommended check-out procedures to further assess the capability of the BLAYER program is found in Appendix F.

Section VIII

CONCLUSIONS AND RECOMMENDATIONS

The primary objective in performing this study was to collect and analyze aerodynamic heating data applicable to the space shuttle launch configuration. In particular, the location and severity of shock impingement areas. This objective has been accomplished quite successfully by obtaining experimental data from a literature survey and from an experimental test program. In addition, several phenomenological aspects associated with the flight of the shuttle were investigated. Included in these aspects were the effect of surface roughness with regard to the operational environment of the shuttle, the leeward surface flowfield of a vehicle in simulated reentry flow, the application of existing computer programs to analyze shuttle environments, and the compilation of a section of a base heating handbook to be used in design studies. Based on the combined results of the entire contract work, the following conclusions were made:

- The effects of shock impingement may result in heat transfer increases of 10-40 times the undisturbed values.
- Available experimental data on shock impingement effects do not exactly simulate proposed shuttle flight conditions.
- No analytical technique is presently available that can accurately predict the effects of shock impingement to shuttle-type vehicles.
- No scaling techniques are available to apply existing experimental data to full-scale configurations.
- The ascent heating tests conducted at Langley Research Center were satisfactory and successful.
- The leeward surface flowfield for blunt delta wings was not conical for Mach numbers of 15 and 20 for angles-of-attack of 20 degrees and less.
- The lee-side peak heating rate occurred off the centerline and on the aft section of the model for a given angle-of-attack.
- Both the local pressure and Stanton numbers were larger for the blunt delta wing than for the sharp leading-edge counterpart on the Leeward surface.
- Flat plate heat transfer prediction methods were not suitable for predicting leeward surface properties.
- A modified Spalding-Patankar boundary layer method can be applied to studying the compressible flow over a sinusoidal wall.

- The modified version of the computer program BLAYER can successfully compute laminar and turbulent boundary layers on two-dimensional and axisymmetric bodies.
- The phase-change paint technique to obtain heat transfer results requires further study to establish a standardized, well-defined procedure.
- More thermocouple instrumentation was required in the interference region to accurately locate the peak heating rates.
- The method of model installation in the test program for the mated configuration needs to be improved for both convenience and alignment accuracy.
- More information is required in the gap region of the shuttle mated configuration to merit improved or different flow visualization techniques than used in the present test program.
- More shock interference data are required before either an analytical or an empirical formulation of the effects of shock impingement can be successful.

Recommendations for future studies based on the results of the present investigations are as follows:

- Plan a model test program and perform test plan duties for conducting wind tunnel tests to establish criteria for shock impingement scaling factors.
- Review the phase-change paint technique and plan an experimental program to ascertain the accuracy of the method. This task should also include a material property study of the model material.
- Plan and execute an experimental program to determine the effects of wall roughness on boundary layer transition and compressible flow parameters.
- Obtain experimental data in the gap region of a mated configuration as a function of Mach number, Reynolds number, angle-of-attack, and geometry for laminar and turbulent boundary layers.
- Perform further leeward surface experimental studies to determine geometry effects, boundary layer transition criteria, Mach number and Reynolds number effects, and establish a prediction technique for the thermal environment.

Section IX

REFERENCES

1. Edney, B., "Anomalous Heat Transfer and Pressure Distributions on Blunt Bodies at Hypersonic Speeds in the Presence of an Impinging Shock", The Aeronautical Research Institute of Sweden, Report No. 115, February 1968.
2. Bechwith, I. E. and Gallagher, J. J., "Local Heat Transfer and Recovery Temperatures on a Yawed Cylinder at a Mach Number of 4.15 and High Reynolds Numbers", NASA TR R-104, 1961.
3. Sayano, S., "Heat Transfer in Shock Wave-Turbulent Boundary Layer Interaction Regions", Douglas Report SM-42567, November 1962.
4. Sayano, S. and Bausch, H. P., "Aerodynamic Heating Due to Shock Impingement on a Cylinder", Douglas Report SM-41420, August 1962.
5. Sayano, S., Bausch, H. P., and Donnelly, R. J., "Aerodynamic Heating Due to Shock Impingement on a Flat Plate", Douglas Report SM-41331, August 1962.
6. Neumann, R. D., "The Influence of Shock Wave-Boundary Layer Effects on the Design of Reusable Space Transportation Systems", Collection of papers presented at the Space Shuttle Symposium held at Smithsonian Museum of Natural History, Washington, D. C., October 16-17, 1969, p. 539.
7. Gulbran, C. E., Redeker, E., Miller, D. S., and Strack, S. L., "Heating in Regions of Interfering Flow Fields", The Boeing Company, Technical Report AFFDL-TR-65-49, Part I - July 28, 1965, Part II - January 1967, Part III - March 1967.
8. Bushnell, D. M., "Interference Heating on a Swept Cylinder in Region of Intersection with a Wedge at Mach Number 8", NASA TN D-3094, December 1965.
9. Hiers, R. S., and Loubsky, W. J., "Effects of Shock-Wave Impingement on the Heat Transfer on a Cylindrical Leading Edge", NASA TN D-3859, February 1967.
10. Beckwith, I. E., "Experimental Investigation of Heat Transfer and Pressures on a Swept Cylinder in the Vicinity of its Intersection with a Wedge and Flat Plate at Mach Number 4.15 and High Reynolds Numbers", NASA TN D-2020, July 1964.
11. Price, E. A., Howard, P. W., and Stallings, R. L., "Heat-Transfer Measurements on a Flat Plate and Attached Fins at Mach Numbers of 3.51 and 4.44", NASA TN D-2340, June 1964.
12. Jones, R. A., "Heat-Transfer and Pressure Investigation of a Fin-Plate Interference Model at a Mach Number of 6", NASA TN D-2028, July 1964.
13. Newlander, R. A., "Effect of Shock Impingement on the Distribution of Heat-Transfer Coefficients on a Right Circular Cylinder at Mach Numbers of 2.65, 3.51, and 4.44", NASA TN D-642, January 1961.

14. Burbank, P. B., Newlander, R. A., and Collins, I. K., "Heat-Transfer and Pressure Measurements on a Flat-Plate Surface and Heat-Transfer Measurements on Attached Protuberances in a Supersonic Turbulent Boundary Layer at Mach Numbers of 2.65, 3.51, and 4.44", NASA TN D-1372, December 1962.
15. Bushnell, D. M., "Effects of Shock Impingement and Other Factors on Leading-Edge Heat Transfer", NASA TN D-4543, April 1968.
16. Ray, A. D. and Palko, R. L., "An Investigation of the Effects of Shock Impingement on a Blunt Leading Edge", AEDC-TR-65-153, July 1965.
17. Siler, L. G. and Deskins, H. E., "Effect of Shock Impingement on the Heat Transfer and Pressure Distributions on a Cylindrical Leading Edge Model at Mach Number 19", AEDC-TDR-64-228, November 1964.
18. Knox, E. C., "Measurements of Shock-Impingement Effects on the Heat-Transfer and Pressure Distributions on a Hemicylinder Model at Mach Number 19", AEDC-TR-65-245, November 1965.
19. Stainback, P. C. and Weinstein, L. M., "Aerodynamic Heating in the Vicinity of Corners at Hypersonic Speeds", NASA TN D-4130, November 1967.
20. Caldwell, A. L., Haugseth, E. G., and Miller, D. S., "The Influence of Aerodynamic Interference Heating on Directional Stability Problems of Hypersonic Vehicles", IAS Paper No. 63-6, January 1963.
21. Miller, D. S., Hijman, R., Redeker, E., Janssen, W. C., and Mullen, C. R., "A Study of Shock Impingements on Boundary Layers at Mach 16", Proceedings of the 1962 Heat Transfer and Fluid Mechanics Institute, June 13-15, 1962.
22. Stainback, P. C., "An Experimental Investigation at a Mach Number of 4.95 of Flow in the Vicinity of a 90° Interior Corner Aligned with the Free-Stream Velocity", NASA TN D-184, February 1960.
23. Stainback, P. C., "Heat-Transfer Measurements at a Mach Number of 8 in the Vicinity of a 90° Interior Corner Aligned with the Free-Stream Velocity", NASA TN D-2417, August 1964.
24. Wisniewski, R. J., "Turbulent Heat-Transfer Coefficients in the Vicinity of Surface Protuberances", NASA Memo 10-1-58E, October 1958.
25. Levin, V. and Fabish, T. J., "Thermal Effects of a Shock Wave-Turbulent Boundary Layer Interaction at Mach Numbers of 3 and 5", North American Aviation Report No. NA 624-795, November 12, 1962.
26. Williams, J. C., III, "Analysis of the Shock-Impingement And Flow Between The Space Shuttle Orbiter and Booster", Consultant, North Carolina State University, June 1971.
27. Click, P. L. and Schmitt, D. A., "Wind Tunnel Test Results from the Thermal Mapping Investigation of 0.325% Scale MDC/MMC Phase B Space Shuttle Vehicles in the NASA/LRC Mach 8 Variable Density Tunnel and the NASA/LRC 31 Inch Continuous Flow Hypersonic Tunnel", Martin Marietta Design Note No. MMC-I-AERO-5002, October 1970.

28. Brevig, O., Otwell, R. L., and Day, R. C., "Aerodynamic Heat Transfer Distribution on Phase B Space Shuttle Booster Vehicles At Angles of Attack from -5° to 60° ", General Dynamics Convair Aerospace Division, Technical Report 76-549-4-083, 584-TP-342, March 1971.
29. Roberge, A. M. and Gordon, C. C., "Heat Transfer Results on Space Shuttle Phase B Launch Configurations at Mach Numbers of 2.5 and 3.7", General Dynamics, Convair Aerospace Division, Technical Report 76-549-4-128, 584-TP-400, April 1971.
30. Doughty, R. O., Brock, O. R., and Erickson, R. C., "Reentry Heat Transfer to a Delta-Wing Space Shuttle Booster at High Angles of Attack", General Dynamics, Convair Aerospace Division, Technical Report FZA-452, March 1971. (Also SADSAC/Space Shuttle Wind Tunnel Test Data Report DMS-DR-1070, March 1971).
31. Ginsky, W. R., "Space Shuttle Mated Booster/Orbiter Model Heat Transfer Test Results Data Report", General Dynamics, Convair Aerospace Division, Preliminary Report 584-TP-281, October 1970.
32. Ginsky, W. R., "Space Shuttle Booster Heat Transfer Model Test Results Data Report", General Dynamics, Convair Aerospace Division, Report 584-TP-270, September 1970.
33. Ginsky, W. R., "Space Shuttle Booster Heat Transfer Model Test Results Data Report", General Dynamics, Convair Aerospace Division, Report 584-TP-265, September 1970.
34. Reardon, J. E. and McKay, G. B., "Space Shuttle Ascent Aerodynamic Heating Tests", REMTECH, Inc., RTR 003-1, December 1971.
35. Lanning, W. D., "Leeward Surface Flowfield on a Blunt Delta Wing in a Simulated Reentry Flow", Northrop Services, Inc., TR-221-993, July 1971.
36. Pell, K. M. and Singh, D., "Effects of Roughness on Compressible Flows", Auburn University, Contract 714-41060, June 1971.
37. Reardon, J. E., "Saturn S-II Base Environment Review", REMTECH, Inc., RTR 003-2, December 1971.
38. Youngblood, W. W., "A Summary of the NASA/Lewis Compressible Laminar and Turbulent Boundary Layer Computer Program (BLAYER) and Northrop-Huntsville Modifications", Northrop-Huntsville, M-794-976, July 1971.

Appendix A

SHOCK INTERFERENCE

Appendix A-1

**SUMMARY OF
LEADING-EDGE SHOCK
INTERFERENCE HEATING
TEST DATA**

INTERFERENCE HEATING ON A SWEPT CYLINDER IN REGION OF
INTERSECTION WITH A WEDGE AT MACH NUMBER 8

By Dennis M. Bushnell

SYMBOLS

D	= cylinder diameter
h	= heat transfer coefficient
h_s	= cylinder stagnation line heat transfer coefficient
L	= distance from front of wedge to cylinder-wedge intersection
l	= distance along cylinder stagnation line from tip
M_∞	= free stream Mach number
M_ω	= wedge flow Mach number
$R_{\infty,D}$	= Reynolds number based on free stream flow and cylinder diameter
$R_{\omega,D}$	= Reynolds number based on wedge flow and cylinder diameter
T_e	= local temperature external to boundary layer
T_o	= tunnel stagnation temperature
T_{wall}	= cylinder wall temperature
ϕ	= angular distance around cylinder in chordwise plane measured from stagnation line
Λ_∞	= sweep angle based on free stream flow
Λ_ω	= sweep angle based on wedge flow

SUMMARY

Local heat-transfer rates and pressures have been measured on a cylinder in the interference flow region between the cylinder and a 12° half-angle wedge. The tests were conducted at a Mach number of 8 with the cylinder at sweep angles of 45° and 60° with respect to the free stream. Tests were also made with the base of the cylinder attached to and then separated from the wedge in order to investigate possible flow-separation effects in the intersection region and to investigate the shock impingement phenomena separately. Test configurations are shown in Figures A-1 and A-2 and results are summarized as follows:

- Figures A-3 through A-7 summarize the effect of shock interaction on cylinder stagnation line heat transfer with different Reynolds numbers.
- For both sweep angles, local heating is increased along the portion of the cylinder subjected to the wedge flow, but the maximum increase can be predicted for both laminar and turbulent boundary-layer flow by using local wedge flow conditions in the infinite swept-cylinder theories of NASA TR R-104.
- Under the test conditions, no local increases in heating were measured in the region of the wedge shock impingement for either laminar or turbulent stagnation-line boundary-layer flow.
- As indicated in Figures A-3, A-4, and A-5, the shock originating from the wedge could increase the cylinder stagnation line heat transfer rate by a factor of 2 at the location of x/D between 1 and 2.
- When the cylinder and the wedge were separated, the separation distance was 0.63 inch which was larger than the local wedge boundary-layer velocity thickness. Therefore the wedge boundary should not affect the flow over the cylinder.
- The extent of the flow separation in the cylinder-wedge juncture was small for the test conditions, and therefore, in the region of the measuring stations, there was no appreciable difference between the data for the cylinder attached and cylinder separated (Figures A-3 and A-5).
- Comparison of the heat transfer data with theory indicates that the boundary-layer flow changed from laminar to fully turbulent over the Reynolds number range used in the test ($R_{\infty, D} = 0.77 \times 10^5 - 8.7 \times 10^5$), (Figures A-8 through A-11).
- The chordwise heat transfer coefficient data are summarized in Figures A-12 through A-14.
- Comparison of the chordwise heat transfer data with infinite swept-cylinder theory indicates that the theoretical turbulent distribution underpredicts the data by 20 percent around the cylinder with 60° sweep angle (Figure A-14).

COMPARISON WITH MSFC SHUTTLE REENTRY STUDY

	<u>BUSHNELL (REF. 5)</u>	<u>MSFC BOOSTER WING</u> (ANGLE OF ATTACK = 12.5°)
M_∞	8	3-6
Shock Strength (Pressure Ratio Across Shock)	6.66	1.72 - 2.46
Cylinder Diameter, D (ft)	1/12	1*
$R_{\infty, D}$	$0.77 \times 10^5 - 8.7 \times 10^5$	$1 \times 10^5 - 14 \times 10^5$
Λ_∞ (Degrees)	45, 60	52
Max. $\frac{h_s \text{ (cylinder and wedge)}}{h_s \text{ (cylinder only)}}$	2	

* Assumed wing leading edge diameter

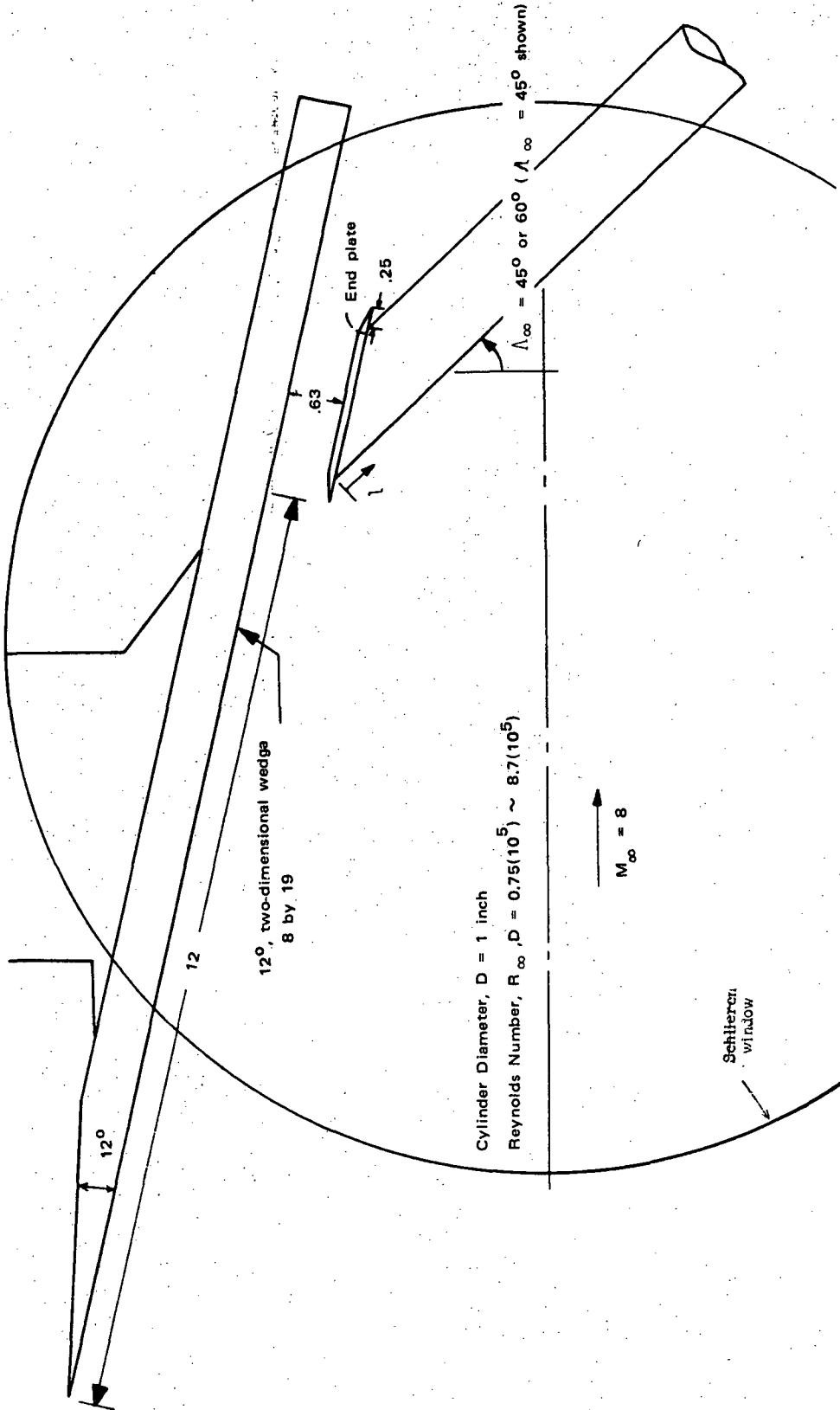


Figure A-1. TEST CONFIGURATIONS - CYLINDER AND WEDGE SEPARATED. (ALL LENGTHS HAVE BEEN NONDIMENSIONALIZED WITH RESPECT TO CYLINDER DIAMETER D.)

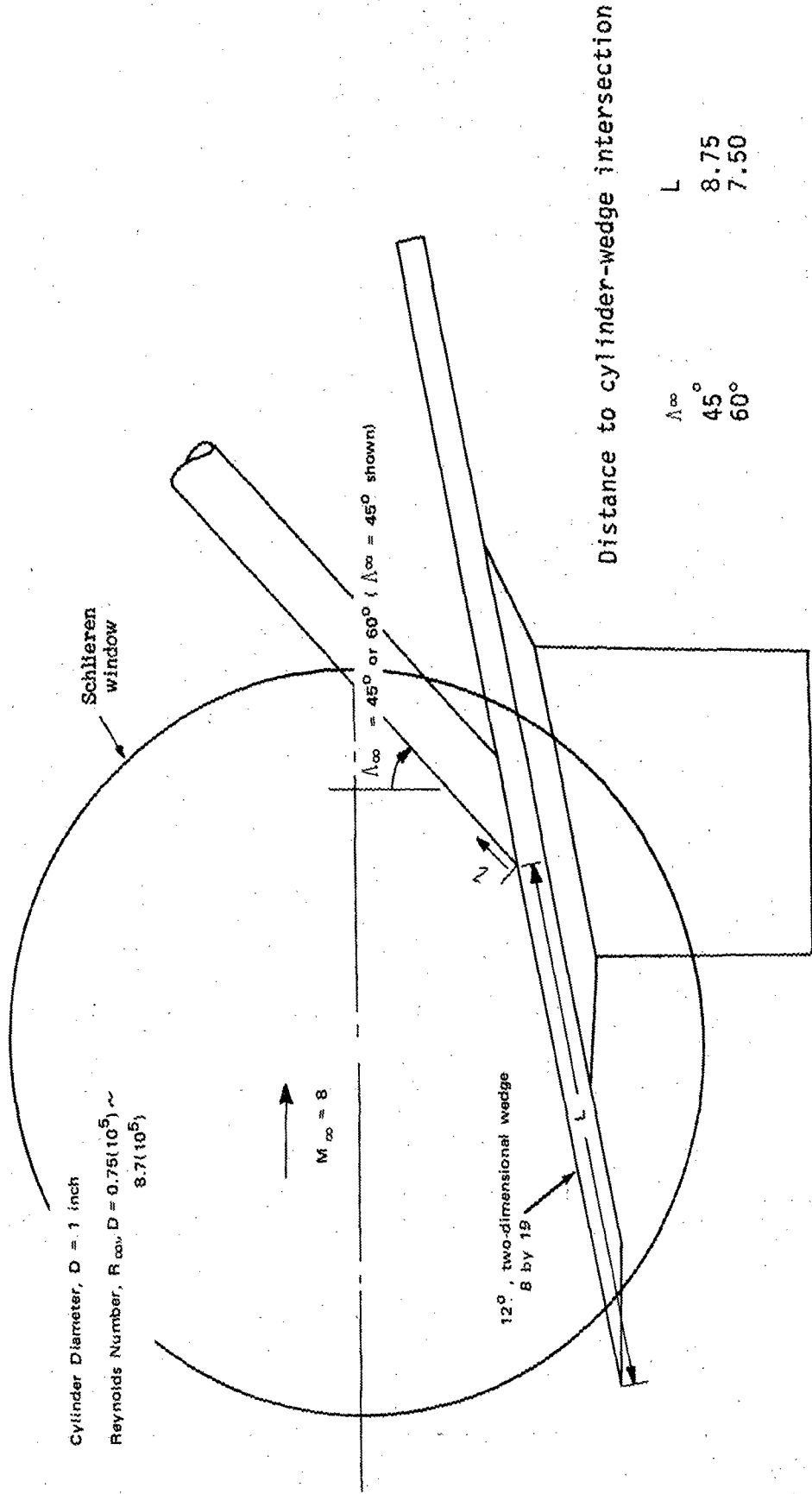


Figure A-2. TEST CONFIGURATION - CYLINDER AND WEDGE ATTACHED (ALL LENGTHS HAVE BEEN NONDIMENSIONALIZED WITH RESPECT TO CYLINDER DIAMETER D.)

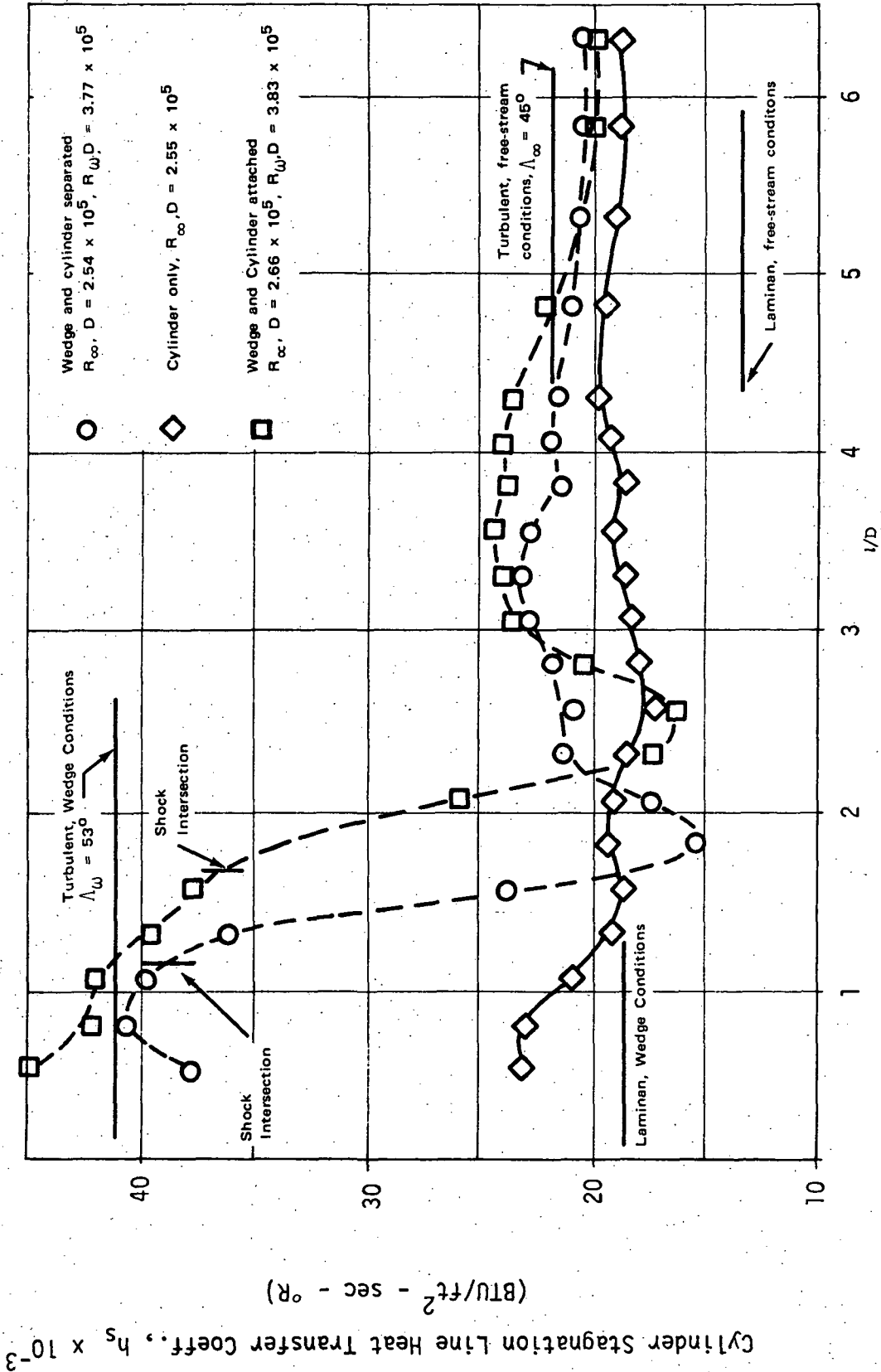


Figure A-3. HEAT-TRANSFER COEFFICIENT DISTRIBUTION ALONG CYLINDER STAGNATION LINE WITH REYNOLDS NUMBER OF ABOUT 2.6×10^5 . $\Lambda_\infty = 45^\circ$ and $\Lambda_w = 53^\circ$

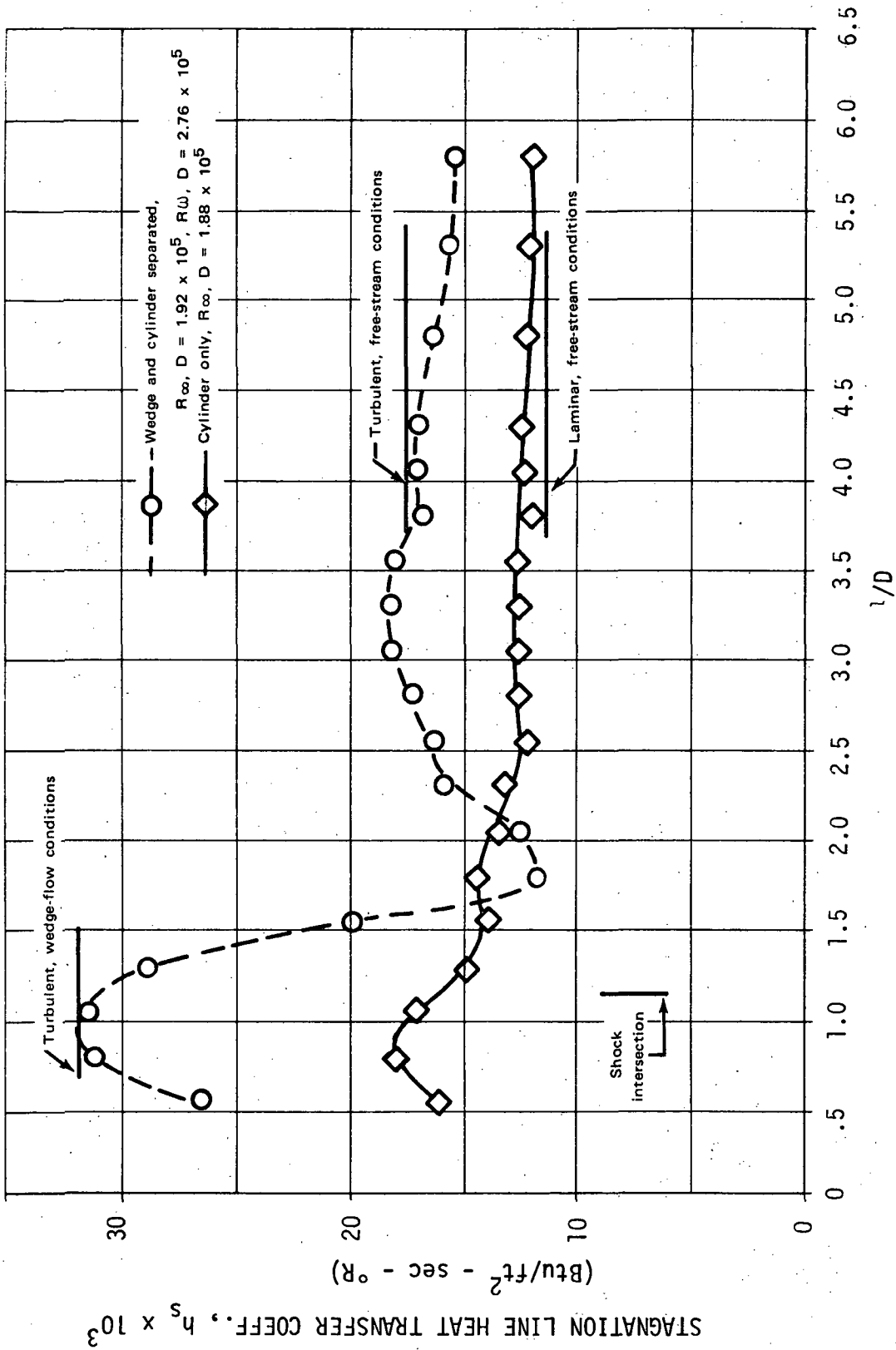


Figure A-4. HEAT-TRANSFER-COEFFICIENT DISTRIBUTION ALONG CYLINDER STAGNATION LINE WITH REYNOLDS NUMBER OF ABOUT 1.9×10^5 . $\Lambda_w = 53^\circ$ and $\Lambda_\infty = 45^\circ$

Wedge and cylinder separated, $R_{\infty}, D = 2.58 \times 10^5$
 $R_{w}, D = 3.7 \times 10^5$

Cylinder only, $R_{\infty}, D = 2.55 \times 10^5$

Wedge and cylinder attached,
 $R_{\infty}, D = 2.46 \times 10^5, R_{w,p} = 3.5 \times 10^5$

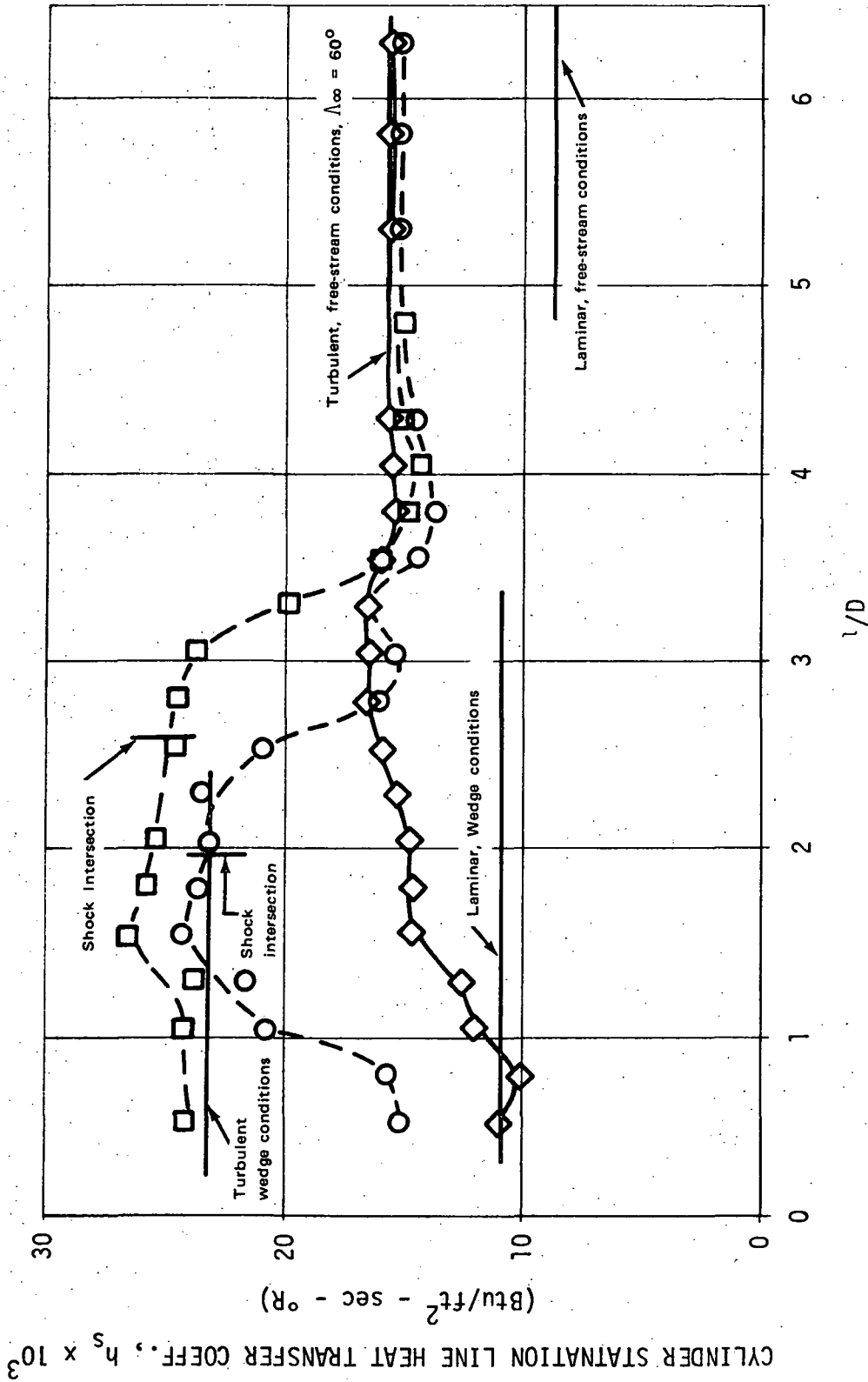


Figure A-5. HEAT-TRANSFER COEFFICIENT DISTRIBUTION ALONG CYLINDER STAGNATION LINE WITH REYNOLDS NUMBER OF ABOUT 2.5×10^5 .

$\Lambda_\infty = 60^\circ, \Lambda_w = 68^\circ$

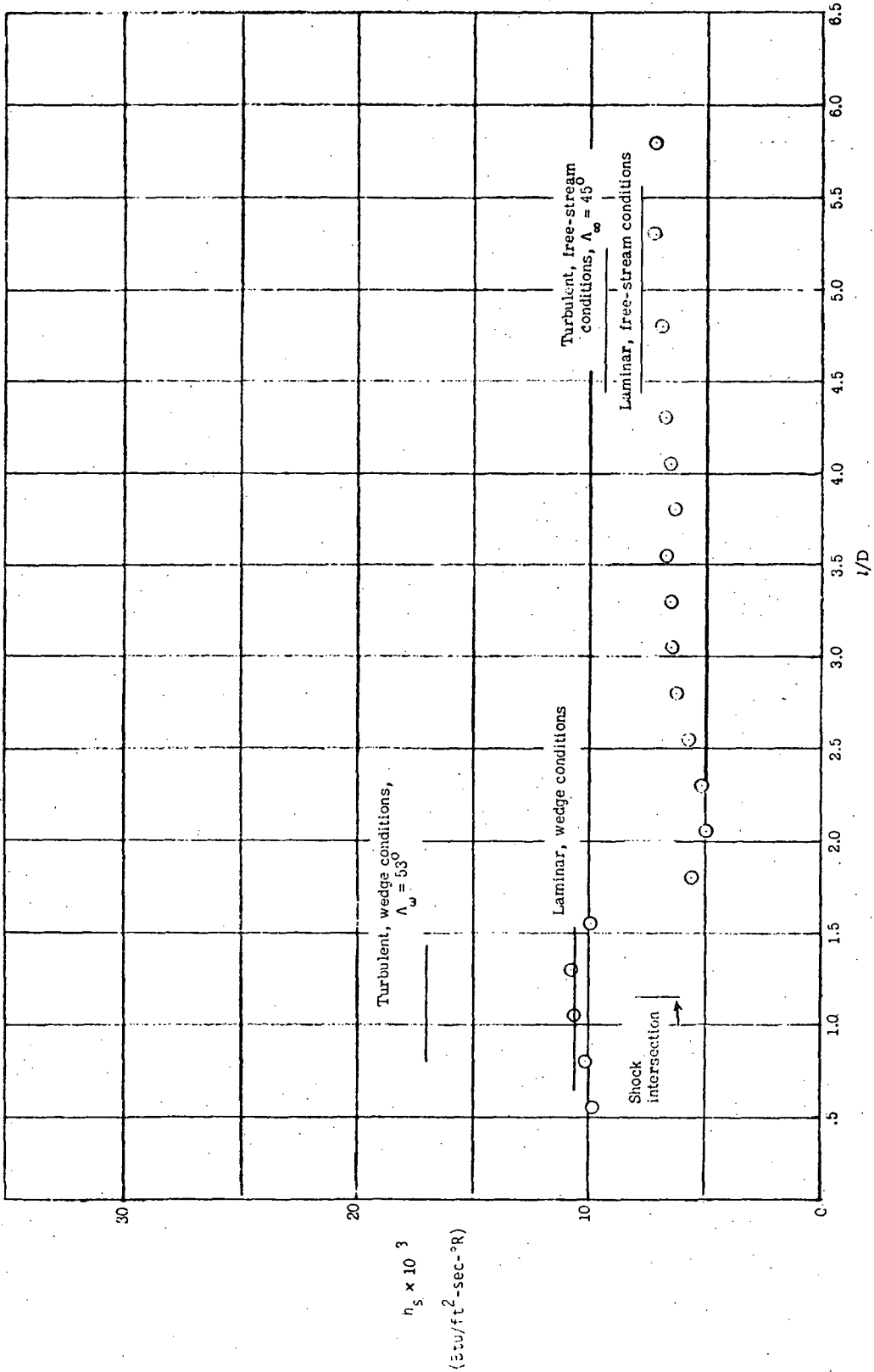


Figure A-6. HEAT TRANSFER COEFFICIENT DISTRIBUTION ALONG CYLINDER STAGNATION LINE WITH LOW REYNOLDS NUMBER (WEDGE AND CYLINDER SEPARATED. $R_{\infty,D} = 0.87 \times 10^5$; $R_{\omega,D} = 1.26 \times 10^5$.)

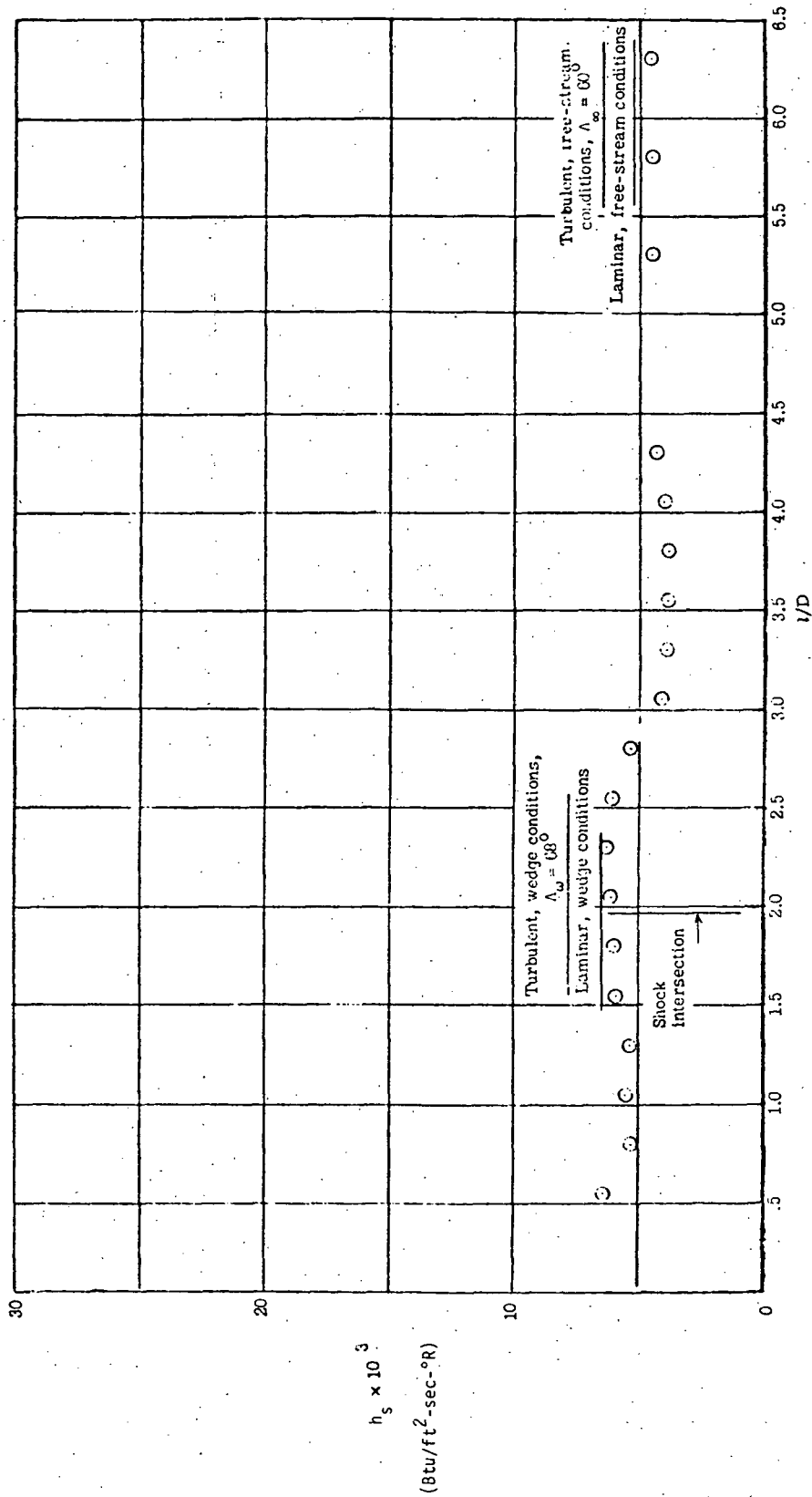


Figure A-7. HEAT TRANSFER COEFFICIENT DISTRIBUTION ALONG CYLINDER STAGNATION LINE WITH LOW REYNOLDS NUMBER (WEDGE AND CYLINDER SEPARATED. $R_{\infty, D} = 0.89 \times 10^5$; $R_{\omega, D} = 1.28 \times 10^5$)

$\Lambda_{60} = 60^\circ$ $\Lambda_{68} = 68^\circ$

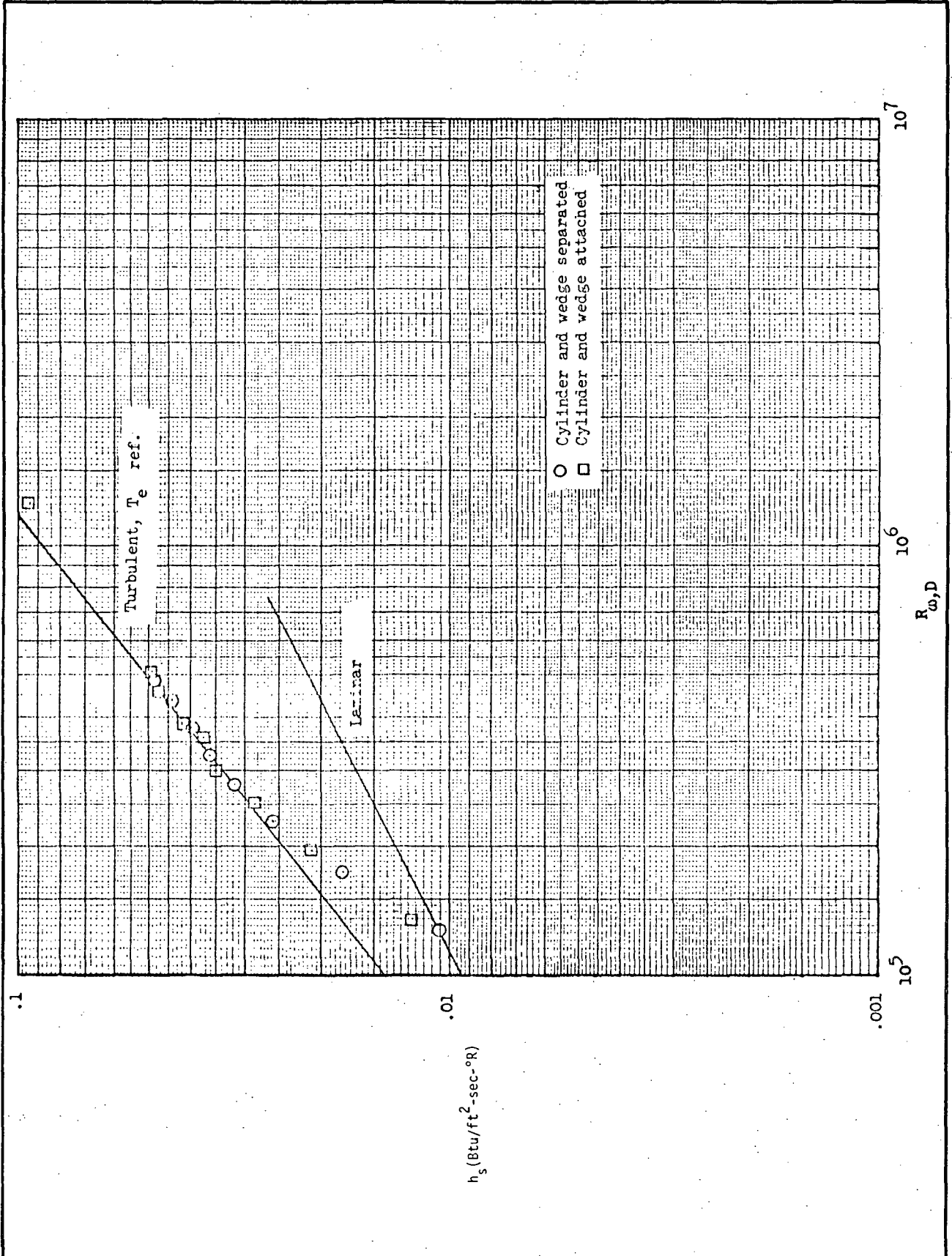


Figure A-8. STAGNATION-LINE HEAT-TRANSFER COEFFICIENT AS A FUNCTION OF UNIT REYNOLDS NUMBER. $\Lambda_{\infty} = 45^\circ$.

Wedge flow region. $l/D = 1.05$; $\Lambda_w = 53^\circ$; $M_w = 5.3$; $T_0 \approx 1360^\circ R$.

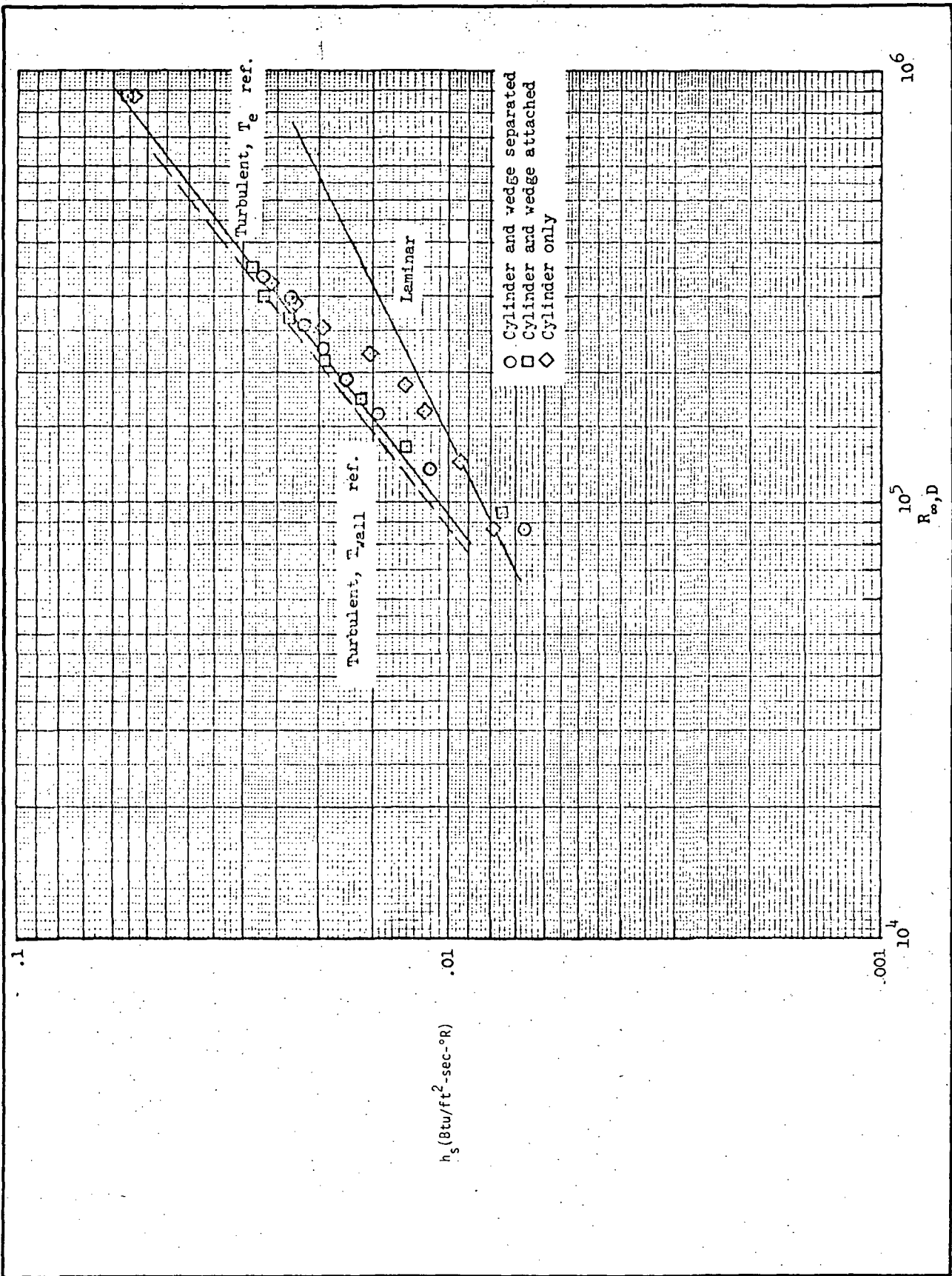


Figure A-9. STAGNATION-LINE HEAT TRANSFER COEFFICIENT AS A FUNCTION OF UNIT REYNOLDS NUMBER. $\Lambda_{\infty} = 45^\circ$.

Undisturbed flow region. $\xi/D = 4.3$; $M_{\infty} = 7.05$; $\Lambda_{\infty} = 45^\circ$; $T_0 \approx 1325^\circ R$.

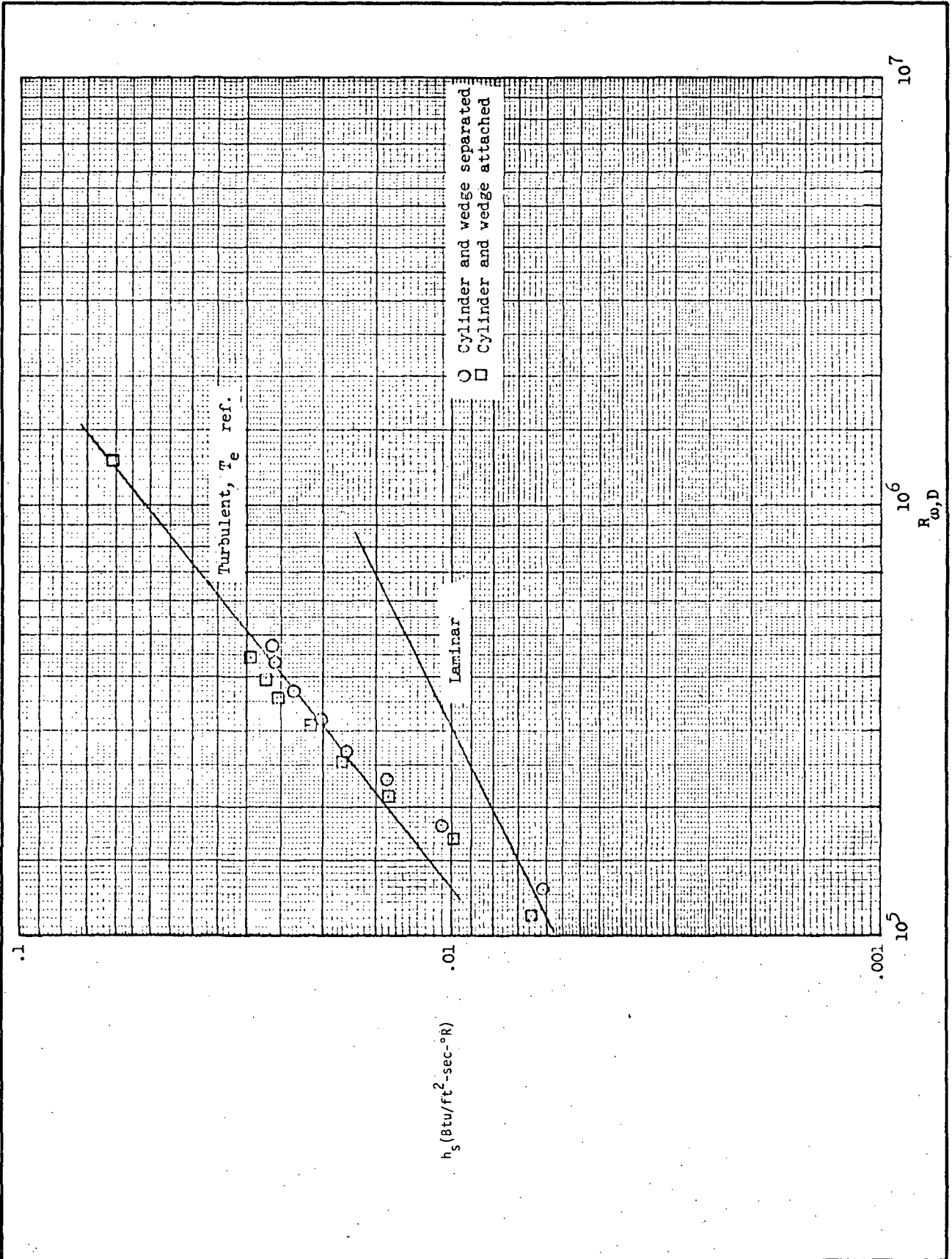


Figure A-10. STAGNATION-LINE HEAT-TRANSFER COEFFICIENT AS A FUNCTION OF UNIT REYNOLDS NUMBER. $\Lambda_\infty = 60^\circ$.

Wedge flow region. $l/D = 2.05$; $\Lambda_w = 68^\circ$; $M_{w,1} = 5.3$; $T_0 \approx 1450^\circ \text{R}$.

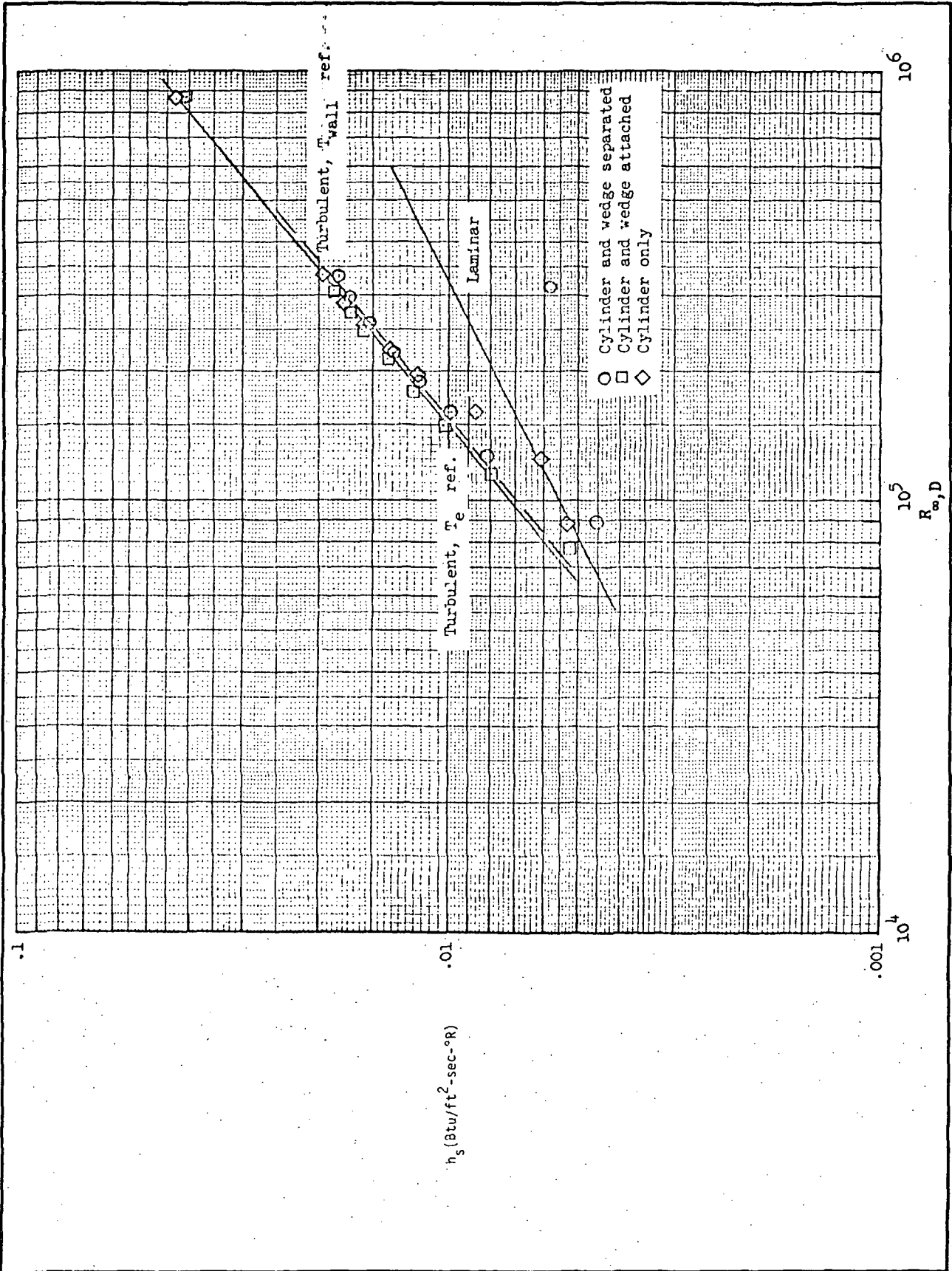
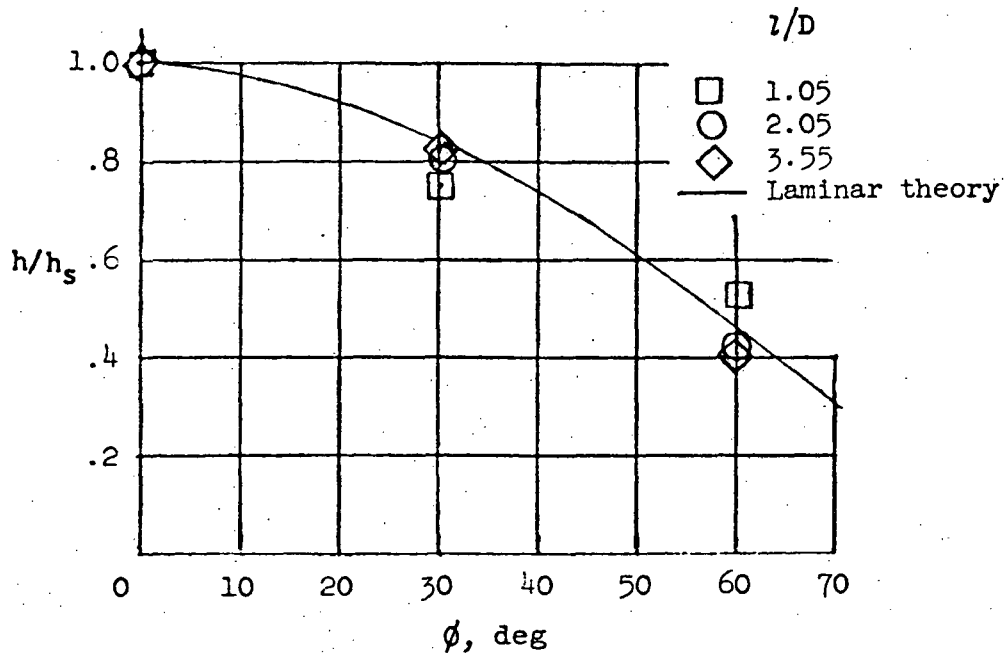
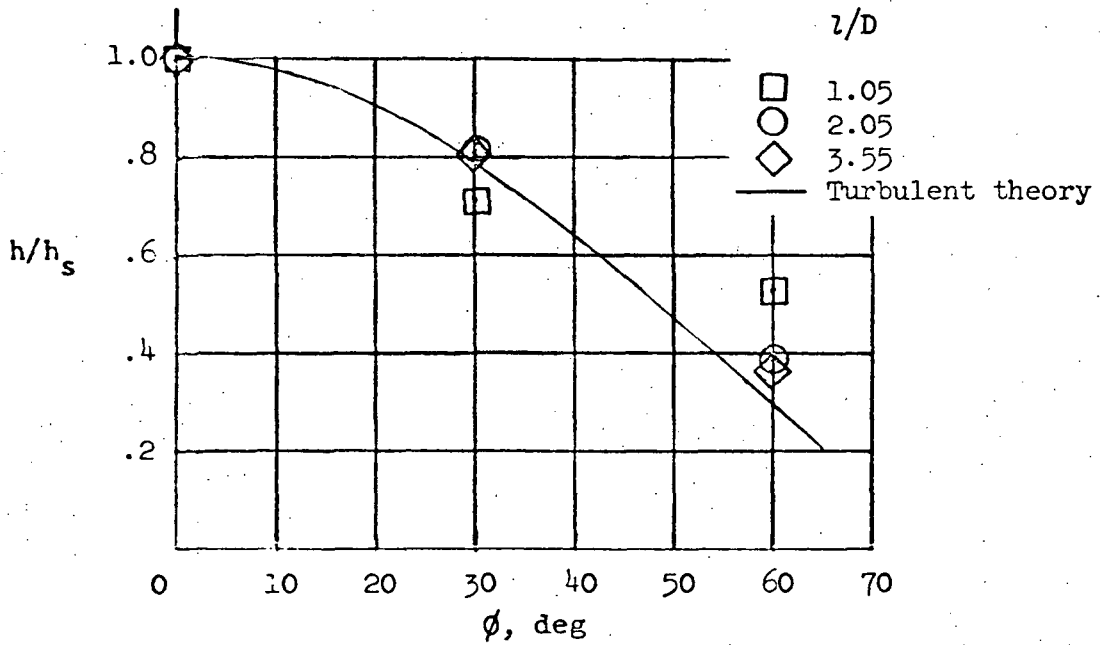


Figure A-11. STAGNATION-LINE HEAT-TRANSFER COEFFICIENT AS A FUNCTION OF UNIT REYNOLDS NUMBER. $\Lambda_{\infty} = 60^\circ$.

Undisturbed flow region. $U/D = 5.3$; $\Lambda_{\infty} = 60^\circ$; $M_{\infty} = 7.95$; $T_0 \approx 1330^\circ \text{R}$.

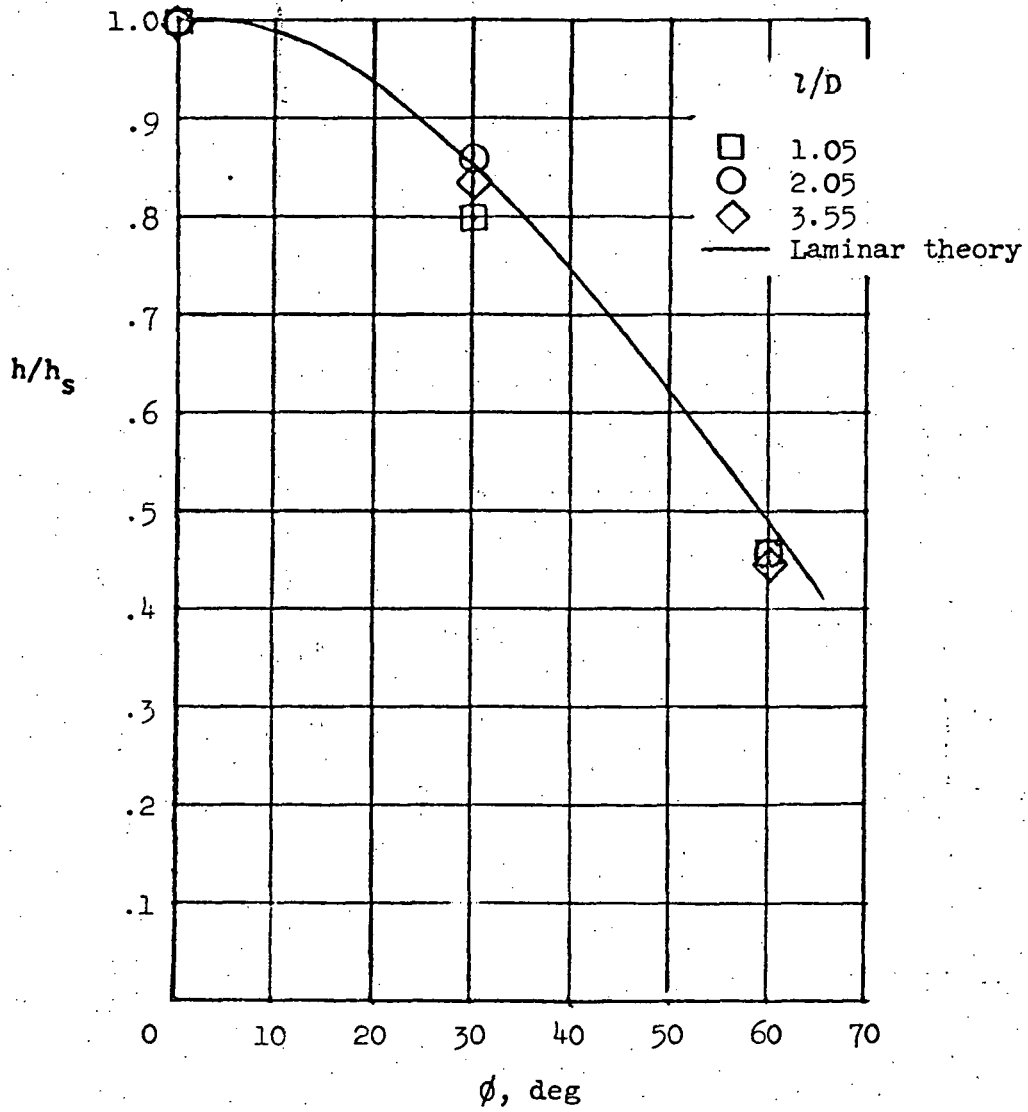


(a) $R_{\infty, D} = 1.25 \times 10^5$; $\Lambda_{\infty} = 60^\circ$.



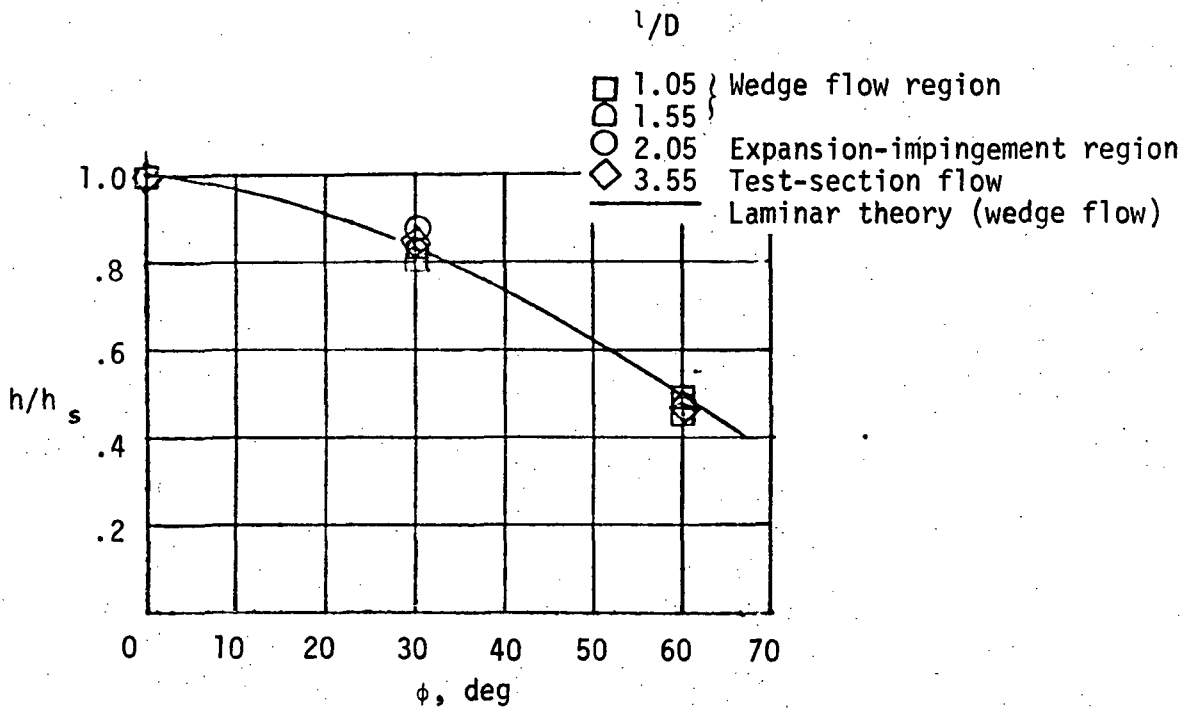
(b) $R_{\infty, D} = 2.56 \times 10^5$; $\Lambda_{\infty} = 60^\circ$.

Figure A-12. CHORDWISE HEAT-TRANSFER DISTRIBUTION, CYLINDER ONLY

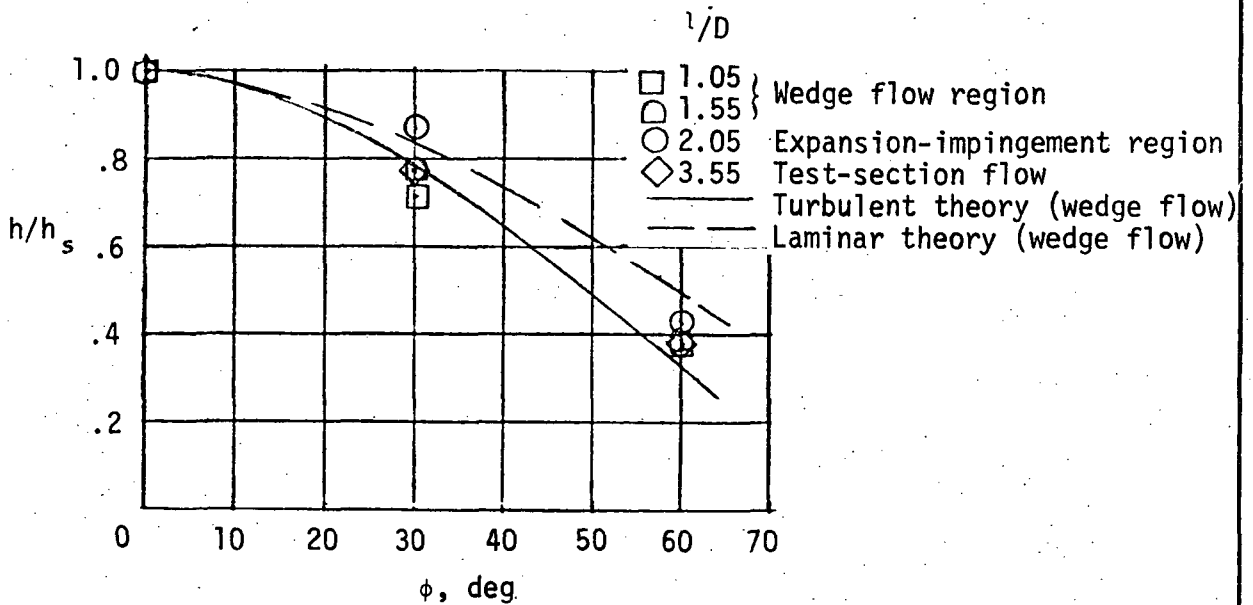


(c) $R_{\infty, D} = 1.24 \times 10^5$; $\Lambda_{\infty} = 45^\circ$.

Figure A-12. CHORDWISE HEAT-TRANSFER DISTRIBUTION, CYLINDER ONLY (Concluded)

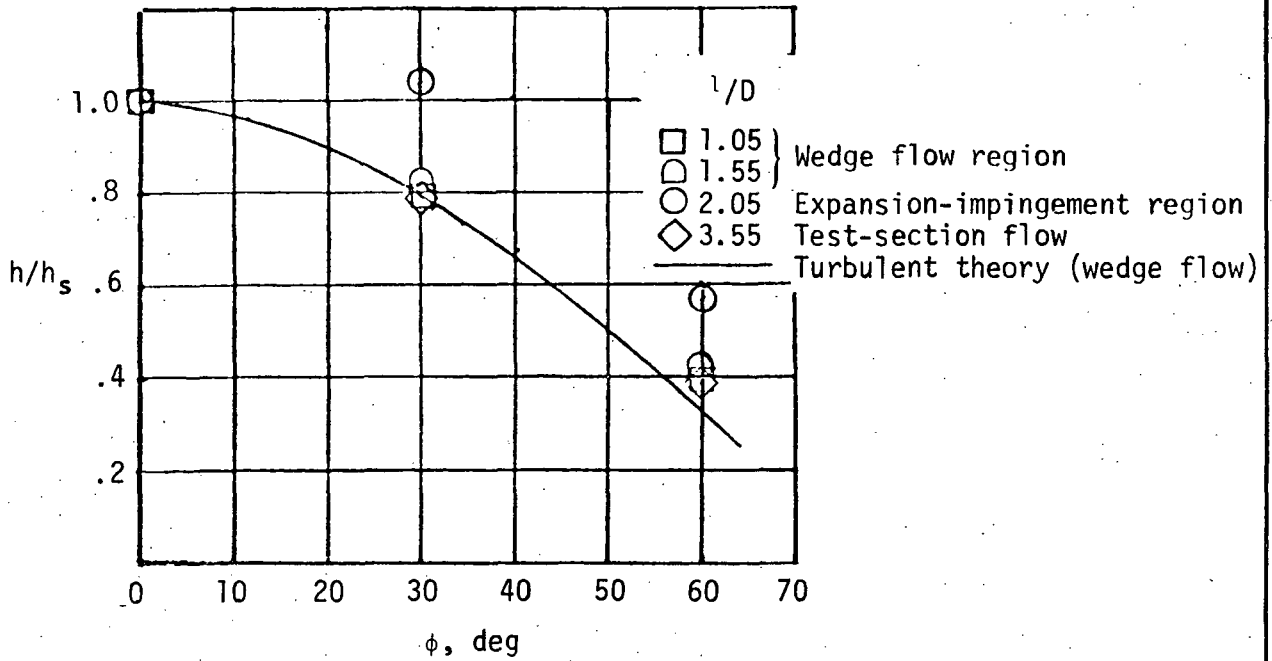


(a) $R_{\infty, D} = 0.94 \times 10^5$.

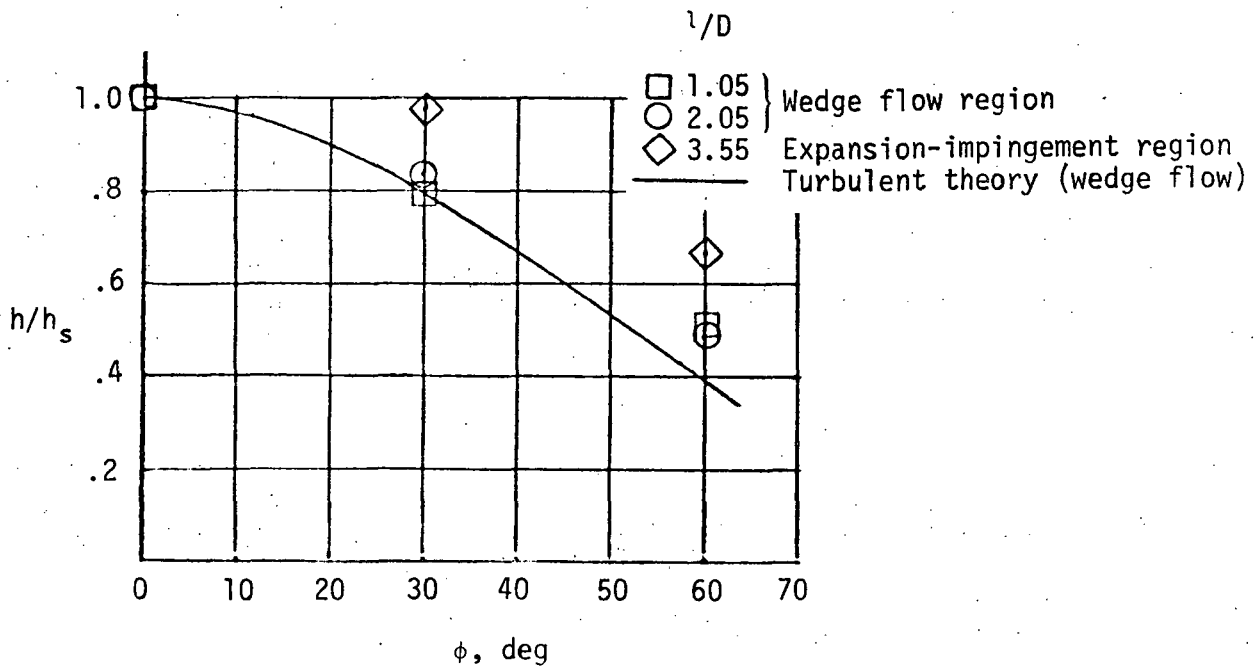


(b) $R_{\infty, D} = 1.34 \times 10^5$.

Figure A-13. CHORDWISE HEAT-TRANSFER DISTRIBUTION FOR LAMINAR AND TRANSITIONAL STAGNATION-LINE BOUNDARY-LAYER FLOW, CYLINDER AND WEDGE ATTACHED. $\Lambda_{\infty} = 45^\circ$



(a) $R_{\infty, D} = 2.66 \times 10^5$; $\Lambda_{\infty} = 45^\circ$



(b) $R_{\infty, D} = 2.46 \times 10^5$; $\Lambda_{\infty} = 60^\circ$

Figure A-14. CHORDWISE HEAT-TRANSFER DISTRIBUTION FOR TURBULENT STAGNATION-LINE BOUNDARY LAYER, CYLINDER AND WEDGE ATTACHED

EXPERIMENTAL INVESTIGATION OF HEAT TRANSFER AND PRESSURES
ON A SWEPT CYLINDER IN THE VICINITY OF ITS INTERSECTION
WITH A WEDGE AND FLAT PLATE AT MACH NUMBER 4.15
AND HIGH REYNOLDS NUMBERS

By Ivan E. Beckwith

NASA TN D-2020
JULY 1964

SYMBOLS

- D = cylinder diameter
- h = heat transfer coefficient
- h_{inf} = measured value of h on infinite cylinder without shock interaction
- K_{∞} = thermal conductivity at free stream condition
- l = upstream length of flat plate or wedge from stagnation line of cylinder
- M_{∞} = free stream Mach number
- $R_{\infty,D}$ = free stream Reynolds number based on cylinder diameter
- y = axial distance along surface of cylinder from wedge intersection line
- y_s = axial distance along cylinder stagnation line from wedge intersection
- δ = wedge half angle
- θ = angular distance from cylinder stagnation line
- A = cylinder sweep angle

SUMMARY

Heat-transfer rates and pressures have been measured on a circular cylinder in the region of flow interference caused by an adjoining 8° half-angle sharp wedge. Data were obtained for sweep angles of 20° and 60° with respect to the free stream flow direction. At the 20° sweep angle some data were obtained with a flat plate (wedge angle = 0) as well as with the wedge. A Mach number of 4.15 was used in the test. A sketch of the model is given in Figure B-1. Results are summarized as follows:

- The test Reynolds numbers were sufficiently large so that the boundary layer was always turbulent on the cylinder and wedge or plate ($R_{\infty, D} = 1.6 \times 10^6 \sim 4.0 \times 10^6$).
- The heat transfer data for 20° sweep angle are given in Figures B-2 and B-3 with both chordwise and spanwise distributions.
- For 20° sweep angle, the peak h/h_{inf} value of 2.5 occurred at about half a cylinder diameter from the wedge and was apparently caused by the local flow conditions and the flow separation on the wedge upstream of the cylinder (Figure B-3).
- For 20° sweep angle, the distribution of heat transfer coefficients along the stagnation line of the cylinder with 8° wedge is compared with the distribution obtained with the flat plate (zero wedge angle) in Figure B-4. The trends of the two curves are similar, but the peak h/h_{inf} ratio with the zero degree plate is only 1.3 as compared with 2.5 for the 8° wedge. For the zero degree plate, the peak heating ratio of 1.3 is caused mainly by the flow separation of the plate-cylinder juncture. The weak shock originating at the sharp leading edge of the plate might also have certain effects on the heat transfer.
- The effect of Reynolds number on h/h_{inf} for $\Lambda = 20^\circ$ at one spanwise station is shown in Figure B-5. Up to $\theta = 30^\circ$, the effect is small; but from $\theta = 60^\circ$ to 120° , the h/h_{inf} values are larger at the smaller Reynolds number.
- Heat transfer data for $\Lambda = 60^\circ$ are shown in Figure B-6.
- When the sweep angle was 60° no separation occurred (based on Schlieren photographs), and the peak heat transfer on the cylinder could be accurately predicted by the theory for turbulent heating on a yawed cylinder from the local conditions on the wedge.
- The local effect on the heating rates of the shock-wave impingement from the wedge was negligible at both sweep angles.

COMPARISON WITH MSFC BOOSTER REENTRY STUDY

	<u>BECKWITH (REF. 6)</u>	<u>MSFC BOOSTER WING</u> (ANGLE OF ATTACK = 12.5°)
M_∞	4.15	3-6
Shock Strength (Pressure Ratio Across Shock)	2.17	1.72 - 2.46
Cylinder Diameter, D (ft)	1.115/12	1*
$R_{\infty,D}$	$16 \times 10^5 - 40 \times 10^5$	$1 \times 10^5 - 14 \times 10^5$
Λ (degrees)	20, 60	52
Max. h/h_{inf}	2.5 (for $\Lambda = 20^\circ$) 1.8 (for $\Lambda = 60^\circ$)	

* Assumed wing leading edge diameter

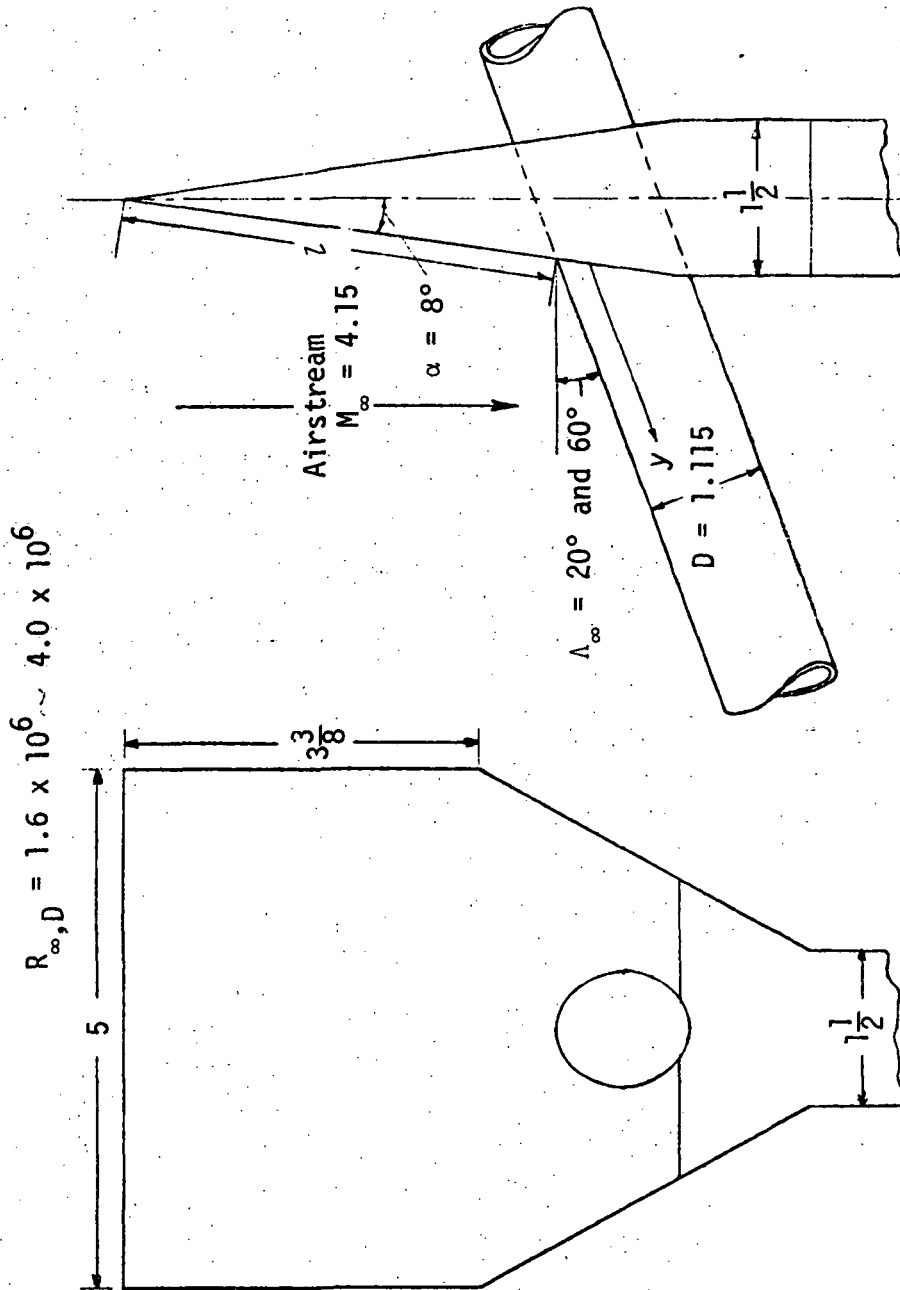


Figure B-1. SKETCH OF MODEL AND INSTRUMENTATION. (ALL DIMENSIONS IN INCHES)

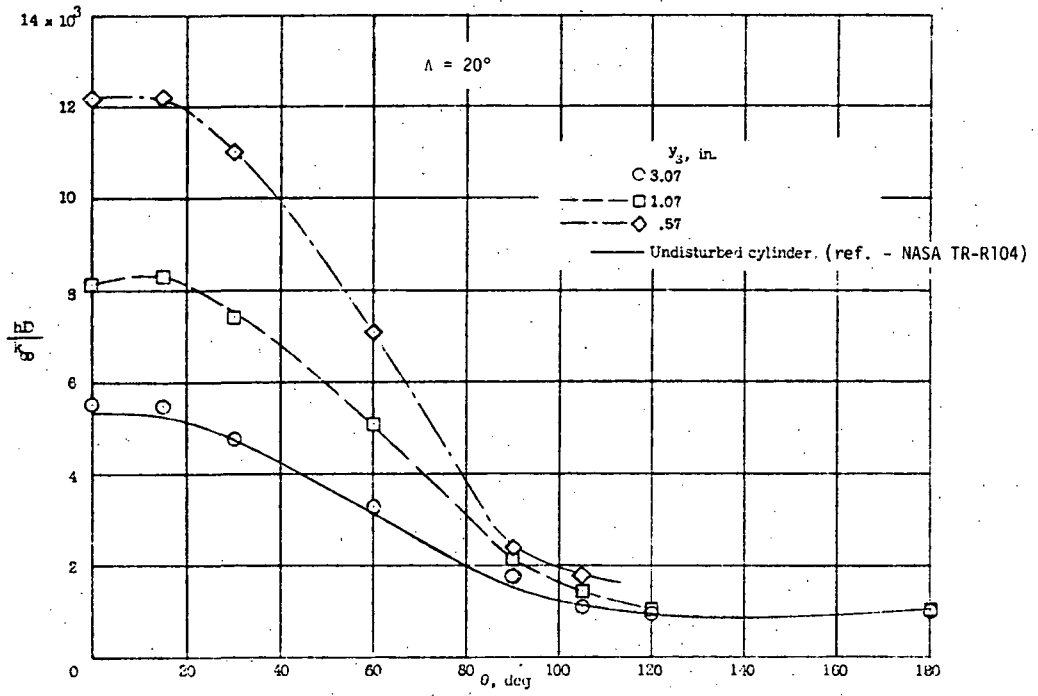


Figure B-2. CHORDWISE HEAT-TRANSFER DISTRIBUTION ON CYLINDER FOR $\Lambda = 20^\circ$, $\alpha = 8^\circ$, $z = 4.16$ INCHES, AND $R_{\infty, D} = 1.56 \times 10^6$

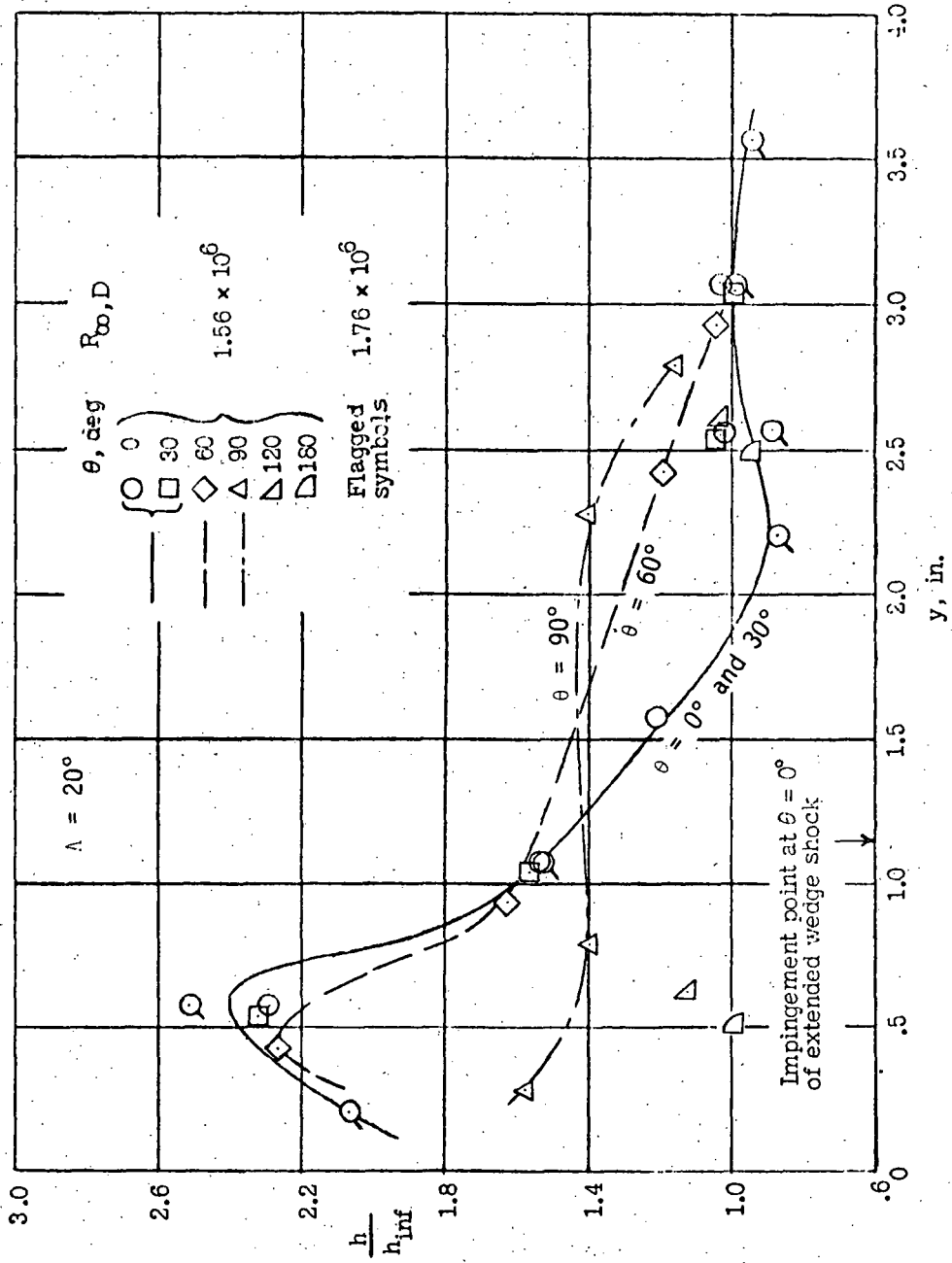


Figure B-3. SPANWISE HEAT-TRANSFER DISTRIBUTION ON CYLINDER FOR $\Lambda = 20^\circ, \alpha = 8^\circ$, AND $l = 4.16$ INCHES

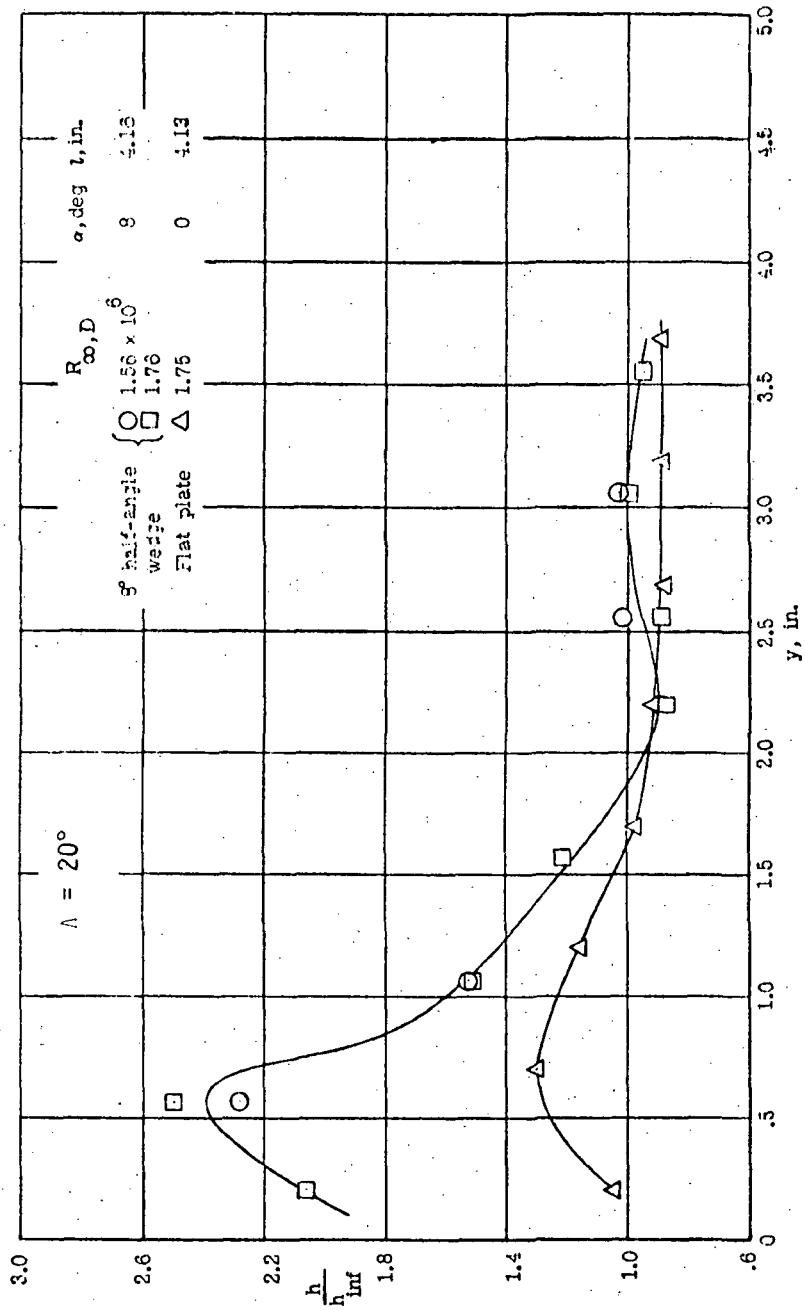


Figure B-4. EFFECT OF WEDGE ANGLE ON THE SPANWISE DISTRIBUTION OF HEAT-TRANSFER COEFFICIENT AT STAGNATION LINE OF CYLINDER FOR $\Lambda = 20^\circ$ AND $Z = 4.16$ INCHES

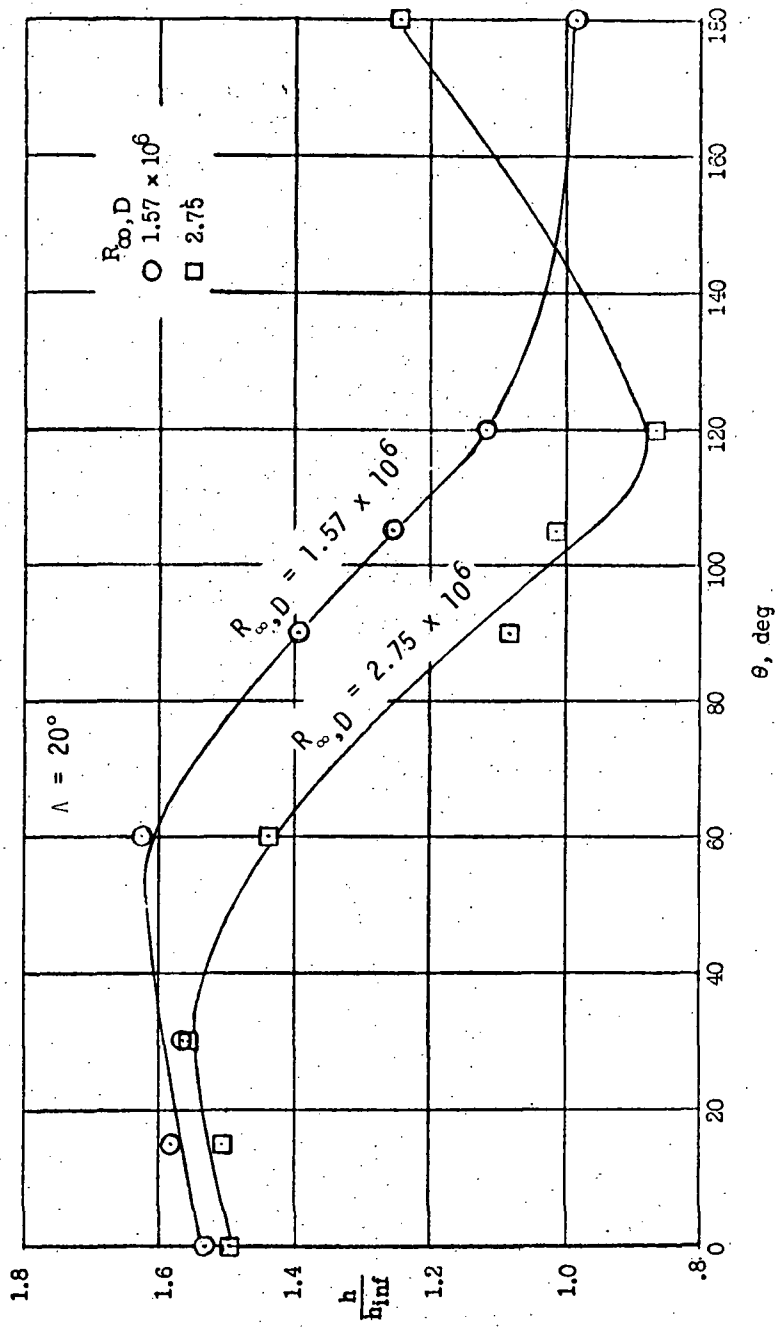


Figure B-5. EFFECT OF REYNOLDS NUMBER ON HEAT-TRANSFER-COEFFICIENT RATIO FOR $\Lambda = 20^\circ$, $y_s = 1.07$ INCHES, $\alpha = 8^\circ$, AND $z = 4.16$ INCHES

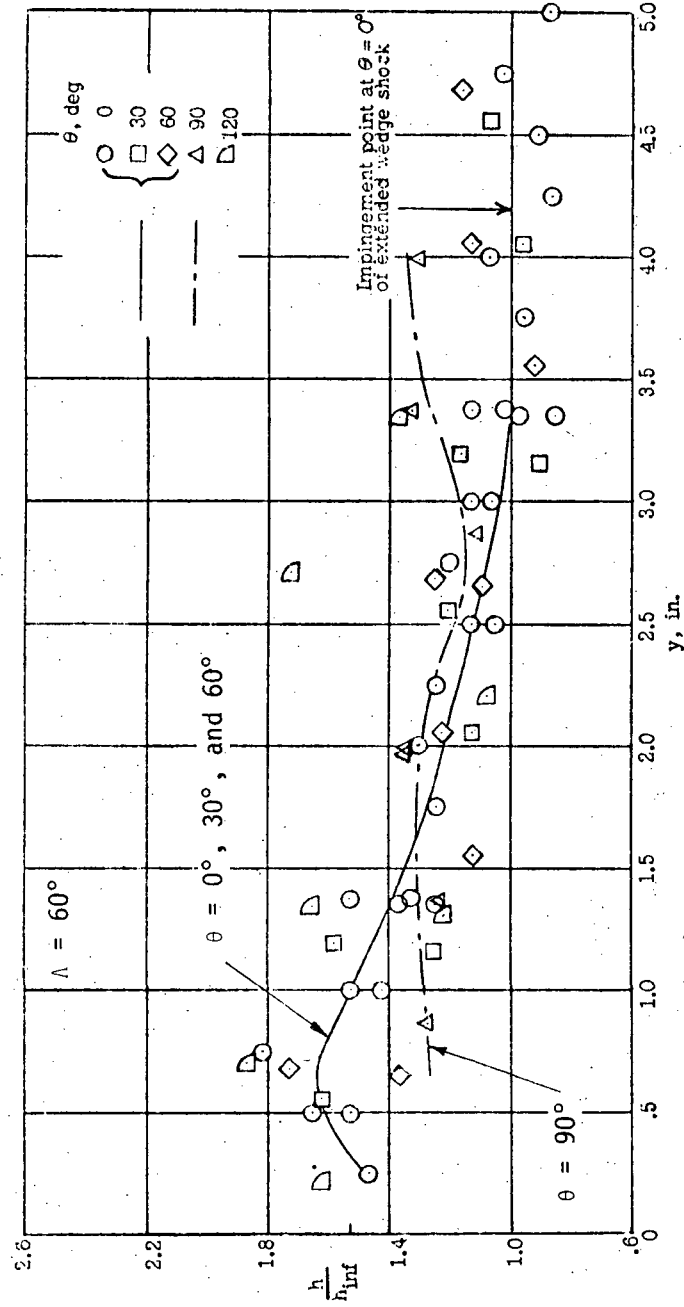


Figure B-6. EFFECT OF 8° HALF-ANGLE WEDGE ON HEAT-TRANSFER COEFFICIENT ON CYLINDER FOR SEVERAL VALUES OF θ WITH $\Lambda = 60^\circ$, $R_{\infty, D} = 1.6 \times 10^6$, AND $L = 3.28$ INCHES

EFFECTS OF SHOCK-WAVE IMPINGEMENT ON THE HEAT TRANSFER
ON A CYLINDRICAL LEADING EDGE

By Robert S. Hiers and William J. Loubsky

SYMBOLS

- d = diameter of leading edge model
- M_{∞} = free stream Mach number
- \dot{q} = local heat transfer rate with leading edge and shock wave generator
- \dot{q}_o = local heat transfer rate with leading edge only
- $R_{\infty, D}$ = Reynolds number based on leading edge diameter and free stream conditions
- R_{le} = leading-edge radius
- y = spanwise distance along stagnation line measured from intersection of shock generator and leading edge
- V_{∞} = free stream velocity
- δ = deflection angle of shock generator
- Λ = leading edge sweep angle

SUMMARY

This appendix describes an experimental study of the influence of shock-wave impingement on leading-edge heat-transfer and flow field characteristics at a Mach number of 14. Heat-transfer measurements were obtained on the cylindrical leading edge of a blunted flat plate model at sweep angles of 0°, 22.5°, and 45°. The impinging shock waves were generated by deflecting a sharp flat plate attached at the root chord of the leading-edge model or were induced by boundary-layer separation on this "shock generator" flat plate. The angle of incidence of the shock generator was varied between 0° and 15°. The tests were conducted at a Reynolds number of 8000 based on the leading-edge diameter. Sketch of model and instrumentation is shown in Figure C-1. Results as shown in Figures C-2, C-3, and C-4 can be summarized as follows.

Average heat-transfer rates as high as 2300 Btu/ft²-sec, more than 10 times the value with no shock impingement, were measured in small localized regions on the stagnation line of the unswept leading edge (Figures C-2a, C-2b, and C-2c). The experimental results presented in this appendix suggest that this extreme interaction-induced effect on heat transfer is associated with the impingement of a vortex sheet or slip line (generated at the intersection of the bow shock wave and the impinging shock wave) onto the leading edge. Simplified boundary-layer calculations based on this vortex impingement model were made to describe the general characteristics of the interaction-induced heat transfer to the unswept leading edge.

It was also observed, as shown in Figures C-2d and C-2e, that two peaks occurred when the deflection angles were 10° and 15°. The position of the inboard peak correlates with the estimated location of the separation shock wave. This suggests that the inboard peak is related to the impingement of the separation shock wave onto an imbedded bow shock wave.

Heat-transfer rates 2-1/2 times the corresponding undisturbed value were measured over large spanwise segments of the stagnation line with leading edge swept 45° with respect to the free stream (Figure C-4). At this sweep angle, however, the interaction-induced increase in heat transfer is not a localized result of the shock impingement similar to that found at zero sweep, since the

vortex sheet associated with the intersecting shock waves does not impinge on the leading edge at this sweep angle. The leading-edge heat transfer in the interaction region can be adequately predicted at $\Lambda = 45^\circ$ by applying infinite cylinder boundary-layer theory to the leading edge flow field and utilizing conditions behind the impinging shock wave as the effective free impingement effects on highly swept leading edges. No flow separation occurred on the wedge when $\Lambda = 45^\circ$.

Intermediate values of maximum heat transfer were obtained with the leading edge swept 22.5° (Figure C-3). These values are apparently associated with the separation phenomena that occur on the shock-generator plate.

COMPARISON WITH MSFC BOOSTER REENTRY STUDY

	<u>Hiers and Loubsky (Ref. 7)</u>	<u>MSFC Booster Wing</u> (angle of attack = 12.5°)
M_{∞}	14	3-6
Shock Strength (Pressure Ratio Across Shock)	9.35**	1.72 - 2.46
Cylinder Diameter, d(ft)	1/12	1*
$R_{\infty, D}$	8000	$1 \times 10^5 - 14 \times 10^5$
Λ (degrees)	0 - 45	52
Max. \dot{q}/\dot{q}_0	2.5***	

*Assumed wing leading edge diameter

**Based on $M_{\infty} = 14$ and $\delta = 10^\circ$ (Figure C-4b)

***For the case of $\delta = 10^\circ$ and $\Lambda = 45^\circ$ (Figure C-4b)

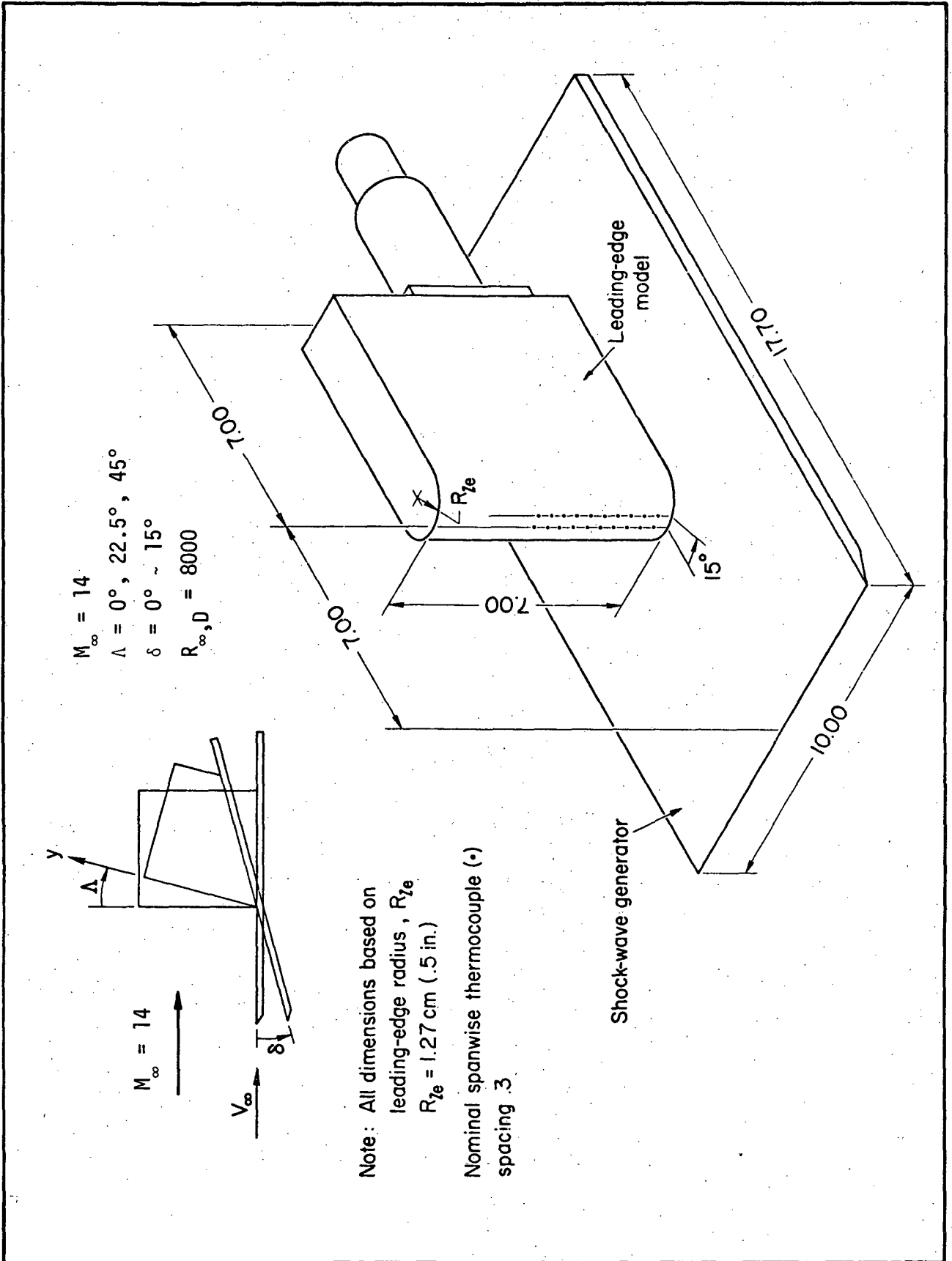


Figure C-1. SKETCH OF MODEL AND INSTRUMENTATION

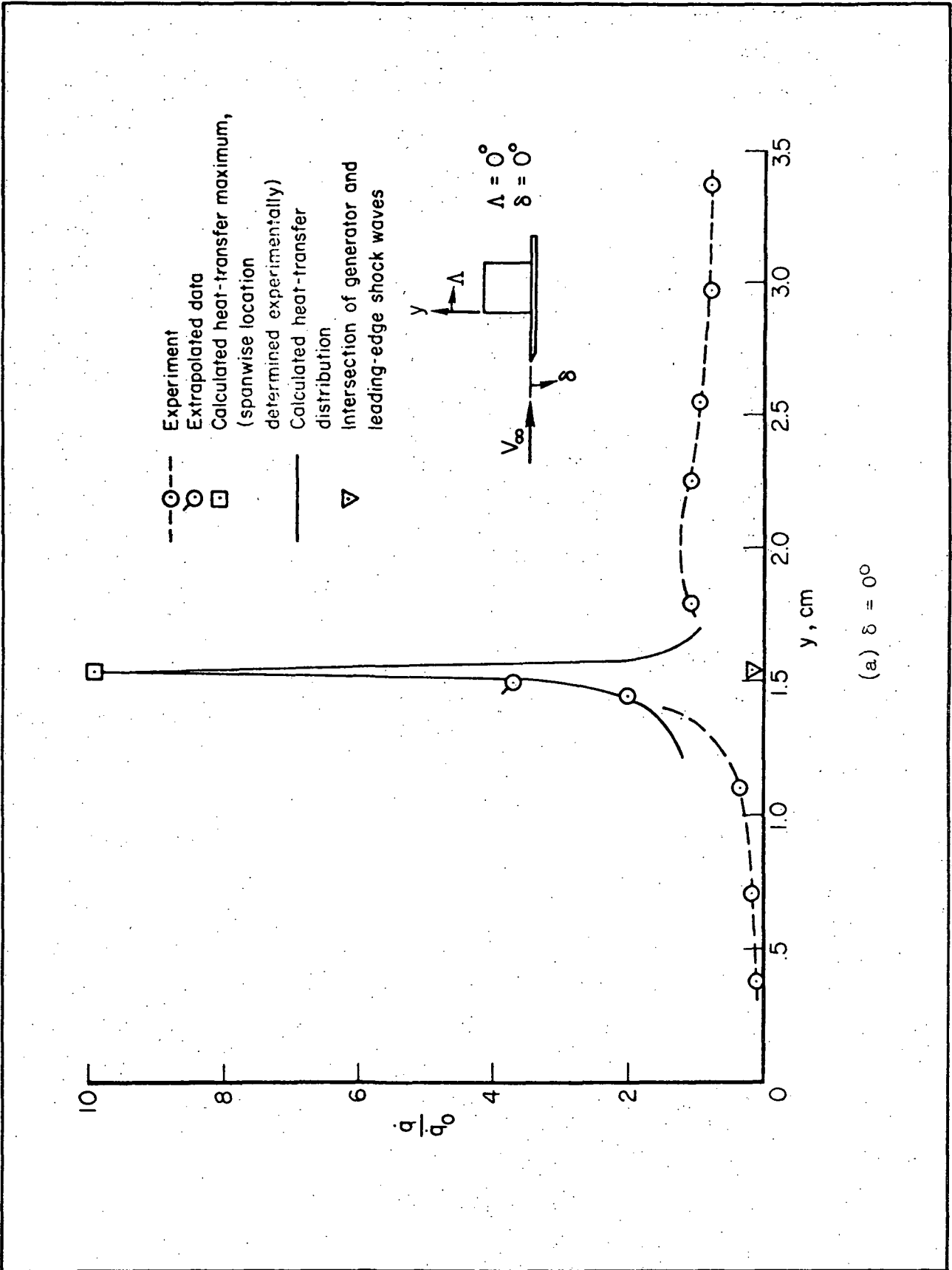


Figure C-2. SPANWISE HEAT-TRANSFER DISTRIBUTIONS ON THE STAGNATION LINE OF THE LEADING EDGE FOR $\Lambda = 0^\circ$

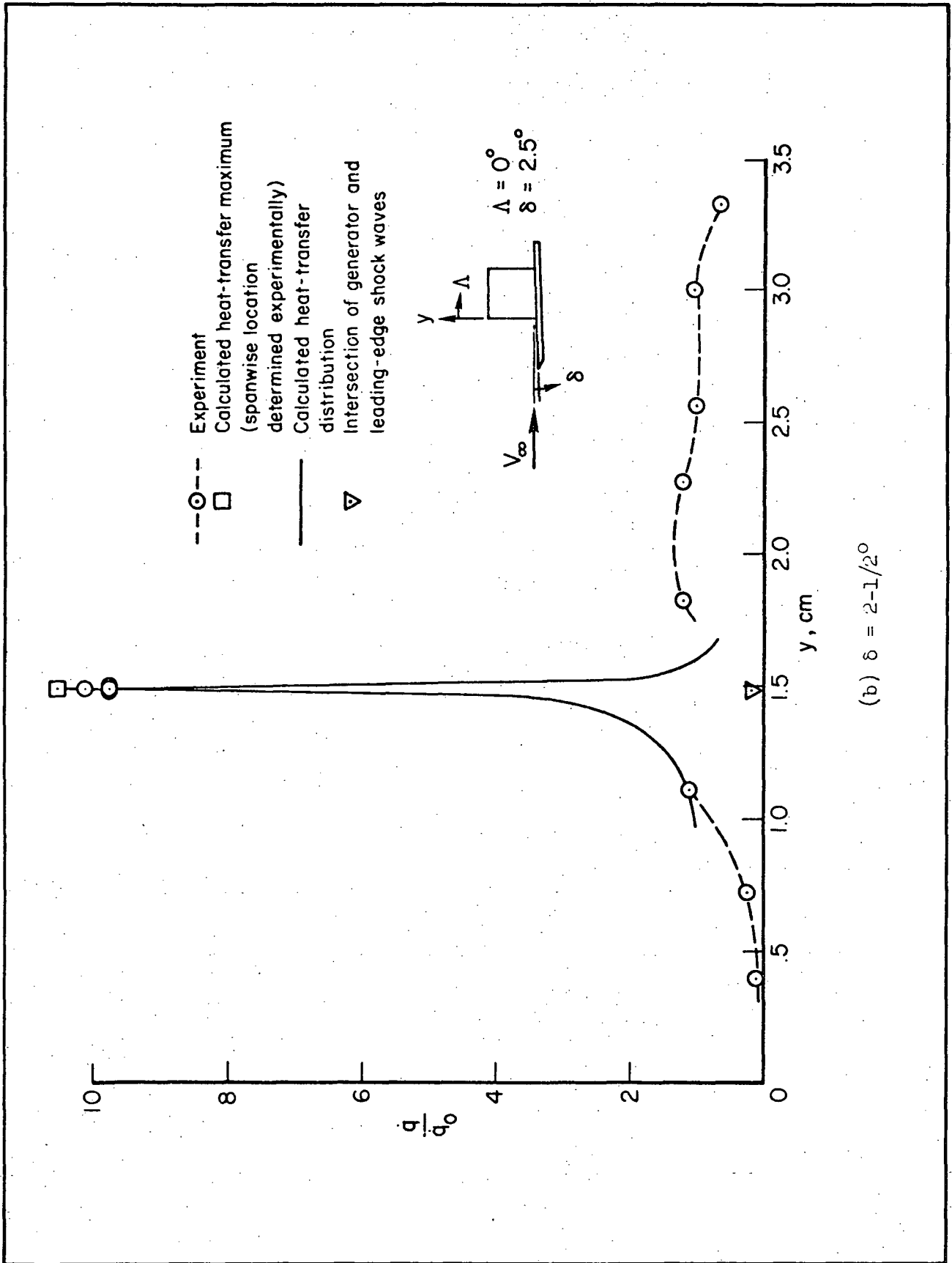
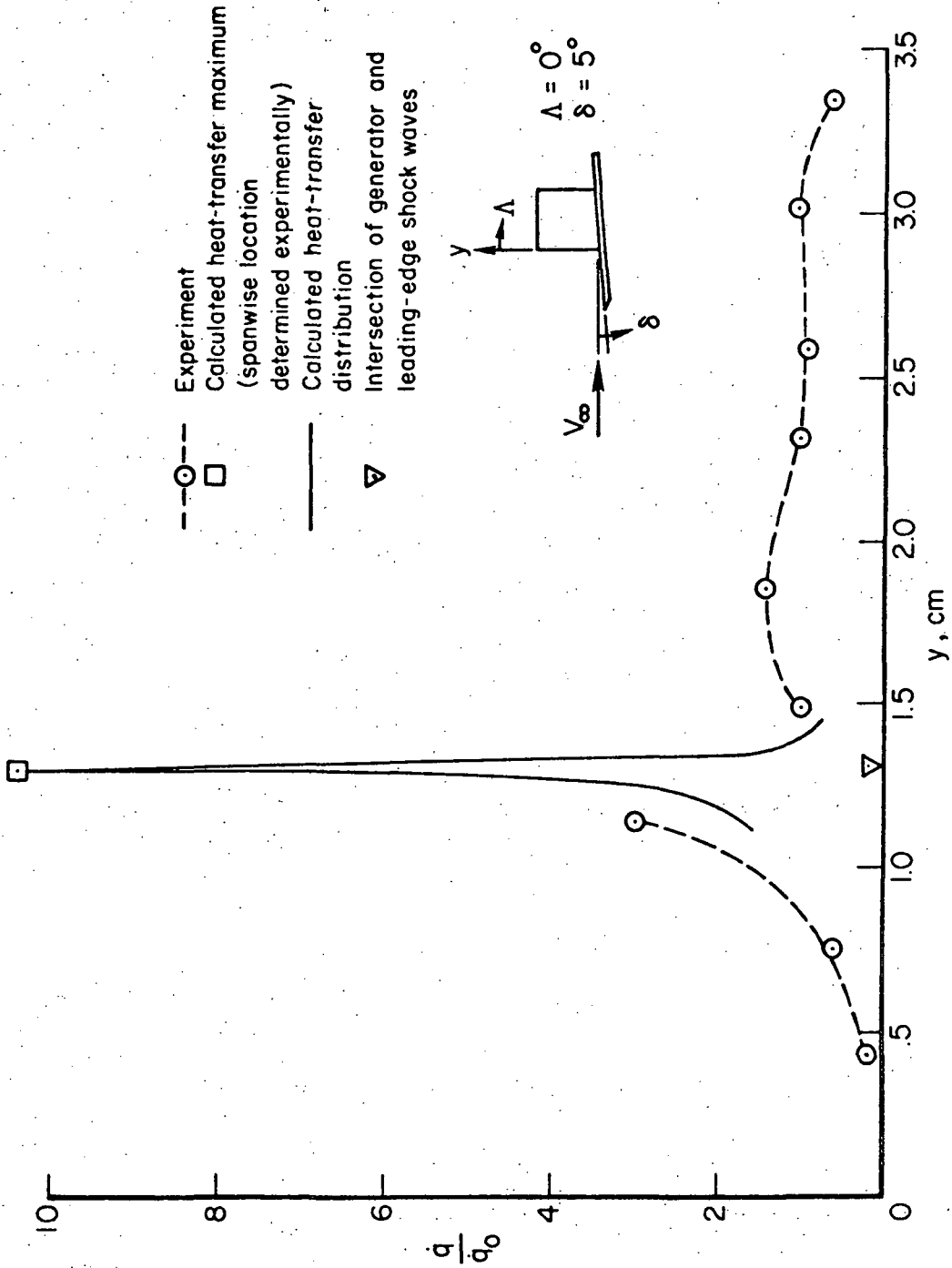


Figure C-2. SPANWISE HEAT-TRANSFER DISTRIBUTIONS ON THE STAGNATION LINE OF THE LEADING EDGE FOR $\Lambda = 0^\circ$ (Continued)



(c) $\delta = 5^\circ$

Figure C-2. SPANWISE HEAT-TRANSFER DISTRIBUTIONS ON THE STAGNATION LINE OF THE LEADING EDGE FOR $\Lambda = 0^\circ$ (Continued)

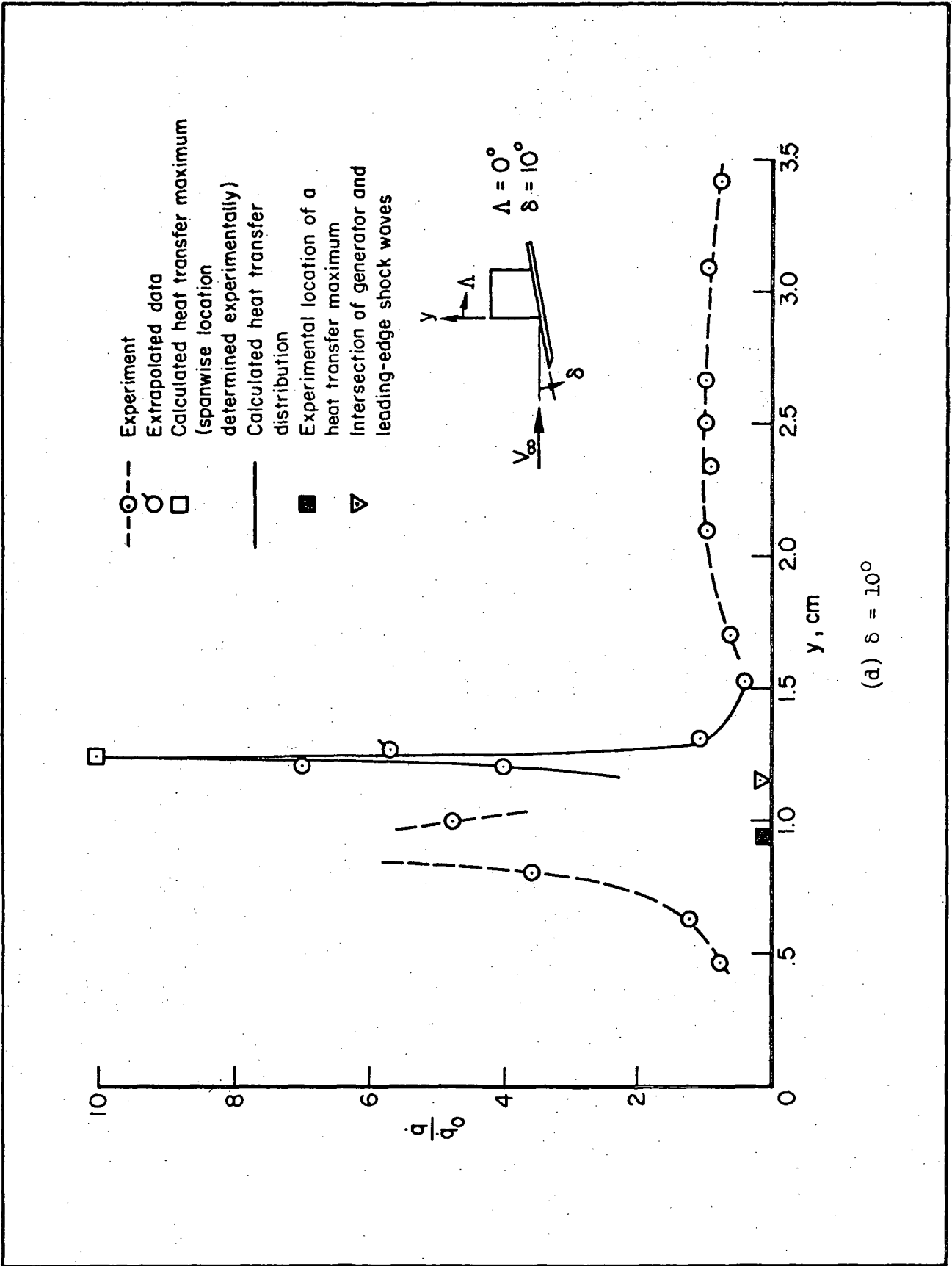


Figure C-2. SPANWISE HEAT-TRANSFER DISTRIBUTIONS ON THE STAGNATION LINE OF THE LEADING EDGE FOR $\Lambda = 0^\circ$ (Continued)

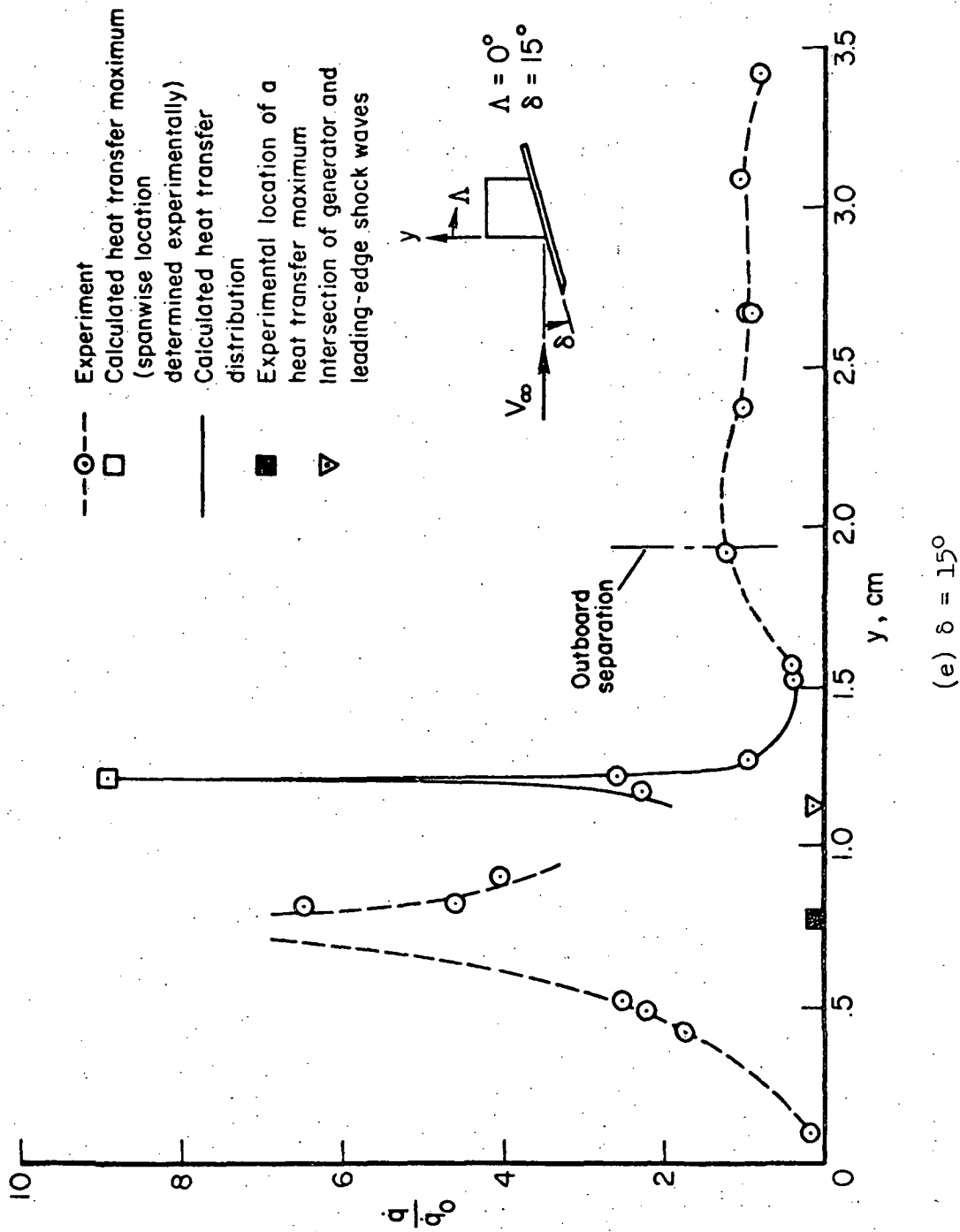


Figure C-2. SPANWISE HEAT-TRANSFER DISTRIBUTIONS ON THE STAGNATION LINE OF THE LEADING EDGE FOR $\Lambda = 0^\circ$ (Concluded)

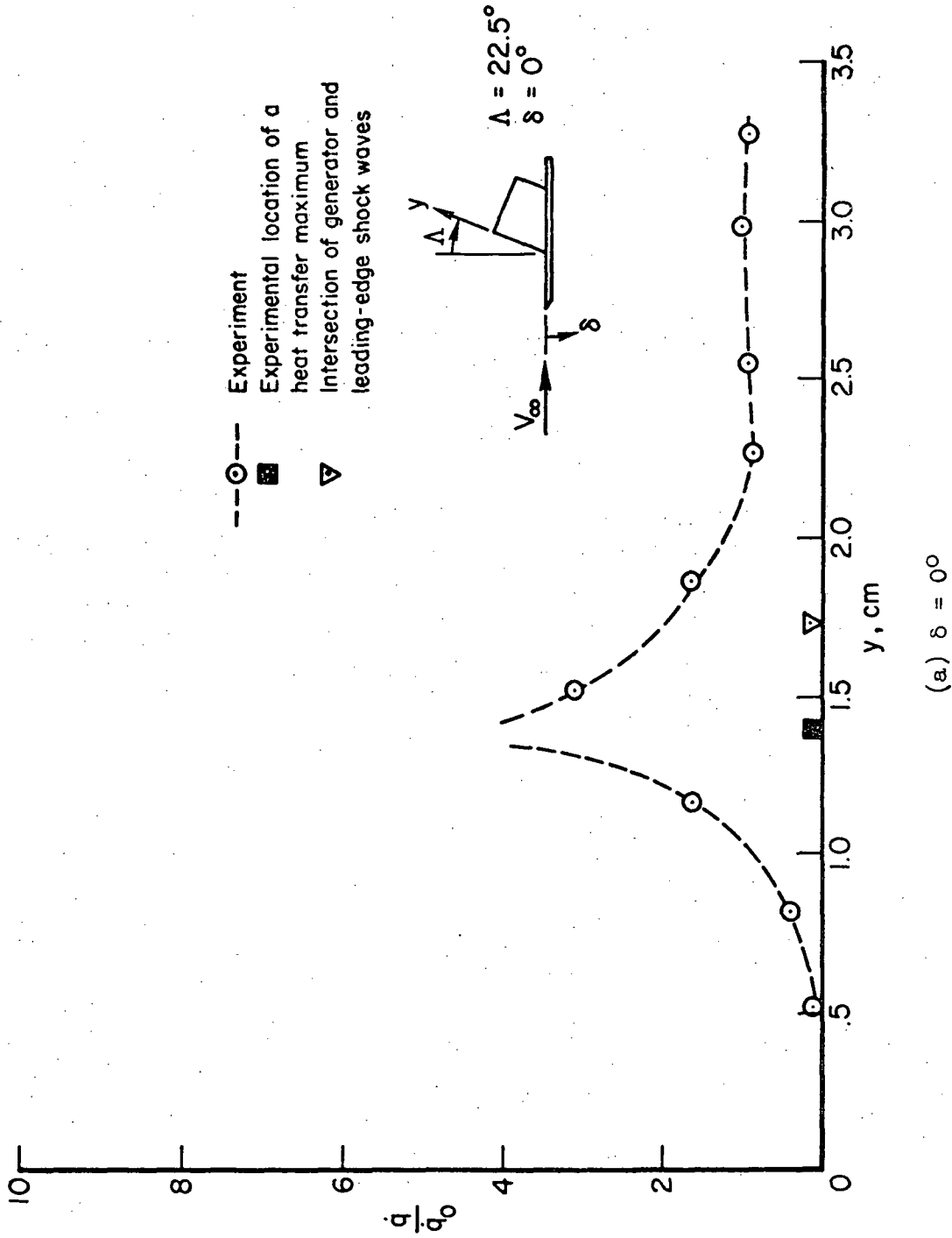


Figure C-3. SPANWISE HEAT-TRANSFER DISTRIBUTIONS ON THE STAGNATION LINE OF THE LEADING EDGE FOR $\Lambda = 22-1/2^\circ$

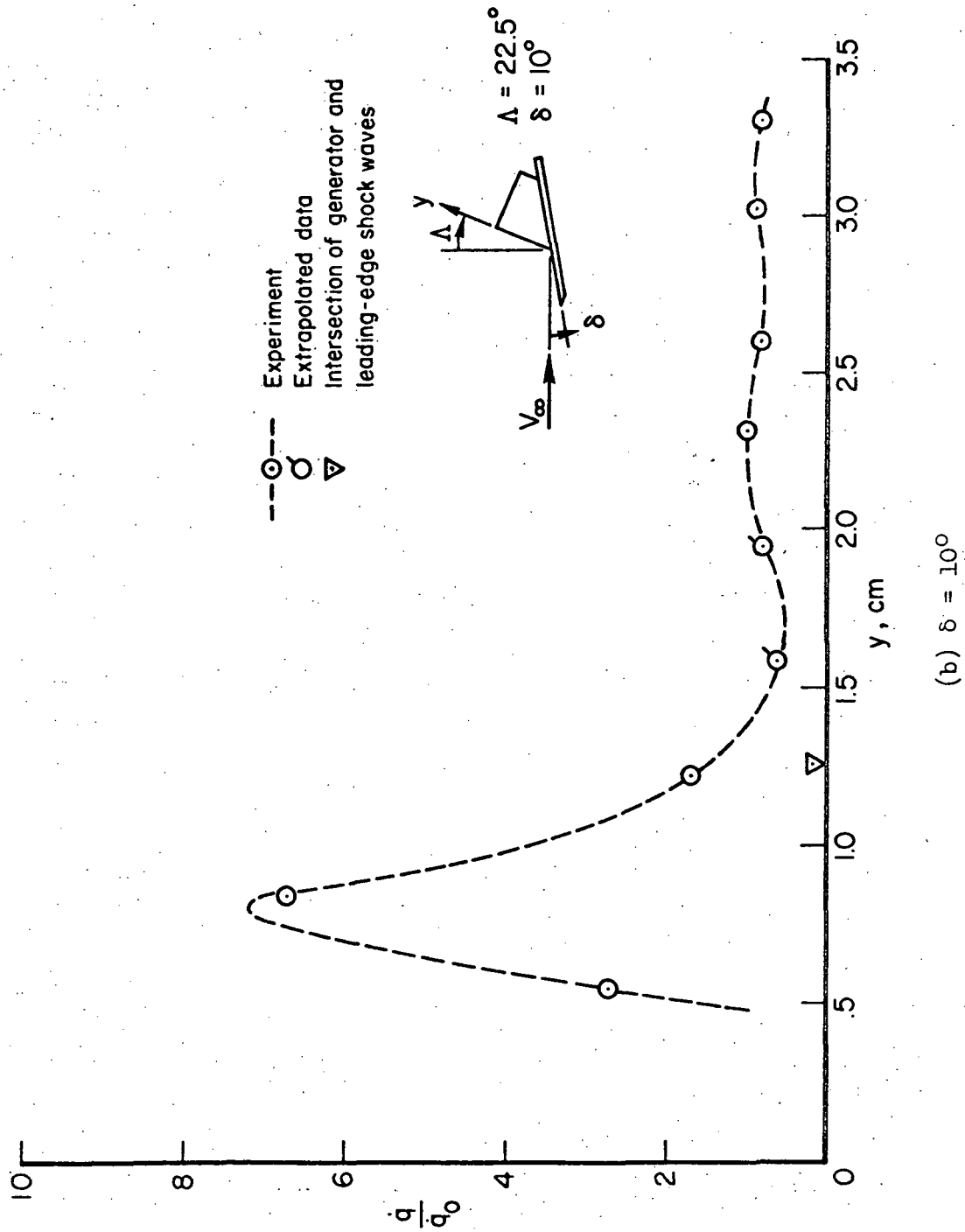


Figure C-3. SPANWISE HEAT-TRANSFER DISTRIBUTIONS ON THE STAGNATION LINE OF THE LEADING EDGE FOR $\Lambda = 22-1/2^\circ$ (Concluded)

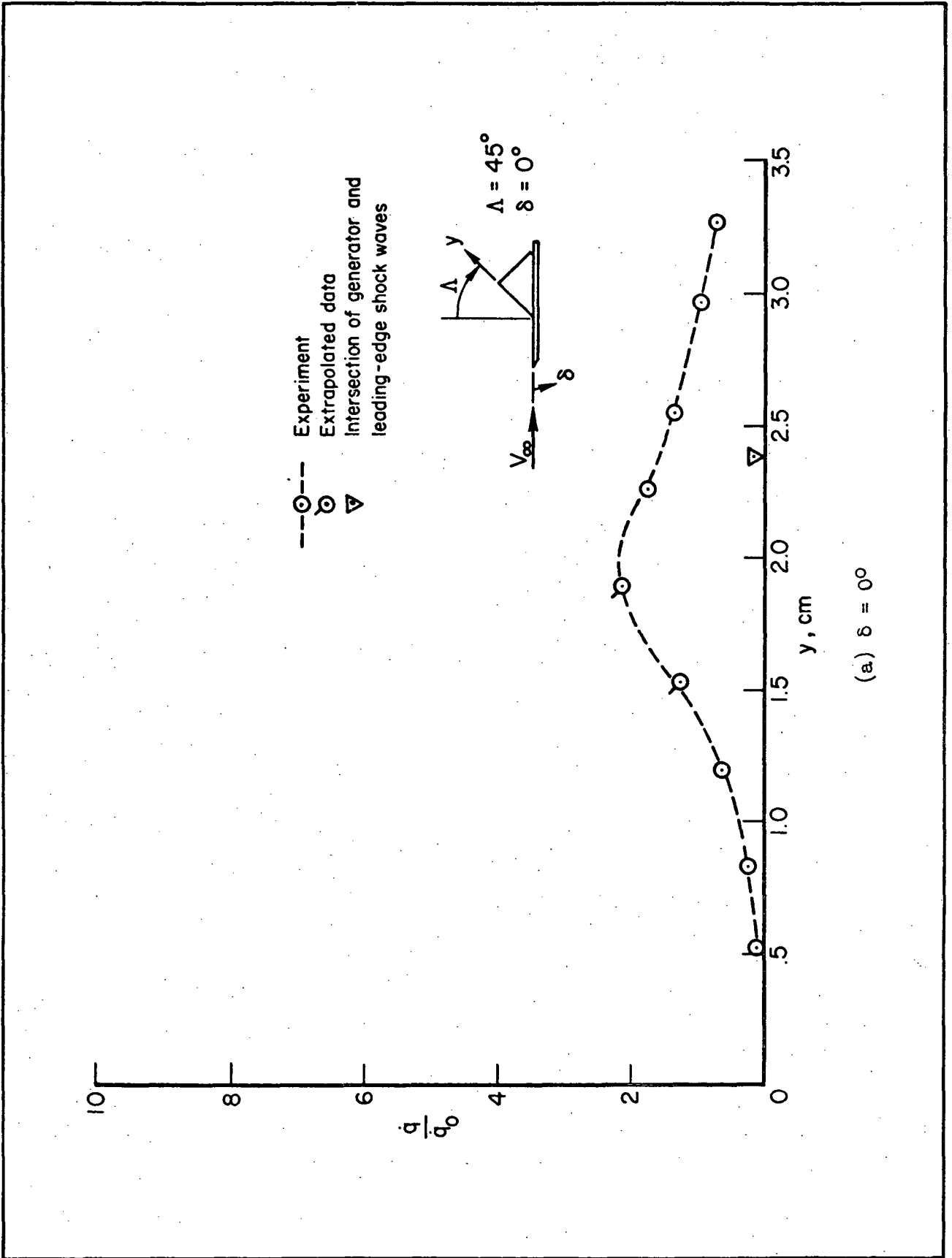
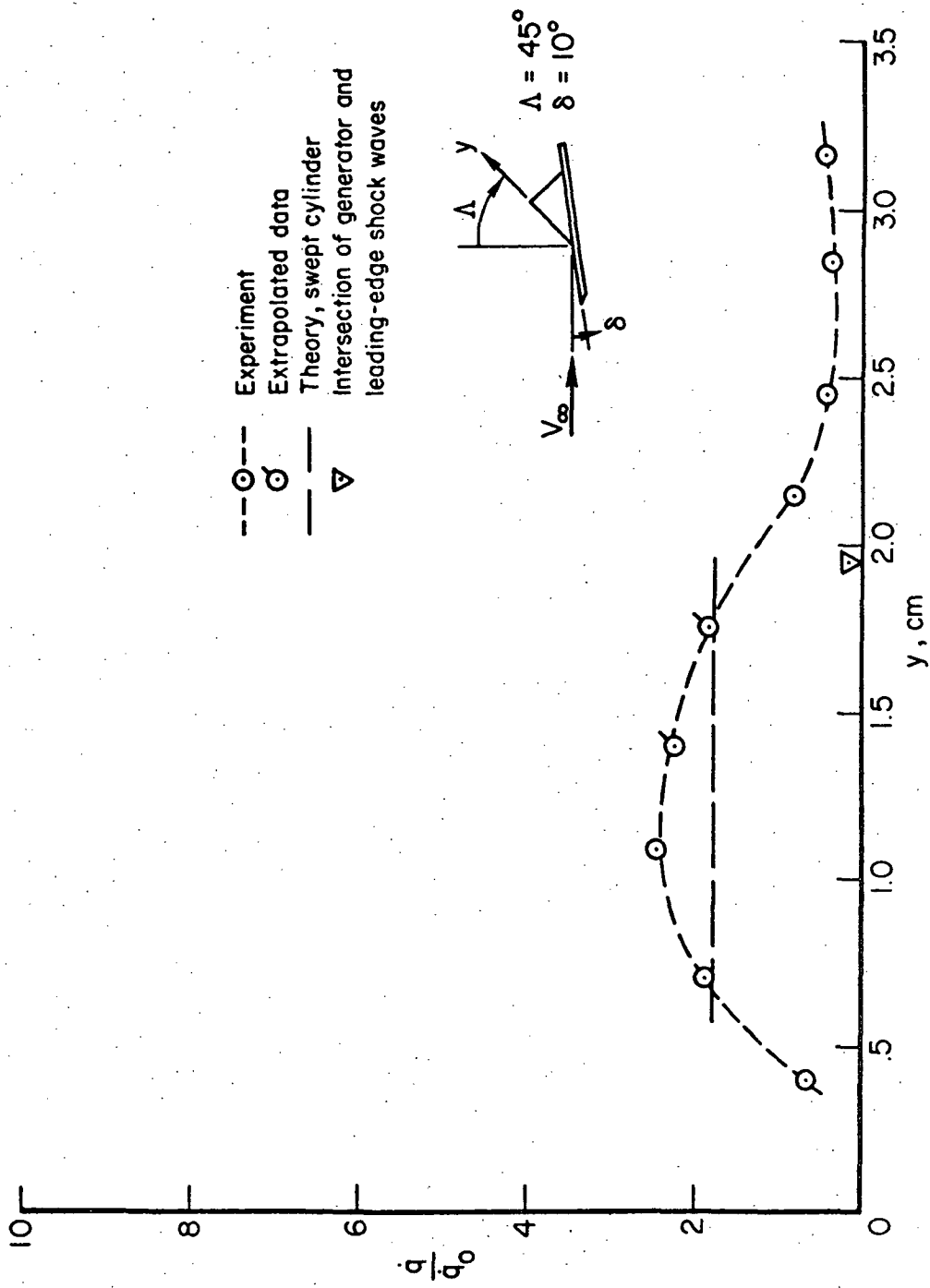


Figure C-4. SPANWISE HEAT-TRANSFER DISTRIBUTIONS ON THE STAGNATION LINE OF THE LEADING EDGE FOR $\Delta = 45^\circ$



(b) $\delta = 10^\circ$

Figure C-4. SPANWISE HEAT-TRANSFER DISTRIBUTIONS ON THE STAGNATION LINE OF THE LEADING EDGE FOR $\Lambda = 45^\circ$ (Concluded)

HEAT-TRANSFER MEASUREMENTS ON A FLAT PLATE AND
ATTACHED FINS AT MACH NUMBERS OF 3.51 AND 4.44

By Earl A. Price, Paul W. Howard,
and Robert L. Stallings, Jr.

SYMBOLS

- b = leading edge span
- d = diameter of leading edge
- h = heat transfer coefficient
- h_o = experimental heat transfer coefficient on plate (or fin) with plate (or fin) only
- h_s = heat transfer coefficient on stagnation line of leading edge
- (hc)s = heat transfer coefficient on stagnation line of leading edge with conduction correction
- h_L = theoretical stagnation line heat transfer coefficient for laminar flow on infinite cylinder
- l = chord length of leading edge (Figure D-1)
- M_∞ = free stream Mach number
- r = longitudinal distance on flat plate from axis of symmetry of leading edge (Figure D-1)
- R = free stream Reynolds number per foot
- S = surface distance from stagnation line of leading edge (Figure D-1)
- X = distance from leading edge of plate (Figure D-1)
- X_c = longitudinal distance (Figure D-1)
- y = distance from center line of plate (Figure D-1)
- z = perpendicular distance from plate (Figure D-1)
- δ = boundary layer thickness
- Λ = sweep angle

SUMMARY

Heating distributions have been obtained on three fixed-sweep fins ($\Lambda_{\infty} = 12.87^{\circ}$) of different diameters partially submerged in a turbulent boundary layer, as well as on the flat plate surface adjacent to these fins. Heating rates have also been obtained on a flat plate adjacent to a fin at sweep angles varying from 0° to 69° . Two Mach numbers were used in the test (3.51 and 4.44) and the Reynolds number (per foot) range was $2.5 \times 10^6 - 4.2 \times 10^6$. Test configurations are shown in Figure D-1 and results are summarized as follows.

The heating rates obtained on the leading edge of the fins outboard of the sidewall boundary-layer effects are in good agreement with laminar theory. The maximum stagnation-line values obtained in the region subjected to the flow of the turbulent sidewall boundary layer are in good agreement with turbulent theory (Figure D-2).

The chordwise heating distributions on the fixed-sweep fins are shown in Figure D-3.

The ratio of heat-transfer coefficients obtained on the center line of the flat plate with the fins mounted to those obtained on the flat plate alone, h/h_0 , upstream of the stagnation line of the fin investigated tends to fall on a single general curve when plotted against the distance from the center line of the fin leading edge in diameters, r/d (Figure D-4). In general, $h/h_0 \approx 1$ for $r/d > 2.5$ and increases asymptotically, within the span of instrumentation, as the fin leading edge is approached. The correlation of data obtained from a 0.155-inch and a 6-inch boundary layer, using the parameters r/d and h/h_0 , indicates that boundary-layer thickness has relatively little, if any, effect on the ratio h/h_0 in the interference region. A maximum h/h_0 of 6.5 was recorded in the test.

The heating distributions on the plate in the direction normal to the flow are shown in Figure D-5.

The general heating distributions on the plate are shown in Figures D-6, D-7 and D-8. In general, increasing sweep resulted in a decrease in both the area affected by interference on the flat plate and the magnitude of the heating rates within this interference region. At the high Reynolds number (4.2×10^6), where the boundary layer was turbulent, the maximum measured heating rate nearest the fin (upstream of the fin stagnation line) decreases from approximately twice the theoretical turbulent flat-plate value at $\Lambda = 0^\circ$ to the undisturbed value at $\Lambda = 40^\circ$ (Figure D-6). Further increases in sweep had only a slight effect on the heating distribution within the entire interference region. At the low Reynolds number (2.5×10^6), the boundary layer remained laminar outside the fin interference region. However, within the interference region the heating rates at the lower sweep angles were of approximately the same magnitude as those obtained at the high Reynolds number, indicating the transitional or turbulent flow (Figure D-8). Due to the apparent transitional flow in this region, the effects of sweep are significant on the flat-plate heating rates in the vicinity of the fin throughout the tested range of sweep.

COMPARISON WITH MSFC BOOSTER REENTRY STUDY

	<u>Price, et. al. (Ref 8)</u>	<u>MSFC Booster Fuselage/ Wing Juncture (Angle of Attack = 12.5°)</u>
M_∞	3.51, 4.44	3 - 6
Diameter of Leading Edge, d (ft)	0.72/12 - 3.4/12	1*
$R_{\infty,d}$	$25 \times 10^5 - 42 \times 10^5$	$1 \times 10^5 - 14 \times 10^5$
Λ (degrees)	0 - 69	52
Max h/h_o		
<u>Fin</u>	1.5 ($\Lambda = 12.87^\circ$, and $d = 3.5$ inches, Figure D-2)	
<u>Plate</u>	1 ($\Lambda = 50^\circ$ and 60° , and turbulent boundary layer, Figure D-6)	
	4 ($\Lambda = 50^\circ$ and 60° ; and laminar boundary layer, Figure D-8)	

*Assumed wing leading edge diameter

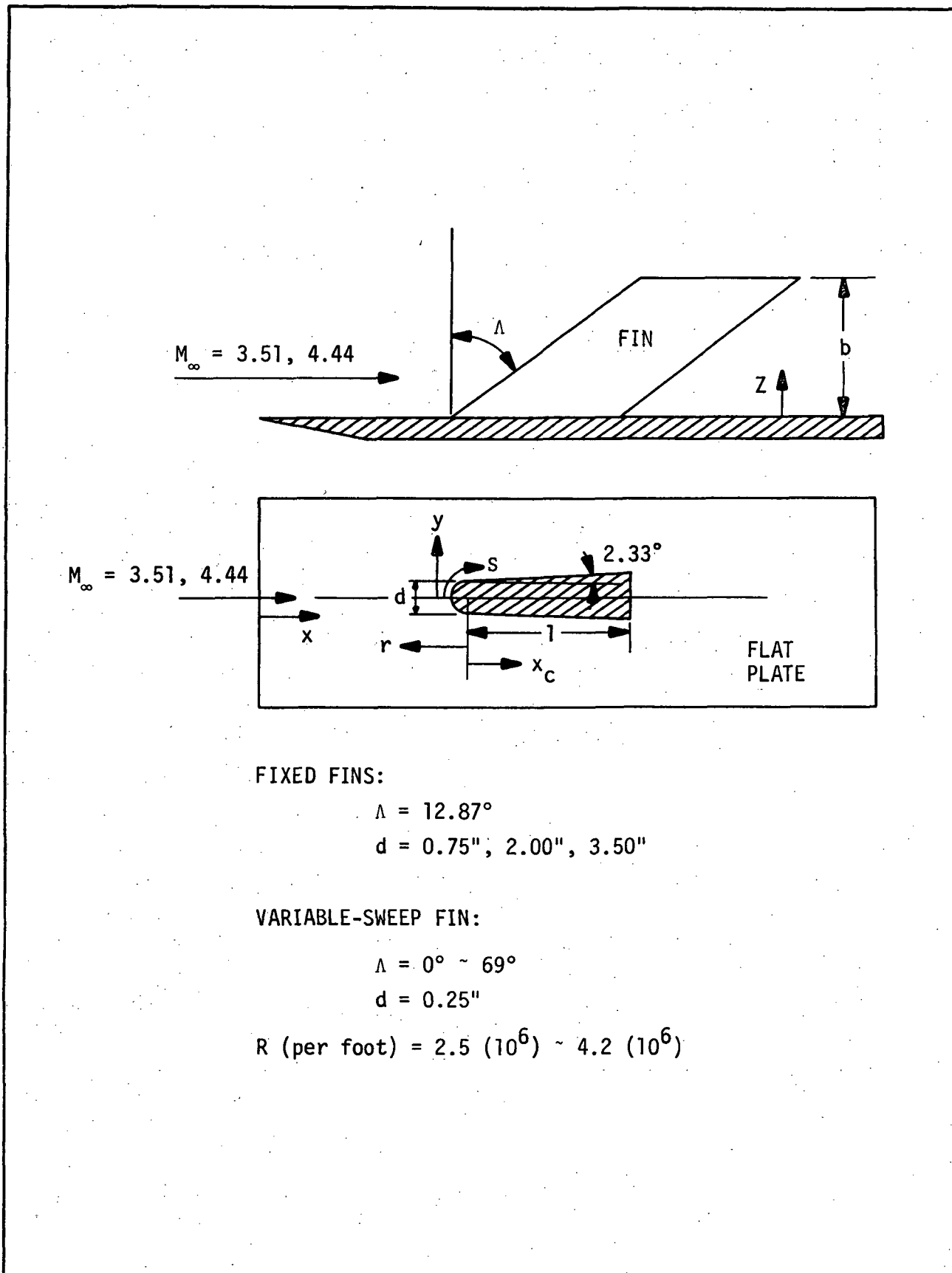


Figure D-1. TEST CONFIGURATIONS

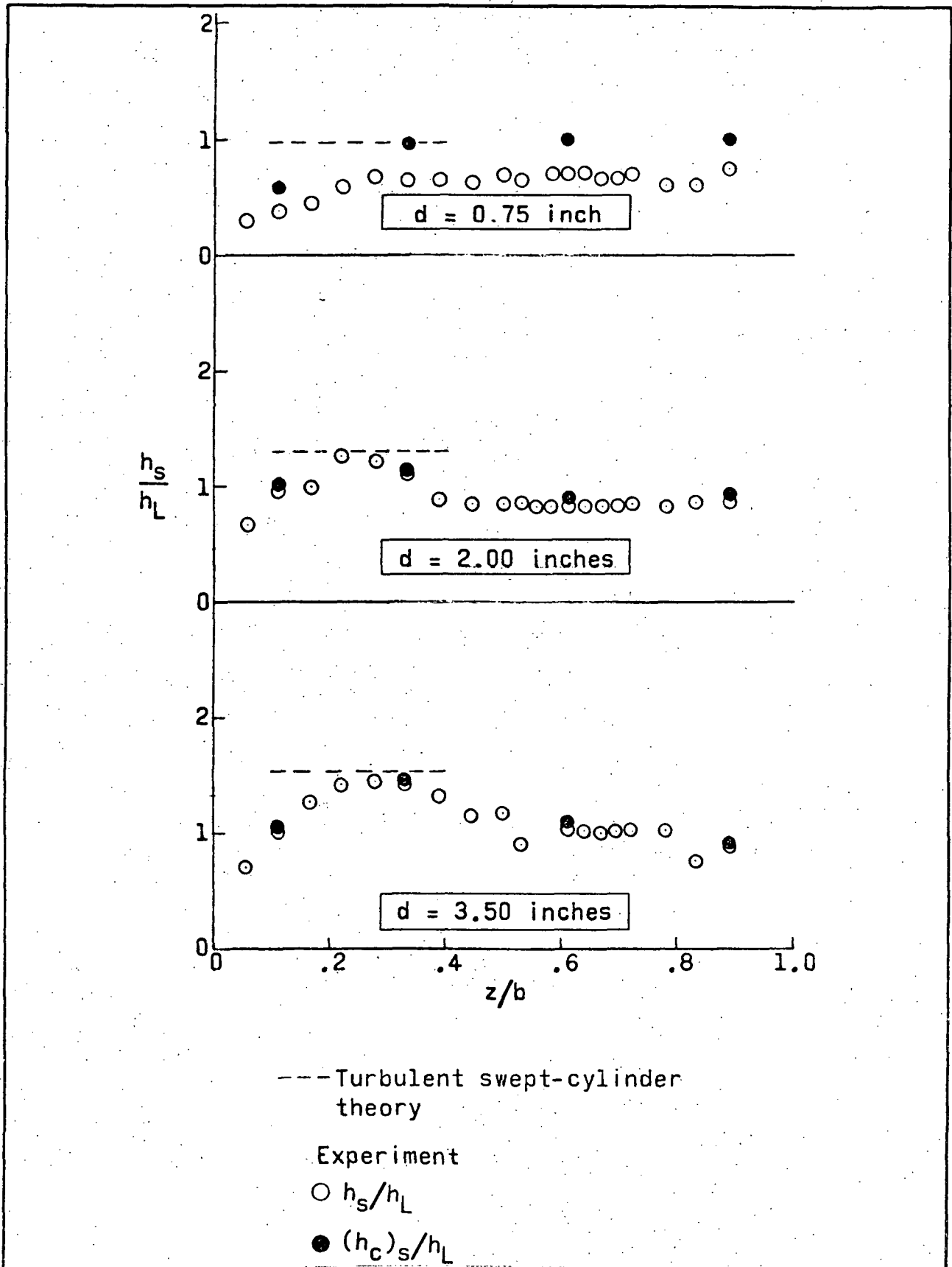


Figure D-2. EFFECT OF LEADING-EDGE DIAMETER ON STAGNATION-LINE HEATING DISTRIBUTION OF FIXED-SWEEP FINS. $M = 3.51$; $R = 4.2 \times 10^6$; $\Lambda = 12.87^\circ$

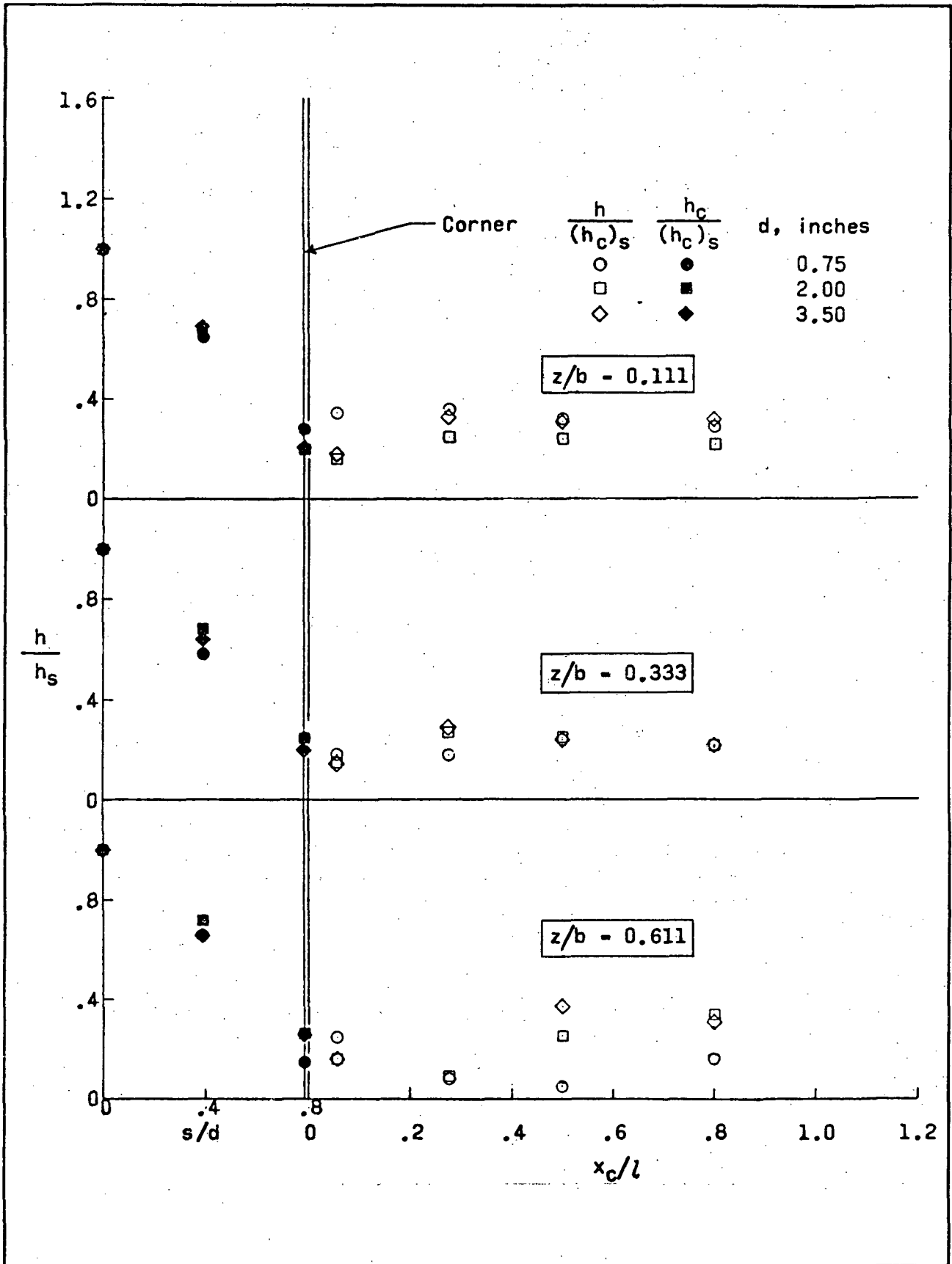


Figure D-3. CHORDWISE HEATING DISTRIBUTION ON FIXED-SWEEP FINS
 $M = 3.51$; $R \approx 4.2 \times 10^6$

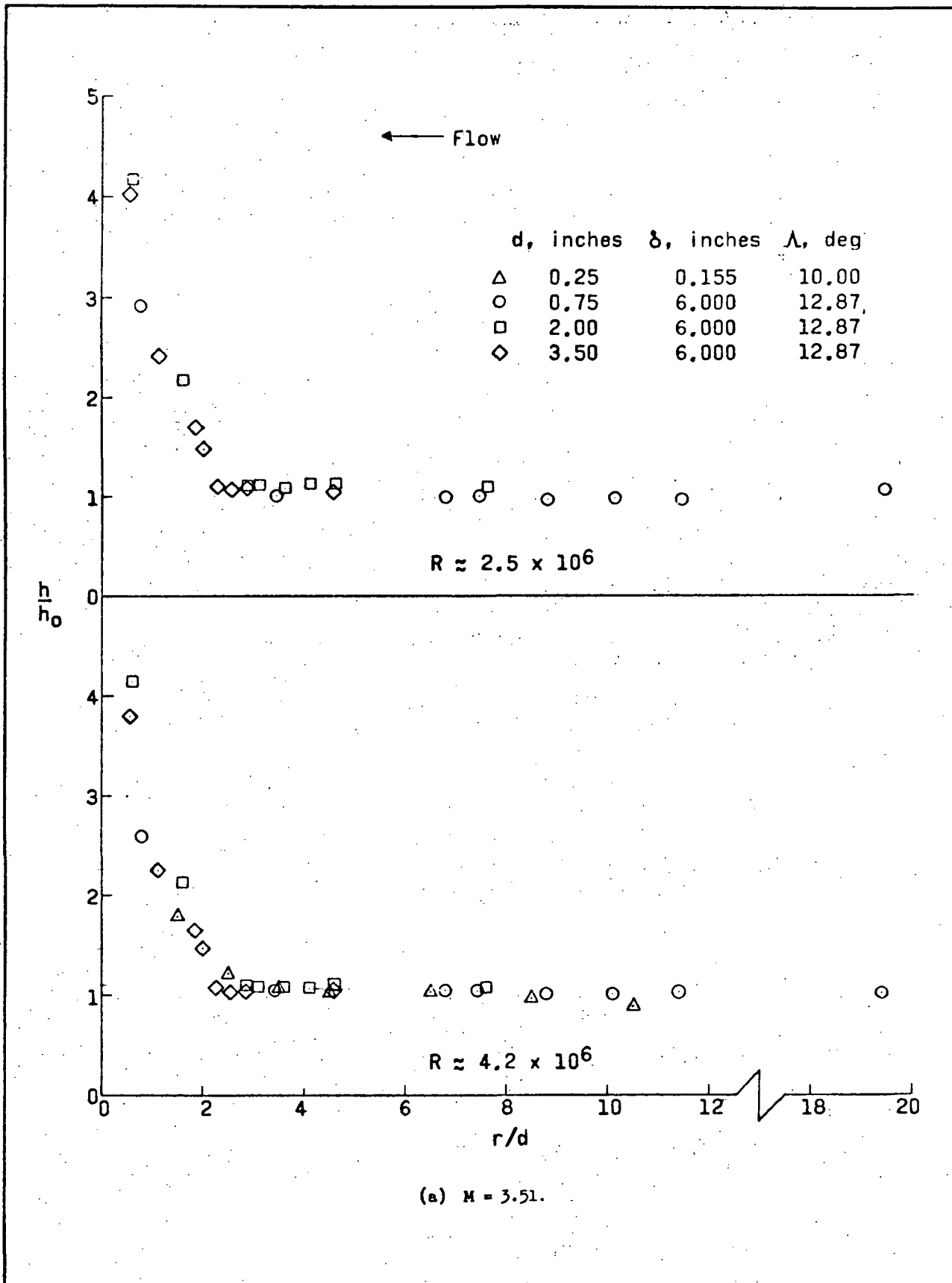


Figure D-4. EFFECT OF FIN LEADING-EDGE DIAMETER AND BOUNDARY-LAYER THICKNESS ON ADJACENT-SURFACE HEATING DISTRIBUTION UPSTREAM OF FIN STAGNATION LINE

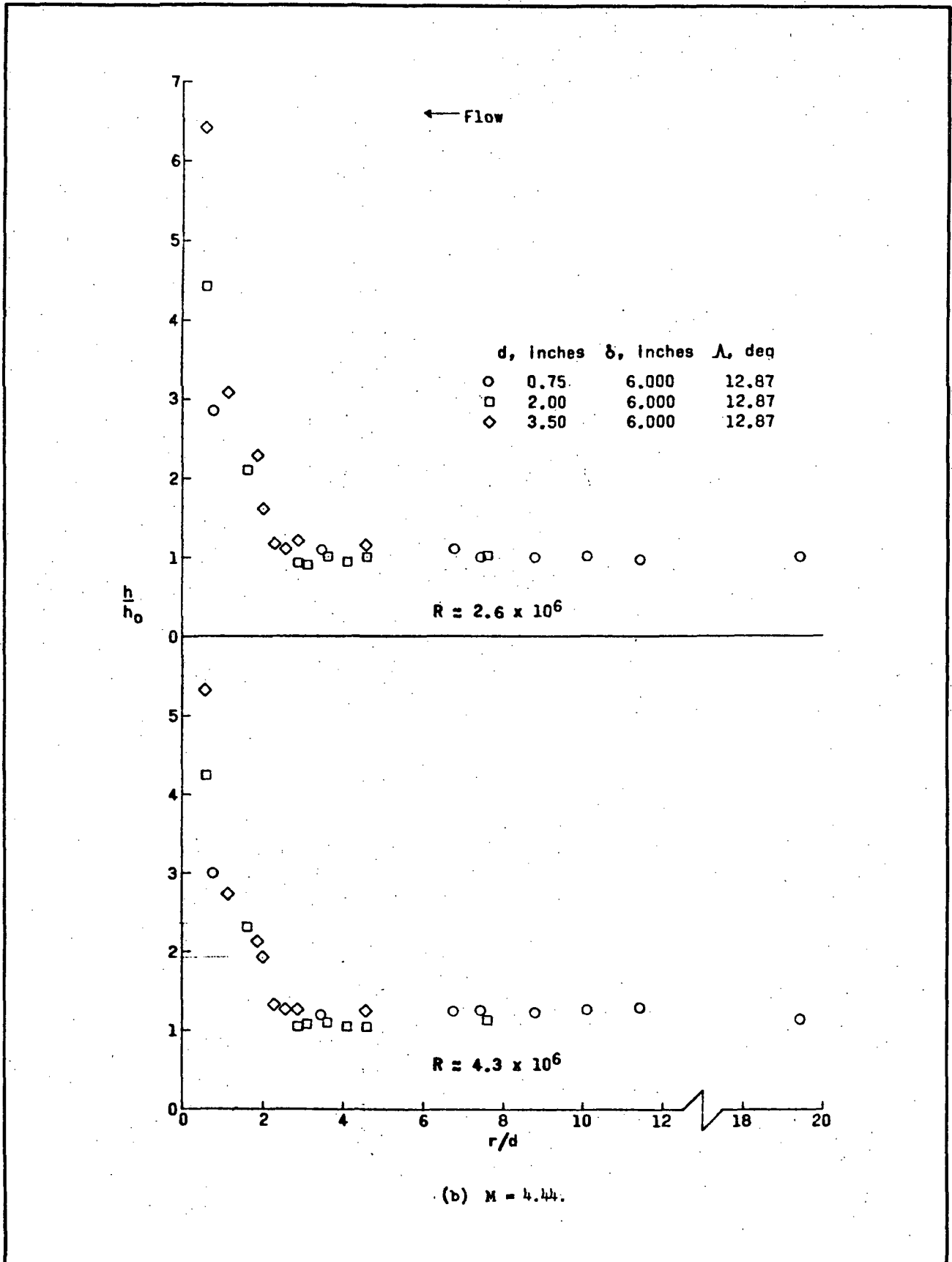


Figure D-4. EFFECT OF FIN LEADING-EDGE DIAMETER AND BOUNDARY-LAYER THICKNESS ON ADJACENT-SURFACE HEATING DISTRIBUTION UPSTREAM OF FIN STAGNATION LINE (Concluded)

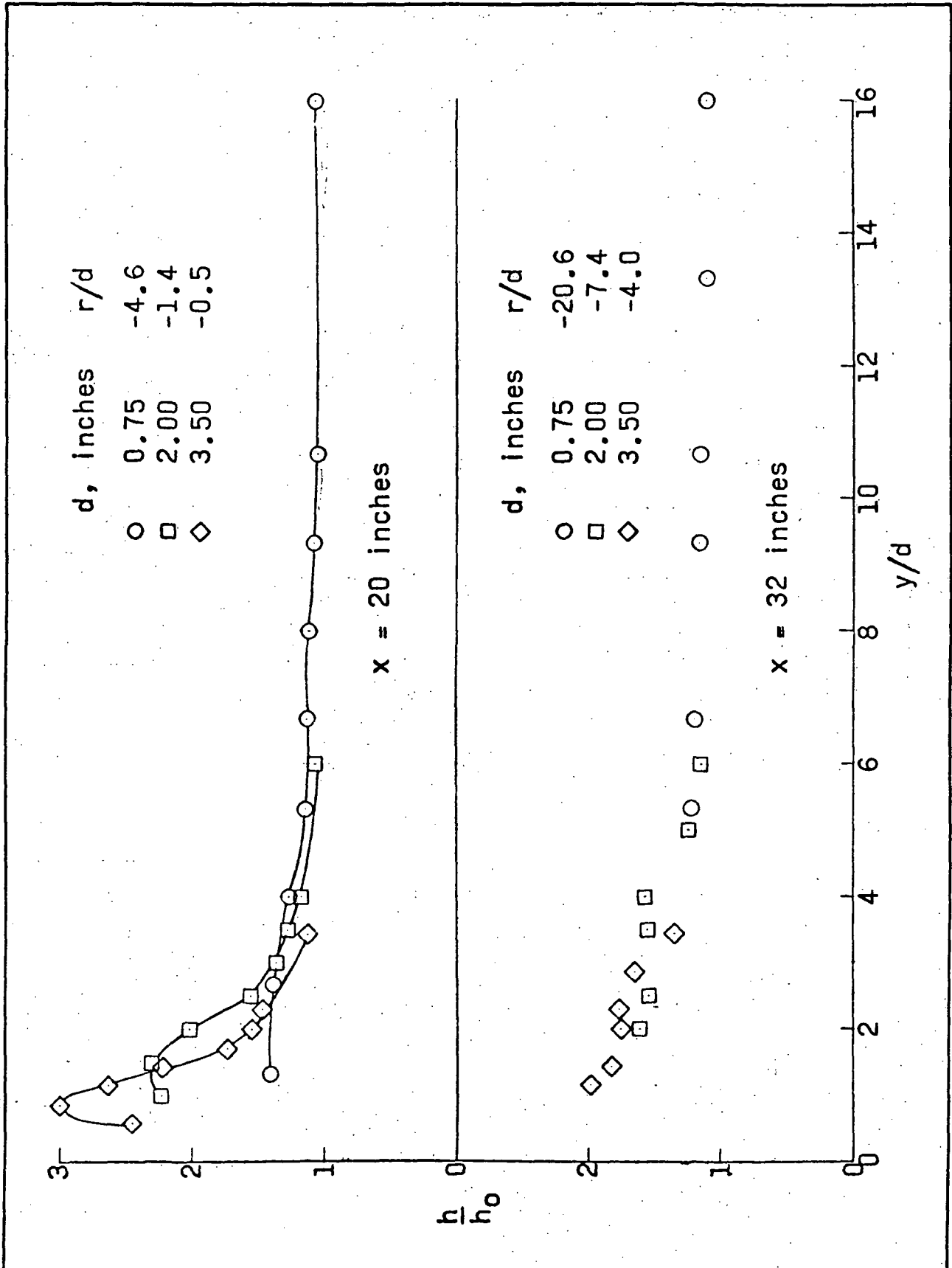


Figure D-5. EFFECT OF FIN LEADING-EDGE DIAMETER ON FLAT-PLATE HEATING DISTRIBUTION NORMAL TO FIN PLANE OF SYMMETRY DOWNSTREAM OF FIN LEADING EDGE. $M = 3.51$; $R \approx 4.2 \times 10^6$; $\delta = 6$ inches; $\Lambda = 12.87^\circ$.

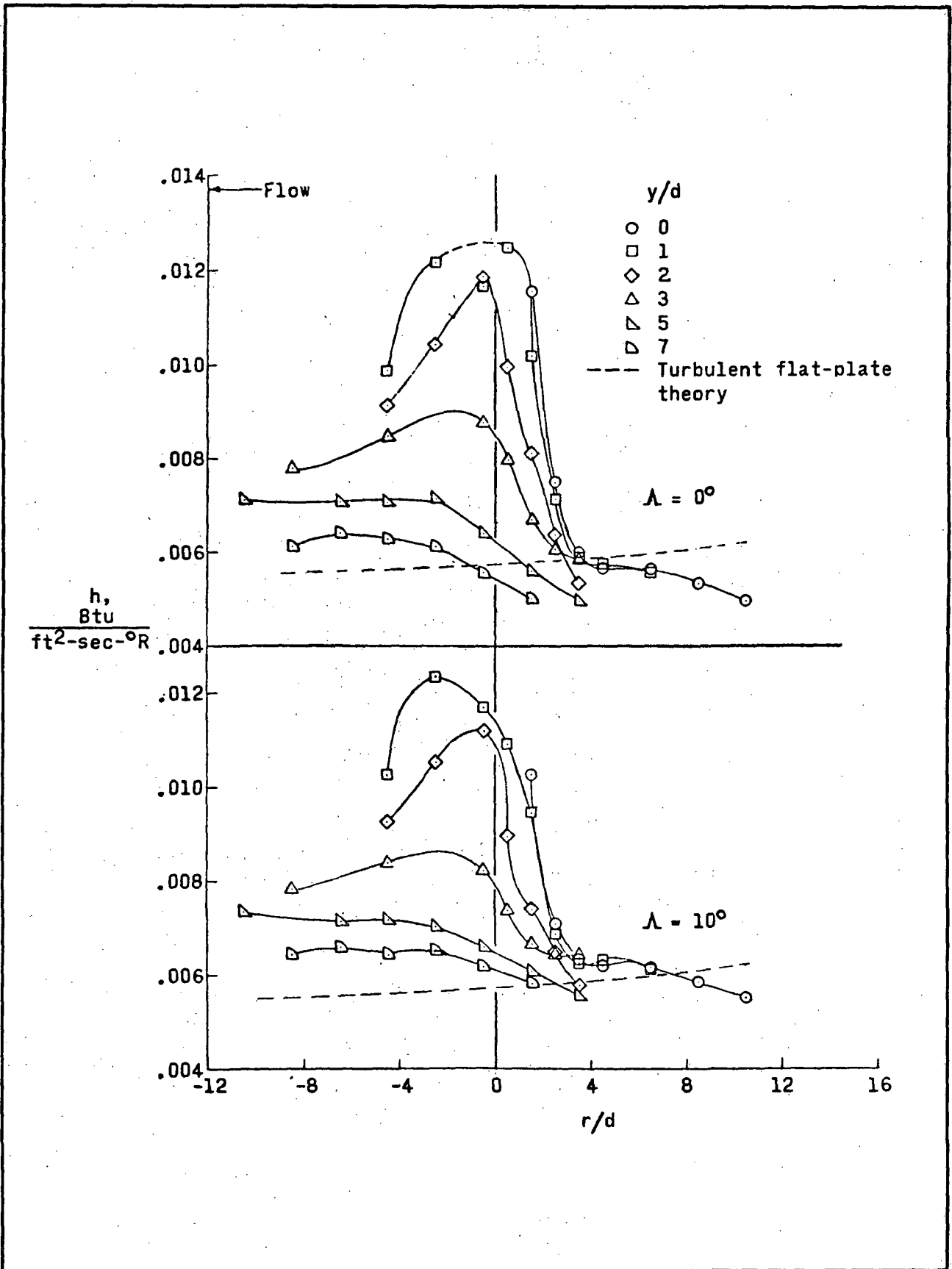


Figure D-6. HEATING DISTRIBUTION ON FLAT PLATE IN VICINITY OF VARIABLE-SWEEP FIN FOR RANGE OF SWEEP FROM 0° TO 69° . $M = 3.51$; $R \approx 4.2 \times 10^6$; $\delta = 0.155$ INCH.

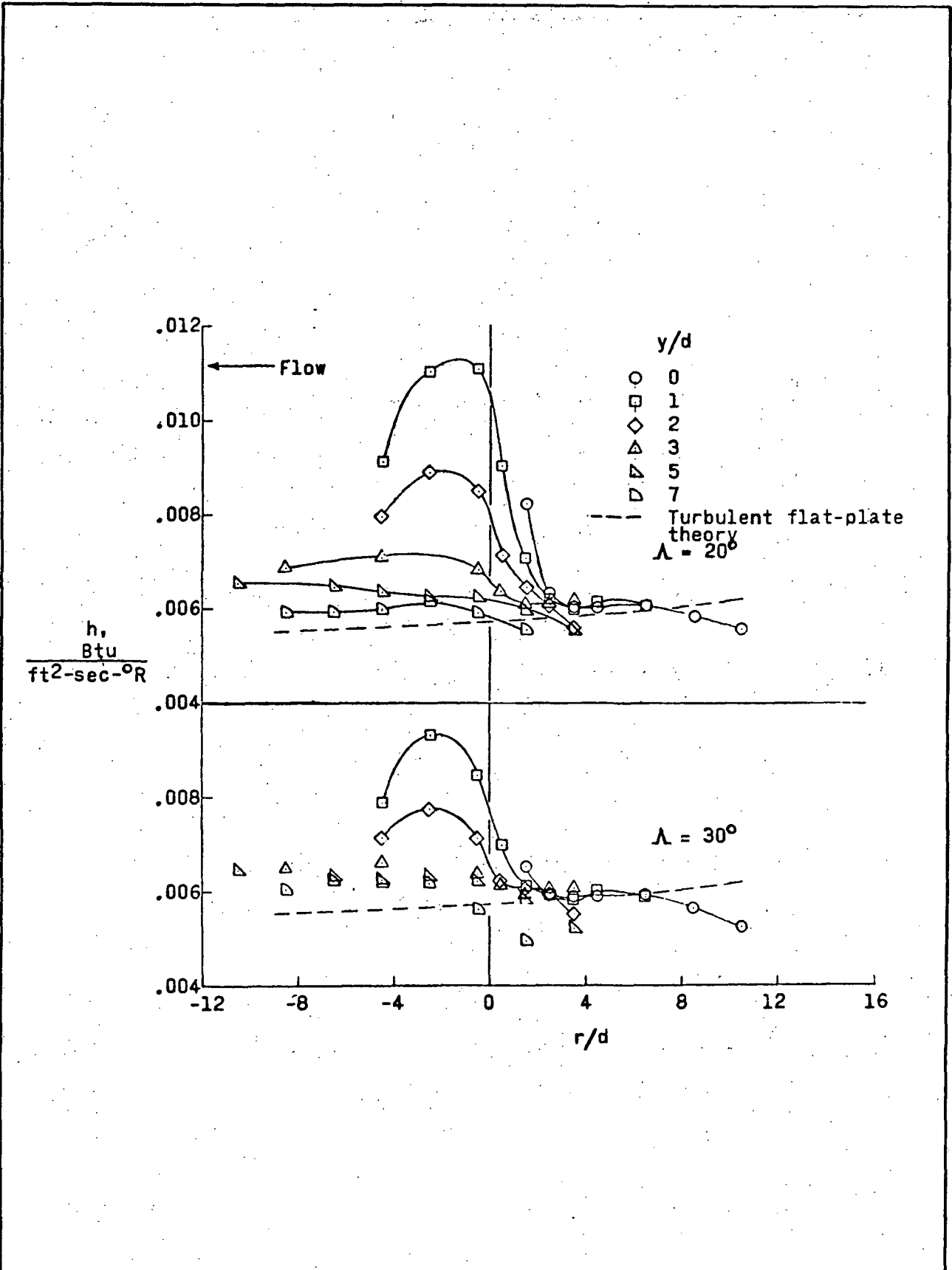


Figure D-6. HEATING DISTRIBUTION ON FLAT PLATE IN VICINITY OF VARIABLE-SWEEP FIN FOR RANGE OF SWEEP FROM 0° TO 69°. $M = 3.51$; $R \approx 4.2 \times 10^6$; $\delta = 0.155$ INCH. (Continued)

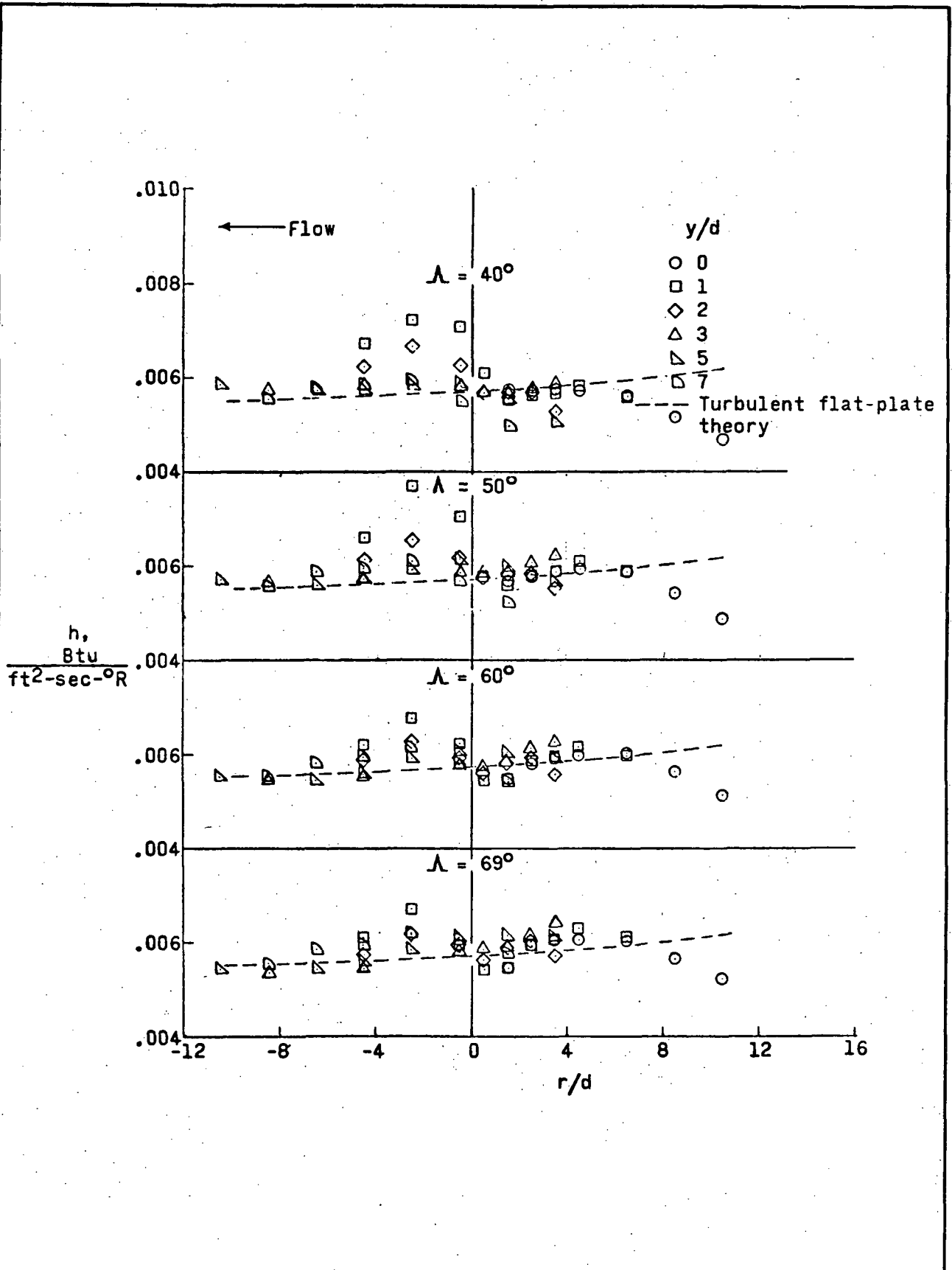


Figure D-6. HEATING DISTRIBUTION ON FLAT PLATE IN VICINITY OF VARIABLE-SWEEP FIN FOR RANGE OF SWEEP FROM 0° TO 69° . $M = 3.51$; $R \approx 4.2 \times 10^6$; $\delta = 0.155$ INCH. (Concluded)

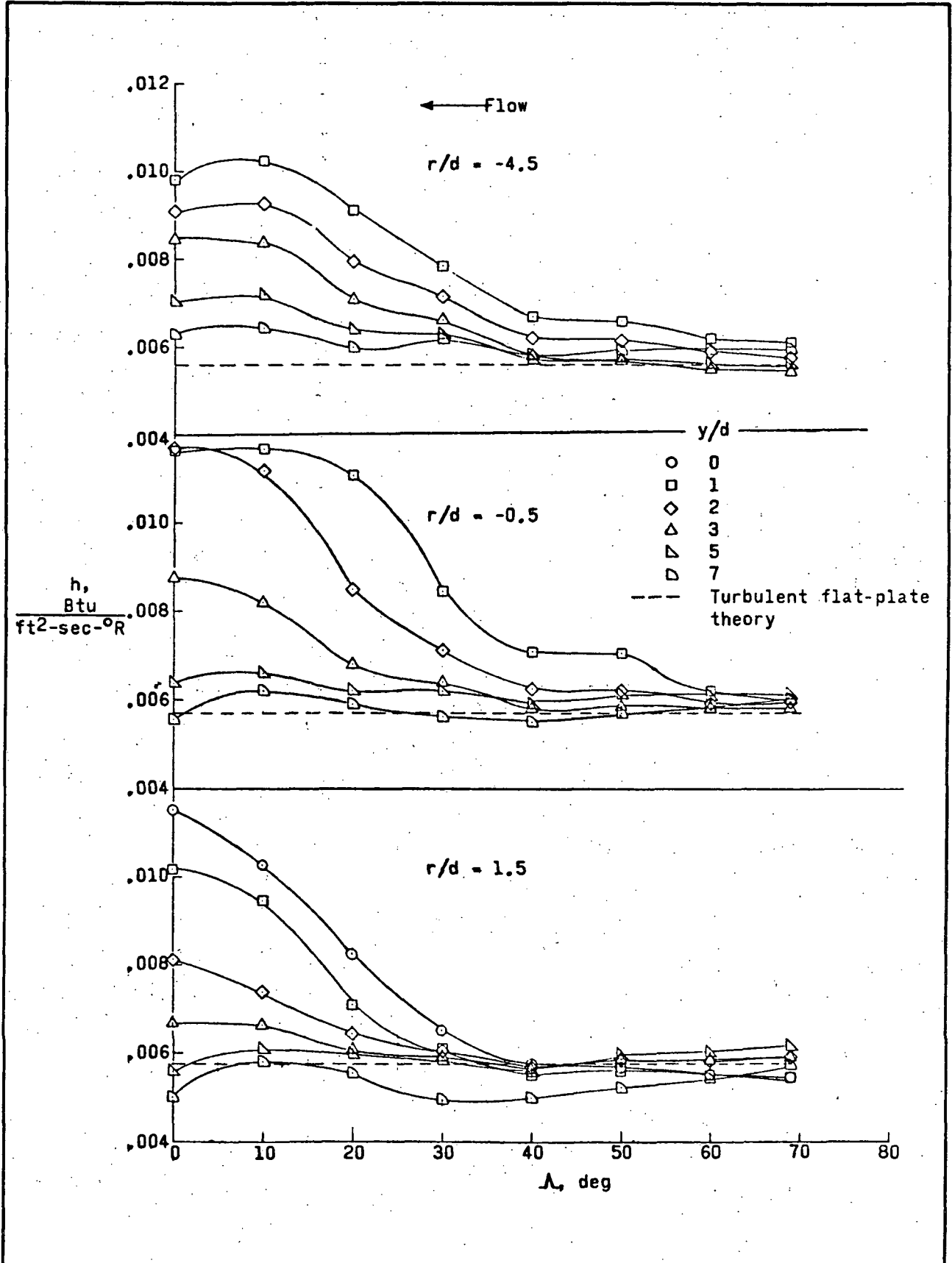


Figure D-7. VARIATION OF HEATING RATES WITH SWEEP ANGLE FOR VARIOUS VALUES OF Y/D AT THREE AXIAL STATIONS. $M = 3.51$; $R \approx 4.2 \times 10^6$; $\delta = 0.155$ INCH.

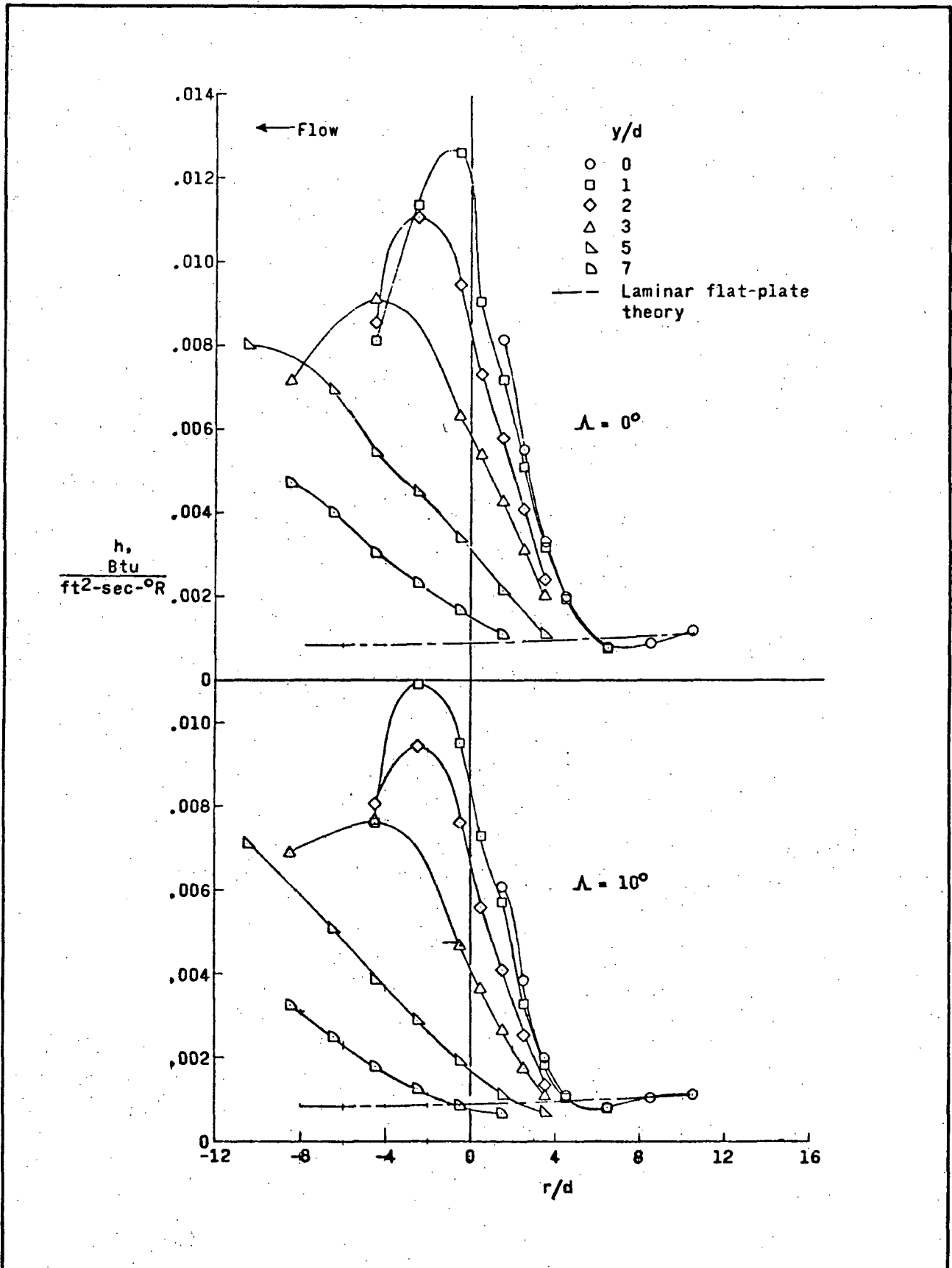


Figure D-8. HEATING DISTRIBUTION ON FLAT PLATE IN VICINITY OF VARIABLE-SWEEP FIN FOR RANGE OF SWEEP FROM 0° TO 69° . $M = 3.51$; $R \approx 2.5 \times 10^6$.

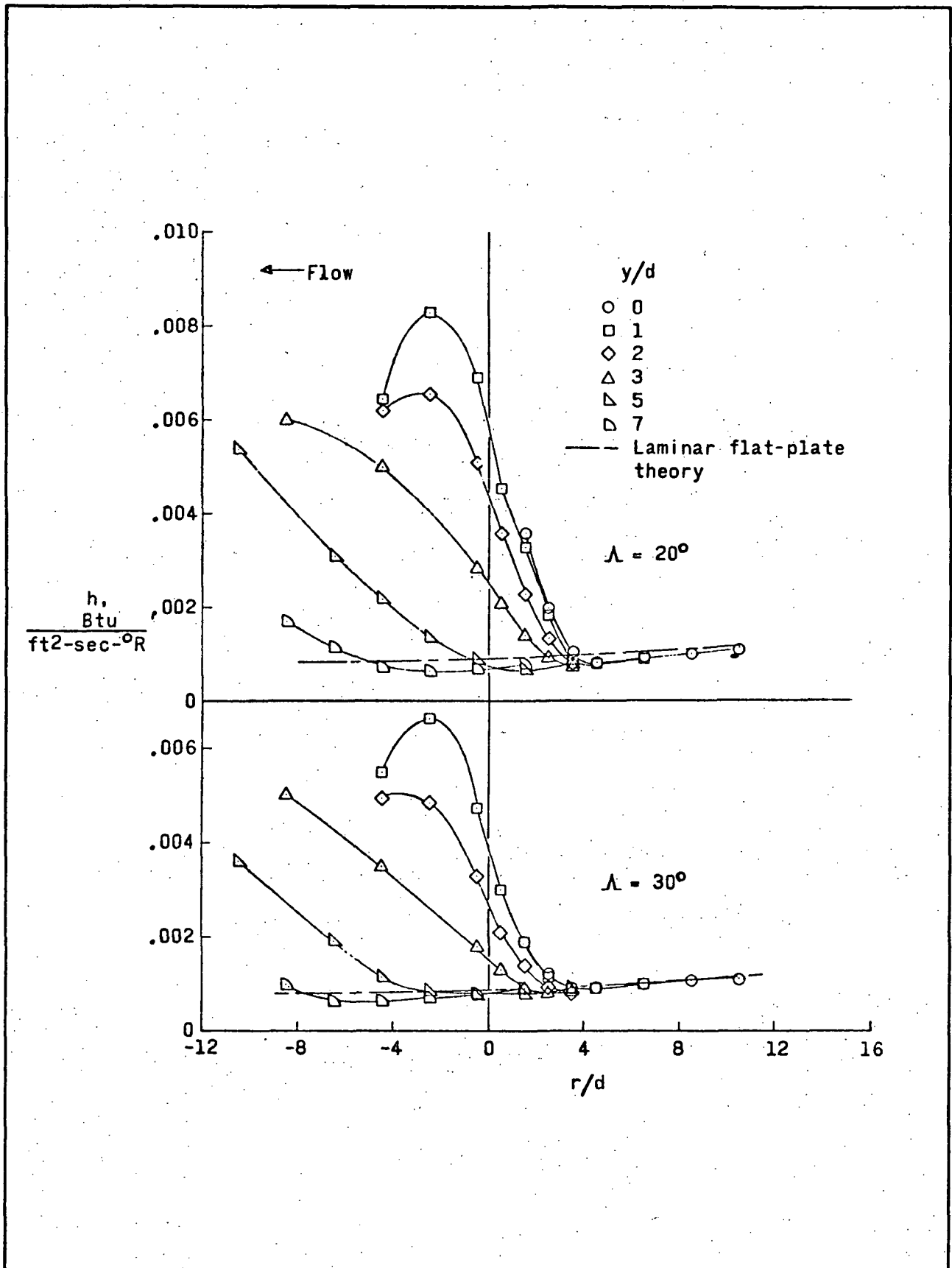


Figure D-8. HEATING DISTRIBUTION ON FLAT PLATE IN VICINITY OF VARIABLE SWEEP FIN FOR RANGE OF SWEEP FROM 0° TO 69° . $M = 3.51$; $R \approx 2.5 \times 10^6$ (Continued)

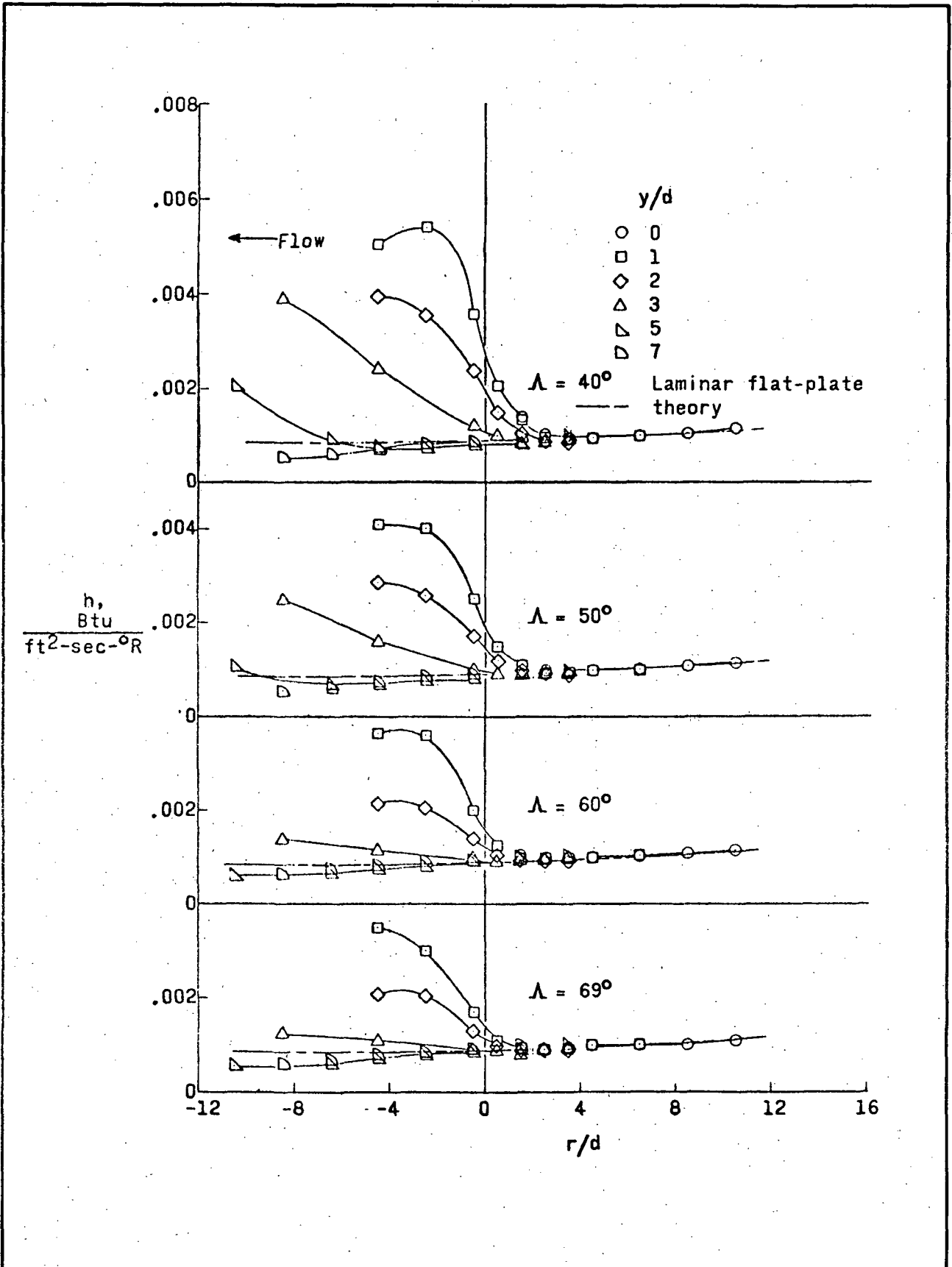


Figure D-8. HEATING DISTRIBUTION ON FLAT PLATE IN VICINITY OF VARIABLE-SWEEP FIN FOR RANGE OF SWEEP FROM 0° TO 69° . $M = 3.51$; $R \approx 2.5 \times 10^6$ (Concluded)

HEAT-TRANSFER AND PRESSURE INVESTIGATION
OF A FIN-PLATE INTERFERENCE MODEL
AT A MACH NUMBER OF 6

By Robert A. Jones

NASA TN D-2028
July 1964

SYMBOLS

- h = heat transfer coefficient
- $h_{no\ fin}$ = measured local heat transfer coefficient on plate without fin
- $h_{\Lambda=0}$ = theoretical heat transfer coefficient at stagnation line on an infinite unswept cylinder at free stream conditions
- l = length of plate
- M_{∞} = free stream Mach number
- p = local surface pressure
- $P_{no\ fin}$ = local surface pressure on plate without fin
- r = radius of fin leading edge
- $R_{D,\infty}$ = Reynolds number based on free stream conditions and fin diameter
- S = surface distance from plane of symmetry of fin leading edge (Figure E-1)
- X = distance from leading edge of plate
- Y = distance along stagnation line of fin measured from plate-fin junction
- β = yaw angle of fin
- Λ = sweep angle

SUMMARY

A 60° swept cylindrical-leading-edge fin mounted on a sharp flat plate was investigated at a Mach number of 6 over a range of Reynolds numbers, based on free-stream conditions and fin leading-edge diameter, from 0.062×10^6 to 0.77×10^6 . The plate was maintained at zero angle of attack and the yaw angle of the fin was varied from 0° to 30°. A relatively weak shock wave which originated at the leading edge of the plate impinged on the leading edge of the fin. Sketch of the model is shown in Figure E-1. Heat-transfer rates and pressures were measured on both the plate and the fin. The measured data on the fin and plate are compared with values calculated from laminar and turbulent theories for an infinitely long 60° swept cylinder and undisturbed plate. Results are summarized below.

The heat transfer distributions on the fin surface are shown in Figures E-2, E-3, and E-4. h is the local experimental heat transfer coefficient and $h_{\Lambda} = 0$ is the theoretical laminar heat transfer coefficient for the stagnation line of an unswept cylinder at free stream conditions.

Tests indicated that the flow over a fin leading edge with no interference was laminar for the Reynolds number range used in the tests. The curves in Figure E-2 represent a theoretical laminar heat transfer coefficient distribution on the swept cylinder without interference.

The shock-wave impingement on the leading edge of the fin, as well as other fin-plate interference effects, caused increases in heat transfer to the leading edge of the fin of approximately one to three times the calculated laminar values (the ratios of data points to the curve value at $S/R = 0$ in Figure E-2), depending on the Reynolds number. The increase was largest at the highest Reynolds number.

Comparisons of the data with values calculated by assuming a turbulent boundary layer indicated that the primary effect of the shock-wave impingement, as well as other inference effects, was to promote transition to turbulent flow and that calculated values based on the assumption of turbulent flow might

be used as an upper limit for estimating the heat-transfer rates to the fin leading edge.

Pressures and heat-transfer coefficients higher than flat-plate theoretical values were measured on the plate (Figure E-5). The highest heat-transfer rates appeared to be for locations near the impingement of the fin shock wave. These high heat-transfer rates occurred at all free-stream Reynolds numbers and the maximum values were considerably above those calculated from turbulent flat-plate theory based on conditions corresponding to the measured local pressure.

COMPARISON WITH MSFC BOOSTER REENTRY STUDY

	<u>Jones (Ref 9)</u>	<u>MSFC Booster Fuselage/ Wing Juncture (Angle of Attack = 12.5°)</u>
M_∞	6	3 - 6
Cylinder Diameter, D(ft)	1.06/12	1*
$R_{\infty, D}$	$0.62 \times 10^5 -$ 7.7×10^5	$1 \times 10^5 - 14 \times 10^5$
Λ	60	52
<u>Max. h (with interference)</u> <u>(without interference)</u>		
<u>Fin</u>	1 (low $R_{\infty, D}$, Figure E-2) 3 (high $R_{\infty, D}$, Figure E-2)	
<u>Plate</u>	8 ($\beta = 15^\circ$, Figure E-5)	

**Assumed wing leading edge diameter*

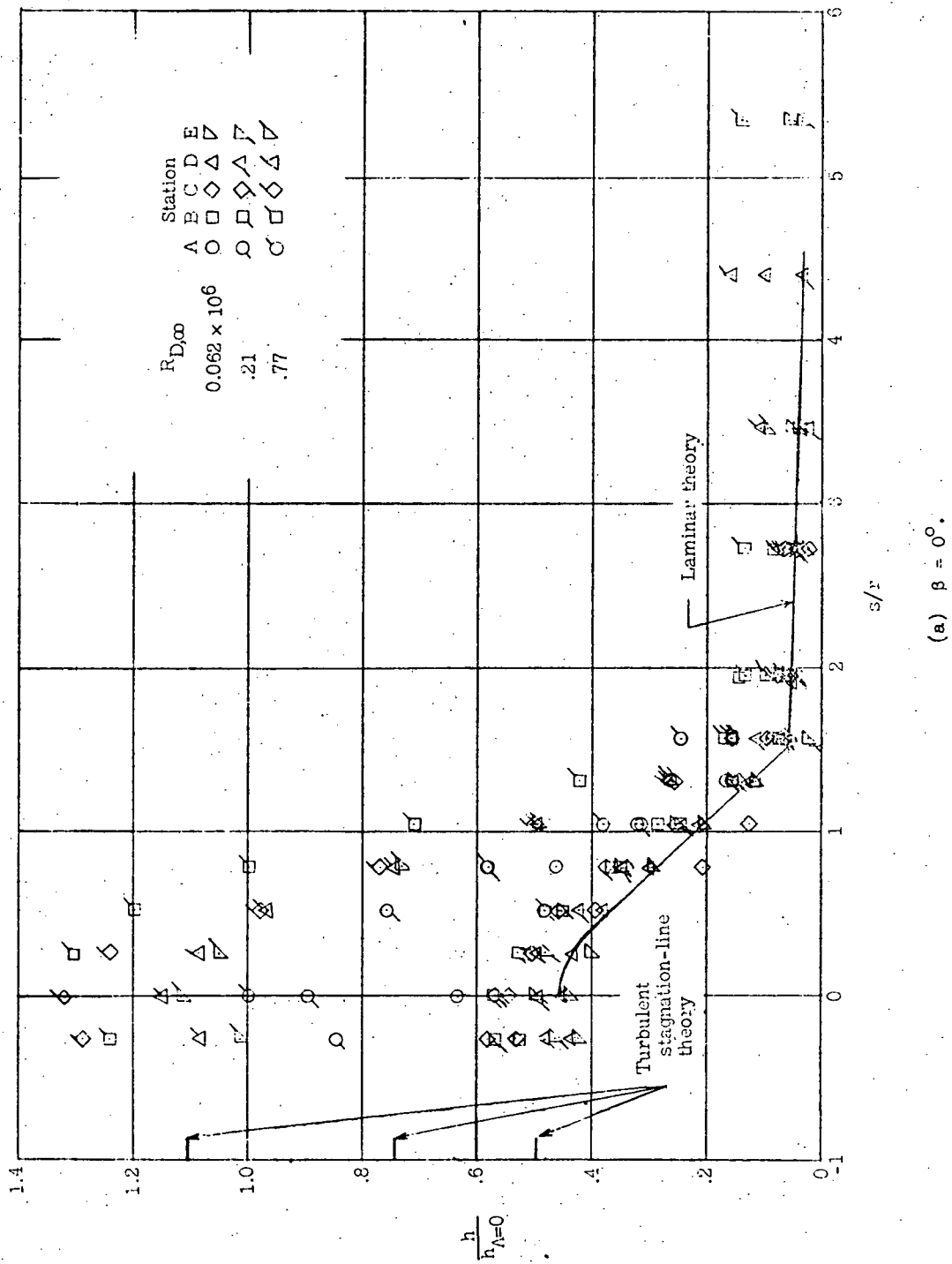
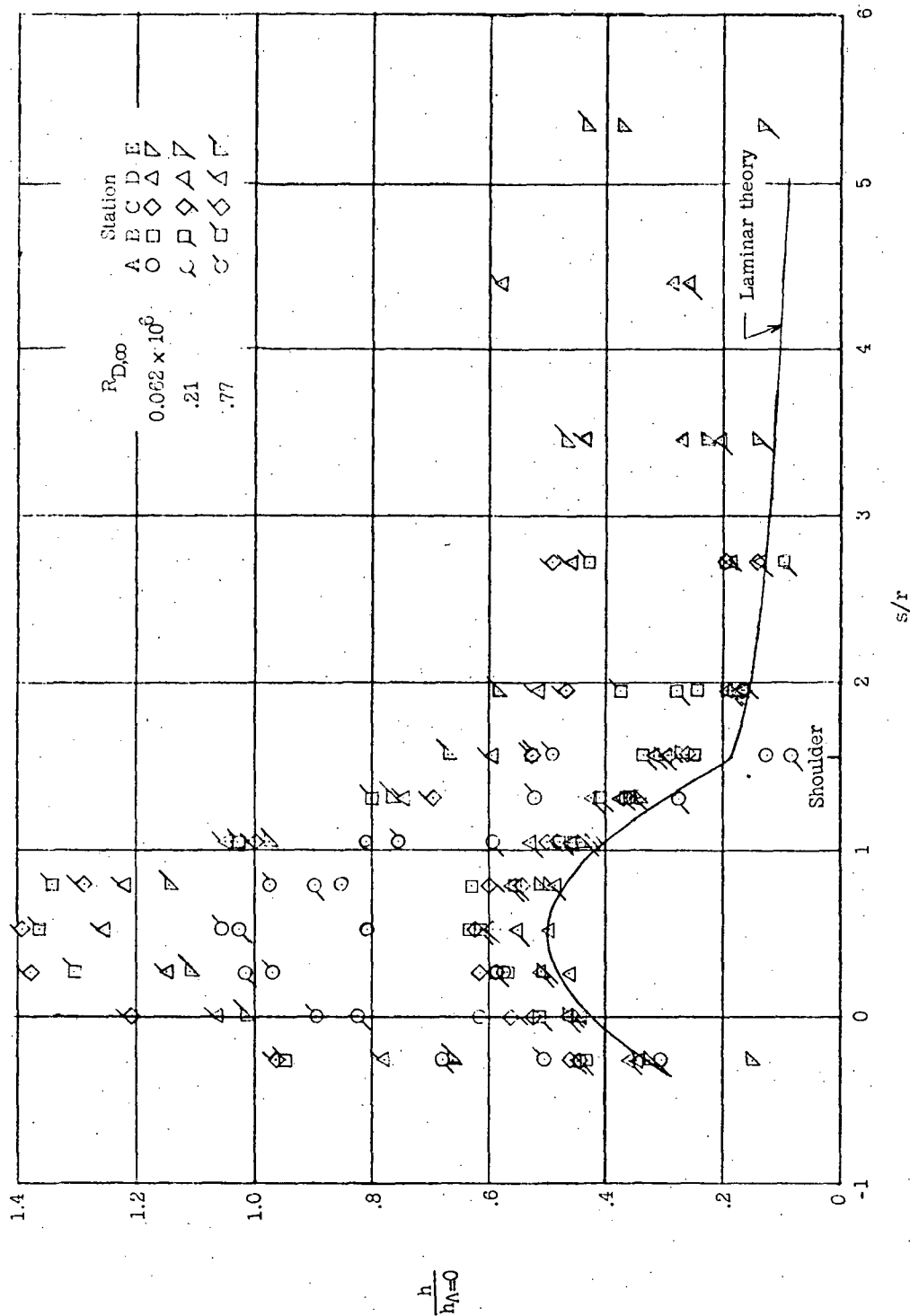


Figure E-2. HEAT-TRANSFER DISTRIBUTION ON FIN (WINDWARD SIDE)



(a) $\beta = 15^\circ$.

Figure E-2. HEAT-TRANSFER DISTRIBUTION ON FIN (WINDWARD SIDE) (Continued)

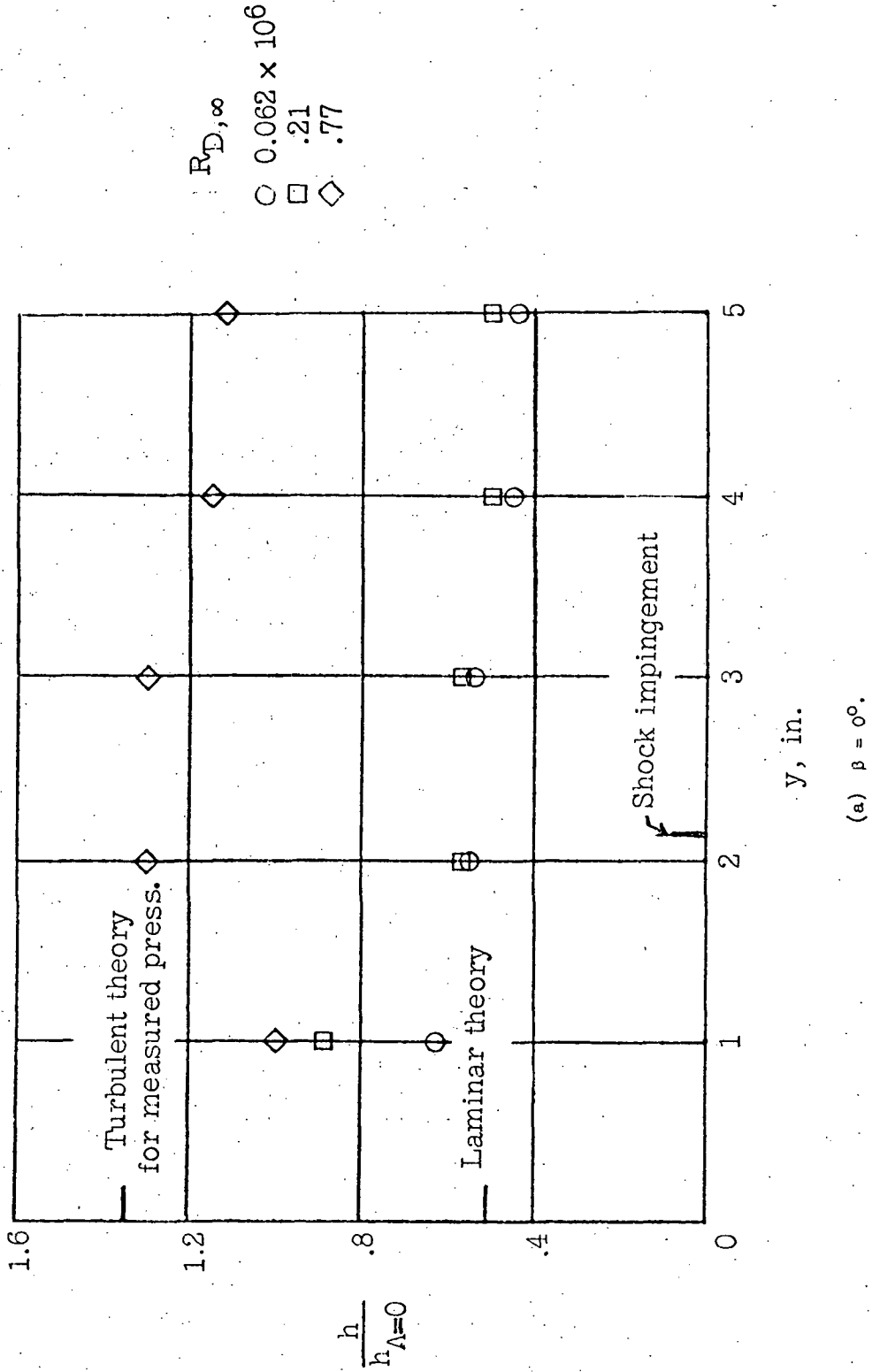
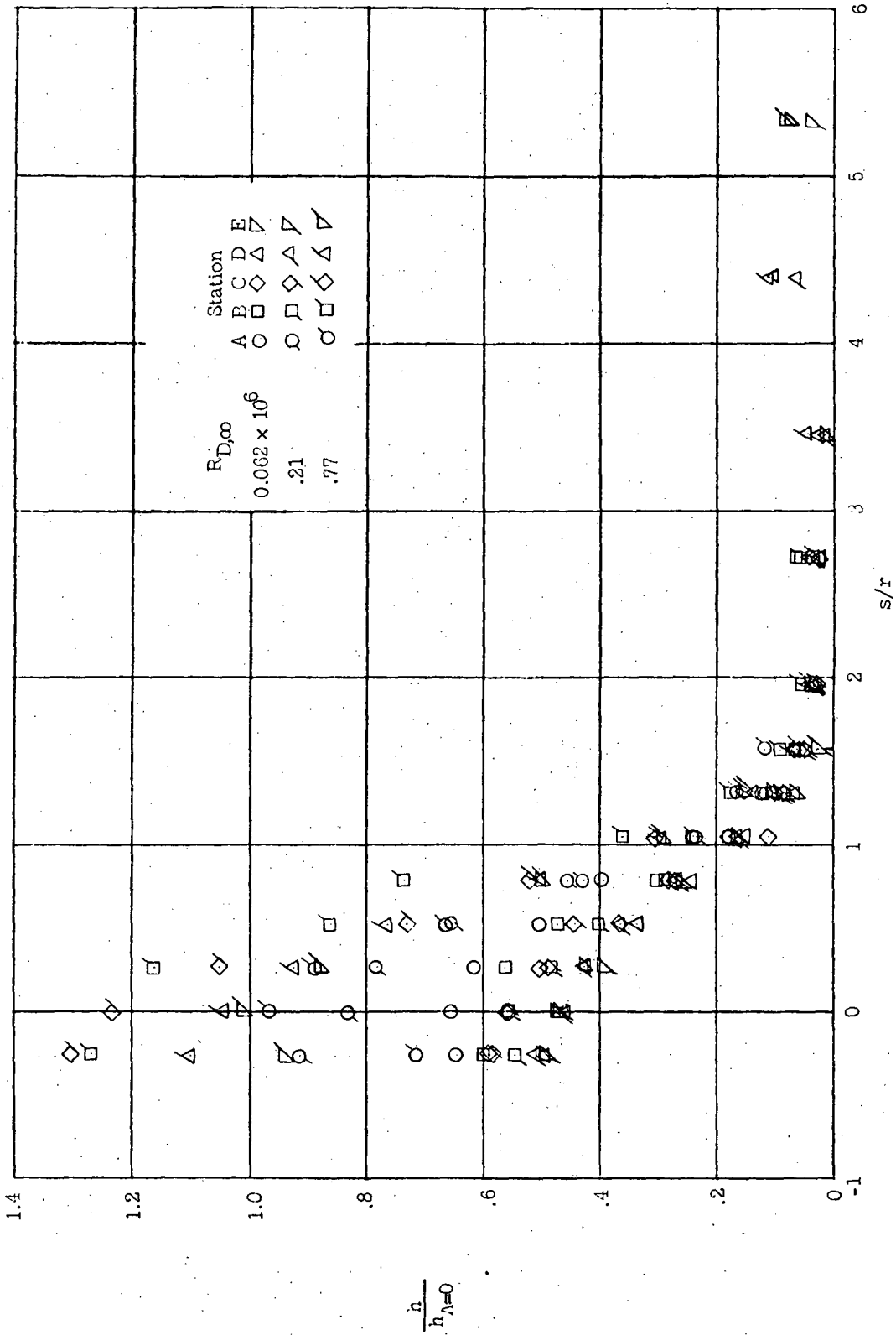


Figure E-3. HEAT-TRANSFER DISTRIBUTION ALONG STAGNATION LINE OF FIN



(a) $\beta = -5^\circ$.

Figure E-4. HEAT-TRANSFER DISTRIBUTION ON FIN (LEEWARD SIDE)

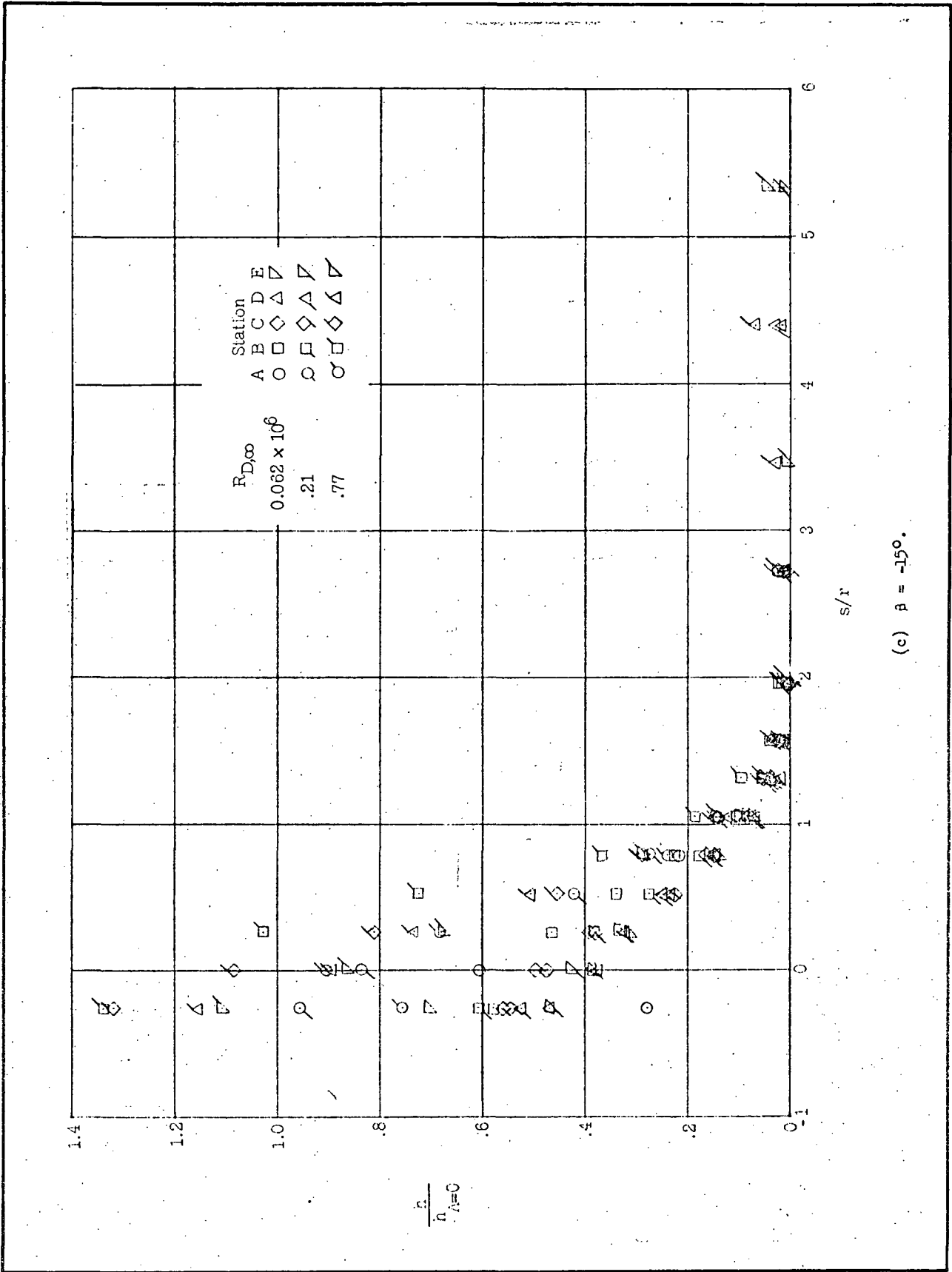
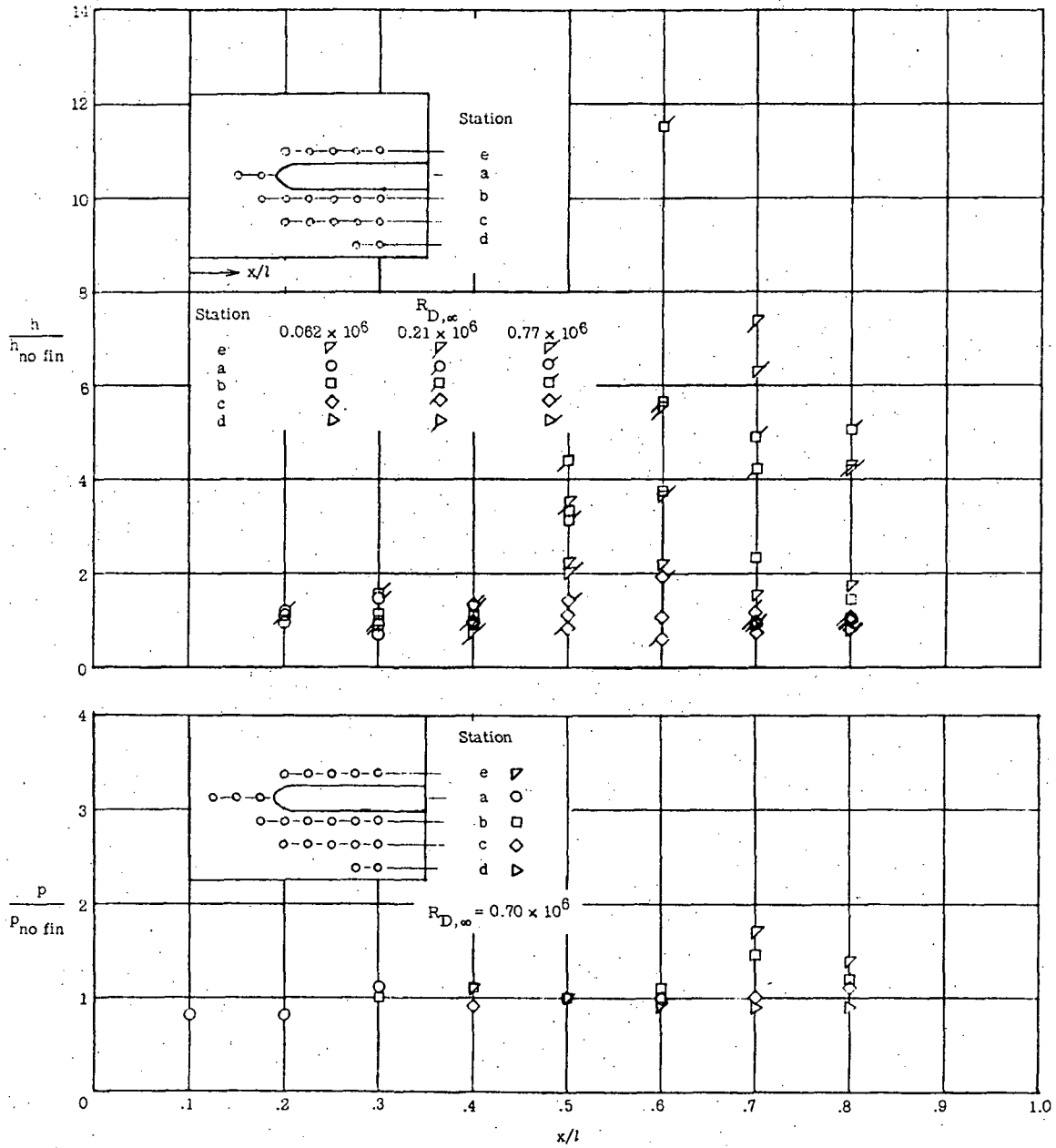
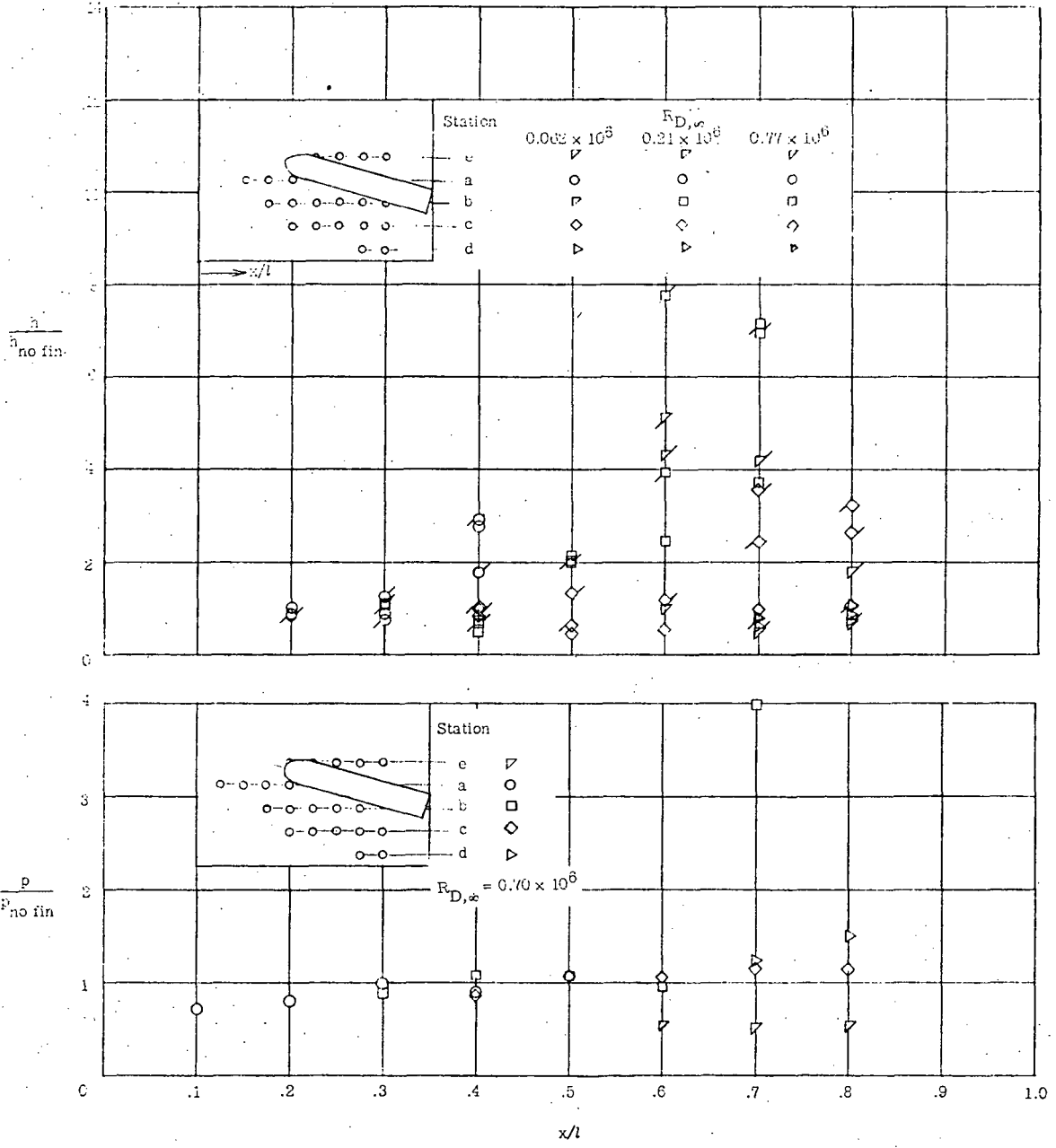


Figure E-4. HEAT-TRANSFER DISTRIBUTION ON FIN (LEEWARD SIDE) (Concluded)



(a) $\beta = 0^\circ$.

Figure E-5. PRESSURE AND HEAT-TRANSFER DISTRIBUTION ON PLATE



(d) $\beta = 15^\circ$.

Figure E-5. PRESSURE AND HEAT-TRANSFER DISTRIBUTION ON PLATE (Continued)

EFFECT OF SHOCK IMPINGEMENT
ON THE DISTRIBUTION OF HEAT-TRANSFER COEFFICIENTS
ON A RIGHT CIRCULAR CYLINDER AT MACH NUMBERS
OF 2.65, 3.51, and 4.44

By Robert A. Newlander

SYMBOLS

- d - diameter of cylinder
- h - measured heat transfer coefficient with protuberance
- h_L - theoretical heat transfer coefficient for laminar flow on cylinder of infinite length
- h_o - measured heat transfer coefficient of flat plate alone
- M - free stream Mach number
- R - Reynolds number per foot
- X - distance along longitudinal axis (Figure 1)
- Y - distance from longitudinal axis (Figure 1)
- Z - vertical distance from flat plate
- δ - boundary layer thickness
- ϕ - circumferential angle

SUMMARY

The heat-transfer distribution on a wedge and cylinder combination mounted on a flat plate has been determined at Mach numbers from 2.65 to 4.44 and Reynolds numbers per foot from 1.27×10^6 to 4.50×10^6 in boundary-layer thicknesses of 6 inches and 0.6 inch. Test model is shown in Figure 1 and the results are summarized as below:

- When an oblique shock and a cylinder bow shock interact, the resulting vortex flow that impinges on the cylinder causes high heating in the area of impingement. The maximum value of heat transfer that occurred on the stagnation line of the cylinder was 3 times the laminar theoretical value for cylinders of infinite length at a Mach number of 4.44 and 1-1/2 times the laminar theoretical value for cylinders of infinite length at a Mach number of 2.65 in a boundary layer of 0.6 inch (Figure 2b).
- For a boundary layer of 6 inches, the maximum heat-transfer coefficient on the cylinder was reduced to 1-1/2 times the shock-free flow heat-transfer coefficient at a Mach number of 4.44 (Figure 2a).
- The cause of the lower heating rates on the cylinder with 6-inch boundary layer on the plate is hypothesized that the 6-inch boundary layer on the plate displaces the wedge shock outward from the plate and no shock interaction occurs with the cylinder. However, a secondary shock pattern resulting from the interaction of the cylindrical bow shock with the boundary layer produces a rise in local heat transfer on the cylinder similar to that noted in Reference 5.
- For the thinner boundary layer case ($\delta = 0.6$ inch), two distinct regions of the high heating occur on the cylinder as shown in Figure 2b. The upper region is the direct result of the oblique shock generating from the wedge. The lower region of the elevated heat transfer can be due to the following hypothetical flow. The high pressure behind the cylinder bow shock feeds upstream into the subsonic region of the detached flow at the back of the wedge. The resulting pressure differential between this subsonic region and the region behind the oblique shock causes a compression shock and therefore a region of high heating on the lower portion of the cylinder. As the Mach number increases, the combination of an increase in pressure behind the cylinder bow shock together with a decrease in the secondary shock angle results in approximately the same impingement point for all the Mach numbers of this investigation. The heat transfer in the area of the secondary shock is of the same magnitude as the heat transfer in the area affected by the primary shock from the wedge.

- On the adjacent flat-plate surface, the proximity of the cylinder to the downstream face of the wedge results in heating rates in the wake of the wedge 10 times the undisturbed flat-plate value at a Mach number of 4.44 for a boundary-layer thickness of 0.6 inch (Figure 3b). When this boundary layer was increased by a factor of 10, the maximum heating rate was reduced by 25 percent (Figure 4).
- The heat transfer distributions on the flat plate are shown in Figures 3a and 4a.

$$R = 1.27 \times 10^6 - 4.50 \times 10^6 \text{ (per foot)}$$

$$M = 2.65 - 4.44$$

$$\delta = 0.6'' \text{ and } 6.0''$$

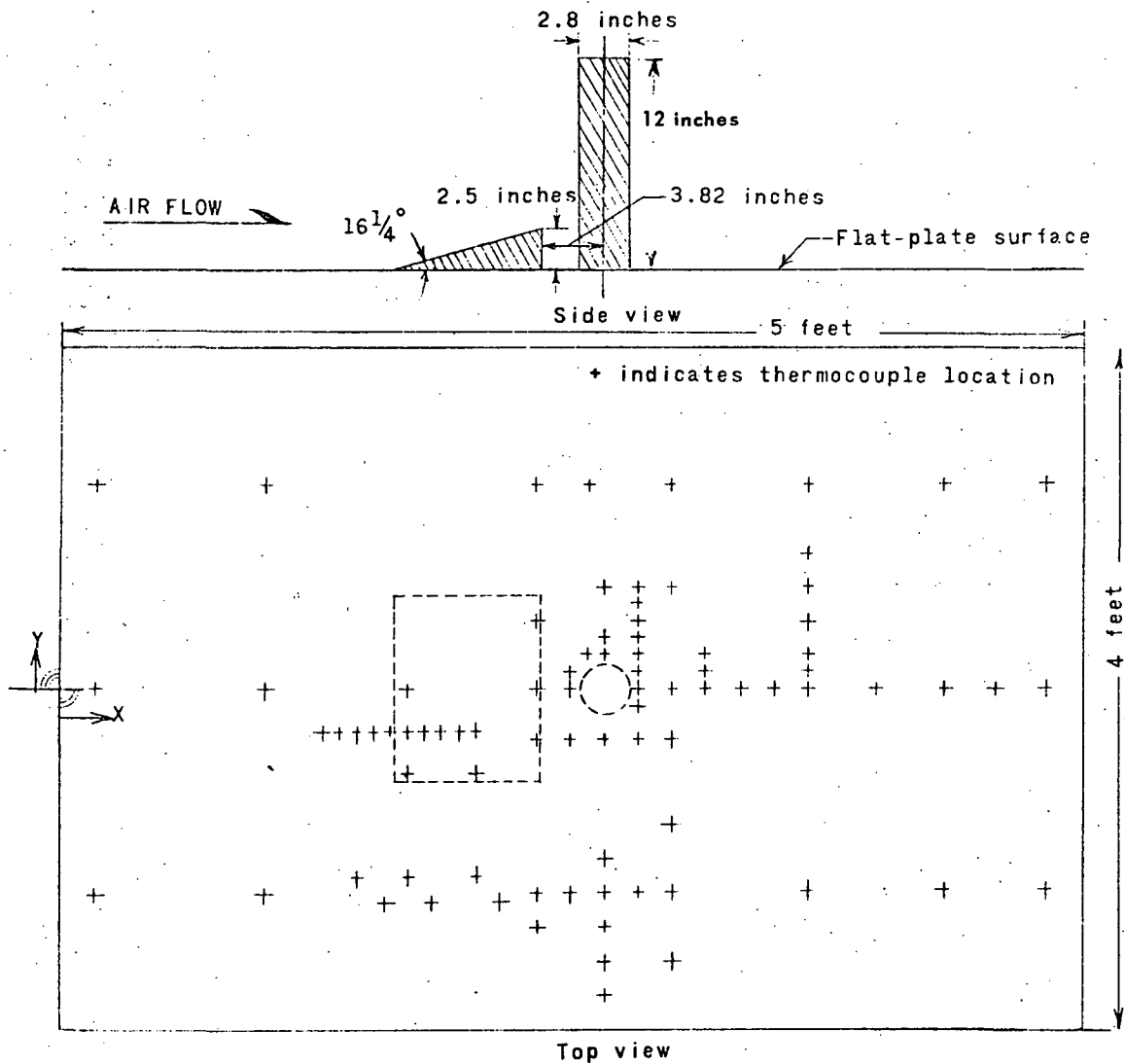
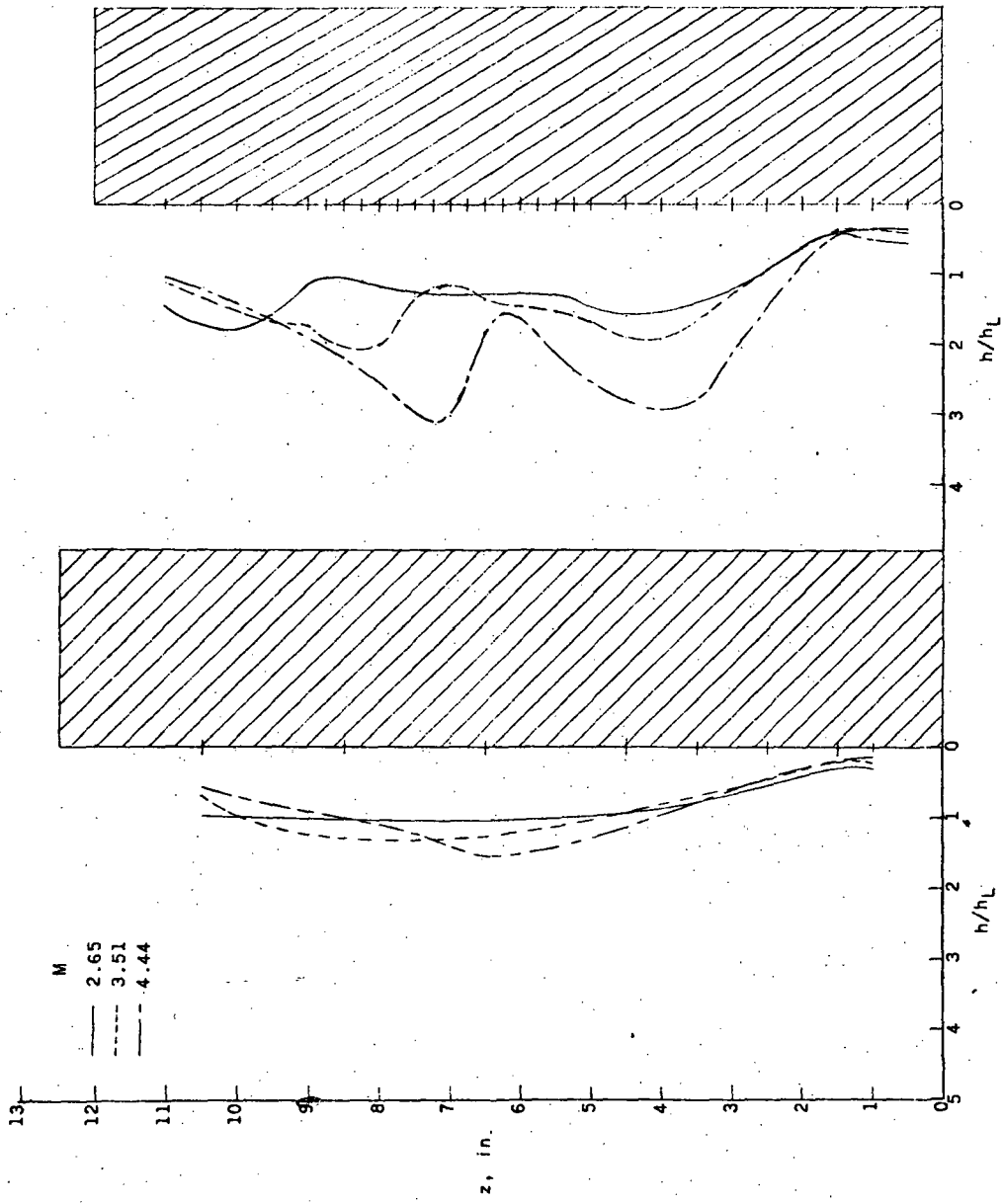
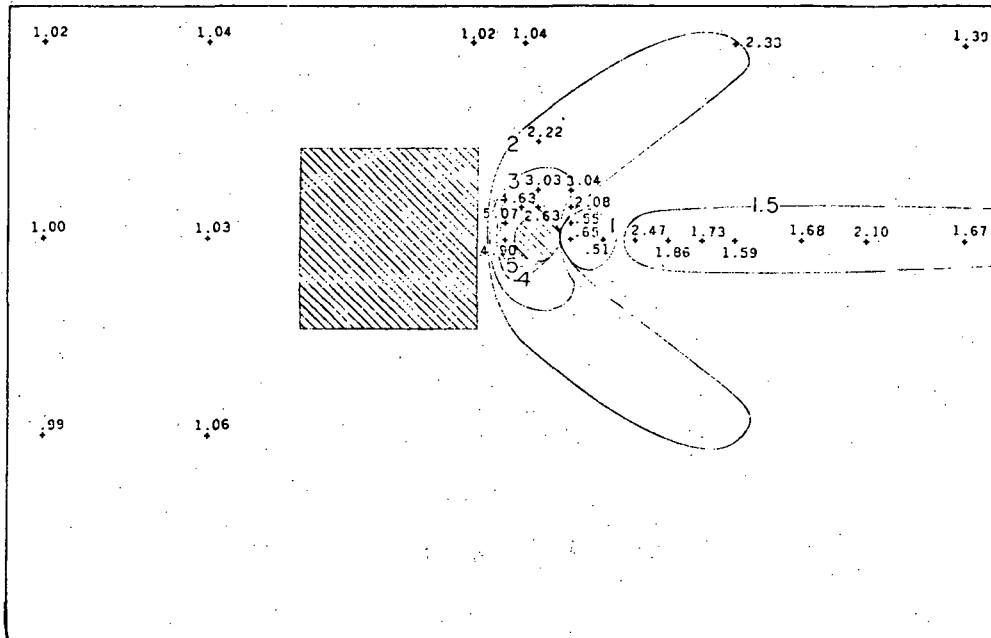


Figure 1. DRAWING OF THERMOCOUPLE AND MODEL LOCATION ON FLAT PLATE

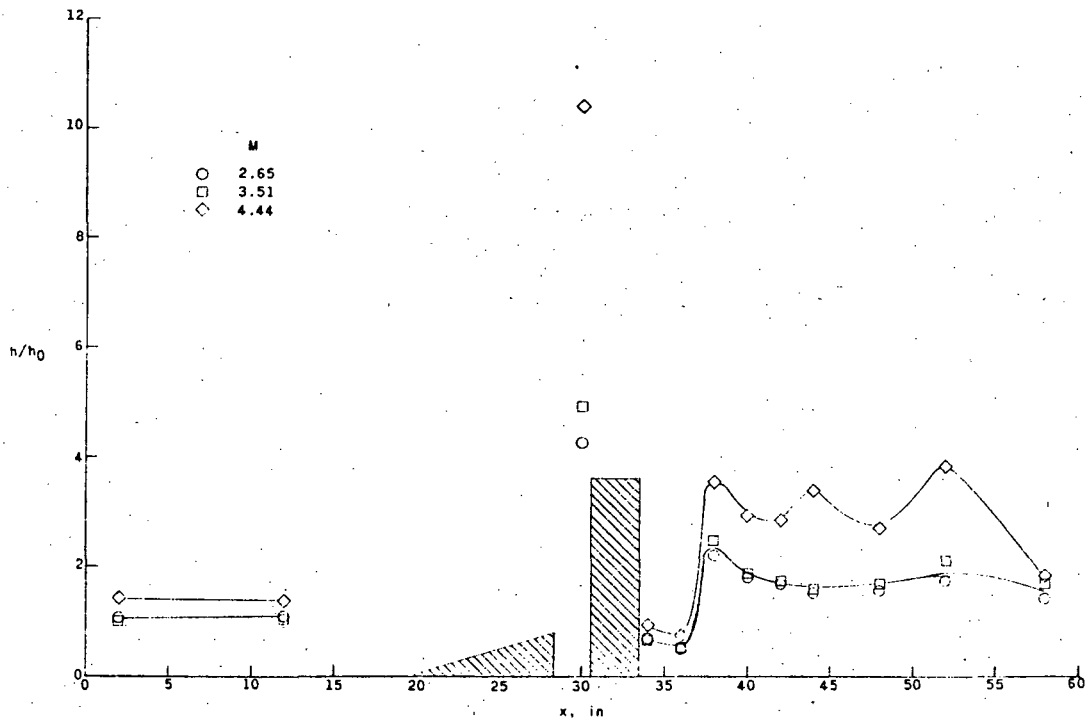


(a) $\delta = 6$ inches. (b) $\delta = 0.6$ inch.

Figure 2. EFFECT OF THE WEDGE ON STAGNATION LINE HEAT-TRANSFER DISTRIBUTION ON SHOCK IMPINGEMENT CYLINDERS $R = 2.76 \times 10^6$

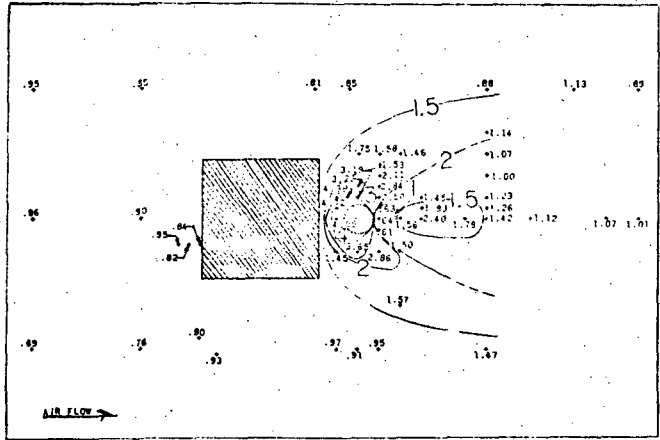


(a) Lines of constant h/h_0 ratio. $M = 3.51$; $R = 2.76 \times 10^6$.

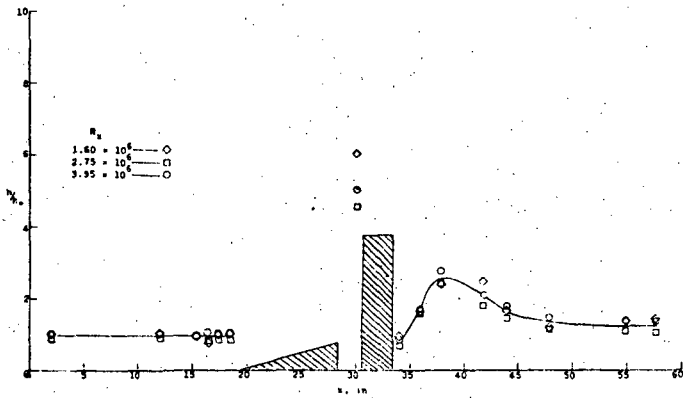


(b) Effect of Mach number along the center line. $R = 2.76 \times 10^6$.

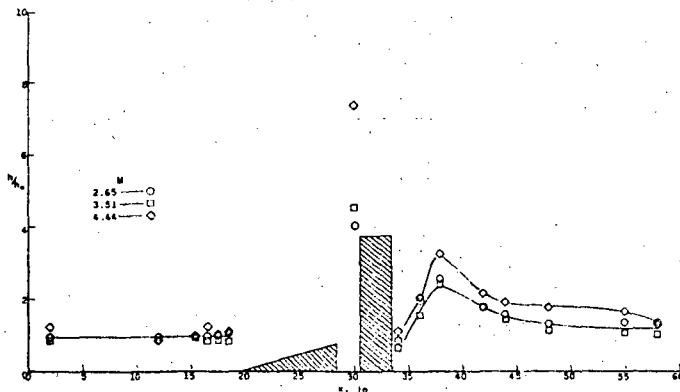
Figure 3. FLAT-PLATE HEAT TRANSFER $\delta = 0.6$ INCH



(a) Lines of constant h/h_0 ratio. $M = 3.51$; $R = 2.75 \times 10^6$.



(b) Effect of Reynolds number along the center line. $M = 3.51$.



(c) Effect of Mach number along the center line. $R = 2.75 \times 10^6$.

Figure 4. FLAT-PLATE HEAT TRANSFER $\delta = 6$ INCHES

HEAT-TRANSFER AND PRESSURE MEASUREMENTS ON A FLAT-PLATE
SURFACE AND HEAT-TRANSFER MEASUREMENTS ON ATTACHED
PROTUBERANCES IN A SUPERSONIC TURBULENT
BOUNDARY LAYER AT MACN NUMBERS
OF 2.65, 3.51, and 4.44

By Paige B. Burbank, Robert A. Newlander, and Ida K. Collins

NASA TN D-1372
December 1962

SYMBOLS

- d - diameter of cylinder
- h - measured heat transfer coefficient
- h_L - theoretical heat transfer coefficient for laminar flow as infinite cylinder
- h_o - measured heat transfer coefficient on flat plate alone
- M - free stream Mach number
- R - Reynolds number per foot
- X - distance along plate longitudinal axis (Figure 58)
- Y - distance from plate longitudinal axis (Figure 58)
- Z - vertical distance from plate
- δ - boundary layer thickness
- ϕ - circumferential angle

SUMMARY

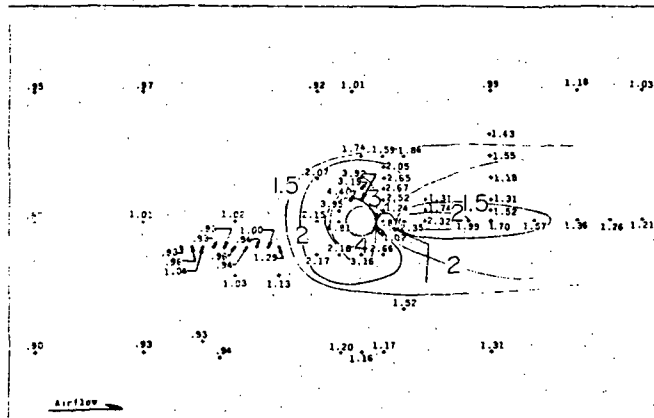
The influence of surface projections, both totally and partially immersed in a turbulent boundary layer, on the distribution of heat-transfer coefficients has been determined on 20 configurations. Surface projections cause separations of the local flow; the extent of these separations both upstream and downstream and the magnitude of the resultant interference heat-transfer coefficients are dependent upon the size and cross-sectional shape of the projection, Mach number, Reynolds number, and boundary-layer thickness. The configurations of this investigation include both three-dimensional simple shapes and hardware-type configurations tested on a flat plate with a turbulent-boundary-layer-thickness variation of approximately 10 to 1. The extent of the interference region can be defined by static-pressure measurements, oil-flow technique, or by heat-transfer measurements.

The windward heating rates increase with decreasing boundary-layer thickness. A maximum value occurs when the projection height is equal to or greater than the boundary-layer thickness. The effects of Mach number and Reynolds number are confined to the immediate vicinity of the windward face of the projection. The magnitude of interference heating expressed as the ratio (at a particular thermocouple) of the heat-transfer coefficient with a protuberance to the heat-transfer coefficient without a protuberance increases with decreasing Reynolds number and increasing Mach number.

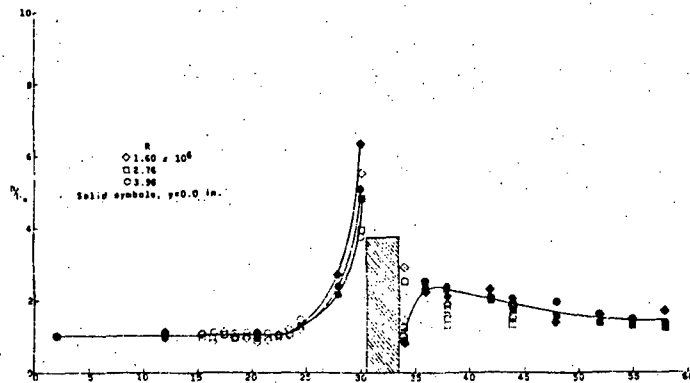
Interference heating in the vicinity of swept cylindrical projections depends upon direction of sweep (forward or back); for example, a cylinder swept back 45° has an interference heating rate 2.07 times that of the undisturbed flat plate, at 0° sweep an interference heating 0.65 times that of the flat plate, and swept forward 45° an interference heating 11.14 times that of the undisturbed flat plate. On the cylindrical projection the lambda-footed bow shock causes a localized region of high heating. The location of this region is dependent upon the free-stream Mach number, boundary-layer thickness, and the ratio of cylinder diameter to boundary-layer thickness. Except for the sweptback cylinder the stagnation-line heating rates outside the interference region are predictable by existing theory. The flat-plate boundary layer on the sweptback cylinder increases the stagnation heat-transfer coefficients.

Location of a protuberance in the influence of another protuberance can cause large variation in the interference heating distribution. The most critical location is in the vicinity of the upstream projection shocks.

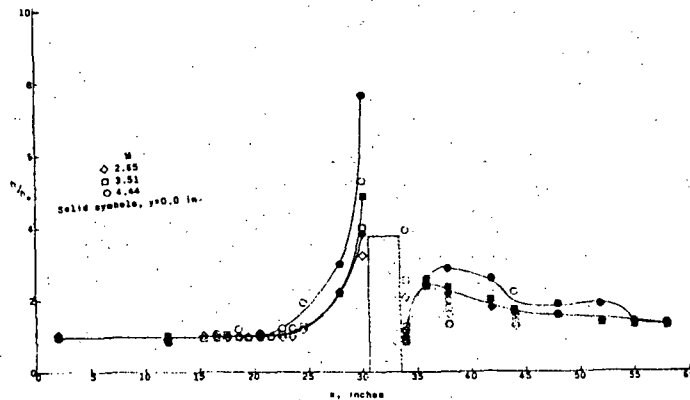
In the wake of a projection placed immediately behind another projection the heating rates are negligible. Further downstream, the wake heat-transfer distribution is greater than that in the undisturbed flow. Cylinders mounted in the wake of other projections and aligned with the flow so that the space between cylinder wall and flat-plate surface is less than 0.01 of the boundary-layer thickness still have heating rates higher than those of the undisturbed region.



(a) Lines of constant h/h_0 . $M = 3.51$; $R = 2.76 \times 10^6$.



(b) Effect of Reynolds number along center line. $M = 3.51$.



(c) Effect of Mach number along center line. $R \approx 3.00 \times 10^6$.

Figure 1. FLAT-PLATE HEAT-TRANSFER RATIO FOR A SINGLE 2.8-INCH-DIAMETER RIGHT CIRCULAR CYLINDER $\delta = 6.00$ INCHES

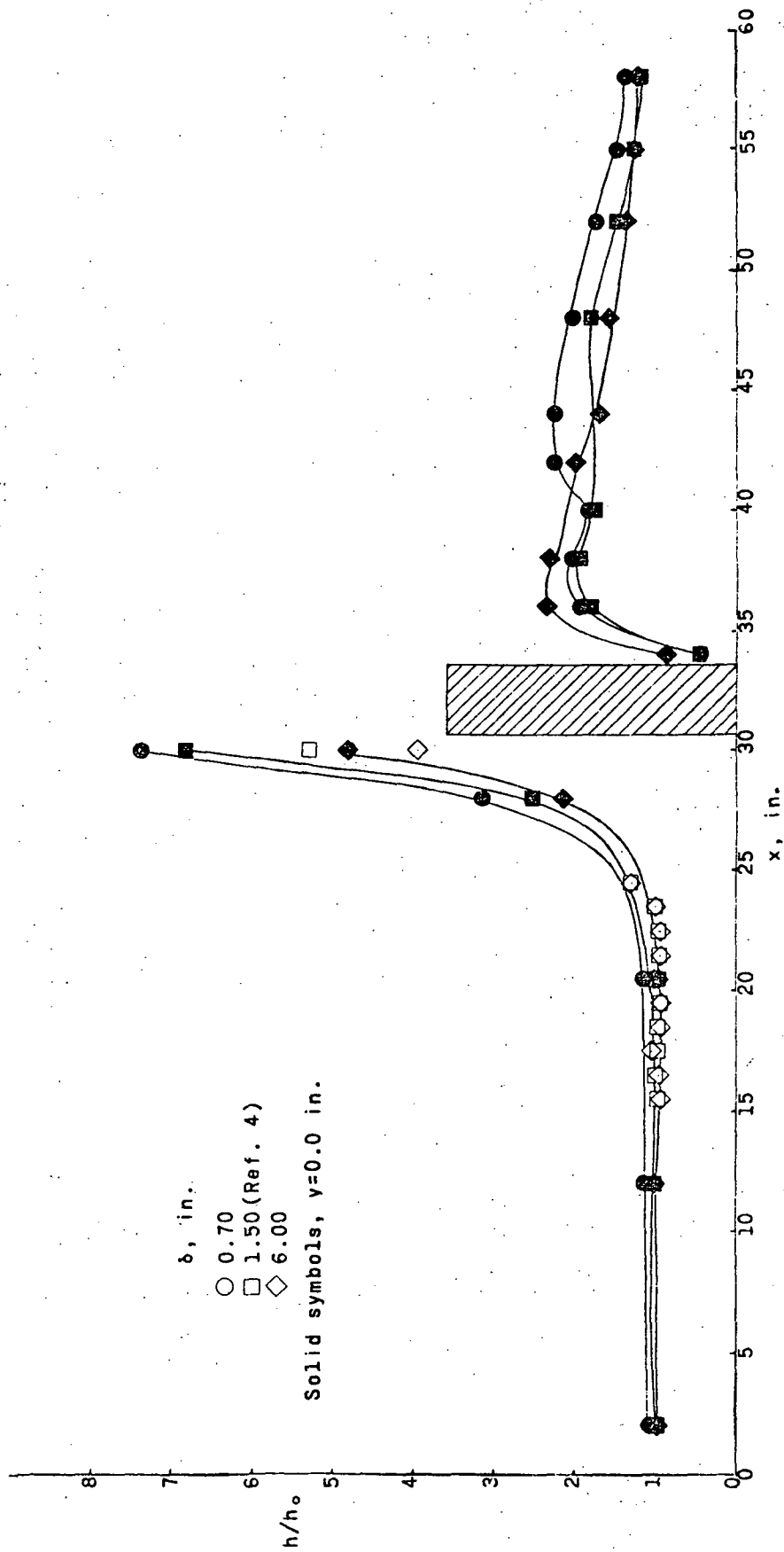
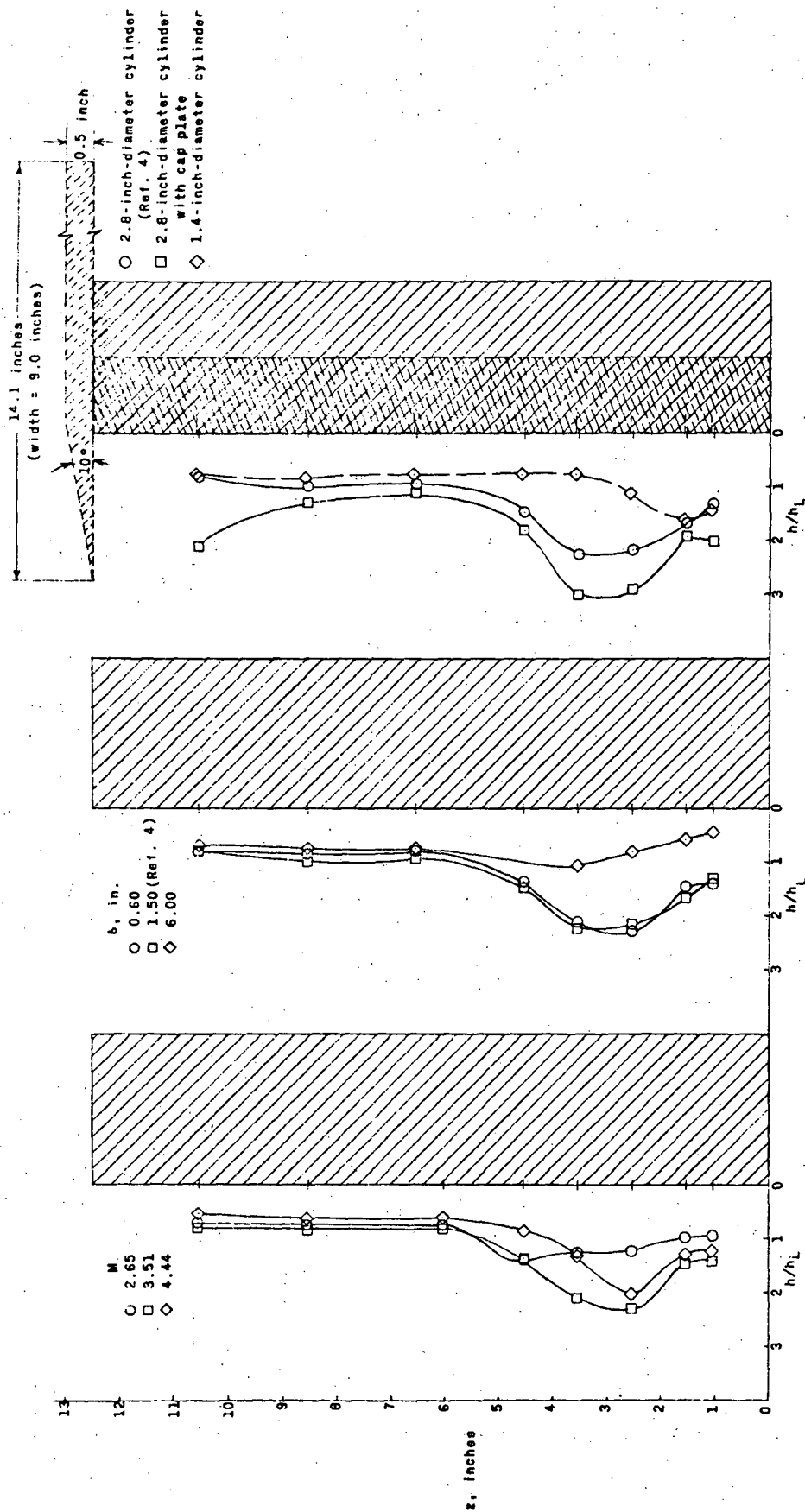


Figure 2. EFFECT OF BOUNDARY-LAYER THICKNESS ON THE DISTRIBUTION OF H/H_0
 WITHIN 2 1/2 INCHES OF THE FLAT-PLATE CENTER LINE FOR A 2.8-
 INCH-DIAMETER RIGHT CIRCULAR CYLINDER $M = 3.51$; $R \approx 2.90 \times 10^6$

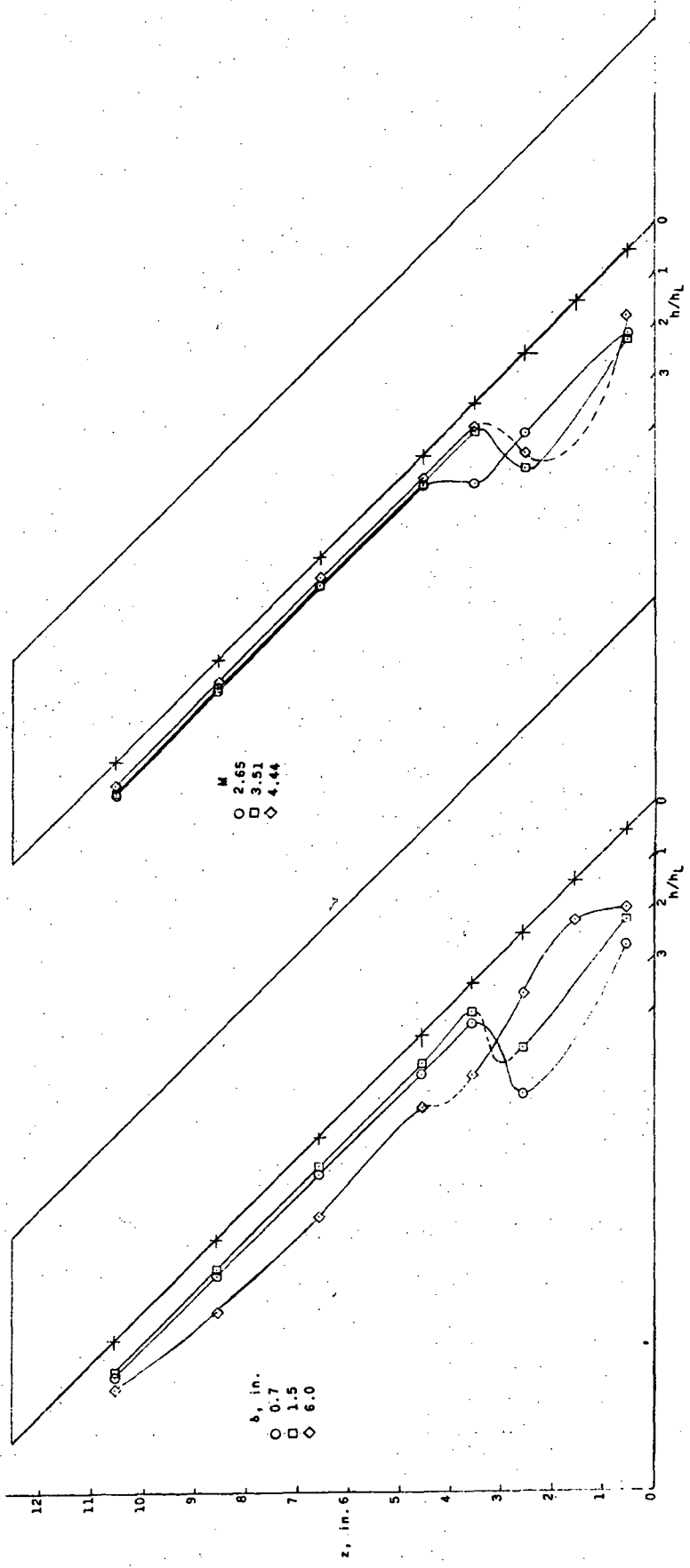


(a) Effect of Mach number. $\delta = 0.70$ inch; $R \approx 3.00 \times 10^6$.

(b) Effect of boundary layer. $M = 3.51$; $R \approx 2.90 \times 10^6$.

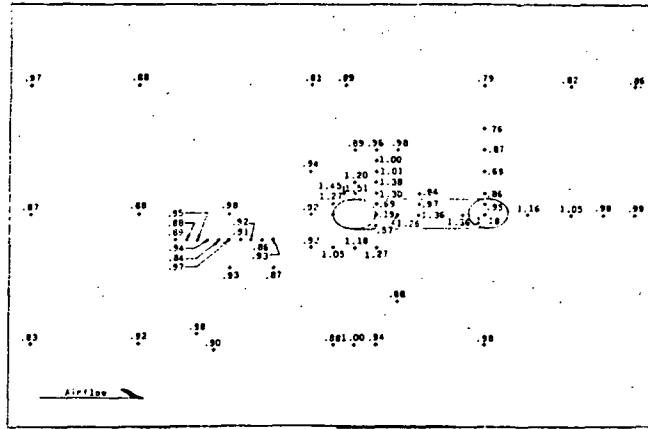
(c) Effect of configuration. $M = 3.51$; $R \approx 2.90 \times 10^6$; $\delta = 1.50$ inches.

Figure 3. RATIO OF EXPERIMENTAL TO THEORETICAL HEAT-TRANSFER COEFFICIENTS ALONG THE STAGNATION LINE ON RIGHT CIRCULAR CYLINDRICAL CONFIGURATIONS

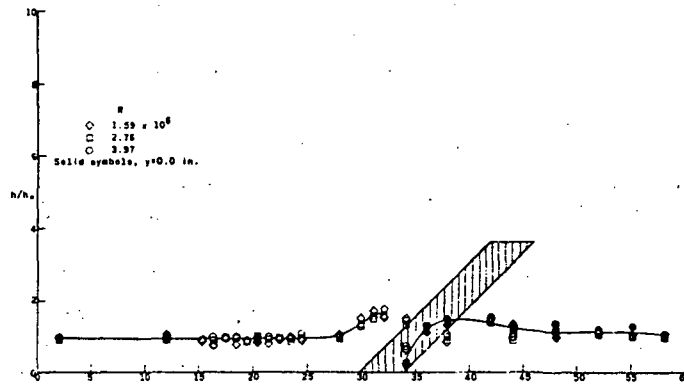


(a) Effect of boundary layer; $M = 3.51$. (b) Effect of Mach number; $\delta = 1.5$.

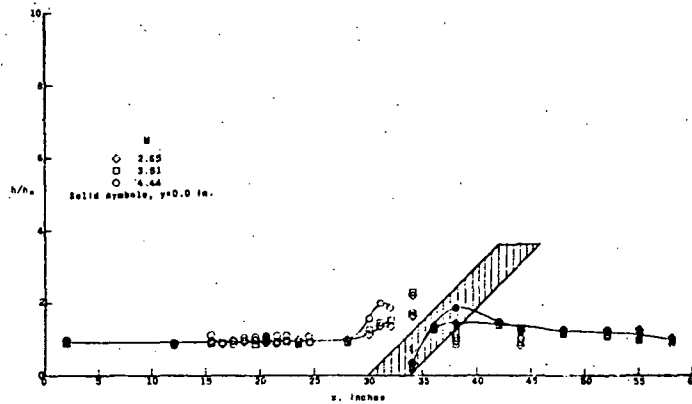
Figure 5. RATIO OF EXPERIMENTAL TO THEORETICAL HEAT-TRANSFER COEFFICIENTS ALONG THE STAGNATION LINE OF A 2.8-INCH-DIAMETER CYLINDER SWEEPED FORWARD 45° $R \approx 3.00 \times 10^5$



(a) Lines of constant h/h_0 . $M = 3.51$; $R = 2.76 \times 10^6$.

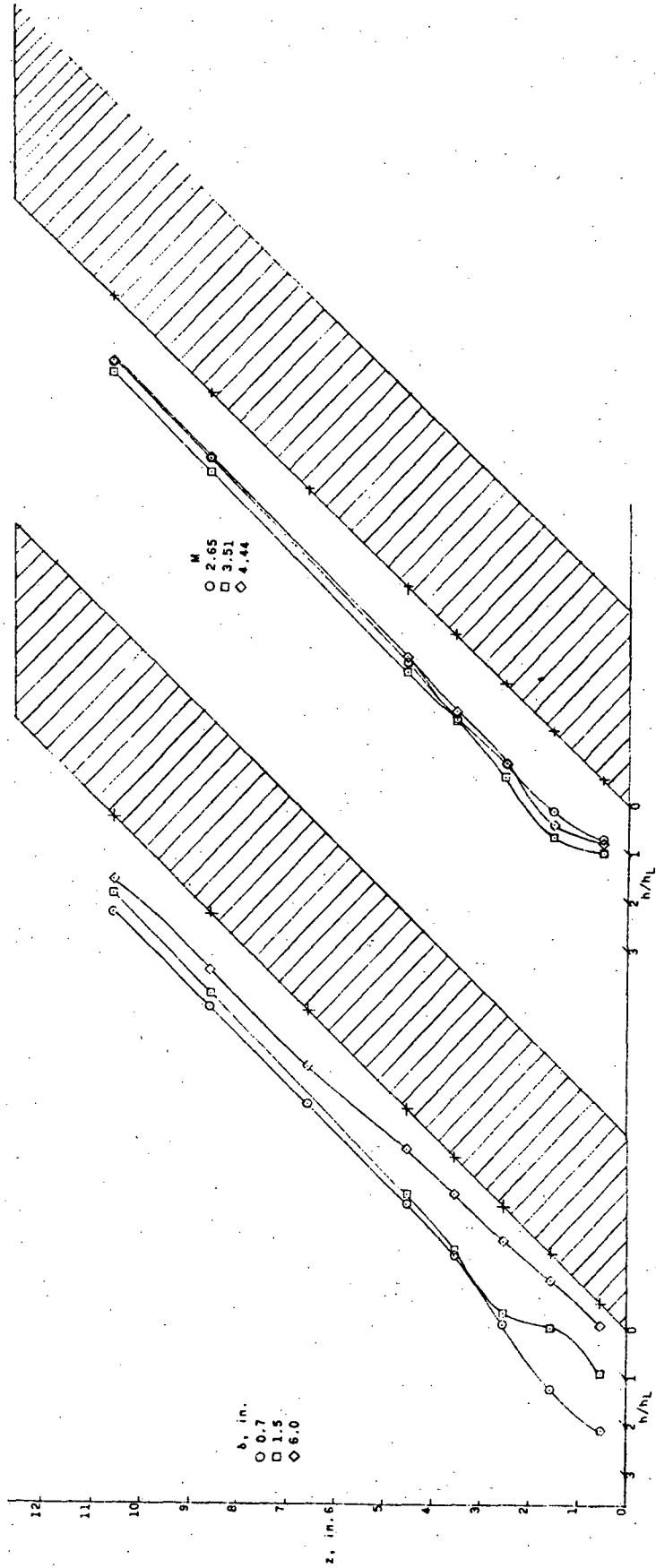


(b) Effect of Reynolds number along center line. $M = 3.51$.



(c) Effect of Mach number along center line. $R \approx 3.00 \times 10^6$.

Figure 6. FLAT-PLATE HEAT-TRANSFER RATIO FOR A 2.8-INCH-DIAMETER CYLINDER SWEPT BACK 45° $\delta = 6.00$ INCHES



(a) Effect of boundary layer; $M = 3.51$. (b) Effect of Mach number; $\delta = 1.50$ inches.

Figure 7. RATIO OF EXPERIMENTAL TO THEORETICAL HEAT-TRANSFER COEFFICIENTS ALONG THE STAGNATION LINE OF A 2.8-INCH-DIAMETER CYLINDER SWEEP BACK 45° $R \approx 3.00 \times 106$.

EFFECTS OF SHOCK IMPINGEMENT AND OTHER FACTORS
ON LEADING-EDGE HEAT TRANSFER

By Dennis M. Bushnell

NASA TN D-4543
April 1968

SYMBOLS

D - leading edge diameter

h_{\max} - maximum heat transfer coefficient

h_1 - undisturbed heat transfer coefficient

M_∞ - free stream Mach number

$R_{\infty, D}$ - Reynolds number based on free stream conditions and leading edge diameter

X - distance along leading edge

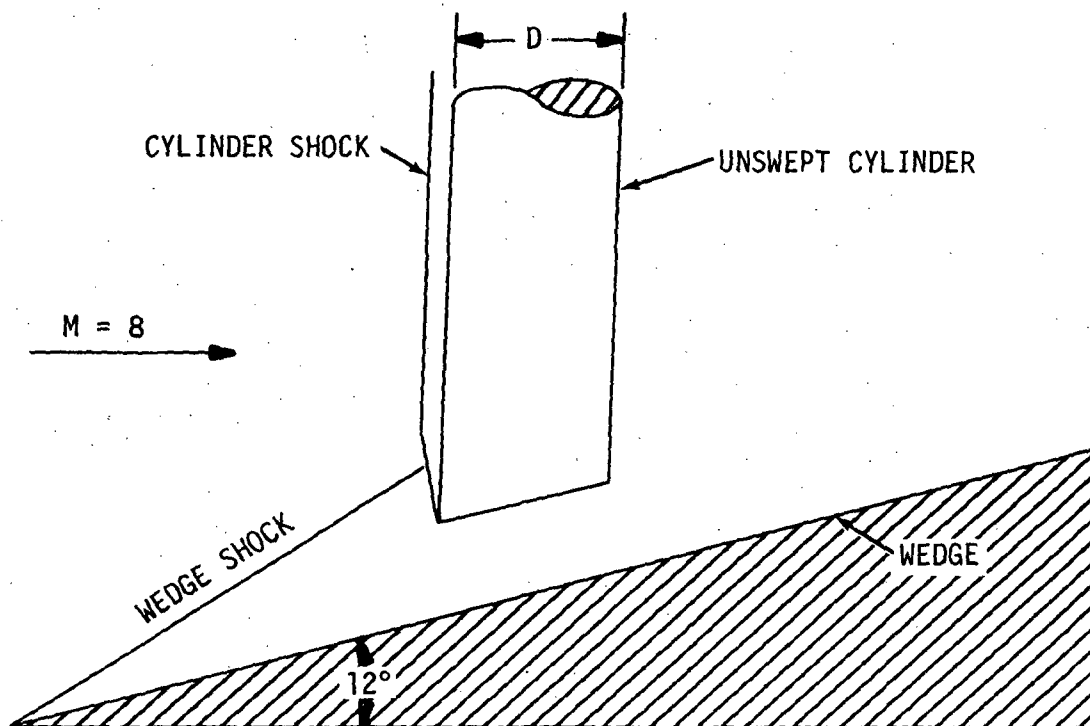
Δ - distance along leading edge from cylinder root to vortex-sheet impingement

Λ - sweep angle

SUMMARY

An investigation was conducted at a Mach number of 8 to determine the effects of stagnation-line heat transfer of shock impingement. The tests were conducted with an unswept cylinder. A flat plate inclined at an angle of 12° to the flow was used as the shock generator. The cylinder was separated from the shock generator to eliminate the effects of flow separation in the root region. Sketch of the test model is shown in Figure 1. Results are summarized as below:

- A local peak in heating that was about twice the undisturbed heating level was observed in the stagnation region of the cylinder where a vortex sheet impinged on the leading edge. The vortex sheet originated at the intersection of the plate and cylinder shocks. Comparison of these data with previous measurements on similar configurations indicates that the magnitude of the peak in heating depends on the proximity of the shock impingement to the tip or root region in which the attacked leading-edge boundary layer first develops. On the basis of this comparison and additional tests in which the shock impingement occurred close to the tip of the cylinder, it is concluded that for leading edges at small sweep angles, shock impingement occurring far from the root of the leading edge causes only moderate increases in heating. If impingement occurs near the root of the leading edge, factors of the order of up to 10 times the undisturbed heating level are possible (Figure 2).
- The tip effect as discussed above is probably, at least in part, due to the occurrence of shock impingement closer to the tip where the bow-shock-layer thickness decreases, and therefore the distance from the origin of the vortex sheet to the impingement region on the leading edge is reduced. Hence the distance over which the vortex sheet grows and diffuses into a mixing layer is smaller.



$$R_\infty, D = 1.8 \times 10^5$$

$$D = 1 \text{ inch}$$

$$\Lambda = 0^\circ$$

Figure 1. SKETCH OF TEST MODEL

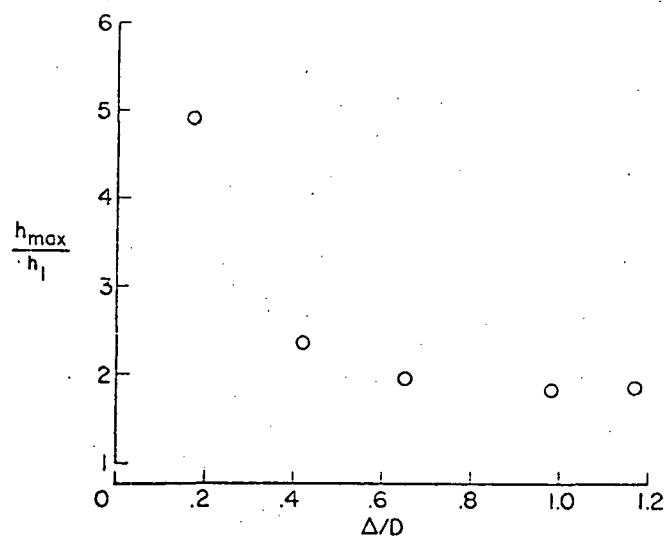


Figure 2. MAXIMUM HEATING AS A FUNCTION OF DISTANCE FROM TIP OF CYLINDER $\Lambda = 0^\circ$; $M_\infty = 8$

AN INVESTIGATION OF THE EFFECTS OF SHOCK
IMPINGEMENT ON A BLUNT LEADING EDGE

By A. D. Ray and R. L. Palko

AEDC-TR-65-153
July 1965

SYMBOLS

- h_s - leading edge heat transfer coefficient with shock impingement
- h_{sN} - leading edge heat transfer coefficient without shock impingement
- M_∞ - free stream Mach number
- P_s - leading edge pressure with short impingement
- P_{sN} - leading edge pressure without short impingement
- Re_∞ - free stream Reynolds number
- X - distance along leading edge (Figure 1)
- δ - angle between shock generator surface and free stream flow
- Λ - sweep angle

SUMMARY

Tests were conducted at hypersonic Mach numbers on a blunt leading edge model both with and without an impinging shock. The effects of Reynolds number, Mach number, leading edge sweep angle, and impinging shock strength on the temperature and pressure distribution for the leading edge were determined. The tests were conducted at nominal Mach numbers of 6, 8, and 10 at unit Reynolds numbers of 0.58×10^6 to 3.55×10^6 per foot with a sweep angle range of 0 to 75 degrees. The test model details are given in Figure 1. Selected results which show the effect of sweep angle at Mach 6 and 10 are presented in Figures 2 and 3. Pressure and heat-transfer coefficients in the presence of an impinging shock, p_S and h_S , have been ratioed to the values p_{NS} and h_{NS} , obtained with the blunt nose configuration without an impinging shock.

The data show the effect of varying leading edge sweep angle on the amplification of local pressure and heat-transfer coefficients resulting from shock interaction for a shock generator angle of 10 degrees relative to the free-stream flow direction. Data for other shock generator angles had similar trends. Two distinct types of shock interaction were observed. At both Mach 6 and 10, the boundary layer on the shock generator plate separated when the angle between the plate and the leading edge was less than approximately 120 degrees. When this angle was greater than 120 degrees, no separation was noted. Shadowgraphs showing these two cases are presented in Figure 6 of the original paper. With a shock generator angle of 10 degrees separation existed for sweep angles of 20 degrees or less, and the increased intensity of the pressure and heat transfer at these angles are shown in Figures 2 and 3. A comparison of Figures 2 and 3 indicates that as Mach number is increased, the shock induced pressures and heat-transfer rates increase in magnitude but occur over a smaller region on the leading edge.

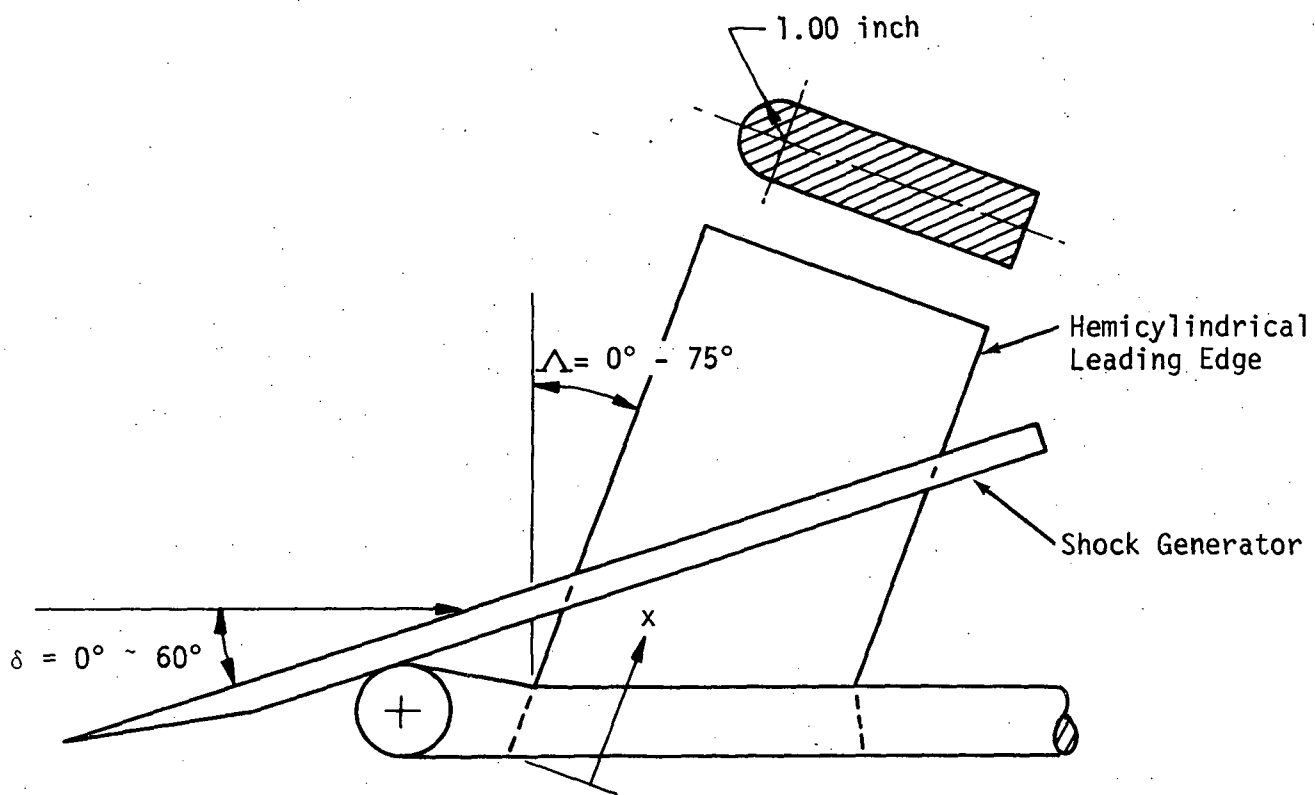


Figure 1. TEST CONFIGURATION-SHOCK GENERATOR AND HEMICYLINDRICAL LEADING EDGE

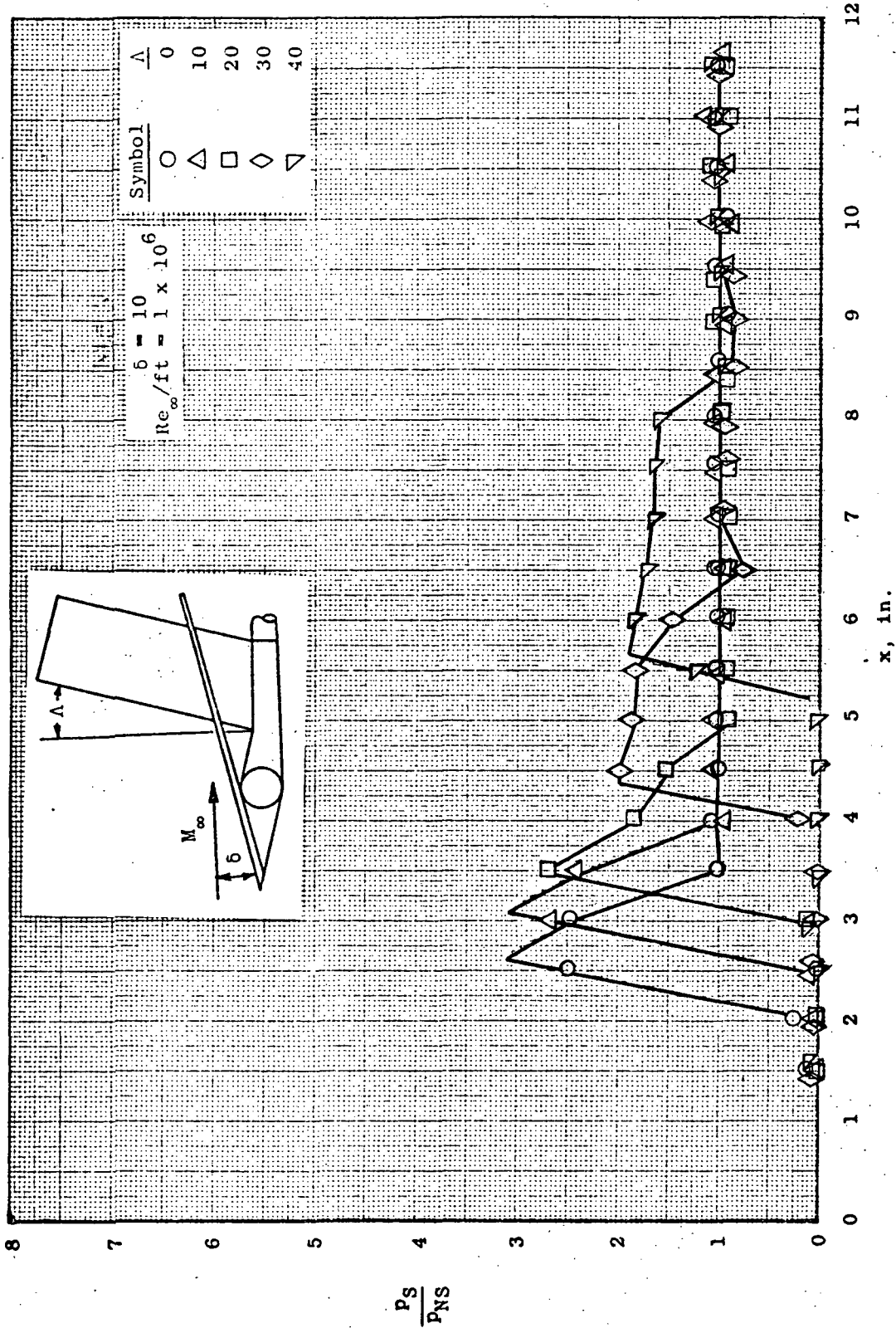
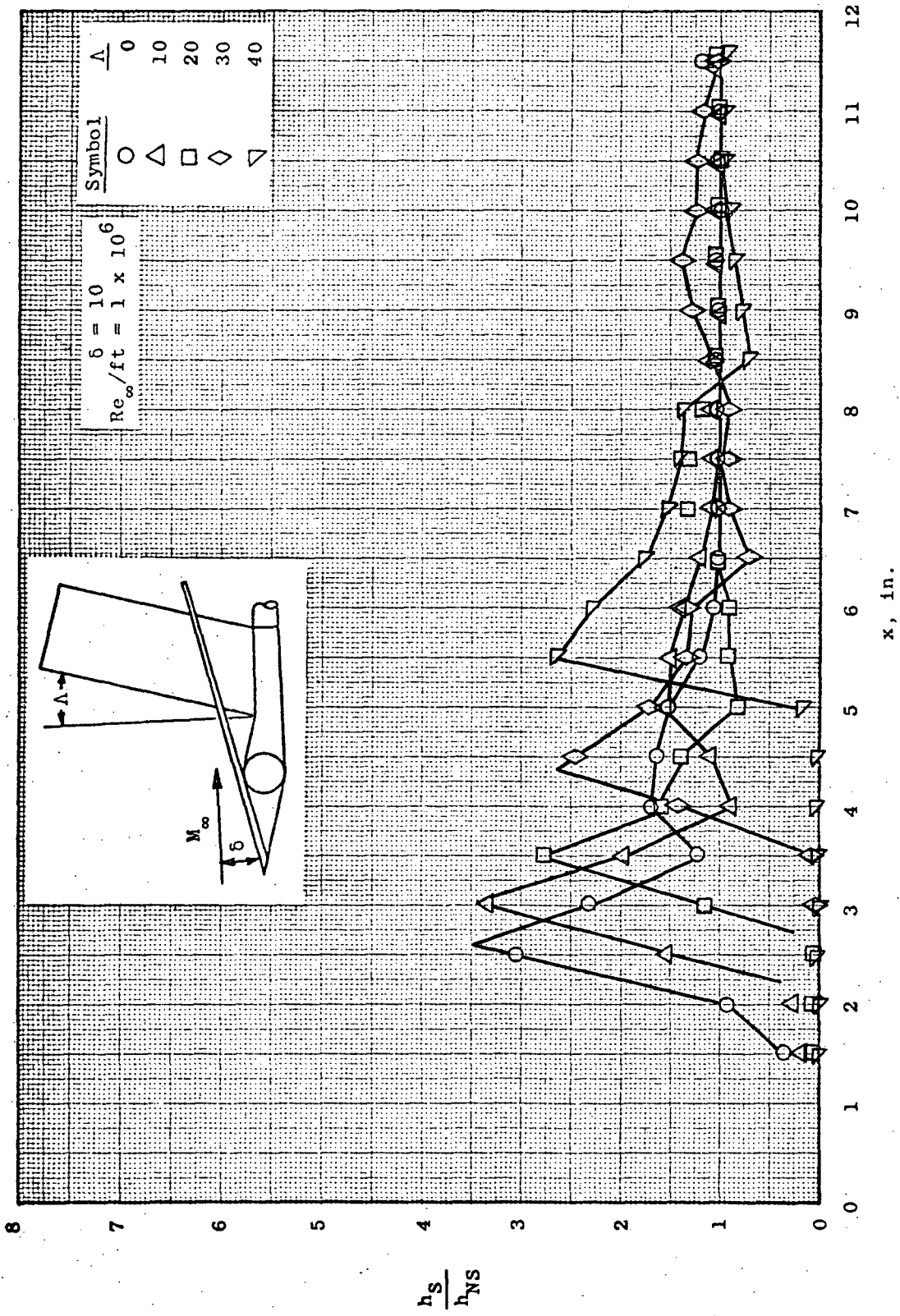
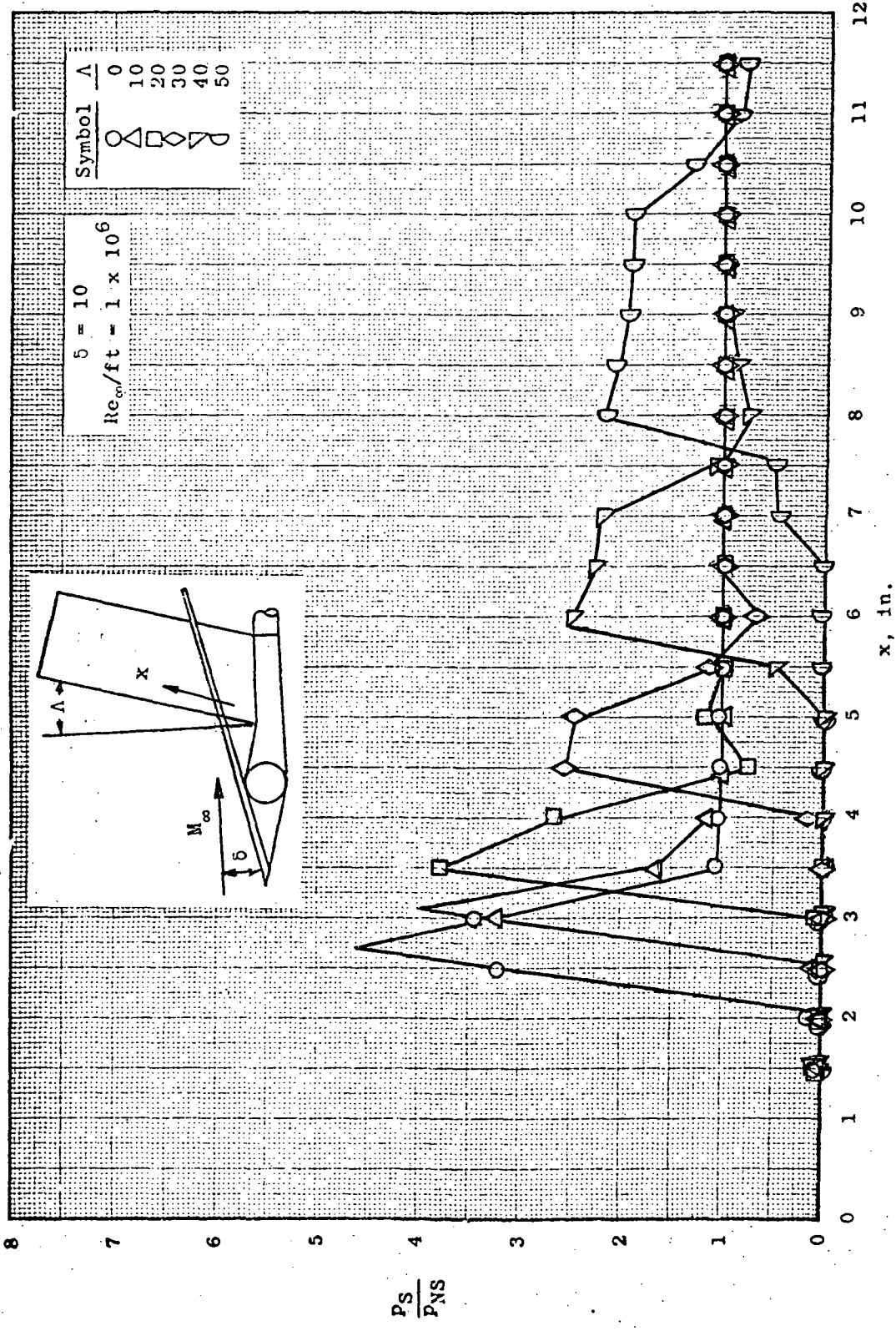


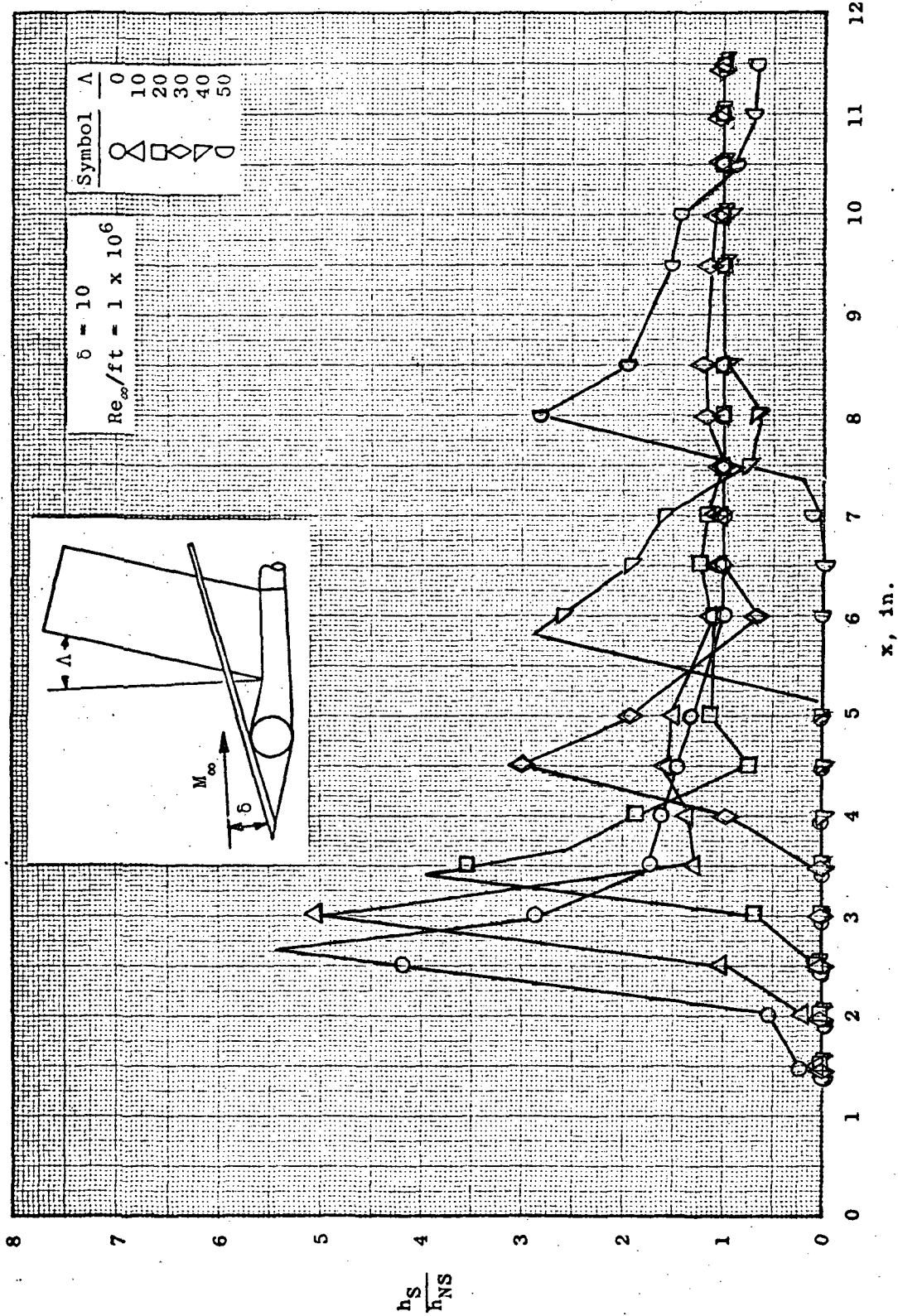
Figure 2. LEADING EDGE STAGNATION LINE SHOCK IMPINGEMENT EFFECTS AT MACH 6



b. Heat Transfer
 Figure 2. LEADING EDGE STAGNATION LINE SHOCK IMPINGEMENT EFFECTS AT MACH 6 (CONCLUDED)



a. Pressure
 Figure 3. LEADING EDGE STAGNATION LINE SHOCK IMPINGEMENT EFFECTS AT MACH 10



b. Heat Transfer

Figure 3. LEADING EDGE STAGNATION LINE SHOCK IMPINGEMENT EFFECTS AT MACH 10 (CONCLUDED)

EFFECT OF SHOCK IMPINGEMENT ON THE HEAT TRANSFER
AND PRESSURE DISTRIBUTIONS ON A CYLINDRICAL LEADING
EDGE MODEL AT MACH NUMBER 19

By L. G. Siler and H. E. Deskins

AEDC-TDR-64-228
November 1964

SYMBOLS

- L - length of leading edge
- M_∞ - free stream Mach number
- p - local pressure on model
- p'_o - total pressure behind normal shock in test section
- \dot{q} - local heat transfer rate on model
- $\dot{q}_{(I)}$ - stagnation heat transfer rate on unyawed and unswept 2-inch diameter hemicylinder
- Re_∞ - free stream Reynolds number per inch
- X - distance from shock generator leading edge to intersection of leading edge and plate
- Y - distance along leading edge of model from model base
- Y_s - distance along leading edge of model from model base to intersection of shock (Figure 3)
- ΔY - distance along leading edge of model from intersection of shock generator plate and model leading edge
- δ - shock generator deflection angle
- θ - angular location of sensor referenced to leading edge centerline
- Λ - leading edge sweep angle

SUMMARY

Pressure and heat-transfer measurements on a cylindrical-leading-edge model with and without the influence of an impinging shock wave were made at about Mach number 19 and Reynolds number of approximately 24,000 per inch. The configuration was evaluated through a sweep range from 0 to 75 degrees while varying the shock generator angle from 0 to 40 degrees. Two cylindrical leading edge models identical in overall dimensions were used for measuring pressure and heating rates. Sketches of the test models are shown in Figures 1 and 2. Test results are summarized as follows:

- The location of the shock-wave impingement point is shown in Figure 3 for each model sweep angle and generator deflection angle.
- The pressure and heat-transfer distributions were measured over the cylindrical-leading-edge model, with the nose fairing attached, through a sweep range from 0 to 75 degrees. Typical variations of pressure and heat-transfer with sweep angle are shown in Figure 4. The measured pressures on the leading edge are compared to a Newtonian distribution whereas the heat-transfer-leading-edge data are compared to the theoretical distribution of Reshotko and Beckwith (Reference 6). Excellent agreement is noted for both the leading-edge pressure and heat-transfer data with theory, as shown in Figure 4.
- The effect of an impinging shock on the pressure and heat-transfer distribution over the cylindrical-leading-edge model ($\Lambda = 30$ degrees) is shown in Figure 5 for a shock generator deflection angle of $\delta = 0$ degrees. The basic model data with no shock generator are shown for comparison purposes. Note that the shock wave impingement on the leading edge caused peak increases in the pressure and heat-transfer data of approximately three times the basic model data. However, as noted by Jones (Reference 7), the increased pressure and heating rates are probably caused by a combination of the shock wave impingement and mutual interference between the leading-edge model and shock generator, causing the peak values to occur inboard of the shock impingement point.
- Shadowgraph of the model and shock generator at a sweep angle of 0 degree and a shock generator deflection angle of 20 degrees shows secondary shocks in the area of the junction between the plate and leading-edge shock waves, as well as flow separation. The pressure and heat-transfer distributions for this configuration are shown in Figure 6 with a max. $\dot{q}/\dot{q}(I)$ of about 5.

- While holding the shock generator deflection angle constant at 0 degrees and varying the sweep angle, the pressure and heat-transfer distributions on the leading edge varied as shown in Figure 7. The distance, Δy , was measured from the plate-model intersection along the model leading edge.

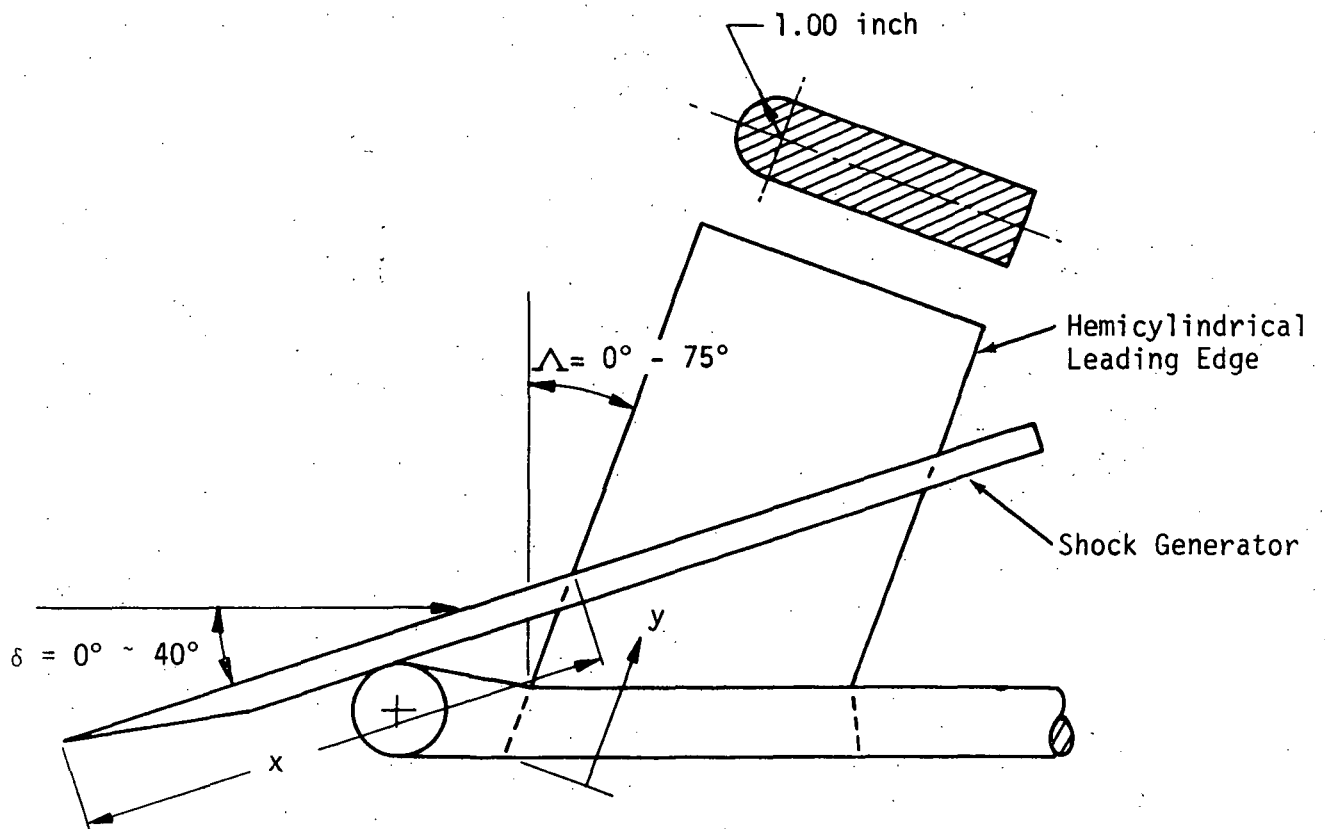


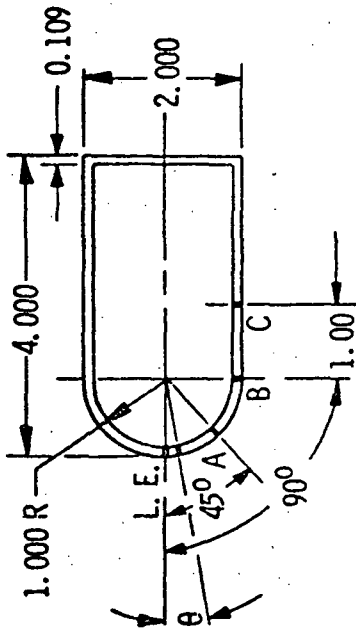
Figure 1. TEST CONFIGURATION-SHOCK GENERATOR AND HEMICYLINDRICAL LEADING EDGE

Gage Locations

Y, in.	Gages	Model No. 1	Model No. 2
1.5	1	P.	P
2.0	2, 2A, 2B, 2C	P	H
2.5	3	P	H
3.0	4	H	P
3.5	5, 5A, 5B, 5C	P	H
4.0	6	P	H
4.5	7	P	P
5.0	8, 8A, 8B	P	H
5.5	9	P	H
6.0	10	H	P
6.5	11, 11A, 11B, 11C	P	H
7.0	12	P	H
7.5	13	P	P
8.0	14, 14A, 14B, 14C	P	H
8.5	15	P	H
9.0	16	H	P
9.5	17, 17A, 17B, 17C	P	H
10.0	18	P	H
10.5	19	P	P
11.0	20, 20A, 20B	P	H
11.5	21	P	-

P - Pressure

H - Heat



Section 1-1

All Dimensions in Inches

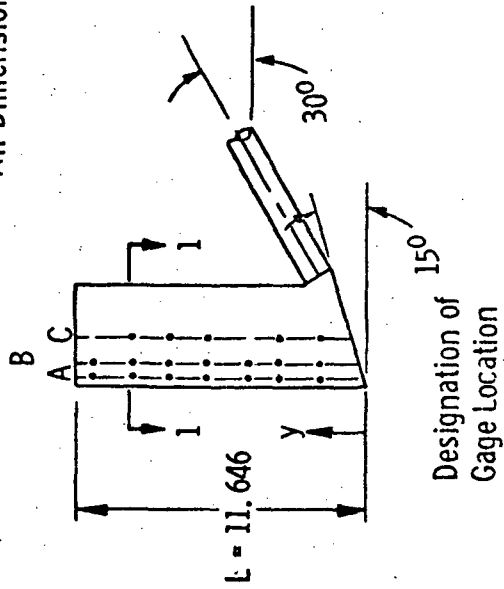


Figure 2. SKETCH OF MODELS 1 AND 2

Intersection of Shock Generator Plate
and Projected Shock with Model

Λ	δ	x	y	y_s
60	0	11.77	7.21	-
50	0	9.88	5.19	8.64
50	10	11.77	7.21	9.29
40	0	8.76	3.91	6.04
40	10	9.88	5.19	6.64
40	20	11.77	7.21	9.94
30	0	8.03	3.01	4.70
30	10	8.76	3.91	4.89
30	30	11.77	7.21	10.50
0	0	6.88	1.29	2.88
0	10	7.15	1.75	2.69
0	20	7.50	2.32	3.09
0	40	8.76	3.91	6.37

All Dimensions in Inches

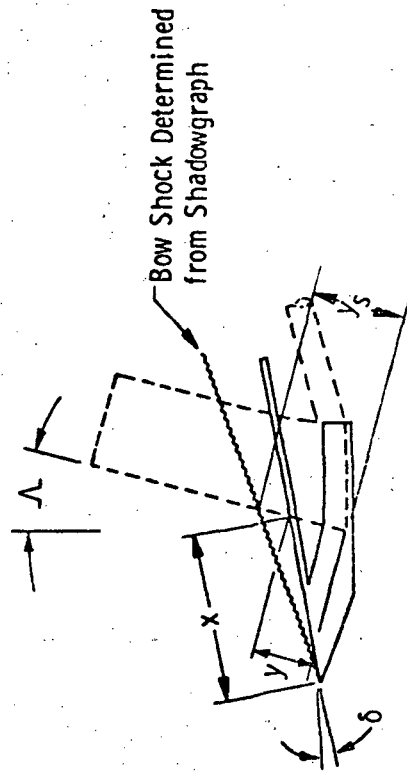
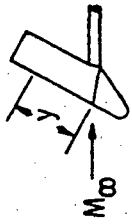


Figure 3. SKETCH OF SHOCK GENERATOR



Sym Gage No.
 ○ 14 (Leading Edge)
 □ 14 A
 △ 14 B
 ◇ 14 C
 (No. 14 Gages at y = 8 in.)

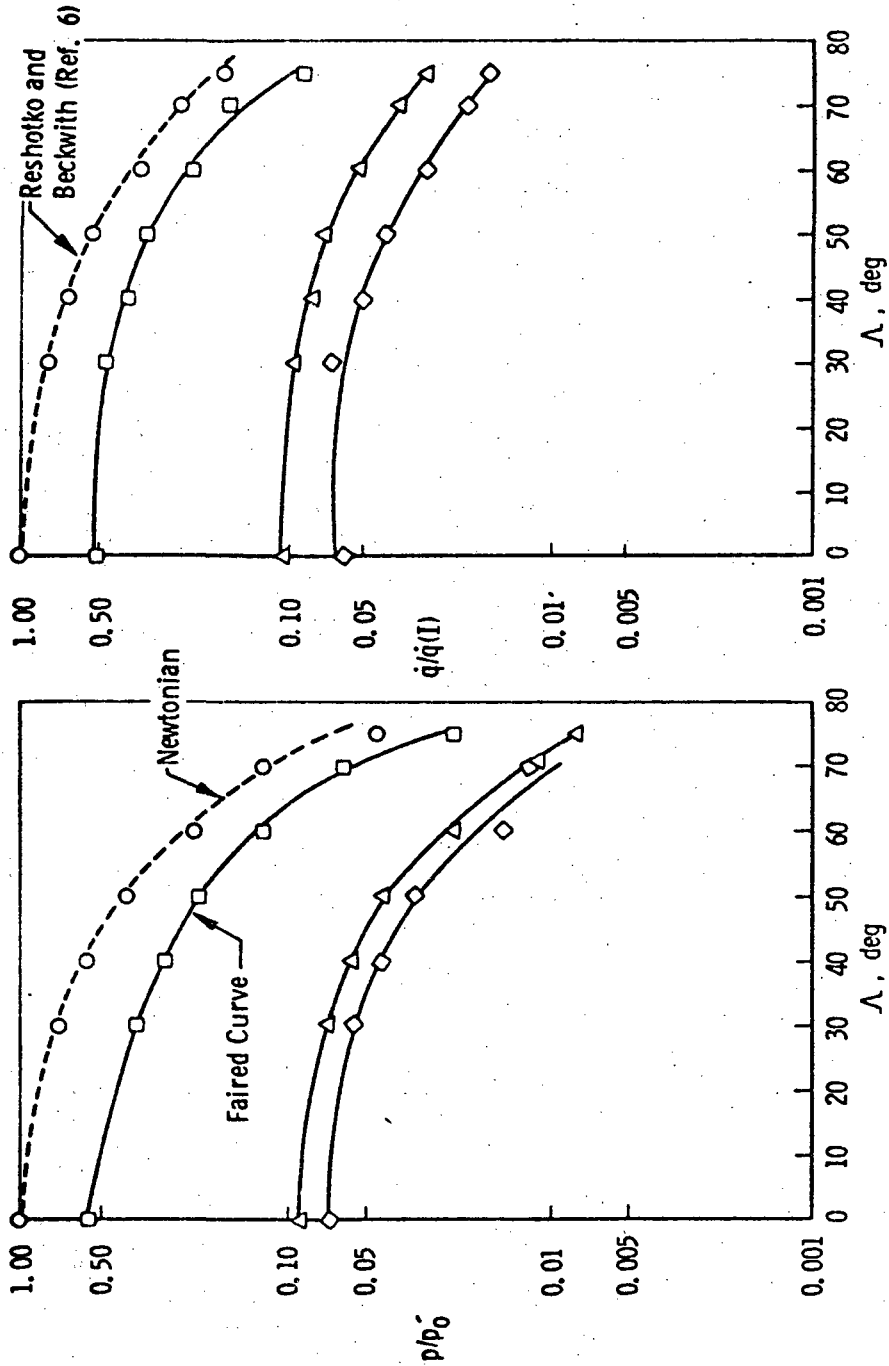
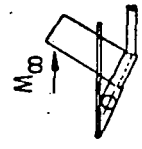


Figure 4. TYPICAL VARIATION OF PRESSURE AND HEAT TRANSFER WITH SWEEP ANGLE FOR MODEL WITH NO SHOCK GENERATOR

Sym Gages
 ○ Leading Edge
 □ A
 △ B
 ◇ C



(Dark Symbols = No Shock Generator)

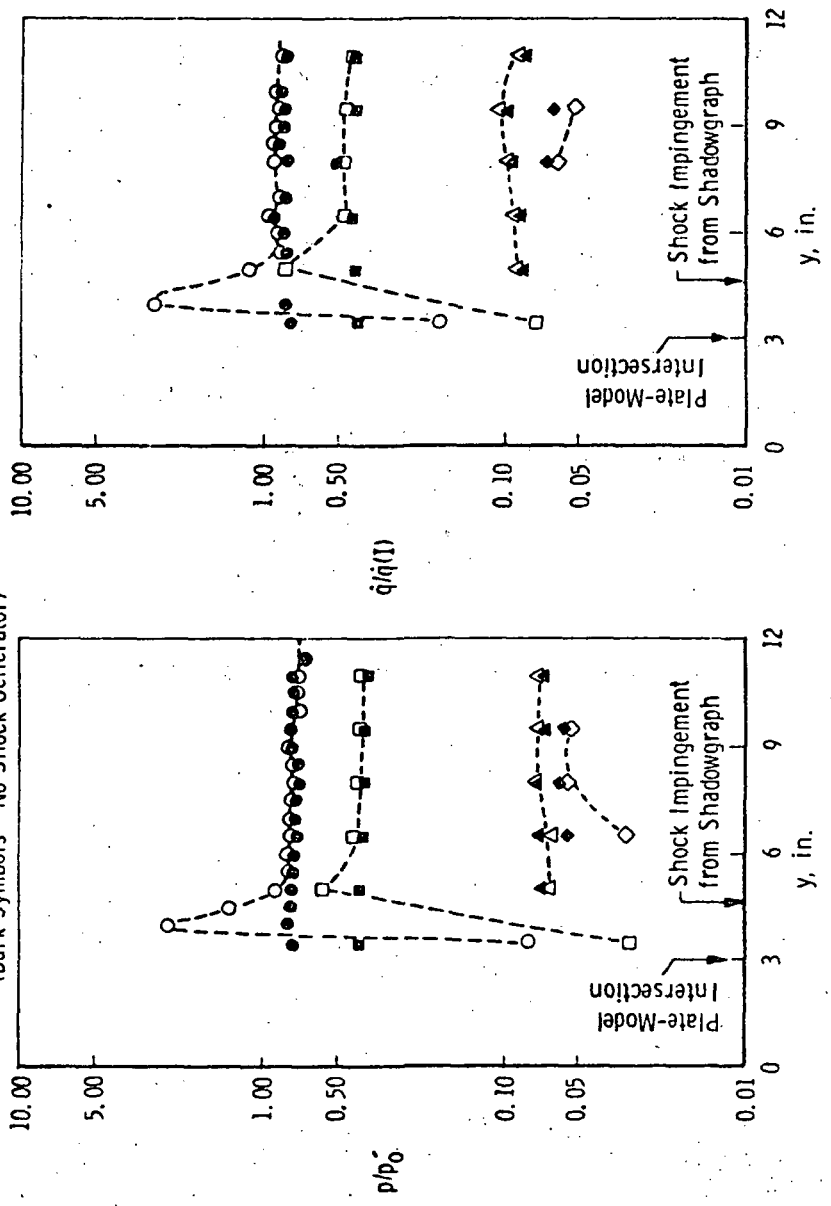


Figure 5. PRESSURE AND HEAT-TRANSFER DISTRIBUTION ON MODEL WITH SHOCK IMPINGEMENT
 ($\lambda = 30$ DEG AND $\delta = 0$)

Sym Gages
 Leading Edge
 A B C
 (Dark Symbols = No Shock Generator)

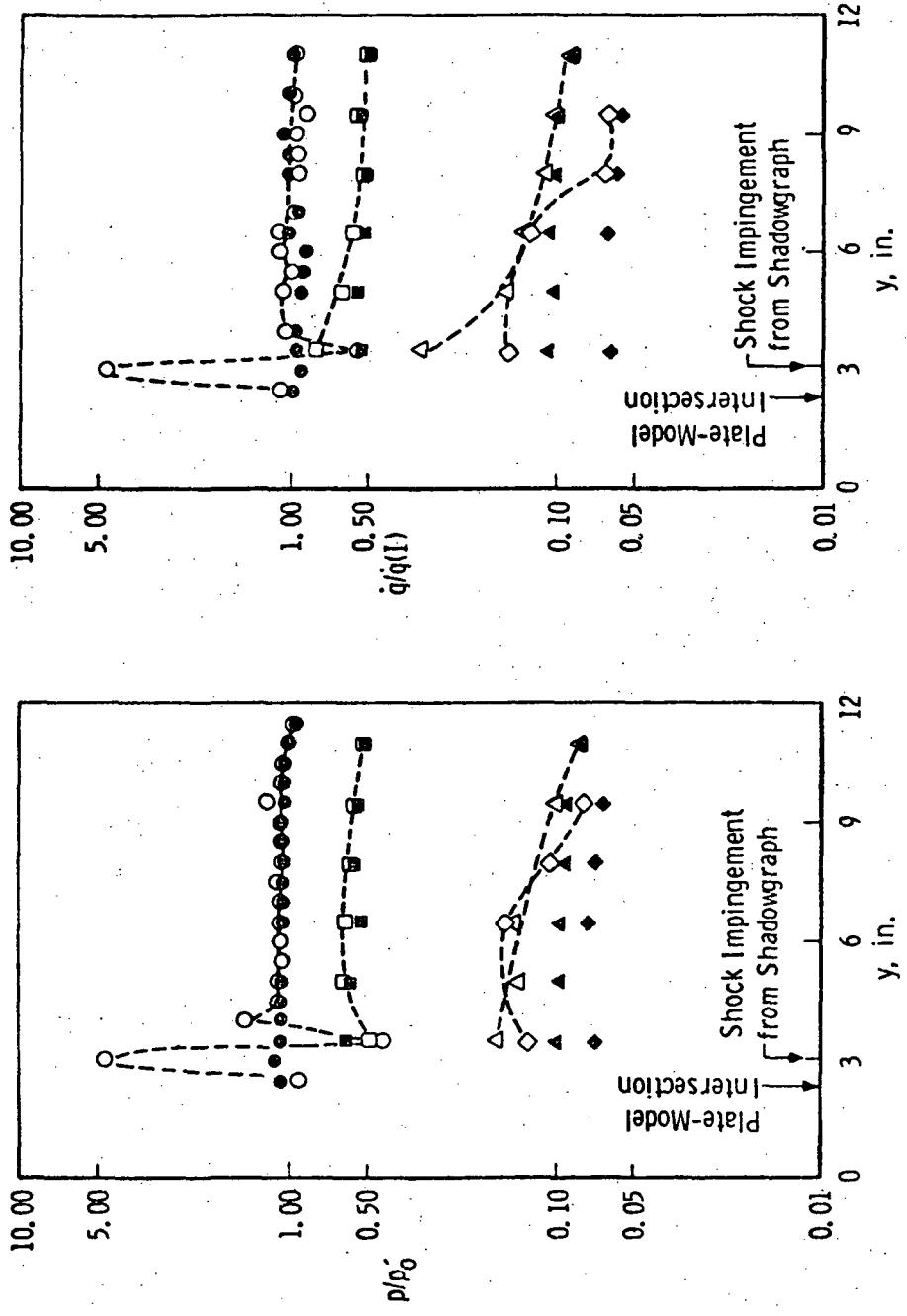
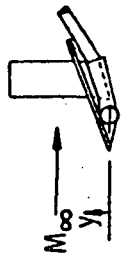


Figure 6. PRESSURE AND HEAT-TRANSFER DISTRIBUTION ON MODEL WITH SHOCK IMPINGEMENT
 ($\Lambda = 0$ AND $\delta = 20$ DEG)

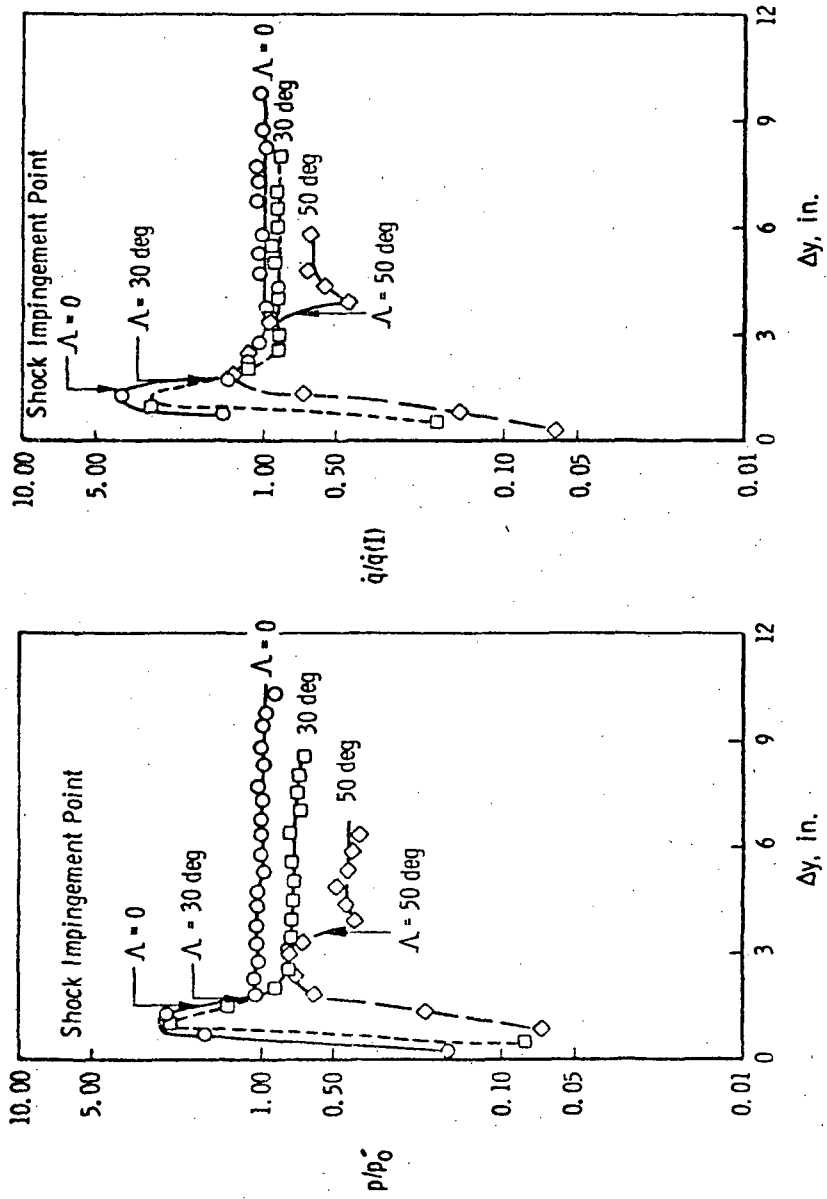
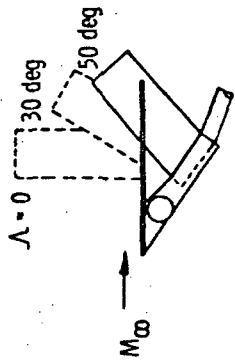


Figure 7. LEADING-EDGE PRESSURE AND HEAT-TRANSFER DISTRIBUTION FOR TYPICAL SWEEP ANGLES. (Λ) AT $\delta = 0$

MEASUREMENTS OF SHOCK-IMPINGEMENT EFFECTS ON THE
HEAT-TRANSFER AND PRESSURE DISTRIBUTIONS ON A
HEMICYLINDER MODEL AT MACH NUMBER 19

By E. C. Knox

AE DC-TR-65-245
November 1965

SYMBOLS

- M_∞ - free stream Mach number
- p - local pressure on model
- p'_o - test section pitot pressure
- p_{ref} - local pressure on model without shock generator
- \dot{q} - local heat transfer rate on model
- \dot{q}_o - stagnation heat transfer rate on 2-inch diameter hemisphere-cylinder
- $\dot{q}_o(I)$ - inferred stagnation heat transfer rate on unyawed and unswept 2-inch diameter hemicylinder
- Re_∞ - free stream unit Reynolds number
- Y - distance along hemicylinder leading edge (Figure 1)
- Λ - sweep angle
- δ - shock generator flow deflection angle

SUMMARY

The effects of leading-edge sweep angle and impinging shock strength on the pressure and heat-transfer distributions on a 2-inch diameter hemicylindrical leading edge were studied. The tests were conducted at a nominal free-stream Mach number of 19 and unit Reynolds number of 300,000 per foot. Test model is shown in Figure 1. Results are summarized as below:

- Typical pressure distributions are shown in Figure 2 for a shock-generator angle of 10 degrees and several leading-edge sweep angles. With the exception of the distribution for the unswept case, all distributions have marked similarities.
- Whenever the leading edge was unswept the flow on the shock generator surface was separated, except for the $\delta = 40$ -degree case. The pressure and heat-transfer distributions for $\delta = 20$ and $\delta = 40$ degrees with the unswept cylinder are shown in Figure 3. The different character of the distributions for $\delta = 40$ degrees (unseparated flow) is readily noted. As shown in Figure 3, max. $\dot{q}/\dot{q}(I)$ values of 5 and 3 were recorded for the case of $\delta = 20$ (with separation) and $\delta = 40$ (without separation) respectively.
- Comparison of the pressure and heat-transfer distributions for $\delta = 20$ degrees in Figure 3 shows almost a direct relationship, whereas, the heat-transfer distribution for $\delta = 40$ degree is notably different from the corresponding pressure distribution. The oscillations observed in the heat-transfer distribution for $\delta = 40$ degrees are attributed to the interaction of the impinging and bow shock waves.
- Utilizing some of the results presented in Reference 2 with the present results, a qualitative assessment of the effect of Mach number is shown in Figure 4 for Mach numbers of 6, 10 and 19 and $\Lambda = 40$ degrees, $\delta = 10$ degrees. The Reference 2 data are presented as the ratio of the measured pressure with shock-wave impingement to the measured pressure for the swept cylinder without shock-wave impingement. Similar measurements for the swept cylinder without shock-wave impingement at Mach 19 were not obtained, so an inferred value ($p'_0 \cos^2 \Lambda$) was used to reference the data at Mach 19. Comparison of the pressure distribution in Figure 4 shows that the recovery pressure at Mach 19 is approximately double that obtained at Mach 6 but with an attendant decrease in the breadth of its influence along the leading edge. As the recovery pressure increases with increasing Mach number, the region of influence decreases because of larger inclination of the impinging shock wave.

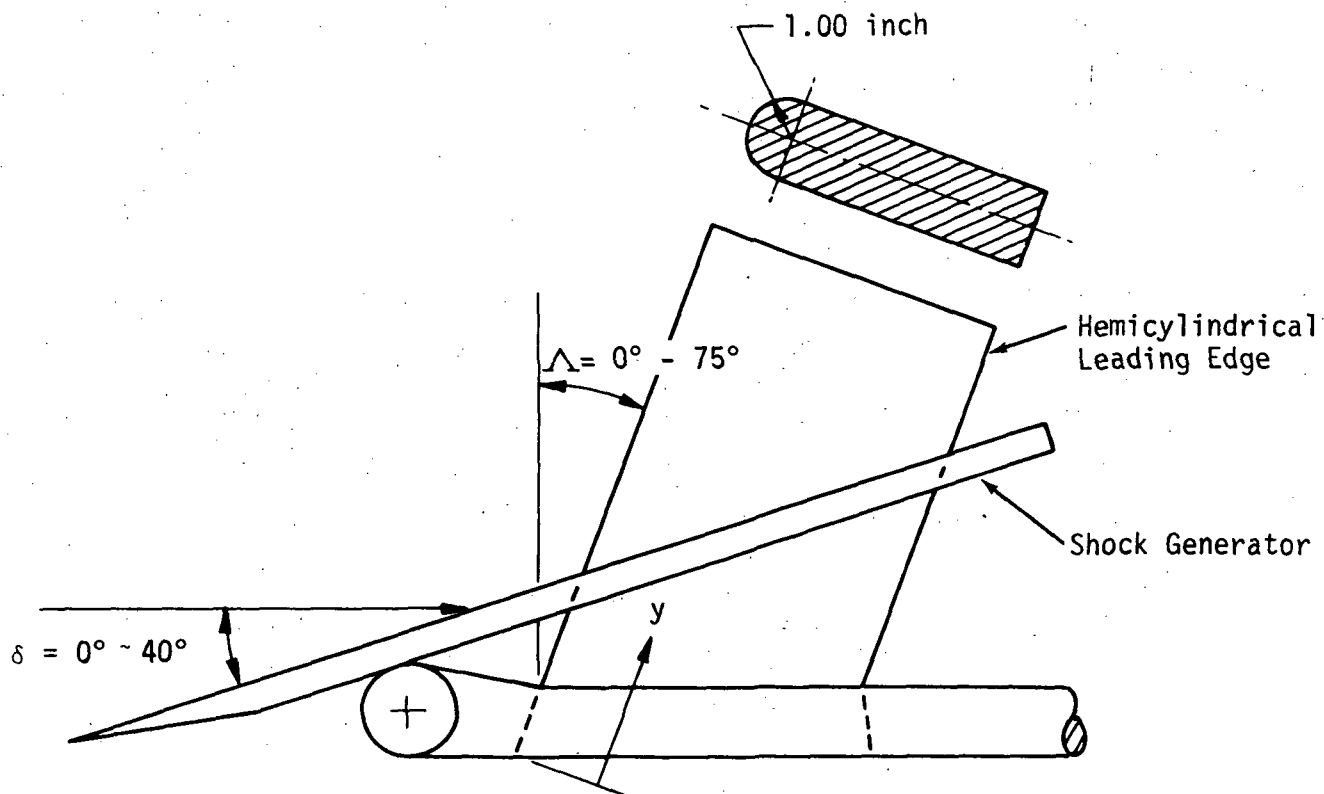


Figure 1. TEST CONFIGURATION-SHOCK GENERATOR AND HEMICYLINDRICAL LEADING EDGE

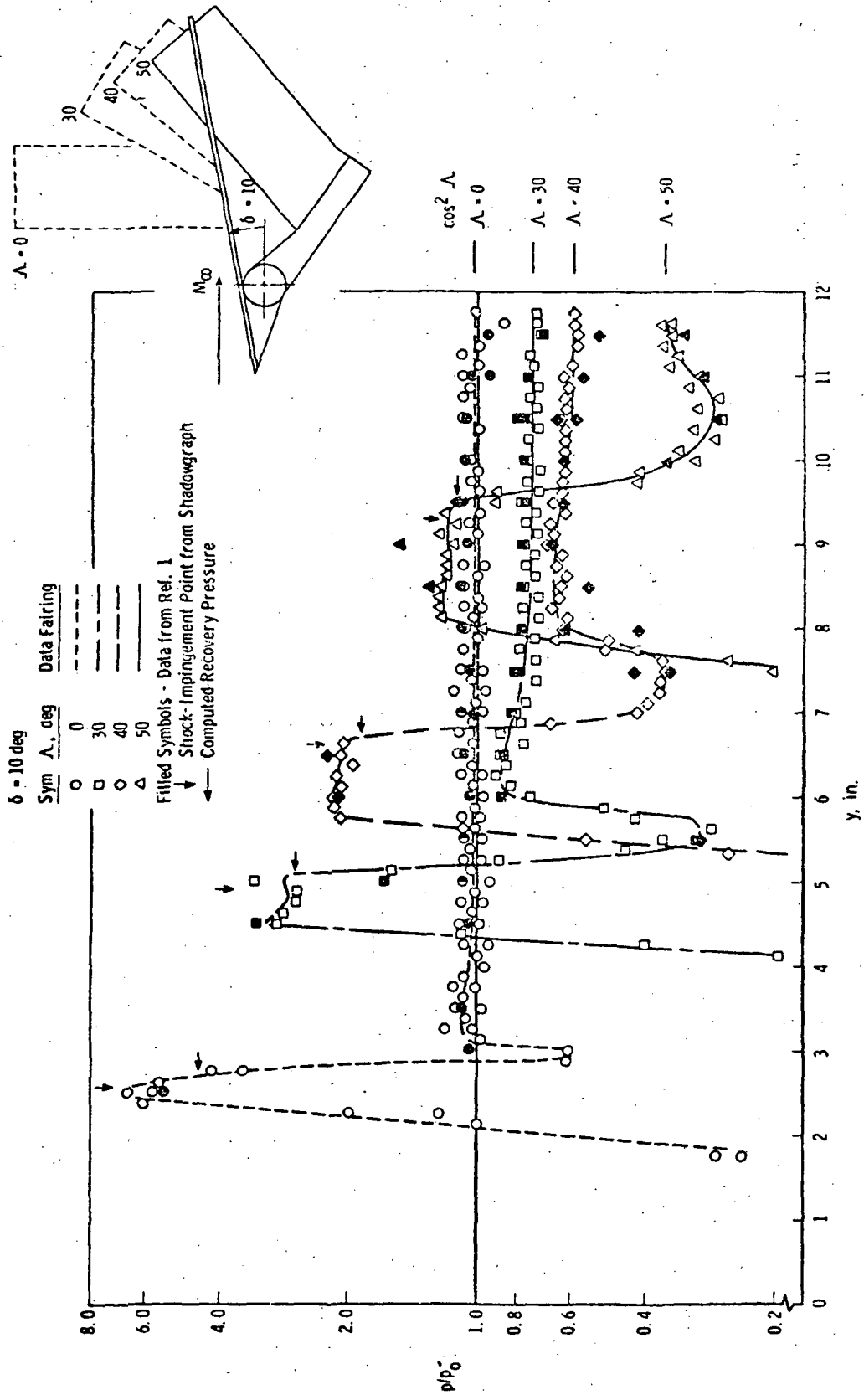
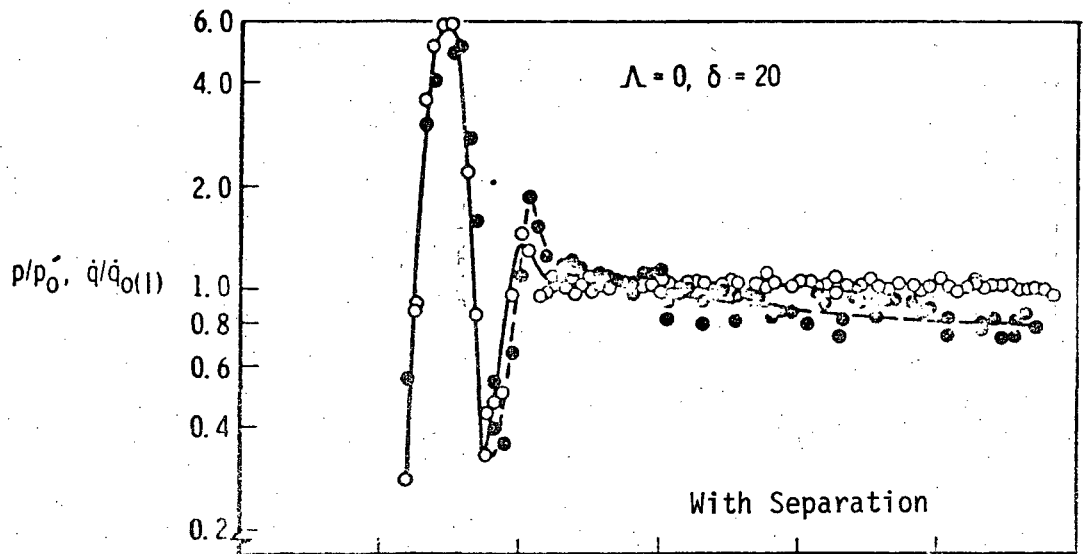


Figure 2. EFFECT OF LEADING-EDGE SWEEP ON PRESSURE DISTRIBUTIONS ALONG LEADING EDGE FOR $\delta = 10$ DEGREES



Sym	Distribution	Data Fairing
○	p/p_0	—
●	$q/q_0(l)$	- - -

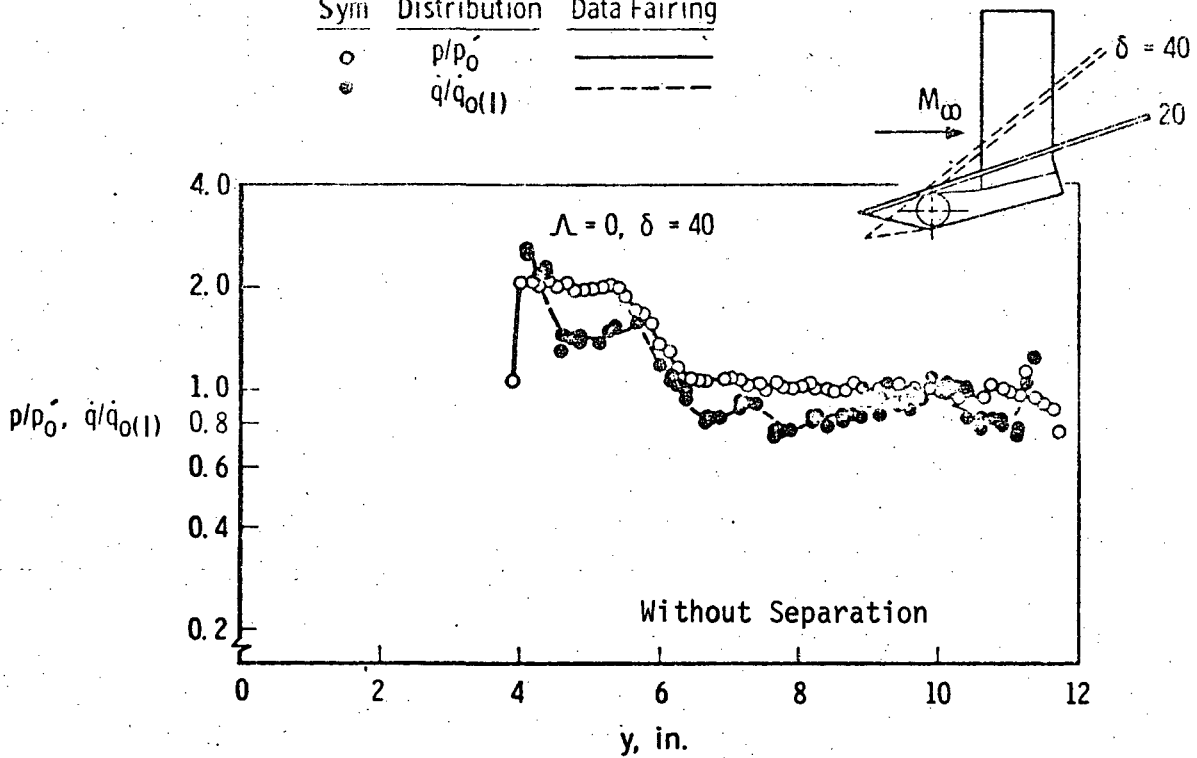


Figure 3. PRESSURE AND HEAT-TRANSFER DISTRIBUTIONS FOR THE UNSWEPT LEADING-EDGE AND TWO SHOCK-GENERATOR ANGLES, $M_\infty \approx 19$

For Mach 6 and 10 (Ref. 2),
 $p/p_{ref} = p(\text{with generator})/p(\text{without generator})$
 For Mach 19,
 $p/p_{ref} = p/p_0 \cos^2 \Lambda$

Experimental Shock
 Impingement Points

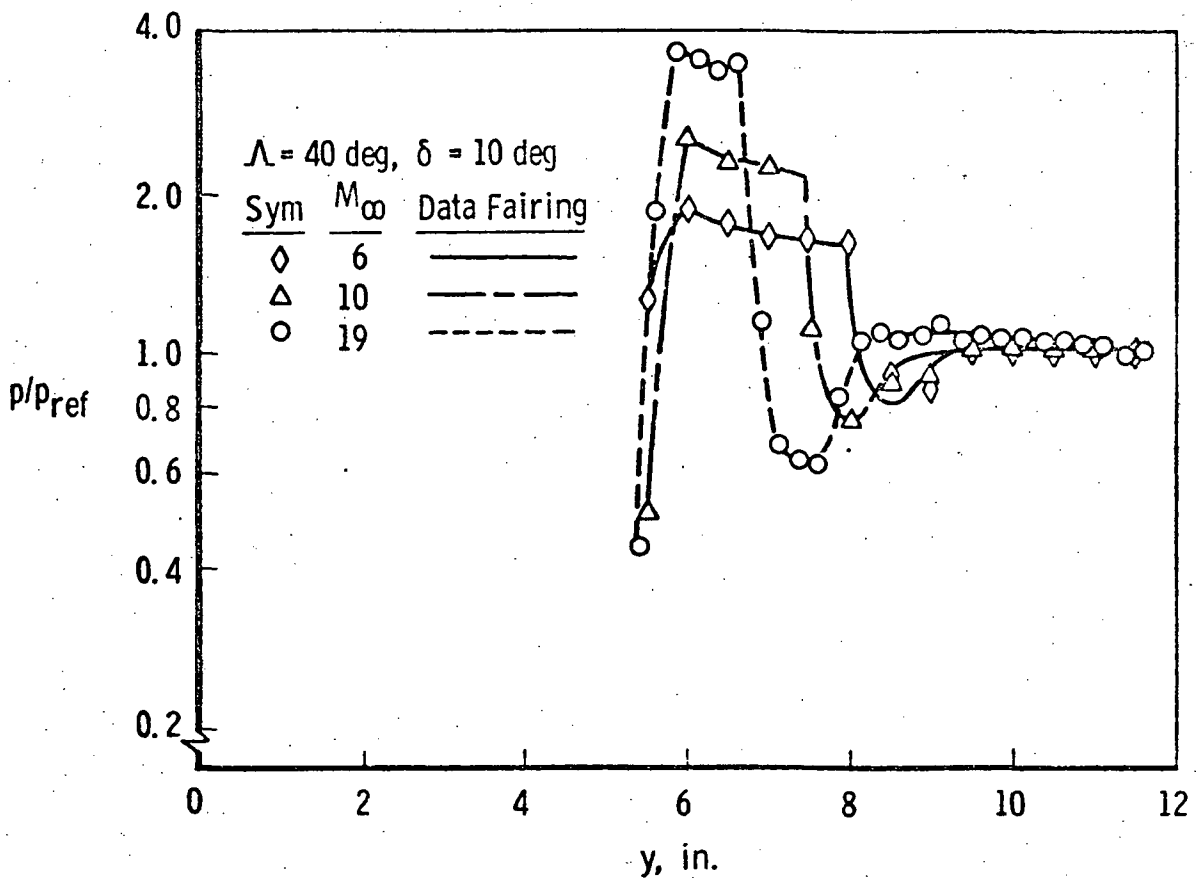
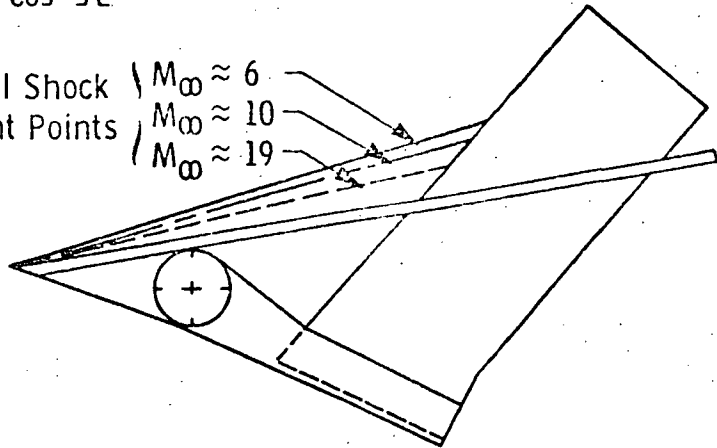


Figure 4. EFFECT OF MACH NUMBER ON THE PRESSURE DISTRIBUTION FOR $\Lambda = 40$ DEGREES AND $\delta = 10$ DEGREES

Appendix A-2

**ANALYSIS OF
SHOCK IMPINGEMENT**

FINAL REPORT

ANALYSIS OF THE SHOCK-IMPINGEMENT AND FLOW BETWEEN
THE SPACE SHUTTLE ORBITER AND BOOSTER

James C. Williams, III

Section I

INTRODUCTION

It is well known that high heating rates occur in the vicinity of the points where shock waves impinge on either the orbiter or the booster in the gap region between the two bodies. It is further known that the maximum rate of heat transfer in the vicinity of shock impingement is closely related to the strength of the impinging shock (ref. 1). The purpose of the proposed study was, then, to determine the location and strength of the impinging shocks in the gap region between the mated orbiter and booster.

It was recognized that any analysis of the flowfield between the orbiter and booster would be extremely complicated. The study was, therefore, limited to an analysis of the flow in the plane of symmetry of the two bodies where it might be possible to perform a quasi-two-dimensional flow analysis. The analysis which resulted, shows that in the plane of symmetry it is possible to cast the equations of motion in a quasi-two-dimensional form. This analysis is presented in Section II.

Once it was established that the equations of motion in the plane of symmetry could be cast in a quasi-two-dimensional form, it was necessary to decide on a solution technique for the equations of motion. A short survey of available techniques indicated that it was not possible, without a very extensive study, to solve even the quasi-two-dimensional equations of motion for the gap region. The most logical method of solution, the method of characteristics, is apparently not developed to the point where flows with interacting shock waves can be handled conveniently.

Regretably, then, it was necessary to abandon the idea of using a quasi-two-dimensional analysis to determine the location of shock impingement in the gap region. It is clear, however, that the exact impingement location could be obtained by other means, say from schlieren or shadowgraph photographs taken of the orbiter-booster model tested in a wind tunnel. This fact raises the question as to whether or not the pressure rise and other flow characteristics associated with a shock impingement can also be determined from

schlieren or shadowgraph pictures. Section III of this report addresses itself to this question. It is shown that if accurate measurements of the impinging and reflected shock wave angles can be made from high resolution schlieren or shadowgraph pictures it is possible to determine uniquely the flowfield parameters in the vicinity of the shock impingement. It is, therefore, possible to determine from schlieren or shadowgraph pictures not only the location of shock impingement, but also the flowfield characteristics necessary to estimate the increase in heat transfer rate due to impingement.

Section II

QUASI-TWO-DIMENSIONAL ANALYSIS OF THE FLOW IN THE PLANE OF SYMMETRY

As mentioned previously, the first phase of the present study involved determining whether or not a quasi-two-dimensional analysis of the flowfield, in the plane of symmetry between the orbiter and booster, is possible. In the following paragraphs it is shown that the equations of motion can be put into a form suitable for a quasi-two-dimensional analysis.

Consider the motion of an inviscid, compressible gas in a rectangular coordinate system (x, y, z) where the velocity components are (u, v, w) respectively, (Figure 1). If the x - y plane is taken as the plane of symmetry, then in the plane of symmetry $w = 0$ and the equations of continuity, x and y momentum and energy are respectively:

$$\frac{\partial \rho u}{\partial x} + \frac{\partial \rho v}{\partial y} + \frac{\partial \rho w}{\partial z} = 0 \quad (1)$$

$$\rho \left\{ u \frac{\partial u}{\partial x} + v \frac{\partial u}{\partial y} \right\} = - \frac{\partial p}{\partial x} \quad (2)$$

$$\rho \left\{ u \frac{\partial v}{\partial x} + v \frac{\partial v}{\partial y} \right\} = - \frac{\partial p}{\partial y} \quad (3)$$

$$\rho \left\{ u \frac{\partial h}{\partial x} + v \frac{\partial h}{\partial y} \right\} = u \frac{\partial p}{\partial x} + v \frac{\partial p}{\partial y} \quad (4)$$

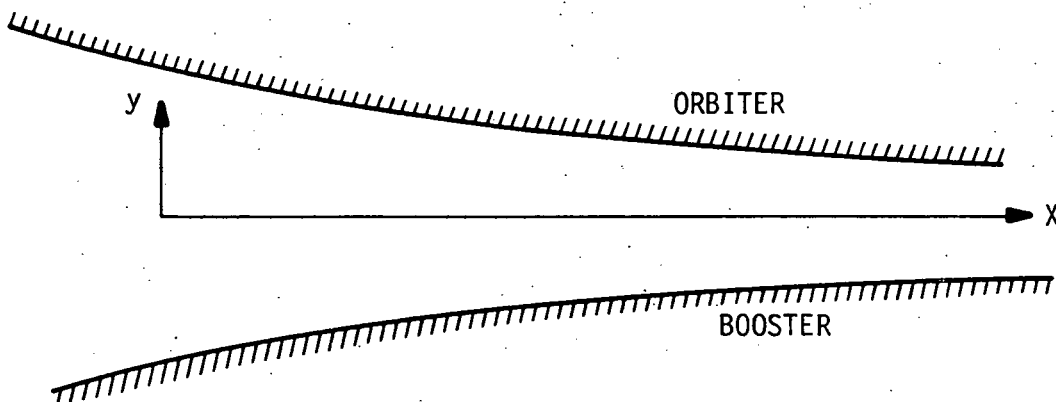


Figure 1.

Here p is the pressure, ρ is the density and h is the enthalpy of the gas.

It is of particular interest to note that except for the term $\frac{\partial \rho \omega}{\partial z}$ in the continuity equation, these equations are identical in form with the equations of motion for two-dimensional motion. Thus, if some convenient method can be found for expressing the term $\frac{\partial \rho \omega}{\partial z}$ in terms of known functions of the other variables, then a quasi-two-dimensional analysis of the problem is possible. In the present analysis, this term will be expressed in terms of the average x component of velocity and the geometry of the gap between the orbiter and booster.

Consider the element of the flowfield bound by two planes parallel to the plane of symmetry and located a distance Δz on either side of it, two planes normal to the x axis and a distance Δx apart, the upper surface of the booster, and the lower surface of the orbiter (Figure 2).

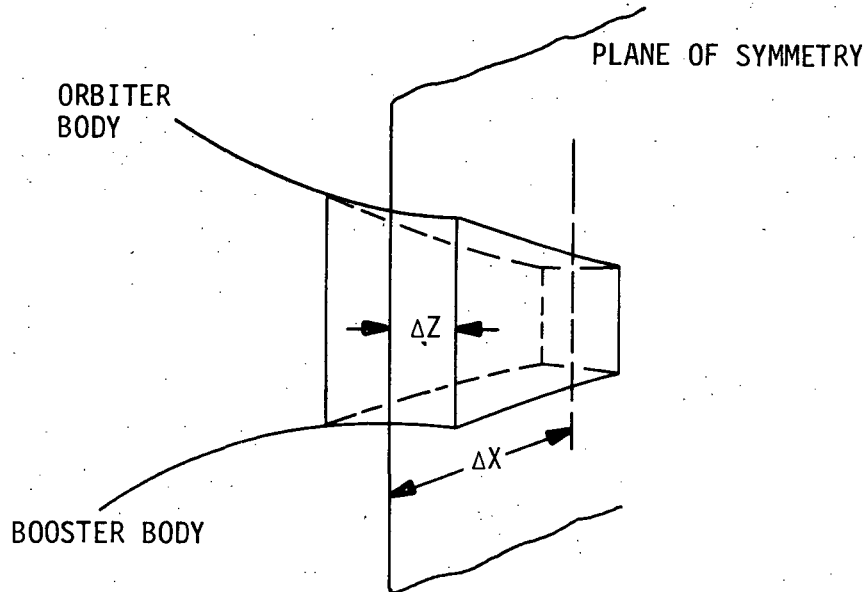


Figure 2.

Now consider the mass flow into and out of the element of volume shown in Figure 2 and resketched in Figure 3. It will now be assumed that $\rho \omega$ is independent of y . The difference between the mass flow entering through the front face, $\overline{\rho u} A$ and that exiting through the rear face $\left(\overline{\rho u} + \frac{d\overline{\rho u}}{dx} \Delta x \right) \cdot \left(A + \frac{dA}{dx} \Delta x \right)$

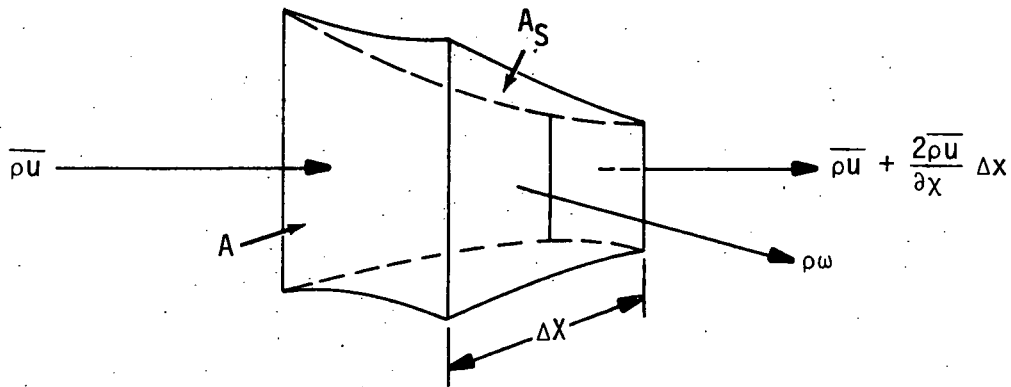


Figure 3.

must be equal to the mass flow out through the two side faces, $2 \rho \omega A_s$ where A_s is the area of the side face. Thus, for the element of volume, mass flow into volume = mass flow out of volume. Therefore one has

$$\overline{\rho u} A = \left(\overline{\rho u} + \frac{d}{dx} \overline{\rho u} \Delta x \right) \cdot \left(A + \frac{dA}{dx} \Delta x \right) + 2 \rho \omega A_s \quad (5)$$

where $\overline{\rho u}$ is the average mass flowrate in the x direction and the factor of two on the right hand side of equation (5) comes from the fact that there are two side faces (one on either side of the plane of symmetry) each with a mass flowrate $\rho \omega$ (per unit area).

Expanding equation (5) and neglecting the higher order terms (which have a coefficient Δx^2) one obtains:

$$0 = \overline{\rho u} \frac{dA}{dx} \Delta x + A \Delta x \frac{d}{dx} \overline{\rho u} + 2 \rho \omega A_s \quad (6)$$

Now from the geometry of the front face (Figure 4) note:

$$A = 2 \left\{ \frac{y_o + \left(y_o + \frac{\partial y_o}{\partial z} \Delta z \right)}{2} \right\}$$

$$\approx 2 y_o \Delta z$$

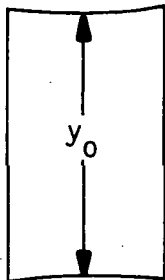


Figure 4.

where y_0 is the distance between the orbiter and the booster at the station in question so that $y_0 = y_0(x)$. Similarly, the area of the side force is given by

$$A_s \approx y_0 \Delta x$$

With these approximations equation 6 becomes

$$2 \rho \omega [y_0 \Delta x] = - \frac{d}{dx} \{2 y_0 \overline{\rho u}\} \Delta x \Delta z \quad (7)$$

Finally, note that since $w = 0$ at the plane of symmetry, the value of $\rho \omega$ (a distance Δz from the plane of symmetry) becomes, using a Taylor series expansion

$$\rho \omega \Big|_{\Delta z} = \frac{\partial \rho \omega}{\partial z} \Big|_{z=0} \Delta z + (\Delta z)^2$$

Introducing this result into equation (7) one obtains

$$\frac{\partial \rho \omega}{\partial z} \Big|_{z=0} \Delta z y_0 \Delta x = - \frac{d}{dx} (y_0 \overline{\rho u}) \Delta z \Delta x$$

or

$$\frac{\partial \rho \omega}{\partial z} = - \frac{1}{y_0} \frac{d}{dx} (y_0 \overline{\rho u}) \quad (8)$$

Employing this result in equation (1), one obtains

$$\frac{\partial \rho u}{\partial x} + \frac{\partial \rho v}{\partial y} - \frac{1}{y_0} (y_0 \overline{\rho u}) = 0$$

or

$$\frac{\partial \rho u}{\partial x} + \frac{\partial \rho v}{\partial y} = \zeta$$

where

$$\zeta = \frac{1}{y_0} \frac{d}{dx} (y_0 \overline{\rho u})$$

Now the flowfield in the plane of symmetry may be solved as a quasi-two-dimensional flowfield in the following manner:

1. Solve the flowfield between the orbiter and booster in the plane of symmetry as a strictly two-dimensional flow problem, i.e., assuming $\zeta = 0$, solve equations (2), (3), (4) and (9).
2. Evaluate ζ_1 , the first iteration of ζ , using the results of step 1.
3. Use ζ_1 , to resolve equations (2), (3), (4) and (9) for a new flowfield. From this flowfield calculate a new ζ and ζ_2 . Using ζ_2 solve the flowfield again.
4. Repeat step 3 as many times as necessary until a converged value of ζ is obtained. At this time one should have a reasonable approximation for the flowfield.

Section III

SHOCK IMPINGEMENT FLOWFIELD PROPERTIES FROM SCHLIEREN PHOTOGRAPHS OR SHADOWGRAPHS

The analysis presented in the previous section would appear to present a logical method for obtaining an approximate solution for the flowfield between the orbiter and booster. The difficulty lies in the fact that there are no solution techniques for the problem as outlined above. The most logical method, the method of characteristics, is apparently not developed to the point where it may be used on flow fields with multiple interacting shock waves such as occur between the orbiter and booster. It is necessary then to seek an alternate method of obtaining the desired information, i.e., the location and strength of the shock waves impinging on the orbiter and booster in the gap region. The location of the shock impingement points may be obtained from schlieren photographs and there appear to be many of these available. What about the shock wave strength and flow characteristics near the impingement points? In this section it is shown that if the angles of the impinging and reflected shock waves can be determined accurately one can determine, from these angles, the necessary information concerning the flowfield in the vicinity of the shock impingement.

Consider the shock wave W impinging on the body, DBE, at point B. The wave, R, is reflected from the body, also at point B. A-B-C is the local tangent to the body at point B. The body is assumed to have a very large radius of curvature at B so that A-B-C and D-B-E almost coincide. The impinging wave W makes an angle θ_1 with the local body tangent while the reflected wave R makes an angle θ_2 with the local body tangent (Figure 5).

It should be noted that in the plane of symmetry, since $w = 0$, the two dimensional shock wave relations are valid. The shock wave relations are true even in the more general case of two and three dimensional curved shock waves. (See reference 2, page 559.) The Mach numbers M_1 and M_2 are related then by (ref. 3)

$$M_2^2 = \frac{(\gamma + 1)^2 M_1^4 \sin^2 \theta_1 - 4(M_1^2 \sin^2 \theta_1 - 1)(\gamma M_1^2 \sin^2 \theta_1 + 1)}{[2 \gamma M_1^2 \sin^2 \theta_1 - (\gamma - 1)][(\gamma - 1) M_1^2 \sin^2 \theta_1 + 2]} \quad (10)$$

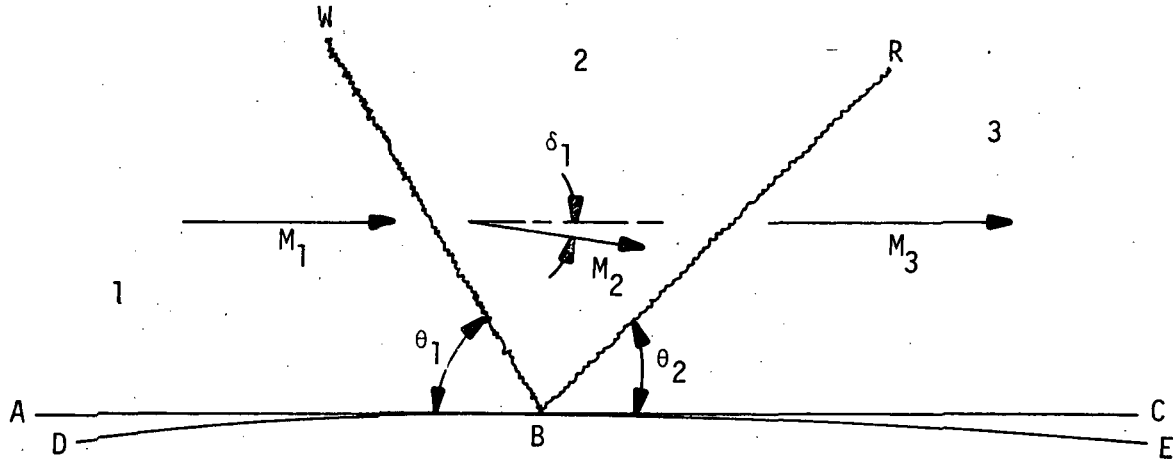


Figure 5.

while the angle through which the flow is deflected in passing through the shock wave, δ_1 is related to M_1 by

$$\text{TAN. } \delta_1 = \frac{2 \cot \theta_1 (M_1^2 \sin^2 \theta_1 - 1)}{2 + M_1^2 (\gamma + 1 - 2 \sin^2 \theta_1)} \quad (11)$$

The flow in region 2 with Mach number M_2 sees a shock wave (the reflected wave) which has a shock angle, with respect to the flow in region 2, of $\theta_2 + \delta_1$. Thus M_2 and M_3 are related by

$$M_3^2 = \frac{(\gamma - 1)^2 M_2^4 \sin^2 (\theta_2 + \delta_1) - 4(M_2^2 \sin^2 (\theta_2 + \delta_1) - 1)(M_2^2 \gamma \sin^2 (\theta_2 + \delta_1) + 1)}{[2 \gamma M_2^2 \sin^2 (\theta_2 + \delta_1) - (\gamma - 1)][(\gamma - 1) M_2^2 \sin^2 (\theta_2 + \delta_1) + 2]} \quad (12)$$

while the angle through which the flow is deflected in passing through the reflected shock wave is given by

$$\text{TAN } \delta_2 = \frac{2 \cot (\theta_2 + \delta_1) (M_2^2 \sin^2 (\theta_2 + \delta_1) - 1)}{2 + M_2^2 (\gamma + 1 - 2 \sin^2 (\theta_2 + \delta_1))} \quad (13)$$

Equations (10), (11), (12), and (13) comprise a system of four equations in five unknowns M_1 , M_2 , M_3 , δ_1 and δ_2 , assuming the wave angles of θ_1 and θ_2

are given. One additional relationship is necessary to complete the systems and determine unique values for each of the five variables. The additional relation necessary comes from the fact that the flows before and after the shock system must be parallel. Thus if the streamlines are turned through an angle δ_1 , by the incident shock wave, they must be turned back through the same angle by the reflected shock wave. Thus

$$\delta_1 = \delta_2 = \delta \quad (14)$$

Now there are five equations in five unknowns. Combining equations (11) and (13) yields

$$M_2 = \frac{2 \text{TAN } \delta + 2 \text{COT } (\theta_2 + \delta)}{2 \text{COT } (\theta_2 + \delta) \sin^2 (\theta_2 + \delta) - \text{TAN } \delta (\gamma + 1 - 2 \sin^2 (\theta_2 + \delta))} \quad (15)$$

which when combined with equation (10) yields

$$\begin{aligned} \text{FN}(M_1) &= \frac{2 \text{TAN } \delta + 2 \text{COT } (\theta_2 + \delta)}{2 \text{COT } (\theta_2 + \delta) \sin^2 (\theta_2 + \delta) - \text{TAN } \delta (\gamma + 1 - 2 \sin^2 (\theta_2 + \delta))} \\ &\quad - \frac{(\gamma - 1)^2 M_1^4 \sin^2 \theta_1 - 4(M_1^2 \sin^2 \theta_1 - 1)(\gamma M_1^2 \sin^2 \theta_1 + 1)}{[2 \gamma M_1^2 \sin^2 \theta_1 - (\gamma - 1)][(\gamma - 1) M_1^2 \sin^2 \theta_1 + 2]} \\ &= 0 \end{aligned} \quad (16)$$

In equation (16) δ is given in terms of M_1 (and θ_1) by

$$\delta = \text{ARC TAN } \frac{2 \text{COT } \theta_1 \cdot (M_1^2 \sin^2 \theta_1 - 1)}{2 + M_1^2 (\gamma + 1 - 2 \sin^2 \theta_1)} \quad (17)$$

Once θ_1 and θ_2 are prescribed one can solve equations (16) and (17) simultaneously to obtain the value of M_1 which satisfies the prescribed conditions. Once M_1 is known, equations (10), (11) and (12) may be solved to obtain M_2 , δ , and M_3 . Other quantities such as pressure and temperature

ratios may be found, once M_1 , M_2 , δ , and M_3 are known, from standard tables, charts or equations (ref. 3).

If equation (17) is inserted in equation (16) and the resulting equation is rearranged it has some of the characteristics of a 6th order polynomial in M_1 or a 3rd order polynomial in M_1^2 . One might expect then six roots, three of which are negative and of no consequence and three of which are positive. The question arises as to which of the positive roots is correct. In practice, there is no problem in choosing the correct root since generally the two which are not correct give rise to impossible physical situations. Generally the false roots show $M_2 < M_1$ and a negative value of δ . This situation is physically impossible.

The analysis developed above has been applied to a number of test cases and found to give correct results. It was then applied to two shock impingement points obtained from a shadowgraph of the orbiter-booster combination tested at a free-stream Mach number of 3.7. The picture from which the wave angles were measured is shadowgraph No. 25 presented in Figure 27 of reference 4. Figure 6 is a sketch of the shadowgraph referred to above indicating the shock impingement points where the present analysis was applied.

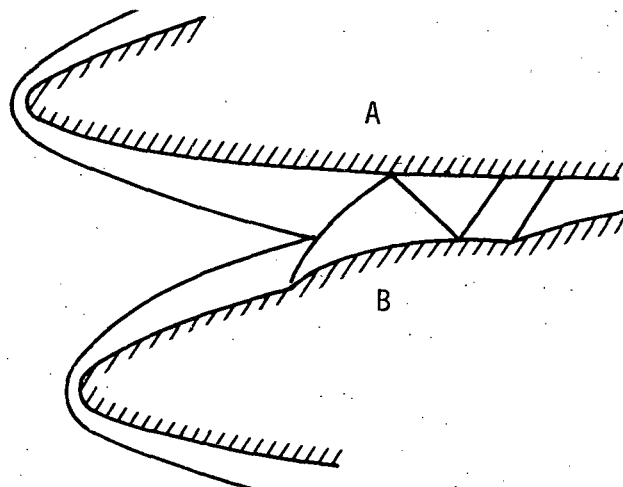


Figure 6.

The roots of equation (16) were obtained by calculating $FN(M_1)$ as a function of M_1 in the range $1 \leq M_1 \leq 4.0$, plotting the results, and determining

the value of M_1 for which $FN(M_1)$ vanishes. The calculations and the listing for the simple computer program used to make the calculations are attached as the Appendix. The curves of $FN(M_1)$ for the two cases are shown in Figure 7. For point A the Mach number M_1 is 3.43 and for point B the Mach number M_1 is 3.02. The remaining properties of the flowfield may be obtained either from solving equations previously presented or from standard tables and charts such as those presented in reference 3. The complete results for points A and B are shown in Table I.

TABLE I
RESULTS FOR POINTS A AND B, SHADOWGRAPH NO. 25

	POINT A	POINT B
θ_1	27.6°	31.0°
θ_2	20.0°	24.2°
M_1	3.43	3.02
M_2	2.67	2.32
M_3	2.10	1.78
δ	12.9°	13.8°
p_2/p_1	2.783	2.636
p_3/p_1	6.36	5.83

It should be pointed out that accurate computations using the above analysis require accurate measurement of the shock wave angles θ_1 and θ_2 . Some error is expected in the results presented herein due to small scale, poor resolution photographs from which θ_1 and θ_2 were taken.

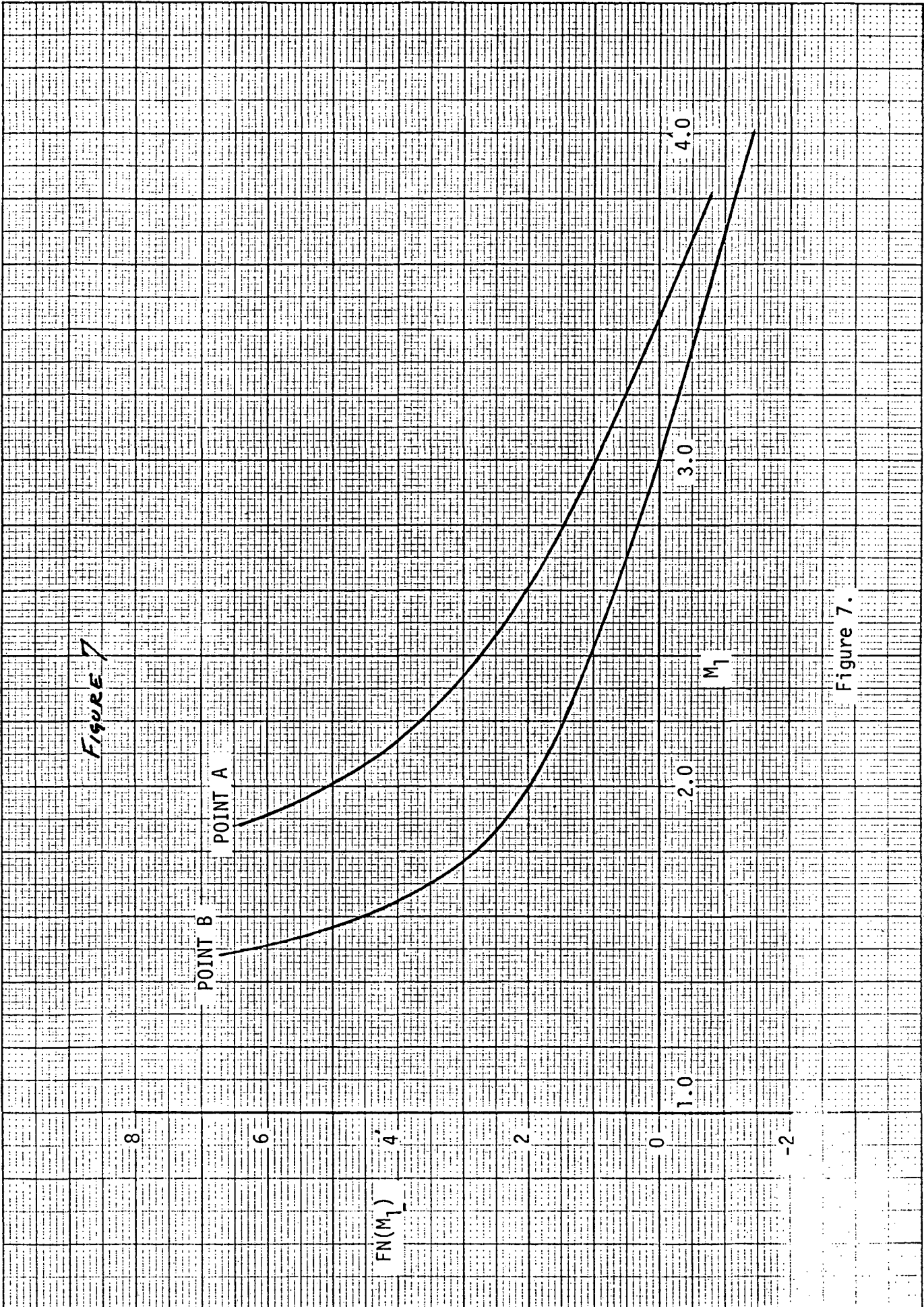


Figure 7.

Section IV

REFERENCES

1. Sayano, S., "Heat Transfer in Shock Wave-Turbulent Boundary Layer Interaction Regions", Douglas Aircraft Company Report SM-42567, November 19, 1962.
2. Shapiro, A. H., "The Dynamics and Thermodynamics of Compressible Fluid Flow, Volume I", The Roland Press Company, New York, New York, 1953.
3. Ames Research Staff, "Equations, Tables and Charts for Compressible Flow" NACA Report 1135, 1953.
4. Roberge, A. M. and C. C. Gordon, "Heat Transfer Results on Space Shuttle Phase B. Launch Configurations at Mach Numbers 2.5 and 3.7" Report 76-549-4-128/584-TP-400, General Dynamics Corporation, Convair Aerospace Division, April 1971.

// JOB T

LOG DRIVE	CART SPEC	CART AVAIL	PHY DRIVE
0000	100A	100A	0000

V2 M08 ACTUAL 8K CONFIG 8K

// FOR

*IOCS(CARD, 1132 PRINTER)

*ONE WORD INTEGERS

*LIST SOURCE PROGRAM

REAL M1,M2,M3,M2P

C ANGL1=ANGLE THETA 1 IN DEGREES

C ANGL2=ANGLE THETA 2 IN DEGREES

C THET1=ANGLE THETA 1 IN RADIANS

C THET2=ANGLE THETA 2 IN RADIANS

C ADELTA=ANGLE DELTA IN DEGREES

C DELTA=ANGLE DELTA IN RADIANS

C M1=MACH NUMBER IN REGION 1

C M2=MACH NUMBER IN REGION 2

C M3=MACH NUMBER IN REGION 3

C GAM=GAMMA

C TAND=TANGENT OF DELTA

C FNM1=THE FUNCTION OF M1 DEFINED IN TEXT

905 FORMAT(1H ,//,10X,'SHADOWGRAPH NO 25,POINT A',)

ANGL1=27.6

ANGL2=20.0

THET1=ANGL1*0.01745329

THET2=ANGL2*0.01745329

WRITE(3,900)ANGL1,ANGL2

900 FORMAT(1H1,//,10X,'THETA1=',1E16.8,'THETA2=',1E16.8)

WRITE(3,905)

WRITE(3,901)

901 FORMAT(1H ,//,17X,'M1',16X,'DELTA',15X,'M2',16X,'M3',15X,'FNM1',)

GAM=1.4

M1=1.0

DM1=0.10

$$1 \text{ TAND} = 2.0 * (\cos(\text{THET1}) / \sin(\text{THET1})) * ((\text{M1}^{**2}) * (\sin(\text{THET1})^{**2}) - 1.0) / (2.0 + (\text{M1}^{**2}) * (\text{GAM} + 1.0 - 2.0 * (\sin(\text{THET1})^{**2})))$$

DELTA=ATAN(TAND)

ADELT=DELTA/0.01745329

THET4=THET2+DELTA

COTAN=COS(THET4)/SIN(THET4)

$$\text{M2} = \sqrt{((2.0 * \text{TAND} + 2.0 * \text{COTAN}) / (2.0 * \text{COTAN} * (\sin(\text{THET4})^{**2}) - \text{TAND} * (\text{GAM} + 1.0 - 2.0 * \sin(\text{THET4})^{**2})))}$$

$$\text{M2P} = (((\text{GAM} + 1.0)^{**2}) * (\text{M1}^{**4}) * (\sin(\text{THET1})^{**2}) - 4.0 * ((\text{M1}^{**2}) * (\sin(\text{THET1})^{**2}) - 1.0) * (\text{GAM} * (\text{M1}^{**2}) * (\sin(\text{THET1})^{**2}) + 1.0)) / ((2.0 * 2 * \text{GAM} * (\text{M1}^{**2}) * (\sin(\text{THET1})^{**2}) - \text{GAM} + 1.0) * ((\text{GAM} - 1.0) * (\text{M1}^{**2}) * (\sin(\text{THET1})^{**2}) + 2.0))$$

$$\text{FNM1} = \text{M2}^{**2} - \text{M2P}$$

$$\text{M3} = \sqrt{(((\text{GAM} + 1.0)^{**2}) * (\text{M2}^{**4}) * (\sin(\text{THET4})^{**2}) - 4.0 * ((\text{M2}^{**2}) * (\sin(\text{THET4})^{**2}) - 1.0) * (\text{GAM} * (\text{M2}^{**2}) * (\sin(\text{THET4})^{**2}) + 1.0)) / ((2.0 * 2 * \text{GAM} * (\text{M2}^{**2}) * (\sin(\text{THET4})^{**2}) - \text{GAM} + 1.0) * ((\text{GAM} - 1.0) * (\text{M2}^{**2}) * (\sin(\text{THET4})^{**2}) + 2.0))}$$

$$3 * (\sin(\text{THET4})^{**2}) + 2.0))$$

WRITE(3,902)M1,ADELTA,M2,M3,FNM1

902 FORMAT(1H ,10X,5(1E16.8,2X))

IF(M1-5.00)10,10,20

10 M1=M1+DM1

GO TO 1

20 CALL EXIT

END

FEATURES SUPPORTED
ONE WORD INTEGERS
IOCS

CORE REQUIREMENTS FOR
COMMON 0 VARIABLES 58 PROGRAM 598

END OF COMPILATION

// XEQ

SHADOWGRAPH NO 25, POINT A

M1	DELTA	M2	M3	FNMI
0.1000002E 01	-0.37113525E 02	0.26711559E 01	0.30741224E 01	-0.55582332E 01
0.1100001E 01	-0.32859077E 02	0.30909023E 01	0.38195877E 01	0.10588681E 01
0.1200000E 01	-0.28650440E 02	0.37940650E 01	0.53261079E 01	0.77953071E 01
0.12999999E 01	-0.24577018E 02	0.52693071E 01	0.12826364E 02	0.22181770E 02
0.13999998E 01	-0.20707771E 02	0.13576553E 02	0.72435464E 01	0.17932434E 03
0.14999997E 01	-0.17089248E 02	0.67986822E 01	0.16252796E 02	0.41565246E 02
0.15999996E 01	-0.13746965E 02	0.47184295E 01	0.72810344E 01	0.17796146E 02
0.16999995E 01	-0.10689065E 02	0.39375381E 01	0.50102625E 01	0.11124328E 02
0.17999994E 01	-0.79107313E 01	0.35207653E 01	0.41096315E 01	0.80316925E 01
0.18999993E 01	-0.53984651E 01	0.32644281E 01	0.36019816E 01	0.62555761E 01
0.19999992E 01	-0.31336555E 01	0.30943985E 01	0.32697687E 01	0.50978441E 01
0.20999994E 01	-0.10952489E 01	0.19763784E 01	0.30332946E 01	0.42741308E 01
0.21999993E 01	0.73839151E 00	0.28920540E 01	0.28555898E 01	0.36479096E 01
0.22999992E 01	0.23882989E 01	0.28306708E 01	0.27168803E 01	0.31460681E 01
0.23999991E 01	0.38742060E 01	0.27854733E 01	0.26055169E 01	0.27262873E 01
0.24999990E 01	0.52142095E 01	0.27519993E 01	0.25141434E 01	0.23626074E 01
0.25999989E 01	0.64246339E 01	0.27271905E 01	0.24378604E 01	0.20384101E 01
0.26999988E 01	0.75200548E 01	0.27088842E 01	0.23732667E 01	0.17426781E 01
0.27999987E 01	0.85134010E 01	0.26955180E 01	0.23179206E 01	0.14679329E 01
0.28999986E 01	0.94160614E 01	0.26859393E 01	0.22700204E 01	0.12089850E 01
0.29999985E 01	0.10238071E 02	0.26792836E 01	0.22282037E 01	0.96217334E 00
0.30999984E 01	0.10988245E 02	0.26748962E 01	0.21914234E 01	0.72489929E 00
0.31999983E 01	0.11674306E 02	0.26722750E 01	0.21588583E 01	0.49531096E 00
0.32999982E 01	0.12303060E 02	0.26710300E 01	0.21298537E 01	0.27205705E 00
0.33999981E 01	0.12880479E 02	0.26708583E 01	0.21038851E 01	0.54181061E-01
0.34999980E 01	0.13411809E 02	0.26715226E 01	0.20805249E 01	-0.15900811E 00
0.35999980E 01	0.13901689E 02	0.26728344E 01	0.20594201E 01	-0.36799806E 00
0.36999979E 01	0.14354194E 02	0.26746425E 01	0.20402765E 01	-0.57315266E 00
0.37999978E 01	0.14772951E 02	0.26768298E 01	0.20228509E 01	-0.77470457E 00
0.38999977E 01	0.15161151E 02	0.26793026E 01	0.20069365E 01	-0.97281372E 00
0.39999976E 01	0.15521640E 02	0.26819858E 01	0.19923577E 01	-0.11675846E 01
0.40999975E 01	0.15856946E 02	0.26848154E 01	0.19789638E 01	-0.13591098E 01
0.41999969E 01	0.16169323E 02	0.26877465E 01	0.19666268E 01	-0.15473988E 01
0.42999963E 01	0.16460773E 02	0.26907386E 01	0.19552350E 01	-0.17324945E 01
0.43999958E 01	0.16733112E 02	0.26937618E 01	0.19446923E 01	-0.19143919E 01
0.44999952E 01	0.16987949E 02	0.26967897E 01	0.19349124E 01	-0.20931077E 01
0.45999946E 01	0.17226730E 02	0.26998047E 01	0.19258236E 01	-0.22686286E 01
0.46999940E 01	0.17450763E 02	0.27027902E 01	0.19173598E 01	-0.24409527E 01
0.47999935E 01	0.17661232E 02	0.27057352E 01	0.19094648E 01	-0.26100759E 01
0.48999929E 01	0.17859188E 02	0.27086286E 01	0.19020860E 01	-0.27760005E 01
0.49999923E 01	0.18045604E 02	0.27114658E 01	0.18951797E 01	-0.29387292E 01
0.50999918E 01	0.18221344E 02	0.27142391E 01	0.18887052E 01	-0.30982694E 01

SHADOWGRAPH NO 25 POINT B

M1

DELTA

M2

M3

FNMI

0.1000000E 01	-0.32294021E 02	0.35546722E 01	0.59330778E 01	0.49355602E 01
0.1100001E 01	-0.27937278E 02	0.52757816E 01	0.12790143E 02	0.22017650E 02
0.1200000E 01	-0.23673961E 02	0.14236076E 02	0.58234205E 01	0.19783551E 03
0.12999999E 01	-0.19592117E 02	0.48856411E 01	0.19785141E 02	0.19600959E 02
0.13999998E 01	-0.15754936E 02	0.36753320E 01	0.55041246E 01	0.95666771E 01
0.14999997E 01	-0.12200710E 02	0.31461768E 01	0.40240097E 01	0.61401863E 01
0.15999996E 01	-0.89460087E 01	0.28507952E 01	0.33567242E 01	0.44569149E 01
0.16999995E 01	-0.59906902E 01	0.26673193E 01	0.29618558E 01	0.34664602E 01
0.17999994E 01	-0.33230118E 01	0.25468282E 01	0.26966047E 01	0.28122816E 01
0.18999993E 01	-0.92414868E 00	0.24653067E 01	0.25047006E 01	0.23420038E 01
0.19999992E 01	0.12283413E 01	0.24094023E 01	0.23589048E 01	0.19805138E 01
0.20999994E 01	0.31580853E 01	0.23710370E 01	0.22442226E 01	0.16869807E 01
0.21999993E 01	0.48883142E 01	0.23450274E 01	0.21516375E 01	0.14376158E 01
0.22999992E 01	0.64409418E 01	0.23278999E 01	0.20753622E 01	0.12178249E 01
0.23999991E 01	0.78360729E 01	0.23172454E 01	0.20114946E 01	0.10183053E 01
0.24999990E 01	0.90918369E 01	0.23113546E 01	0.19572970E 01	0.83296156E 00
0.25999989E 01	0.10224382E 02	0.23089861E 01	0.19107863E 01	0.65770614E 00
0.26999988E 01	0.11247978E 02	0.23092284E 01	0.18704903E 01	0.48977840E 00
0.27999987E 01	0.12175163E 02	0.23114028E 01	0.18352899E 01	0.32730281E 00
0.28999986E 01	0.13016925E 02	0.23149943E 01	0.18043158E 01	0.16897574E 00
0.29999985E 01	0.13782873E 02	0.23196196E 01	0.17768895E 01	0.13955833E 01
0.30999984E 01	0.14481424E 02	0.23249797E 01	0.17524638E 01	-0.13836127E 00
0.31999983E 01	0.15119924E 02	0.23308501E 01	0.17306003E 01	-0.28833234E 00
0.32999982E 01	0.15704803E 02	0.23370571E 01	0.17109398E 01	-0.43619281E 00
0.33999981E 01	0.16241714E 02	0.23434667E 01	0.16931860E 01	-0.58207750E 00
0.34999980E 01	0.16735599E 02	0.23499770E 01	0.16770923E 01	-0.72604060E 00
0.35999980E 01	0.17190822E 02	0.23565096E 01	0.16624510E 01	-0.86809575E 00
0.36999979E 01	0.17611209E 02	0.23630056E 01	0.16490888E 01	-0.10082163E 01
0.37999978E 01	0.18000156E 02	0.23694200E 01	0.16368577E 01	-0.11463720E 01
0.38999977E 01	0.18360656E 02	0.23757186E 01	0.16256287E 01	-0.12825067E 01
0.39999976E 01	0.18695369E 02	0.23818769E 01	0.16152944E 01	-0.14165666E 01
0.40999975E 01	0.19006649E 02	0.23878789E 01	0.16057598E 01	-0.15484869E 01
0.41999969E 01	0.19296611E 02	0.23937106E 01	0.15969426E 01	-0.16782195E 01
0.42999963E 01	0.19567127E 02	0.23993654E 01	0.15887718E 01	-0.18057148E 01
0.43999958E 01	0.19819873E 02	0.24048380E 01	0.15811836E 01	-0.19309220E 01
0.44999952E 01	0.20056366E 02	0.24101276E 01	0.15741238E 01	-0.20538163E 01
0.45999946E 01	0.20277938E 02	0.24152340E 01	0.15675442E 01	-0.21743488E 01
0.46999940E 01	0.20485817E 02	0.24201598E 01	0.15614011E 01	-0.22925100E 01
0.47999935E 01	0.20681087E 02	0.24249057E 01	0.15556552E 01	-0.24082827E 01
0.48999929E 01	0.20864749E 02	0.24294776E 01	0.15502734E 01	-0.25216460E 01
0.49999923E 01	0.21037696E 02	0.24338808E 01	0.154522261E 01	-0.26326022E 01
0.50999918E 01	0.21200737E 02	0.24381165E 01	0.15404837E 01	-0.27411637E 01

Appendix A-3

INTERFERENCE HEATING AT FIN-PLATE CORNERS

TR-794-921A
APRIL 1971

SHOCK INTERFERENCE HEATING IN THE VICINITY OF FIN-PLATE CORNERS

Prepared for:

**NATIONAL AERONAUTICS AND SPACE ADMINISTRATION
GEORGE C. MARSHALL SPACE FLIGHT CENTER
Aero-Astrodynamics Laboratory**

UNDER CONTRACT NAS8-26268

**NORTHROP CORPORATION
ELECTRO-MECHANICAL DIVISION
P. O. BOX 1484
HUNTSVILLE, ALABAMA 35807
TELEPHONE (205)837-0580**

SHOCK INTERFERENCE HEATING IN THE VICINITY OF FIN-PLATE CORNERS

April 1971

by

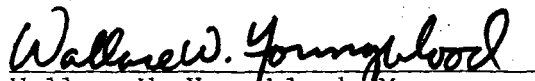
F. T. Hung

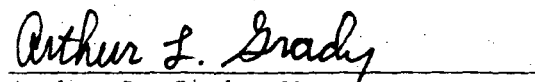
PREPARED FOR:

**NATIONAL AERONAUTICS AND SPACE ADMINISTRATION
GEORGE C. MARSHALL SPACE FLIGHT CENTER
AERO-ASTRODYNAMICS LABORATORY**

Under Contract NAS8-26268

REVIEWED AND APPROVED BY:


Wallace W. Youngblood, Manager
Aerothermodynamics


Arthur L. Grady, Manager
Aerophysics

FOREWORD

This report presents the results of a space shuttle interference heating analysis performed by Northrop-Huntsville. The results of this analysis is presented as part of the tasks being performed under Aero-Astroynamics Laboratory Contract NAS8-26268. Mr. John Warmbrod is the Contracting Officer's Technical Representative for the contract. A note of appreciation is due Mr. J. A. Forney for his assistance in coordinating this task with other study efforts.

SUMMARY

Interference heating data for simple geometry fin-flat plate models tested in wind tunnels were compiled and analyzed in order to predict interference heating on the space shuttle booster fuselage due to the presence of booster wings or canards. The swept shock wave generating from the wing or canard interacts with the fuselage boundary layer and causes boundary layer separation and/or transition which in turn causes high heating rates on the fuselage surface.

The thermocouple measured heating data, presented as the ratio of interference heat transfer coefficients to the undisturbed values, have been correlated with different flow conditions and model configurations. The study results may be summarized as below:

- Interference heating on the plate increases with fin deflection angle and fin leading edge diameter.
- Interference heating on the plate decreases with increasing fin sweep angle and cant angle.
- The Mach number effect on the plate interference heating is related to boundary layer separation. The high Mach number flow provides a strong swept shock wave which in turn causes boundary layer separation on the plate and consequently high heating, whereas no boundary layer separation occurs for low Mach number cases. In general, the interference heating effect increases with increasing Mach number.
- The Reynolds number effect on the plate interference heating is related to boundary-layer transition. For a certain Reynolds number, the swept shock wave may cause boundary layer transition on plate and consequently a high heating rate, whereas for low Reynolds number flows the incoming laminar boundary layer may still remain laminar after the shock wave. For the case of very high Reynolds number flows, the incoming boundary layer on the plate is already turbulent and consequently no transition will occur across the shock wave.
- The plate heating increase caused by swept-shock/laminar boundary layer interaction is larger than the case of swept-shock/turbulent-boundary-layer interaction.

The correlations derived in this study are applicable to the booster fuselage interference heating prediction in the presence of wings and canards.

TABLE OF CONTENTS

<u>Section</u>	<u>Title</u>	<u>Page</u>
	FOREWORD	ii
	SUMMARY	iii
	LIST OF ILLUSTRATIONS	v
I	INTRODUCTION	1
II	DISCUSSION OF RESULTS	3
III	CONCLUSIONS	9
IV	REFERENCES	10

LIST OF ILLUSTRATIONS

<u>Figure</u>	<u>Title</u>	<u>Page</u>
1	FIN-PLATE MODEL FOR INTERFERENCE HEATING TEST	11
2	FIN-PLATE INTERFERENCE HEATING DISTRIBUTION (h_i/h_u on plate) (Ref. 1)	12
3	FIN-PLATE INTERFERENCE HEATING DISTRIBUTION (h_i/h_u on plate) (Ref. 1)	13
4	FIN-PLATE INTERFERENCE HEATING DISTRIBUTION (h_i/h_u on plate) (Ref. 4)	14
5	FIN-PLATE INTERFERENCE HEATING DISTRIBUTION (h_i/h_u on plate) (Ref. 4)	15
6	EFFECT OF FIN DEFLECTION ANGLE ON FLAT PLATE PEAK INTERFERENCE HEATING (Ref. 1)	16
7	EFFECT OF FIN DEFLECTION ANGLE ON FLAT PLATE PEAK INTERFERENCE HEATING (Ref. 1)	17
8	EFFECT OF FIN DEFLECTION ANGLE ON FLAT PLATE PEAK INTERFERENCE HEATING (Ref. 3)	18
9	EFFECTS OF FIN DEFLECTION ANGLE ON FLAT PLATE PEAK INTERFERENCE HEATING (Ref. 4)	19
10	EFFECT OF FIN DEFLECTION ANGLE ON FLAT PLATE PEAK INTERFERENCE HEATING (Ref. 2)	20
11	EFFECT OF FIN SWEEP ANGLE ON FLAT PLATE PEAK INTERFERENCE HEATING (Ref. 1)	21
12	EFFECT OF FIN SWEEP ANGLE ON FLAT PLATE PEAK INTERFERENCE HEATING (Ref. 5)	22
13	EFFECT OF FIN SWEEP ANGLE ON FLAT PLATE PEAK INTERFERENCE HEATING (Ref. 2)	23
14	EFFECT OF FLAT PLATE ANGLE-OF-ATTACK ON FLAT PLATE PEAK INTERFERENCE HEATING (Ref. 1)	24
15	EFFECT OF FLAT PLATE ANGLE-OF-ATTACK ON FLAT PLATE PEAK INTERFERENCE HEATING (Ref. 1)	25
16	EFFECT OF FIN LEADING EDGE DIAMETER ON FLAT PLATE PEAK INTERFERENCE HEATING (Ref. 1)	26
17	EFFECT OF FIN LEADING EDGE DIAMETER ON FLAT PLATE PEAK INTERFERENCE HEATING (Ref. 2)	27
18	EFFECT OF FIN CANT ANGLE ON FLAT PLATE PEAK INTERFERENCE HEATING (Ref. 2)	28
19	EFFECT OF FIN CANT ANGLE ON FLAT PLATE PEAK INTERFERENCE HEATING (Ref. 7)	29

LIST OF ILLUSTRATIONS (Concluded)

<u>Figure</u>	<u>Title</u>	<u>Page</u>
20	EFFECT OF FIN DEFLECTION ANGLE AND MACH NUMBER ON FLAT PLATE PEAK INTERFERENCE HEATING (Ref. 8)	30
21	EFFECT OF FIN DEFLECTION ANGLE AND MACH NUMBER ON FLAT PLATE PEAK INTERFERENCE HEATING (Ref. 8)	31
22	EFFECT OF MACH NUMBER ON FLAT PLATE PEAK INTERFERENCE HEATING (Refs. 1 and 3).	32
23	EFFECT OF MACH NUMBER ON FLAT PLATE PEAK INTERFERENCE HEATING (Refs. 2, 4 & 5)	33
24	EFFECT OF MACH NUMBER ON FLAT PLATE CENTER LINE INTERFERENCE HEATING (Ref. 6).	34
25	EFFECT OF REYNOLDS NUMBER ON FLAT PLATE PEAK INTERFERENCE HEATING (Ref. 7) (LAMINAR FLOW DATA ONLY).	35
26	COMPARISON OF LAMINAR AND TURBULENT INTERFERENCE HEATING ON FLAT PLATE (Ref. 7)	36
27	EFFECT OF REYNOLDS NUMBER ON THE FLAT PLATE CENTER LINE INTERFERENCE HEATING (Ref. 6).	37
28	FLAT PLATE PEAK INTERFERENCE HEATING AT DIFFERENT LOCATIONS (X) (Ref. 7)	38
29	EFFECT OF FIN LOCATION ON FLAT PLATE PEAK INTERFERENCE HEATING (Ref. 1)	39
30	EFFECT OF BOUNDARY-LAYER THICKNESS ON THE FLAT PLATE CENTERLINE INTERFERENCE HEATING (Ref. 6)	40

Section I INTRODUCTION

The design of space shuttle systems for operation at supersonic and hypersonic speeds requires an understanding of the intense aerodynamic heating generated through the interference of shock waves. This knowledge is of great importance in the determination of an optimum thermal protection system. Of the different kinds of shock interference involved in the shuttle flight, only the interference heating on booster fuselage due to the presence of booster wings and canards are considered in this study.

Interference heating data (thermocouple measurements, refs. 1 through 8) with simple geometry fin-flat plate models tested in wind tunnels were compiled and analyzed in this study. The heating data have been correlated with different flow conditions and model configurations such as Mach number, Reynolds number, fin deflection angle, fin sweep angle, etc. These correlations are applicable to the interference heating prediction on the booster fuselage due to the presence of wings and canards.

The booster fuselage and wing (or canard) can be simulated by a flat plate and a fin, respectively, as shown in Figure 1. The fins with different deflection angles and sweep angles can be either blunt or sharp (wedges). Flat plates with sharp leading edges were used in all the tests and with zero angle-of-attack in most of the cases. The swept shock wave generating from the fin interacts with the flat plate boundary layer as shown in Figure 1 and effects the plate heating as a result of one of the following sets of conditions:

- Low Reynolds Number and Weak Shock. The approaching boundary layer on plate is laminar and remains laminar after the shock. Separation does not occur. Heating on the plate is affected by the flow field change across the shock.
- Low Reynolds Number and Strong Shock. The approaching laminar boundary layer separates and reattaches in the interaction region. The boundary layer after the interaction can be either laminar or turbulent. High heating rates are due to both boundary layer separation and transition.
- Higher Reynolds Number and Weak Shock. The approaching laminar boundary layer may undergo transition due to shock interference but not necessarily separate. Heating increases are due to boundary layer transition and flow field change.

- Still Higher Reynolds Number and Weak Shock. The approaching boundary layer is turbulent, does not separate, and remains turbulent after the shock. Heating rates are affected by the flow field change across the shock.
- High Reynolds Number and Strong Shock. The approaching turbulent boundary layer separates and remains turbulent after shock. High heating is caused by separation.

The above discussion indicates that interference heating on the plate is caused by one or the combination of any of the following three mechanisms:

- Boundary layer separation
- Boundary layer transition
- Flow field change across shock wave.

To predict interference heating analytically, the criteria for predicting boundary layer separation and transition due to shock interference have to be available and, unfortunately, no adequate criteria exist at the present time. Assuming that separation does occur, the analytical methods to predict heating rate in the separation-reattachment region are also very limited due to the complexity of the problem. At the present time, analytical methods are limited to the unswept shock/boundary layer interaction (two-dimensional) and to laminar flows (refs. 9 and 10). Much less is known about the swept shock/boundary layer interaction (the case considered in this study) as the problem is further complicated by the fact that the boundary layer is three-dimensional. (Reference 11 provides useful definitions of swept shock/and unswept shock/boundary layer interactions) Consequently an empirical approach was chosen in this study to correlate existing interference heating data with different flow conditions and model configurations.

Section II

DISCUSSION OF RESULTS

The collected thermocouple test data with fin-flat plate models as listed in references 1 through 8 have been analyzed and are summarized in Table 1. The heating data on the flat plate were presented in the form of h_i/h_u , the ratio of the interference heat transfer coefficient to the undisturbed value. Typical heating distributions on flat plates are shown in Figures 2 through 5. The maximum h_i/h_u values at different X-locations on the plate were then chosen and correlated with the following flow conditions and model configurations:

- Fin Deflection Angle, δ
- Fin Sweep Angle, Λ
- Flat Plate Angle-of-Attack, α
- Fin Leading Edge Diameter, D
- Fin Cant Angle, ϕ
- Free Stream Mach Number, M_∞
- Free Stream Reynolds Number, R_N
- Boundary Layer State
- Fin Location on Flat Plate, L
- Thermocouple Location on Flat Plate, X
- Boundary Layer Thickness, t

Results of the data correlation are summarized below:

Fin Deflection Angle, δ (Figures 6 through 10, 20, and 21):

It is quite clear that peak interference heating on the plate increases with increasing fin deflection angle. This results since the high fin deflection angle provides a stronger shock which in turn causes boundary layer separation and stronger flow field change across the shock.

Fin Sweep Angle, Λ (Figures 11 through 13):

Figures 11 through 13 show a clear correlation between plate heating and fin sweep angle. As expected, heating decreases with increasing fin sweep angle.

Flat Plate Angle of Attack, α (Figures 14 and 15):

When the flat plate angle-of-attack is positive, no significant effect on maximum h_i/h_u values is observed as shown in Figures 14 and 15.

Table 1. SUMMARY OF FIN-FLAT PLATE INTERFERENCE HEATING EXPERIMENTS

REF. NO.	AUTHOR(S)	D (inches)	M_∞	R_N/FT	δ (Degrees)	Λ (Degrees)	α (Degrees)	REMARKS
1	Gulbran et al.	0 ~ 0.5	8	2×10^6 ($0.5 - 3.0 \times 10^6$)	-10 ~ +15	0 ~ 75	-10 ~ +20	Laminar B. L.
2	Caldwell et al.	0.5 (0 ~ 1)	16	2×10^5	-5 ~ +10	0 ~ 75	0 ~ 10	Laminar B. L. $L = 0$
3	Miller et al.	0	16	2×10^5	-10 ~ +15	0	0	Laminar B. L. $L = 0$
4	Jones	1.06	6	0.7×10^6 8.7×10^6	0 ~ 30	60	0	Lam. - $R_N = 0.7 \times 10^6$ $R_N = 2.38 \times 10^6$ $R_N = 8.7 \times 10^6$, $X+L < 6"$ Turb. - $R_N = 8.7 \times 10^6$, $X+L > 6"$ $L \neq 0$
5	Price et al.	0.75 ~ 3.5	3.51 4.44	2.5×10^6 4.2×10^6	0	0 ~ 69	0	Turb. - $R_N = 4.2 \times 10^6$ Lam. - $R_N = 2.5 \times 10^6$ $L \neq 0$
6	Burbank et al.	2.8	2.65 3.51 4.44	1.6×10^6 2.76×10^6 3.96×10^6	--	0 ~ 45	0	Turbulent B. L. (Trip) $L \neq 0$ Cylinder - Flat Plate Model
7	Stainback & Weinstein	0 ~ 0.5	8	0.42×10^6 10×10^6	-10 ~ +10	0	-10 ~ +10	Laminar B. L. (with some Turb. data) $L = 0$
8	Neumann	0	6 8	1×10^6 3.5×10^6	5 ~ 20	0 ~ 75	0	Laminar & Turbulent (Trip) $L \neq 0$

Fin Leading Edge Diameter, D (Figures 16 and 17)

Interference heating on the plate increases with fin leading edge diameter for both the fin with high deflection angle and low sweep angle (Figure 16) and the fin with low deflection angle and high sweep angle (Figure 17).

Fin Cant Angle, ϕ (Figures 18 and 19):

As expected, plate interference heating decreases with increasing fin cant angle as indicated in Figures 18 and 19.

Free Stream Mach Number, M_∞ (Figures 20 through 24):

The effect of Mach number on plate peak interference heating is not conclusive. This is due to the limited heating data and also due to the fact that the Mach number effect on interference heating is complicated by boundary layer separation. It is known that a high Mach number provides stronger swept shock wave which in turn causes boundary layer separation and high heating whereas no separation is normally associated for low Mach number flows. Direct comparisons between Mach 6 and Mach 8 data for both laminar and turbulent flows show no Mach number effect (Figures 20 and 21). The comparisons shown in Figures 22 and 23 furnish little in direct comparisons due to the different flow conditions and model configurations used in different tests as indicated in these figures. For the case of the unswept cylinder/flat plate model as shown in Figure 24, the plate interference heating in the region up-stream of the cylinder increases with Mach number whereas the 45-degree swept cylinder does not have any effect on plate heating with all three Mach numbers. This is because the unswept cylinder causes flow separation and consequently higher heating on the plate whereas no separation occurs for the swept cylinder cases in the region of measurement.

Free Stream Reynolds Number, R_N , and Boundary Layer State (Figures 9, 12, 25 through 27):

The effect of Reynolds number on interference heating is interrelated to the boundary layer state. The shock wave may cause the laminar boundary layer to undergo transition for higher Reynolds number flows whereas the boundary layer may still be laminar after the shock for lower Reynolds number cases.

Data in Figure 25 indicate that the Reynolds number does not have significant effect on maximum h_i/h_u for laminar flows. The fact that lower Reynolds numbers cause higher h_i/h_u values as indicated in Figures 12 and 26 is due to difference in boundary layer state. As indicated in both figures, the boundary layers upstream of the shocks are turbulent for the higher Reynolds number flows, whereas the boundary layers are laminar for the lower Reynolds number cases. Why the swept shock wave has less heating effect on turbulent boundary layer remains to be answered even though speculations have been made by different authors (ref. 7, for instance).

The Reynolds number effect as shown in Figure 9 may be explained as follows:

- For low Reynolds number ($R_N = 0.7 \times 10^6/\text{ft}$), the approaching laminar boundary layer remains laminar after the shock. Interference heating is caused by boundary layer separation.
- For intermediate Reynolds number ($R_N = 2.38 \times 10^6$), the approaching laminar boundary layer separates and may also become turbulent. The combination of separation and transition causes higher heating rates.
- For high Reynolds number ($R_N = 8.7 \times 10^6/\text{ft}$), the interference heating rates are somewhat lower because the approaching boundary layer is turbulent. As just discussed, the shock wave has less heating effect on turbulent boundary layers.

It should be noted that thermocouple spacings used to obtain heating data in Figure 9 are quite large (1 inch as shown in Figures 4 and 5). Some of the maximum h_i/h_u values may have been missed in the tests.

Fin and Thermocouple Locations, L and X, and Boundary Layer Thickness, t (Figures 6-8, 11, 14, 15, 20, 21, 25, 28-30):

The fin and thermocouple locations on flat plate and the boundary layer thickness are all interrelated and are, therefore, discussed together in this section. The maximum h_i/h_u increases with increasing X as shown in Figures 6-8, 11, 14, 15, 25, and 29. On the other hand, data in Figures 20, 21, and 28 indicate that maximum h_i is not significantly effected by X. This can be explained by comparing Figures 25 and 28 (both are deduced from the same original data in ref. 7). The maximum h_i (or $N_{ST,MAX}$) does not vary appreciably with X (or Re_x) as shown in Figure 28 and the maximum h_i/h_u increase with X as shown in Figure 25 is due to the fact that h_u decreases with X as shown by the solid lines in Figure 28.

The effects of fin location (on the plate) and plate boundary layer thickness on interference heating are important for shuttle heating studies, since both the wings and the canards are located far away from the booster fuselage nose. Unfortunately, both effects are not known due to the limited data as shown in Figures 29 and 30 which indicate the h_i/h_u increases with both decreasing L and t.

The study results are summarized in Table 2.

Table 2. SUMMARY OF SWEEP SHOCK WAVE/BOUNDARY LAYER INTERACTION HEATING STUDY

FLOW CONDITIONS OR MODEL CONFIGURATIONS	EFFECT ON FLAT PLATE INTERFERENCE HEATING (h_i/h_u)	FIGURE NUMBERS
Fin Deflection Angle, δ	h_i/h_u increases with δ	6 through 10, 20, 21
Fin Sweep Angle, Λ	h_i/h_u decreases with Λ	11 through 13
Plate Angle-of-Attack, α	h_i/h_u does not vary with α when α is positive	14, 15
Fin Leading Edge Diameter, D	h_i/h_u increases with D	16, 17
Fin Cant Angle, ϕ	h_i/h_u decreases with ϕ	18, 19
Free Stream Mach No., M_∞	<ul style="list-style-type: none"> * Not conclusive * M_∞ effect is inter-related with B. L. separation 	20 through 24
Free Stream Reynolds No., R_N and Boundary Layer State	<ul style="list-style-type: none"> * R_N effect is inter-related with B. L. transition * $(h_i/h_u)_{\text{Laminar}}$ is not effected by R_N * $(h_i/h_u)_{\text{Laminar}} > (h_i/h_u)_{\text{Turbulent}}$ 	9, 12, 25 through 27
Fin and Thermocouple Locations, L and X, and Boundary Layer Thickness, t	<ul style="list-style-type: none"> * h_i/h_u increases with X * h_i does not increase with X * h_i/h_u decreases with L * h_i/h_u decreases with t 	6, 7, 8, 11, 14, 15, 20, 21, 25, 28 through 30

Section III

CONCLUSIONS

The complexity of the swept shock/boundary layer interaction prevents an analytical approach for predicting interference heating on the flat plate. An empirical approach to correlate heating with different flow conditions and model configurations seems more fruitful.

In this study, heating correlations with different flow conditions and model configurations have been made. Different mechanisms which cause high heating rates in the interference region were also analyzed in order to have a better physical understanding. It is expected that, based on this study and the interference heating data deduced from the MDC/MMC Phase B Space Shuttle Model Tests (refs. 12 and 13), a set of empirical equations may be developed for reliable interference heating prediction on shuttle booster fuselage.

It should be noted that test data collected and used in this study are limited in the following two respects:

- As indicated in Table 1, most of the available data are laminar whereas most of the booster fuselage boundary layer during the actual flight will be turbulent. More turbulent data are needed.
- Most of the data used in this study were taken on models with a fin located very close to the plate leading edge (i.e., $L = 0$ for most of the cases). This is different from the booster fuselage/wing or fuselage/canard configurations since both wing and canard are quite a distance from the fuselage nose. More data are needed to study the effect of fin location and plate boundary layer thickness on plate interference heating.

Section IV
REFERENCES

1. Gulbran, C. E., Redeker, E., Miller, D. S., and Strack, S. L., "Heating in Regions of Interfering Flow Fields," The Boeing Company, Technical Report AFFDL-TR-65-49, Part I - July 28, 1965, Part II - January 1967, Part III - March 1967.
2. Caldwell, A. L., Haugseth, E. G., and Miller, D. S., "The Influence of Aerodynamic Interference Heating on Directional Stability Problems of Hypersonic Vehicles," IAS Paper No. 63-6, January 1963.
3. Miller, D. S., Hijman, R., Redeker, E., Janssen, W. C., and Mullen, C. R., "A Study of Shock Impingements on Boundary Layers at Mach 16," Proceedings of the 1962 Heat Transfer and Fluid Mechanics Institute, June 13-15, 1962.
4. Jones, R. A., "Heat-Transfer and Pressure Investigation of a Fin-Plate Interference Model at a Mach Number of 6," NASA TN D-2028, July 1964.
5. Price, E. A., Howard, P. W., and Stallings, R. L., "Heat-Transfer Measurements on a Flat Plate and Attached Fins at Mach Numbers of 3.51 and 4.44," NASA TN D-2340, June 1964.
6. Burbank, P. B., Newlander, R. A., and Collins, I. K., "Heat-Transfer and Pressure Measurements on a Flat-Plate Surface and Heat-Transfer Measurements on Attached Protuberances in a Supersonic Turbulent Boundary Layer at Mach Numbers of 2.65, 3.51, and 4.44," NASA TN D-1372, December 1962.
7. Stainback, P. C., and Weinstein, L. M., "Aerodynamic Heating in the Vicinity of Corners at Hypersonic Speeds," NASA TN D-4130, November 1967.
8. Neumann, R. D., "The Influence of Shock Wave-Boundary Layer Effects on the Design of Reusable Space Transportation Systems," Collection of papers presented at the Space Shuttle Symposium held at Smithsonian Museum of Natural History, Washington, D. C., October 16-17, 1969, p. 539.
9. Holden, M. S., "An Analytical Study of Separated Flows Induced by Shock Wave - Boundary Layer Interaction," NASA CR-600, 1966.
10. Martellucci, A., and Lipfert, F. W., "Shock Wave-Laminar Boundary Layer Interaction - Integral Analysis and Experimental Results," AGARD Separated Flows Meeting, Brussels, May 1966, p. 635.
11. Wuerer, J. E., and Clayton, F. I., "Flow Separation in High Speed Flight - A Review of the State-of-The-Art," Douglas Report SM-46429, April 1965.
12. Hung, F. T., "Shock Interference Heating Analysis Based on MDC/MMC Phase B Space Shuttle Model Test Data," Northrop Memorandum M-794-887, February 1971.
13. Click, P. L. and Schmitt, D. A., "Wind Tunnel Test Results from the Thermal Mapping Investigation of 0.325% Scale MDC/MMC Phase B Space Shuttle Vehicles in the NASA/LRC Mach 8 Variable Density Tunnel and the NASA/LRC 31 Inch Continuous Flow Hypersonic Tunnel," Martin Marietta Design Note No. MMC-I-AERO-5002, October 1970.

- M_∞ = FREE-STREAM MACH NUMBER
- R_N = FREE-STREAM REYNOLDS NUMBER
- α = FLAT PLATE ANGLE-OF-ATTACK
- D = FIN LEADING EDGE DIAMETER
 (D = 0 FOR WEDGE WITH SHARP L.E.)
- δ = FIN DEFLECTION ANGLE
- Λ = FIN SWEEP ANGLE
- ϕ = FIN CANT ANGLE
- t = BOUNDARY LAYER THICKNESS

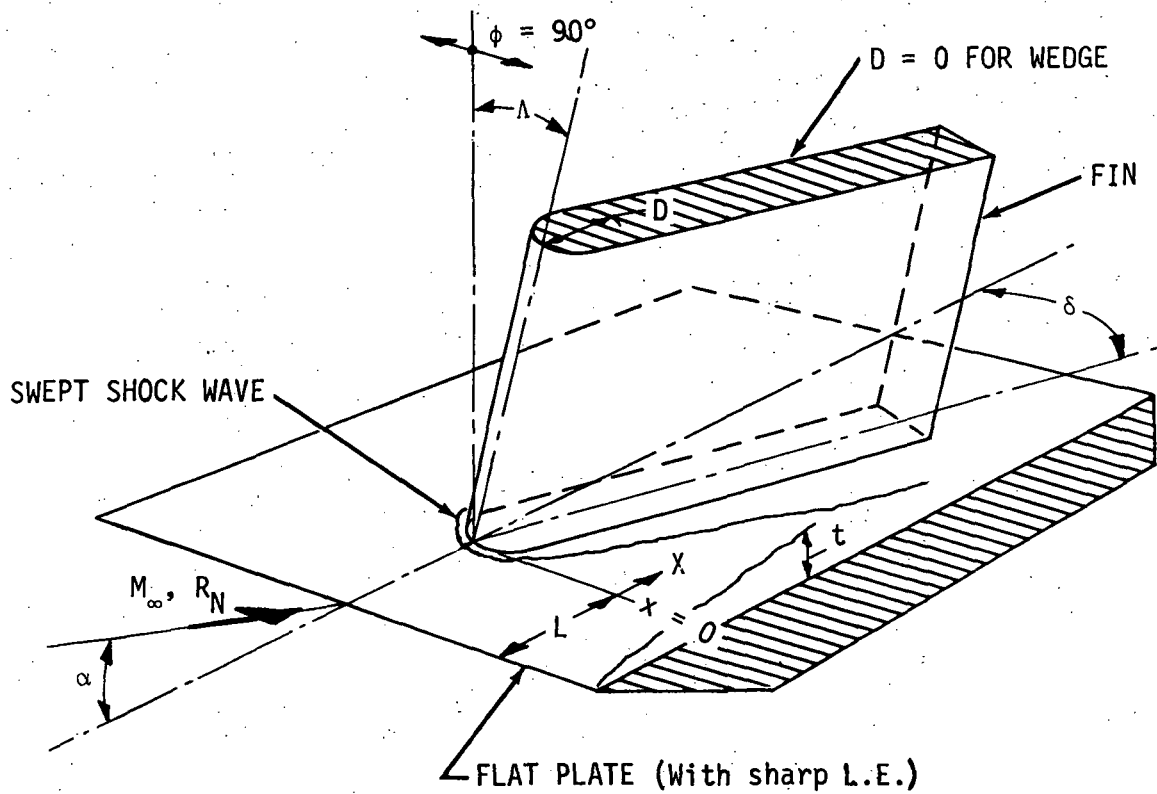


Figure 1. FIN-PLATE MODEL FOR INTERFERENCE HEATING TEST

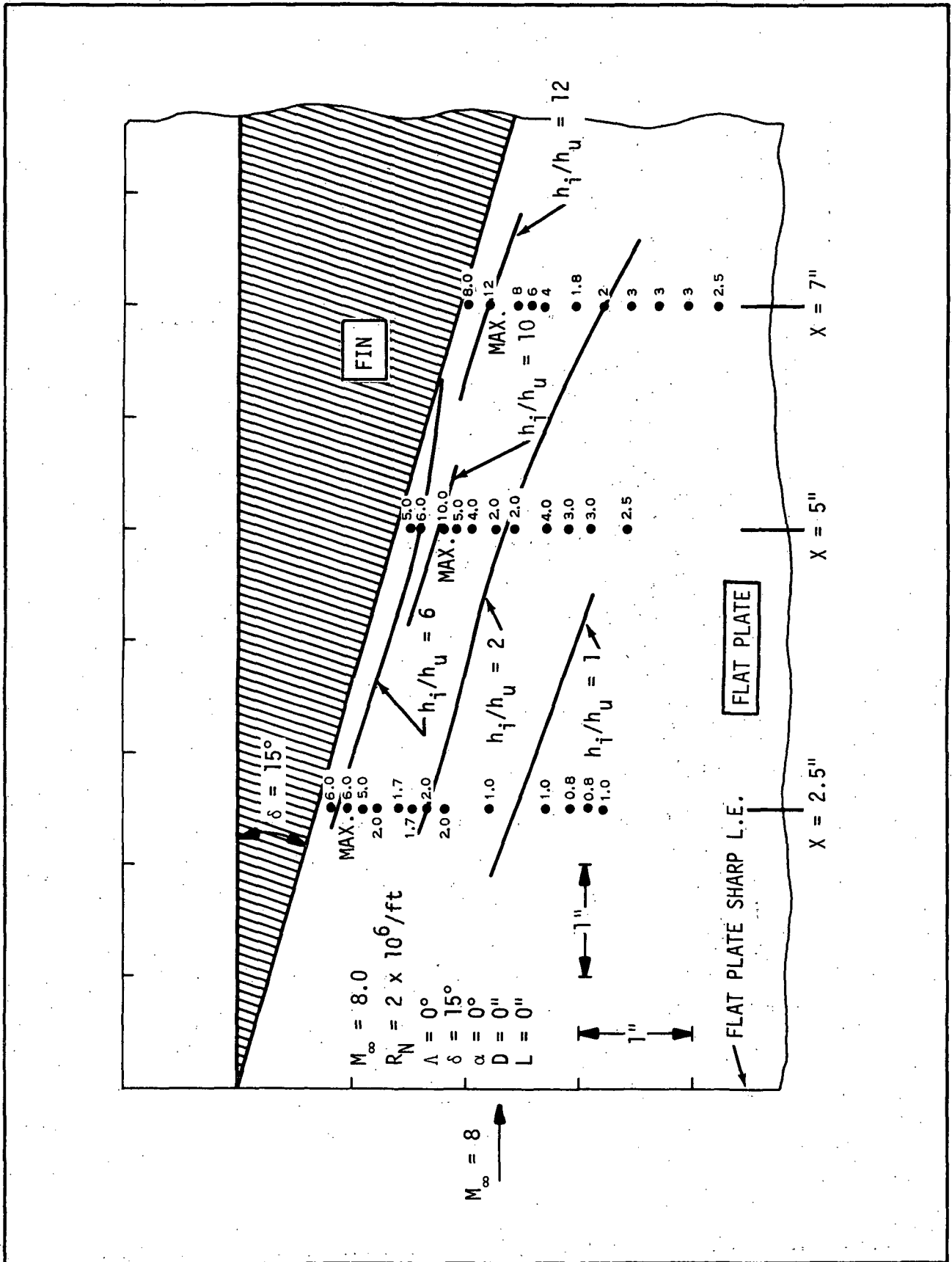


Figure 2. FIN-PLATE INTERFERENCE HEATING DISTRIBUTION (h_i/h_u on plate) (Ref. 1)

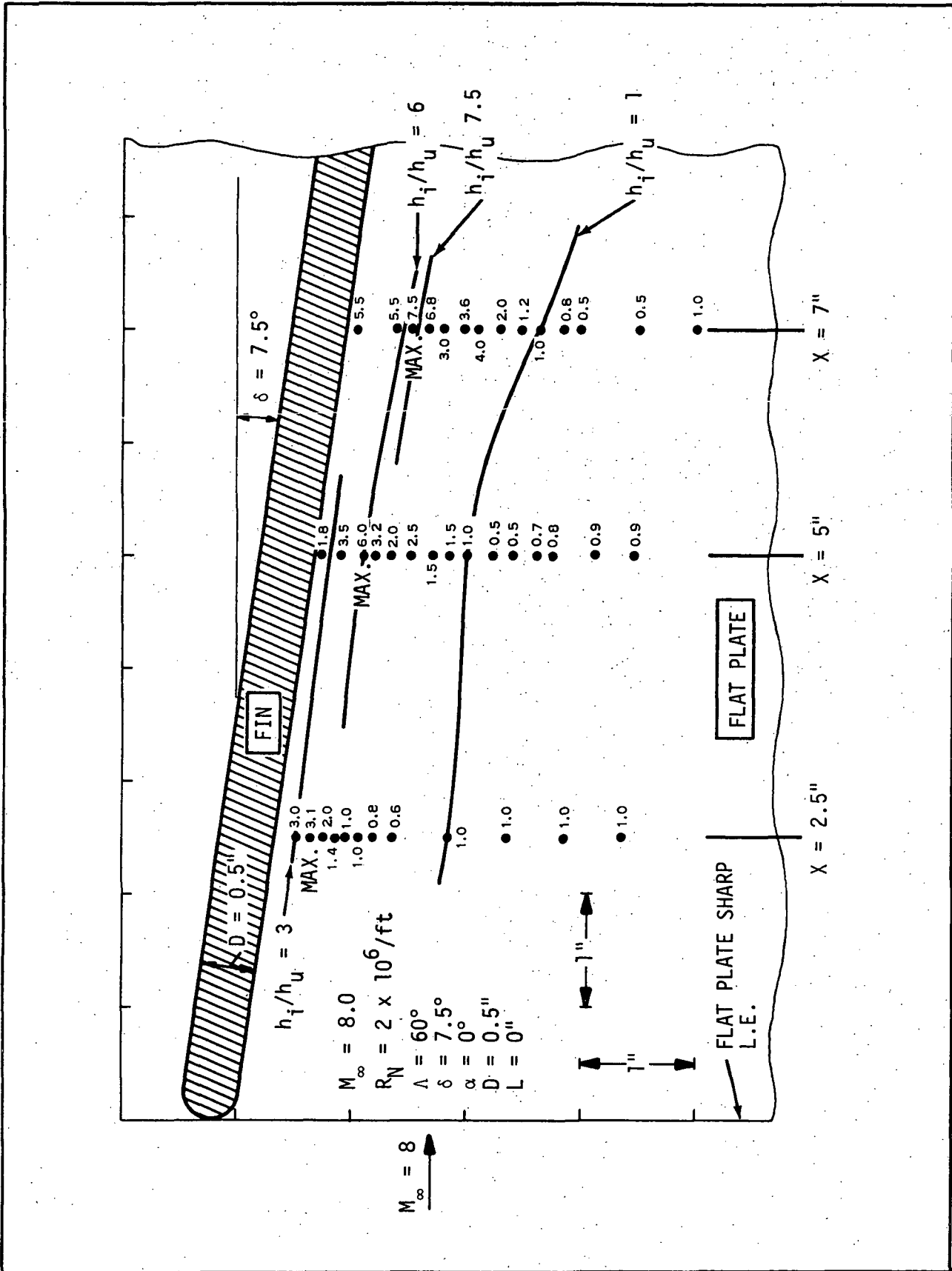


Figure 3. FIN-PLATE INTERFERENCE HEATING DISTRIBUTION (h_i/h_u on plate) (Ref. 1)

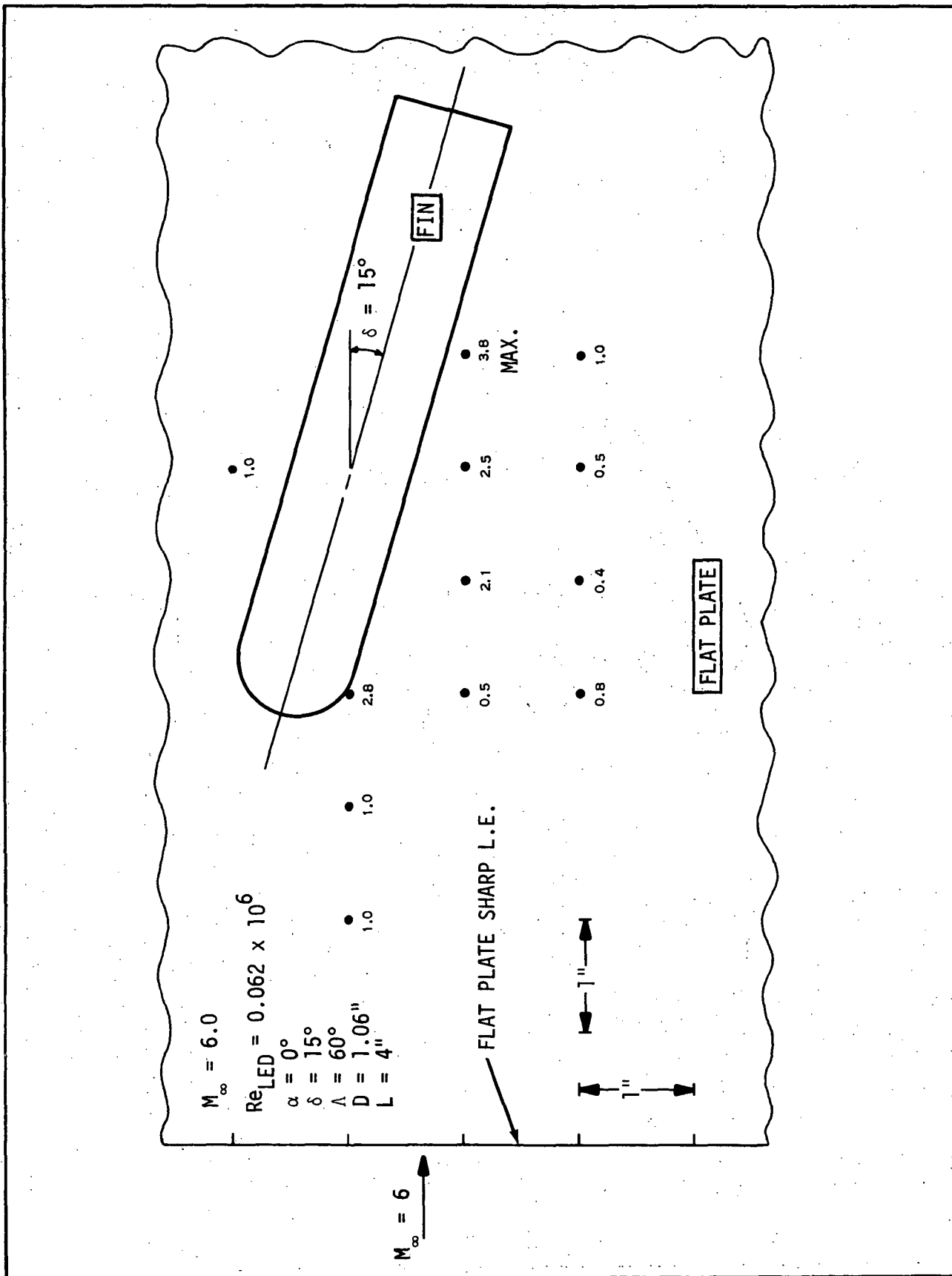


Figure 4. FIN-PLATE INTERFERENCE HEATING DISTRIBUTION (h_i/h_u on plate) (Ref. 4)

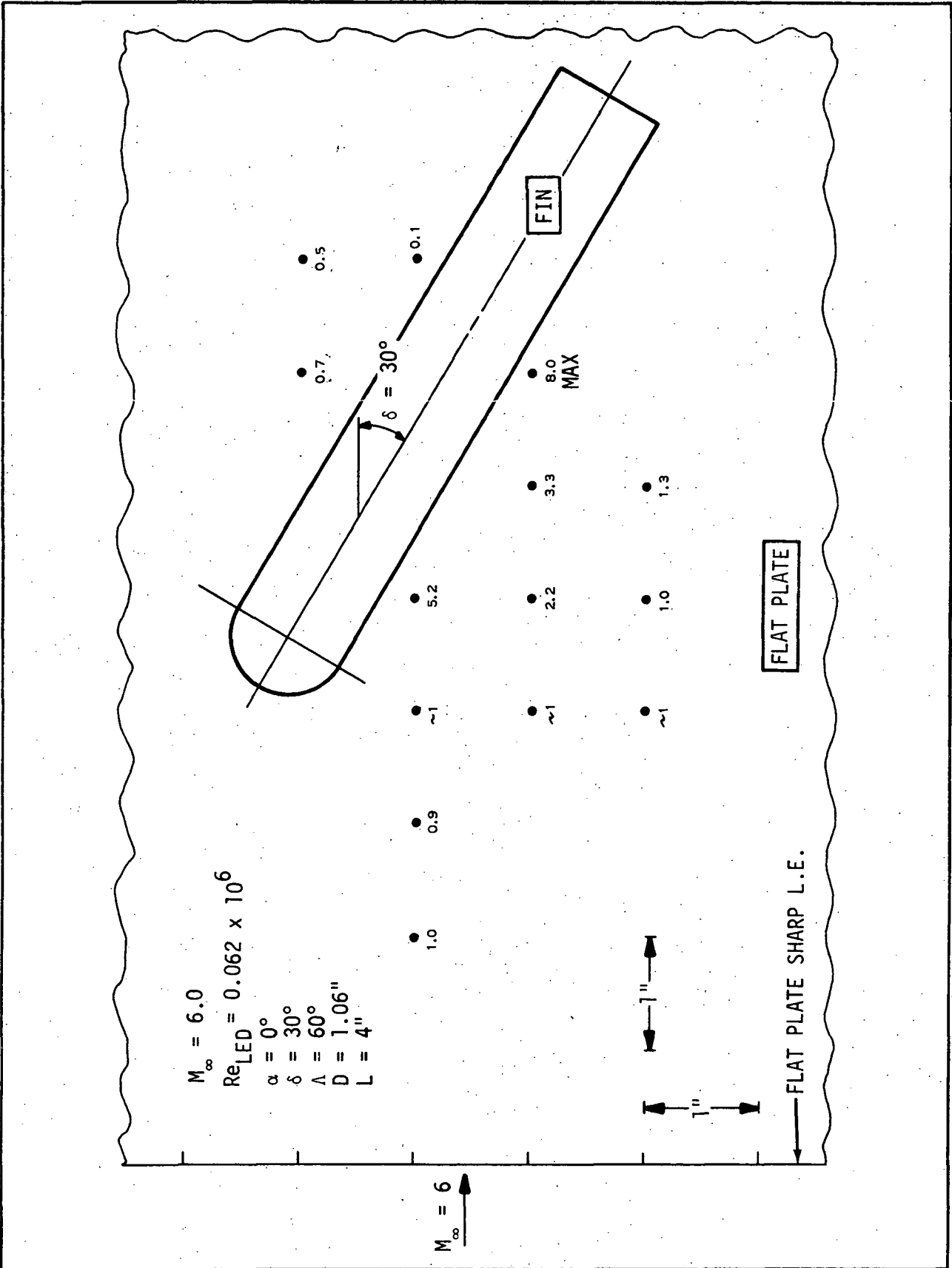


Figure 5. FIN-PLATE INTERFERENCE HEATING DISTRIBUTION (h_i/h_u on plate) (Ref. 4)

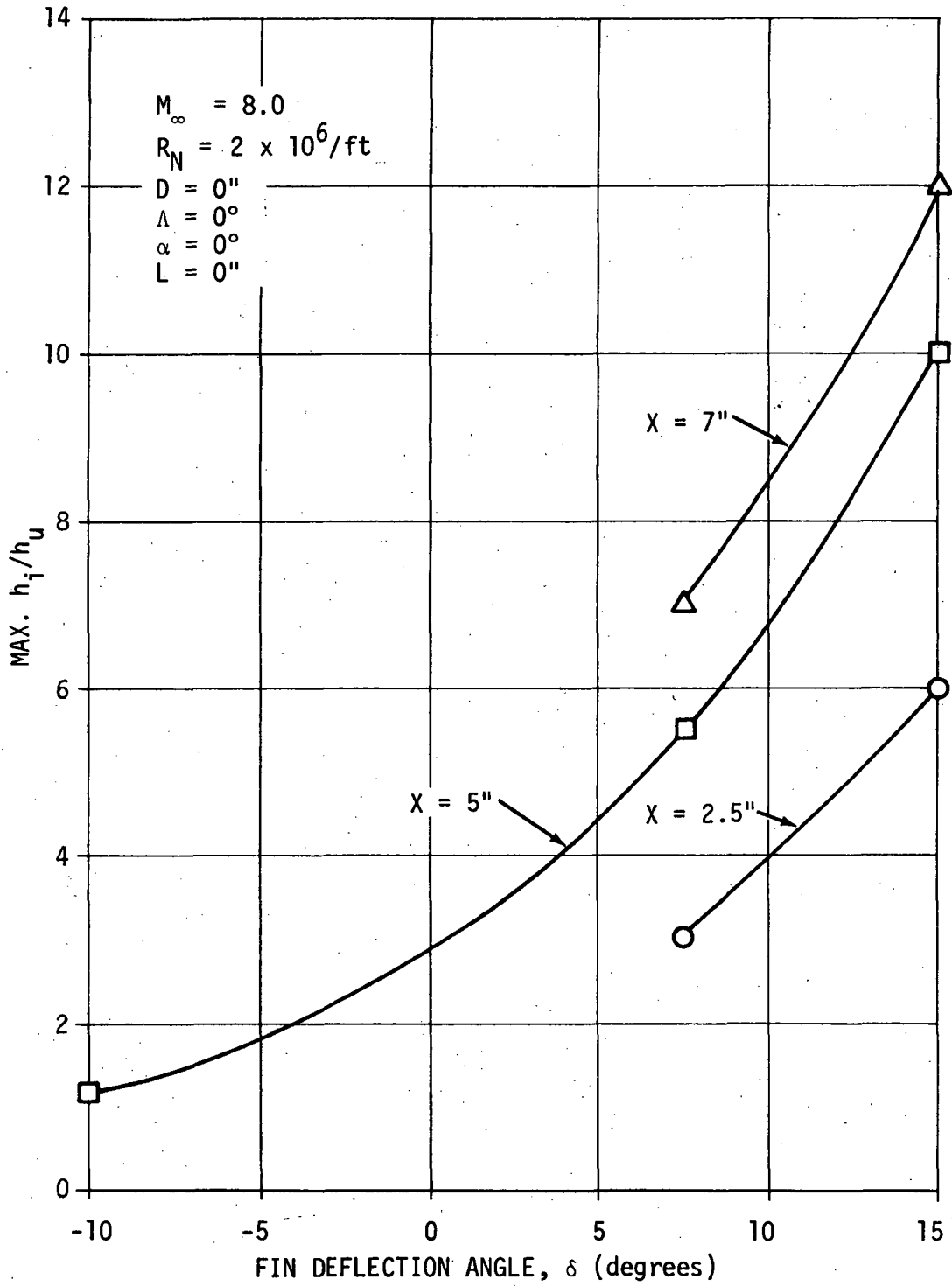


Figure 6. EFFECT OF FIN DEFLECTION ANGLE ON FLAT PLATE PEAK INTERFERENCE HEATING (Ref. 1)

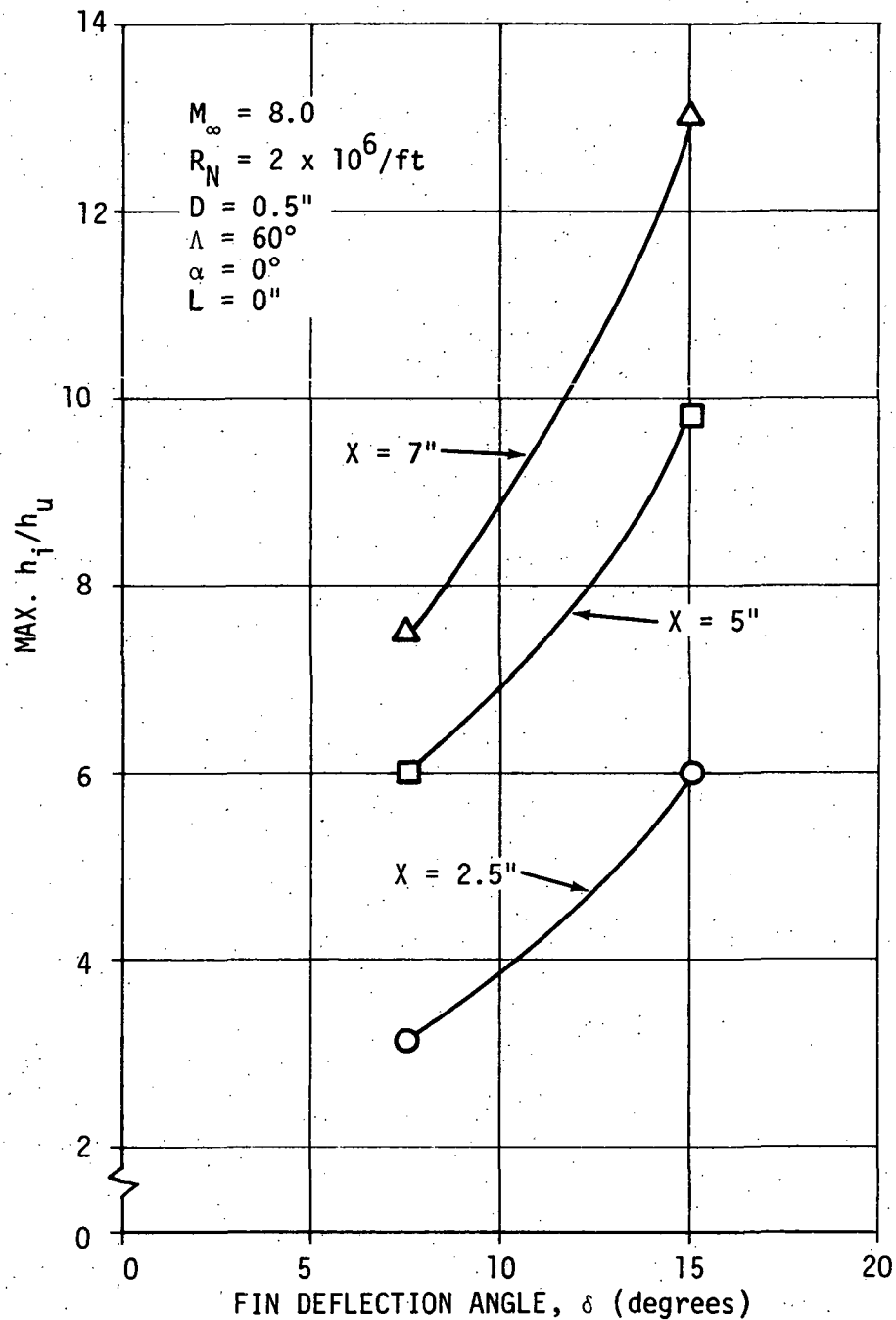


Figure 7. EFFECT OF FIN DEFLECTION ANGLE ON FLAT PLATE PEAK INTERFERENCE HEATING (Ref. 1)

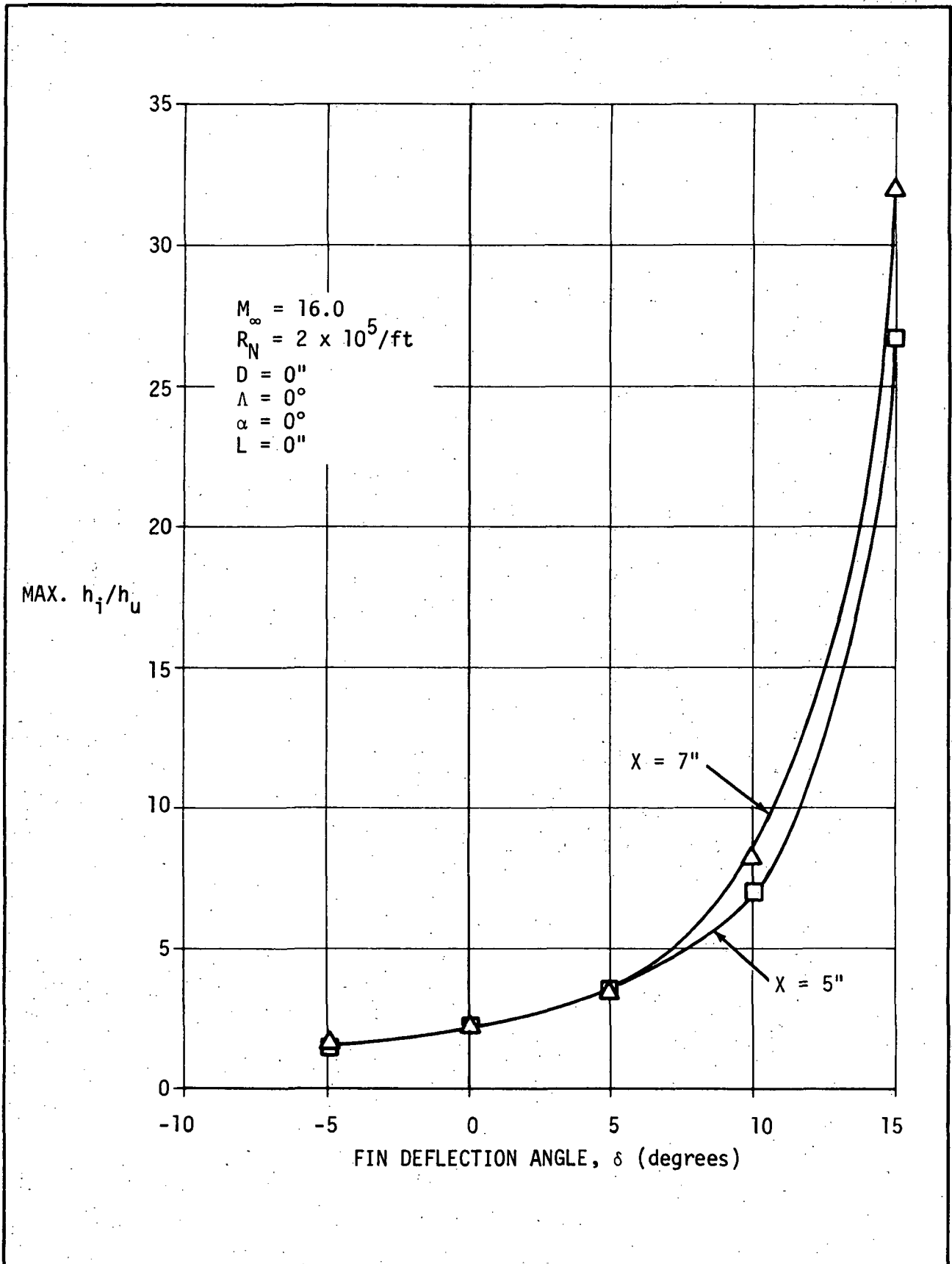


Figure 8. EFFECT OF FIN DEFLECTION ANGLE ON FLAT PLATE PEAK INTERFERENCE HEATING (Ref. 3)

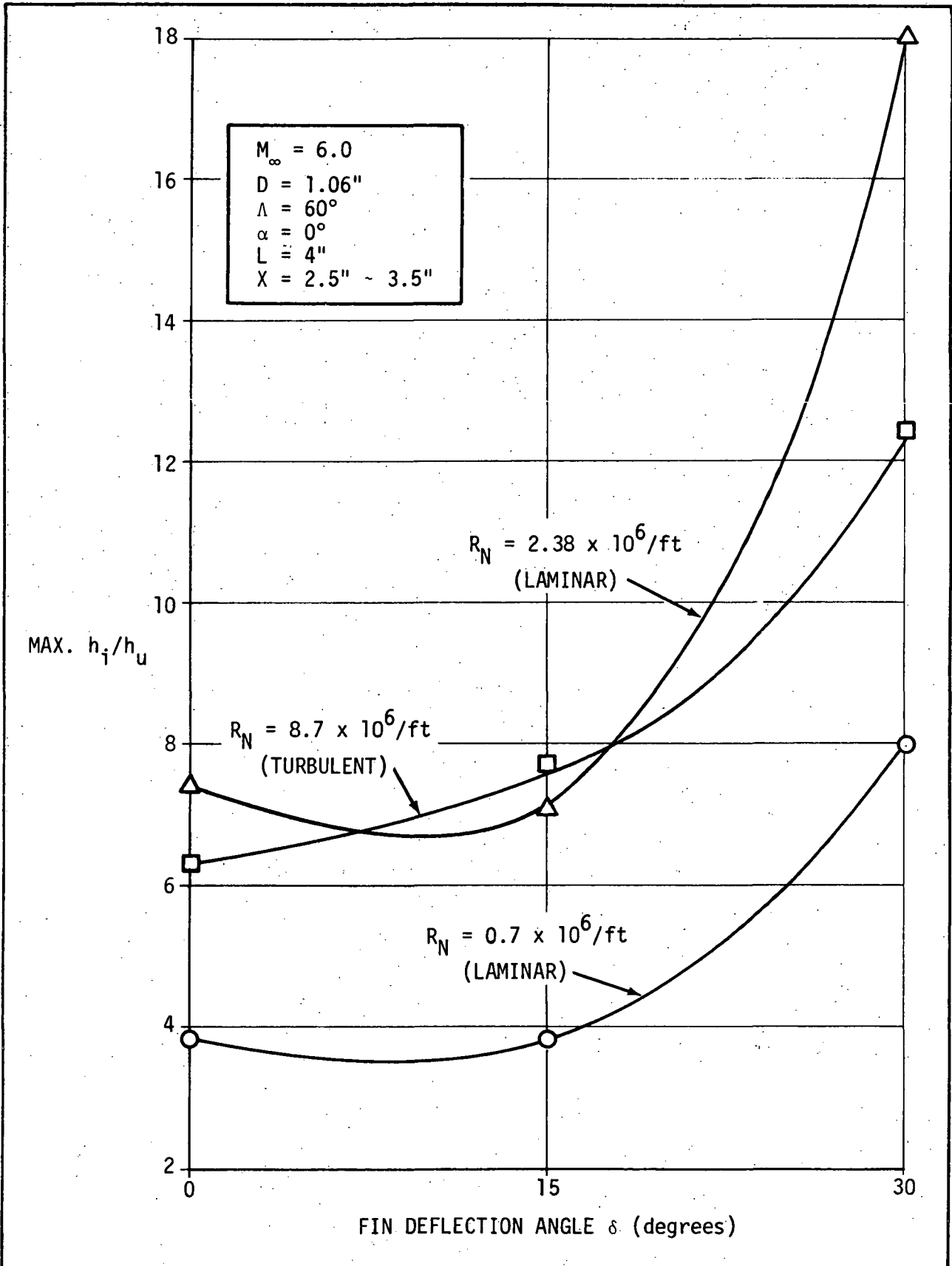


Figure 9. EFFECTS OF FIN DEFLECTION ANGLE ON FLAT PLATE PEAK INTERFERENCE HEATING (Ref. 4)

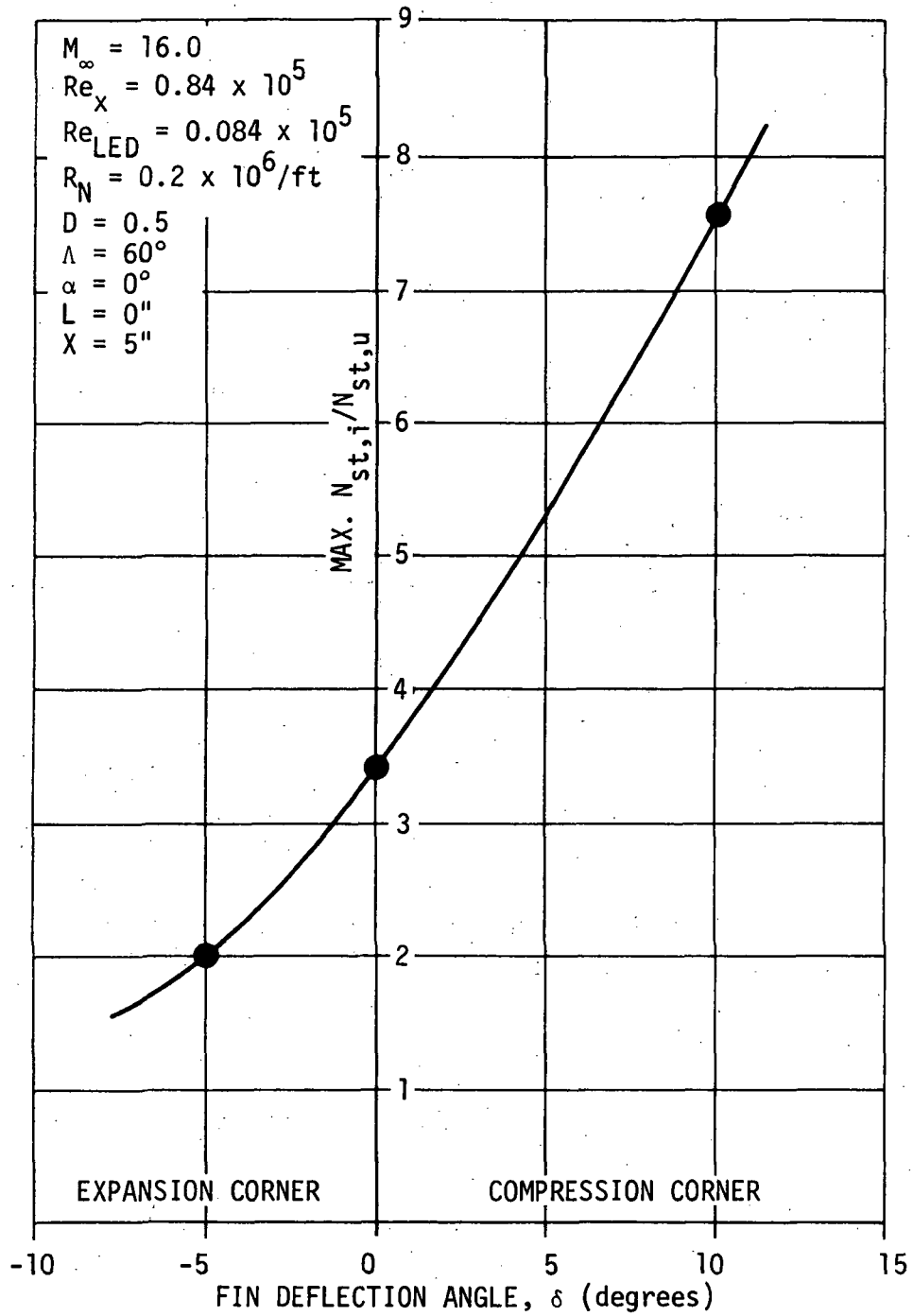


Figure 10. EFFECT OF FIN DEFLECTION ANGLE ON FLAT PLATE PEAK INTERFERENCE HEATING (Ref. 2)

$M_\infty = 8.0$
 $R_N = 2 \times 10^6/\text{ft}$
 $D = 0.5''$
 $\delta = 0^\circ$
 $\alpha = 0^\circ$
 $L = 0''$

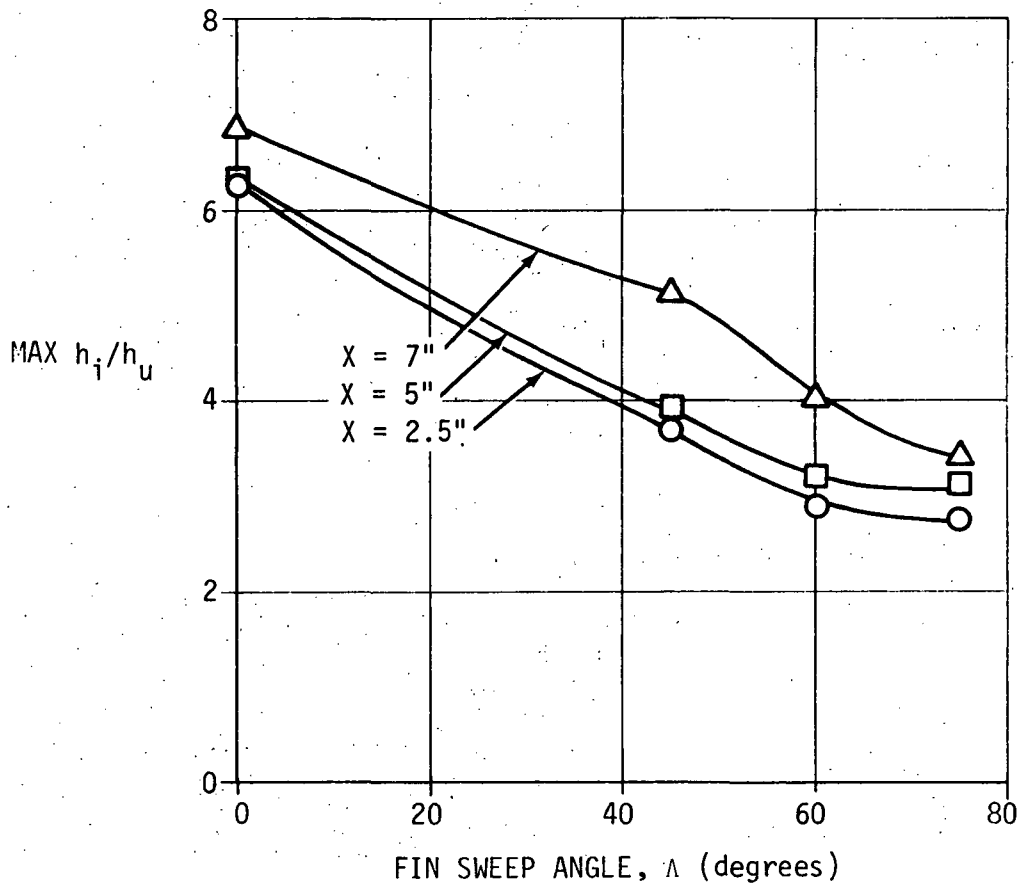


Figure 11. EFFECT OF FIN SWEEP ANGLE ON FLAT PLATE PEAK INTERFERENCE HEATING (Ref. 1)

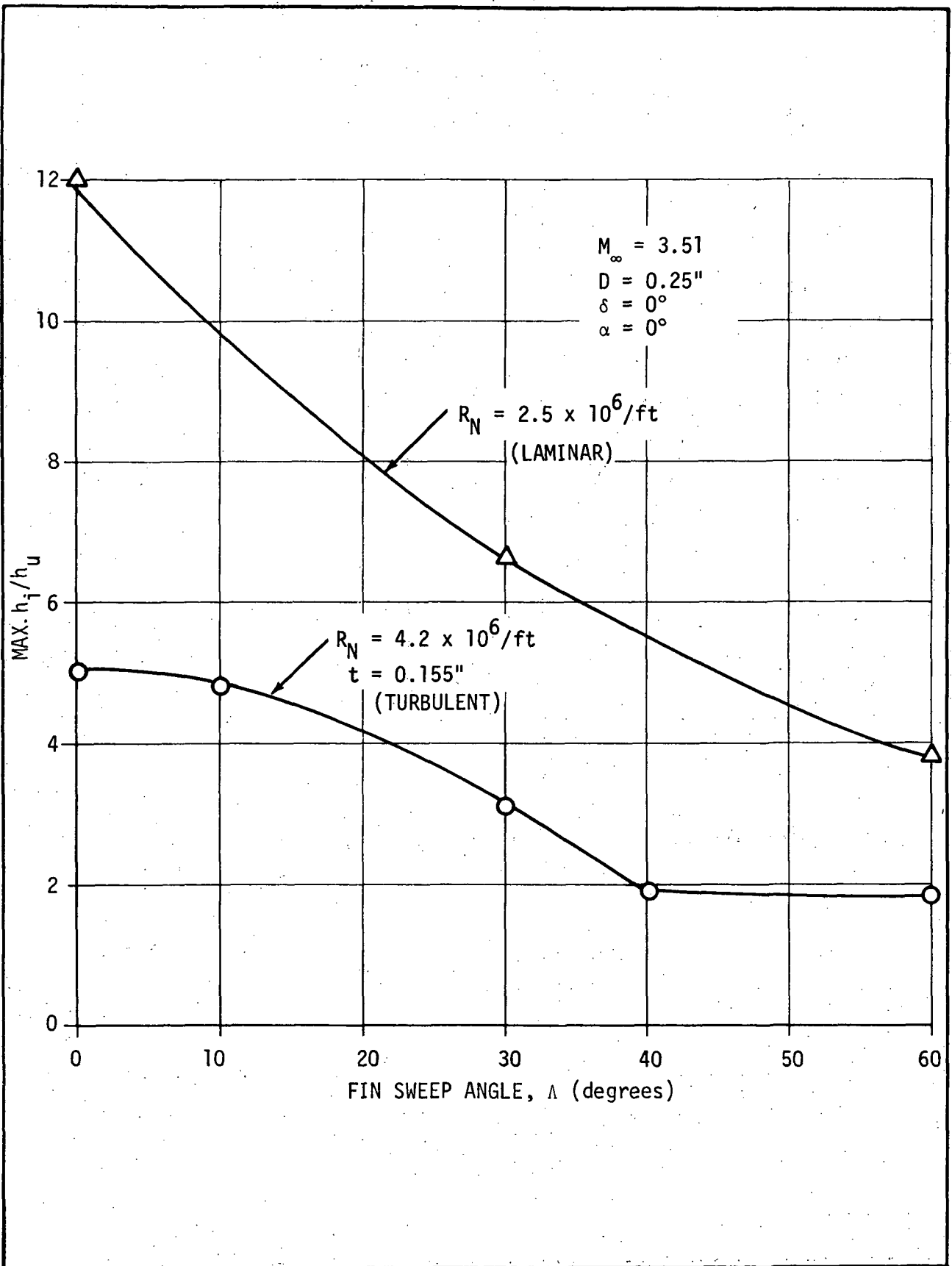


Figure 12. EFFECT OF FIN SWEEP ANGLE ON FLAT PLATE PEAK INTERFERENCE HEATING (Ref. 5)

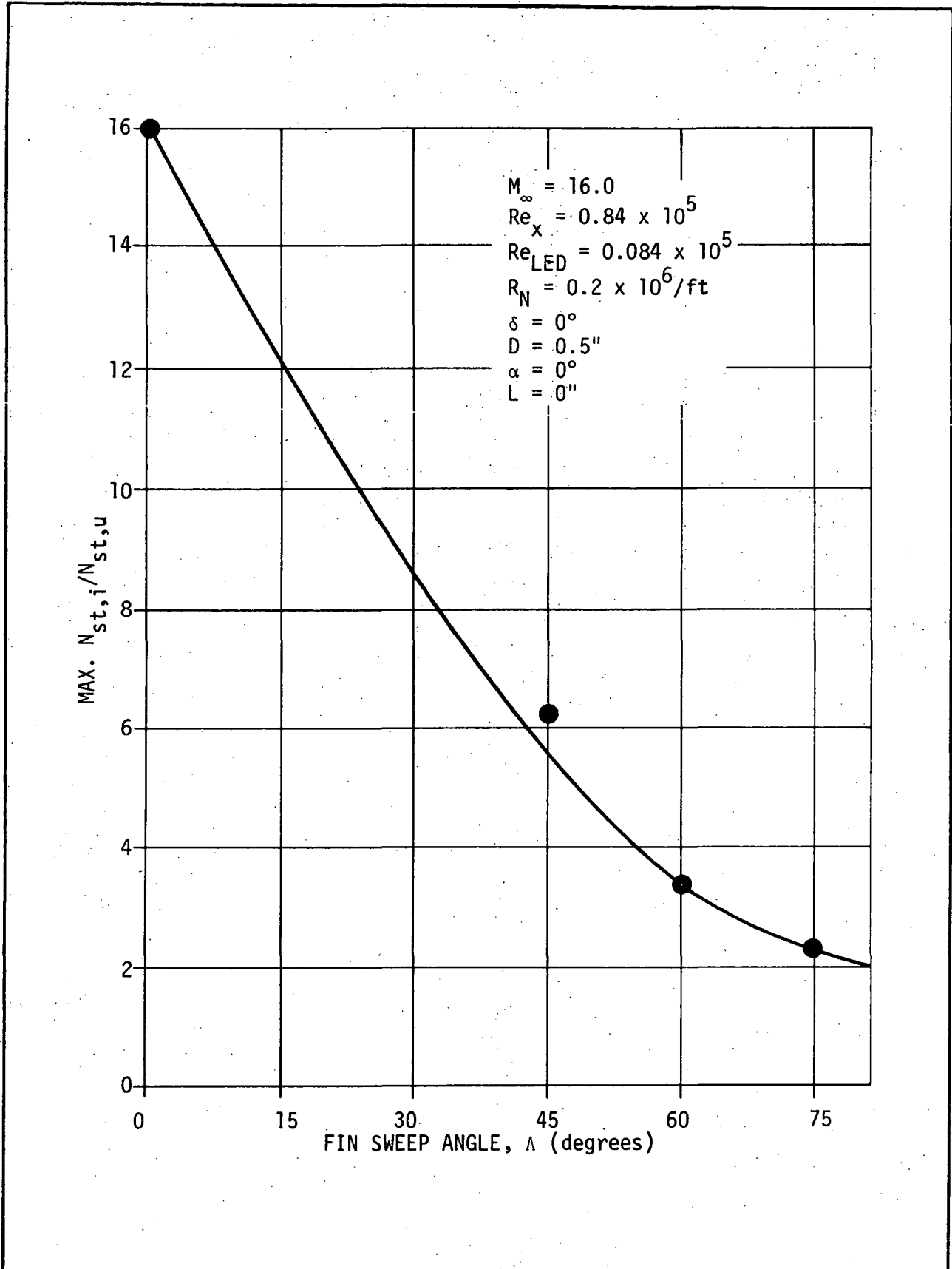


Figure 13. EFFECT OF FIN SWEEP ANGLE ON FLAT PLATE PEAK INTERFERENCE HEATING (Ref. 2)

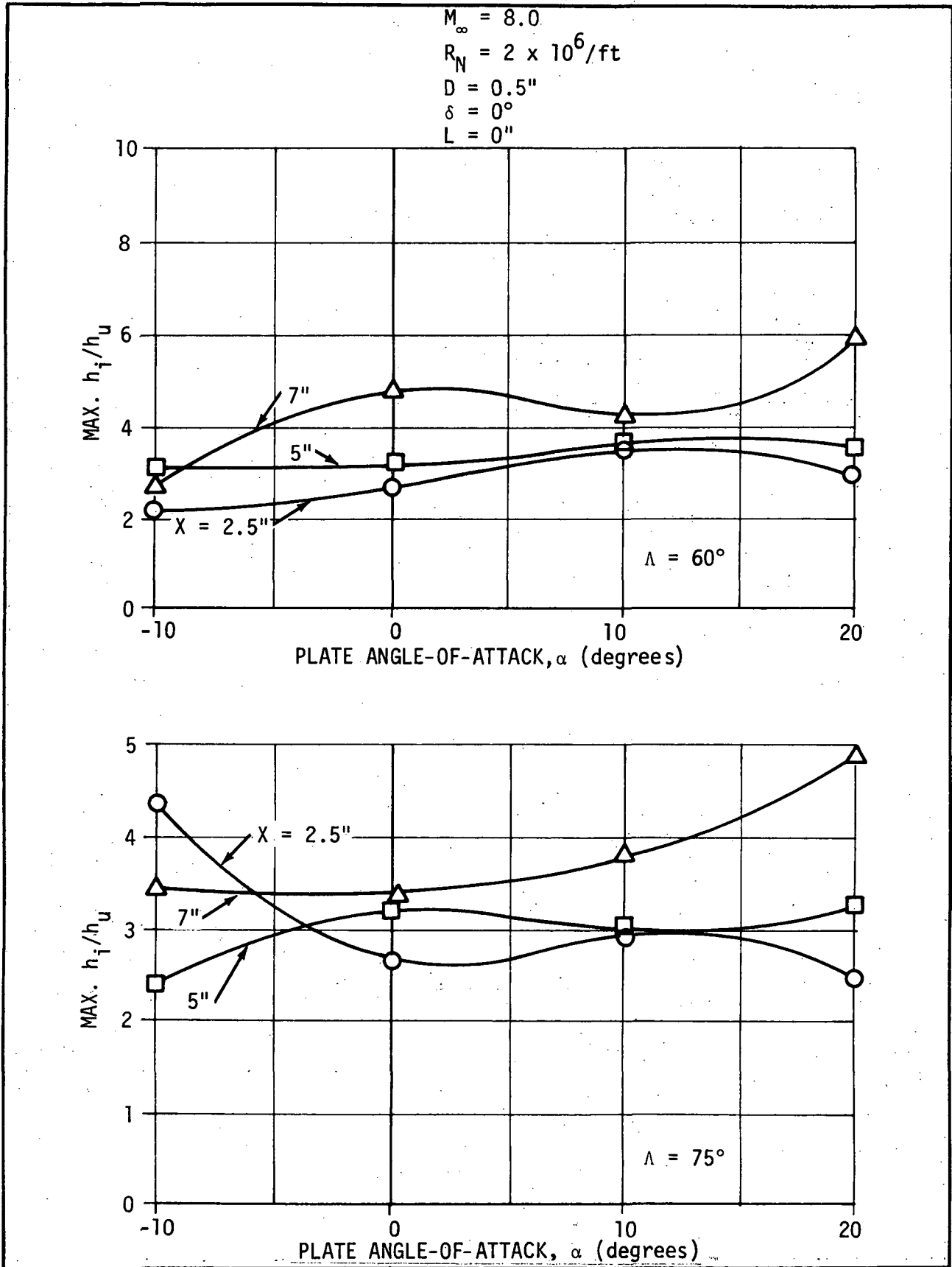


Figure 14. EFFECT OF FLAT PLATE ANGLE-OF-ATTACK ON FLAT PLATE PEAK INTERFERENCE HEATING (Ref. 1)

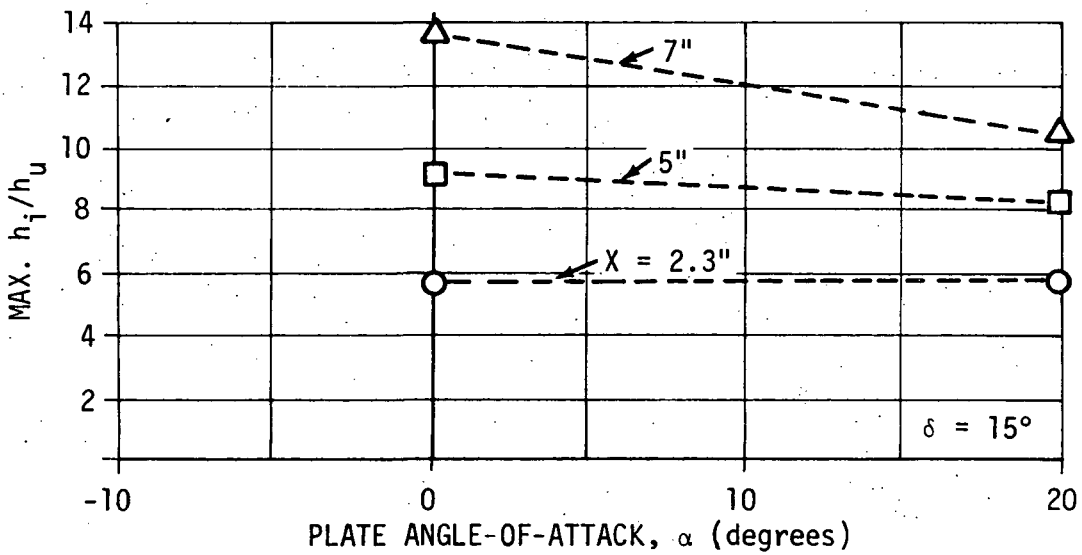
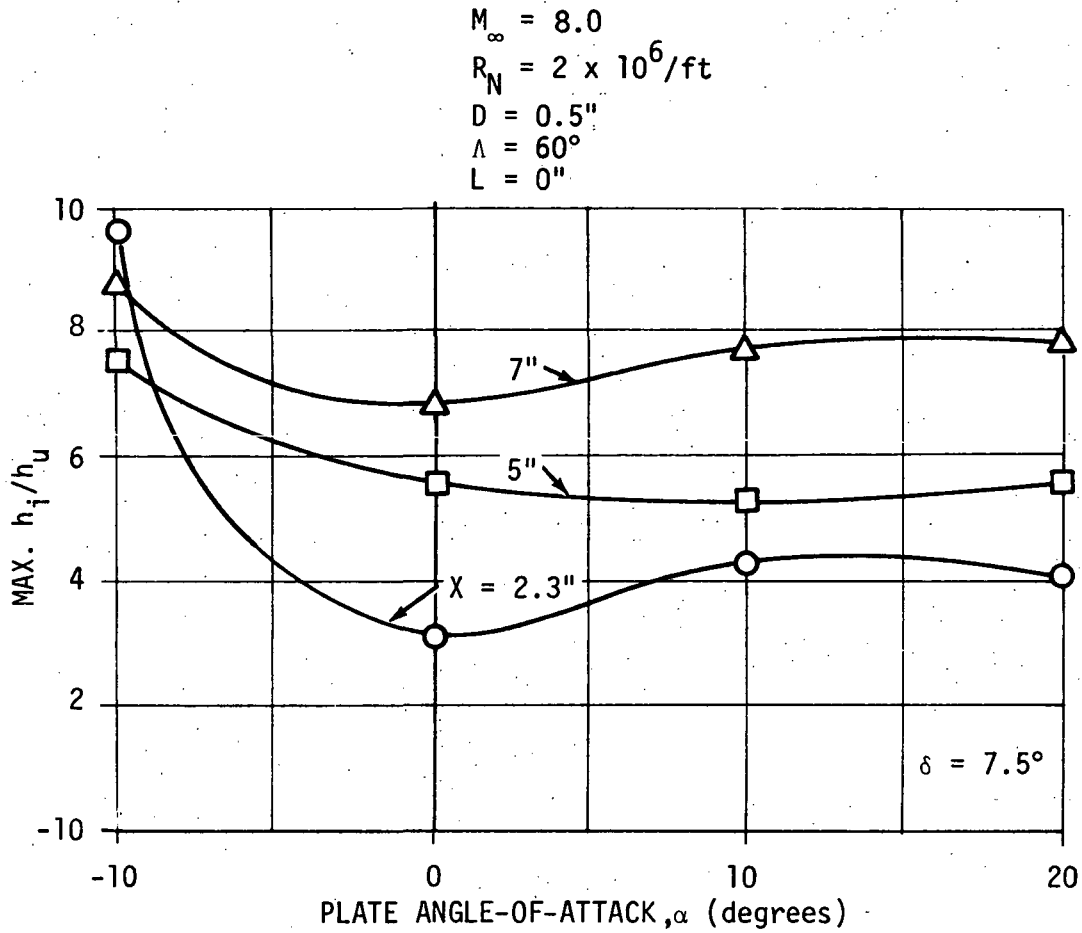


Figure 15. EFFECT OF FLAT PLATE ANGLE-OF-ATTACK ON FLAT PLATE PEAK INTERFERENCE HEATING (Ref. 1)

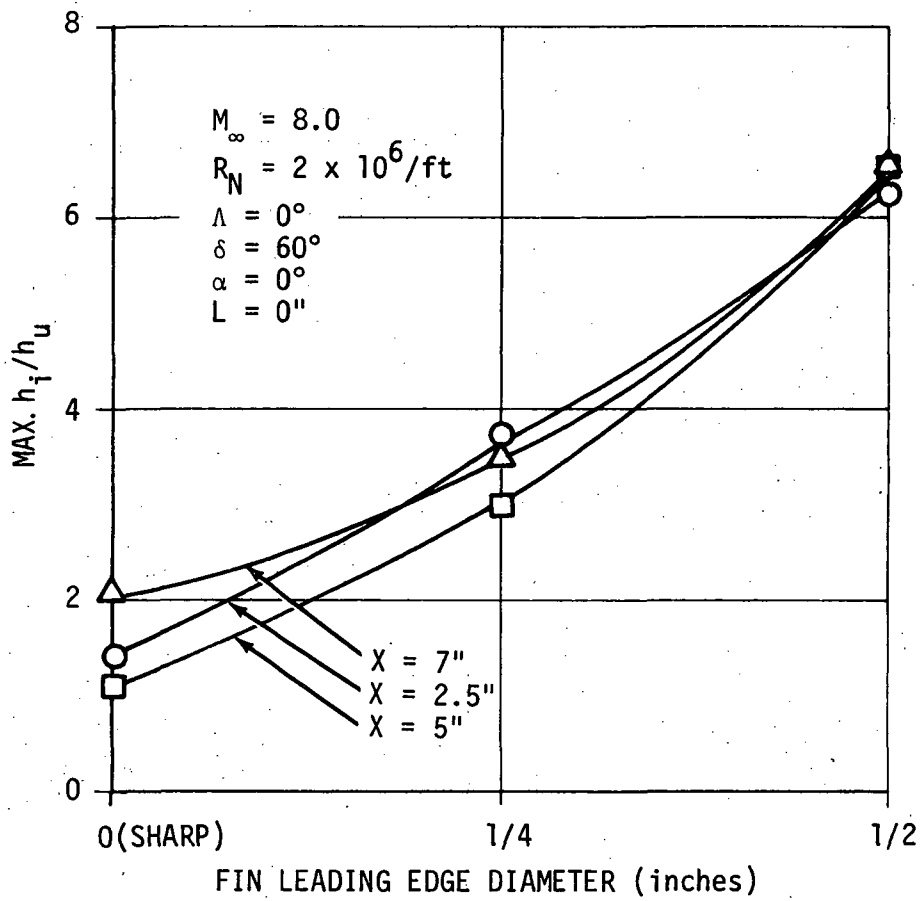


Figure 16. EFFECT OF FIN LEADING EDGE DIAMETER ON FLAT PLATE PEAK INTERFERENCE HEATING (Ref. 1)

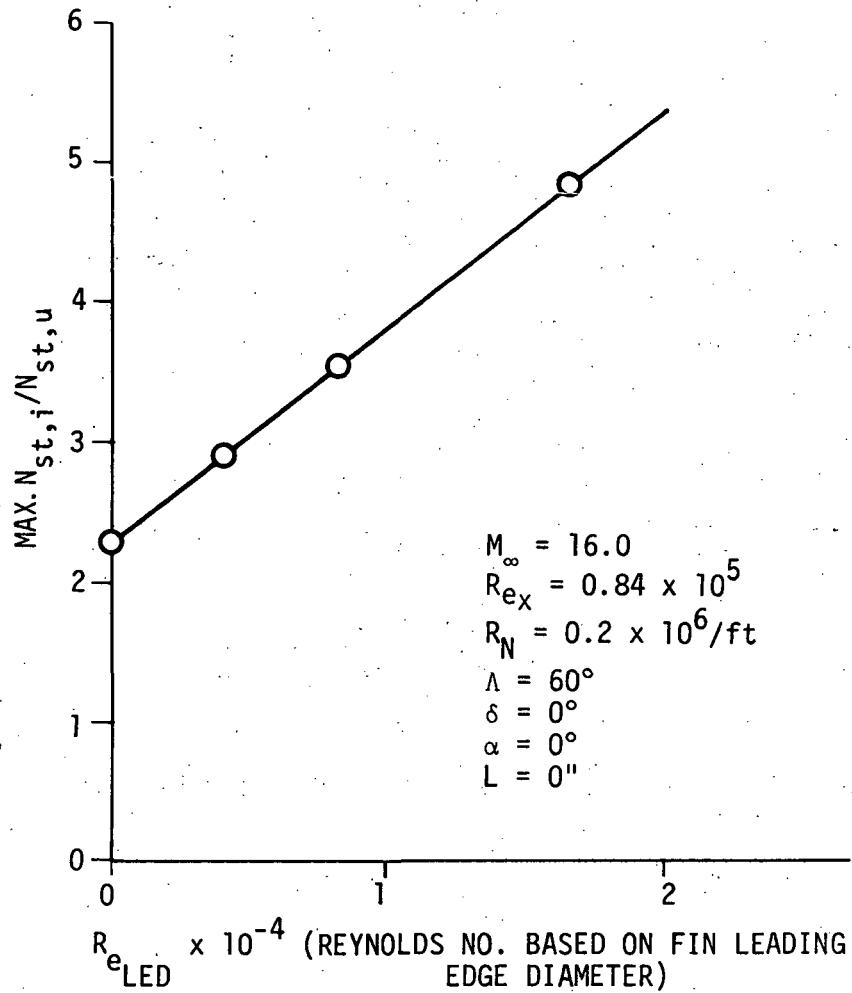


Figure 17. EFFECT OF FIN LEADING EDGE DIAMETER ON FLAT PLATE PEAK INTERFERENCE HEATING (Ref. 2)

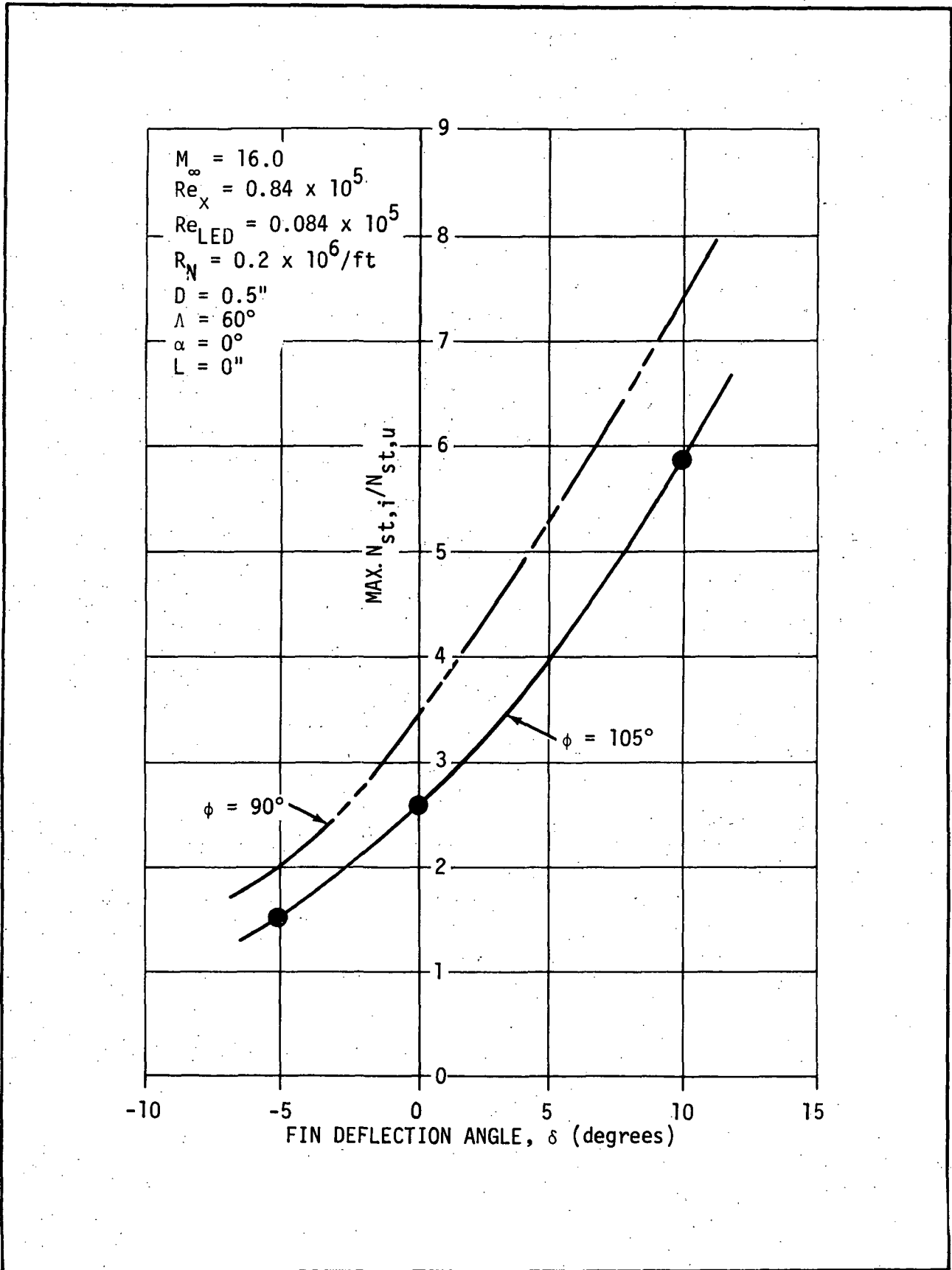


Figure 18. EFFECT OF FIN CANT ANGLE ON FLAT PLATE PEAK INTERFERENCE HEATING (Ref. 2)

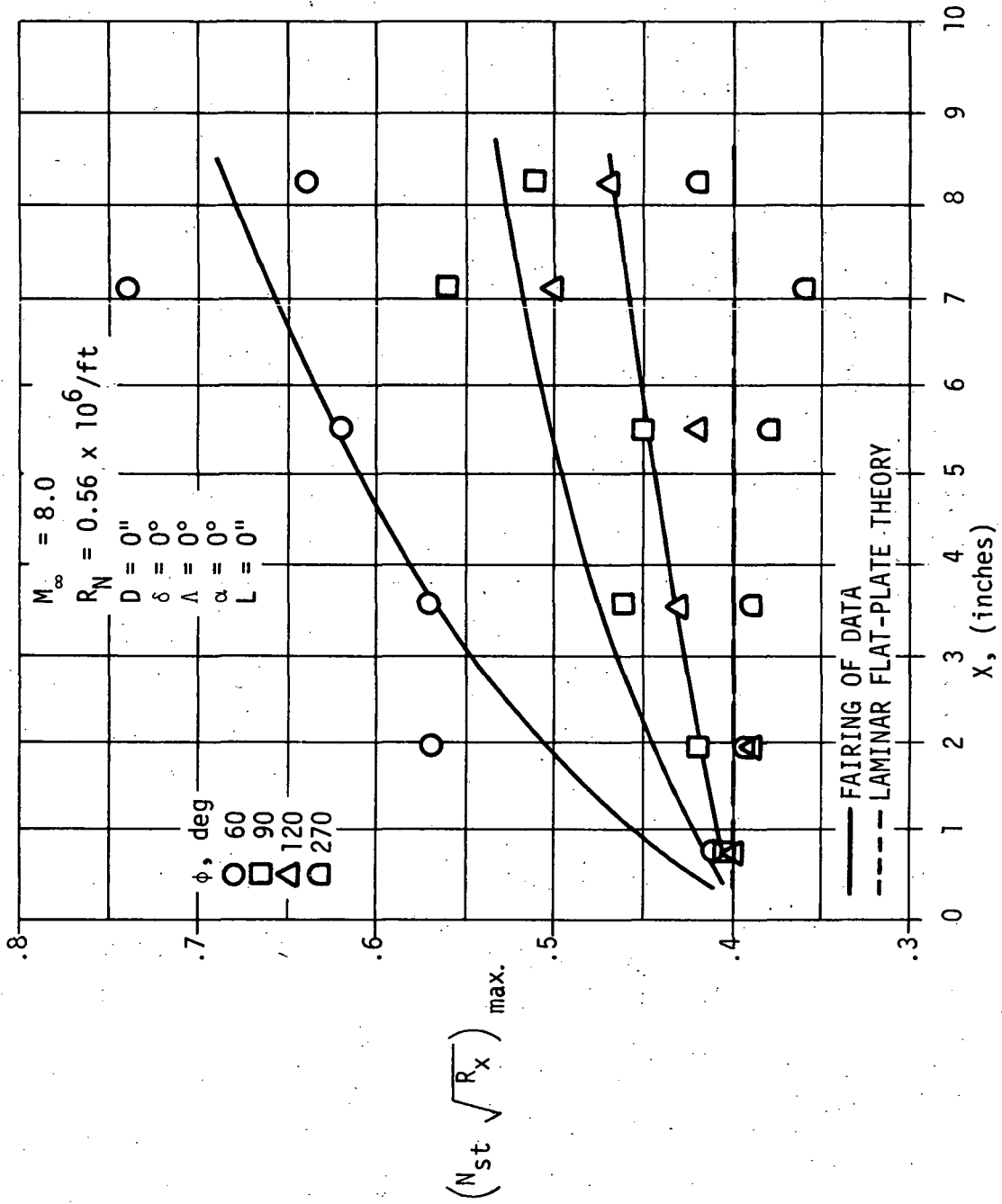


Figure 19. EFFECT OF FIN CANT ANGLE ON FLAT PLATE PEAK INTERFERENCE HEATING (Ref. 7)

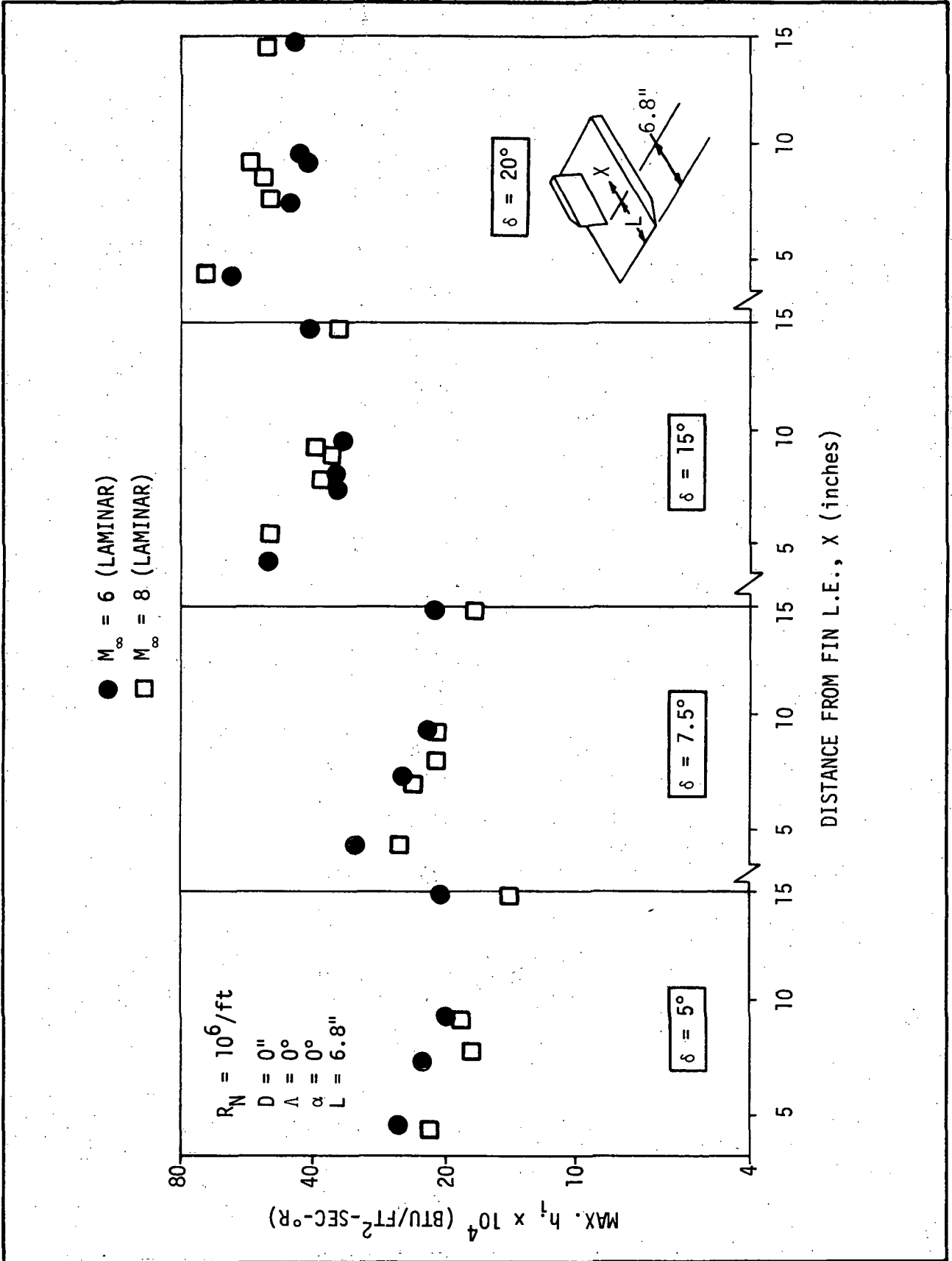


Figure 20. EFFECT OF FIN DEFLECTION ANGLE AND MACH NUMBER ON FLAT PLATE PEAK INTERFERENCE HEATING (Ref. 8)

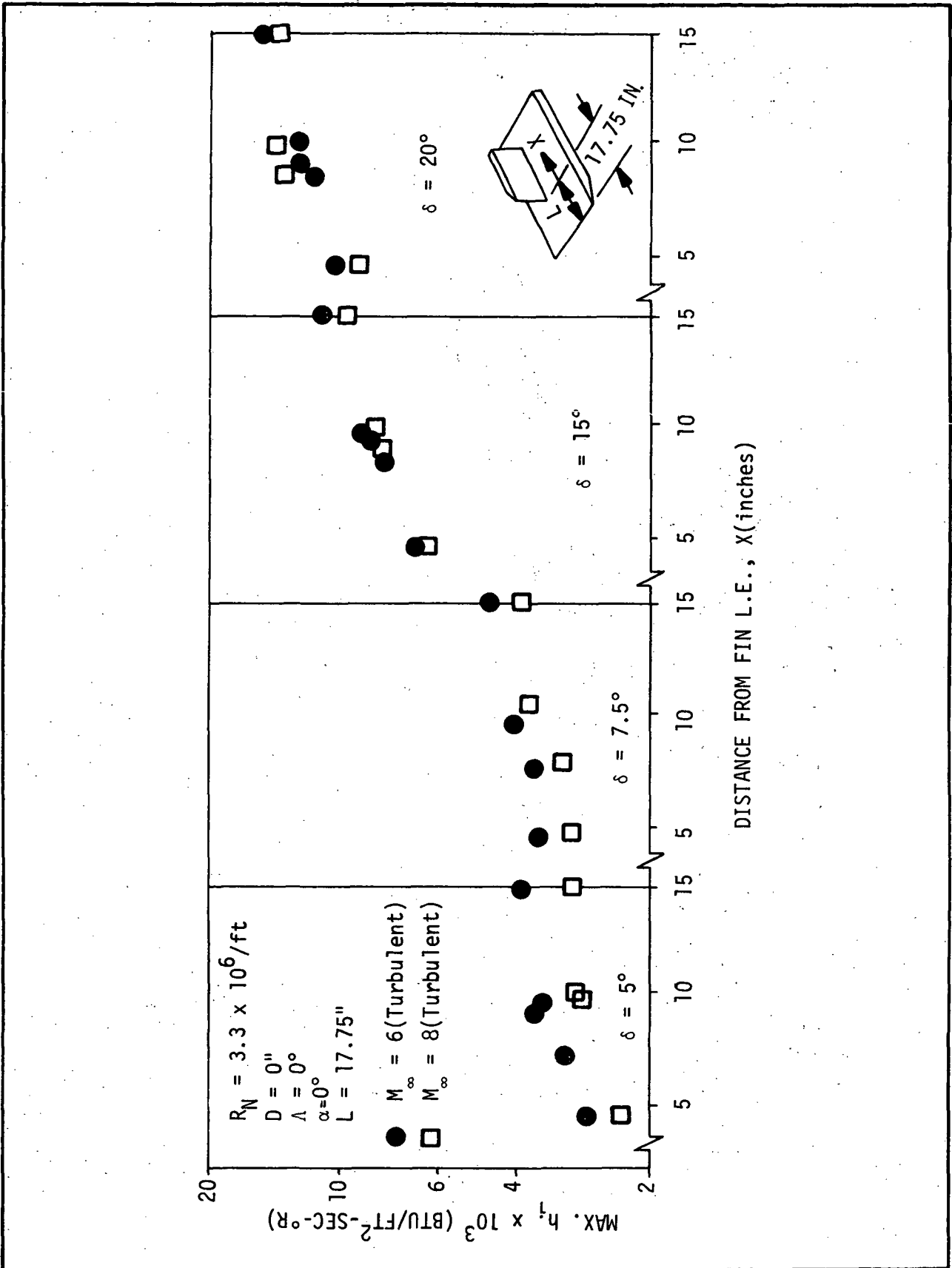


Figure 21. EFFECT OF FIN DEFLECTION ANGLE AND MACH NUMBER ON FLAT PLATE PEAK INTERFERENCE HEATING (Ref. 8)

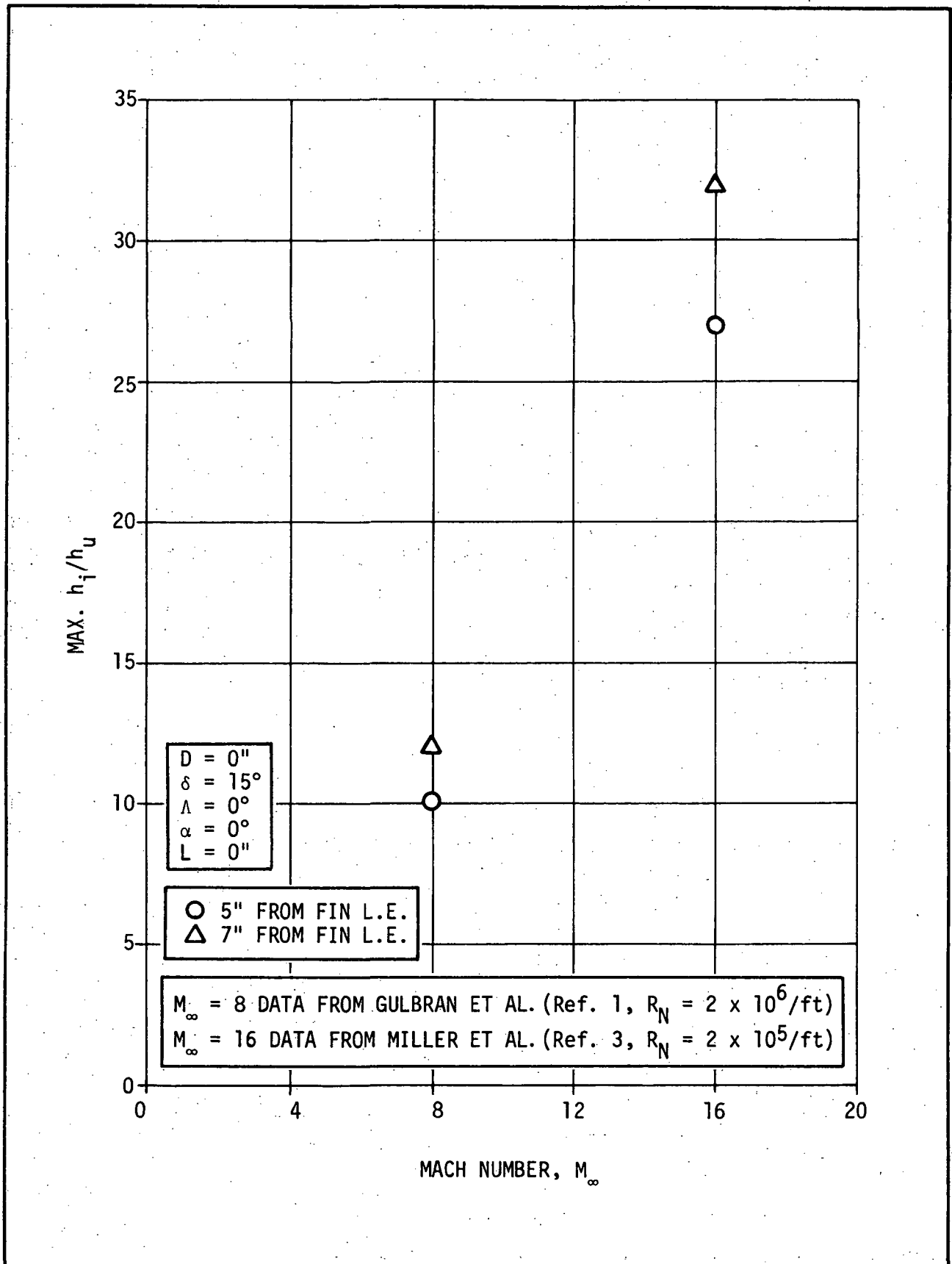


Figure 22. EFFECT OF MACH NUMBER ON FLAT PLATE PEAK INTERFERENCE HEATING (Refs. 1 and 3)

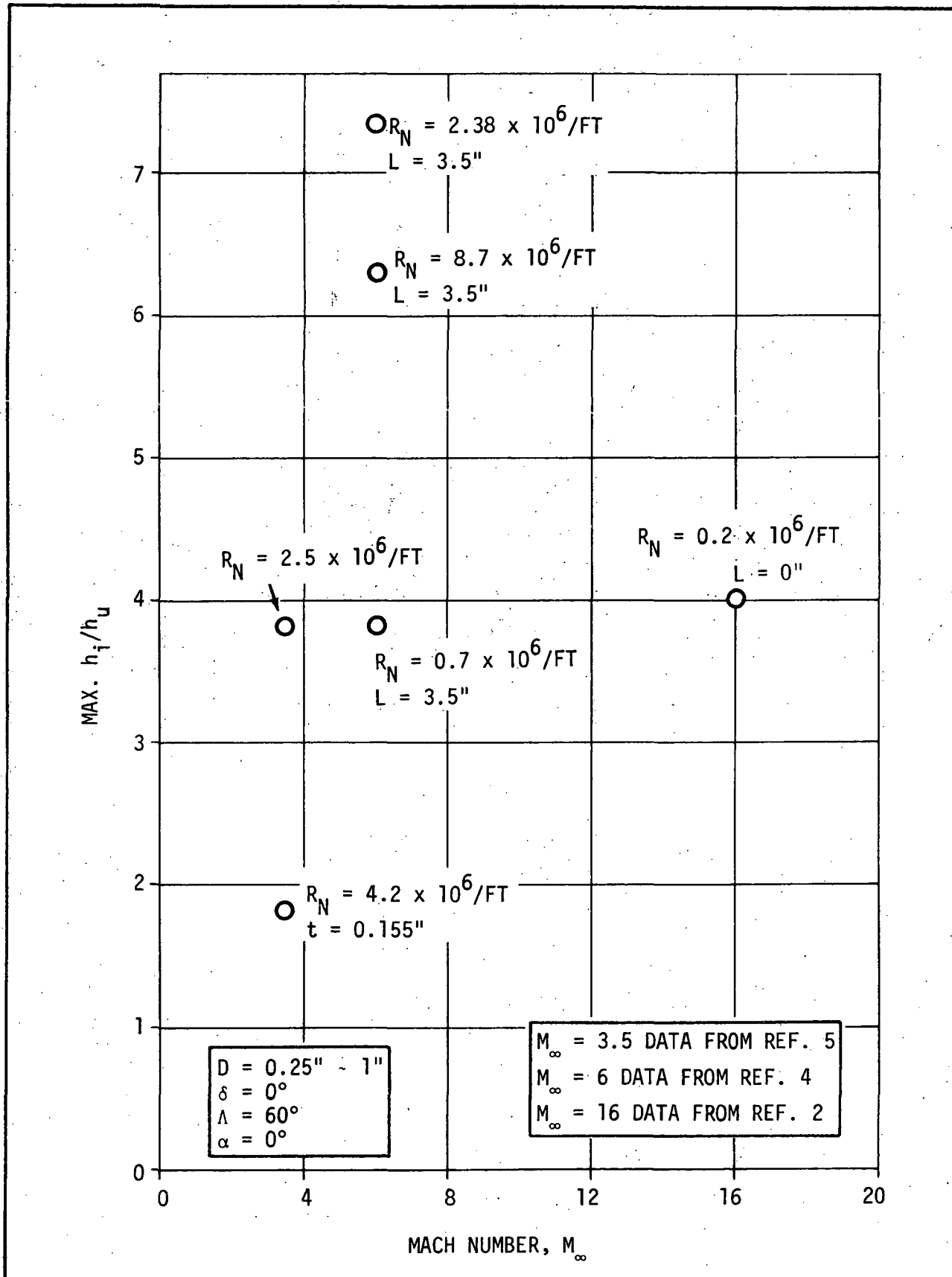


Figure 23. EFFECT OF MACH NUMBER ON FLAT PLATE PEAK INTERFERENCE HEATING (Refs. 2, 4 & 5)

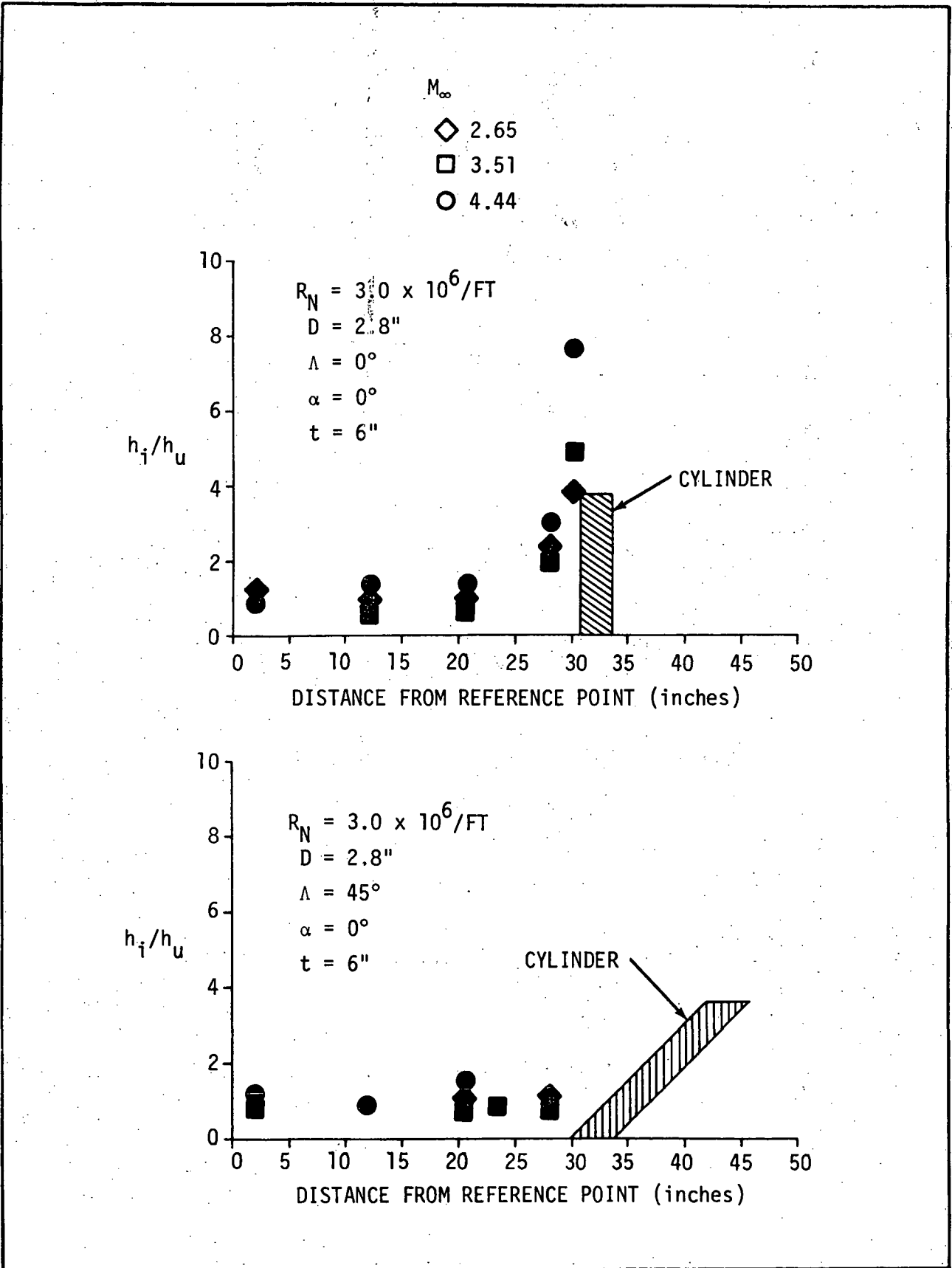


Figure 24. EFFECT OF MACH NUMBER ON FLAT PLATE CENTER LINE INTERFERENCE HEATING (Ref. 6)

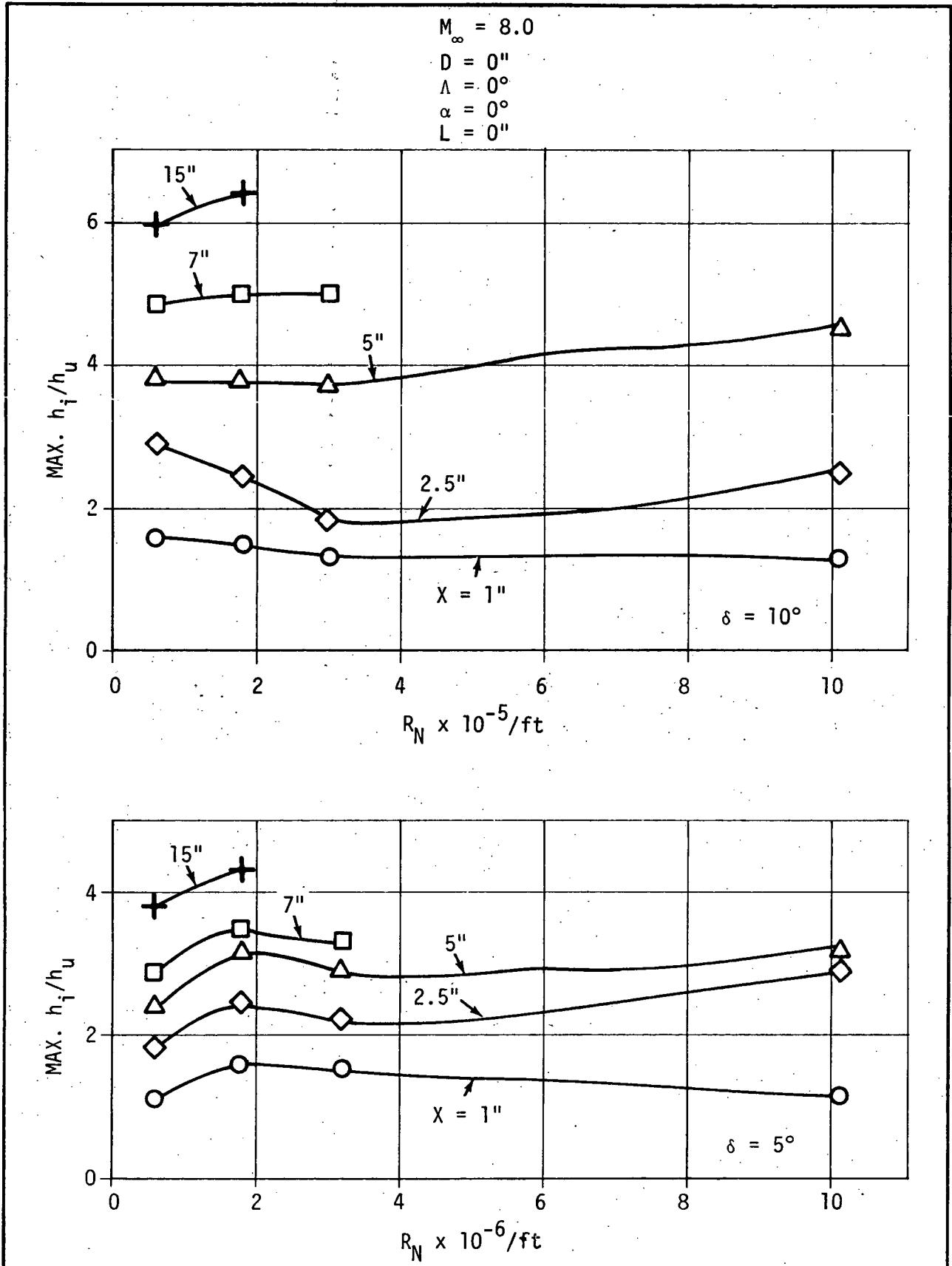


Figure 25. EFFECT OF REYNOLDS NUMBER ON FLAT PLATE PEAK INTERFERENCE HEATING (Ref. 7) (LAMINAR FLOW DATA ONLY)

$M_\infty = 8.0$
 $D = 5''$
 $\delta = 0^\circ$
 $\Lambda = 0^\circ$
 $\alpha = 0^\circ$
 $X = 14.5''$
 $L = 0''$

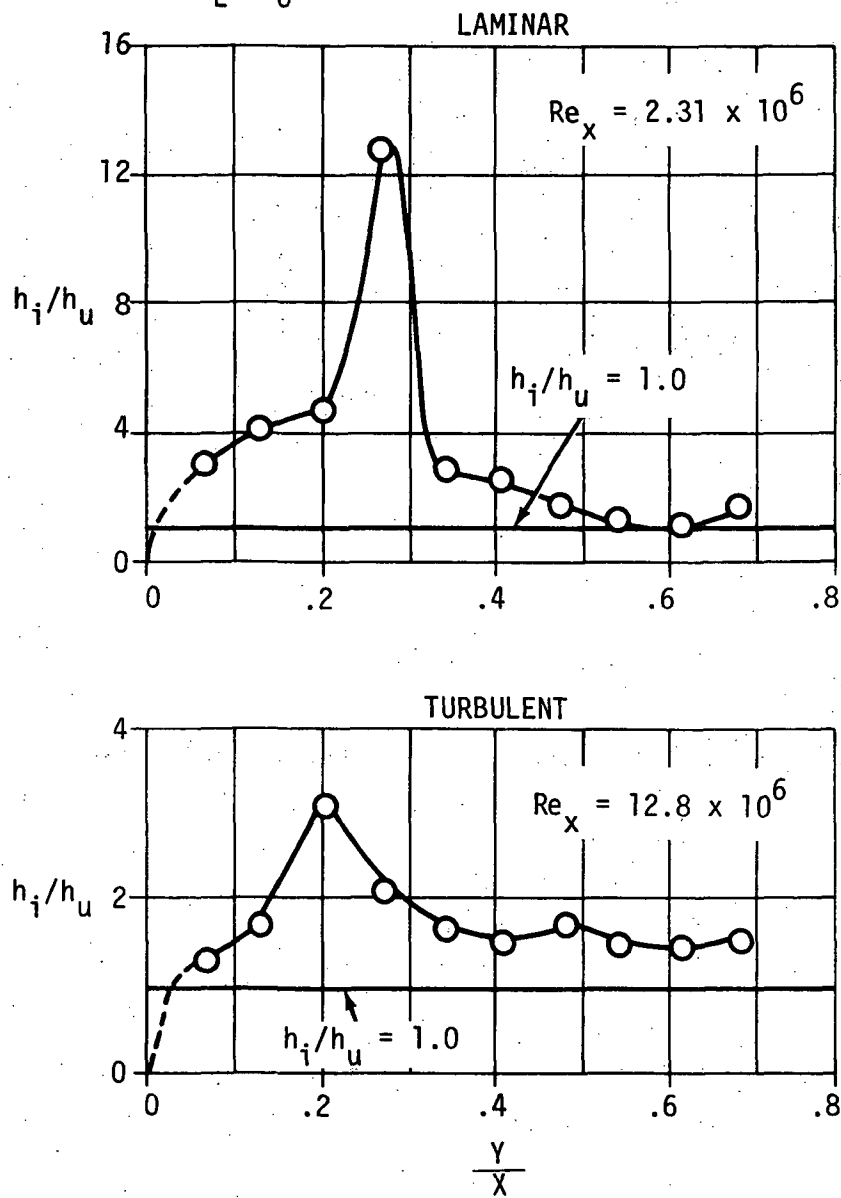
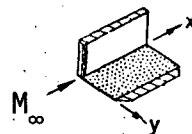


Figure 26. COMPARISON OF LAMINAR AND TURBULENT INTERFERENCE HEATING ON FLAT PLATE (Ref. 7)

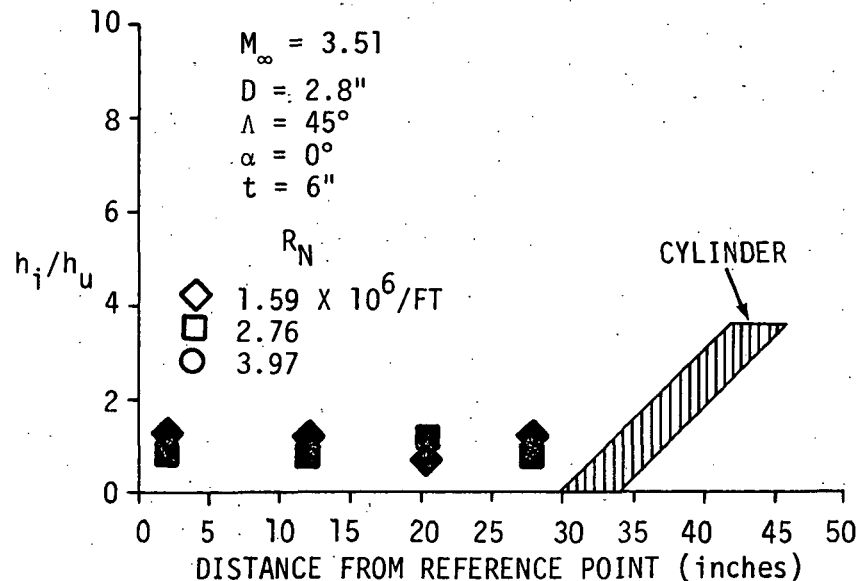
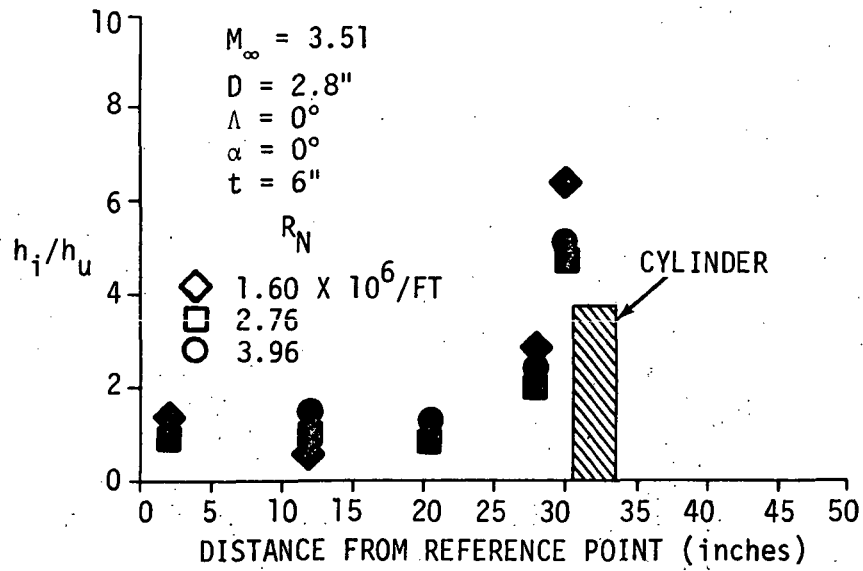


Figure 27. EFFECT OF REYNOLDS NUMBER ON THE FLAT PLATE CENTER LINE INTERFERENCE HEATING (Ref. 6)

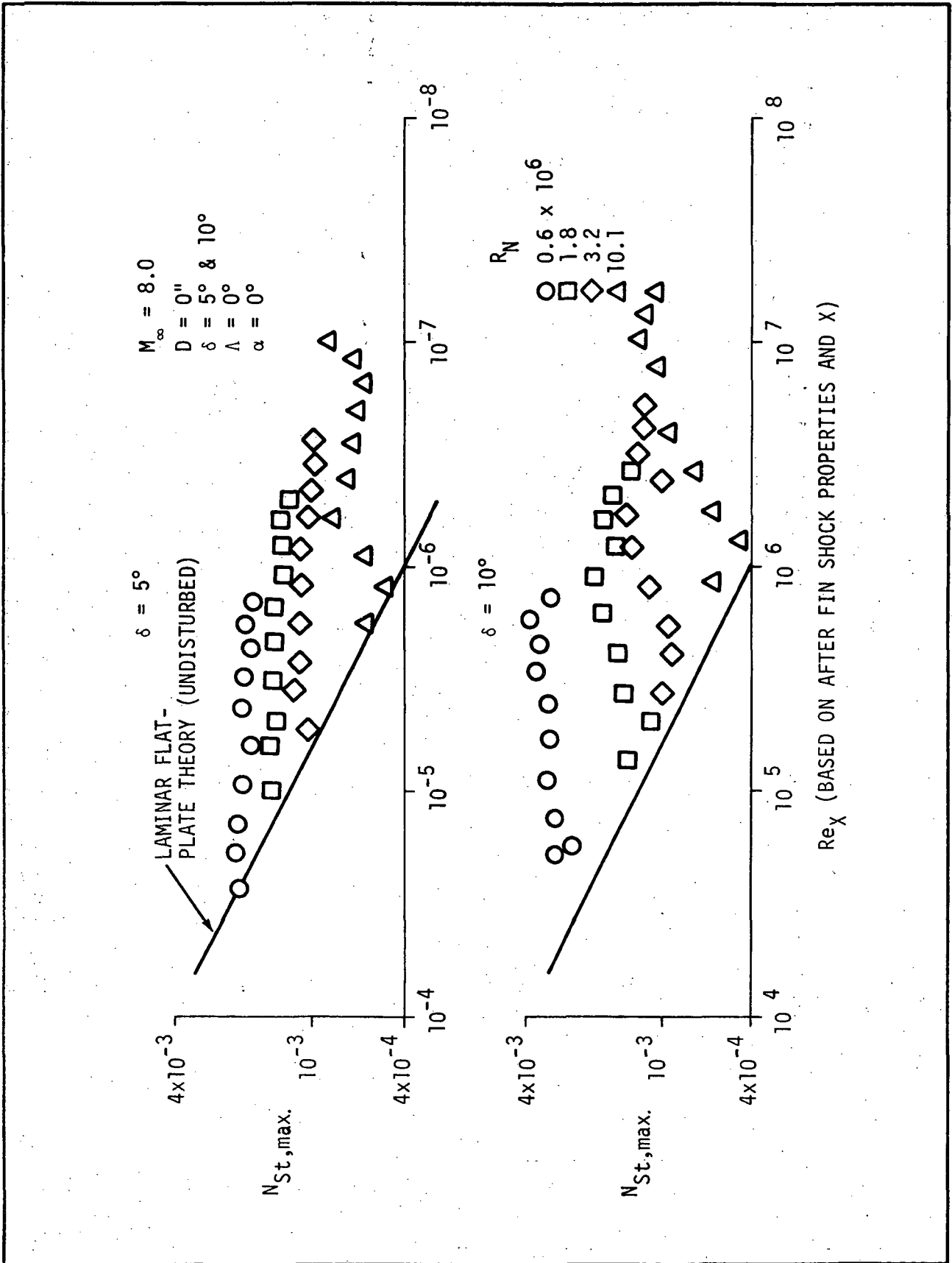


Figure 28. FLAT PLATE PEAK INTERFERENCE HEATING AT DIFFERENT LOCATIONS (X) (Ref. 7)

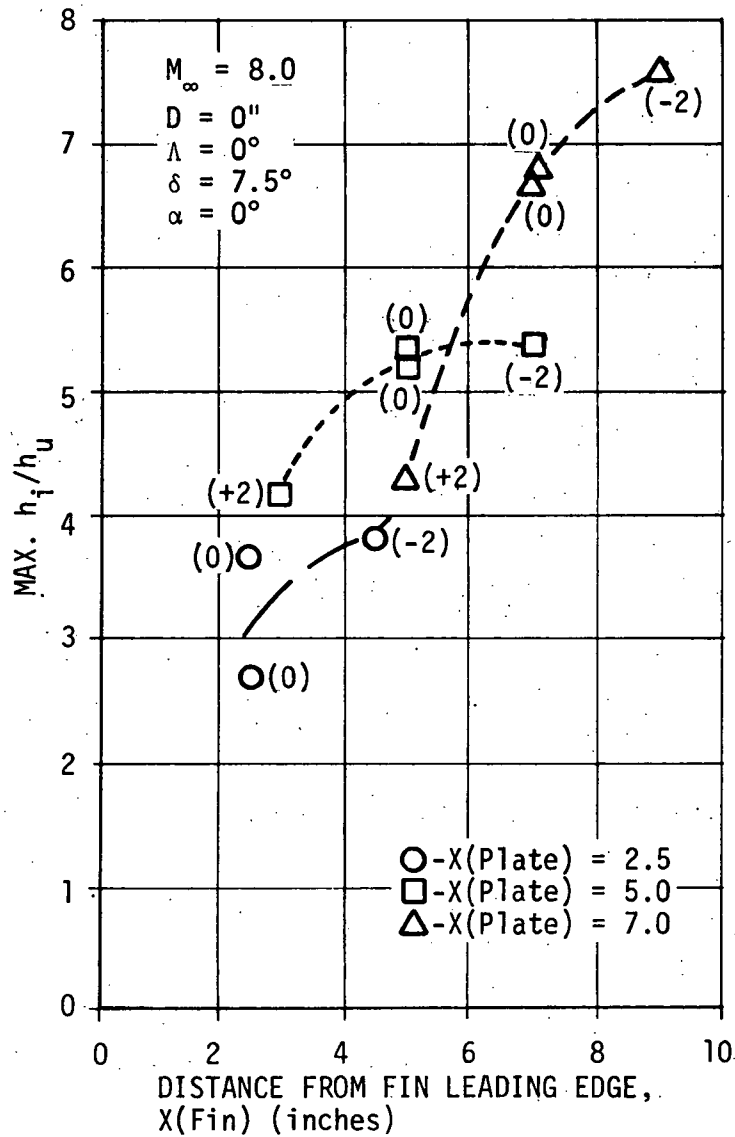
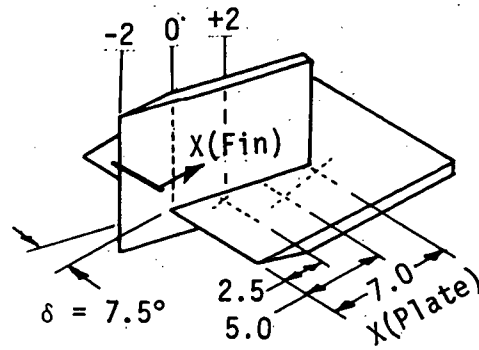


Figure 29. EFFECT OF FIN LOCATION ON FLAT PLATE PEAK INTERFERENCE HEATING (Ref. 1)

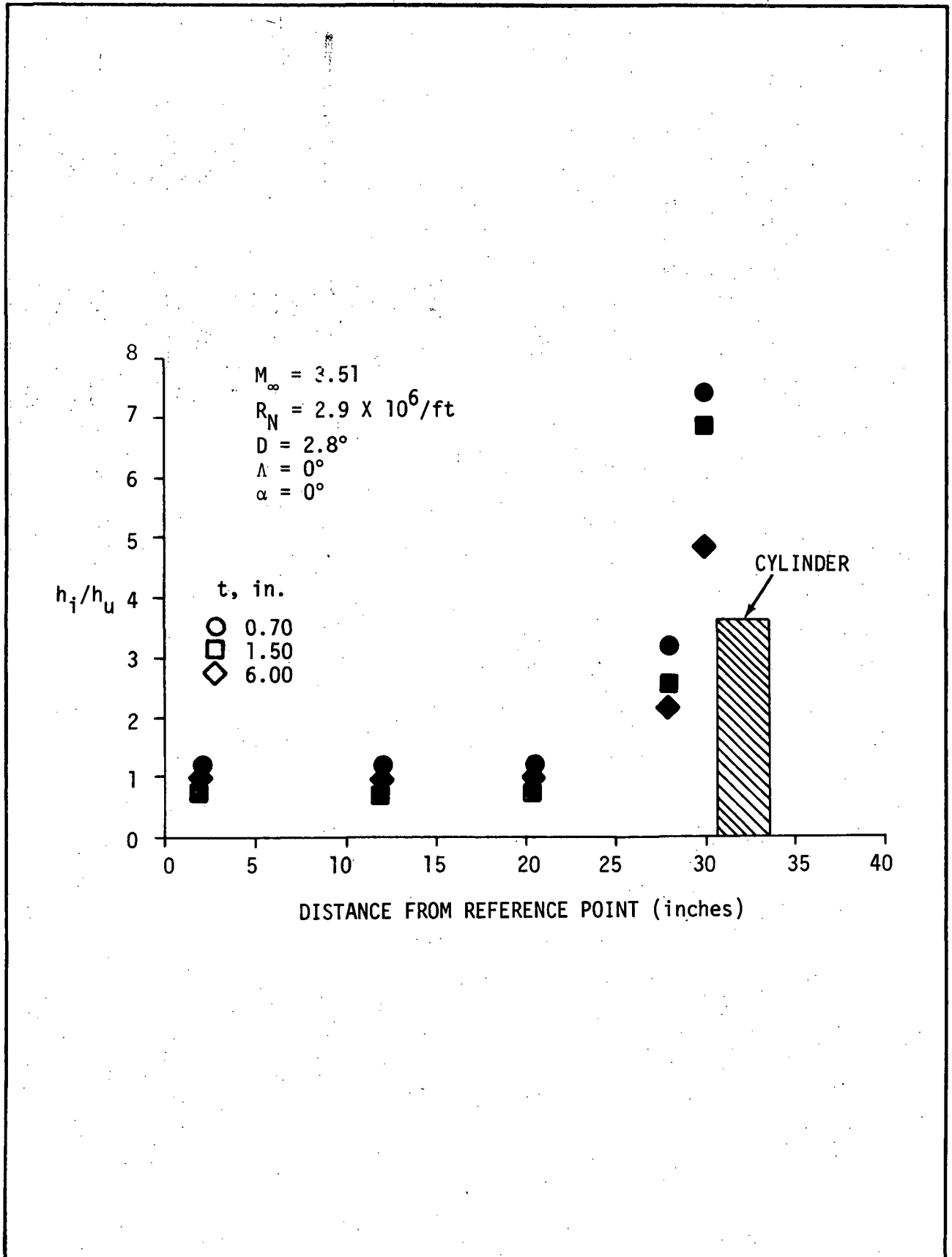


Figure 30. EFFECT OF BOUNDARY-LAYER THICKNESS ON THE FLAT PLATE CENTERLINE INTERFERENCE HEATING (Ref. 6)

Appendix A-4

**MDC/MMC HEATING
TEST DATA**

**SHOCK INTERFERENCE HEATING ANALYSIS BASED ON MDC/MMC
PHASE B SPACE SHUTTLE MODEL TEST DATA**

February 1971

by

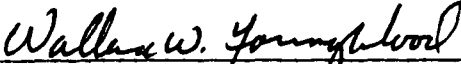
F. T. Hung

PREPARED FOR:

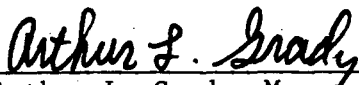
**NATIONAL AERONAUTICS AND SPACE ADMINISTRATION
GEORGE C. MARSHALL SPACE FLIGHT CENTER
AERO-ASTRODYNAMICS LABORATORY**

Under Contract NAS8-26268

REVIEWED AND APPROVED BY:



Wallace W. Youngblood, Manager
Aerothermodynamics



Arthur L. Grady, Manager
Aerophysics

**NORTHROP CORPORATION
HUNTSVILLE, ALABAMA**

205/837-0680

8 February 1971

TO: J. A. Forney, S&E-AERO-AT

FROM: F. T. Hung

SUBJECT: Shock Interference Heating Analysis based on MDC/MMC
Phase B Space Shuttle Model Test Data

REFERENCE: 1. Click, P. L. and Schmitt, D. A., "Wind Tunnel Test Results from the Thermal Mapping Investigation of 0.325% Scale MDC/MMC Phase B Space Shuttle Vehicles in the NASA/LRC Mach 8 Variable Density Tunnel and the NASA/LRC 31 Inch Continuous Flow Hypersonic Tunnel", Martin Marietta Design Note No. MMC-I-AERO-5002, October 1970.

A study was made of the effect of shock interference on MDC/MMC Phase B Space Shuttle aerodynamic heating. By using the phase change coating test data of reference 1, the shock interference effects were derived and presented as the ratios of the shock interference heat transfer coefficients to the undisturbed values, h_i/h_u . Of the shock interference heating involved in the shuttle flight as shown in Figure 1, only the areas at the booster (B1) canard/fuselage juncture and between the booster (B1) and the orbiter (O1) fuselages were considered in this study. The test conditions are listed in Table 1.

Figures 2(a) through 2(d) show the h_i/h_u values on the O1 and B1 fuselage centerlines in the shock interference region. Test data with the O1 or B1 model alone at 0 degree angle-of-attack were used as h_u values.

It is also of interest to have the interference heating data on the O1 and B1 fuselage centerlines without the presence of a canard as shown in Figures 2(a'), 2(b'), and 2(d'). In this case, the h_u values on B1 fuselage without canard are not available for the entire body. Extrapolation was made based on B1 and O1 test data at 0 degree angle-of-attack as shown in Figure 6.

Figures 3(a) through 3(h') show the interference heating data at the B1 canard/fuselage juncture with 0 degree angle-of-attack. Again, the h_u values at higher X/L ratios were obtained by extrapolation. Consequently, both an approximately constant h_u value (based on Figures A265 and A267 of reference 1) and the extrapolated variable h_u values as shown in Figure 6 were used to generate Figures 3(a) through 3(h) and Figures 3(a') through 3(h') respectively.

Figures 4(a) through 4(f) present the interference heating data near the B1 canard/fuselage juncture at 30 degrees angle-of-attack. It is noted that B1 and B2 configurations are exactly the same except B1 has high wing and low canard whereas B2 has low wing and high canard. This indicates that h_i/h_u data for B1 can easily be derived by combining the B1 and B2 data both with 30 degrees angle-of-attack.

Figures 5(a) through 5(e) show the interference heating data near B1 canard/fuselage juncture at 60 degrees angle-of-attack.

The results of this study will be used to correlate interference heating with test flow conditions. The collected thermocouple data with simple geometry test models will also be used in the data correlation.

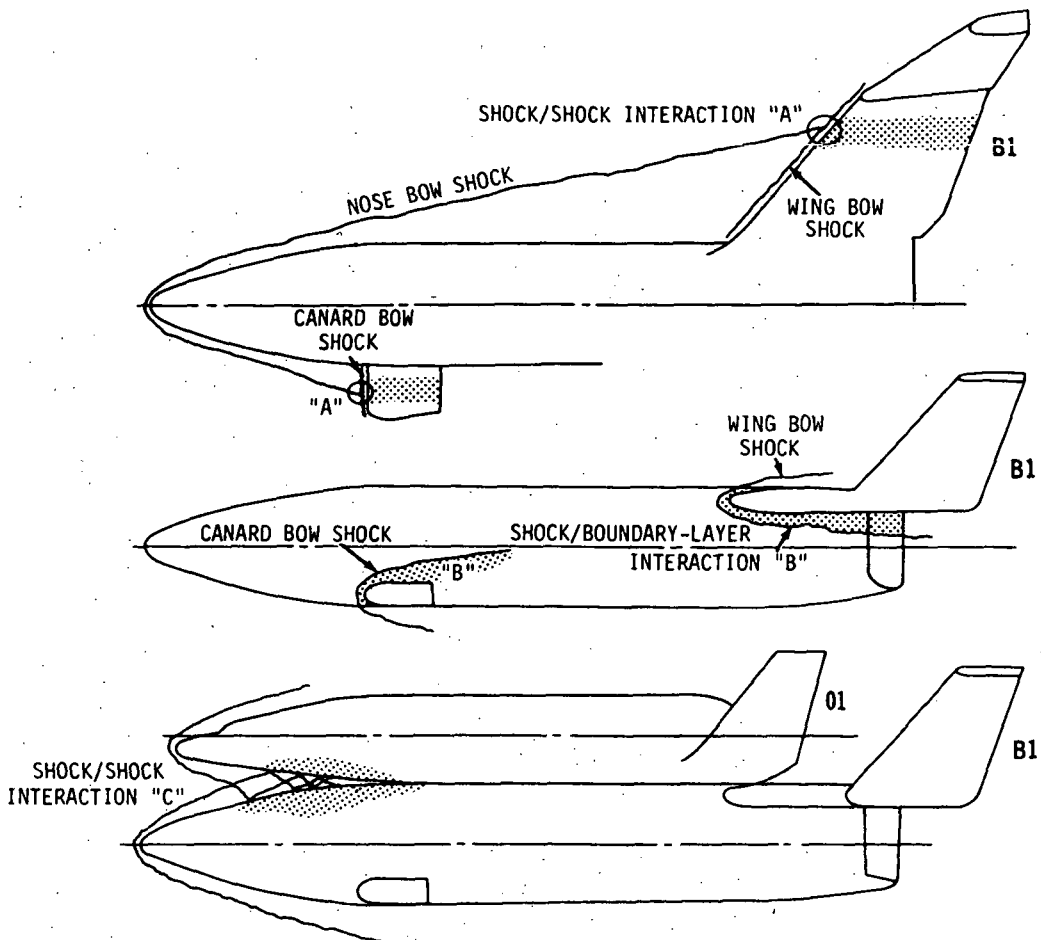


Figure 1. SPACE SHUTTLE SHOCK INTERFERENCE

Table 1. SHOCK INTERFERENCE HEATING STUDY SUMMARY

FIGURE NO.	MODEL	INTERFERENCE REGION	ANGLE-OF-ATTACK α (deg)	MACH NO., M_∞	REYNOLDS NO. R_N (per foot)	REMARKS
2(a)	01 + B1	01/B1 FUSELAGES	0	7.71	0.553×10^6	WITH CANARD ↓ NO CANARD
2(b)				7.81	1.008×10^6	
2(c)				7.95	5.614×10^6	
2(d)				10.28	0.513×10^6	
2(a')				7.71	0.553×10^6	
2(b')				7.81	1.008×10^6	
2(d')				10.28	0.513×10^6	
3(a)	B1			CANARD/FUSELAGE JUNCTURE	0	
3(b)		7.81	1.014×10^6			
3(c)		7.81	1.014×10^6			
3(d)		7.95	5.437×10^6			
3(e)		7.95	5.738×10^6			
3(f)		10.28	0.518×10^6			
3(g)		10.28	0.508×10^6			
3(h)		10.28	0.523×10^6			
3(a')		7.71	0.569×10^6			
3(b')		7.81	1.014×10^6			
3(c')		7.81	1.014×10^6			
3(d')		7.95	5.437×10^6			
3(e')		7.95	5.738×10^6			
3(f')		10.28	0.518×10^6			
3(g')		10.28	0.508×10^6			

Table 1. SHOCK INTERFERENCE HEATING STUDY SUMMARY (Concluded)

FIGURE NO.	MODEL	INTERFERENCE REGION	ANGLE-OF-ATTACK α (deg)	MACH NO., M_∞	REYNOLDS NO. R_N (per foot)	REMARKS
3(h')	B1	CANARD/FUSELAGE JUNCTURE	0	10.28	0.523×10^6	VARIABLE h_u
4(a)	B1	CANARD/FUSELAGE JUNCTURE	30	7.81	0.985×10^6	
4(b)				7.81	0.985×10^6	
4(c)				7.81	1.062×10^6	
4(d)				7.81	1.062×10^6	
4(e)				7.95	4.845×10^6	
4(f)				7.95	4.845×10^6	
5(a)	B1	CANARD/FUSELAGE JUNCTURE	60	7.71	0.584×10^6	
5(b)				7.81	1.044×10^6	
5(c)				7.95	5.707×10^6	
5(d)				7.95	5.707×10^6	
5(e)				10.28	0.534×10^6	

$$\alpha = 0^\circ$$

$$M_\infty = 7.71$$

$$R_N = 0.553 \times 10^6 / \text{FT}$$

DATA FROM REF. 1, FIGURES A246, A272, A265, A267, A161

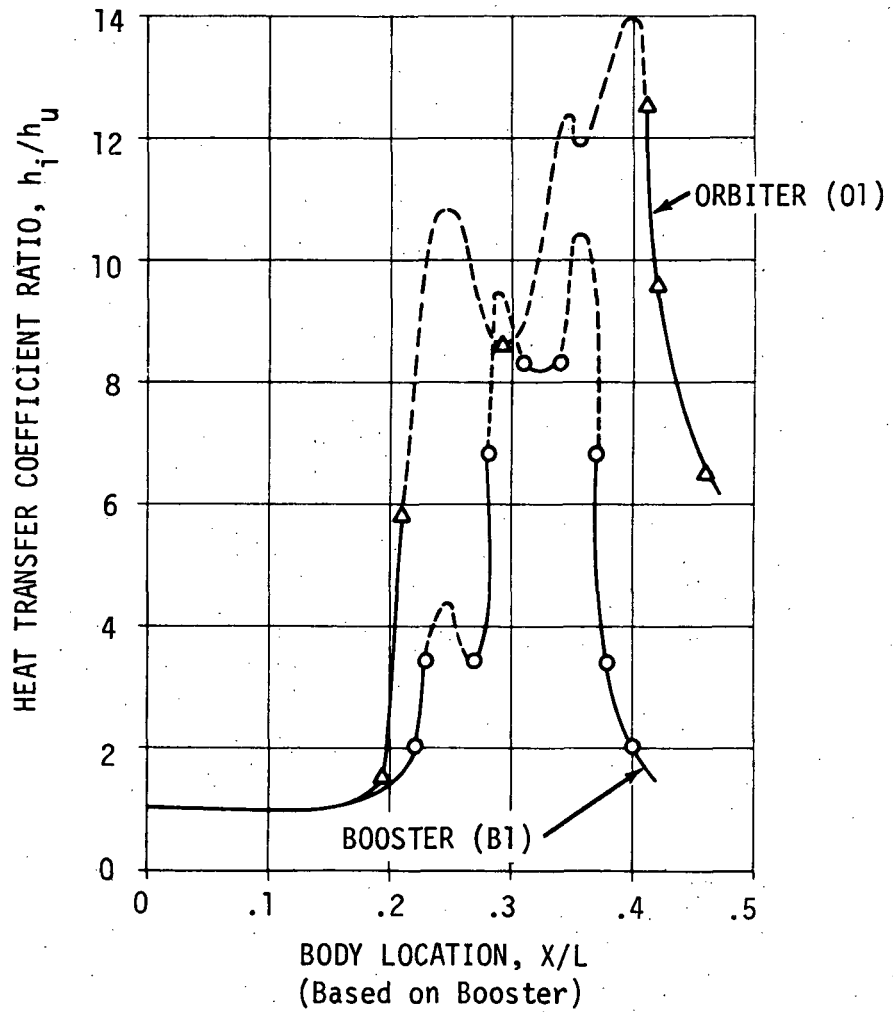


Figure 2(a). SHOCK INTERFERENCE HEATING ON ORBITER (O1) AND BOOSTER (B1) FUSELAGE CENTERLINES

$$\alpha = 0^\circ$$

$$M_\infty = 7.81$$

$$R_N = 1.008 \times 10^6 / \text{FT}$$

● DATA FROM REF. 1, FIGURES A254, A272, A265, A267, A161

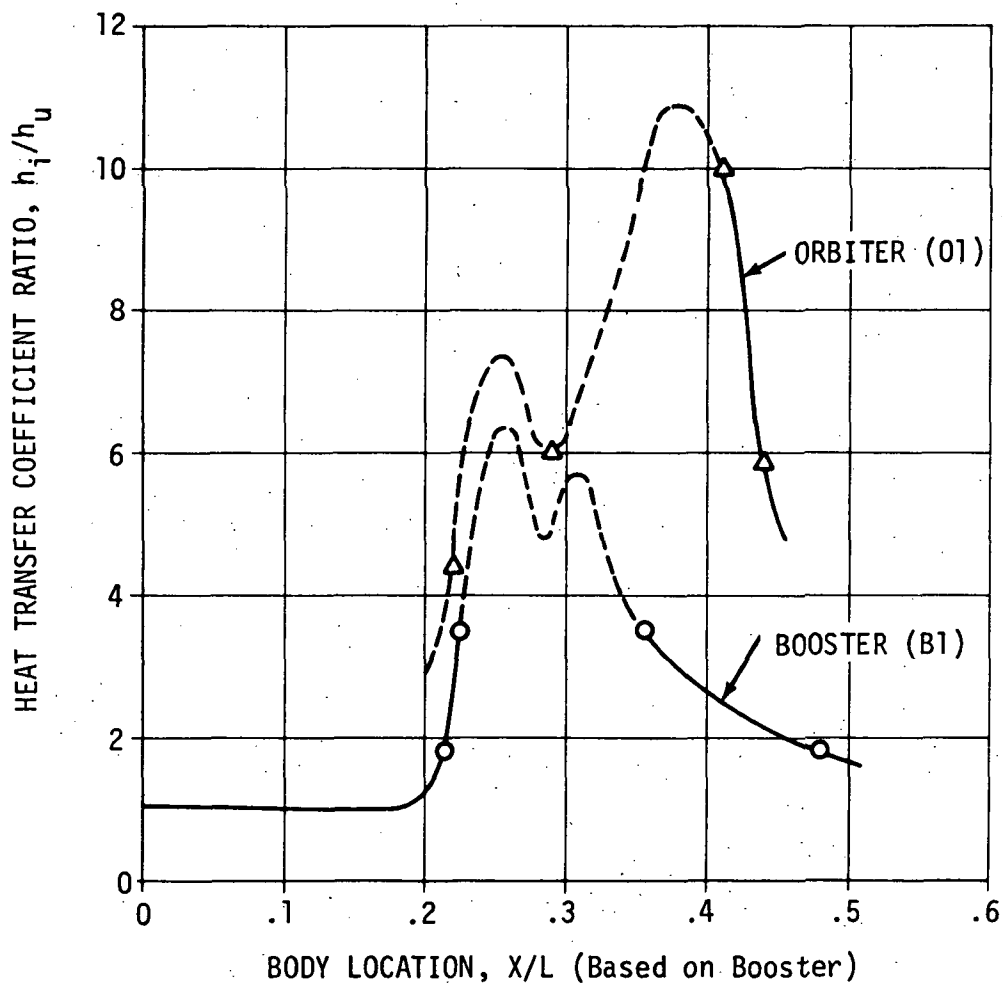


Figure 2(b). SHOCK INTERFERENCE HEATING ON ORBITER (O1) AND BOOSTER (B1) FUSELAGE CENTERLINES

$$\alpha = 0^\circ$$

$$M_\infty = 7.95$$

$$R_N = 5.614 \times 10^6 / \text{FT}$$

INSUFFICIENT BOOSTER DATA

• DATA FROM REF. 1, FIGURES A222, A161

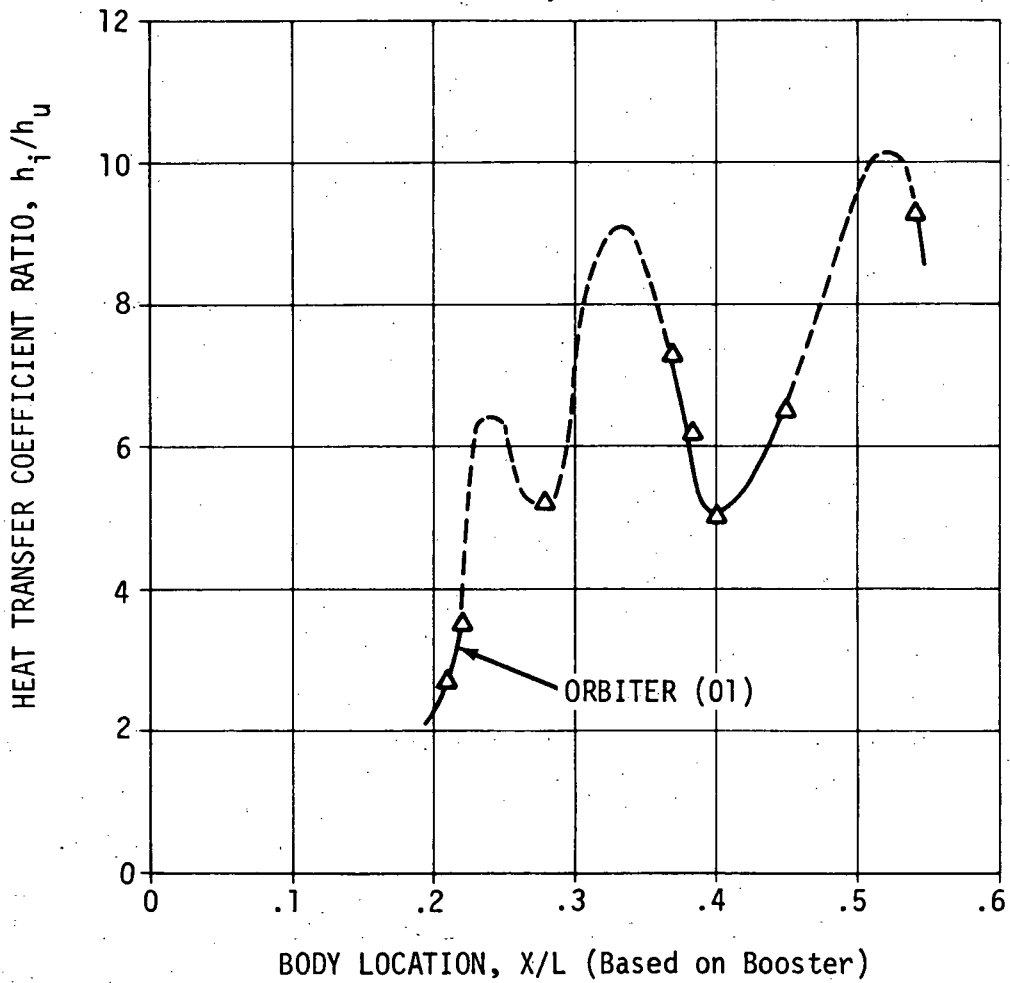


Figure 2(c). SHOCK INTERFERENCE HEATING ON ORBITER (01) AND BOOSTER (B1) FUSELAGE CENTERLINES

$\alpha = 0^\circ$

$M_\infty = 10.28$

$R_N = 513,000/\text{FT (OR } 503,000/\text{FT)}$

- DATA FROM REF. 1, FIGURES A63, A65, A272, A265, A267, A161

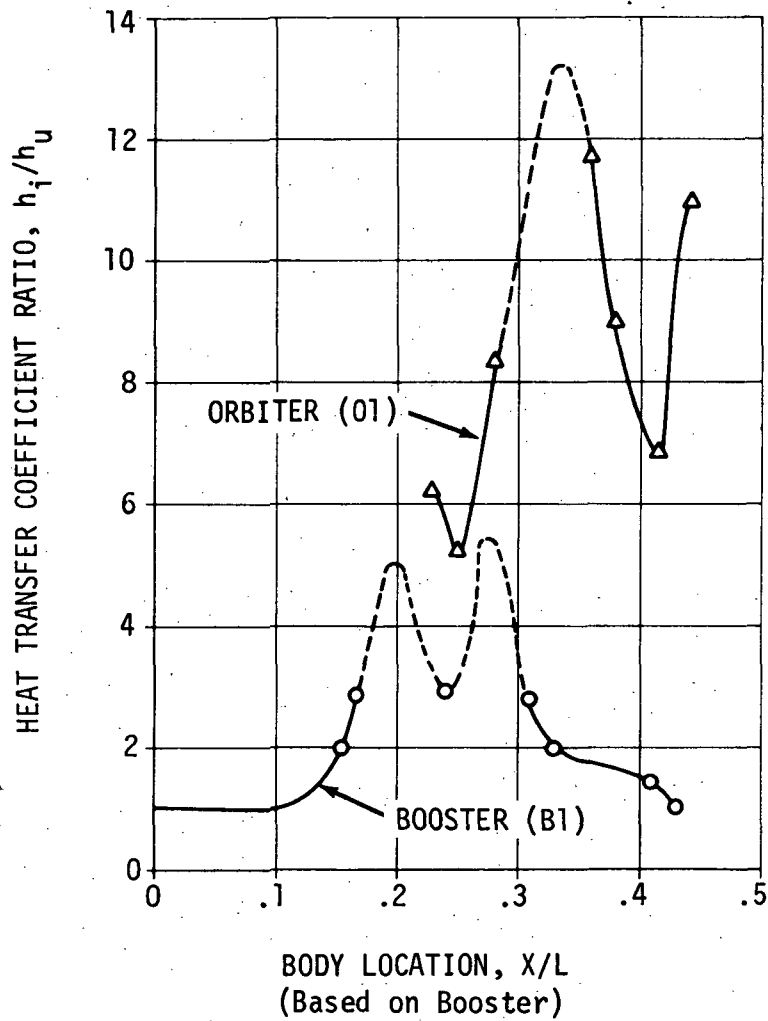


Figure 2(d). SHOCK INTERFERENCE HEATING ON ORBITER (O1) AND BOOSTER (B1) FUSELAGE CENTERLINES

$$\alpha = 0^\circ$$

$$M_\infty = 7.71$$

$$R_N = 0.553 \times 10^6/\text{FT}$$

- DATA FROM REF. 1, FIGURES A246, A265, A267, A161
- NO CANARD ON B1

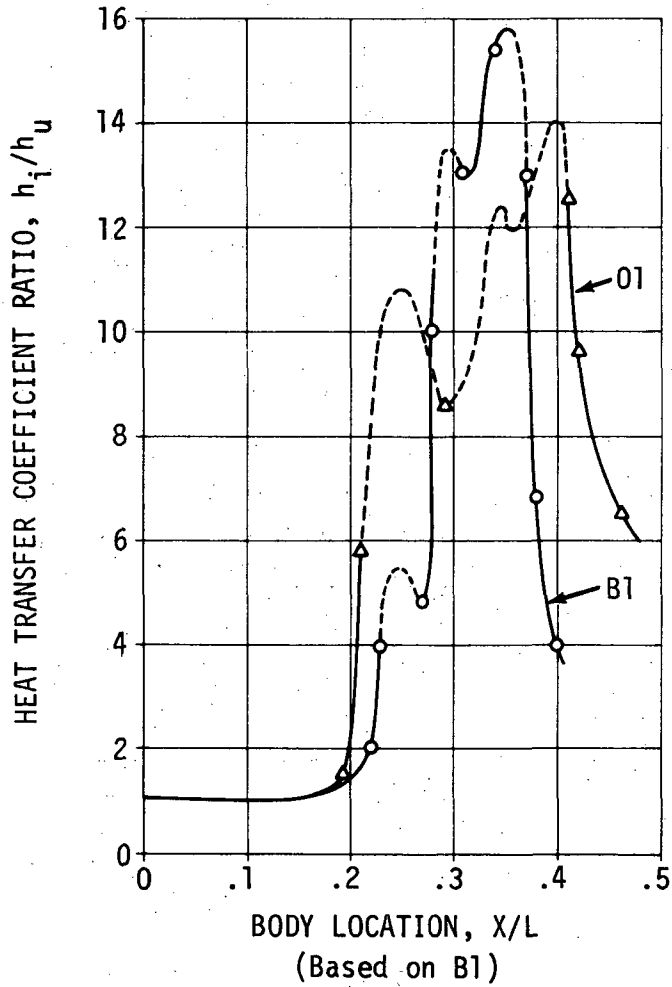


Figure 2(a'). SHOCK INTERFERENCE HEATING ON ORBITER (O1) AND BOOSTER (B1) FUSELAGE CENTERLINES

$$\alpha = 0^\circ$$

$$M_\infty = 7.81$$

$$R_N = 1.008 \times 10^6 / \text{FT}$$

- DATA FROM REF. 1, FIGURES A254, A265, A267, A161
- NO CANARD ON B1

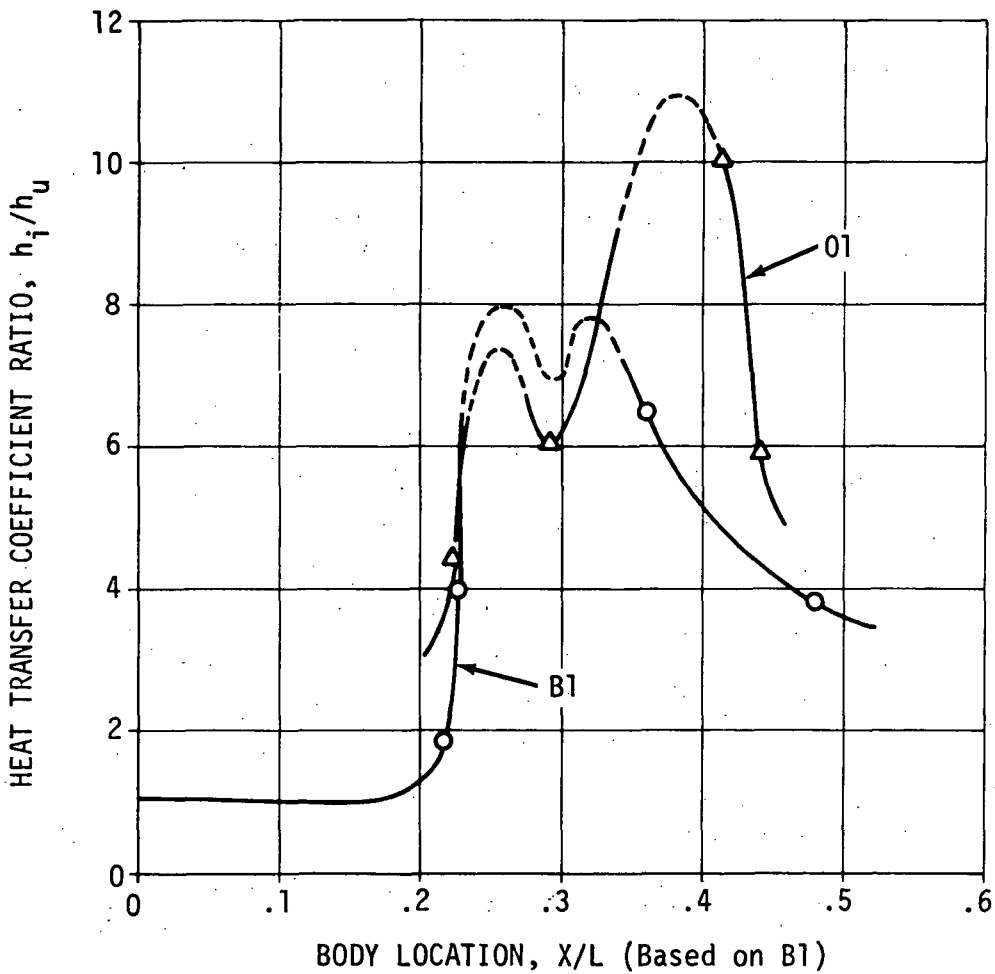


Figure 2(b'). SHOCK INTERFERENCE HEATING ON ORBITER (O1) AND BOOSTER (B1) FUSELAGE CENTERLINES

$\alpha = 0^\circ$

$M_\infty = 10.28$

$R_N = 513,000/FT$ (OR 503,000/FT)

- DATA FROM REF. 1, FIGURES A63, A65, A265, A267, A161
- NO CANARD ON B1

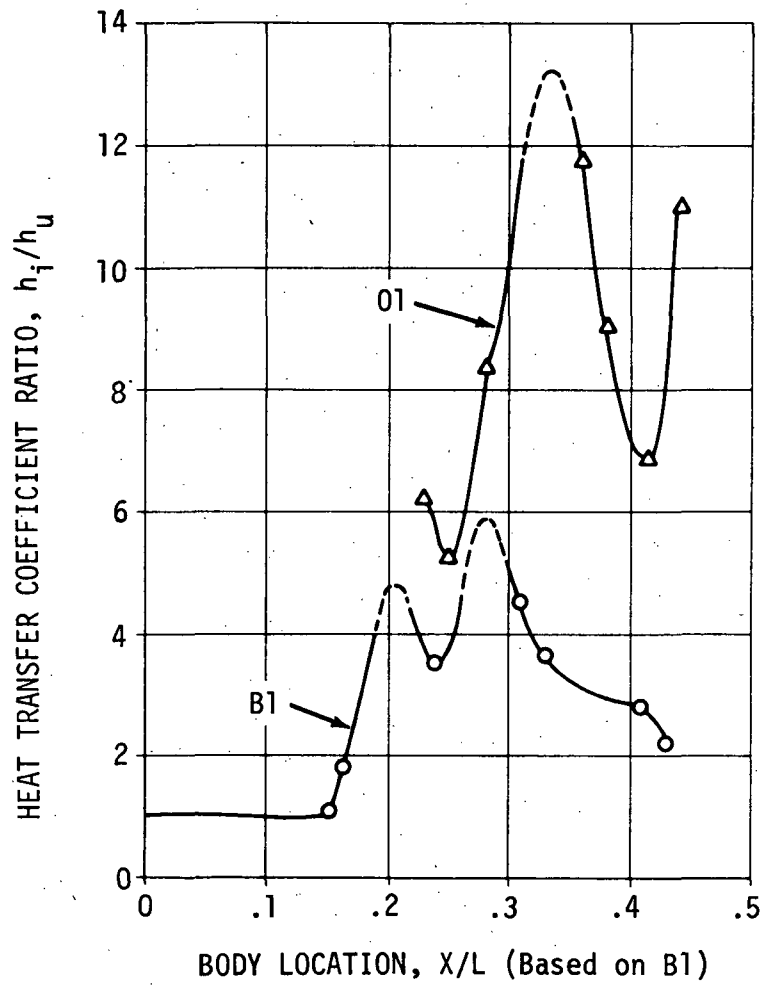


Figure 2(d'). SHOCK INTERFERENCE HEATING ON ORBITER (O1) AND BOOSTER (B1) FUSELAGE CENTERLINES

$$\alpha = 0^\circ$$
$$M_\infty = 7.71$$
$$R_N = 0.569 \times 10^6 / \text{FT}$$

- DATA FROM REF. 1, FIGS. A260, A 272, A265, A267
- CONSTANT h FOR UNDISTURBED CASE ($h/h_{r=1} = \text{CONST.} = 0.023$)

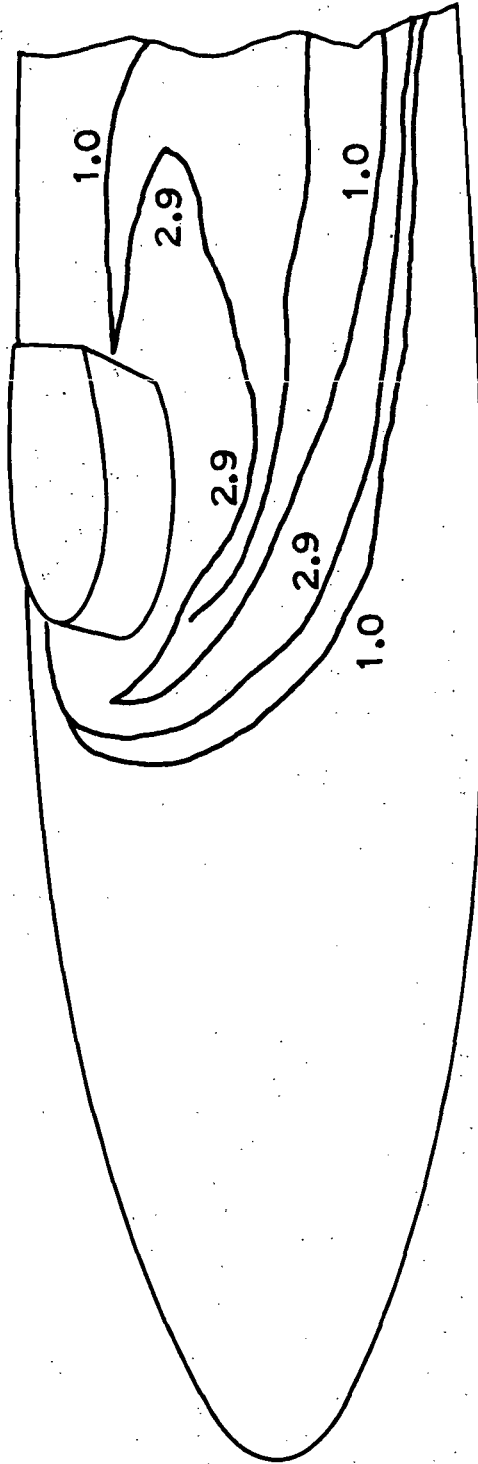


Figure 3(a). SHOCK INTERFERENCE HEATING NEAR BOOSTER (B1) CANARD/FUSELAGE JUNCTURE (HEAT TRANSFER COEFFICIENT RATIO WITH AND WITHOUT INTERFERENCE, h_i/h_u)

$$\begin{aligned}\alpha &= 0^\circ \\ M_\infty &= 7.81 \\ R_N &= 1.014 \times 10^6/\text{FT}\end{aligned}$$

- DATA FROM REF. 1, FIGS. A269, A272, A265, A267
- CONSTANT h FOR UNDISTURBED CASE ($h/h_{r=1} = \text{CONST.} = 0.023$).

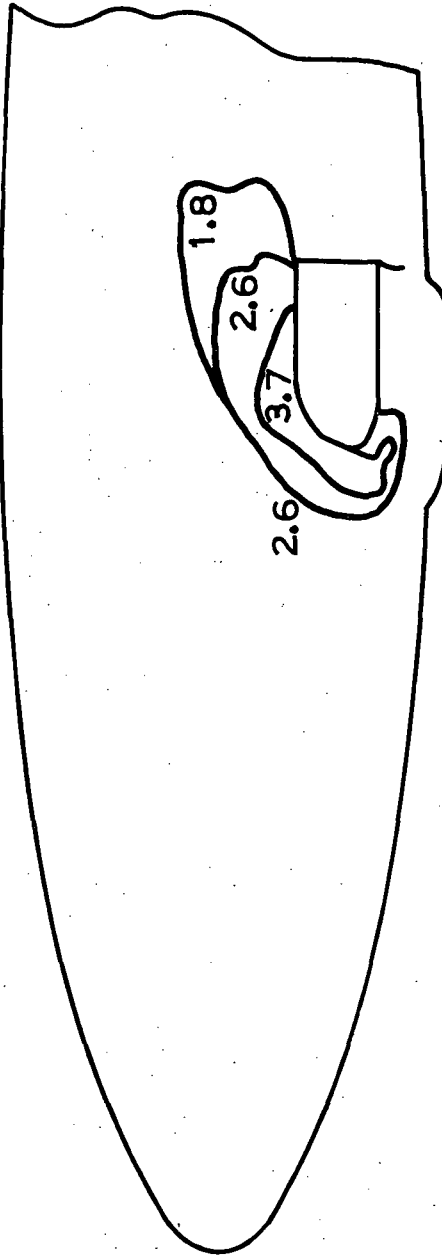


Figure 3(b). SHOCK INTERFERENCE HEATING NEAR BOOSTER (B1) CANARD/FUSELAGE JUNCTURE (HEAT TRANSFER COEFFICIENT RATIO WITH AND WITHOUT INTERFERENCE, h_i/h_u)

$\alpha = 0^\circ$
 $M_\infty = 7.81$
 $R_N = 1.014 \times 10^6 / \text{FT}$

- DATA FROM REF. 1, FIGS. A268, A272, A265, A267
- CONSTANT h FOR UNDISTURBED CASE ($h/h_{r=1} = \text{CONST.} = 0.023$)

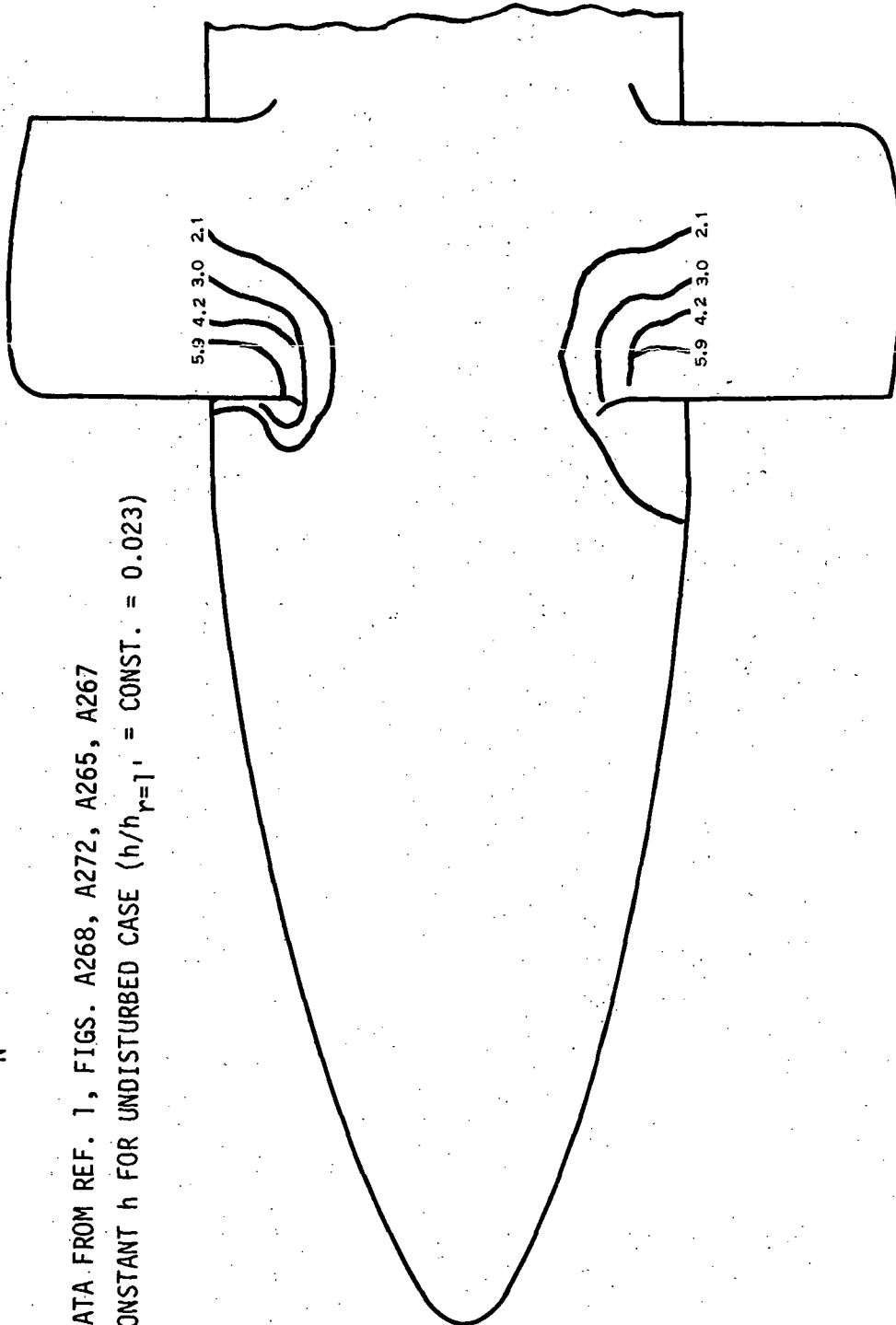


Figure 3(c). SHOCK INTERFERENCE HEATING NEAR BOOSTER (B1) CANARD/FUSELAGE JUNCTURE (HEAT TRANSFER COEFFICIENT RATIO WITH AND WITHOUT INTERFERENCE, h_j/h_u)

$$\begin{aligned}\alpha &= 0^\circ \\ M_\infty &= 7.95 \\ R_N &= 5.437 \times 10^6/\text{FT}\end{aligned}$$

- DATA FROM REF. 1, FIGS. A264, A272, A265, A267
- CONSTANT h FOR UNDISTURBED CASE ($h/h_{r=1} = \text{CONST.} = 0.023$)

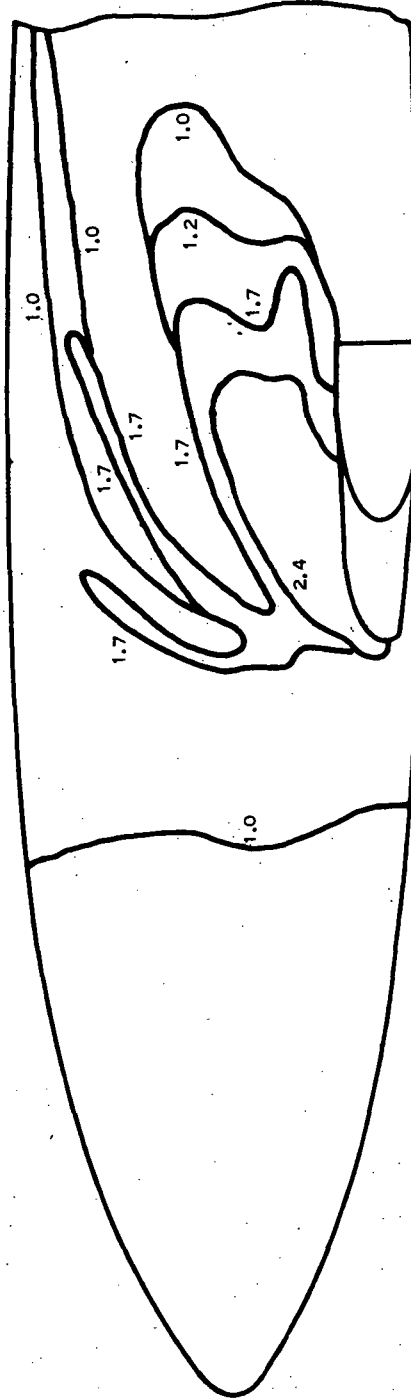


Figure 3(d). SHOCK INTERFERENCE HEATING NEAR BOOSTER (B1) CANARD/FUSELAGE JUNCTURE (HEAT TRANSFER COEFFICIENT RATIO WITH AND WITHOUT INTERFERENCE, h_i/h_u)

$\alpha = 0^\circ$
 $M_\infty = 7.95$
 $R_N = 5.738 \times 10^6 / \text{FT}$

- DATA FROM REF. 1, FIGS. A272, A265, A267
- CONSTANT h FOR UNDISTURBED CASE ($h/h_{r=1} = \text{CONST.} = 0.023$)

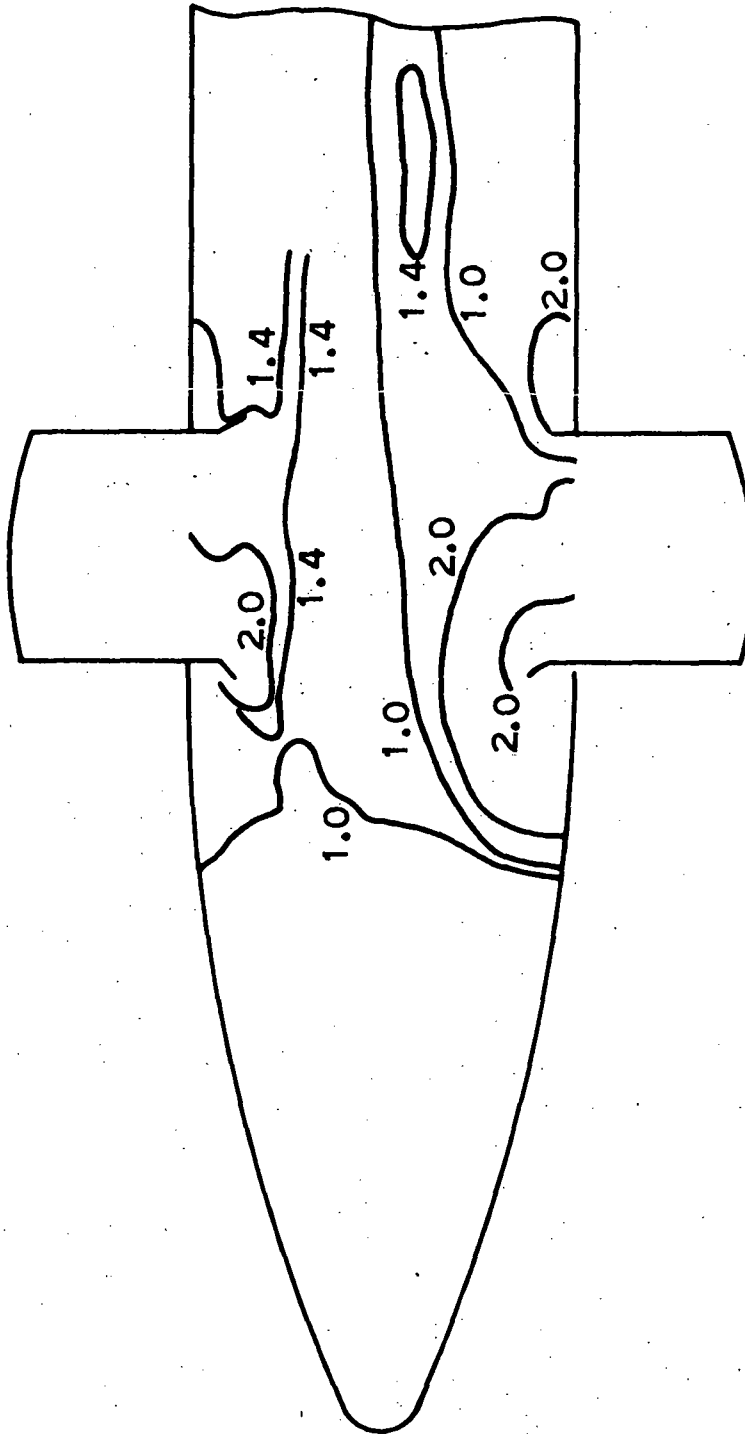


Figure 3(e). SHOCK INTERFERENCE HEATING NEAR BOOSTER (B1) CANARD/FUSELAGE JUNCTURE (HEAT TRANSFER COEFFICIENT RATIO WITH AND WITHOUT INTERFERENCE, h_i/h_u)

$\alpha = 0^\circ$
 $M_\infty = 10.28$
 $R_N = 518,000/\text{FT}$

- DATA FROM REF. 1, FIGS. A52, A272, A265, A267
- CONSTANT h FOR UNDISTURBED CASE ($h/h_{\gamma=1} = \text{CONST.} = 0.023$)

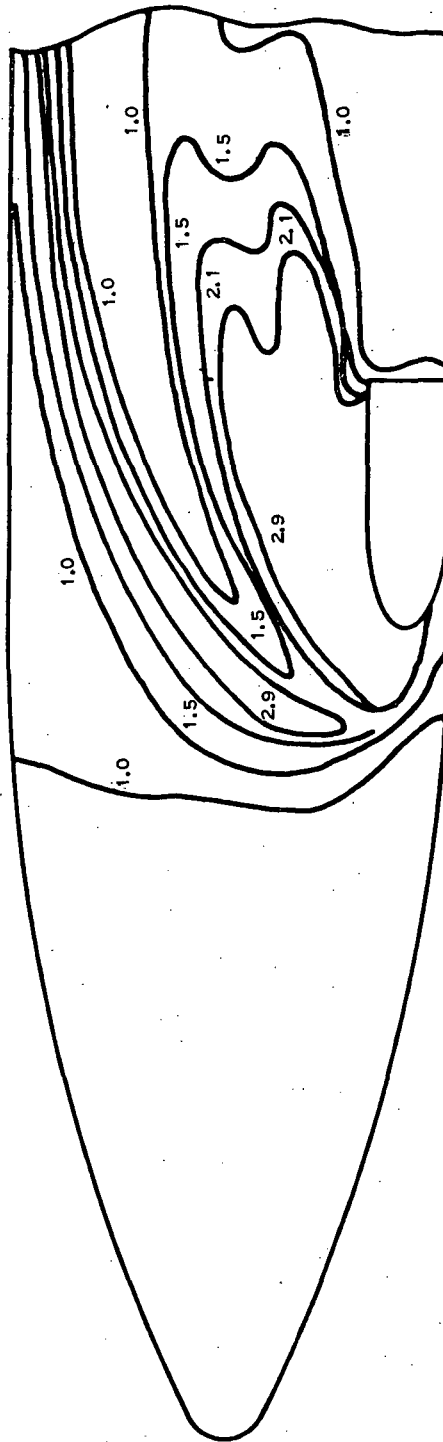


Figure 3(f). SHOCK INTERFERENCE HEATING NEAR BOOSTER (B1) CANARD/FUSELAGE JUNCTURE (HEAT TRANSFER COEFFICIENT RATIO WITH AND WITHOUT INTERFERENCE, h_i/h_u)

$\alpha = 0^\circ$
 $M_\infty = 10.28$
 $R_N = 508,000/\text{FT}$

- DATA FROM REF. 1, FIGS. A53, A272, A265, A267
- CONSTANT h FOR UNDISTURBED CASE ($h/h_{r=1} = \text{CONST.} = 0.023$)

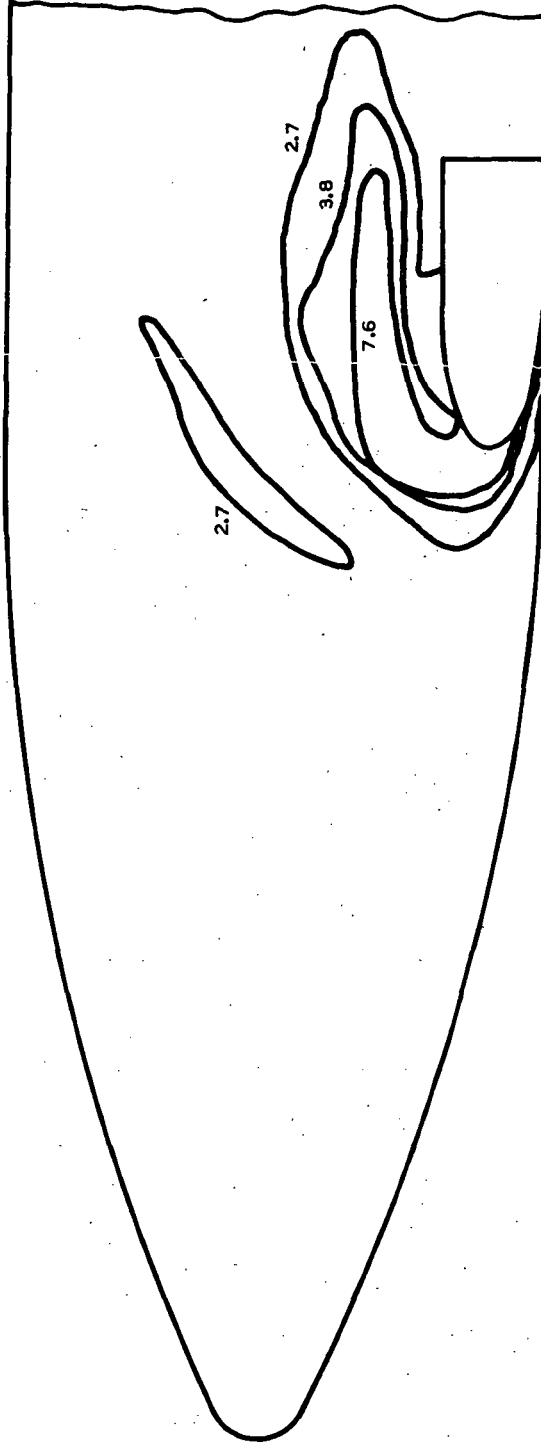


Figure 3(g). SHOCK INTERFERENCE HEATING NEAR BOOSTER (B1) CANARD/FUSELAGE JUNCTURE (HEAT TRANSFER COEFFICIENT RATIO WITH AND WITHOUT INTERFERENCE, h_i/h_u)

$\alpha = 0^\circ$
 $M_\infty = 10.28$
 $R_N = 523,000/\text{FT}$

- DATA FROM REF. 1, FIGS. A51, A272, A265, A267
- CONSTANT h FOR UNDISTURBED CASE ($h/h_{r=1} = \text{CONST.} = 0.023$)

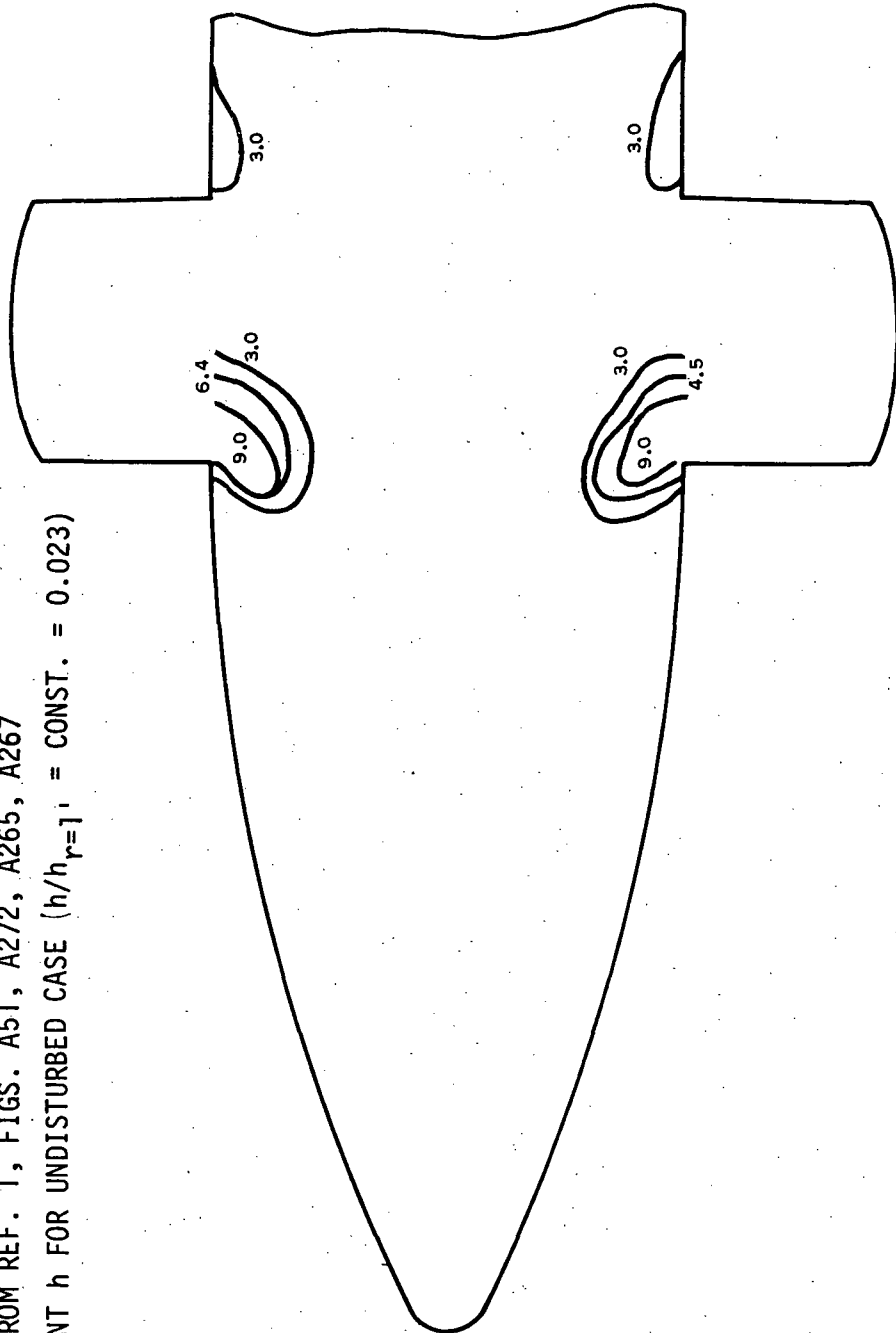


Figure 3(h). SHOCK INTERFERENCE HEATING NEAR BOOSTER (B1) CANARD/FUSELAGE JUNCTURE (HEAT TRANSFER COEFFICIENT RATIO WITH AND WITHOUT INTERFERENCE, h_i/h_u)

$\alpha = 0^\circ$
 $M_\infty = 7.71$
 $R_N = 0.569 \times 10^6/\text{FT}$

- DATA FROM REF. 1 FIG. 260
- EXTRAPOLATED VARIABLE h FOR UNDISTURBED CASE (SEE FIG. 6)

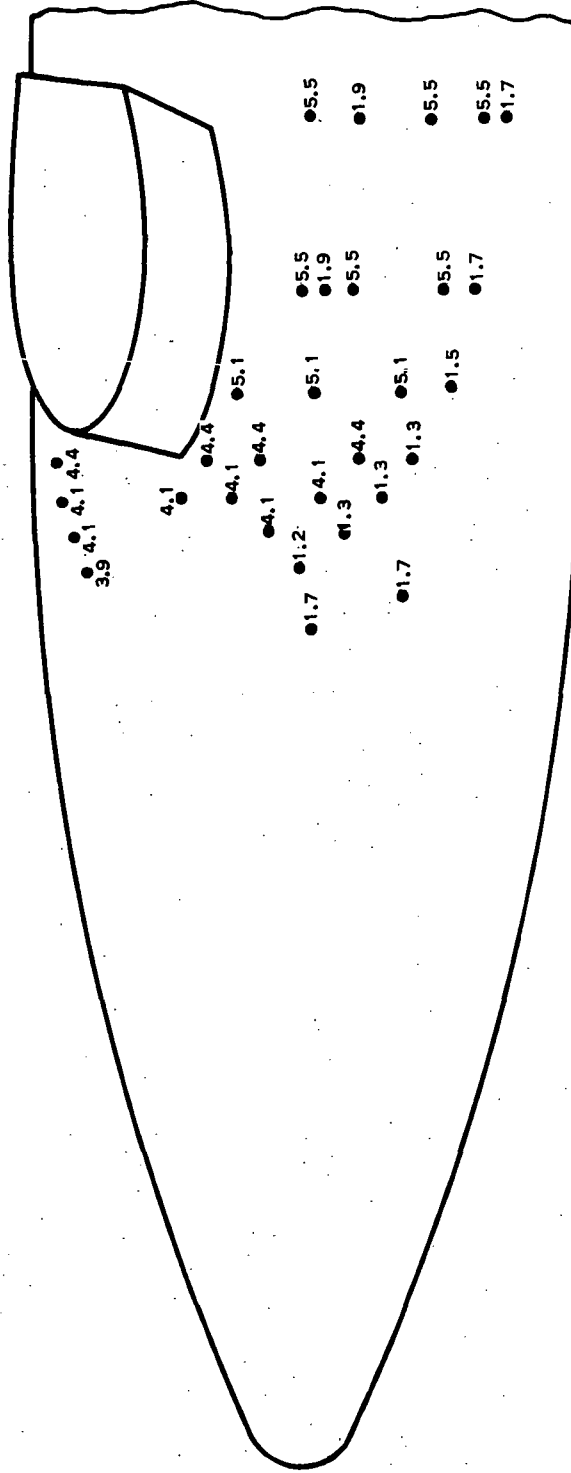


Figure 3(a'). SHOCK INTERFERENCE HEATING NEAR BOOSTER (B1) CANARD/FUSELAGE JUNCTURE (HEAT TRANSFER COEFFICIENT RATIO WITH AND WITHOUT INTERFERENCE, h_i/h_u)

$$\alpha = 0^\circ$$

$$M_\infty = 7.81$$

$$R_N = 1.014 \times 10^6/\text{FT}$$

- DATA FROM REF. 1, FIG. 269
- EXTRAPOLATED VARIABLE h FOR UNDISTURBED CASE (SEE FIG. 6)

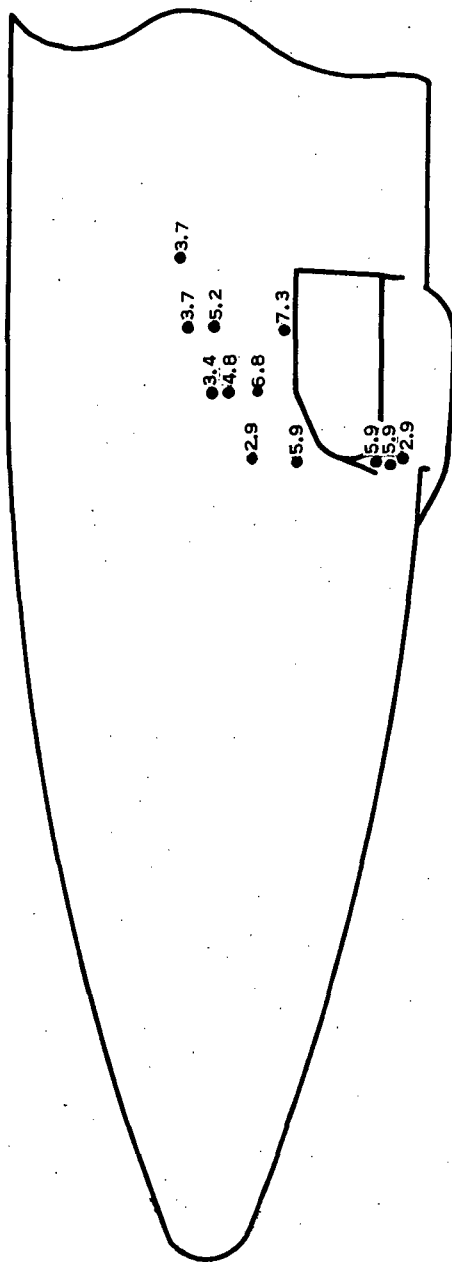


Figure 3(b'). SHOCK INTERFERENCE HEATING NEAR BOOSTER (B1) CANARD/FUSELAGE JUNCTURE (HEAT TRANSFER COEFFICIENT RATIO WITH AND WITHOUT INTERFERENCE, h_1/h_u)

$\alpha = 0^\circ$
 $M_\infty = 7.81$
 $R_N = 1.014 \times 10^6/\text{FT}$

- DATA FROM REF. 1, REF. A268
- EXTRAPOLATED VARIABLE h FOR UNDISTURBED CASE (SEE FIG. 6)

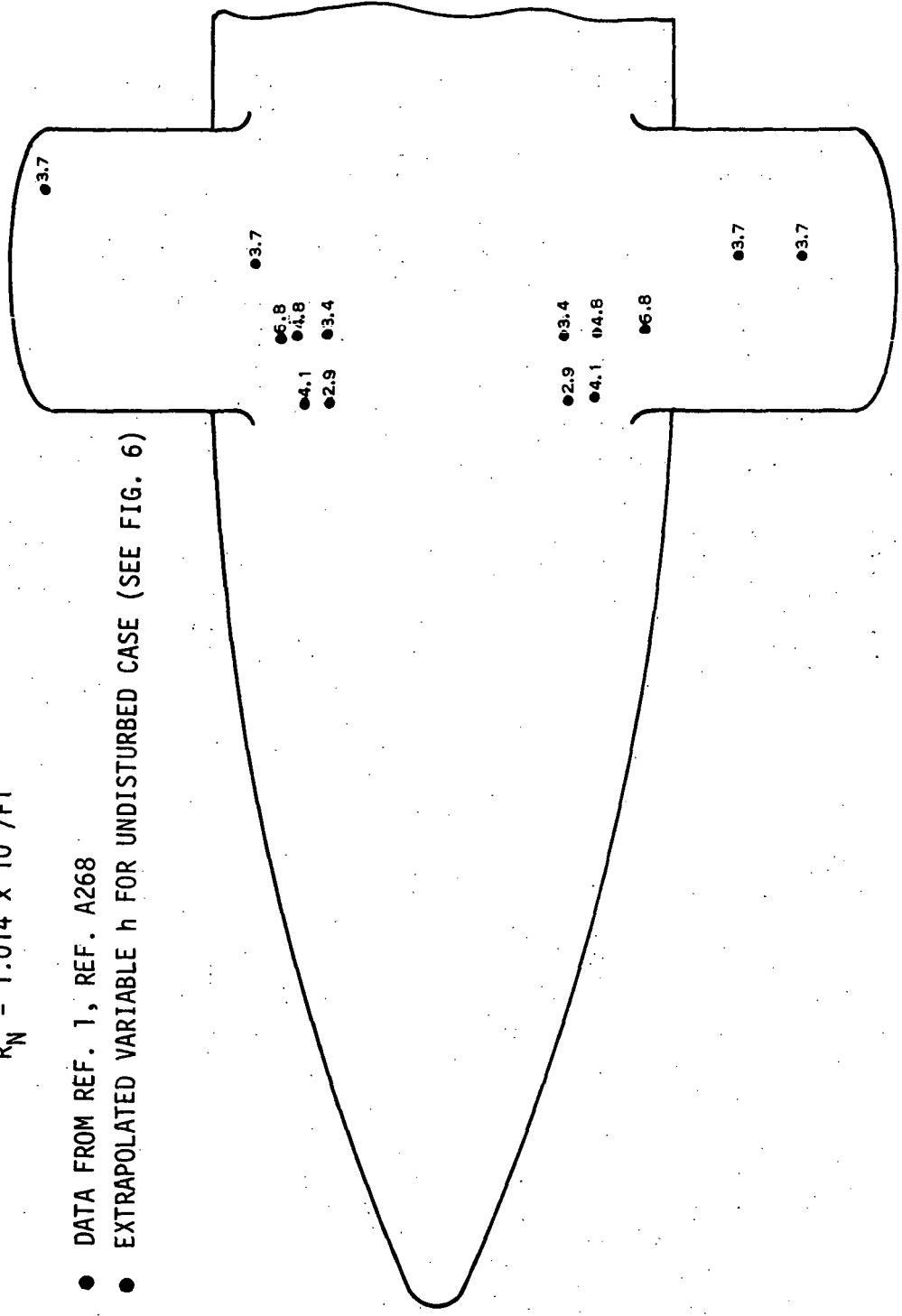


Figure 3(c'). SHOCK INTERFERENCE HEATING NEAR BOOSTER (B1) CANARD/FUSELAGE JUNCTURE (HEAT TRANSFER COEFFICIENT RATIO WITH AND WITHOUT INTERFERENCE) h_s/h_u

$\alpha = 0^\circ$
 $M_\infty = 7.95$
 $R_N = 5.437 \times 10^6 / \text{FT}$

- DATA FROM REF. 1, FIG. 264
- EXTRAPOLATED VARIABLE h FOR UNDISTURBED CASE (SEE FIG. 6)

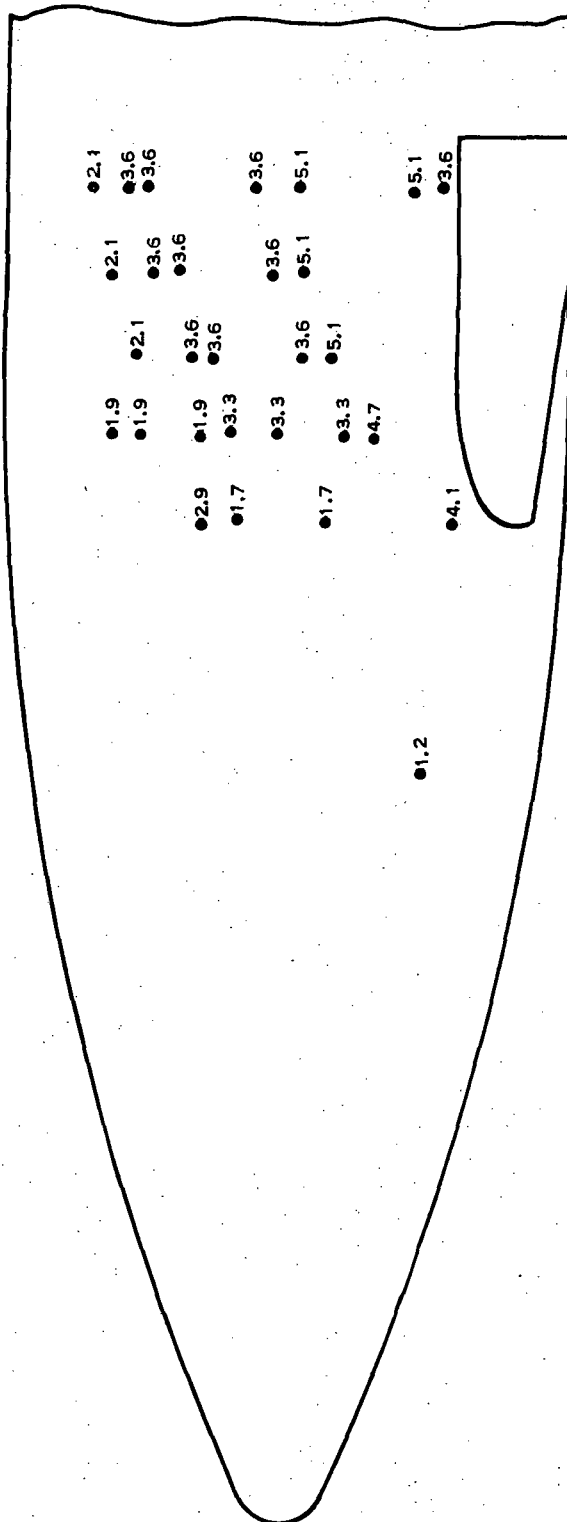


Figure 3(d'): SHOCK INTERFERENCE HEATING NEAR BOOSTER (B1) CANARD/FUSELAGE JUNCTURE (HEAT TRANSFER COEFFICIENT RATIO WITH AND WITHOUT INTERFERENCE, h_i/h_u)

$\alpha = 0^\circ$
 $M_\infty = 7.95$
 $R_N = 5.738 \times 10^6 / \text{FT}$

- DATA FROM REF. 1, FIG. 272
- EXTRAPOLATED VARIABLE h FOR UNDISTURBED CASE (SEE FIG. 6)

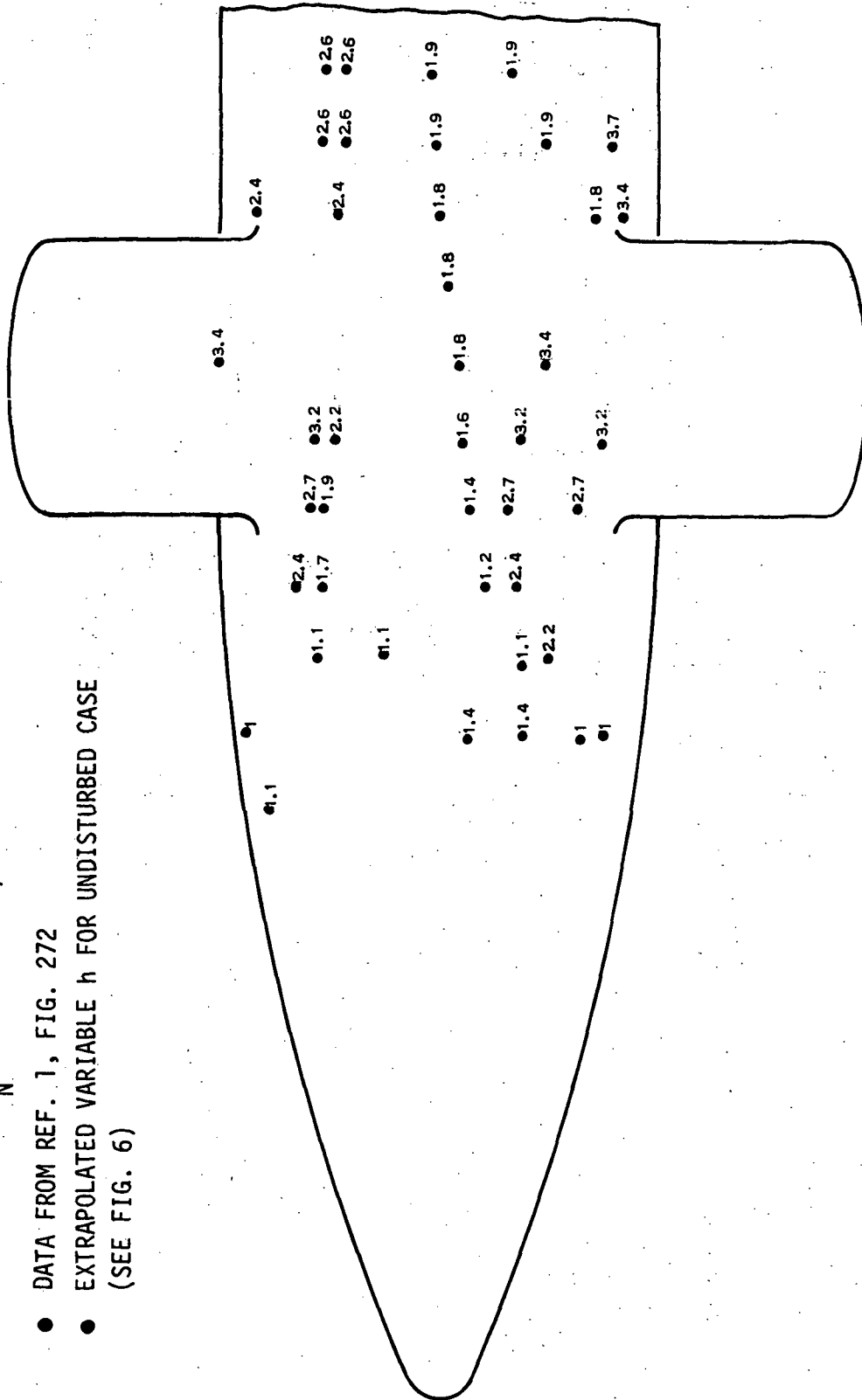


Figure 3(e'). SHOCK INTERFERENCE HEATING NEAR BOOSTER (B1) CANARD/FUSELAGE JUNCTURE (HEAT TRANSFER COEFFICIENT RATIO WITH AND WITHOUT INTERFERENCE, h_i/h_u)

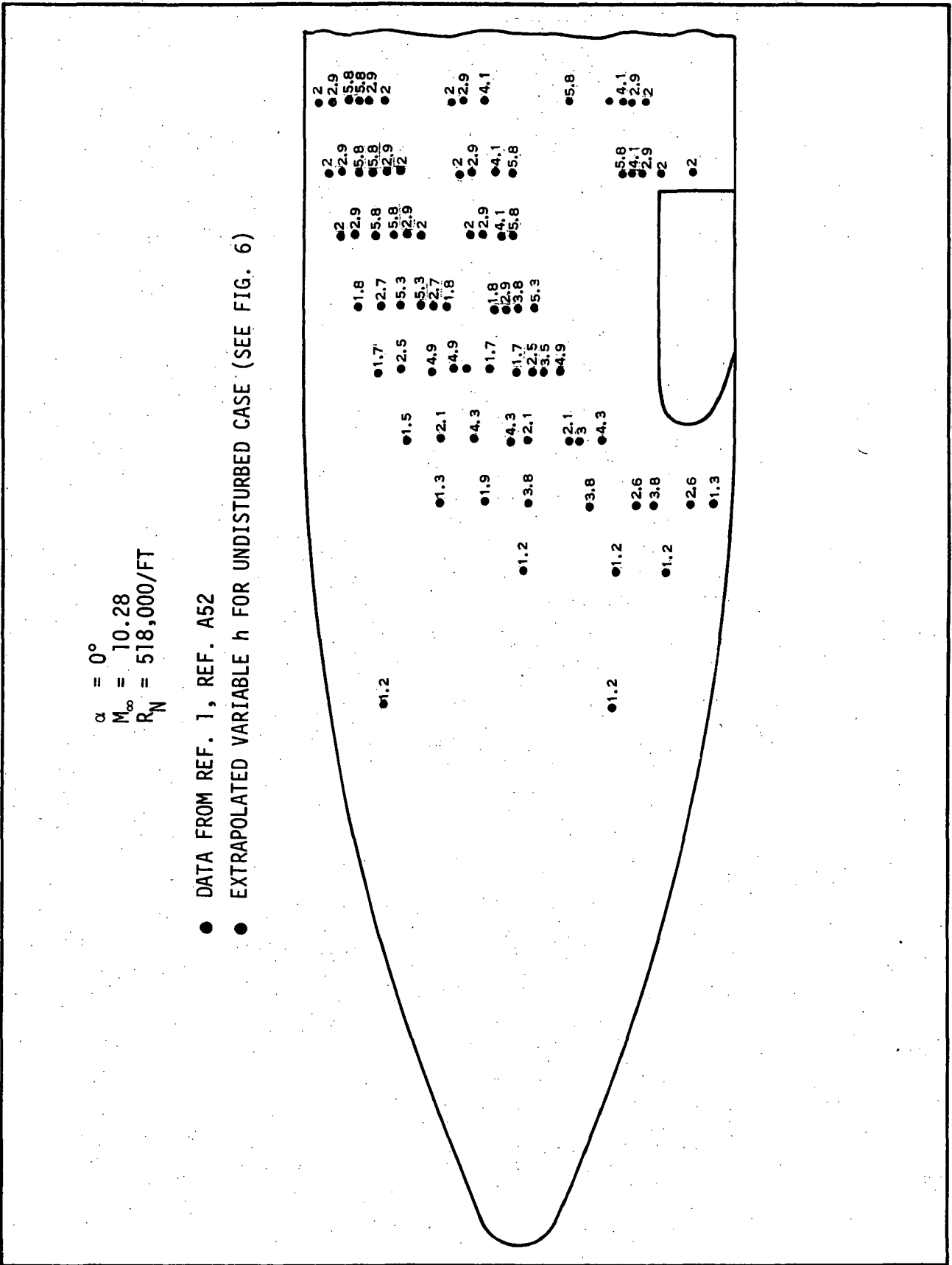


Figure 3(f'). SHOCK INTERFERENCE HEATING NEAR BOOSTER (B1) CANARD/FUSELAGE JUNCTURE (HEAT TRANSFER COEFFICIENT RATIO WITH AND WITHOUT INTERFERENCE, h_i/h_u)

$\alpha = 0^\circ$
 $M_\infty = 10.28$
 $R_N = 508,000/\text{FT}$

- DATA FROM REF. 1, FIG. 53
- EXTRAPOLATED VARIABLE h FOR UNDISTRIBUED CASE (SEE FIG. 6)

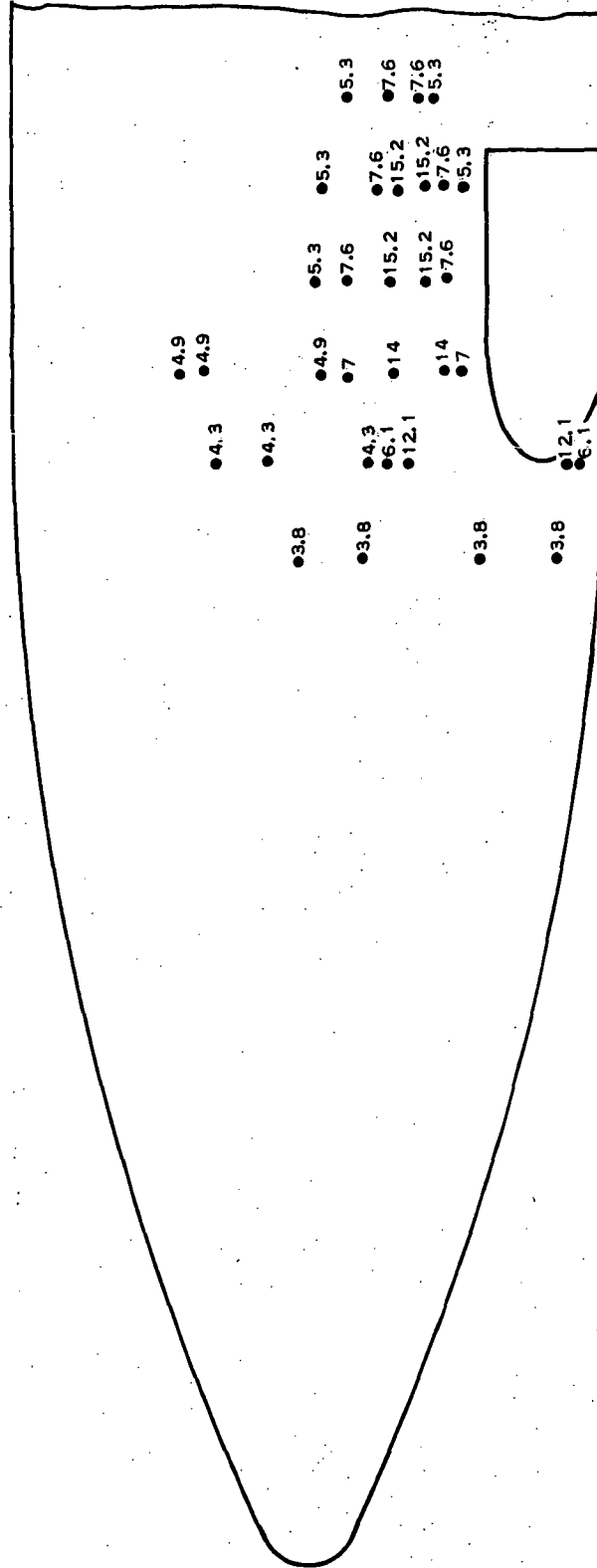


Figure 3(g'). SHOCK INTERFERENCE HEATING NEAR BOOSTER (B1) CANARD/FUSELAGE JUNCTURE (HEAT TRANSFER COEFFICIENT RATIO WITH AND WITHOUT INTERFERENCE, h_1/h_u)

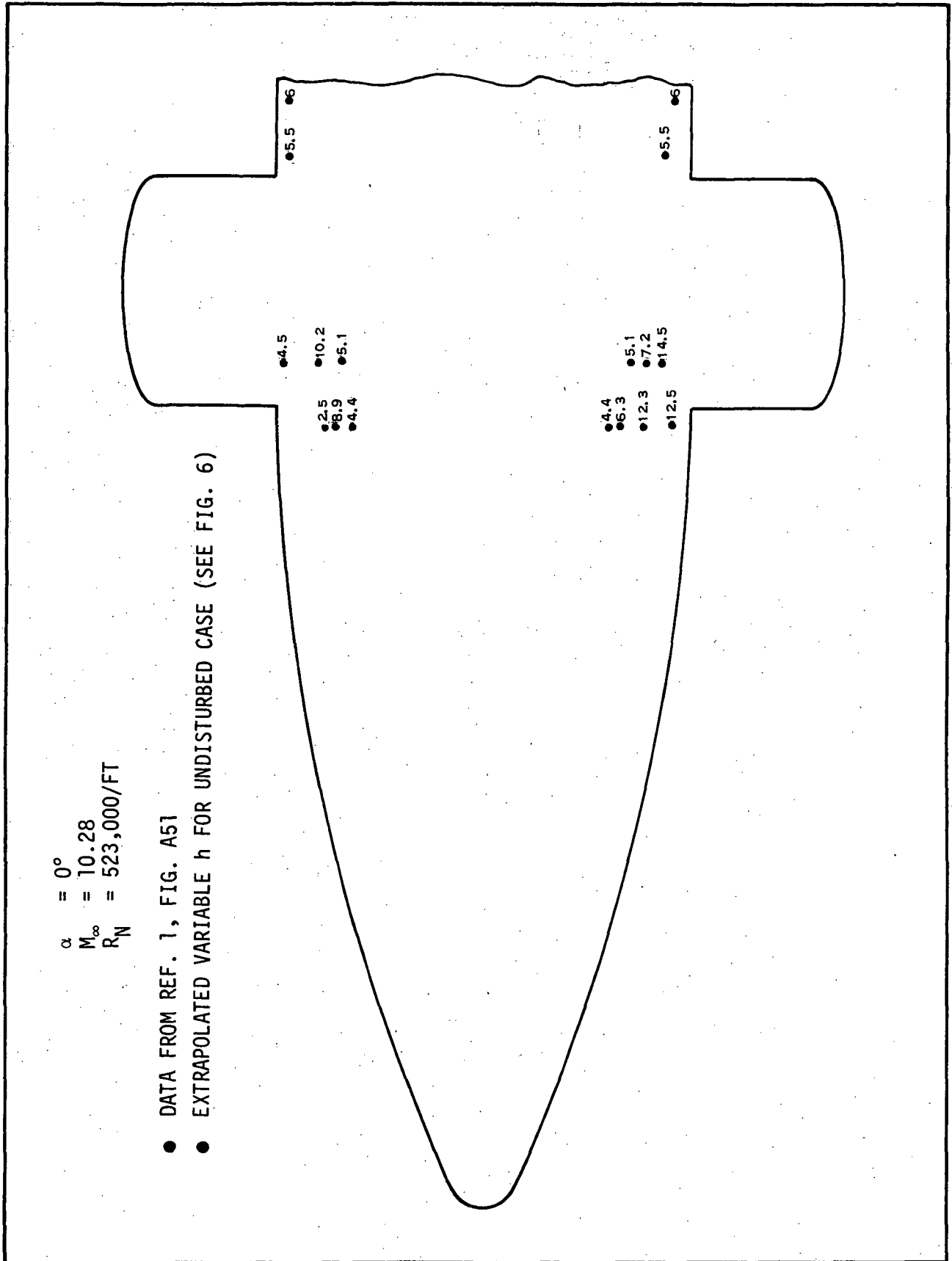


Figure 3(h'). SHOCK INTERFERENCE HEATING NEAR BOOSTER (B1) CANARD/FUSELAGE JUNCTURE (HEAT TRANSFER COEFFICIENT RATIO WITH AND WITHOUT INTERFERENCE, h_j/h_U)

$\alpha = 30^\circ$

$M_\infty = 7.81$

$R_N = 0.985 \times 10^6 / \text{FT}$

● DATA FROM REF. 1, FIGURES A201, A199

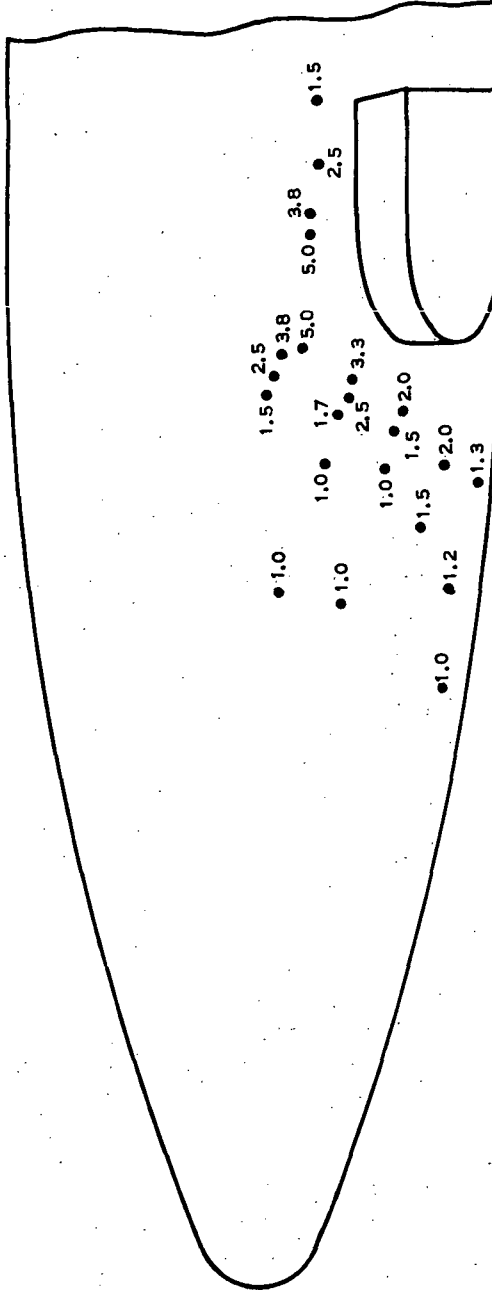


Figure 4(a). SHOCK INTERFERENCE HEATING NEAR BOOSTER (B1) CANARD/FUSELAGE JUNCTURE
(HEAT TRANSFER COEFFICIENT RATIO WITH AND WITHOUT INTERFERENCE) h_2/h_u

$$\alpha = 30^\circ$$

$$M_\infty = 7.81$$

$$R_N = 0.987 \times 10^6/\text{FT}$$

● DATA FROM REF. 1, FIGURES A200, A198

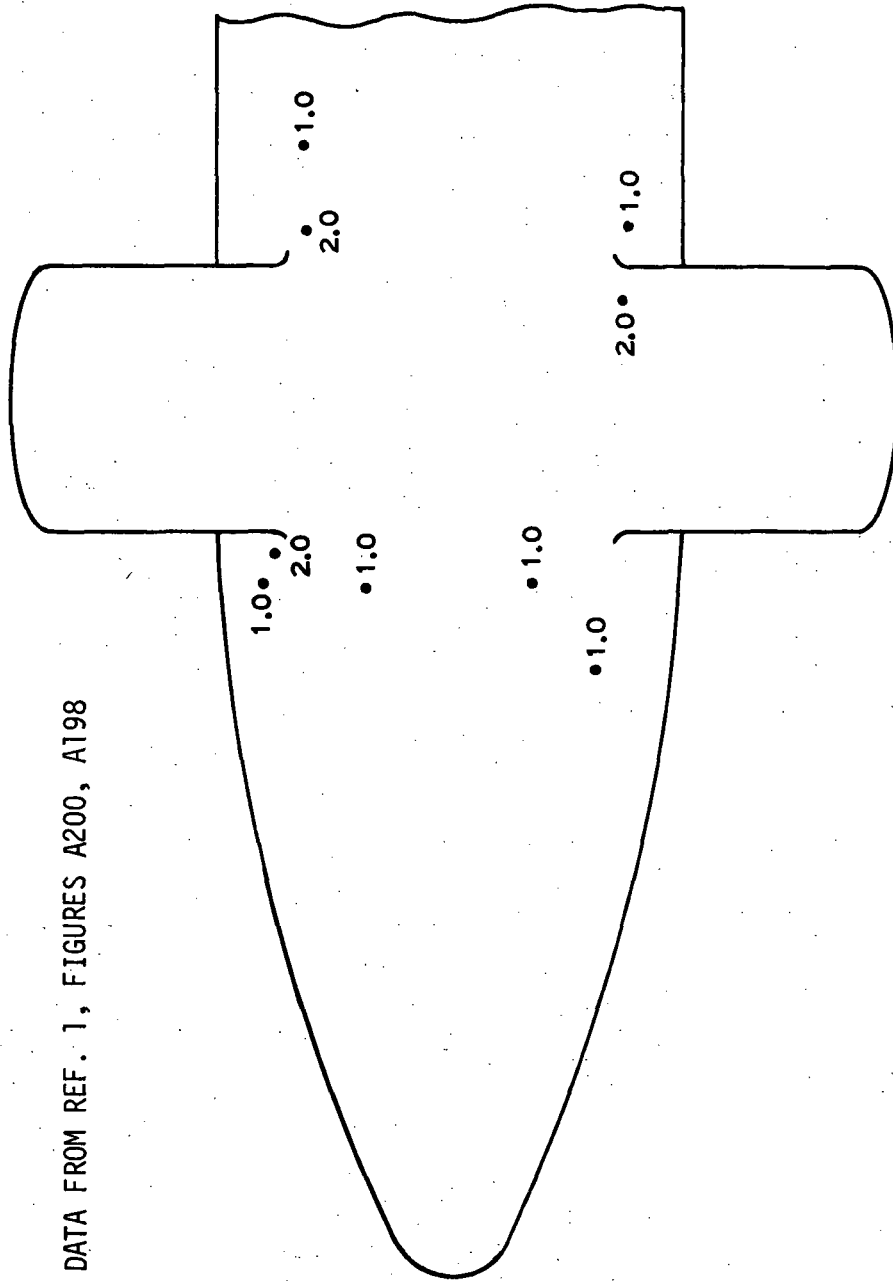


Figure 4(b). SHOCK INTERFERENCE HEATING NEAR BOOSTER (B1) CANARD/FUSELAGE JUNCTURE
(HEAT TRANSFER COEFFICIENT RATIO WITH AND WITHOUT INTERFERENCE, h_i/h_u)

$$\alpha = 30^\circ$$

$$M_\infty = 7.81$$

$$R_N = 1.062 \times 10^6/\text{FT}$$

• DATA FROM REF. 1, FIGURES A197, A199

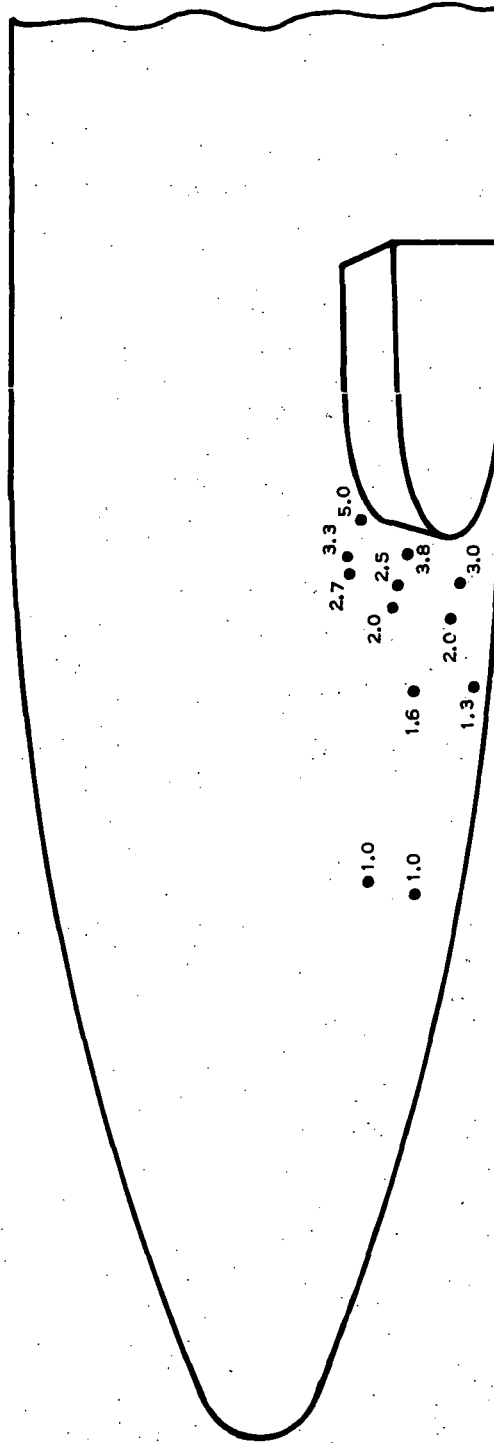


Figure 4(c). SHOCK INTERFERENCE HEATING NEAR BOOSTER (B1) CANARD/FUSELAGE JUNCTURE
(HEAT TRANSFER COEFFICIENT RATIO WITH AND WITHOUT INTERFERENCE, h_i/h_u)

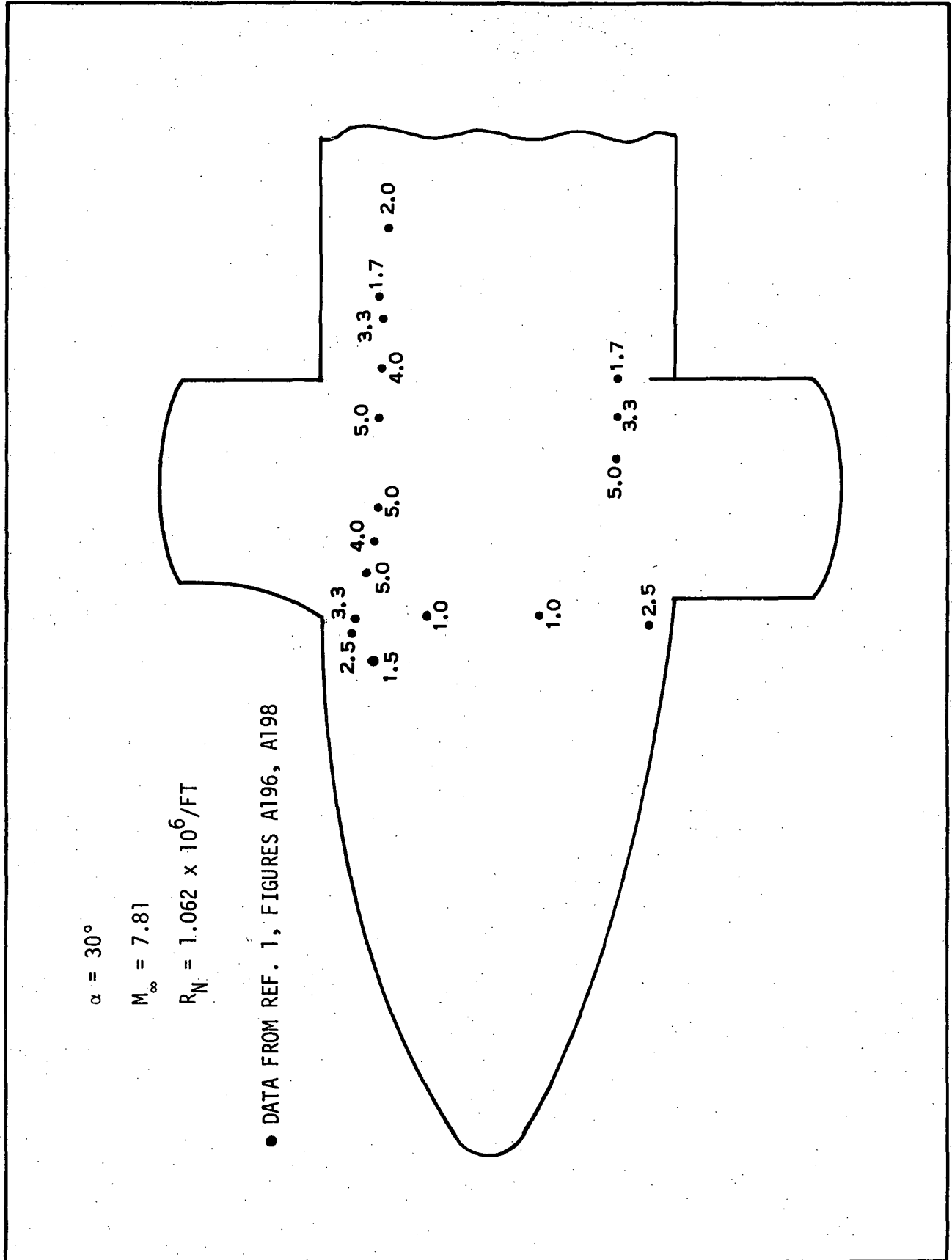


Figure 4(d). SHOCK INTERFERENCE HEATING NEAR BOOSTER (B1) CANARD/FUSELAGE JUNCTURE (HEAT TRANSFER COEFFICIENT RATIO WITH AND WITHOUT INTERFERENCE, h_i/h_u)

$$\alpha = 30^\circ$$

$$M_\infty = 7.95$$

$$R_N = 4.845 \times 10^6 / \text{FT}$$

● DATA FROM REF. 1, FIGURES A350, A352

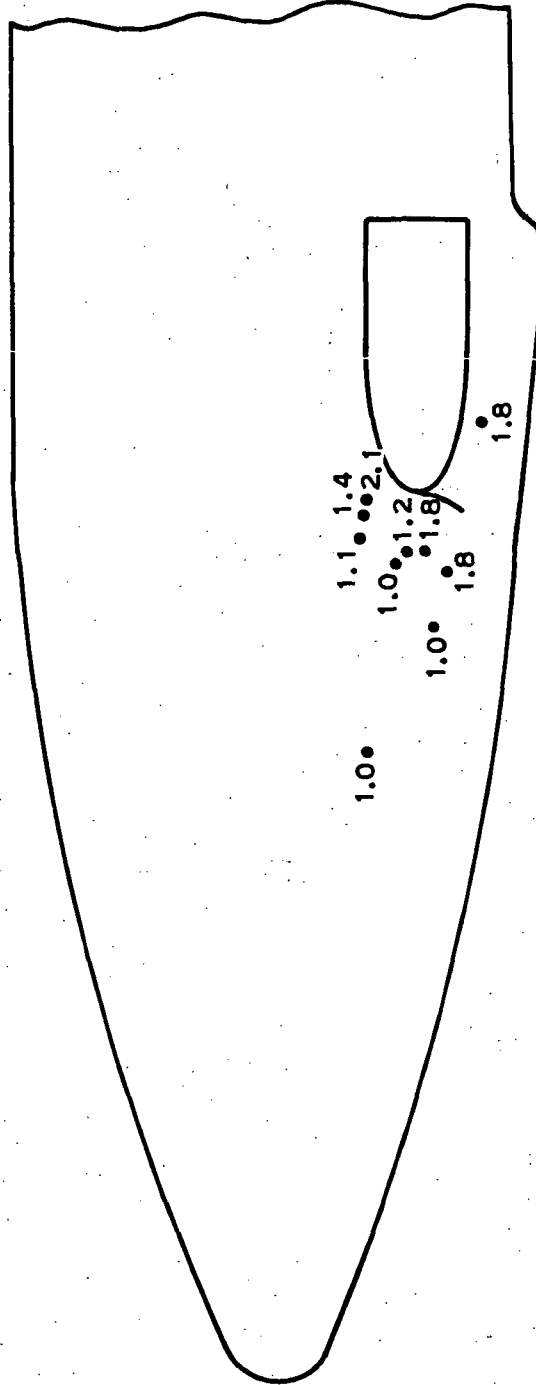


Figure 4(e). SHOCK INTERFERENCE HEATING NEAR BOOSTER (B1) CANARD/FUSELAGE JUNCTURE
(HEAT TRANSFER COEFFICIENT RATIO WITH AND WITHOUT INTERFERENCE, h_i/h_u)

$$\alpha = 60^\circ$$

$$M_\infty = 7.71$$

$$R_N = 0.584 \times 10^6/\text{FT}$$

● DATA FROM REF. 1, FIGURES A164, A173

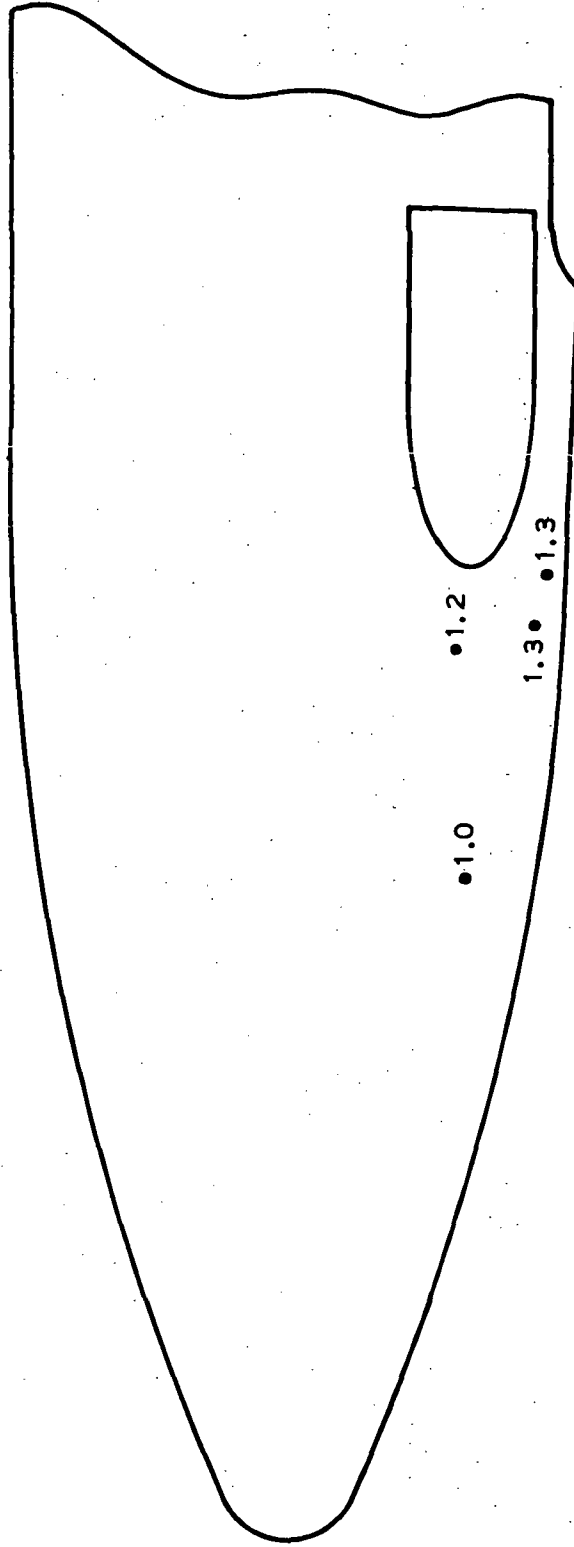


Figure 5(a). SHOCK INTERFERENCE HEATING NEAR BOOSTER (B1) CANARD/FUSELAGE JUNCTURE
(HEAT TRANSFER COEFFICIENT RATIO WITH AND WITHOUT INTERFERENCE, h_i/h_u)

$$\alpha = 60^\circ$$

$$M_\infty = 7.95$$

$$R_N = 5.707 \times 10^6/\text{FT}$$

• DATA FROM REF. 1, FIGURES A170, A171

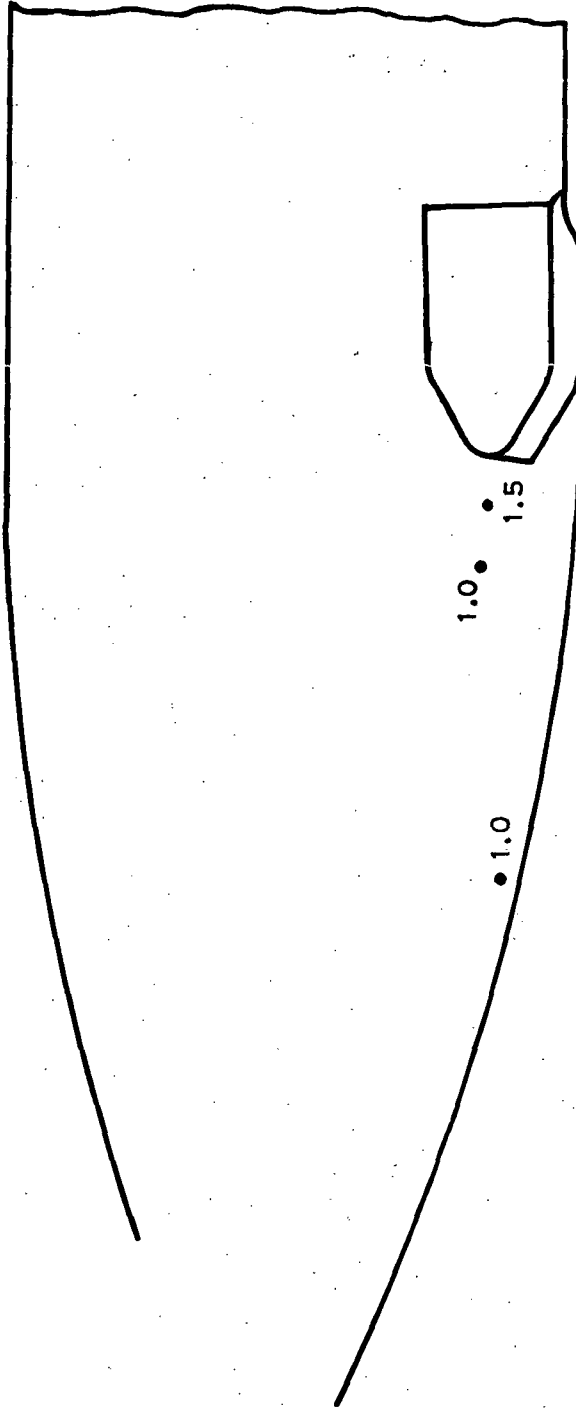


Figure 5(c). SHOCK INTERFERENCE HEATING NEAR BOOSTER (B1) CANARD/FUSELAGE JUNCTURE
(HEAT TRANSFER COEFFICIENT RATIO WITH AND WITHOUT INTERFERENCE, h_i/h_u)

$$\alpha = 60^\circ$$

$$M_\infty = 7.95$$

$$R_N = 5.707 \times 10^6 / \text{FT}$$

• DATA FROM REF. 1, FIGURES A169, A343

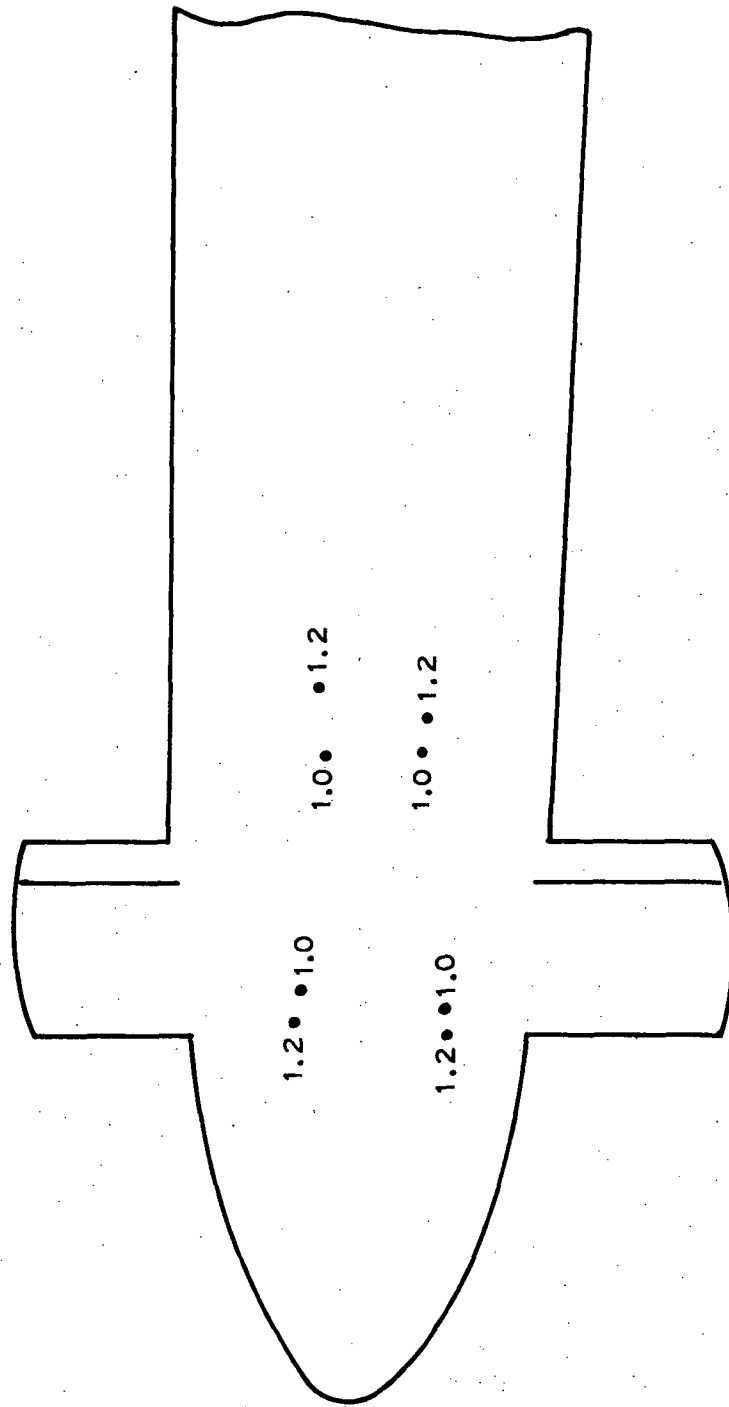


Figure 5(d). SHOCK INTERFERENCE HEATING NEAR BOOSTER (B1) CANARD/FUSELAGE JUNCTURE (HEAT TRANSFER COEFFICIENT RATIO WITH AND WITHOUT INTERFERENCE, h_i/h_u)

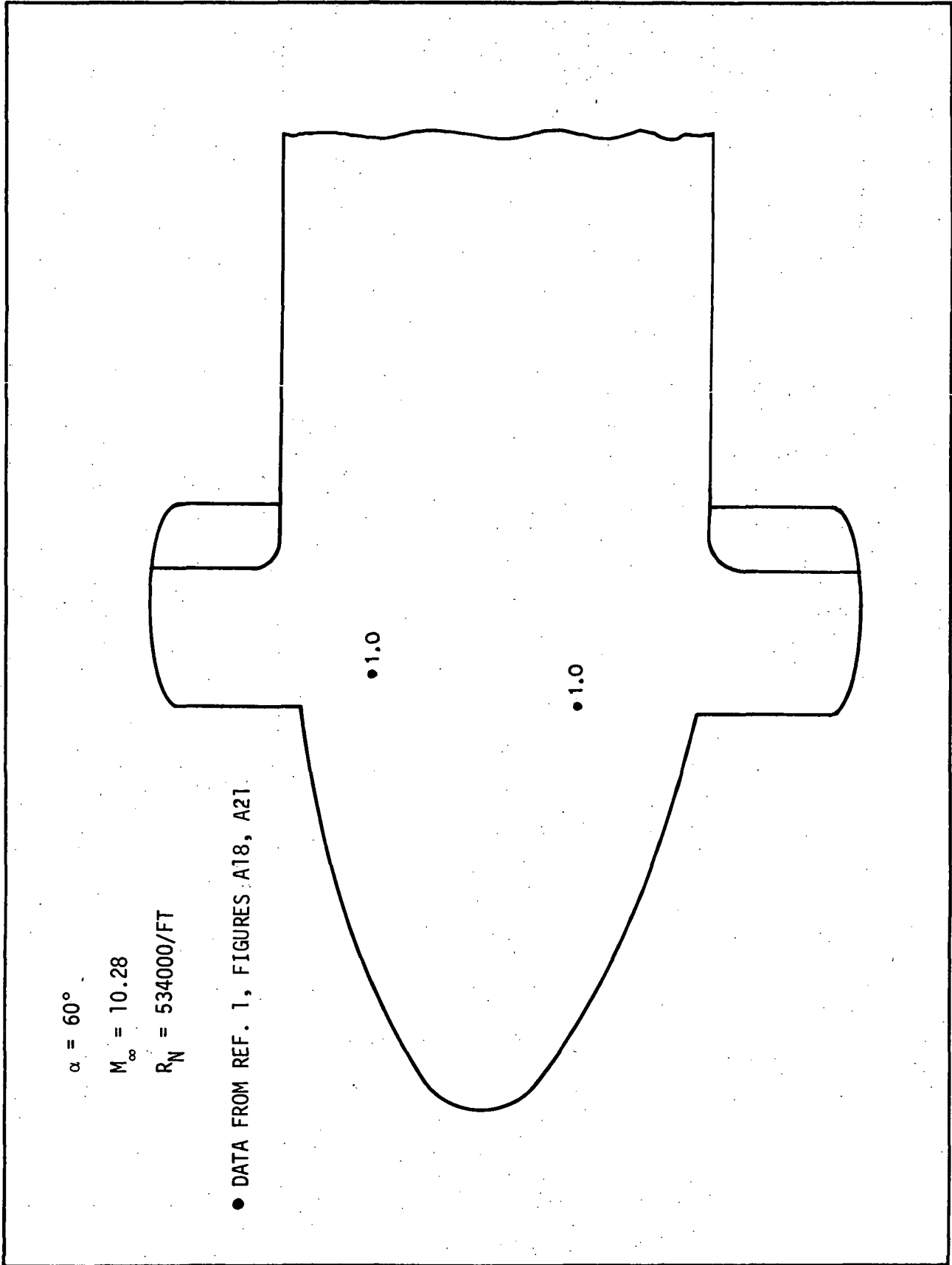


Figure 5(e). SHOCK INTERFERENCE HEATING NEAR BOOSTER (B1) CANARD/FUSELAGE JUNCTURE (HEAT TRANSFER COEFFICIENT RATIO WITH AND WITHOUT INTERFERENCE, h_i/h_u)

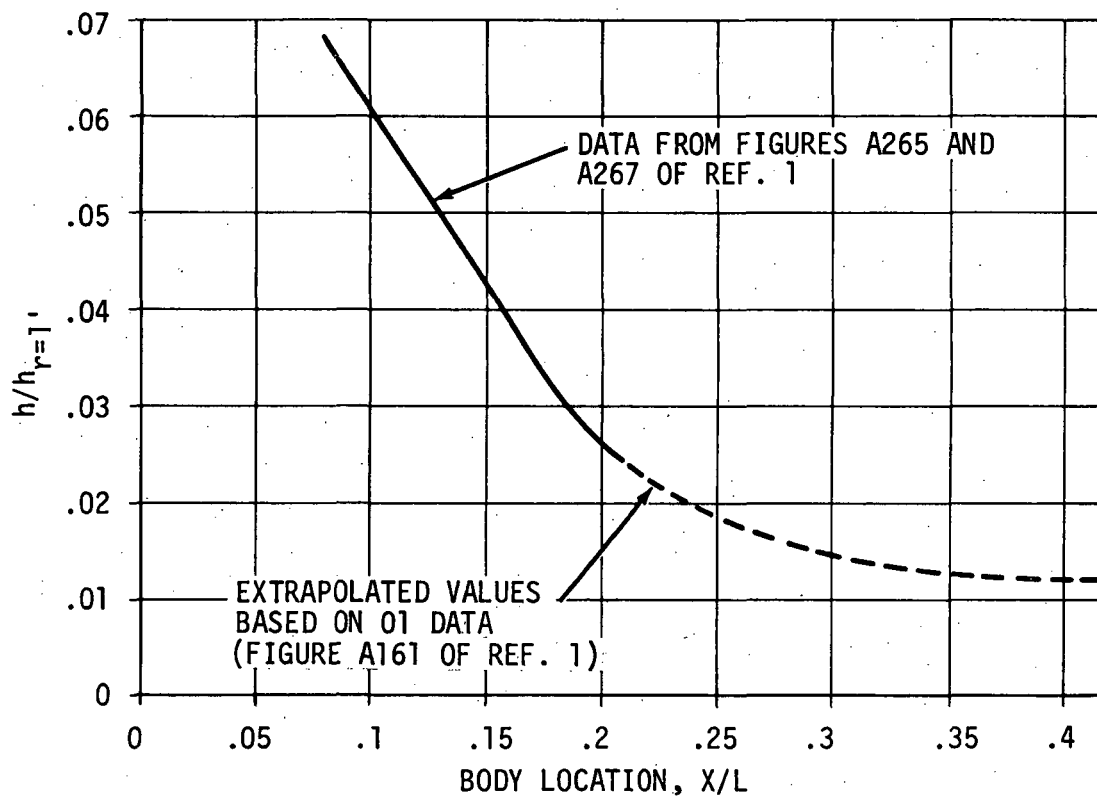


Figure 6. B1 FUSELAGE CENTERLINE HEATING DATA WITHOUT O1 AND CANARD INTERFERENCE

Distribution:

NASA/MSFC

J. A. Forney (3)
J. D. Warmbrod

NORTHROP:

D. O. Barnett
J. A. Roux
J. Y. Parker
7946, File

ADDENDUM

By using the same methods as discussed in the original Memorandum (M-794-887), the interference heating near Bl canard/fuselage juncture at 15 and 45 degrees angle-of-attack was analyzed in order to complete the study. Results are given in Figures 7 and 8.

Efforts have also been made to correlate the peak interference heating on fuselage ($\max. h_i/h_u$) with Mach number, Reynolds number, and angle-of-attack. Results are shown in Table 2 which indicate that peak interference heating increases with increasing Mach number. Reynolds number and angle-of-attack do not show any definite effects on interference heating.

Table 2. PEAK HEATING ON B1 FUSELAGE DUE TO CANARD INTERFERENCE

α (Degrees)	R_N/FT	MAX h_i/h_u ($M_\infty \approx 8$)		MAX h_i/h_u ($M_\infty \approx 10$)		REMARKS
0	0.5×10^6	2.9*	---**	7.6*	9.0**	Constant h_u
	1×10^6	3.7	5.9	---		
	5×10^6	2.4	2.0	---		
0	0.5×10^6	5.5	---	15.2	14.5	Variable h_u
	1×10^6	7.3	6.8	---		
	5×10^6	5.1	3.7	---		
15	0.5×10^6	---	---	---		
	1×10^6	---	---	---		
	5×10^6	3.0	2.0	---		
30	0.5×10^6	---	---	---		
	1×10^6	5.0	2.0	---		
	1×10^6	5.0	5.0	---		
	5×10^6	2.1	2.0	---		
45	0.5×10^6	---	---	---		
	1×10^6	5.2	5.2	---		
	1×10^6	6.6	7.6	---		
	1×10^6	2.4	1.4	---		
	5×10^6	2.6	2.6	---		
60	0.5×10^6	1.3	---	---	1.0	
	1×10^6	1.3	---	---		
	5×10^6	1.5	1.2	---		

* Max. h_i/h_u in B1 Side view

** Max. h_i/h_u in B1 Bottom view

$\alpha = 15^\circ$

$M_\infty = 7.95$

$R_N = 5.495 \times 10^6 / \text{FT}$

● DATA FROM REF. 1, FIGURES A354, A356

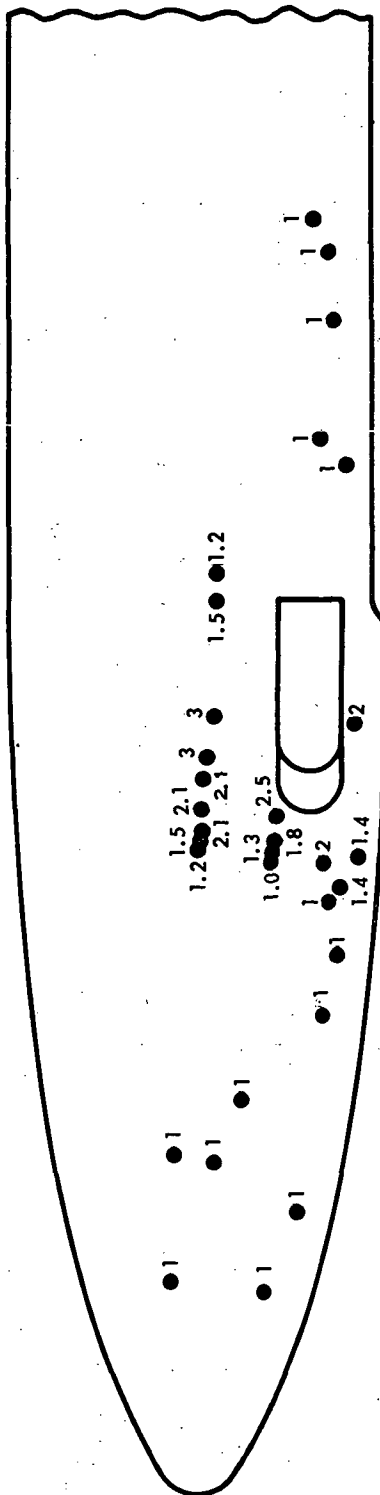


Figure 7(a). SHOCK INTERFERENCE HEATING NEAR BOOSTER (B1) CANARD/FUSELAGE JUNCTURE
(HEAT TRANSFER COEFFICIENT RATIO WITH AND WITHOUT INTERFERENCE, h_i/h_u)

$$\alpha = 15^\circ$$

$$M_\infty = 7.95$$

$$R_N = 5.495 \times 10^6 / \text{FT}$$

● DATA FROM REF. 1, FIGURES A353, A355

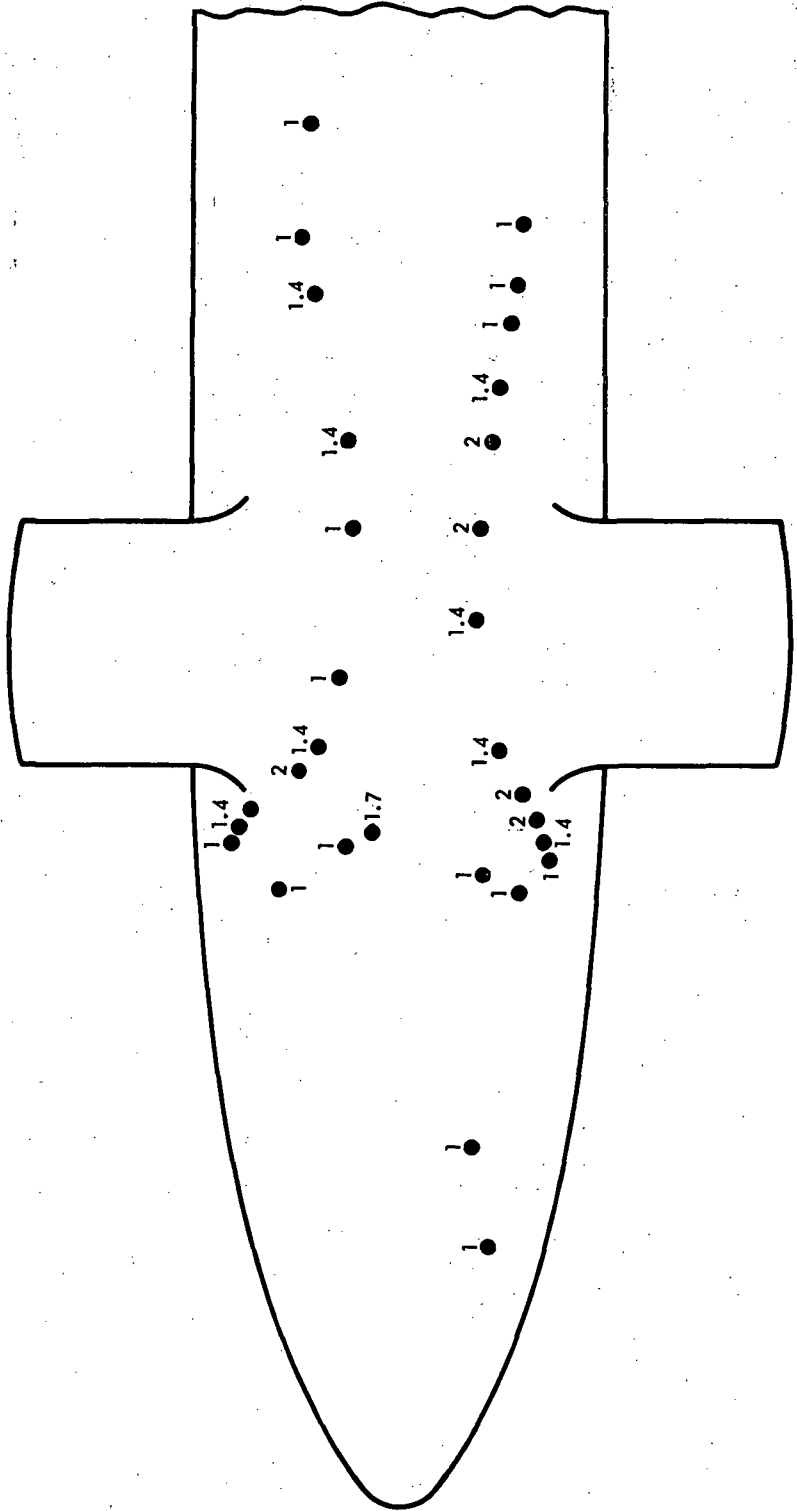


Figure 7(b). SHOCK INTERFERENCE HEATING NEAR BOOSTER (B1) CANARD/FUSELAGE JUNCTURE
(HEAT TRANSFER COEFFICIENT RATIO WITH AND WITHOUT INTERFERENCE, h_i/h_u)

$$\alpha = 45^\circ$$

$$M_\infty = 7.81$$

$$R_N = 0.997 \times 10^6 / \text{FT}$$

● DATA FROM REF: 1, FIGURES A185, A179

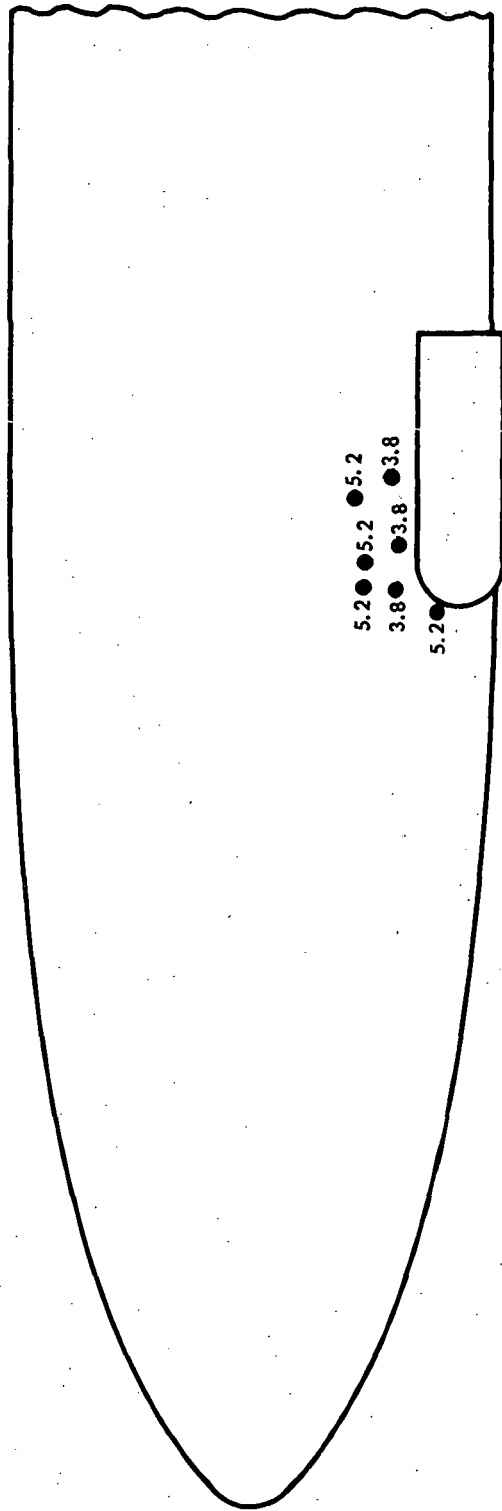


Figure 8(a). SHOCK INTERFERENCE HEATING NEAR BOOSTER (B1) CANARD/FUSELAGE JUNCTURE
(HEAT TRANSFER COEFFICIENT RATIO WITH AND WITHOUT INTERFERENCE, h_i/h_u)

$$\alpha = 45^\circ$$

$$M_\infty = 7.81$$

$$R_N = 0.997 \times 10^6 / \text{FT}$$

● DATA FROM REF. 1, FIGURES A184, A178

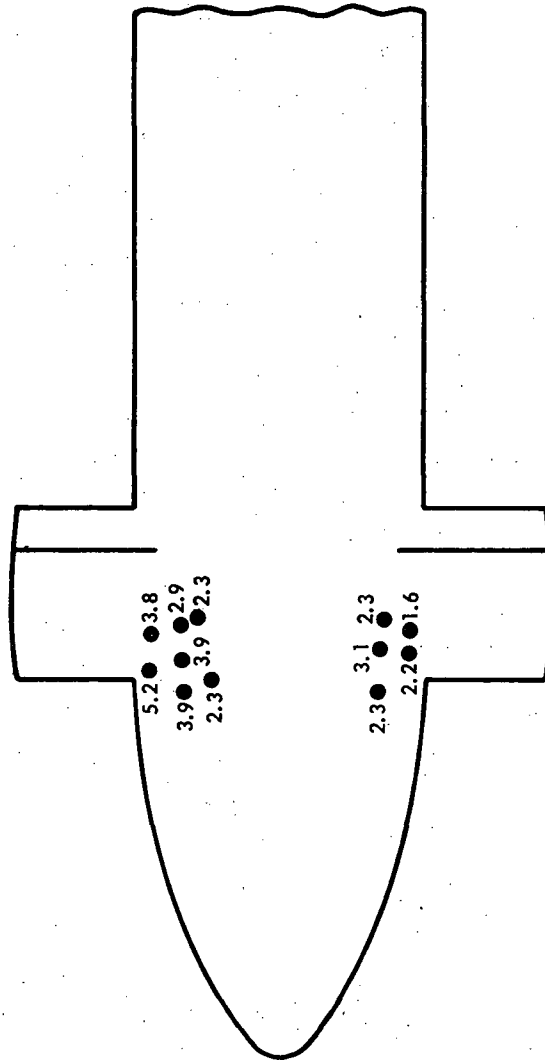


Figure 8(b). SHOCK INTERFERENCE HEATING NEAR BOOSTER (B1) CANARD/FUSELAGE JUNCTURE (HEAT TRANSFER COEFFICIENT RATIO WITH AND WITHOUT INTERFERENCE, h_i/h_u)

$$\alpha = 45^\circ$$

$$M_\infty = 7.81$$

$$R_N = 1.020 \times 10^6 / \text{FT}$$

● DATA FROM REF. 1, FIGURES A189, A179

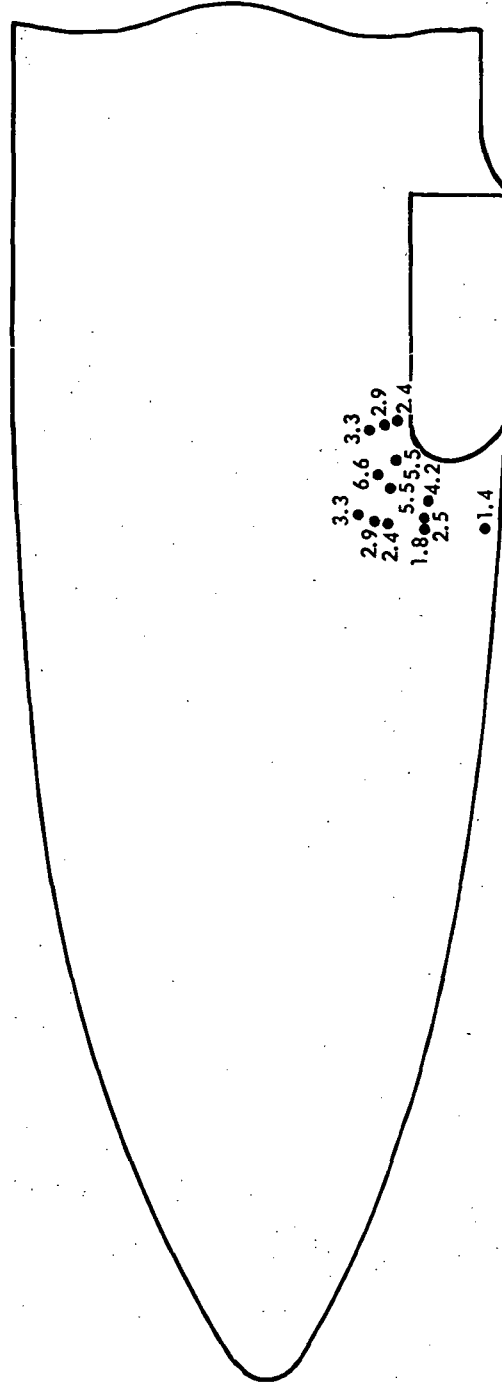


Figure 8(c). SHOCK INTERFERENCE HEATING NEAR BOOSTER (B1) CANARD/FUSELAGE JUNCTURE
(HEAT TRANSFER COEFFICIENT RATIO WITH AND WITHOUT INTERFERENCE, h_i/h_u)

$$\alpha = 45^\circ$$

$$M_\infty = 781$$

$$R_N = 1.020 \times 10^6 / \text{FT}$$

● DATA FROM REF. 1, FIGURES A188, A178

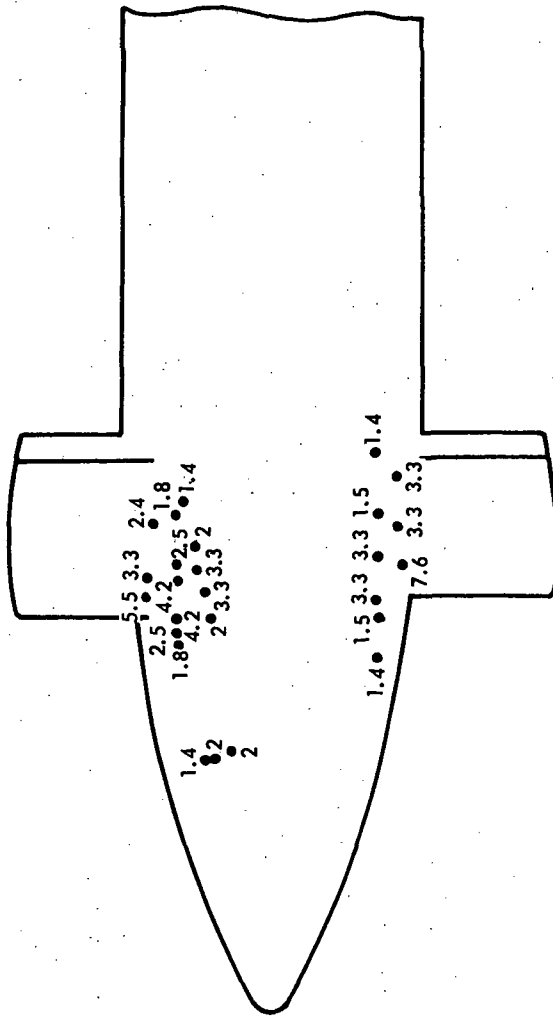


Figure 8(d): SHOCK INTERFERENCE HEATING NEAR BOOSTER (B1) CANARD/FUSELAGE JUNCTURE
(HEAT TRANSFER COEFFICIENT RATIO WITH AND WITHOUT INTERFERENCE, h_i/h_u)

$$\alpha = 45^\circ$$

$$M_\infty = 7.81$$

$$R_N = 1.026 \times 10^6 / \text{FT}$$

● DATA FROM REF. 1, FIGURES A181, A179

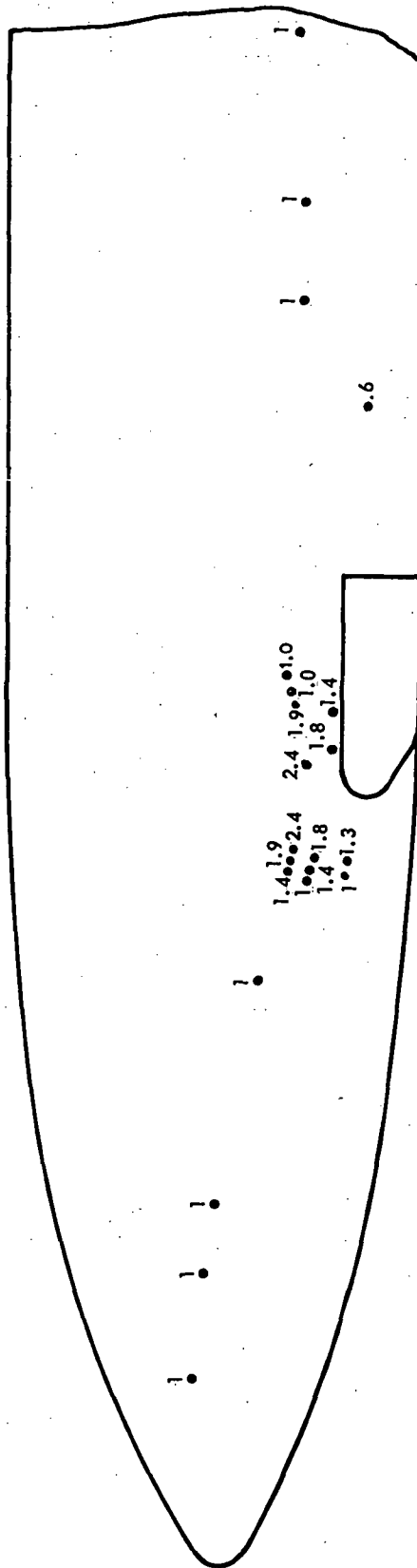


Figure 8(e). SHOCK INTERFERENCE HEATING NEAR BOOSTER (B1) CAVARD/FUSELAGE JUNCTURE
(HEAT TRANSFER COEFFICIENT RATIO WITH AND WITHOUT INTERFERENCE, h_i/h_u)

$$\alpha = 45^\circ$$

$$M_\infty = 7.81$$

$$R_N = 1.026 \times 10^6 / \text{FT}$$

● DATA FROM REF. 1, FIGURES A180, A178

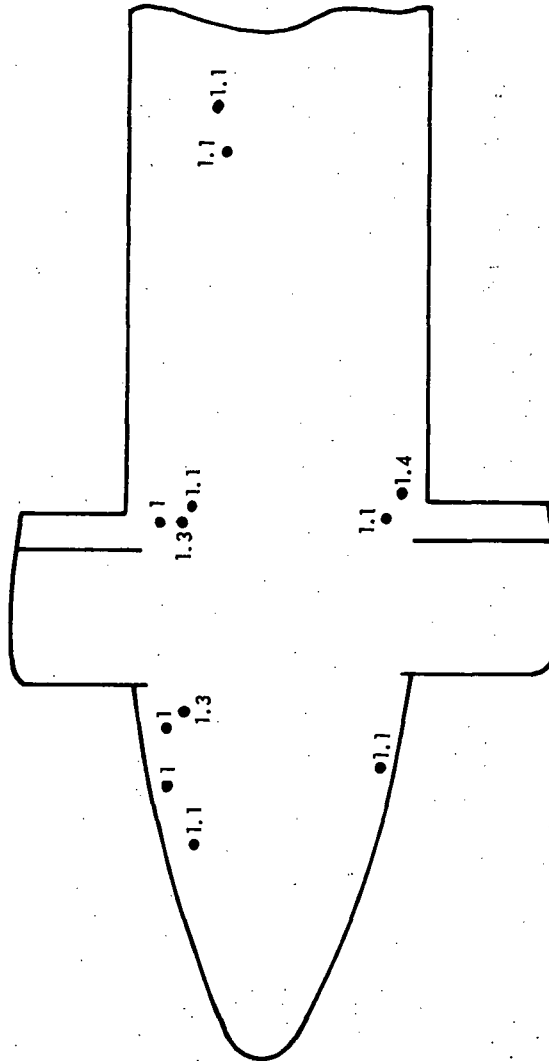


Figure 8(f). SHOCK INTERFERENCE HEATING NEAR BOOSTER (B1) CANARD/FUSELAGE JUNCTURE
(HEAT TRANSFER COEFFICIENT RATIO WITH AND WITHOUT INTERFERENCE, h_i/h_u)

$$\alpha = 45^\circ$$

$$M_\infty = 7.95$$

$$R_N = 5.323 \times 10^6 / \text{FT}$$

● DATA FROM REF. 1, FIGURES A348, A346

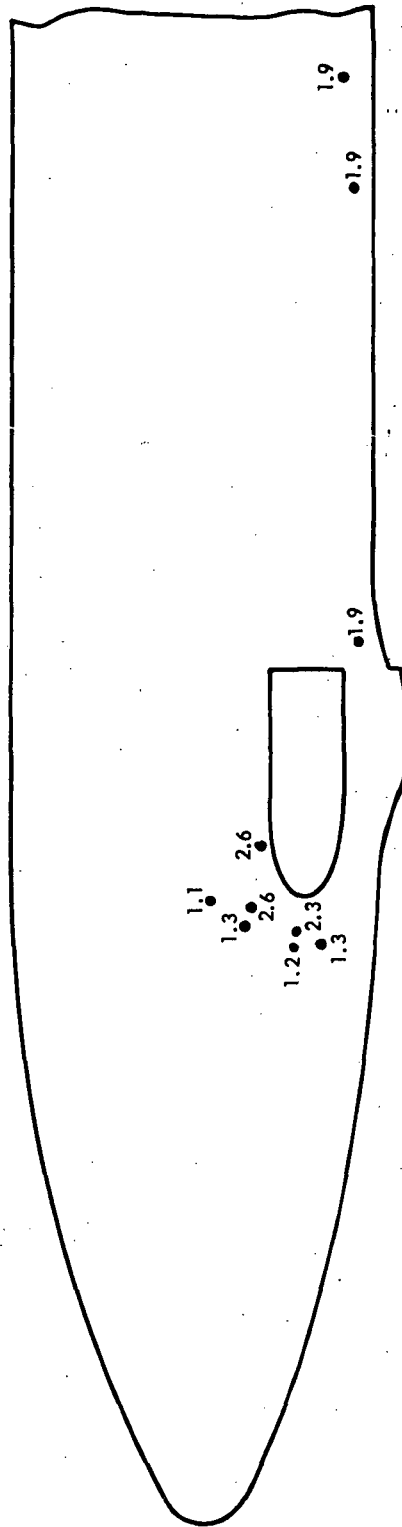


Figure 8(g). SHOCK INTERFERENCE HEATING NEAR BOOSTER (B1) CANARD/FUSELAGE JUNCTURE
(HEAT TRANSFER COEFFICIENT RATIO WITH AND WITHOUT INTERFERENCE, h_f/h_u)

$$\alpha = 45^\circ$$

$$M_\infty = 7.95$$

$$R_N = 5.323 \times 10^6/\text{FT}$$

● DATA FROM REF. 1, FIGURES A347, A345

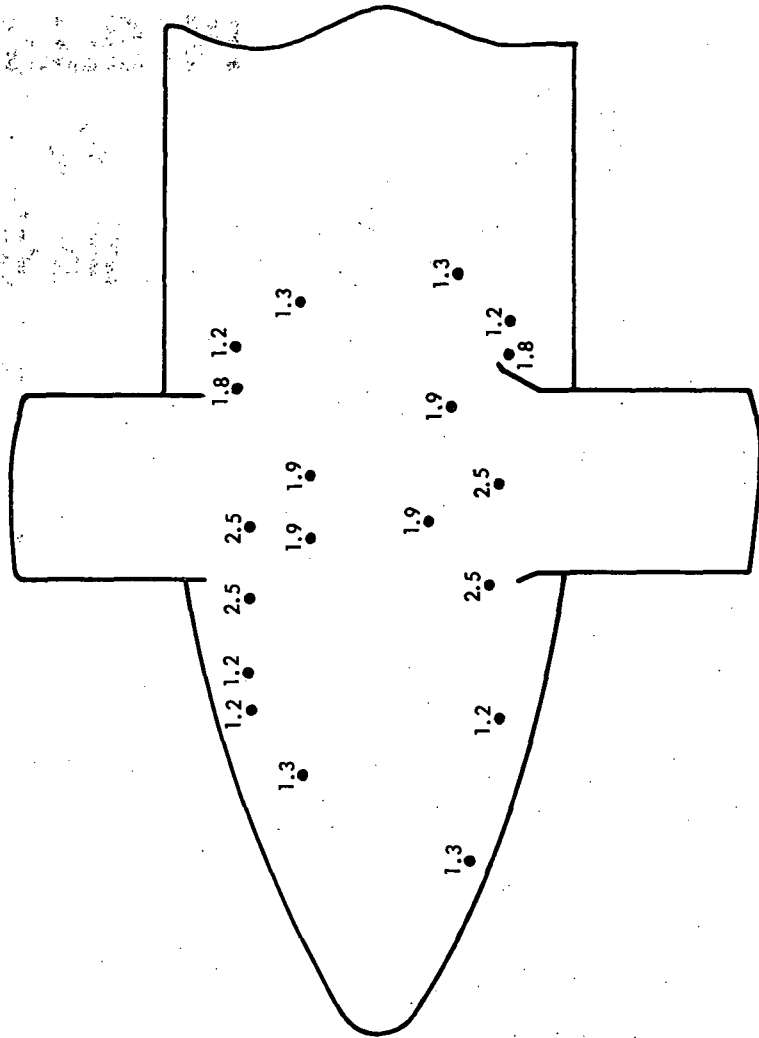


Figure 8(h). SHOCK INTERFERENCE HEATING NEAR BOOSTER (B1) CANARD/FUSELAGE JUNCTURE (HEAT TRANSFER COEFFICIENT RATIO WITH AND WITHOUT INTERFERENCE, h_1/h_u)

Appendix A-5

INTERFERENCE HEATING ON MDC/MMC BASELINE BOOSTER

**INTERFERENCE HEATING ON MDC/MMC BASELINE BOOSTER DURING
ASCENT AND REENTRY FLIGHTS – A QUALITATIVE STUDY**

April 1971

by

F. T. Hung

PREPARED FOR:

**NATIONAL AERONAUTICS AND SPACE ADMINISTRATION
GEORGE C. MARSHALL SPACE FLIGHT CENTER
AERO-ASTRODYNAMICS LABORATORY**

Under Contract NAS8-26268

REVIEWED AND APPROVED BY:

Wallace W. Youngblood

Wallace W. Youngblood, Manager
Aerothermodynamics

A. L. Grady

A. L. Grady, Manager
Aerophysics

**NORTHROP CORPORATION
HUNTSVILLE, ALABAMA**

April 1971

To: J. A. Forney, S&E-AERO-AT

From: F. T. Hung, Northrop-Huntsville

Subject: Interference Heating on MDC/MMC Baseline Booster During Ascent and Reentry Flights - A Qualitative Study

Reference: 1. Click, P. L. and Schmitt, D. A, "Wind Tunnel Test Results from the Thermal Mapping Investigation of 0.325% Scale MDC/MMC Phase B Space Shuttle Vehicles in the NASA/LRC Mach 8 Variable Density Tunnel and the NASA/LRC 31 Inch Continuous Flow Hypersonic Tunnel", Martin Marietta Design Note No. MMC-I-AERO-5002, October 1970.

MDC/MMC Phase B baseline (B1) booster interference heating during ascent and reentry flights has been analyzed qualitatively based on paint test data contained in reference 1. Typically, the test conditions were as listed below.

- Free stream Mach number, $M_\infty \approx 6$ and 8
- Free stream Reynolds number, $R_N \approx 0.5 \times 10^6$, 1×10^6 and 5×10^6 /ft
- Booster angle-of-attack, $\alpha = -5^\circ$, 0° , 15° , 30° , 45° and 60°
- Booster model scale : 0.00325

The interference heating data in reference 1 can be analyzed only in a qualitative manner since peak interference heating data are not available at the present time. This is due to the fact that paints used in the tests have fairly low phase change temperature (as low as 113°F), which is not adequate for the high interference heating measurements. Examination of movie films taken during the tests indicates that high interference heating causes the paint phase change on the very first movie frame in most of the runs.

Study of both Schlieren photographs, Figures 1 and 2, and the test data indicates that, depending on the angle-of-attack, the booster will experience

interference heating in nine regions during ascent and reentry flights as shown in Figure 3. The study results can be summarized below.

- Area(A) - Fuselage Heating Due to Canard Shock. The interference heating on the fuselage exists for any angle-of-attack as shown in Figure 4 which also indicates that the heating pattern varies significantly with α .
- Area(B) - Fuselage Heating Due to Wing Shock. This is similar to the fuselage/canard (Area(A)) case as shown in Figure 4.
- Area(C) - Wing Heating Due to Canard or Fuselage Shock. As indicated in Figure 5, no interference heating on the wing occurs for zero α . For $\alpha = 15$ degrees and 30 degrees, the interference heating area near the wing tip is caused by either the canard or fuselage nose shocks. For $\alpha = 45$ degrees and 60 degrees, the wing experiences two interference heating areas. The one near the wing root is expected to be caused by the fuselage cylinder body shock impingement. The cause of the other interference heating area near the wing tip cannot be explained due to lack of Schlieren photographs.
- Area(D) - Wing Tip Heating Due to Fin Shock. Interference heating should exist for any α even though only $\alpha = 0$ data are available as shown in Figure 6.
- Area(E) - Fin Root Heating Due to Wing Shock. This is similar to Area(D) as shown in Figure 6.
- Area(F) - Fin Heating Due to Canard Shock. The canard shock wave impinges on fin only when $\alpha = 0$ degree as shown in Figure 7. No interference heating exists for $\alpha \geq 15$ degrees.
- Area(G) - Fin Outboard Surface Heating Due to Wing Tip Flow Separation. For high angle-of-attack ($\alpha \geq 30$ degrees), the flow at the wing tip separates and reattaches on the fin outboard surface and consequently causes high interference heating on the fin as shown in Figure 8.
- Area(H) - Canard Heating Due to Fuselage Nose Shock. The fuselage nose shock wave impinges on canard for $\alpha \leq 45$ degrees as shown in Figure 9.
- Area(I) - Fuselage Heating Due to Orbiter Fuselage. For mated configuration, high interference heating on both booster and orbiter fuselages is shown in Figure 10.

The overall interference heating on the booster is shown in Figure 11. The interference heating Area(J) in Figure 11 is caused by the two shock waves generating from the canards.

Booster interference heating can be analyzed quantitatively once the peak interference heating data (thermocouple tests with booster and orbiter models) become available. It is also suggested that paints with high phase change

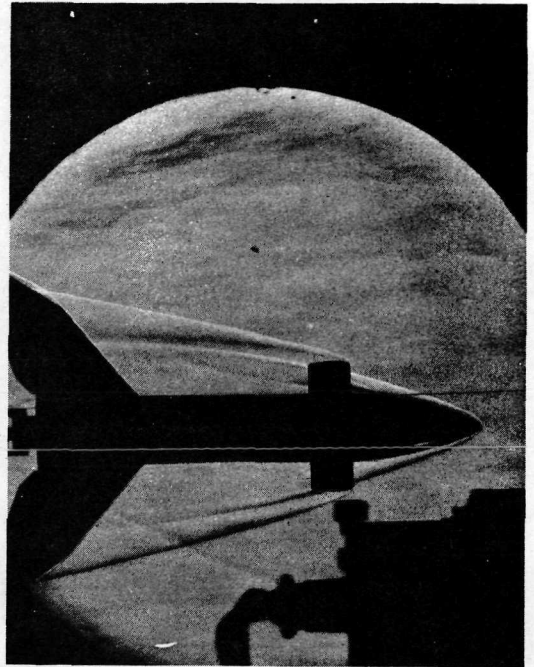
temperature should be used during future paint tests in order to provide peak interference heating data.

The results of this study can be used as a guideline to locate possible interference heating areas on the booster.

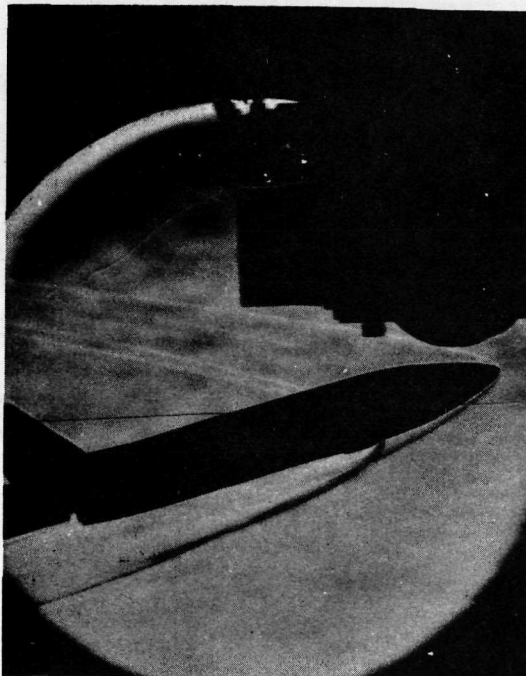
Run 264, B1, $\alpha = 0^\circ$



Run 260, B1, $\alpha = 0^\circ$



Run 232, B1, $\alpha = 15^\circ$



Run 224, B1, $\alpha = 30^\circ$

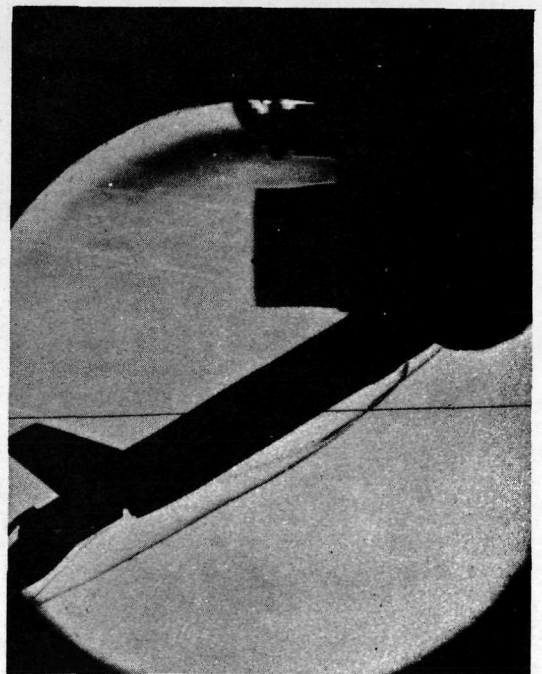
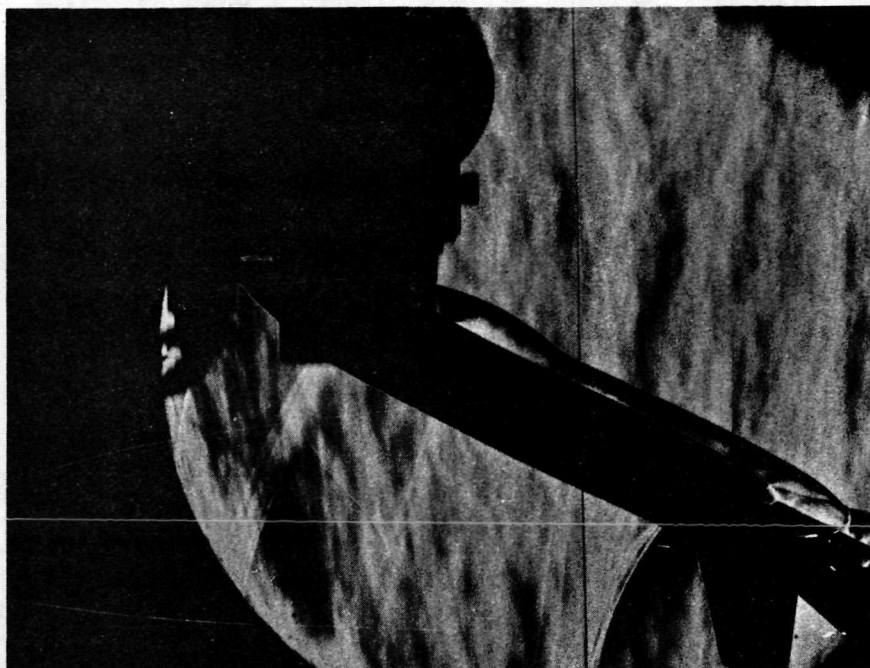


Figure 1. MDC/MMC BASELINE BOOSTER (B1) SCHLIEREN PHOTOGRAPHS

Run 209, B1, $\alpha = 60^\circ$



Run 220, B1, $\alpha = 45^\circ$

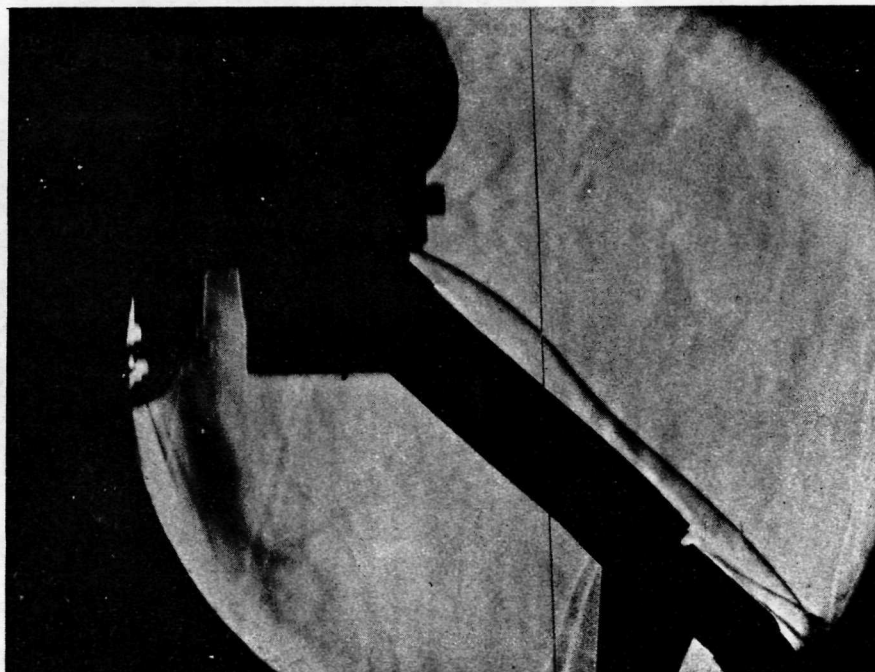
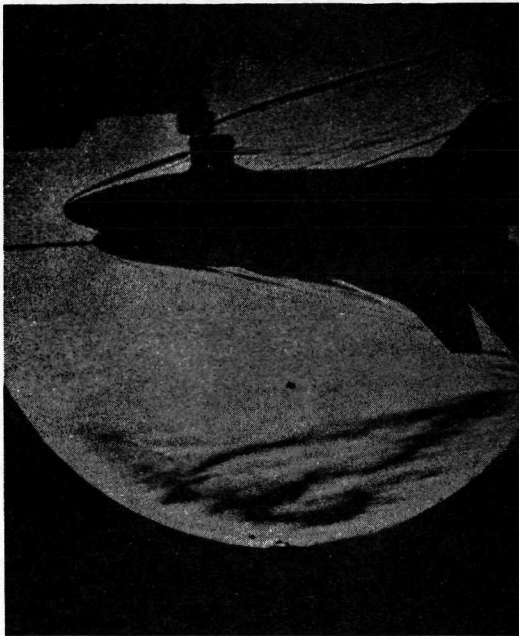
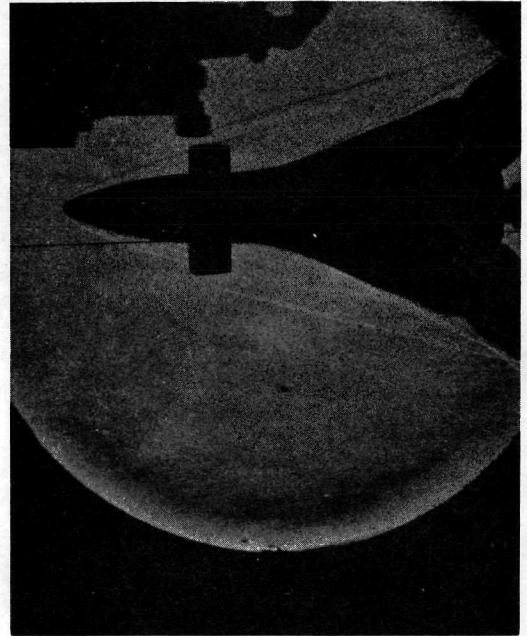


Figure 1. MDC/MMC BASELINE BOOSTER (B1) SCHLIEREN PHOTOGRAPHS (Concluded)

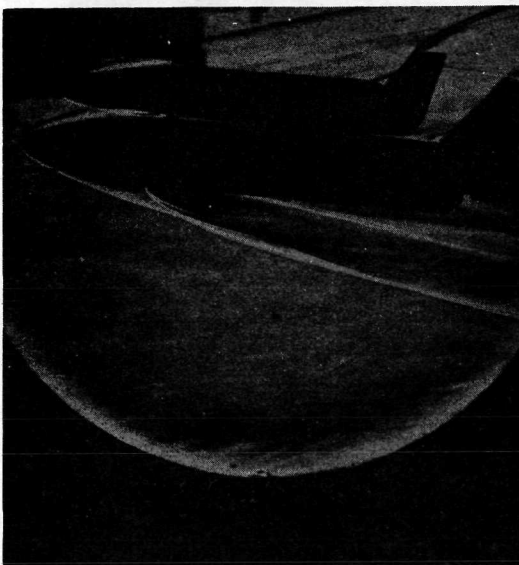
Run 237, O1+ B1, $\alpha = 0^\circ$



Run 255, O1+ B1, $\alpha = 0^\circ$



Run 270, O1+ B1, $\alpha = 5^\circ$



Run 272, O1+ B1, $\alpha = -5^\circ$

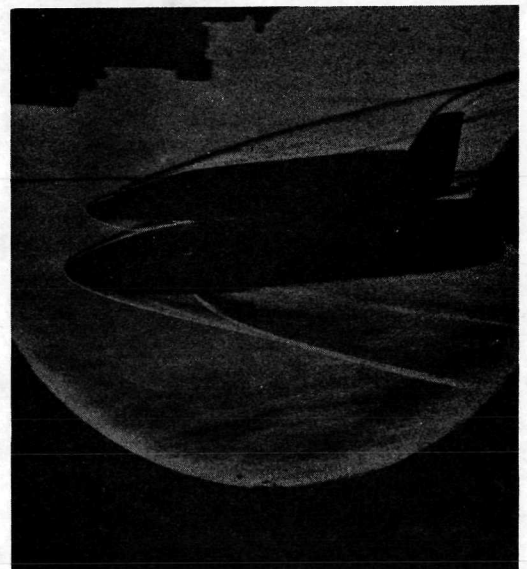


Figure 2. ASCENT CONFIGURATION SCHLIEREN PHOTOGRAPHS (BASELINE BOOSTER, B1, AND BASELINE ORBITER, O1)

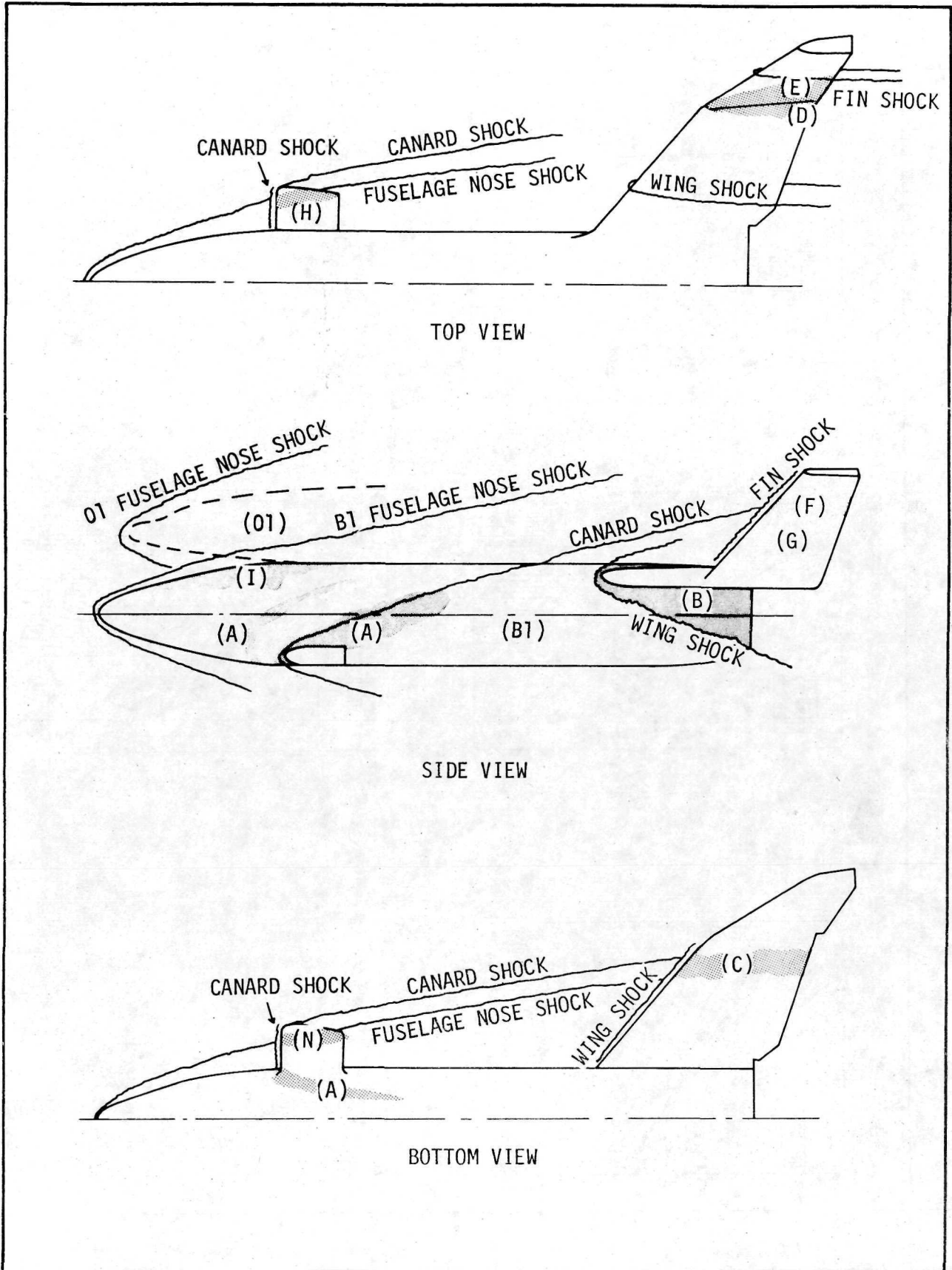


Figure 3. OVERALL SHOCK WAVE INTERFERENCE DIAGRAM ON BOOSTER

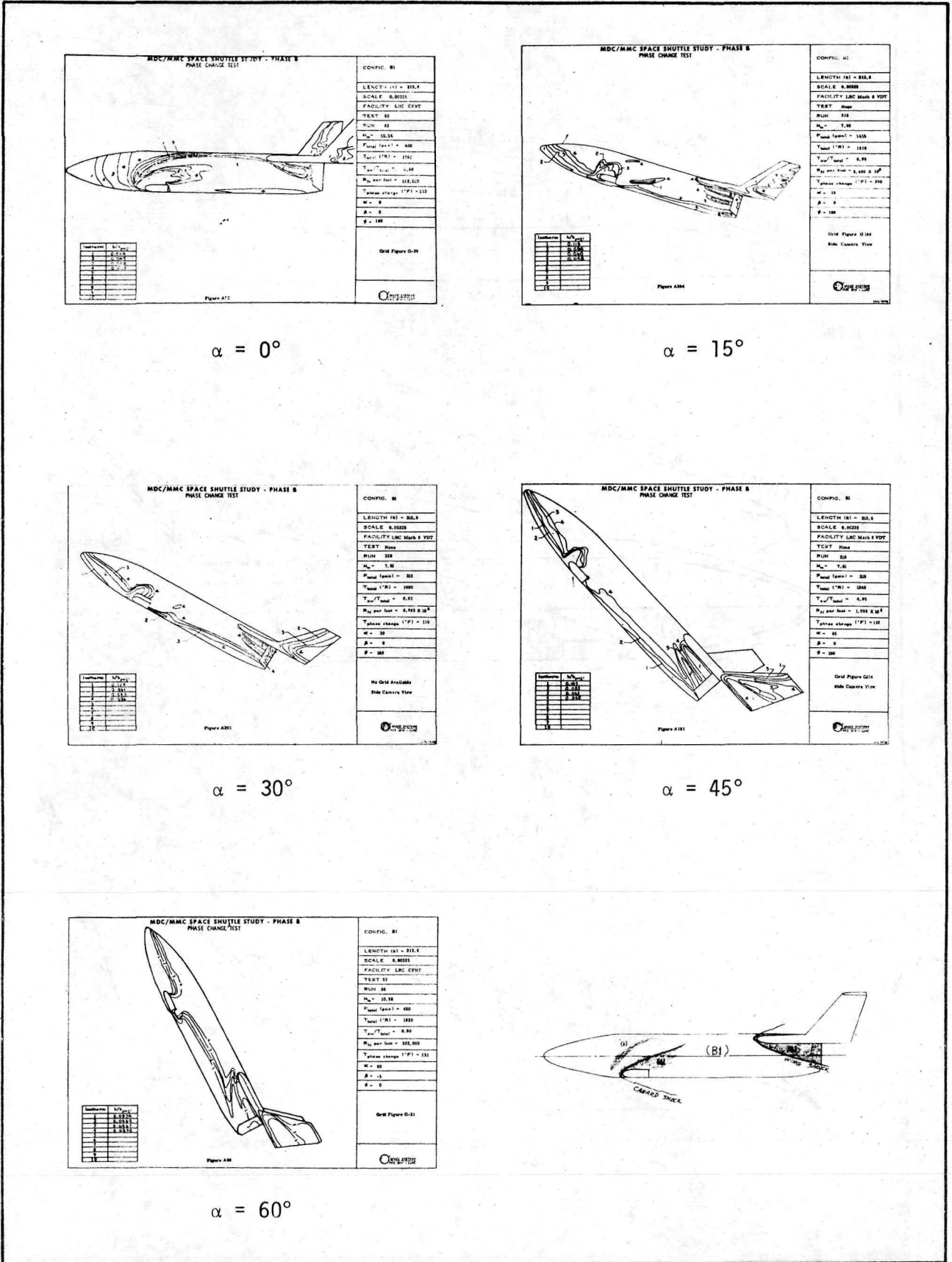
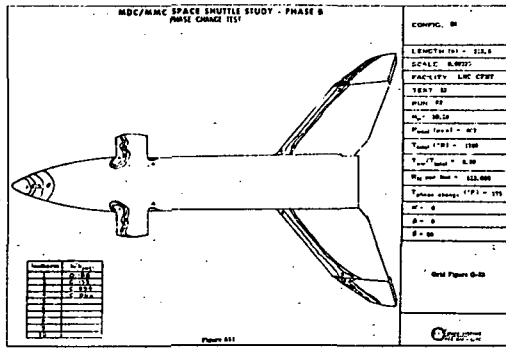
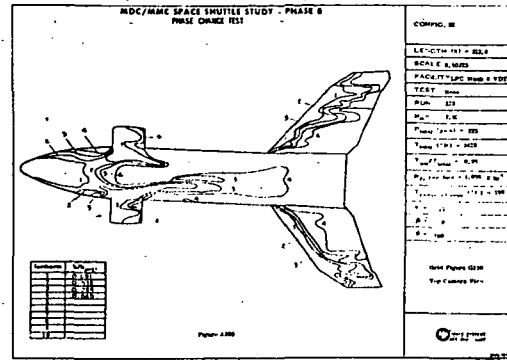


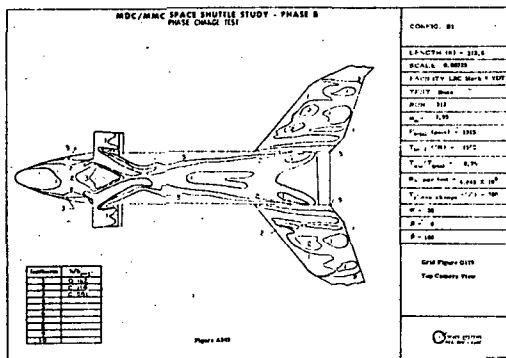
Figure 4. INTERFERENCE HEATING ON FUSELAGE DUE TO CANARD SHOCK WAVE (AREA A) AND WING SHOCK WAVE (AREA B)



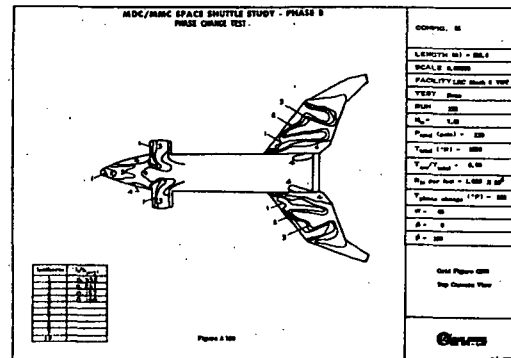
$\alpha = 0^\circ$



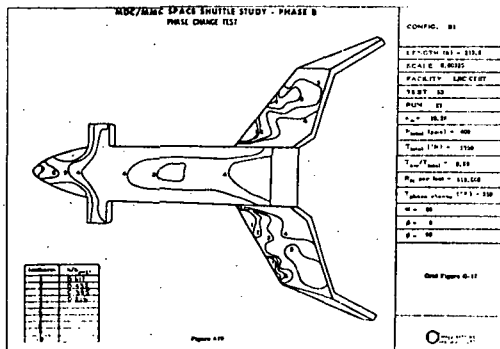
$\alpha = 15^\circ$



$\alpha = 30^\circ$



$\alpha = 45^\circ$



$\alpha = 60^\circ$

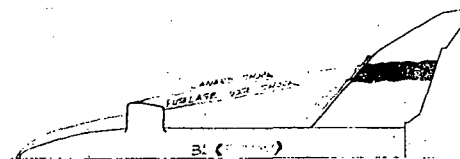
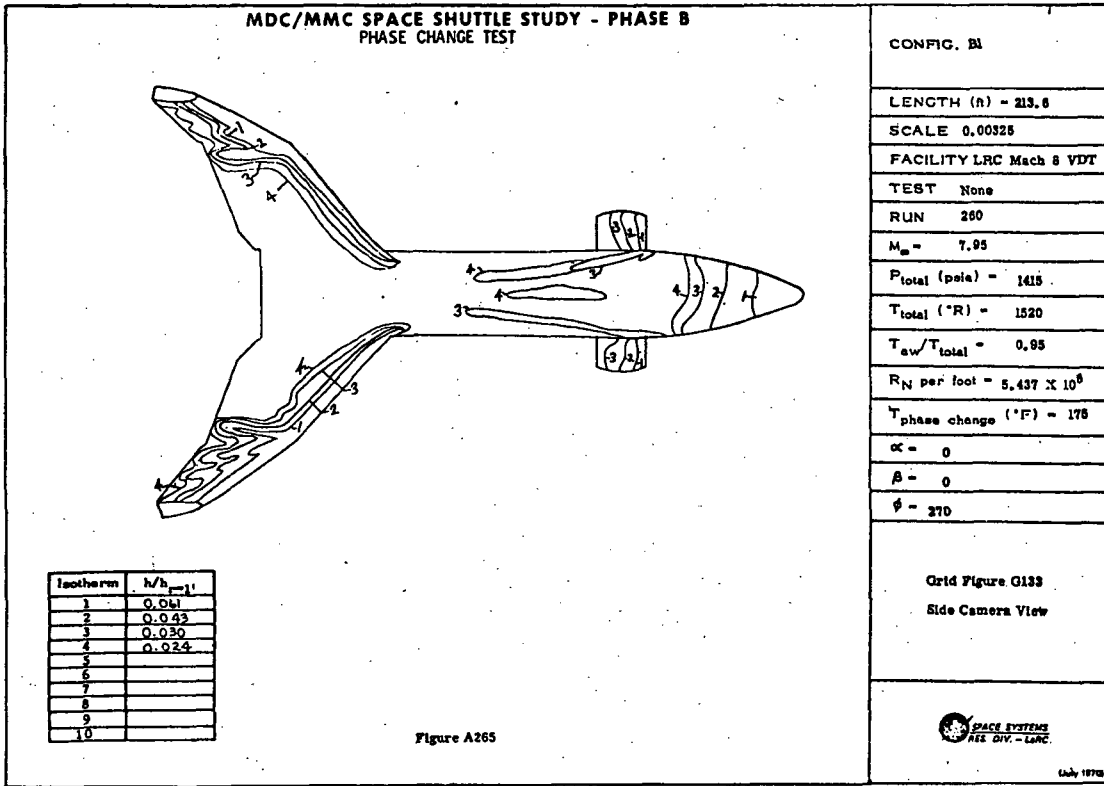


Figure 5. INTERFERENCE HEATING ON WING DUE TO CANARD OR FUSELAGE NOSE SHOCK WAVE (AREA C).



$\alpha = 0^{\circ}$

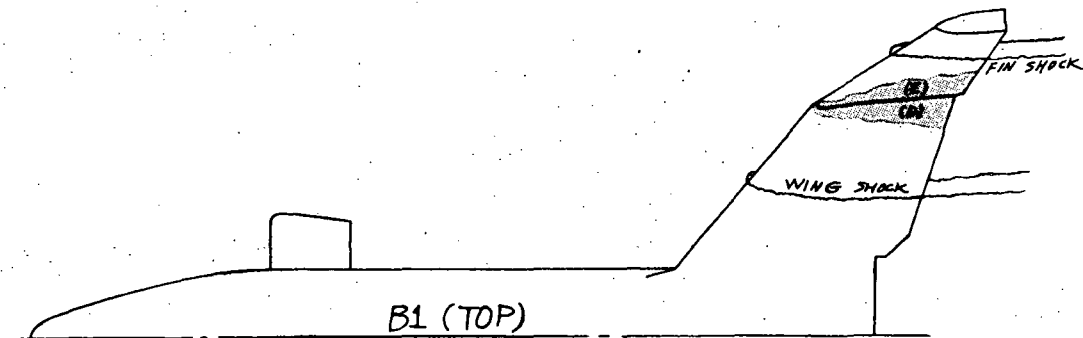
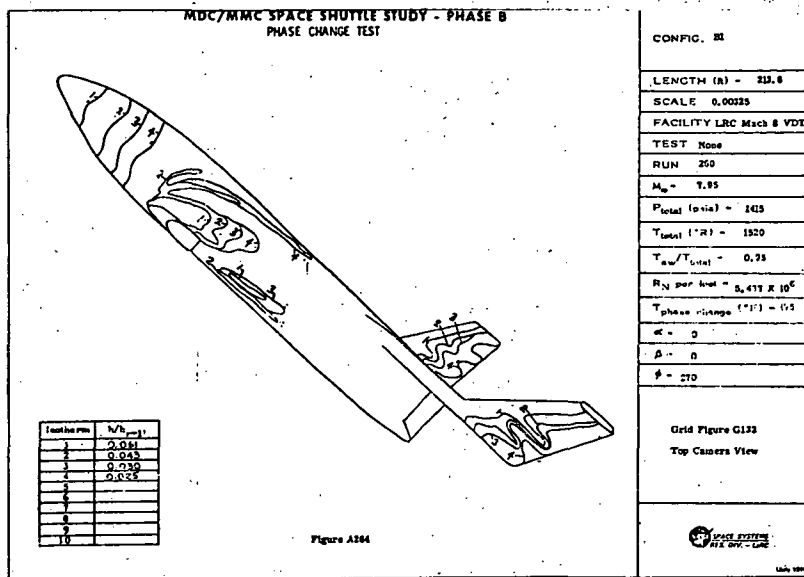
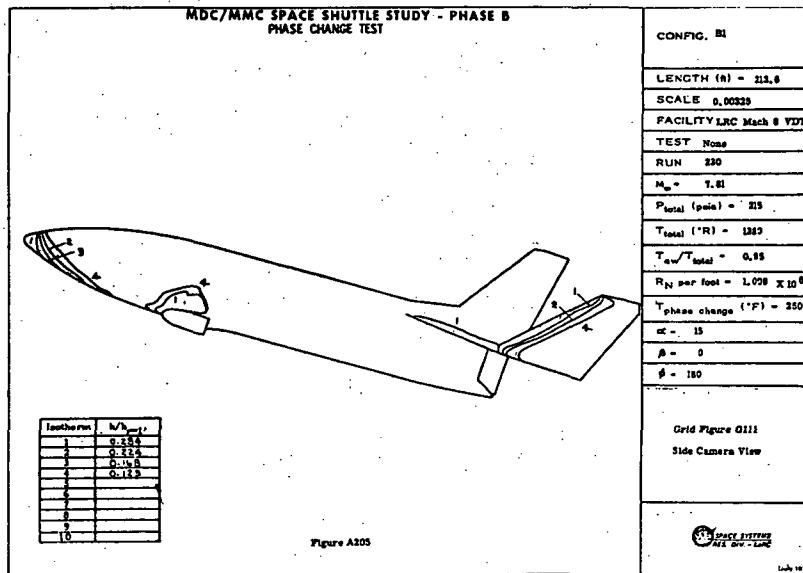


Figure 6. INTERFERENCE HEATING ON WING TIP (AREA D) AND FIN ROOT (AREA E) DUE TO WING-SHOCK/FIN-SHOCK INTERACTION.



$\alpha = 0^\circ$



$\alpha = 15^\circ$

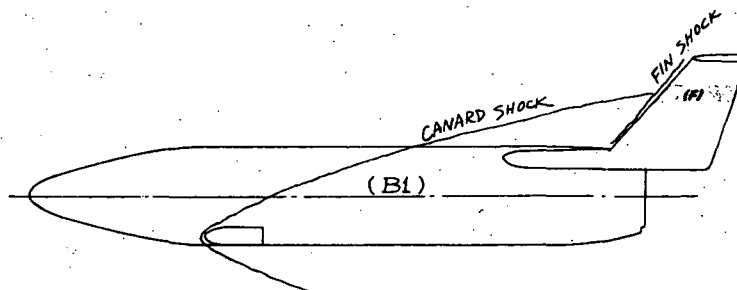


Figure 7. INTERFERENCE HEATING ON FIN DUE TO CANARD SHOCK WAVE (AREA F)

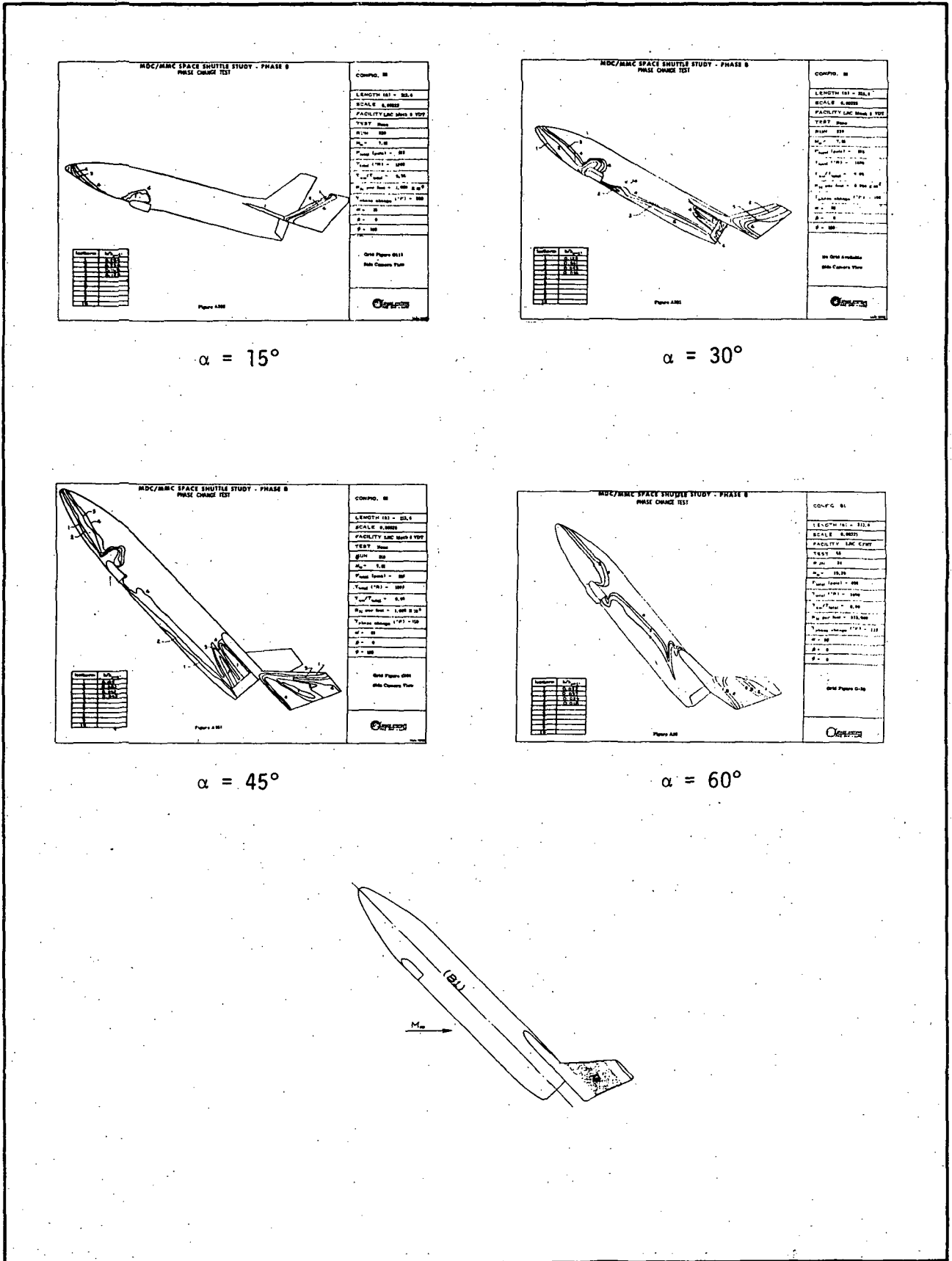
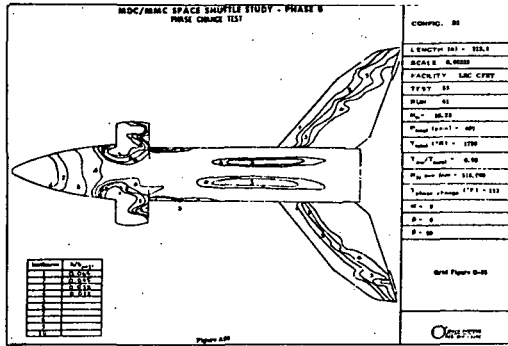
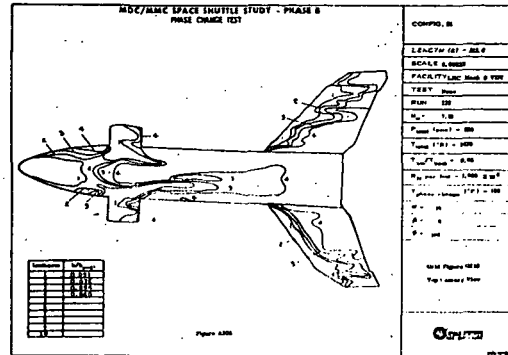


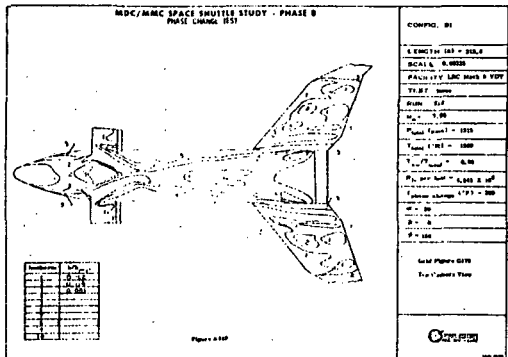
Figure 8. INTERFERENCE HEATING ON FIN OUTBOARD SURFACE (AREA G) DUE TO WING TIP FLOW SEPARATION AT HIGH ANGLE-OF-ATTACK



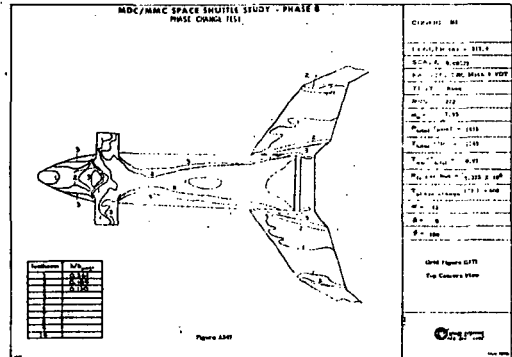
$\alpha = 0^\circ$



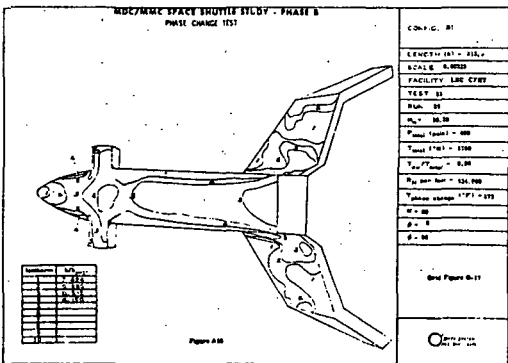
$\alpha = 15^\circ$



$\alpha = 30^\circ$



$\alpha = 45^\circ$



$\alpha = 60^\circ$

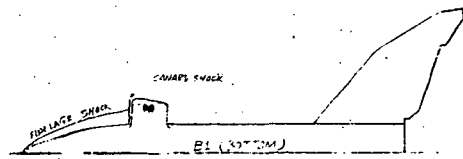
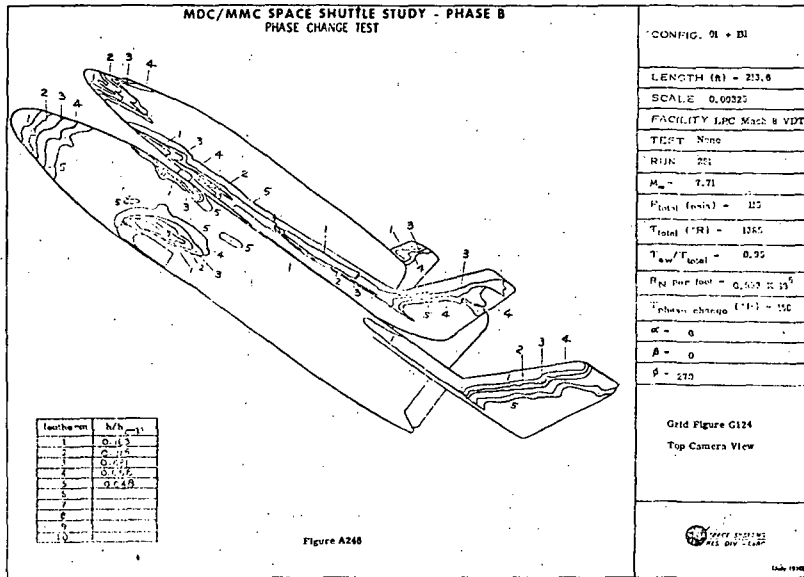
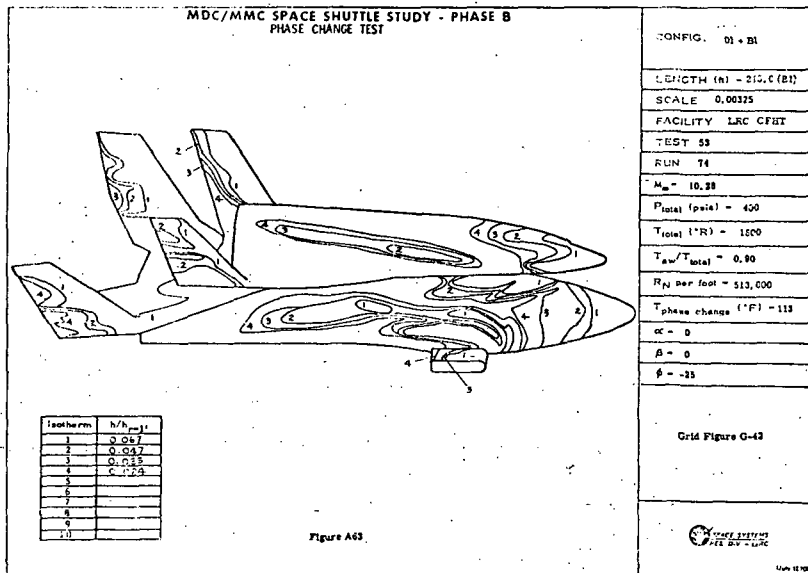


Figure 9. INTERFERENCE HEATING ON CANARD DUE TO FUSELAGE NOSE SHOCK WAVE (AREA H)



$\alpha = 0^\circ$



$\alpha = 0^\circ$

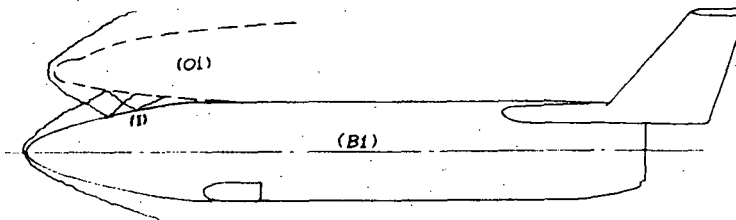


Figure 10. INTERFERENCE HEATING ON B1 FUSELAGE (AREA I) DUE TO O1 FUSELAGE SHOCK WAVE

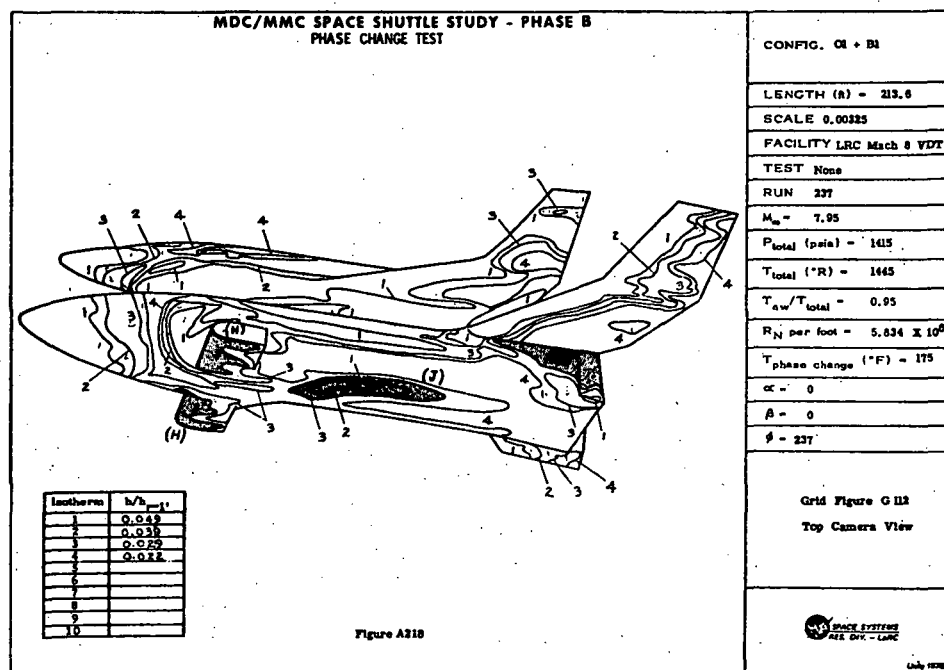
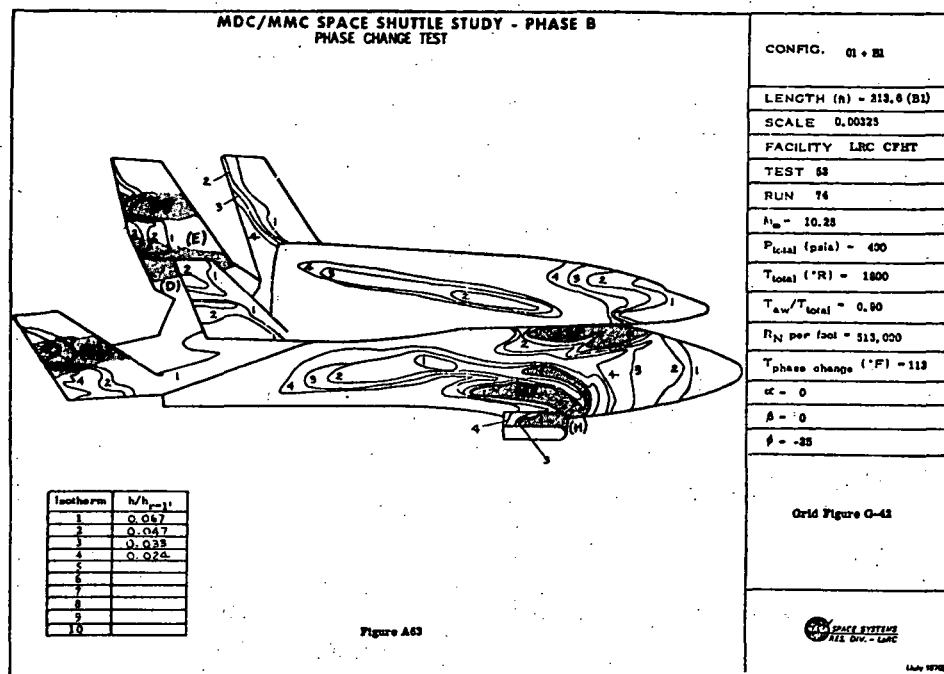


Figure 11. OVERALL INTERFERENCE HEATING ON BOOSTER

Distribution:

NASA/MSFC

J. A. Forney (3)

J. D. Warmbrod

Northrop

W. W. Youngblood

D. O. Barnett

J. A. Roux

J. Y. Parker

F. T. Hung (3)

7946, File

Appendix A-6

**INTERFERENCE HEATING
TO GDC BOOSTER**

**INTERFERENCE HEATING
ON GENERAL DYNAMICS PHASE B DELTA WING BOOSTER
DURING ASCENT AND REENTRY FLIGHTS**

July 1971

by

F. T. Hung

PREPARED FOR:

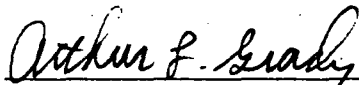
**NATIONAL AERONAUTICS AND SPACE ADMINISTRATION
GEORGE C. MARSHALL SPACE FLIGHT CENTER
AERO-ASTRODYNAMICS LABORATORY**

Under Contract NAS8-26268

REVIEWED AND APPROVED BY:



Dr. D. O. Barnett, Chief
Aerothermodynamics Branch



Arthur L. Grady, Manager
Aerophysics Section

**NORTHROP-HUNTSVILLE
HUNTSVILLE, ALABAMA**

July 1971

TO: H. B. Wilson, S&E-AERO-AT

FROM: F. T. Hung, Northrop-Huntsville

SUBJECT: Interference Heating on General Dynamics
Phase B Delta Wing Booster During Ascent
and Reentry Flights

Shock interference heating on the General Dynamics, Phase B, Delta Wing Booster has been analyzed and correlated with Mach number and angle-of-attack. This study is based on the thermocouple and paint test results contained in references 1 through 6 which cover a wide range of Mach number, Reynolds number, and angle-of-attack. Mated orbiter-booster models were used to study the interference heating on the booster fuselage due to orbiter-generated shock waves during ascent flight. A summary of test conditions and model configurations is given in Table 1.

It should be noted that even though a large amount of heating data has been taken during the tests, the shock interference heating data available at the present time are somewhat limited. For the case of thermocouple measurements, the thermocouple spacings on the booster models were not close enough to measure the localized peak heating values. For the paint tests, the quality of the measurements was affected by the difficulty involved in photographing the paint phase change history at some booster surface areas. In other tests the paints employed had extremely low phase change temperatures. As a consequence, some test data were lost since the movie films showed phase change on the very first frame. The preceding considerations deem it probable that some interference heating peaks were missed in both the paint and the thermocouple measurements.

In this study, the interference heating data are presented in the form of h_i/h_u , the ratio of interference heat transfer coefficient to the undisturbed value. The effects of Mach number and booster angle-of-attack on h_i/h_u were

also analyzed and correlated. The Reynolds number effect could not be determined quantitatively due to the quality and limited amount of data. The different interference heating areas on the booster (during ascent and reentry flights) are shown in Figure 1 and details are summarized below:

- Area (A) - Fuselage Heating due to Orbiter Fuselage Shock

The Maximum h_1/h_u values on booster fuselage upper surface centerline with different Mach numbers, Reynolds numbers, orbiter/booster positions, and orbiter/booster gaps are shown in Figure 2. Only the Mach number effect can be derived from these data points. A straight line was drawn above all the data to account for the fact that peak heating values might have been missed for the reasons discussed. It is also assumed that maximum $h_1/h_u = 1$ when Mach number $M_\infty = 1$ as indicated in Figure 2. Some typical heating distributions and locations of maximum h_1/h_u on the fuselage upper surface centerline are given in Figures 3 through 5. It is expected that the heating distribution should vary drastically with Mach number, angle-of-attack, and orbiter/booster position due to the variation of shock/shock interaction pattern.

The peripheral heating distribution on the booster fuselage varies drastically with fuselage axial location (X/L) due to the complicated shock/shock interaction pattern between the orbiter and the booster fuselages. The peripheral heating data are also very limited at the present time. In this study only the peripheral heating distributions at the locations (X/L) of maximum h_1/h_u have been roughly correlated as shown in Figure 6. It has been assumed that no interference heating occurs for peripheral angles, ϕ , less than 60 degrees as indicated in Figure 6. For $\phi > 60$ degrees, it is assumed that h_1/h_u increases linearly with ϕ . The h_1/h_u values at $\phi = 180$ degrees (fuselage upper surface centerline) in Figure 6 are taken from Figure 2.

For certain flow conditions and model configurations, shock waves impinge on the booster canopy and cause high heating rates during ascent flights. Shadowgraphs, contained in references 1 and 2, indicate that the booster nose shock impinges on its own canopy for high Mach number flows ($M_\infty > 7$ for $\alpha = 0^\circ$ and -5°). Typical heating data are shown in Figures 7 and 8. For certain combinations of Mach number and orbiter/booster position, the orbiter nose shock wave also impinges on the booster canopy with similar interference heating effects as shown in Figures 3, 4, and 5. The canopy peak interference heating data are summarized in Figure 9. Since the booster canopy had been eliminated in the latest booster configuration to reduce the interference heating rates, no detailed correlation of canopy heating was made.

- Area (B) - Fuselage Heating due to Wing Shock:

Maximum h_1/h_u data are available only for high Mach number tests as shown in Figure 10. Two correlations are presented to account for high and low angle-of-attack cases. Again, corrections were made to account for the missing of the heating peaks. It is also assumed that maximum $h_1/h_u = 1$ when $M_\infty = 1$. The interference heating area on the fuselage varies with angle-of-attack as indicated in Figure 1.

- Area (C) - Fuselage Heating due to Canard Shock

Of the four delta wing booster models used in reference 3 (Configuration B-15B, Models A, B, C and D), only data from Model C (booster with a pivoting contoured canard) are considered in this study. Maximum h_i/h_u data are shown in Figure 11. The single correlation in Figure 11 should apply to any angle-of-attack since the interference heating should not be affected significantly by the booster angle-of-attack because the pivoting canard always has a zero angle-of-attack.

- Area (D) - Fuselage Heating due to Fin Shock

The swept shock wave generating from the fin impinges on the booster fuselage only for the case of low angle-of-attack. The maximum h_i/h_u was again correlated with Mach number as shown in Figure 12. It was assumed that maximum $h_i/h_u = 1$ when $M_\infty = 1$.

- Area (E) - Wing Heating due to Fuselage Shock

The interference heating on booster wing due to a fuselage shock wave is a strong function of booster angle-of-attack. Schlieren photographs indicate that:

- (1) For high angles-of-attack ($\alpha > 40^\circ$), the fuselage shock does not impinge on wing. Consequently $h_i/h_u = 1$.
- (2) For intermediate angles-of-attack ($20^\circ < \alpha < 40^\circ$), the fuselage shock impinges on wing for any Mach number. Based on the limited data, a simple crude correlation is made as shown in Figure 13 with the assumption that maximum $h_i/h_u = 1$ when $M_\infty = 1$.
- (3) For low angle-of-attack ($\alpha < 20^\circ$), the fuselage nose shock does not impinge on the wing for low Mach number flows ($M_\infty < 4$) so that $h_i/h_u = 1$. However, the nose shock wave does impinge on the wing for high Mach number cases ($M_\infty > 4$). The same heating correlation as shown in Figure 13 can be used.

The shock impingement point on wing varies with angle-of-attack as shown in Figure 14 for the $M_\infty = 10$ case.

- Area (F) - Fin Heating due to Fuselage Shock

The booster fuselage shock wave impinges on the fin only for very low angles-of-attack and high Mach numbers. The very limited heating data are shown in Figure 15. A linear correlation was derived with the usual assumption that maximum $h_i/h_u = 1$ when $M_\infty = 1$.

- Area (G) - Canard Heating due to Fuselage Shock

The fuselage shock wave impinges on the canard for certain angles-of-attack and Mach numbers. No interference heating data are available at the present time.

It should be noted that only the booster models used to generate low Mach number heating data ($M=2.5$ and 3.7 in reference 2) had boundary layer trips on the fuselage nose to increase the probability that turbulent flow would occur

for the ascent flight configurations. For the rest, and predominant portion of the data discussed in this study, the undisturbed flow on the booster wing, fin, canard, and most of the fuselage should be laminar due to the small booster models and the tunnel flow conditions used during the tests. This indicates that in this study most of the interference heating data have been referenced to the laminar undisturbed heating values, $(h_i/h_u)_{\text{laminar}}$. This differs from the actual flight cases where turbulent boundary layers are expected. In general, the effect of an impinging shock wave on the interference heating is less for a turbulent boundary layer than for a laminar boundary layer as discussed in references 7 and 8, i.e., $(h_i/h_u)_{\text{turbulent}} < (h_i/h_u)_{\text{laminar}}$. This means the data correlated in this study are considered to be conservative when they are applied to the actual booster flight cases.

It should be noted that improved correlations can be developed when more and better heating data become available.

REFERENCES

1. Brevig, O., Otwell, R. L., and Day, R. C., "Aerodynamic Heat Transfer Distribution on Phase B Space Shuttle Booster Vehicles At Angles of Attack from -5° to 60° ", General Dynamics Convair Aerospace Division, Technical Report 76-549-4-083, 584-TP-342, March 1971.
2. Roberge, A. M. and Gordon, C. C., "Heat Transfer Results on Space Shuttle Phase B Launch Configurations at Mach Numbers of 2.5 and 3.7", General Dynamics, Convair Aerospace Division, Technical Report 76-549-4-128, 584-TP-400, April 1971.
3. Doughty, R. O., Brock, O. R., and Erickson, R. C., "Reentry Heat Transfer to a Delta-Wing Space Shuttle Booster at High Angles of Attack", General Dynamics, Convair Aerospace Division, Technical Report FZA-452, March 1971. (Also SADSAC/Space Shuttle Wind Tunnel Test Data Report DMS-DR-1070, March 1971).
4. Ginsky, W. R., "Space Shuttle Mated Booster/Orbiter Model Heat Transfer Test Results Data Report", General Dynamics, Convair Aerospace Division, Preliminary Report 584-TP-281, October 1970.
5. Ginsky, W. R., "Space Shuttle Booster Heat Transfer Model Test Results Data Report", General Dynamics, Convair Aerospace Division, Report 584-TP-270, September 1970.
6. Ginsky, W. R., "Space Shuttle Booster Heat Transfer Model Test Results Data Report", General Dynamics, Convair Aerospace Division, Report 584-TP-265, September 1970.
7. Hung, F. T., "Shock Interference Heating in the Vicinity of Fin-Plate Corners", Northrop-Huntsville Technical Report TR-794-921A, April 1971.
8. Stainback, P. C., and Weinstein, L. M., "Aerodynamic Heating in the Vicinity of Corners at Hypersonic Speeds", NASA TN D-4130, November 1967.

Table 1. WIND TUNNEL TEST SUMMARY

REFERENCE	1	2	3	4	5	6
Wind Tunnel(s)	LaRC Mach 10 Hypersonic LaRC Mach 8 VDT Ames 3.5 ft Hypersonic	LaRC UPT	LaRC Mach 8 VDT	LaRC Mach 8 VDT	LaRC Mach 8 VDT	LaRC Mach 10 Hypersonic
Measurements	Paint (LaRC) T/C (Ames)	T/C	Paint	Paint	Paint	Paint
M_∞	7.4 - 10	2.5, 3.7	7.8 - 7.95	8	8	10
$Re \times 10^6 / ft$	0.7 - 7	2.5 - 5.0	1 - 6	1.2 - 4.0	5.5	1
α (deg)	-5 - 60	0, -5	40 - 65	0, -5	20 - 60	0 - 60
Model Scales	0.0035 (paint) 0.0060 (T/C)	0.006	0.0032	0.0035	0.0035	0.0035
Models	Delta Wing Booster Straight Wing Booster Delta Wing Orbiter Straight Wing Orbiter	Delta Wing Booster Delta Wing Orbiter Straight Wing Orbiter	Delta Wing Boosters	Delta Wing Booster Straight Wing Booster Delta Wing Orbiter Straight Wing Orbiter	Delta Wing Booster Straight Wing Booster	Delta Wing Booster Straight Wing Booster
Remarks		Boundary Layer Trips Used				

LIST OF SYMBOLS

G = gap between orbiter and booster fuselages, inches

h_i/h_u = ratio of interference heat transfer coefficient to undisturbed values

λ = distance between orbiter and booster noses, positive for orbiter in forward position, inches

L = booster fuselage length, inches

M_∞ = freestream Mach number

Re = freestream Reynolds number per foot

X = booster fuselage axial distance measuring from booster nose, inches

α = angle of attack, degrees

ϕ = fuselage peripheral angle measuring from fuselage bottom surface centerline, degrees

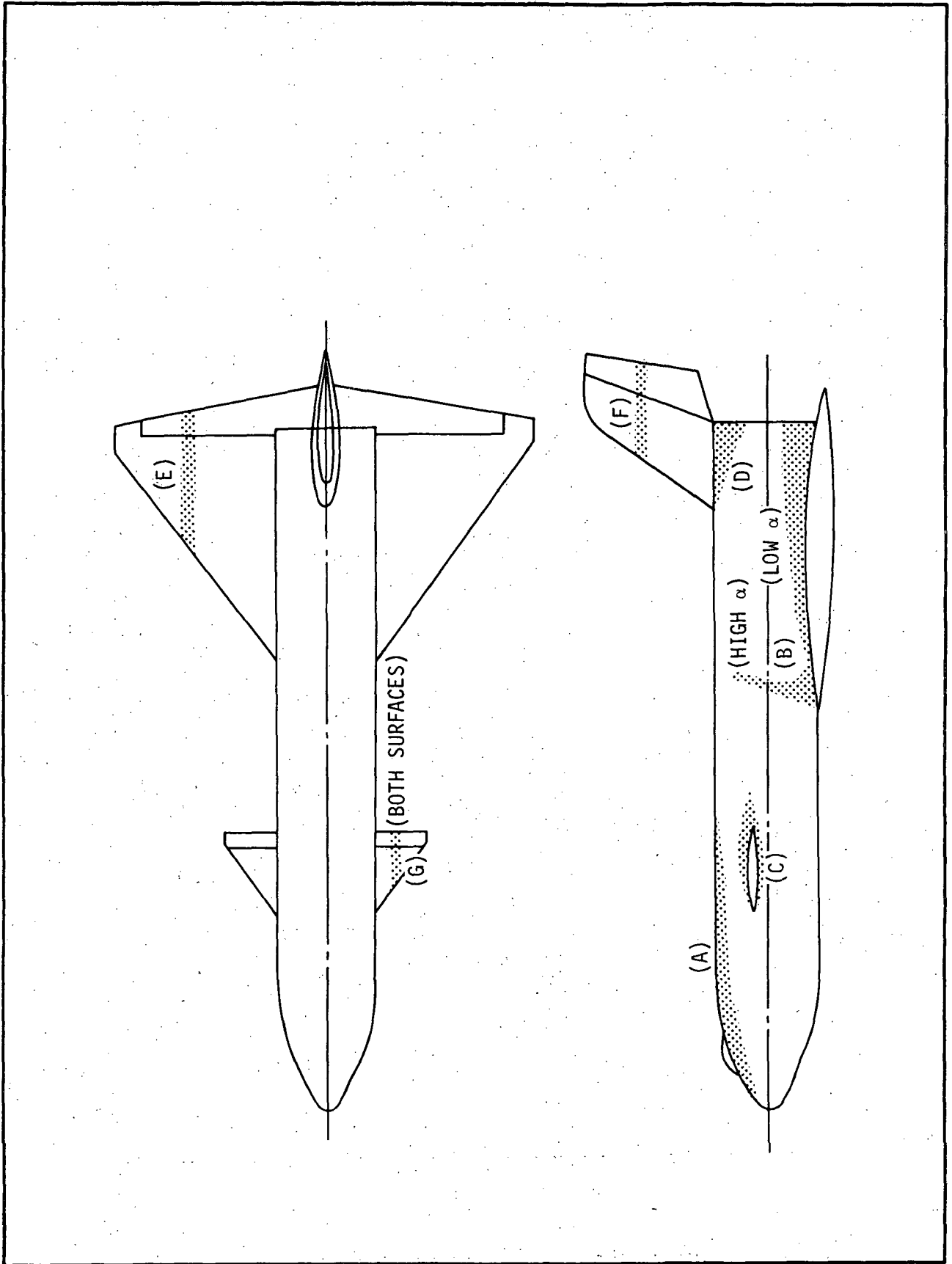


Figure 1. SHOCK INTERFERENCE HEATING AREAS ON GDC DELTA WING BOOSTER

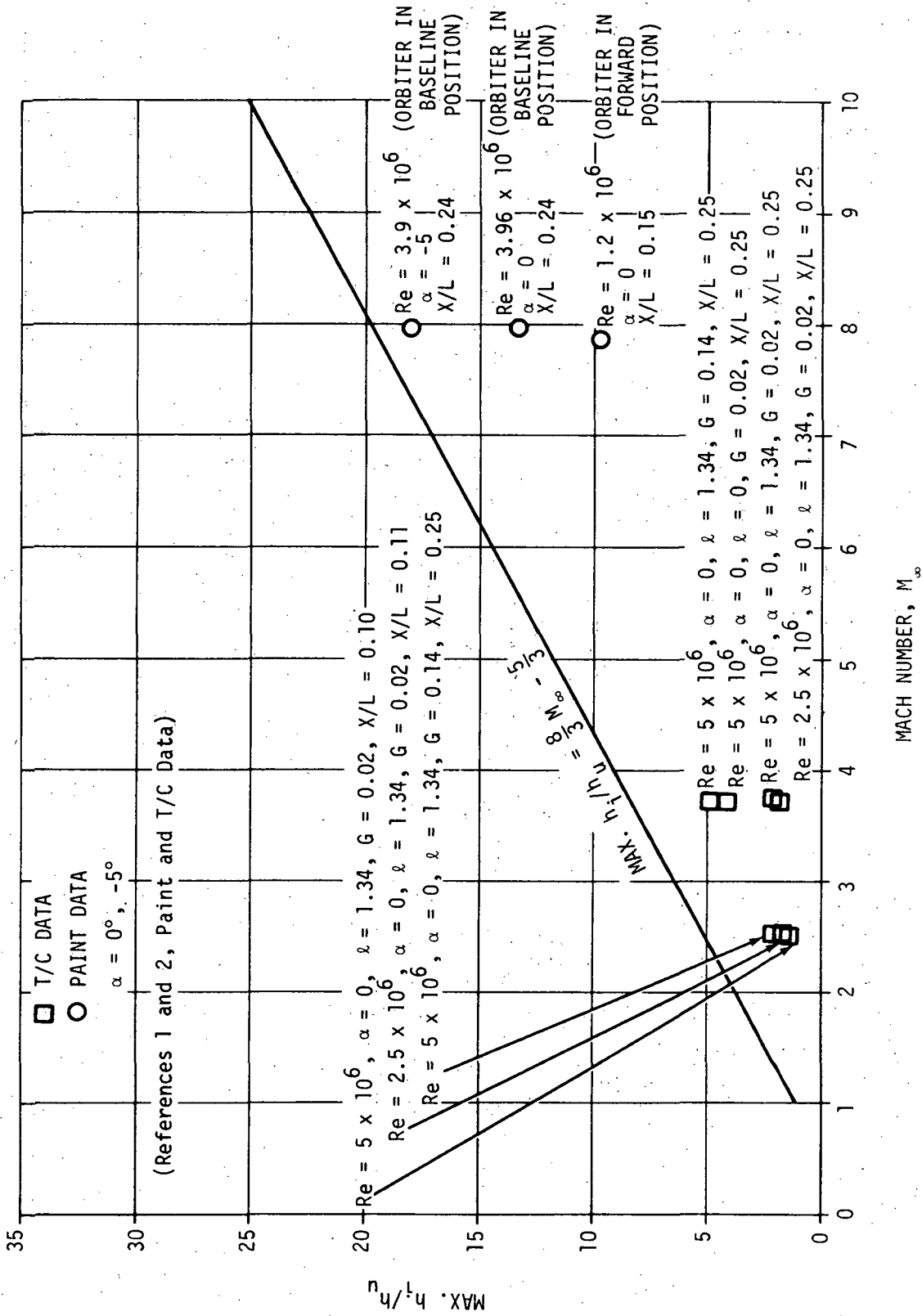


Figure 2. BOOSTER FUSELAGE UPPER SURFACE CENTERLINE HEATING DUE TO ORBITER SHOCK INTERFERENCE (AREA (A))

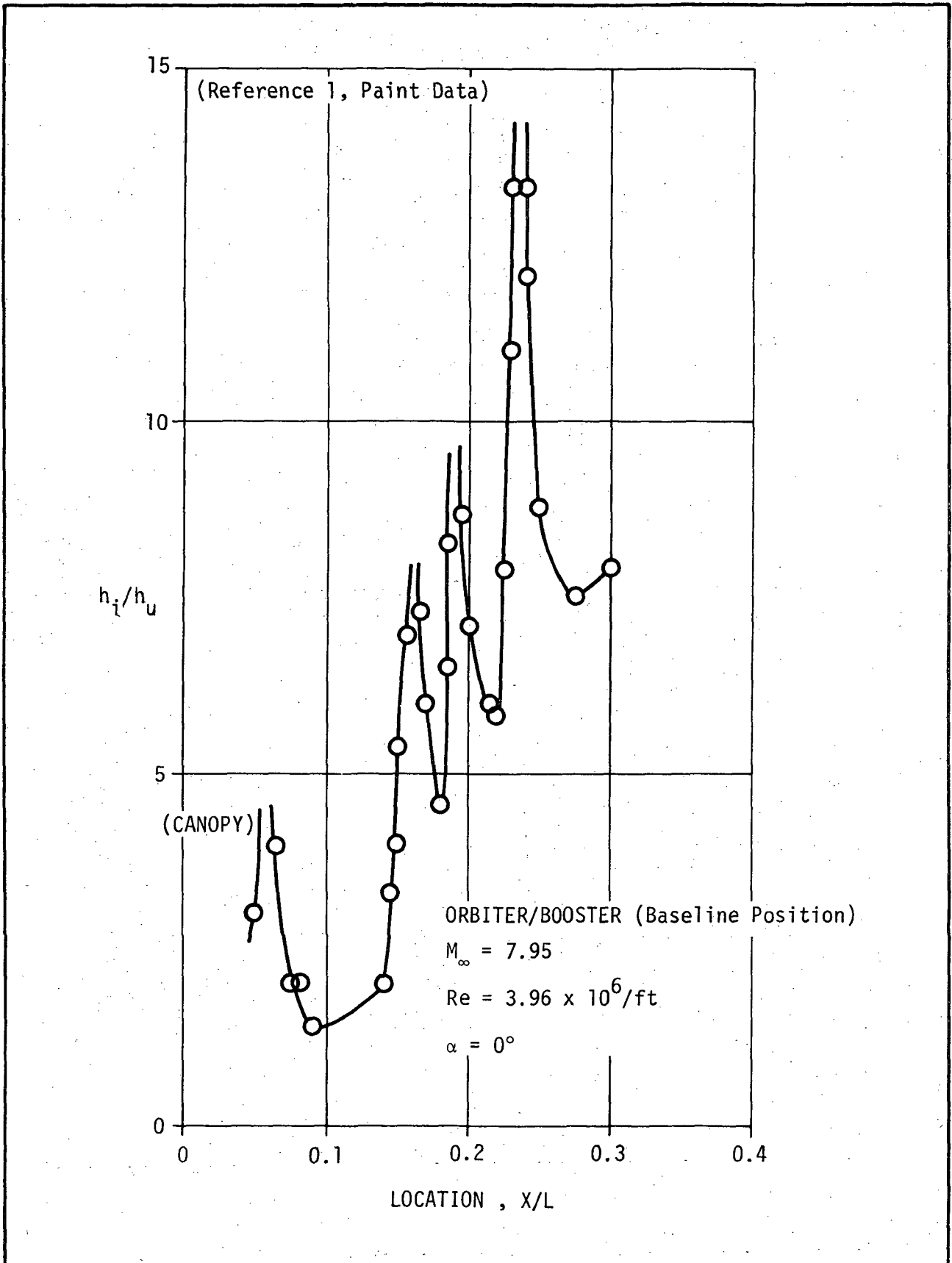


Figure 3. BOOSTER FUSELAGE UPPER CENTERLINE SHOCK INTERFERENCE HEATING DISTRIBUTION (AREA (A))

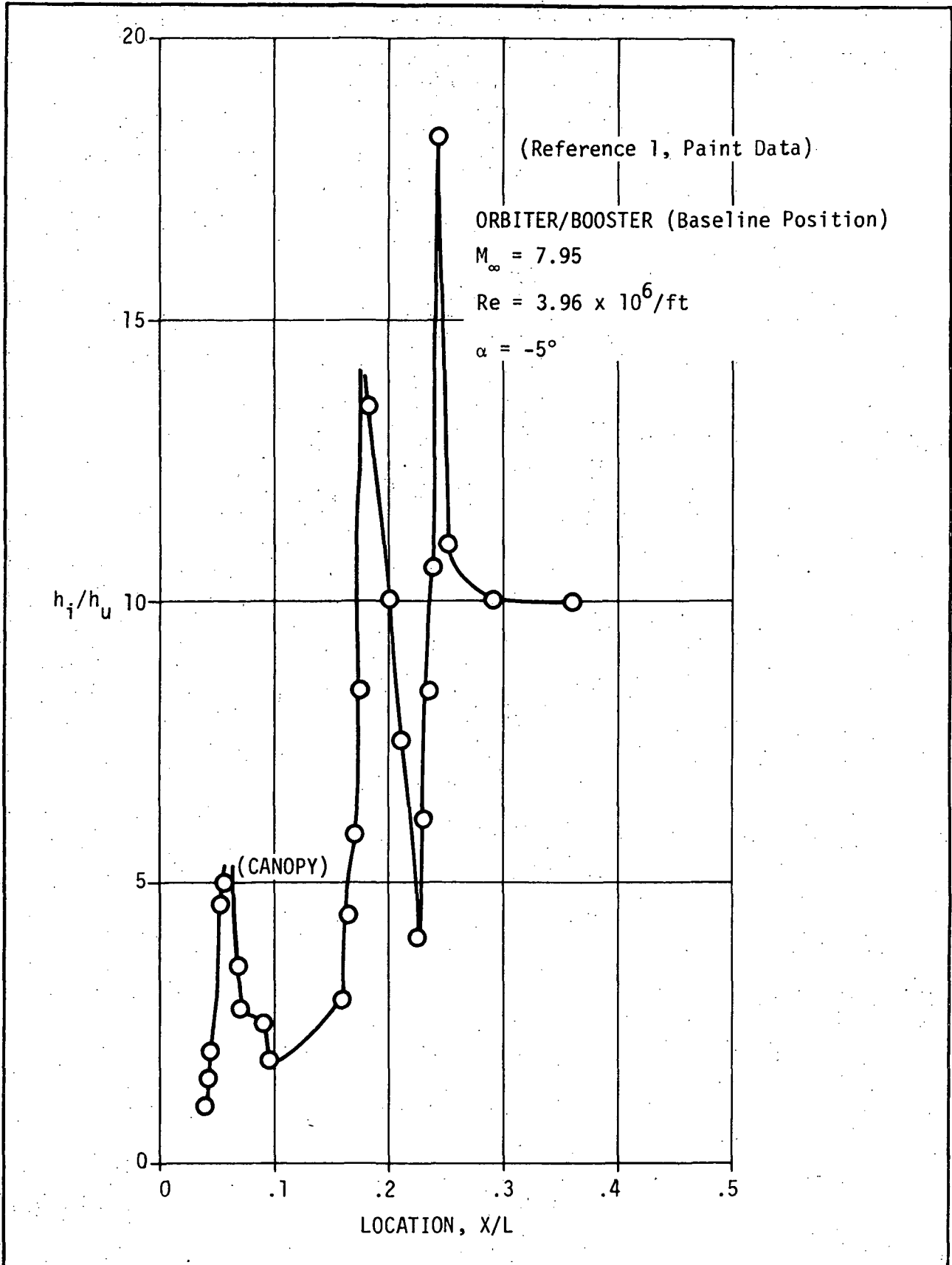


Figure 4. BOOSTER FUSELAGE UPPER CENTERLINE SHOCK INTERFERENCE HEATING DISTRIBUTION (AREA (A))

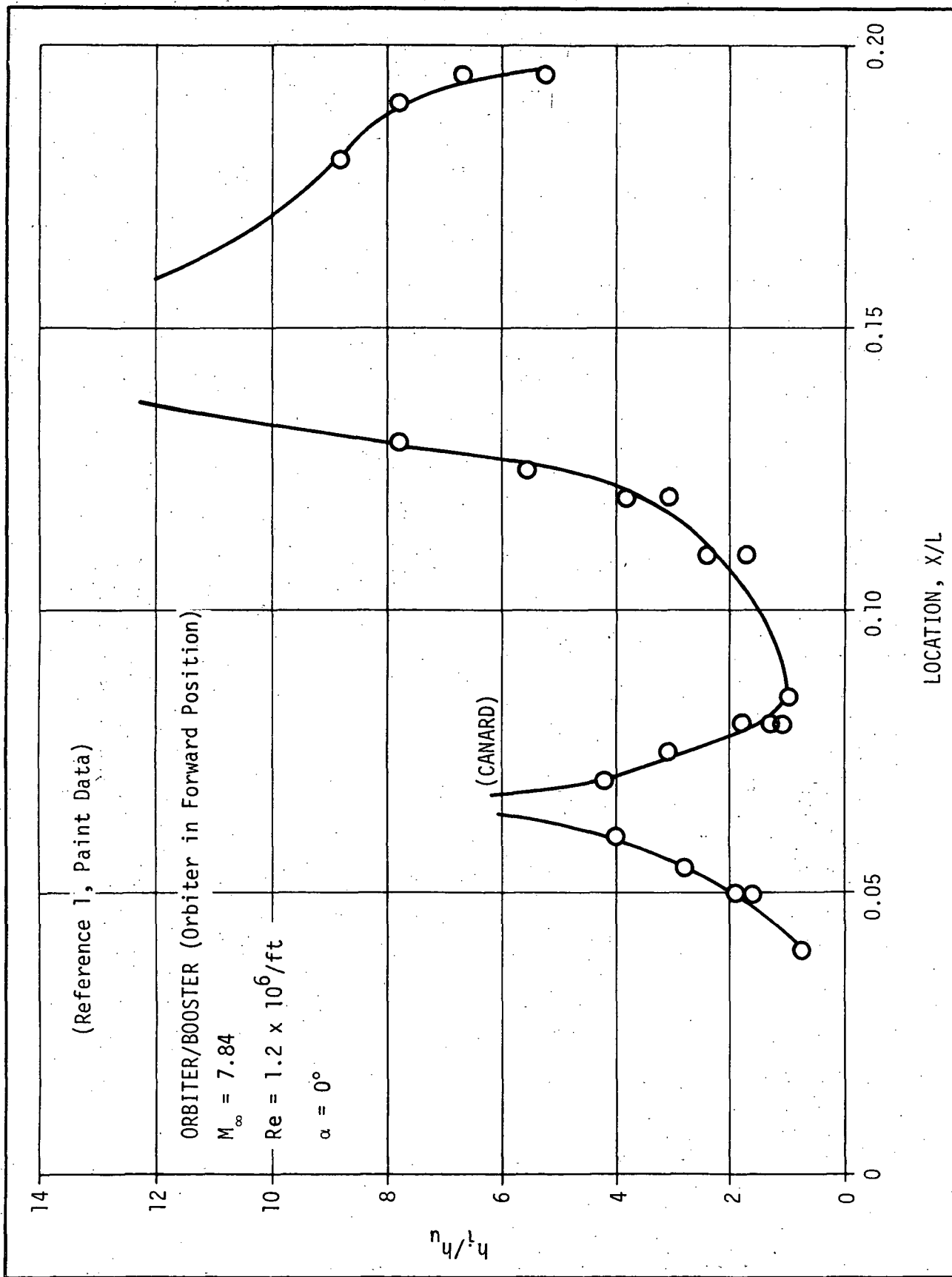


Figure 5. BOOSTER FUSELAGE UPPER SURFACE CENTERLINE SHOCK INTERFERENCE HEATING DISTRIBUTION (AREA (A))

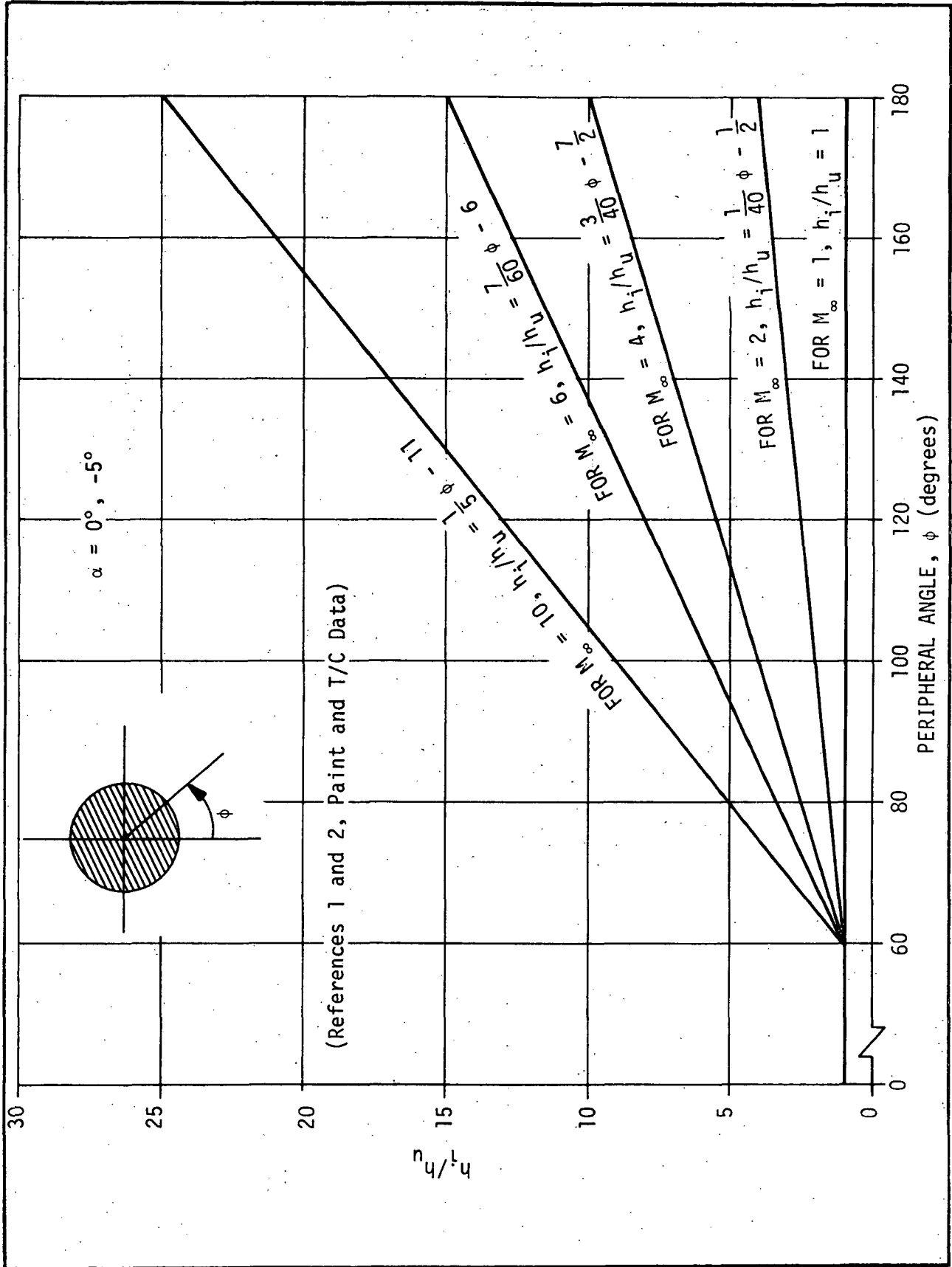


Figure 6. BOOSTER FUSELAGE PERIPHERAL HEATING DISTRIBUTION AT LOCATION (X/L) OF MAX. h_i/h_u DUE TO ORBITER SHOCK INTERFERENCE (AREA (A))

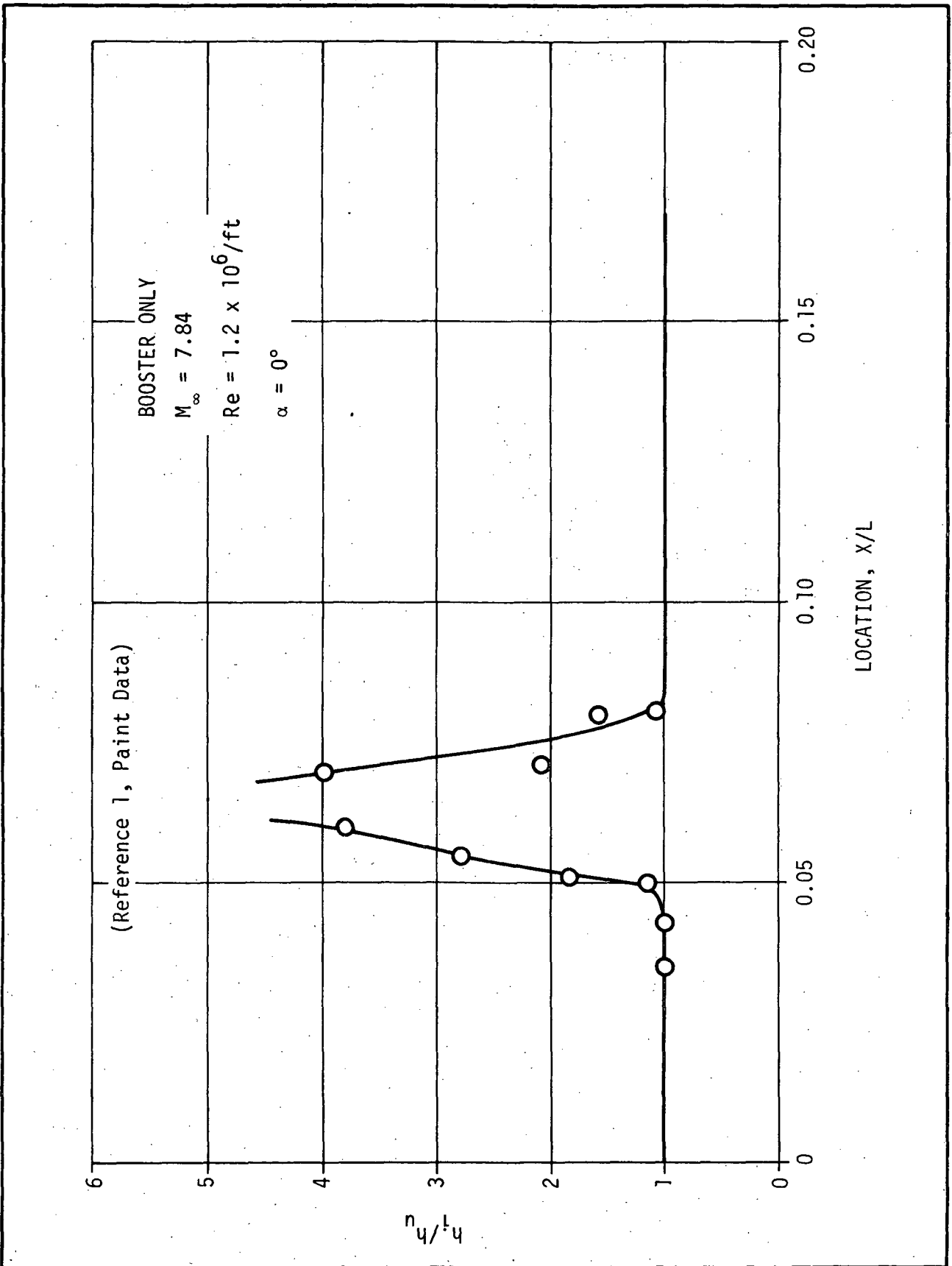


Figure 7. INTERFERENCE HEATING DISTRIBUTION ON BOOSTER CANOPY CENTERLINE (AREA (A))

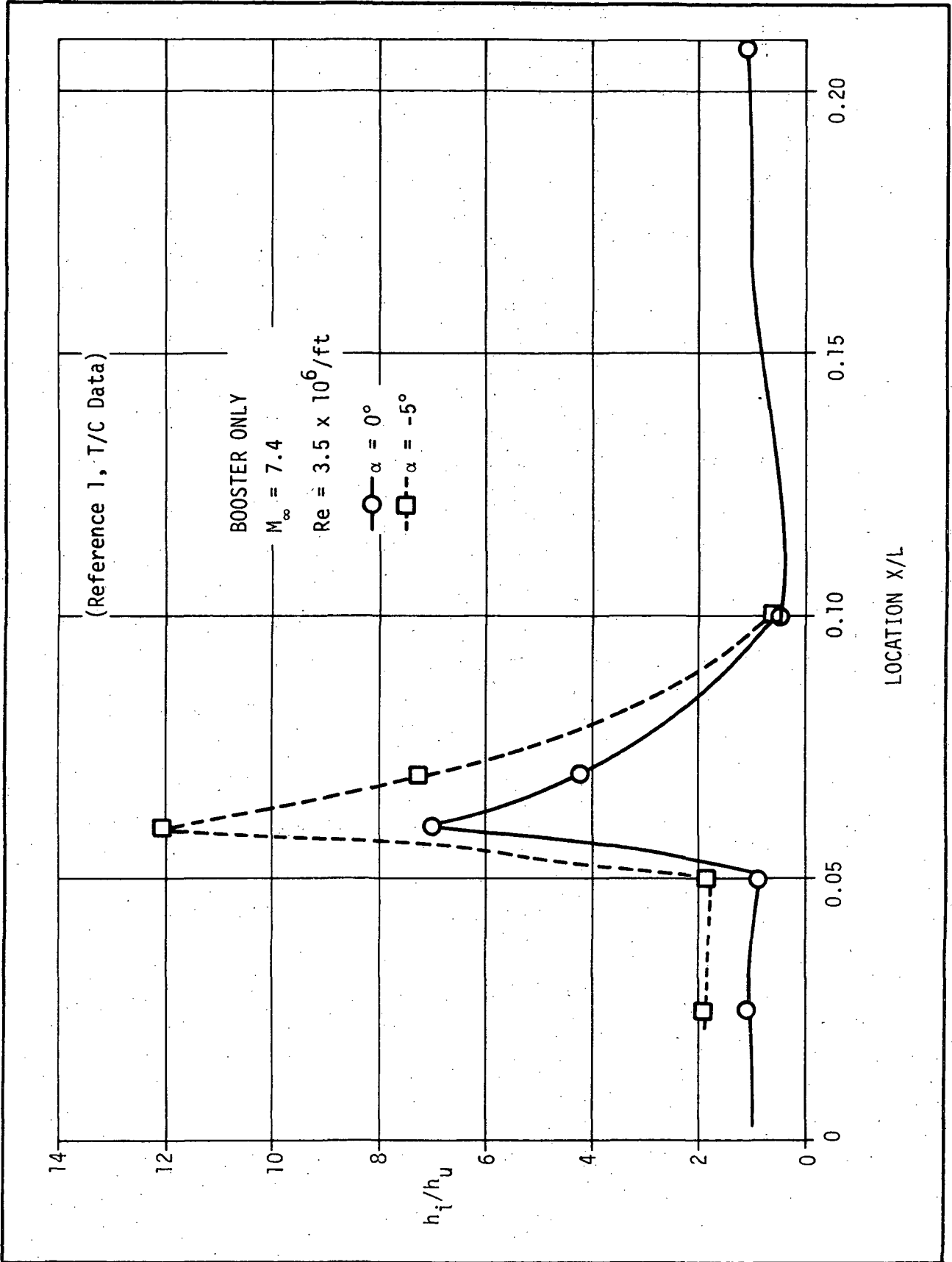


Figure 8. INTERFERENCE HEATING DISTRIBUTION ON BOOSTER CANOPY CENTERLINE (AREA (A))

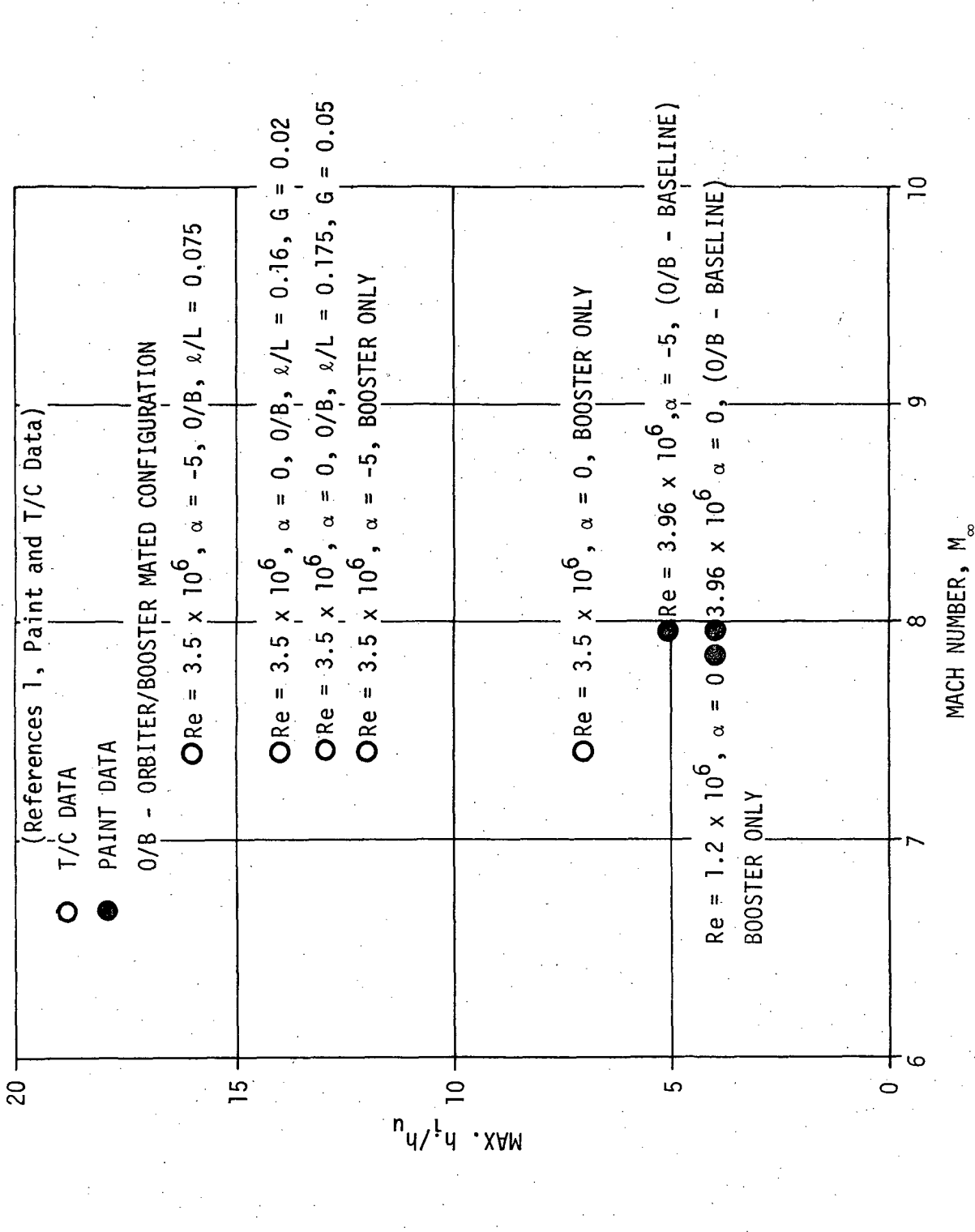


Figure 9. BOOSTER CANOPY CENTERLINE MAX. INTERFERENCE HEATING (AREA(A))

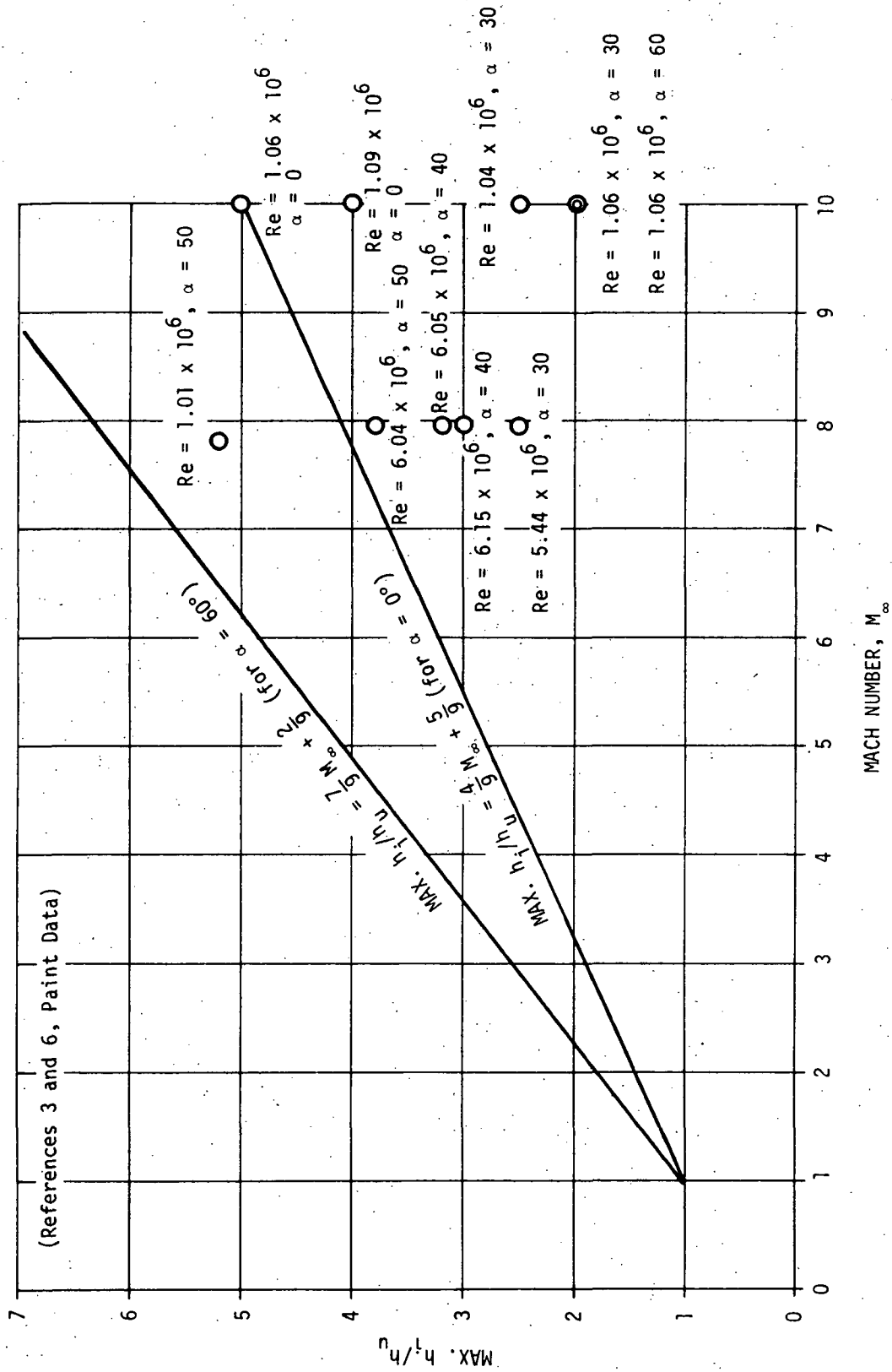


Figure 10. FUSELAGE HEATING DUE TO WING SHOCK INTERFERENCE (AREA (B))

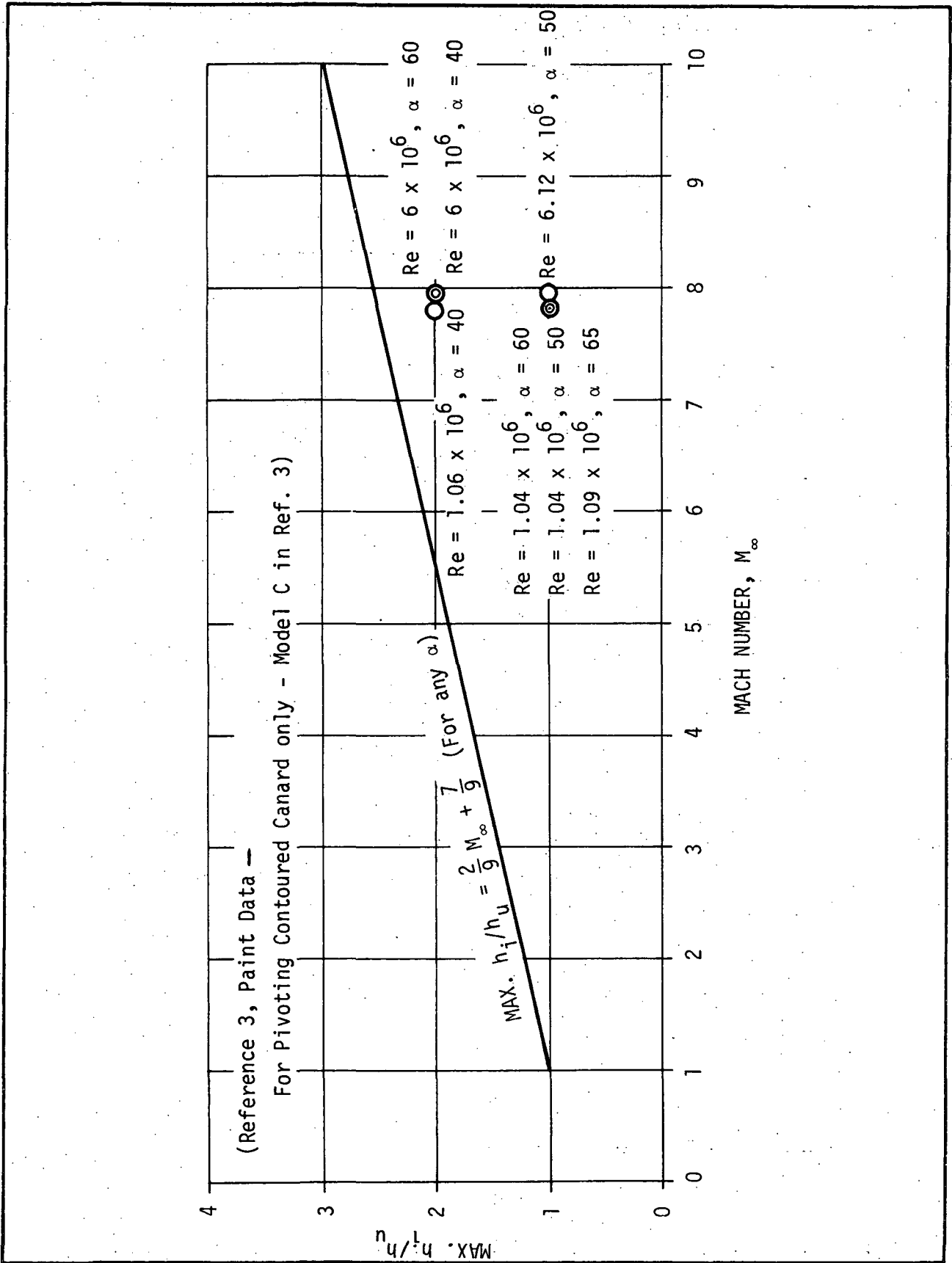


Figure 11. FUSELAGE HEATING DUE TO CANARD SHOCK INTERFERENCE (AREA (C))

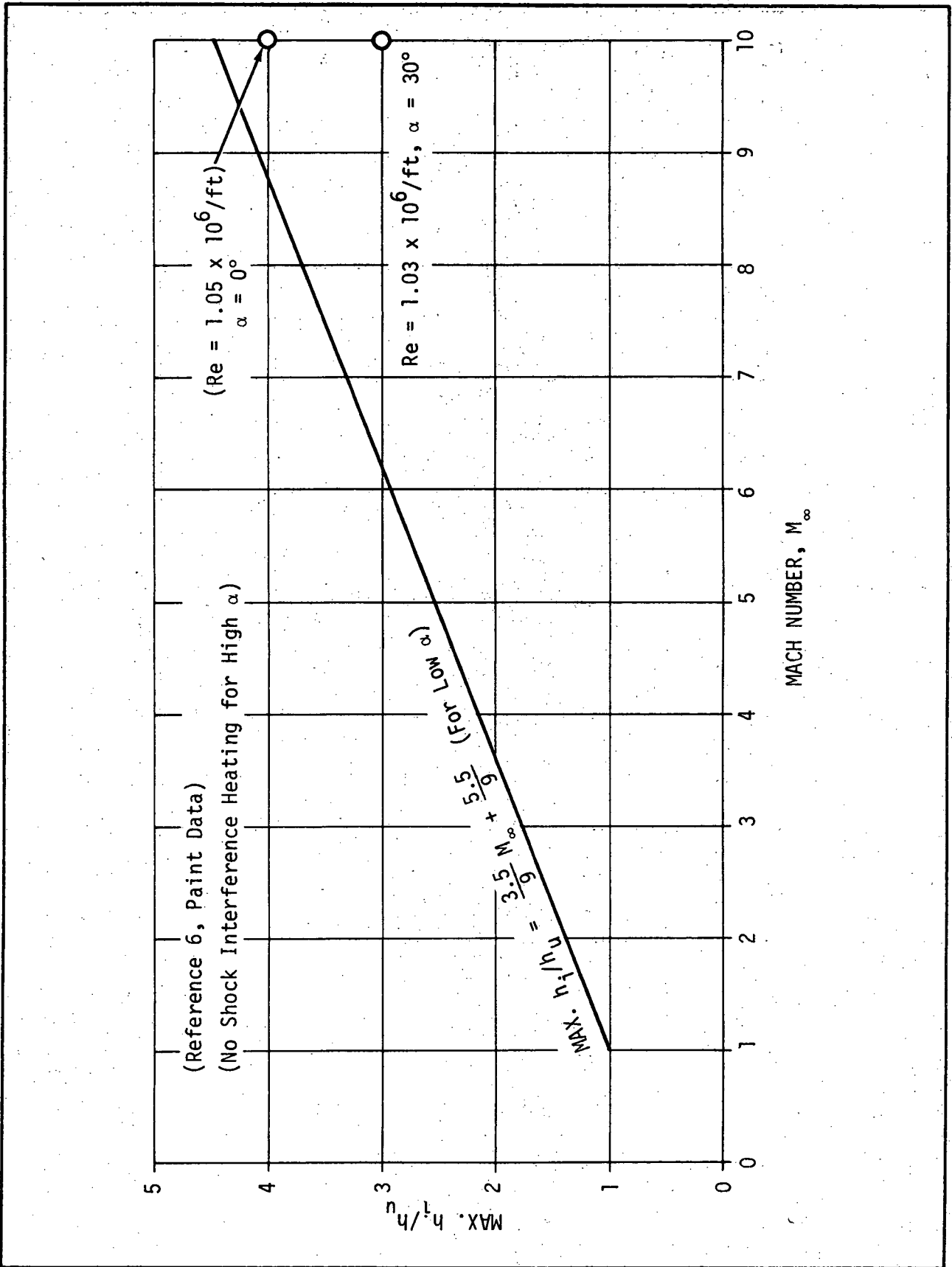


Figure 12. FUSELAGE HEATING DUE TO FIN SHOCK INTERFERENCE (AREA (D))

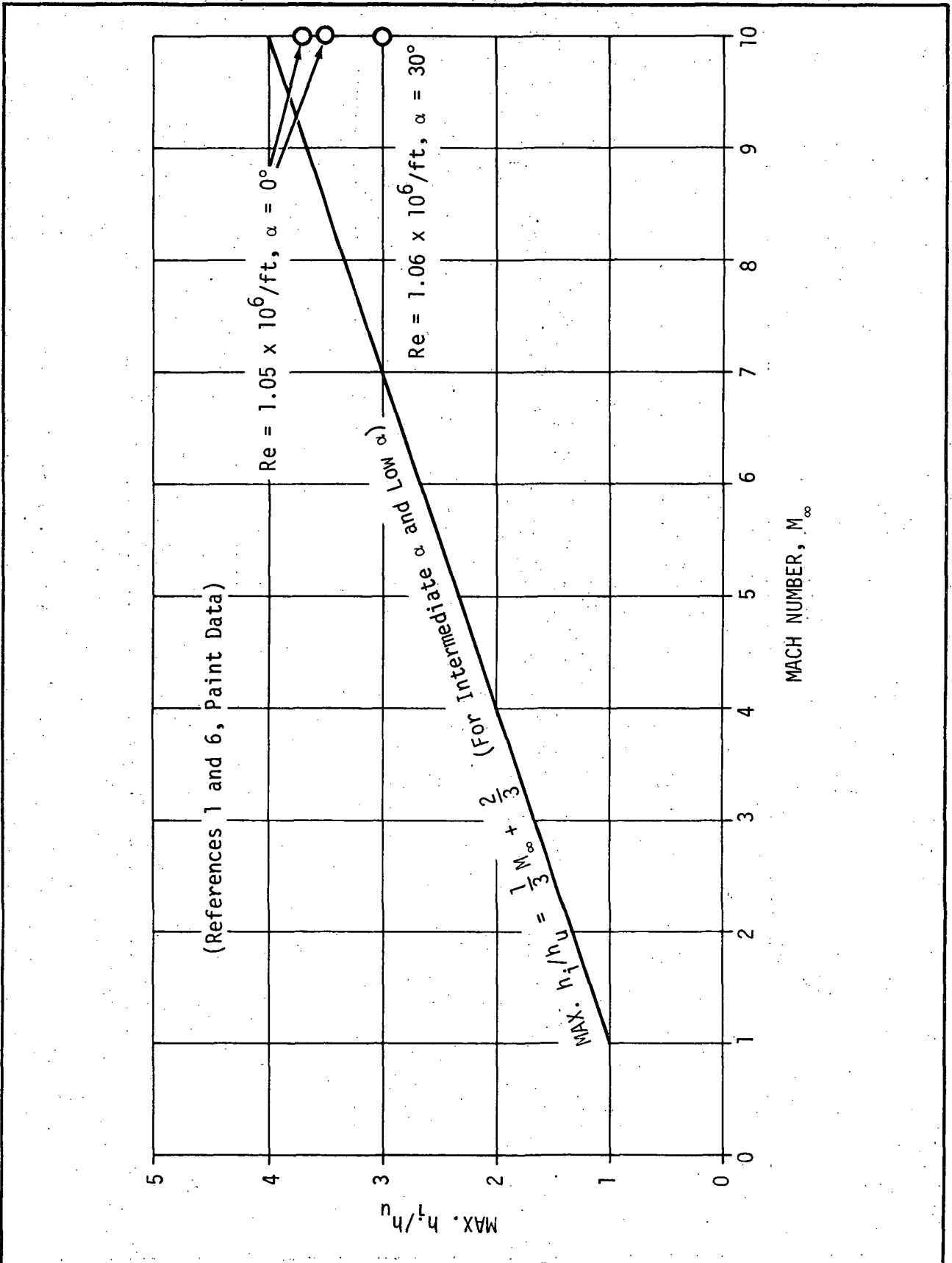


Figure 13. WING HEATING DUE TO FUSELAGE SHOCK INTERFERENCE (AREA (E))

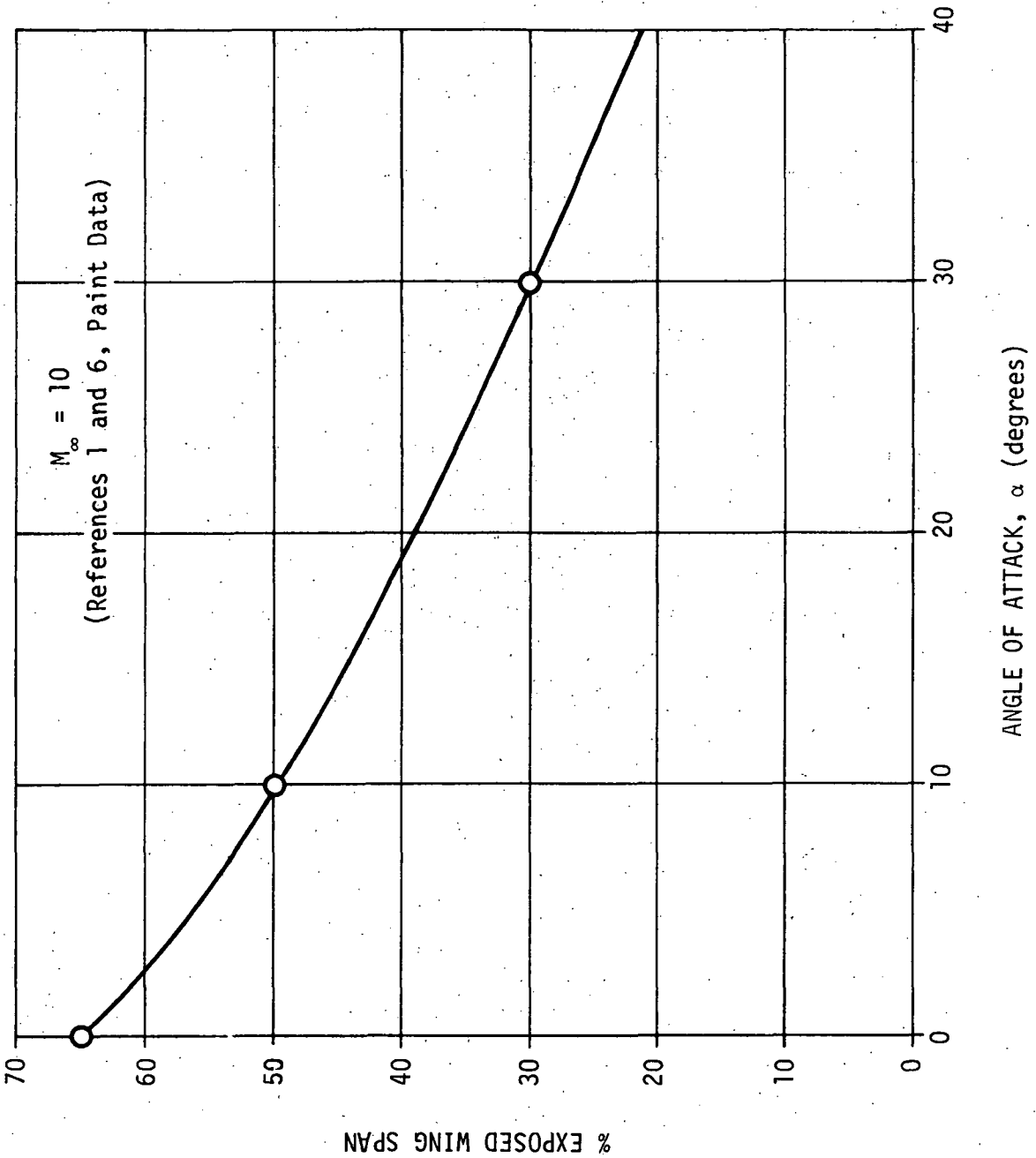


Figure 14. SHOCK IMPINGEMENT POINT ON BOOSTER WING (AREA (E))

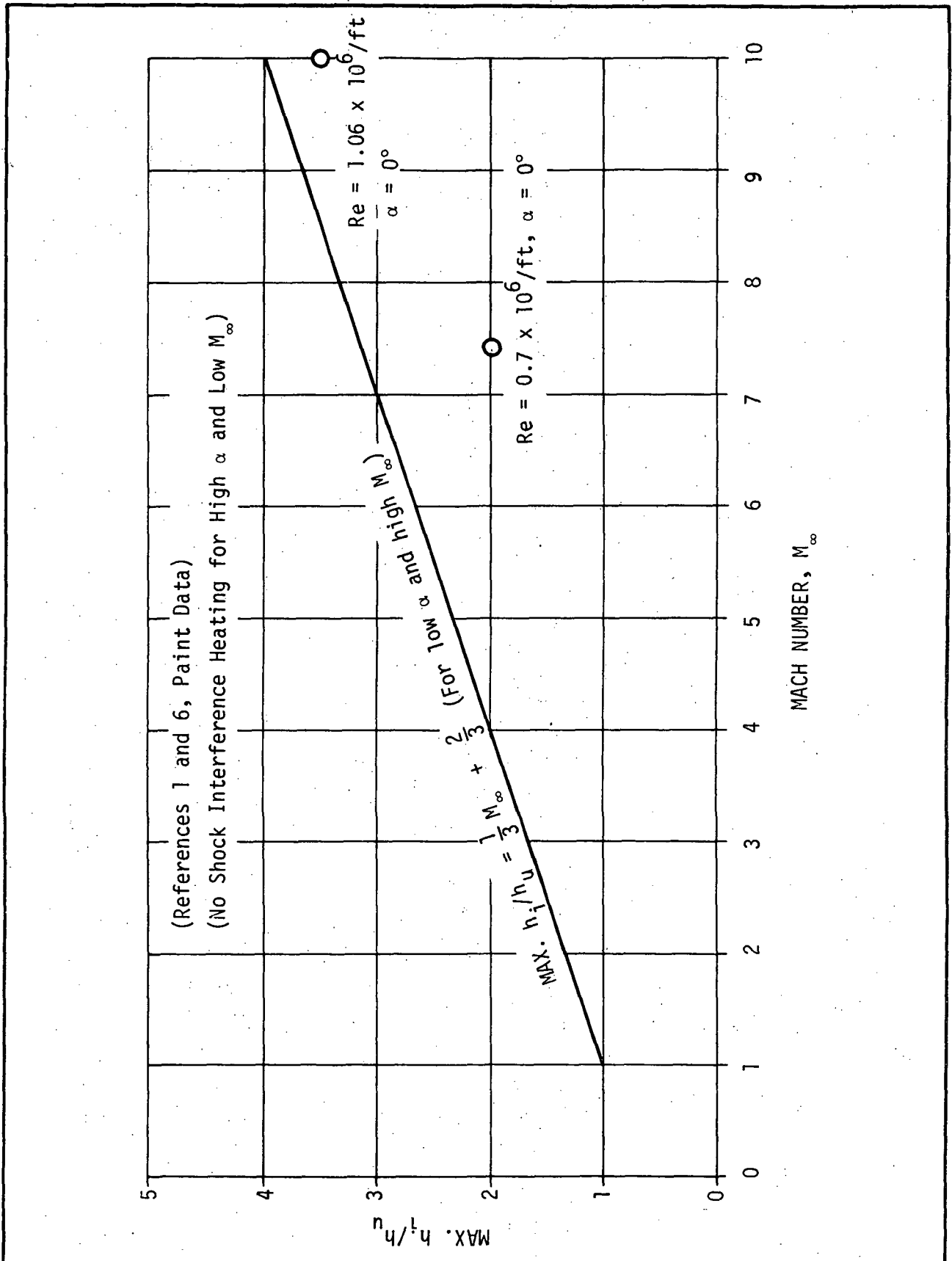


Figure 15. FIN HEATING DUE TO FUSELAGE SHOCK INTERFERENCE (AREA(F))

Distribution:

NASA/MSFC

H. B. Wilson (3)
J. A. Forney
J. D. Warmbrod

Northrop

W. W. Youngblood
D. O. Barnett
J. A. Roux
J. Y. Parker
F. T. Hung (3)
7946, File

ADDENDUM

Part of the GDC orbiter/booster T/C model test results (AEDC-Tunnel B) have been analyzed. The high quality orbiter/booster gap interference heating factors were reduced and presented in Figures 1A - 3A. The heating peaks from these figures should be used to update the data in Figure 2 of the original memorandum.

The AEDC test data used in this study is from AEDC-ARO Test Data Book, "NASA Space Shuttle Heating Test - GDC Booster - NAR Orbiter Mated (0.009 scale)."

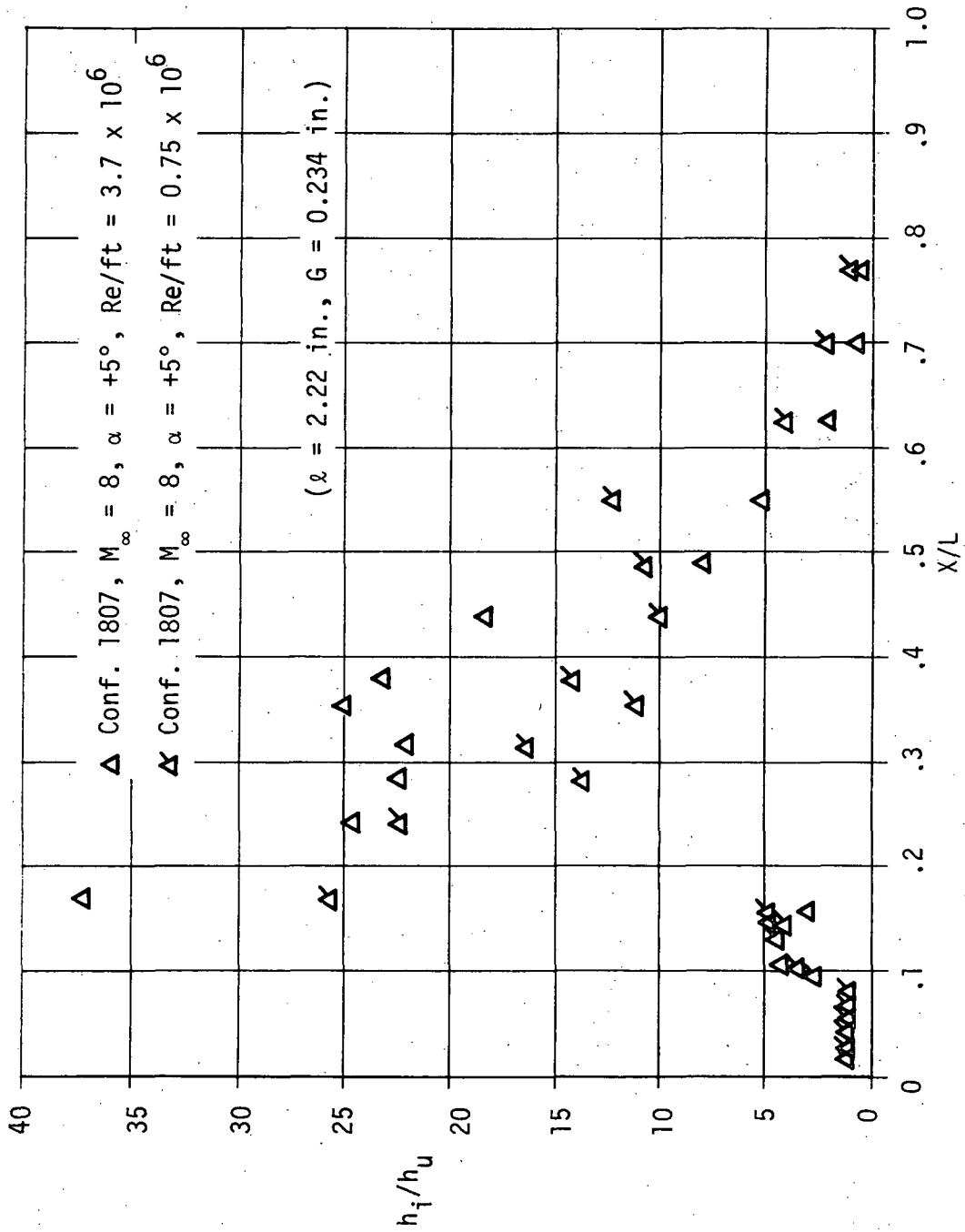


Figure 1A. EFFECT OF REYNOLDS NUMBER ON BOOSTER UPPER SURFACE CENTERLINE INTERFERENCE HEATING

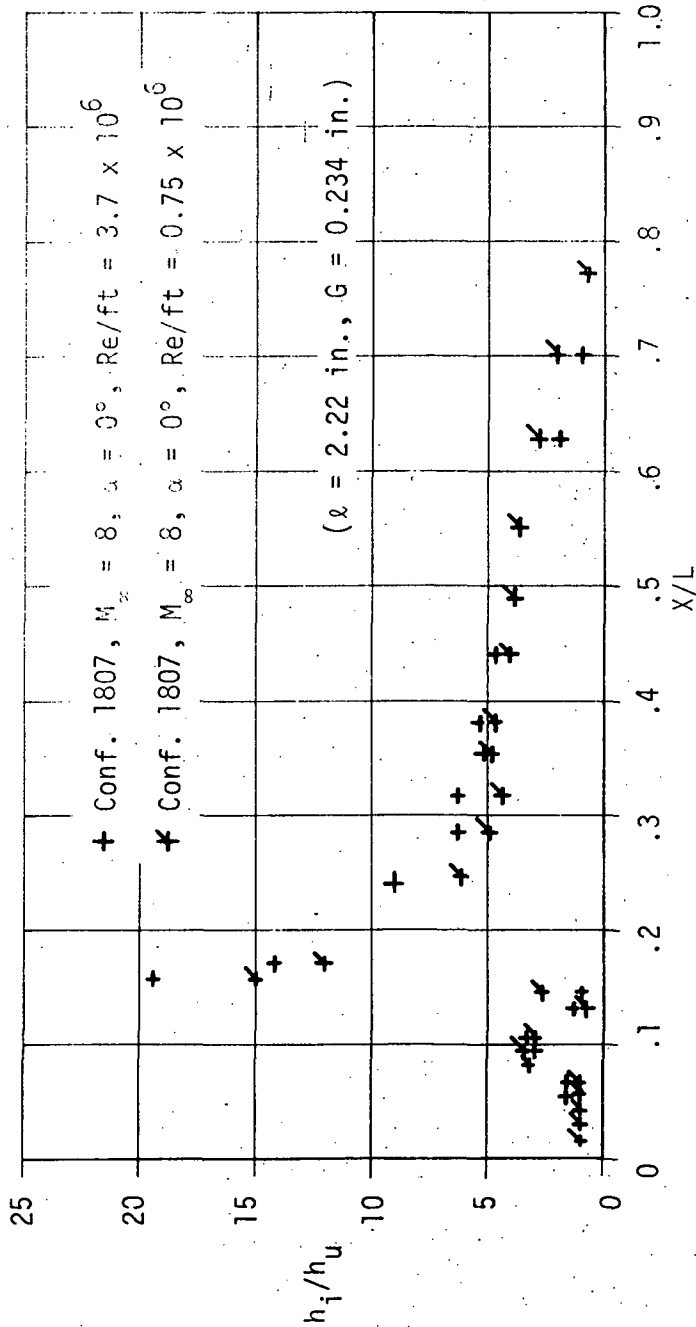


Figure 2A. EFFECT OF FREE-STREAM REYNOLDS NUMBER ON BOOSTER UPPER SURFACE CENTERLINE INTERFERENCE HEATING

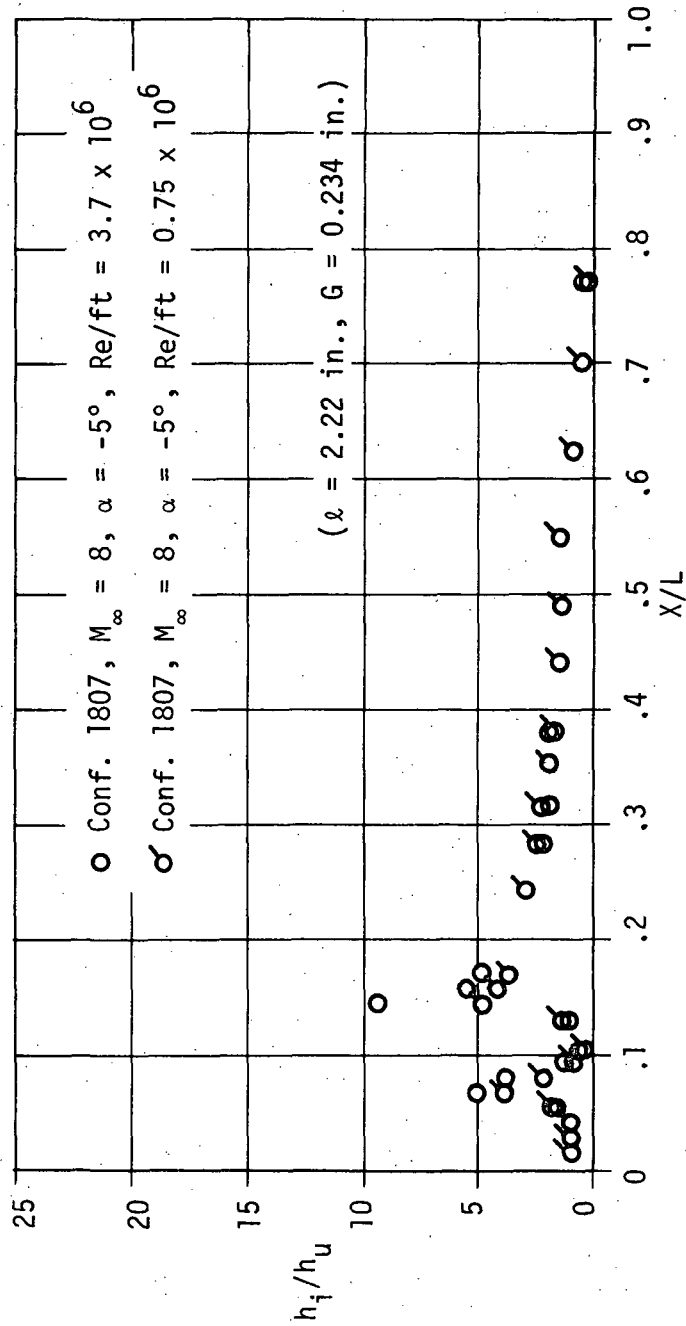


FIGURE 3A. EFFECT OF FREE-STREAM REYNOLDS NUMBER ON BOOSTER UPPER SURFACE CENTERLINE INTERFERENCE HEATING

Appendix B

HEATING TESTS

REMTECH Inc.
1744 Oxmoor Road
Birmingham, Alabama 35209

RTR 003-1

D R A F T C O P Y

SPACE SHUTTLE ASCENT
AERODYNAMIC HEATING TESTS

Final Report
on
Subcontract 510-41028

1 December 1971

Prepared for

Northrop Services Inc.
6025 Technology Drive
Huntsville, Alabama 35805

Prepared by

John E. Reardon and Gordon B. McKay

FOREWORD

This work was prepared under subcontract for Northrop Services Incorporated as a portion of the research under Marshall Space Flight Center Contract NAS8-26268. Additional work under the subcontract on a base thermal environment review is reported in REMTECH Report RTR 003-2.

TABLE OF CONTENTS

FOREWORD	ii
NOMENCLATURE	iv
INTRODUCTION AND SUMMARY	1
MODEL DESCRIPTION	2
M=6 TEST PROGRAM	6
M=10 TEST PROGRAM	10
SUPERSONIC TEST PROGRAM	14
DATA REDUCTION EVALUATION	20
CONCLUSIONS AND RECOMMENDATIONS	22
REFERENCES	23

NOMENCLATURE

Symbol

- a Cylinder or sphere radius or slab thickness
- c Specific heat
- h Heat transfer coefficient
- k Thermal conductivity
- q Heat transfer rate per unit area
- r Recovery factor-see T_R
- T_e Equilibrium wall temperature
- T_i Initial model temperature at $\tau = 0$
- T_0 Stagnation temperature
- T_R Adiabatic wall temperature, $T_R = T_\infty + r(T_0 - T_\infty)$
- T_w Wall temperature
- T_∞ Free-stream static temperature

- α Thermal diffusivity or angle of attack
- β Angle of yaw
- δ Model skin thickness
- ρ Model skin density
- τ Time
- θ Fourier modulus, $\alpha\tau/a^2$

INTRODUCTION AND SUMMARY

A test program was planned and conducted for ascent heating tests on a 0.0065 scale thin-skin model of the MDAC 256-20 space shuttle booster mated with a Stycast model of the MDAC Internal Tank Orbiter. The test work included review of test facility characteristics and data reduction methods, coordination of the model fabrication and verification of the model stress analysis, liaison on model installation problems, preparation of test plans, and monitoring of the tests when they were conducted. This report presents a description of the models and a review of the test facilities, test conditions, and data reduction methods. In addition, the results of a brief study of possible errors in data reduction for phase-change models are summarized.

The general performance of the model was satisfactory throughout the test program, but difficulties in model adjustments during configuration changes impeded testing somewhat. Tests were made in three facilities at the NASA Langley Research Center (LRC): the 20-inch $M=6$ tunnel, the 31-inch $M=10$ tunnel, and the 48-inch Unitary Plan Tunnel ($M=2.3$ and 3.7). The model configurations and test conditions are summarized in Table 1.

The results of phase-change data reduction evaluation indicated possible errors in treating cylindrical and spherical sections as semi-infinite slabs, but the restrictions required in the analysis limit the application of the results.

MODEL DESCRIPTION

The test model consisted of a 0.0065 scale thin-skin model of the MDAC 256-20 space shuttle booster with provisions for mounting a Stycast model of the MDAC internal tank orbiter to simulate the mated ascent configuration. The nominal launch configuration is illustrated in Figure 1 with the orbiter nose 1.1 inches aft of the booster nose ($\Delta X = -1.1$) and no gap between the booster and orbiter ($\Delta Y = 0$). The orbiter sting adjustment allows a fore and aft movement of +5 or -1 inches from the nominal position and shims were provided for the orbiter sting splice to allow the minimum gap between the booster and orbiter to be increased to 0.0325 or 0.065 inches (5 or 10 inches full scale).

The booster was designed and manufactured by Ellico Engineering Company. It was machined from Armco 17-4 PH stainless steel which was heat treated to the H-900 condition before final finishing. The model was designed for a safety factor of 4 based on yield at 300F for the tunnel conditions and angle of attack range shown in Figures 2 and 3.

A skin thickness of approximately 0.030 inches was maintained over most of the left half of the fuselage where the thermocouple instrumentation was concentrated while the right half was kept heavy to provide strength. The canard was also instrumented on the left side, but the wing and fin instrumentation was split between the right and left wing to provide clearance for the thermocouple wiring. Due to the limited thickness of the fins, it was not possible to provide a thin-skin thermocouple installation with a metal cover. Therefore, the fin thermocouples were installed on the interior of the thin-skin surface to be instrumented and the area around the wires was filled with Sauereisen* No. 31 cement contoured to approximate the required airfoil shape.

A total of 217 iron-constantan thermocouples were installed in area

* Sauereisen Cements Co.-Wesrep Corp., Factory Representatives, 369 South Robertson Blvd., Beverly Hills, Calif., 90211, Phone (213) 655-9784

groupings as follows:

Orbiter/booster interference	47
Canard/fuselage interference	44
Wing/fuselage interference	19
Canard	25
Wing	39
Lower fuselage	26

In addition to the thermocouples, ten surface pressure ports were located on the upper forward fuselage.

The thermocouples were formed by spot welding 30 gage (0.010 inch diameter) thermocouple wires to the inside surface of the model skin. When installing the wires, a space of approximately 0.03 inches was maintained between the wires to assure that the wires made a good joint with the skin. The thermocouple bundle was routed out of the model base and leads 35 feet long were supplied to satisfy installation requirements at all anticipated test facilities. Initially the thermocouples were wired into 19 24-pin plugs with copper pins which were required by the LRC 20-inch M=6 Tunnel. These plugs were also used at the LRC 31-inch M=10 tunnel, but they were removed for supersonic tests in the Unitary Plan Tunnel and replaced with 24 pin plugs using iron and constantan pins. The plug wiring sequence which is used in the test descriptions is listed in Table 2, and the location of all thermocouples and the local skin thicknesses are listed in Table 3.

The pressure tubing was 0.0625 O.D. x 0.006 wall stainless steel which was silver brazed in position and routed out through the model base with the thermocouple wire. In order to prevent interference with the thermocouples, the first seven pressure ports were located 0.2 inches to the right of the top fuselage centerline at stations between the thermocouples. The locations of the pressure ports are listed in Table 4.

The Stycast (castable plastic) orbiter models were manufactured by the Lockheed Huntsville Research and Engineering Center. Three models were

provided: one with a tape grid to use for dimensional reference pictures, and two with thermocouples installed for use as test models. The test models each had two chromel-alumel thermocouples installed approximately 1/8 inch below the model surface near the upper and lower fuselage surfaces to indicate the initial model temperature before testing.

When the orbiter was mounted with the booster, it was not possible to maintain the exact gap (ΔY) listed in the test summary of Table 1. In the initial tests in the 20-inch M=6 tunnel, it was necessary to cement spacers on the top of the booster (at X=7.40) where it was locally reinforced, so that model bounce caused by the high injection accelerations would not damage the thin-skin sections. Because of this, the nominal zero gap was a minimum of 0.002 inches which was the spacer shim thickness. However, difficulty in installing the orbiter generally caused larger gaps as listed in the individual test descriptions, but an attempt was made to keep the nominal zero gap less than 0.0065 inches (1 inch full scale). Since this precedent was set in the initial test, it was continued through the remaining tests although no spacers were cemented to the top of the booster.

The overall operation of the model was satisfactory, but difficulties were encountered in assembly of the mated configuration which should be avoided in future models. The cause of the difficulties in order of importance were: (1) variations in orbiter/sting alignment, (2) poor orbiter sting splice design, and (3) inconvenient booster sting splice design.

In the process of molding the orbiters, the sting shifted from its design position, and the amount of the shift varied slightly with each of the three models. The angle of the orbiter sting splice was changed by machining the mating portion of the sting in an attempt to account for the sting shift, but the variation between orbiters still required shimming to produce the

desired fit.

The orbiter sting splice design was difficult to work with because there was no positive method of assuring alignment in yaw, and the screws were so close together that significant pitch changes could occur while tightening the joint on several thicknesses of shim material. Approximately 1/2 inch of yaw movement was possible at the orbiter nose before tightening the splice screws, so the booster and orbiter were aligned by eye after each configuration change before tightening the joint.

The splice between the two sections of booster sting was held together by either a plain splice plate (for booster alone tests) or by the orbiter sting mount. The splice design provided tight fitting dowels to give positive booster alignment, but it was inconvenient to try to support the booster without damaging the instrumentation bundle while the splice plate was changed to either install or remove the orbiter sting mount. In future designs of this type it would be desirable to allow removal of the orbiter sting mount without disturbing the booster sting continuity.

M=6 TEST PROGRAM

The M=6 test program was conducted in the LRC 20-inch Mach 6 Tunnel from September 1 thru 13, 1971. During this period seven shifts of testing were accomplished with 55 test runs completed. The facility, test conditions, and data reduction methods for this test will be described in this section.

Facility

The LRC 20-inch Mach 6 Tunnel is a blowdown type using air from a 600 psi tank field which is heated by electrical resistance heaters to obtain the range of test conditions shown in Figure 4. The test Mach number is achieved with a fixed geometry two-dimensional contour nozzle with parallel side walls. The throat is 0.339 x 20.0 inches and the test section 89.4 inches downstream of the throat is 20.5 x 20.0 inches. The shuttle model was installed with the booster centerline on the centerline of the test section with the orbiter in the upper half of the tunnel. Previous surveys of the test section for the pressure range used in this test have indicated that the uniform test core is approximately 6.8 x 10 inches at the booster nose increasing to a minimum of 12 x 13 inches near the tail. Therefore, the model was assumed to be essentially outside of the tunnel boundary layer (with the possible exception of the orbiter and booster vertical fin tips) at all test conditions.

The model was mounted on a bottom injection system which held the model in a chamber under the tunnel for approximately 30 seconds until the desired tunnel operating condition was achieved. Although the chamber was not isolated from the test section by a door, there were no apparent temperature effects due to hot air circulation from the tunnel into the chamber around the model. For heat transfer tests, the injection system is set to move the model the last 9.8 inches from near the tunnel wall to the centerline in less than 0.3 seconds with a maximum acceleration of 6G.

Data on 99 analog channels plus run and configuration coding on seven digital channels are sent to a central LRC data processing system where the data are digitized and converted to engineering units for data reduction. Since 6 of the analog channels are required for tunnel operating data, only 93 channels are usable for model data, so the model data was recorded in parts with complete data obtained only for the booster and nominal mated configuration.

Test Conditions

Three Reynolds Numbers were selected for the test. The two lower values (1.27 and 5.72 million per foot) were selected to agree with tests of a 0.011 scale model of the same configuration at AEDC (M=8) while the maximum value (8 million per foot) was selected to provide high Reynolds Number data. Most of the tests were conducted at the intermediate Reynolds Number since the operational problems at the extreme values would have reduced the run frequency. The approximate tunnel stagnation conditions at each Reynolds Number are tabulated below.

Re/Ft x 10 ⁻⁶	Stagnation Pressure-psia	Stagnation Temperature - °F
1.27	75	450
5.72	325	400
8	460	400

Tests were made with the booster and orbiter alone as well as the mated configuration so the effects of interference heating in the mated configuration could be evaluated. A complete tabulation of the various configurations and test conditions are presented in Table 5. All planned test conditions (ref.1) in Run Series 1, 4, and 6 were completed with the exception of the low Reynolds Number runs on the orbiter and on the booster and mated configurations with instrumentation group 3(wing data). Run Series 2 was reduced due to the time required to prepare the model for oil flow patterns and photograph the results. Run Series 3 was reduced to half of the planned runs by only using one phase change temperature at each test condition. In Run Series 5, tests at the intermediate Reynolds

Number with $\Delta Y=0.065$ and 0.0325 were omitted.

Six runs were added to Run Series 1. Five to investigate canard heating and one angle of attack run accidentally made at the wrong Reynolds Number. In the five runs to investigate canard heating the model was rolled so the bow shock impingement on the canard would be visible on the Schlieren photographs. Then the model was yawed in an attempt to move the shock impingement across an instrument station on the canard so the peak interference heating could be evaluated. Unfortunately the bow shock position was not very sensitive to yaw and not much movement occurred. Further evaluation of the test results will be necessary to determine if the desired effect was achieved.

Data Reduction

The data reduction performed by LRC on this test consisted of two steps. First, appropriate calibration factors were applied to convert the electrical temperature and pressure signals to engineering units, and second, the temperature time results were reduced to give heat transfer coefficients. The reduction to engineering units and the computation of standard dimensionless parameters are relatively straightforward and require no explanation. However, the methods used in determining the heat transfer coefficients are pertinent to the evaluation of the results and will be described.

The data recording system digitized the temperature of each thermocouple at a rate of 10/sec. throughout each test run. Zero time for starting the data reduction procedure was determined by the model injection marker output (on data channel 8). Normally the injection marker reads about 4000 counts at the bottom limit and jumps to about 8000 counts when the model is approximately on the tunnel centerline. Unfortunately the injection marker did not work normally on all of the tests, so the tunnel test engineer selected the times to be used as zero based on his evaluation of the injection marker indication.

Using the zero time input for each test, the data reduction computer program takes the first 20 points (1.9 seconds of data) and makes a least squares curve fit of a second degree polynomial to the points. This gives an equation of the form

$$T_w = A + B\tau + C\tau^2 \quad (1)$$

where τ is measured from the zero time.

The normal assumptions are made that there is negligible internal resistance in the thin skin, that there is no heat transfer to surrounding points by lateral conduction, and that there is negligible heat loss to the interior of the model and thermocouple wire. With these assumptions, the heat gain by the skin is equal to the heating rate on the exterior of the model.

$$q = \delta\rho c(dT/d\tau) \quad (2)$$

In reducing the data, δ was taken as the actual skin thickness listed in Table 3, while ρ and c were assumed to be 488 lbm/ft³ and 0.11 Btu/lbm-R.

Equations (1) and (2) can be substituted in the definition of heat transfer coefficient

$$h = q/(T_R - T_w) \quad (3)$$

to yield

$$h = \delta\rho c(B + 2C\tau)/(T_R - T_w) \quad (4)$$

In the data reduction, equation (4) was evaluated for each of the twenty times used in fitting the curve. Each of these twenty points is listed in the tabulated results for review, and a summary table is prepared listing only the heat transfer coefficient at zero time when errors due to lateral conduction and other losses should be a minimum.

Since the adiabatic wall temperature varies over the model, the data reduction program allows the selection of two recovery factors. The two selected for this test correspond to laminar and turbulent values (0.847 and 0.895), and the adiabatic wall temperature is computed based on the undisturbed free stream conditions.

M=10 TEST PROGRAM

The test program at the LRC 31-inch Mach 10 Tunnel was conducted from October 7 thru 13, 1971. During this time the tunnel was operated four shifts and 32 test runs were made. Descriptions of the facility, test conditions, and data reduction methods will be presented in this section.

Facility

The LRC 31-inch Mach 10 Tunnel can be operated either as a continuous flow or blow down tunnel. The test section and nozzle are both square. A uniform test core approximately 12 x 12 inches is available for the test conditions used, so only the model fin tips would be in the tunnel boundary layer.

The model is injected from a chamber on the right side of the test section. A door is provided to protect the model from the hot gas prior to injection and cooling air jets are directed on the model to cool it between runs. Since the model is not accessible while it is in the injection chamber, no configuration changes can be made between runs, but angles of attack and yaw can be remotely adjusted. When the tunnel is used with the injection system, no schlieren pictures can be made.

In the injection sequence the protective door is retracted 1 to 2 seconds before model injection. The injection requires approximately 1 second, but the time from the model entering the tunnel ^{until} it is on the centerline is only about 0.5 seconds.

A special model support strut was designed and built by MSFC in order to move the model far enough back in the test section so it would clear the injection opening. There was little clearance allowable on the model length and a slight error in the design of the support strut made the resulting nose clearance very small. Because of this, the model could not be run with the orbiter nose forward of the booster nose. In addition, since yawing the model to

the right tends to move the nose forward, the right yaw angle was limited to 1° .

The data recording system is similar to that described previously for the Mach 6 test, but the Mach 10 tunnel is not configured to handle iron-constantan thermocouples. Because of this, auxiliary cold junction reference boxes were brought in and put next to the tunnel. The temperature of the cold junctions in the boxes was approximately room temperature and was indicated by a thermometer which was recorded before each run.

Test Conditions

The allowable tunnel pressure was limited below the facility capability to minimize maintenance problems, so the minimum unit Reynolds Number of $1.27 \times 10^6/\text{ft.}$ used in the Mach 6 test could not be obtained. The tunnel was run at the maximum allowable stagnation pressure of 750 psia which produced a unit Reynolds Number of $10^6/\text{ft.}$ with a stagnation temperature of approximately 1360 F.

Due to tunnel occupancy limitations, no data were obtained on the orbiter alone, but runs were made with the booster alone and the mated configuration. A summary of all the test conditions is presented in Table 6. All the planned test conditions (ref. 2) of Run Series 1 and 4 were completed with the exception of the runs at a unit Reynolds Number of $1.27 \times 10^6/\text{ft.}$, and two yawed runs were added to improve canard and wing shock impingement definition. Run Series 2 was planned for oil flow studies, but was eliminated because of time limitations. Run Series 3 was shortened by reducing the number of phase change temperatures used at the $\pm 5^\circ$ angles of attack, but one run was added with the model rolled to try to identify shock impingement locations on the canard and wing. In Run Series 5, the high Reynolds Number run ($1.27 \times 10^6/\text{ft.}$) with a gap ($\Delta Y=0.065$) was omitted because of the tunnel operating limitation and the runs with $\Delta X=1.1$ were eliminated because of the model clearance problems. Three runs were substituted for the planned runs with $\Delta X=1.1$ in which the orbiter was moved in 0.1 inch

increments around the nominal location of -1.1 inches. The purpose of these tests was to move the orbiter/booster shock positions relative to the thermocouple locations to assure that the peak interference heating rate would be recorded.

Normal test duration was set at 5 seconds to prevent model damage, but this was extended to 8 seconds when pressures were being recorded to provide more time for them to stabilize. However, when the orbiter was in the $\Delta X=0$ position the 8 second run time allowed the orbiter lower surface to be badly scorched and a slight crack developed, so the time was reduced for the remaining runs of this configuration. The run times appeared to be sufficient for the pressures in the interference region between the orbiter and the booster to stabilize, but the pressures were not always steady and often appeared to change significantly during the run. It has been proposed that the changes are caused by the effects of increasing wall temperature on the boundary layers and this should be considered during the data evaluation.

Data Reduction

The data reduction procedure used for the Mach 10 test was similar to that used for the Mach 6 tests with slight variations in timing, recovery factors, and material properties. The data system digitized the data at the rate of 20/sec. and two least squares second degree curve fits of the temperature data were made starting at 0 time and at 0.5 seconds. As in the Mach 6 test, there was some question as to the accuracy of the injection marker indication of the zero time, so the test engineer selected the zero time frame for each test by evaluating the rate of change of temperature at a point with a high heating rate.

The heat transfer coefficient was evaluated at the beginning of each curve fit (0 and 0.5 second) using equation 4. These values were tabulated

REMTECH INCORPORATED

and a summary table was prepared for all thermocouples listing the data evaluated at zero time. The constants used in equation 4 were slightly different from those used for the Mach 6 test. The skin density was taken to be 485 lbm/ft³ and the specific heat was represented by the

$$c = 0.10734 + 0.000056T$$

where T is in degrees F. Since turbulent flow was not expected in this test, the turbulent recovery factor was omitted and the values chosen corresponded to the laminar value of 0.84 and unity.

SUPERSONIC TEST PROGRAM

The supersonic test program was conducted at the LRC Unitary Plan Tunnel from November 15, thru 23, 1971, but the model was reinstalled December 3 to repeat booster schlieren photographs. During the tests in November, 24 heat transfer and 22 schlieren runs were made. The high speed test cell was used for all tests to obtain data at Mach Numbers of 2.3 and 3.7. Heat transfer tests outside of this range are not feasible although the tunnel has a much wider operating range. The test facility, test conditions, and data reduction methods will be described in this section.

Facility

The LRC Unitary Plan Tunnel (UPT) is a continuous-flow facility with two supersonic test cells 4 feet square and 7 feet long. The lower speed test cell (No.1) covers the range of Mach Numbers from 1.47 to 2.86 while the high speed test cell (No.2) is used for Mach 2.29 to 4.63. However, only the high speed test cell can be used for heat transfer tests, and most satisfactory operation is achieved if the Mach number is limited to the 2.3 to 3.7 range.

The model remains in the tunnel at all times and the heat pulse used for heat transfer tests is achieved by by-passing the tunnel coolers. This causes a temperature increase from approximately 135 F to 250 F in a period of less than 5 seconds. Due to the rapid heating of the test section during heat transfer tests, the large windows in the test section walls are replaced with steel doors to prevent thermal stress cracks in the glass, so separate runs must be made to obtain heat transfer data and schlieren or shadowgraph pictures.

Data recording at the UPT is similar to the other tunnels except that more data can be recorded. Temperatures can be recorded on 199 channels (197 from the model and 2 stagnation probes) which are connected to the LRC central

data processing system, while pressures are recorded and punched on computer cards at the tunnel. The tunnel uses a special connector for the thermocouple wires which has iron and constantan pins to prevent a dissimilar metal junction in the thermocouple circuit. Since all the model plugs were removed from the model so it could be rewired for the facility, 20 thermocouples were eliminated to reduce the number to be recorded to the limit of 197. Some of the thermocouples deleted were inoperative or questionable in the Mach 10 test and are noted in the list of thermocouples omitted in Table 7.

Test Conditions

Most of the tests were conducted at a unit Reynolds Number of $3.5 \times 10^6/\text{ft}$ with boundary layer trips cemented 1.1 inches aft of the model noses, but a few runs were also made at $1.27 \times 10^6/\text{ft}$ and $5.5 \times 10^6/\text{ft}$ without trips so Mach Number effects could be evaluated by comparison with Mach 6 results. The approximate tunnel stagnation conditions for the heat transfer runs were as follows:

<u>Mach No.</u>	<u>Stagnation Pressure - psia</u>	<u>Stagnation Temperature - R</u>	<u>Re/Ft $\times 10^{-6}$</u>
2.3	22.5	700	3.5
3.7	17.3	700	1.27
	47.7	700	3.5
	75.0	700	5.5

Tests were made with the booster alone and with the mated configuration, but no phase change data could be obtained on the orbiter because a model injection system was not available. A tabulation of all the test conditions is presented in Table 8. All tests which were planned (ref.3) were completed with the exception of the low Reynolds Number runs on the booster and nominal mated configuration, and the mated configuration with the orbiter 1.1 inches forward of the booster. Schlieren photographs were not obtained on some of the runs

due to camera difficulties, but after the repeat runs scheduled for December 3, shadowgraphs will be available on all the flow visualization runs (Run Series 2 and 3).

Conduction effects on the model were noted which caused a change in test procedure in order to obtain equilibrium temperatures for use in data reduction. Normally the tunnel is heated by running with the coolers by-passed for approximately 30 minutes. Then the coolers are introduced in the circuit to cool the air and the model for about 20 minutes before they are by-passed again to produce the heat bump. When this procedure was tried initially on the booster, it appeared that the temperatures near the top of the model well aft of the nose were too high after the normal cooling period. It was postulated that this behavior might be caused by conduction from the heated mass of metal on the right side of the model which cooled too slowly. The higher heat transfer coefficients near the model nose could drop the thin skin temperature in spite of conduction from the heavy side of the model while the lower coefficients further back would not cool the thin skin as effectively, so a higher temperature would result from conduction. When the orbiter was installed the temperatures on the top of the model tended to be cooler after the short cooling process due to the higher heat transfer coefficients resulting from the interference between the booster and orbiter, but still the temperature far back under the orbiter would remain high.

Since the equilibrium temperature of the model is necessary in the data reduction procedure, it was decided that the safest policy would be to record equilibrium temperature profiles on the model for each test condition before the coolers were by-passed to heat the tunnel. This caused some delay in the test since all test points were run cold before the tunnel could be heated.

Since the booster runs had been completed before this procedure was used, the booster equilibrium temperatures were recorded during the flow visualization runs on the booster (Run Series 2).

Data Reductions

The data reduction procedure normally used for the UPT is being modified for this test, so the final description of the data reduction procedure will be transmitted to MSFC with the reduced data. The description presented below is based on descriptions of the method previously used and discussions of the probable changes with the LRC test engineer.

Data from the test is digitized at 0.5 second intervals, and the heat transfer coefficient is calculated using an integral method which includes lateral conduction corrections where instrumentation is spaced close enough to allow it.

The data reduction model is derived from the expression

$$h = \delta \rho c (dT_w/d\tau) / (T_e - T_w) \tag{5}$$

where T_e is the equilibrium skin temperature rather than the adiabatic wall temperature. If there is a significant change in recovery factor over a short distance on the model, conduction in the skin under equilibrium conditions could cause T_e to differ slightly from T_R . Equation (5) is integrated numerically using the form

$$h = \frac{\delta \rho c (T_{w,\tau} - T_{w,0})}{(T_e/T_0) \sum_0^t T_0 \Delta\tau - \sum_0^t T_w \Delta\tau} \tag{6}$$

in which the summations are evaluated at 0.5 second intervals according to the trapezoidal rule

$$\sum_0^t T \Delta\tau = (0.5 T_{\tau=0} + 0.5 T_t + T_1 + T_2 + \dots + T_{t-1}) \Delta\tau \tag{7}$$

The temperature T_0 and T_w are both recorded during the test and the ratio T_e/T_0 is determined from the equilibrium temperature run before the test.

If conduction corrections are possible, a term is added to equation (6) to account for the integrated conduction

$$h = \frac{\delta \rho c (T_{w,t} - T_{w,0}) - k \delta \sum_0^t [(\partial^2 T_w / \partial x^2) + (\partial^2 T_w / \partial y^2)] \Delta \tau}{(T_e/T_0) \sum_0^t T_0 \Delta \tau - \sum_0^t T_w \Delta \tau} \quad (8)$$

The wall temperature derivatives are approximated in the data reduction program by

$$(\partial^2 T_w / \partial x^2) = \frac{[(T_{n+1} - T_n) / (x_{n+1} - x_n)] - [(T_n - T_{n-1}) / (x_n - x_{n-1})]}{0.5(x_{n+1} - x_{n-1})} \quad (9)$$

$$(\partial^2 T_w / \partial y^2) = \frac{[(T_{n+1} - T_n) / (y_{n+1} - y_n)] - [(T_n - T_{n-1}) / (y_n - y_{n-1})]}{0.5(y_{n+1} - y_{n-1})} \quad (10)$$

Either the x or y correction may be omitted if it is considered to be unnecessary.

In previous tests, zero time was taken just after the temperature bump had raised the stagnation temperature to the high temperature level, but with the high heat transfer coefficients experienced in interference regions this allowed appreciable skin heating before the data reduction was started. Previous trials at starting the data reduction at the beginning of the temperature bump while the model is still cool have indicated that the quality of the resulting data was improved. Therefore, the zero time for this test will be selected at the beginning of the temperature bump.

The upper limit of integration for equation 8 was formerly determined by an elaborate system of tests designed to select the best probable value of h,

but these tests will be disregarded in the reduction of the data from the current test. The test engineer will select the upper integration limit based on his analysis of the data, and the present indication is that a value of four seconds will be used.

DATA REDUCTION EVALUATION

In the process of planning the ascent heating tests for the space shuttle, data reduction methods used with phase-change models were studied and an attempt was made to define a criteria for accepting or rejecting data taken on portions of models which had a small radius of curvature. Although no straight forward analysis was found, computations were made which might indicate the magnitude of the error.

The approach taken was to attempt to put analytical expressions for heating of cylinders, spheres, and semi-infinite solids into similar forms so relative effects could be evaluated. It was not possible to compare the semi-infinite solid with the dimensioned shapes, so the heating of a slab of thickness "a" with the back side insulated was used. Since the slab surface temperature will behave essentially the same as that of a semi-infinite solid for $(\alpha\tau/a^2) < 0.2$, the analysis is limited to this range.

The case for which comparison of shapes was desired was that for constant heat transfer coefficient and adiabatic wall temperature, but solutions for this case were not found. Therefore, the case of constant heat flux was chosen. This approximates the actual case when the difference between the initial model temperature and the phase change temperature is small compared to the adiabatic wall temperature, but can only be used as an approximate indication of other cases.

The solutions for constant heat flux (ref. 5) were arranged to evaluate the parameter $(T_w - T_i)k/qa$ as a function of θ , where

$$\theta = k\tau/a^2 \quad (11)$$

and a is the radius of the cylinder or sphere or the thickness of the slab. Solutions for the various shapes from ref. 5 were evaluated for the surface temperature, T_w . They are as follows:

Cylinder

$$(T_w - T_i)k/qa = 2\theta + 0.25 - 2 \sum_{n=1}^{\infty} (\exp(-\gamma_n^2 \theta)) / \gamma_n^2 \quad (12)$$

where $\gamma_n, n = 1, 2, \dots$ are the positive roots of

$$J_1(\gamma) = 0$$

Sphere

$$(T_w - T_i)k/qa = 3\theta + 0.2 - 2 \sum_{n=1}^{\infty} (\exp(-\gamma_n^2 \theta)) / \gamma_n^2 \quad (13)$$

where $\gamma_n, n = 1, 2, \dots$ are the positive roots of

$$\tan \gamma = \gamma$$

Slab

$$(T_w - T_i)k/qa = \theta + 1/3 - 2/\pi^2 \sum_{n=1}^{\infty} (\exp(-n^2 \pi^2 \theta)) / n^2 \quad (14)$$

where $n = 1, 2, 3, \dots$

The ratios of equations (12) and (13) to equation (14) were computed and the resulting ratios are presented as a function of θ in Figure 5. These ratios can be interpreted as ratios of temperature difference for equal flux or as ratios of flux which will give the same temperature difference. In application to phase change data reduction, the ratio gives a direct indication of the possible error in the heat transfer coefficient.

The results presented in Figure 5 may be used to estimate experimental errors, but their use should be limited to values of $\theta \leq 0.2$ and $(T_w - T_i)/(T_R - T_i) < 0.2$. Further studies should be made to obtain an indication of errors over a larger range.

CONCLUSIONS AND RECOMMENDATIONS

Most of the objectives of the test were achieved, and if the data quality proves to be satisfactory, the results should be useful in the development of analytical predictions of interference heating on space shuttle configurations. Additional data on configuration variations and more complete oil flow patterns for flow visualization could have been obtained if the model configuration changes could have been made more quickly. In model designs for future tests, careful attention should be given to ease of configuration changes and positive alignment methods to use when setting up the models should be provided.

Additional work would also be useful in perfecting attachment designs which would minimize conduction from the structural parts of the model into the thin-skin. This is particularly important in designs for the Unitary Plan Tunnel. Previous model designs for the UPT used heavy transverse bulkheads which caused non-isothermal wall effects in the flow down the model. Every effort was made to avoid this problem in the present model, but the design appears to suffer from circumferential conduction from the heavy side of the model into the top of the thin skin half. Consideration should be given to using insulating materials to minimize conduction through attachments and to lightening structural members as much as possible to promote rapid temperature changes.

REFERENCES

1. Reardon, J., "Test Program for Ascent Heating Tests of a MDAC Model 256-20 Booster at M=6, REMTECH RM003-2, Aug., 1971.
2. Reardon, J., "Test Program for Ascent Heating Tests of a MDAC Model 256-20 Booster at M=10," REMTECH RM003-3, Sept. 1971.
3. Reardon, J., "Test Program for Ascent Heating Tests of a MDAC Model 256-20 Booster at Mach Numbers of 2.3 and 3.7," REMTECH RM003-4, Oct. 1971.
4. Jones, R. A. and Hunt, J.L., "Use of Fusible Temperature Indicators for Obtaining Quantitative Aerodynamic Heat-Transfer Data," NASA TR-R-230, 1966.
5. Carslaw, H.S., and Jaeger, J.C., CONDUCTION OF HEAT IN SOLIDS. (Oxford: Clarendon Press, 1959)

TABLE 1
TEST CONDITION SUMMARY

Nominal Mach No.	Configuration	$\Delta X/\Delta Y$	Angle of		Approximate Re/Ft $\times 10^{-6}$ **					
			Attack	Yaw	1.0	1.3	3.5	5.5	5.7	8.0
6	Booster	-	-5,0,5	-		X			X	X
	Orbiter Mated	-	0	1,2,3,4					X	X
		-1.1/0	-5,0,5	-					X	X
		-1.1/0.065	-5,0,5	-		X			X	X
		0/0	0	-		X				X
	1.1/0	-5,0,5	-					X		
10	Booster	-	-5,0,5	-	X					
	Mated	-	0	1	X					
		-1.1/0	-5,0,5	-	X					
		-1.1/0.065	0	2	X					
		-1.2/0	0	-	X					
		-1.0/0	0	-	X					
		-0.9/0	0	-	X					
0/0	-5,0,5	-	X							
3.7	Booster	-	-5,0,5	-			X			
	Mated*	-1.1/0	0	-		X		X		
		-1.1/0.065	-5,0,5	-		X		X		
		0/0	0	-			X			
		-5,0,5	-			X				
2.3	Booster	-	-5,0,5	-			X			
	Mated*	-1.1/0	-5,0,5	-			X			
		-1.1/0.065	0	-			X			
		0/0	-5,0,5	-			X			

ΔX is the axial distance between the booster and the orbiter noses and is positive for the orbiter forward of the booster.

ΔY is the minimum vertical gap between the booster and orbiter.

*Data on booster only.

**Runs at Re/Ft = 3.5×10^{-6} were made with boundary layer trips on the booster and orbiter noses.

TABLE 2

INITIAL THERMOCOUPLE WIRING CONFIGURATION

Plug	PINS											
	1,13	2,14	3,15	4,16	5,17	6,18	7,19	8,20	9,21	10,22	11,23	12,24
1	1	2	3	4	16	26	27	28	29	38	39	192
2	5	6	7	17	18	19	30	31	40	41	42	46
3	8	9	10	20	21	22	32	33	34	43	44	47
4	11	12	13	14	15	23	24	25	35	36	37	45
5	48	49	50	51	52	53	60	61	62	69	70	71
6	54	55	56	57	58	59	63	64	65	66	67	68
7	72	73	74	79	80	81	86	87	88	89	90	91
8	75	76	77	78	82	83	84	85	113	199	200	201
9	111	112	114	115	116	117	118	119	120	121	122	123
10	124	125	126	127	128	129	130	131	132	133	134	135
11	92	93	94	95	98	99	100	153	154	155	156	157
12	96	97	101	102	103	104	105	106	107	108	109	110
13	158	159	160	161	162	163	164	165	166	167	168	171
14	136	137	138	139	140	141	142	143	169	170	172	173
15	174	175	176	177	178	179	180	181	-	-	-	-
16	182	183	184	185	186	187	188	189	190	191	-	-
17	144	145	146	147	148	149	150	151	152	-	-	-
18	193	194	195	196	197	198	208	209	210	213	214	215
19	202	203	204	205	206	207	211	212	216	217	-	-

Notes:

- 1) Thermocouple numbering order shown on instrumentation installation drawing EE-5434-1110 (Eilco Engineering).
- 2) Plug consists of an insert, Amphenol 26-1328, and a housing, Amphenol 26-4501-24, which match the connectors in the Langley M=6 20-inch wind tunnel.
- 3) Each plug has 24 numbered pins. The iron wires are soldered to pins 1 thru 12 and the constantan wires are soldered to pins 13 thru 24. The plug insert is installed in the plug so that pin 1 is on the end of the housing marked 1.

TABLE 3

THERMOCOUPLE LOCATION AND SKIN THICKNESS*

FUSELAGE

Thermocouples 1-110 and 192-217

L = 18.88 inches

ϕ Measured counter clockwise looking forward

Z Measured above (+) and below (-) the booster centerline

T.C. No.	X	X/L	ϕ	Z	Skin Thickness Inches
1	0.5	0.026	0		0.031
2	1.0	0.053			0.031
3	1.5	0.079			0.025 (0.023-0.027)
4	2.0	0.106			0.032 (0.030-0.035)
5	2.5	0.132			0.026 (0.024-0.028)
6	3.0	0.159			0.028
7	3.5	0.185			0.028
8	4.0	0.212			0.027
9	4.5	0.238			0.029 (0.028-0.032)
10	5.0	0.265			0.033
11	5.5	0.291			0.034
12	6.0	0.318			0.032
13	6.5	0.344			0.029
14	7.0	0.371			0.028
15	8.0	0.424	V		0.032
16	2.0	0.106	15		0.029 (0.027-0.031)
17	2.5	0.132			0.030 (0.029-0.031)
18	3.0	0.159			0.030
19	3.5	0.185			0.031
20	4.0	0.212			0.030
21	4.5	0.238			0.030 (0.029-0.031)
22	5.0	0.265			0.032
23	5.5	0.291			0.031
24	6.5	0.344			0.027 (0.026-0.028)
25	7.0	0.371	V		0.026
26	1.0	0.053	30		0.031
27	1.5	0.079			0.022 (0.022-0.025)
28	2.0	0.106			0.030 (0.029-0.031)
29	2.5	0.132			0.029
30	3.0	0.159			0.031
31	3.5	0.185			0.032
32	4.0	0.212			0.030 (0.029-0.032)
33	4.5	0.238			0.033
34	5.0	0.265			0.035
35	5.5	0.291			0.035
36	6.5	0.344			0.032 (0.031-0.035)
37	7.0	0.371	V		0.033 (0.031-0.035)
38	2.0	0.106	45		0.027
39	2.5	0.132			0.029 (0.028-0.031)
40	3.0	0.159			0.030 (0.028-0.032)
41	3.5	0.185			0.028
42	4.0	0.212	V		0.026 (0.025-0.027)

*Skin thickness measured within 3/8 inch radius of thermocouple location. If thickness variation is not less than ± 0.001 , the range is listed in parenthesis.

T.C. No.	X	X/L	ϕ	Z	Skin Thickness Inches
43	4.5	0.238	45		0.025 (0.024-0.027)
44	5.0	0.265			0.024 (0.023-0.025)
45	5.5	0.291			0.024 (0.023-0.025)
46	4.0	0.212	60		0.027
47	5.0	0.265	60		0.026
48	10.0	0.530	45		0.025
49	11.0	0.583	45		0.027
50	8.0	0.424	60		0.026
51	9.0	0.477			0.025
52	10.0	0.530			0.026
53	11.0	0.583	∇		0.028
54	5.37	0.284	81.4	±0.2	0.030
55	5.77	0.306			0.029
56	6.17	0.327			0.030 (0.029-0.031)
57	6.57	0.348			0.030 (0.028-0.032)
58	6.97	0.369			0.028 (0.026-0.031)
59	8.0	0.424			0.022
60	9.0	0.477			0.023
61	10.0	0.530			0.024
62	11.0	0.583	∇		0.023
63	5.37	0.284	98.6	-0.2	0.030
64	5.77	0.306			0.027
65	6.17	0.327			0.028 (0.026-0.030)
66	6.57	0.348			0.026
67	6.97	0.369			0.025
68	8.0	0.424			0.028
69	9.0	0.477			0.026
70	10.0	0.530			0.029
71	11.0	0.583	∇		0.028
72	5.0	0.265	117.5	-0.62	0.024 (0.023-0.025)
73	5.3	0.281			0.027
74	5.6	0.297			0.025 (0.024-0.027)
75	5.9	0.312			0.025 (0.021-0.027)
76	6.2	0.328			0.026 (0.020-0.028)
77	6.5	0.344			0.027
78	6.8	0.360	∇		0.027
79	5.0	0.265	130.5	-0.86	0.023
80	5.3	0.281			0.020
81	5.6	0.297			0.020
82	5.9	0.312			0.020
83	6.2	0.328			0.024
84	6.5	0.344			0.020
85	6.8	0.360	∇		0.020
86	5.0	0.265	143.5	-1.06	0.028
87	5.3	0.281	∇		0.028
88	5.6	0.297	∇		0.033
89	5.0	0.265	156.5	-1.22	0.031
90	5.3	0.281	∇		0.030
91	5.6	0.297	∇		0.035
92	15.1	0.803	62.3	+0.8	0.030 (0.028-0.032)
93	15.5	0.824	62.3	+0.8	0.029 (0.027-0.031)

TABLE 3 (continued)

T.C. No.	X	X/L	ϕ	Z	Skin Thickness Inches
94	15.9	0.846	62.3	+0.8	0.026 (0.025-0.028)
95	16.3	0.867	↓	↓	0.025 (0.023-0.028)
96	16.7	0.888	↓	↓	0.029 (0.028-0.031)
97	17.1	0.910	↓	↓	0.030 (0.029-0.031)
98	15.5	0.824	75.3	+0.4	0.032 (0.031-0.033)
99	15.9	0.846	↓	↓	0.032
100	16.3	0.867	↓	↓	0.031
101	16.7	0.888	↓	↓	0.030
102	17.1	0.910	↓	↓	0.029
103	17.5	0.931	↓	↓	0.028
104	17.9	0.952	↓	↓	0.028 (0.027-0.029)
105	16.7	0.888	90	0	0.030
106	17.1	0.910	↓	↓	0.031
107	17.5	0.931	↓	↓	0.031
108	17.9	0.952	↓	↓	0.031
109	17.5	0.931	104.7	-0.4	0.029 (0.027-0.031)
110	17.9	0.952	104.7	-0.4	0.028
192	0	0	180		0.029
193	0.5	0.026	↓		0.028
194	1.0	0.053	↓		0.030
195	1.5	0.079	↓		0.030 (0.028-0.031)
196	2.0	0.106	↓		0.022
197	3.0	0.159	↓		0.030
198	4.0	0.212	↓		0.028 (0.025-0.030)
199	5.0	0.265	↓		0.030
200	6.0	0.318	↓		0.030
201	7.0	0.371	↓		0.033 (0.032-0.035)
202	8.0	0.424	↓		0.033
203	9.0	0.477	↓		0.030
204	11.0	0.583	↓		0.026
205	13.0	0.689	↓		0.028 (0.027-0.030)
206	15.0	0.794	↓		0.031
207	17.0	0.900	↓		0.033 (0.031-0.034)
208	1.0	0.053	160		0.030
209	2.0	0.106	↓		0.020
210	3.0	0.159	↓		0.030
211	9.0	0.477	↓		0.027
212	11.0	0.583	↓		0.024
213	1.0	0.053	140		0.030
214	2.0	0.106	↓		0.023
215	3.0	0.159	↓		0.030
216	9.0	0.477	↓		0.025
217	11.0	0.583	↓		0.030

TABLE 3 (continued)

LEFT CANARD

Thermocouples 111-135

Y Measured along exposed semi-span with Y=0 at 1.2 inches from model center.

b/2 is the exposed semi-span of 1.565 inches

X is approximate. Thermocouples installed on leading edge (LE) and 0.3 and 0.6 inches along the surface from the leading edge on the upper (US) and lower (LS) surfaces.

T.C. No.	X	X/L	Location	Y	Y/b/2	Skin Thickness Inches
111	6.1	0.323	LS	0.2	0.128	0.026
112	5.8	0.307	LS			0.025
113	5.6	0.297	LE			0.030
114	5.8	0.307	US			0.030
115	6.1	0.323	US	∇	∇	0.032
116	6.1	0.323	LS	0.5	0.319	0.028
117	5.8	0.307	LS			0.027
118	5.6	0.297	LE			0.030
119	5.8	0.307	US			0.031
120	6.1	0.323	US	∇	∇	0.032
121	6.1	0.323	LS	0.88	0.562	0.031
122	5.8	0.307	LS			0.028
123	5.6	0.297	LE			0.030
124	5.8	0.307	US			0.030
125	6.1	0.323	US	∇	∇	0.032
126	6.1	0.323	LS	1.14	0.728	0.031
127	5.8	0.307	LS			0.030
128	5.6	0.297	LE			0.030
129	5.8	0.307	US			0.032
130	6.1	0.323	US	∇	∇	0.031
131	6.1	0.323	LS	1.38	0.882	0.032
132	5.8	0.307	LS			0.031
133	5.6	0.297	LE			0.030
134	5.8	0.307	US			0.030
135	6.1	0.323	US	∇	∇	0.032

TABLE 3 (continued)

FIN

Thermocouples 136-143 on outboard side of Left Fin
 Thermocouples 144-152 on inboard side of Right Fin
 X is measured from leading edge
 C is the chord length
 Y is measured along the fin from the fin - wing joint
 b/2 is the fin semispan of 1.794 inches.

T.C. No.	X	X / C	Fin	Y	Y/b/2	Skin Thickness Inches	
136	0.341	0.30	Left ↓ ↓ ↓ ↓ ↓ ↓ ↓ ↓ ↓ ↓ ↓ ↓	1.56	0.870	0.033	
137	0.113	0.10		1.56	0.870	0.033	
138	0.397	0.30		1.20	0.669	0.030	
139	0.132	0.10		1.20	0.669	0.032	
140	0.460	0.30		0.80	0.446	0.028	
141	0.153	0.10		0.80	0.446	0.033	
142	0.546	0.30		0.25	0.139	0.029	
143	0.182	0.10		↓	↓	0.030	
144	0	0		Right	↓	↓	0.029
145	0.182	0.10		↓	↓	0.032	
146	0.546	0.30		↓	↓	0.031	
147	0	0		↓	0.80	0.446	0.032
148	0.153	0.10		↓	↓	0.031	
149	0.460	0.30	↓	↓	0.028		
150	0	0	↓	1.20	0.669	0.031	
151	0.132	0.10	↓	↓	0.029		
152	0.397	0.30	↓	↓	0.030		

TABLE 3 (concluded)

WING

Thermocouples 153-173 Left Wing

Thermocouples 174-191 Right Wing

S is the distance along surface from leading edge parallel to vehicle centerline

Y is measured normal to fuselage centerline along the wing surface from the wing root. The origin for Y is 1.528 inches from the booster center

b/2 is the wing exposed semi-span of 4.197 inches

T.C. No.	S	Wing	Location	Y	Y/b/2	Skin Thickness Inches
153	0.8	Left	LS	0.64	0.152	0.031
154	0.4		LS	↓	↓	0.030 (0.029-0.032)
155	0.		LE	↓	↓	0.029 (0.028-0.031)
156	0.4		US	↓	↓	0.027 (0.026-0.028)
157	0.8		US	↓	↓	0.029
158	0.4		LS	1.04	0.248	0.030 (0.029-0.032)
159	0.		LE	↓	↓	0.028 (0.026-0.030)
160	0.4		US	↓	↓	0.028 (0.026-0.031)
161	0.8		LS	1.44	0.343	0.030
162	0.4		LS	↓	↓	0.030
163	0.		LE	↓	↓	0.028 (0.026-0.030)
164	0.4		US	↓	↓	0.028 (0.026-0.031)
165	0.8		US	↓	↓	0.030
166	0.4		LS	1.84	0.438	0.029
167	0.		LE	↓	↓	0.029 (0.027-0.031)
168	0.4		US	↓	↓	0.028 (0.026-0.031)
169	0.8		LS	2.24	0.534	0.032
170	0.4	LS	↓	↓	0.031	
171	0.	LE	↓	↓	0.029 (0.027-0.031)	
172	0.4	US	↓	↓	0.028 (0.026-0.030)	
173	0.8	Right	US	↓	↓	0.028
174	0.4		LS	2.44	0.581	0.029
175	0.		LE	↓	↓	0.028 (0.026-0.030)
176	0.4		US	↓	↓	0.030
177	0.8		LS	2.84	0.677	0.030
178	0.4		LS	↓	↓	0.030
179	0.		LE	↓	↓	0.029 (0.027-0.031)
180	0.4		US	↓	↓	0.030
181	0.8		US	↓	↓	0.028 (0.027-0.030)
182	0.4		LS	3.24	0.772	0.030
183	0.		LE	↓	↓	0.030 (0.029-0.031)
184	0.4		US	↓	↓	0.028
185	0.8		US	↓	↓	0.028
186	1.2		US	↓	↓	0.030 (0.028-0.032)
187	0.4		LS	3.64	0.867	0.031 (0.030-0.033)
188	0.		LE	↓	↓	0.029 (0.027-0.031)
189	0.4		US	↓	↓	0.030 (0.028-0.032)
190	0.8		US	↓	↓	0.028 (0.026-0.030)
191	1.2	US	↓	↓	0.030 (0.028-0.032)	

TABLE 4
 PRESSURE TAP LOCATIONS ON FUSELAGE

Pressure Number	X	X/L	ϕ
1	2.25	0.119	11.5
2	2.75	0.146	11
3	3.25	0.172	9.5
4	3.75	0.199	9
5	4.25	0.225	8.5
6	4.75	0.252	8.5
7	5.25	0.278	8.5
8	2.75	0.146	38
9	4.25	0.225	21.5
10	4.25	0.225	36

TABLE 5

RUN LOG FOR LRC M=6 TESTS

MSFC Run No.	LRC Test No.	LRC Run No.	Model	$\Delta X/\Delta Y$ (3)	Approx. Re/Ft $\times 10^{-6}$	Angle of		Booster Inst. Group (5)	Phase Change Temp.	
						Attack α	Yaw β		Booster F	Orbiter F
1-1	6386	5	Booster	-	1.3	0	0	1		
2		3			5.7	0	0	4		
3		9			5.7	-5	↑	4		
4		8			5.7	+5	↓	1		
5		4			8.0	0	0	1		
6		6387			5	1.3	0	2		
7					2	5.7	0	2		
8					4	5.7	-5	↑		
9					3	5.7	+5	↓		
10					31	8.0	0	2		
11					8	1.3	0	3		
12					6	5.7	0	3		
13		9			5.7	-5	↓	3		
14		7			↑	+5	0	5		
-	11	0(1)	0	4						
-	12	-1	-1	4						
-	13	-2	-2	4						
-	14	-3	-3	4						
-	15	-4	-4	5						
-	6386	6	5.7	0(1)	-4	5				
-			8.0	+5	0	1				
2-1	6387	16	Mated	-1.1/0	5.7	0	0	?(2)	Oil Flow	
-3	6386	13		-1.1/0	5.7	+5	0	1(2)		
3-2	6387	18	Mated	-1.1/0	5.7	0	0	2	125	150
-4		20		-1.1/0	5.7	-5	0	2	125	125
-6		19		-1.1/0	5.7	+5	0	2	125	125
4-1	6386	17	Mated	-1.1/0	1.3	0	0	1		
2		11		5.7	0	↑	↑			
3		16		5.7	-5	↑	↑			
4		15		5.7	+5	↓	↓			
5		29		8.0	0	0	1		250	
6		6387		24	1.3	0	2			
7				21	5.7	0	↑			
8				23	5.7	-5	↓			
9				22	5.7	+5	↓			
10				26	8.0	0	2			
11				27	8.0	0	3			
12				28	5.7	0	↑			
13		30		5.7	-5	↓				
14		29		↓	+5	0	3			
14			-1.1/0	5.7						
5-2	6386	27	Mated	-1.1/0.06	1.3	0	0	4		175
4		28		-1.1/0.06	8.0	0	↑	↑		250
5		23		0/0	5.7	0	↓	↓		175
6		25		0/0	5.7	-5	↓	↓		175
7		24		0/0	5.7	+5	0	4		175

(Continued)

TABLE 5 (Continued)

MSFC Run No.	LRC Test No.	LRC Run No.	Model	$\Delta X/\Delta Y$ (3)	Approx. Re/Ft $\times 10^{-6}$	Angle of		Booster Inst. Group (5)	Phase Change Temp.	
						Attack α	Yaw β		Booster F	Orbiter F
8	6386	19	Mated	+1.1/0	5.7	0	0	4(4)		175
9		21		+1.1/0	5.7	-5	0	4		175
10		22		+1.1/0	5.7	+5	0	4(4)		175
6-3	6387	37	Orbiter	-	5.7	0	0	-		150
4		41		↑	0	0	↑		113	
5		39			-5				150	
6		40			-5				113	
7		38			+5				150	
8		42			+5				113	
9		36			0		↓		200	
10		35			0		0		150	

- NOTES: 1) Model rolled 90° clockwise to visualize shock on canard and yawed using angle of attack adjustment. Negative yaw moved the nose to the right (or down with the model rolled 90° clockwise).
- 2) Oil flow tests. Booster instrumentation uncertain on first run so LRC data must be used. Due to short run time for oil flow (≈ 7 sec.) pressures are probably not good on LRC Test 6386 Run 13.
- 3) Nominal zero gap was run with a 0.002 shim on the back of the booster, and the actual gap varied from 0.002 to 0.005 before the run. On some occasions the gap would open during the run or during model retraction. On most runs this would only amount to a few thousandths, but on LRC Test 6387 Run 19 (MSFC 3-6) the gap after the test was ≈ 0.02 and the orbiter was nose up. The schlieren pictures can be used to evaluate actual gap during the test.
- 4) During MSFC Run 5-8, pressure P5 was noted to be above the 20 psia limit, and a higher pressure transducer was added in parallel on data channel 99. On MSFC Run 5-10 both P5 and P6 exceeded the 20 psia gage limit, but data was obtained on P5 from the high pressure transducer.
- 5) Booster instrumentation groups are:

Group	Thermocouple Plugs	Pressures
1	1,2,3,4,6,18	P1 thru P10
2	5,6,7,8,9,10,19	
3	11,12,13,14,15,16,17,	
4	1,2,3,4,9,10	
5	9,10,13,14,15,16,17	P1 thru P10

See Table 2 for thermocouple/plug wiring details.

TABLE 6

RUN LOG FOR LRC M=10 TESTS

MSFC Run No.	LRC Run (T)	Model	$\Delta X/\Delta Y$	Angle of		Booster Inst. Group(3)	Phase Change Temp.	
				Attack α	Yaw $\beta(4)$		Booster F	Orbiter F
1-1	1	Booster		0		1		
2	2		-5		1			
3	3		+5		1			
5	4		0		2			
6	5		-5		2			
7	6		+5		2			
-	8		0		2	-1		
9	9		0		3			
10	10		-5		3			
11	11		+5		3			
3-1	29		Mated	-1.1/0.003	0		4	305
2	30	-1.1/0.002		0		↓	200	200
3	31	-1.1/0.003		-5		↓	275	275
5	32	-1.1/0.002		+5		↓	275	275
-	33	-1.1/0.002		0(2)		↓	275	275
4-1	12	Mated	-1.09/0.003	0		1		
2	13		-5		1			
3	14		+5		1			
5	15		0		2			
6	16		-5		2			
7	17		+5		2			
9	18		0		3			
10	19		-5		3			
11	20		+5		3			
-	21		0	↓	+2	3		
5-1	28		Mated	-1.1/0.063	0		4	
3	25	0/0.003		0		↓		400
4	26	-5			↓			350
5	27	+5			↓			350
-	22	-1.19/0.003		0		↓		
-	23	-0.99/0.003		0		↓		
-	24	-0.89/0.003		0		↓		

- Notes: 1) All runs are part of LRC Test 78. The Mach number was 10.2 and the unit Reynolds Number was approximately 10^6 . The model was rolled 0.5° left wing down for all tests due to support tolerance.
 2) Model rolled 90° to get indication from phase change pictures of bow shock impingement on the canard and wings.
 3) Booster instrumentation groups are:

Group	Thermocouple Plugs	Pressures
1	1,2,3,4,6,18	P5,P6,P7,P9
2	5,6,7,8,9,10,19	
3	11,12,13,14,15,16,17	
4	1,2,3,4,9,10	P5,P6,P7,P9

See Table 2 for thermocouple/plug wiring details

- 4) Yaw positive with nose left viewed from the rear.

TABLE 7
THERMOCOUPLES OMITTED FOR SUPERSONIC TESTS

<u>Item</u>	<u>Thermocouple Number</u>	<u>Inoperative</u>	<u>Questionable Operation</u>	<u>Deleted</u>
1	64	X		
2	69		X	
3	114	X		
4	123		X	
5	129		X	
6	131		X	
7	138	X		
8	153		X	
9	156	X		
10	157			X
11	160			X
12	165			X
13	173		X	
14	177		X	
15	181			X
16	185		X	
17	186			X
18	190			X
19	191			X
20	206		X	

Note: Thermocouple 46 has also exhibited questionable operation but has been retained because of its important location on the upper fuselage.

TABLE 8

RUN CONDITIONS FOR SUPERSONIC TESTS

MSFC Run No.	LRC No.		$\Delta X/\Delta Y$	Mach No.	Approx. Re/Ft $\times 10^{-6}$	Angle of		Heat Transfer	Schlieren	Shadowgraph	
	Run	Pt (2)				Attack	Roll				
1-1	1	5,6	Booster	3.7	3.5	0		X			
2	1	7			3.5	-5					
3	1	8			3.5	+5					
4	6	3			1.3	0					
5	6	4			5.5	0					
6	1	1			2.3	3.5	0				
7	1	2			3.5	-5					
8	1	3,4			3.5	+5			X		
2-1	10	4	Booster	3.7	3.5	0			X	X	
2	↓	5			↓	-5					
3	↓	6			↓	+5					
4	↓	1			2.3	0					
5	↓	2			↓	-5					
6	↓	3			↓	+5				X	
3-1	7	6	-1.1/0 ↓ 0/0 ↓	3.7	3.5	0			X	X	
2	↓	7			↓	-5				X	
3	↓	8			↓	+5				X	
4	↓	9			↓	0	90				
5	↓	2			2.3	0				X	
6	↓	3			↓	-5					
7	↓	4			↓	+5					
8	↓	5			↓	0	90				
9	8	4			0/0	3.7	0			X	
10	↓	5			↓	↓	-5				
11	↓	6			↓	2.3	0			X	
12	↓	1			↓	↓	-5				
13	↓	2			↓	↓	+5				
14	↓	3			↓	↓	0				
21	9	2	-1.1/0.068	3.7	0			X			
22	9	1	-1.1/0.068	2.3	↓	0		X	X		
4-1	2	7	-1.075/0.004 ↓ -1.1/0.003 ↓ -1.1/0.003 ↓ -1.075/0.004 ↓ -1.075/0.004 ↓ -1.075/0.004	3.7	3.5	0		X			
2	2	8			↓	-5					
3	2	9			↓	+5					
4	5	4			-1.1/0.003	5.5	0				
5	5	5			-1.1/0.003	1.3	0				
6	2	10			-1.075/0.004	2.3	3.5	0			
7	2	11			-1.075/0.004	↓	-5				
8	2	12			-1.075/0.004	↓	+5			X	

TABLE 8 (continued)

MSFC Run No.	LRC No.		$\Delta X/\Delta Y$	Mach No.	Approx. Re/Ft $\times 10^{-6}$	Angle of		Heat Transfer	Schlieren	Shadowgraph
	Run	Pt (2)				Attack	Roll			
5-1	3	7	0/0.007 ↓ ▽	3.7	3.5 ↓ ↓ ↓ ↓ ▽	0		X X		
2		8								
3		9								
4		10				2.3				
5		11								
6		12								
13	4	3	-1.09/0.063	3.7		0				
14	4	4	-1.09/0.063	2.3		0				

- Notes: 1) Grit boundary layer trips were cemented around the booster and orbiter noses approximately 1.1 inches aft of the tip for all runs at a unit Reynolds Number of 3.5×10^6 . One row of No. 40 grit (0.018 in.) was used with a spacing between particles of about 3 times the particle dimension.
- 2) Occasionally double points were taken because of problems with the pressure recording. Equilibrium runs were made before heating up the tunnel for all heat transfer runs to obtain the true equilibrium skin temperature without non-steady conduction effects from the heavy structure of the model. These runs are not listed.

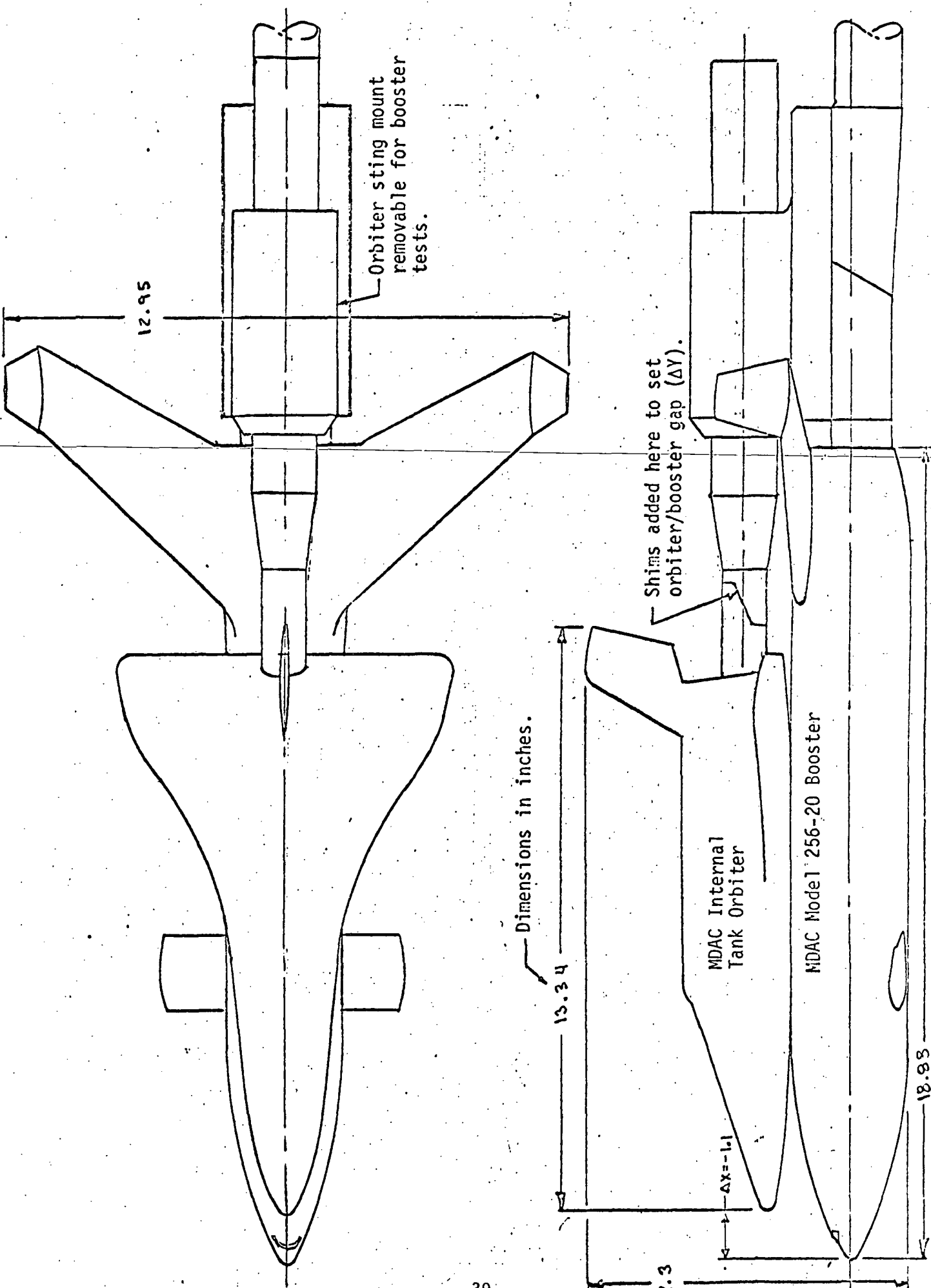


Figure 1 - Model arrangement.

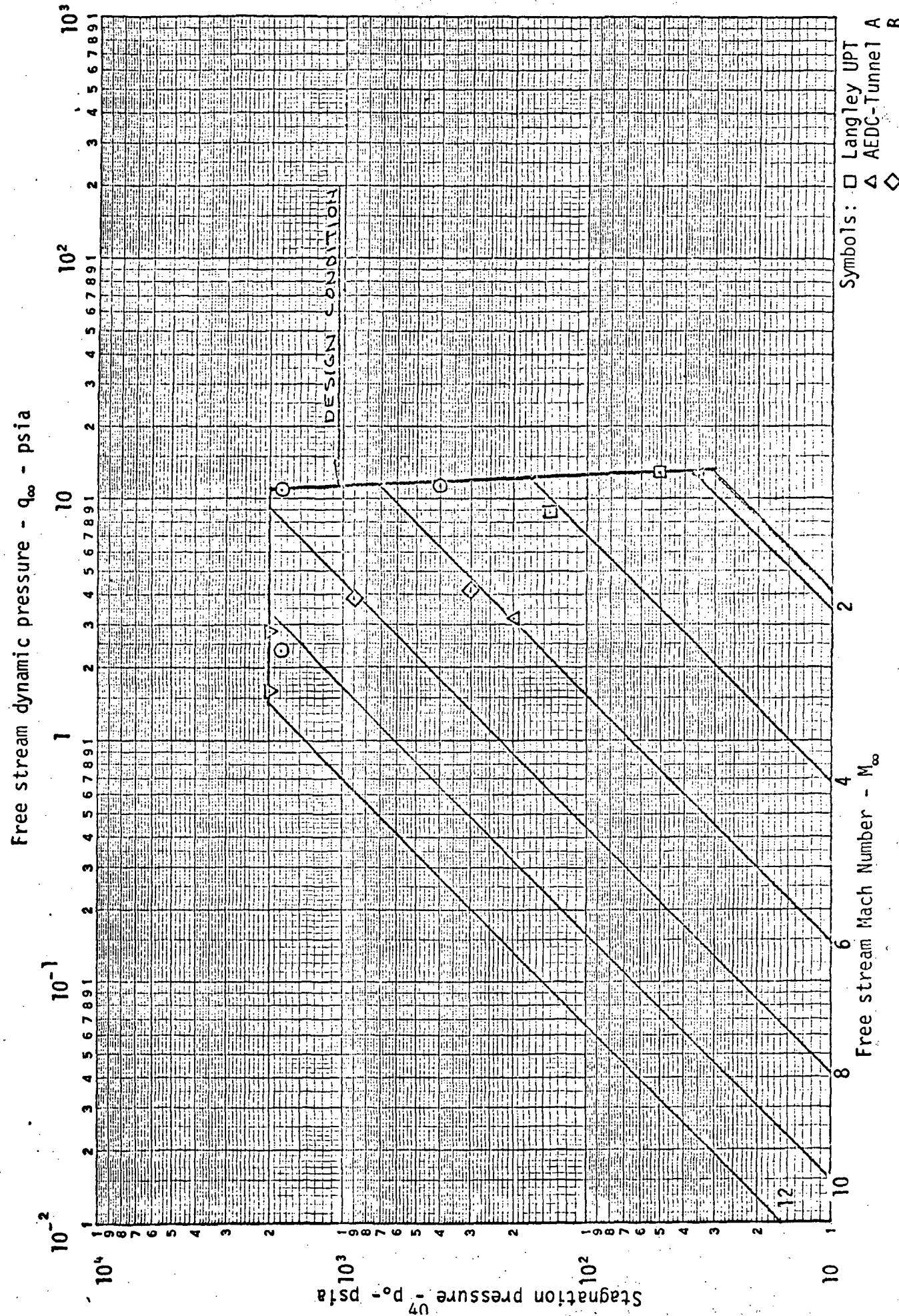


Figure 2. Design envelope for model loads.

NOTE: Limits shown are for booster alone. The launch configuration will be limited to $\pm 10^\circ$.

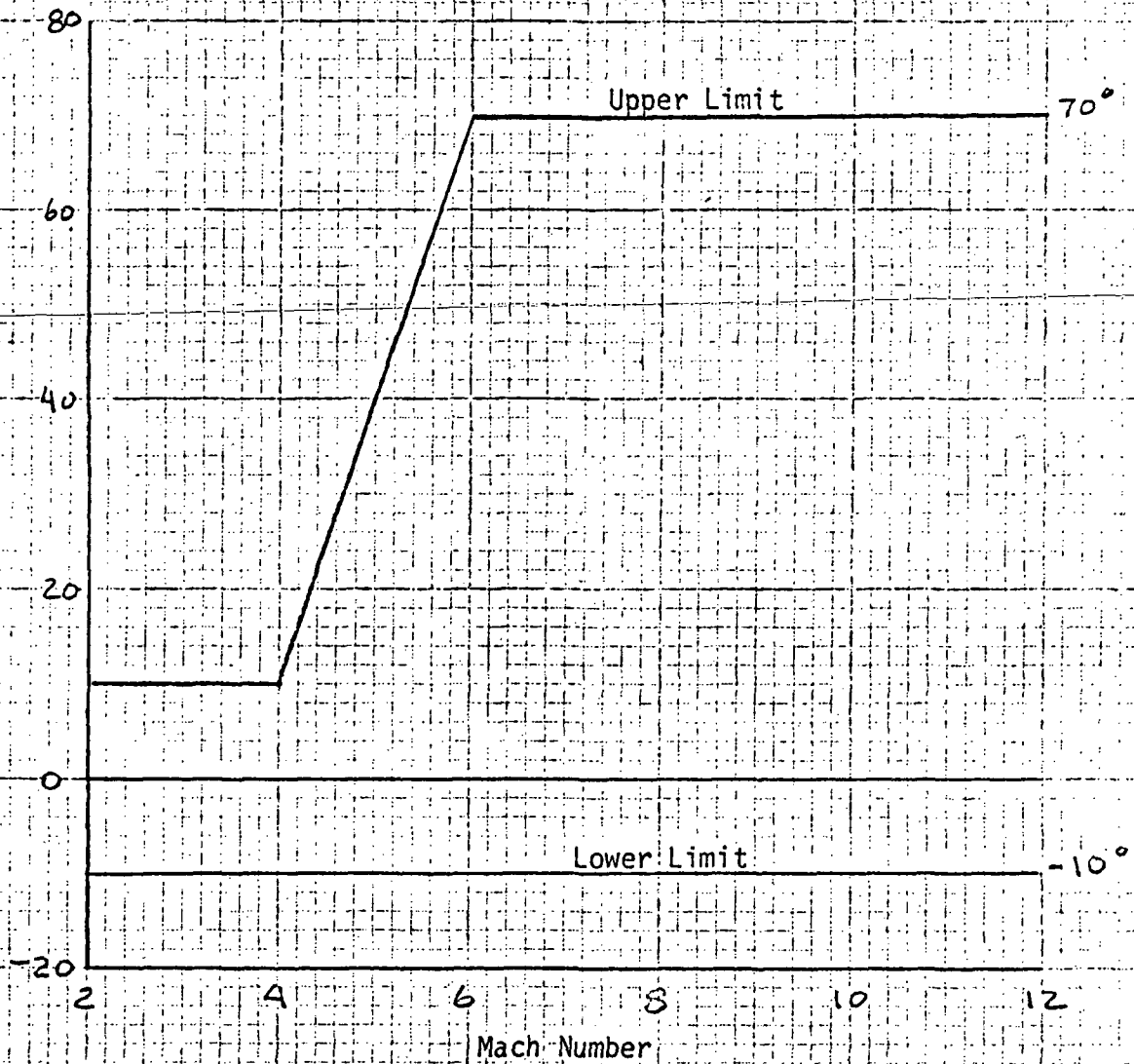
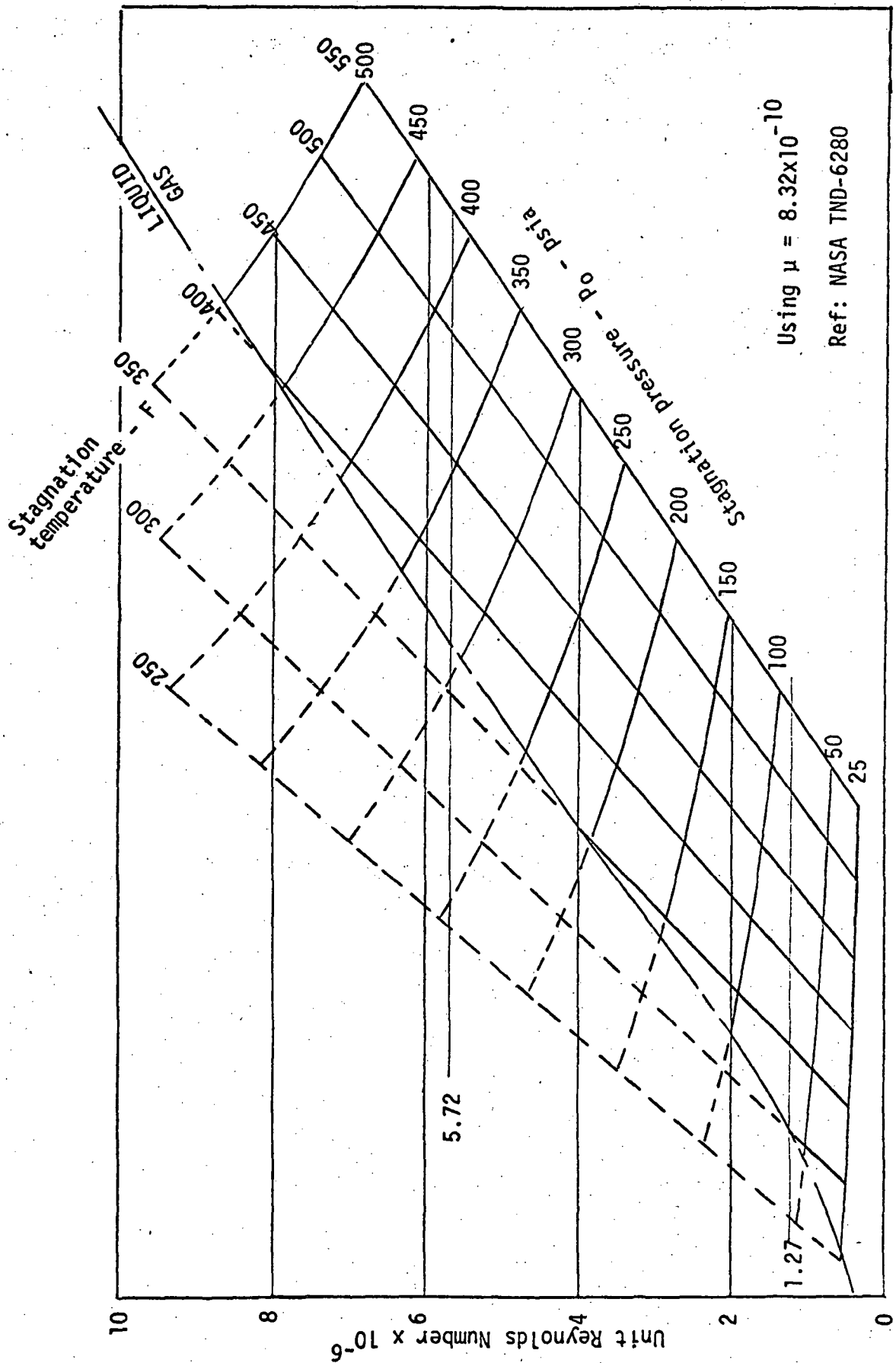


Figure 3 - Design range for angle of attack.



Using $\mu = 8.32 \times 10^{-10}$
 Ref: NASA TND-6280

Figure 4. Tunnel operating conditions as a function of unit Reynolds Number for M=6.

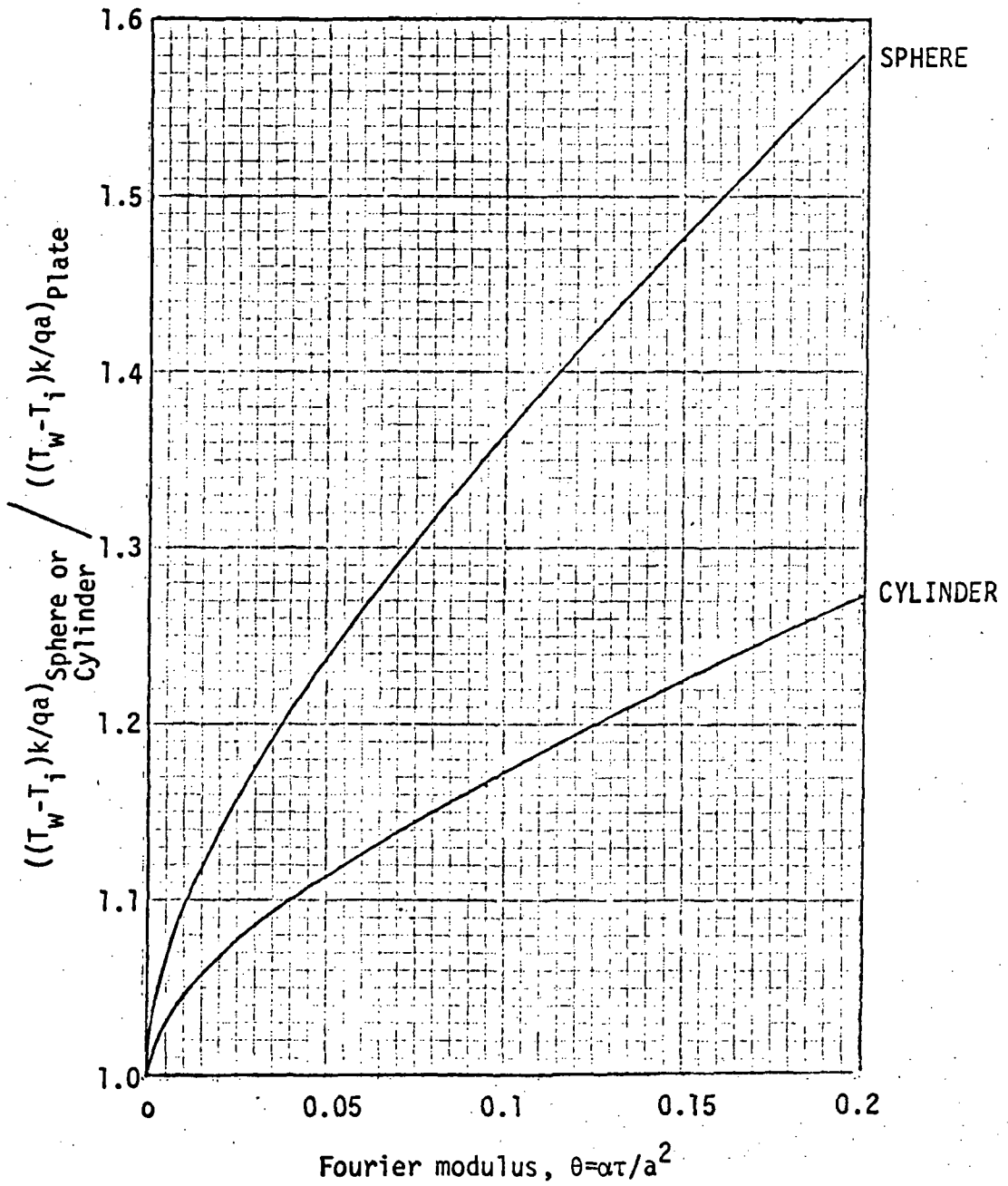


Figure 5 - Estimated variation in heat transfer conditions as a function of body geometry.

Appendix C

LEEWARD SURFACE FLOWFIELD

TR-221-993
JULY 1971

LEEWARD SURFACE FLOWFIELD ON A BLUNT DELTA WING IN A SIMULATED REENTRY FLOW

Prepared for:

**NATIONAL AERONAUTICS AND SPACE ADMINISTRATION
GEORGE C. MARSHALL SPACE FLIGHT CENTER
Aero-Astroynamics Laboratory**

Under Contract NAS8-26268

NORTHROP SERVICES, INC.

P. O. BOX 1484
HUNTSVILLE, ALABAMA 35807
TELEPHONE (205) 837 0580

**LEEWARD SURFACE FLOWFIELD ON A BLUNT DELTA WING
IN A SIMULATED REENTRY FLOW**

July 1971

By

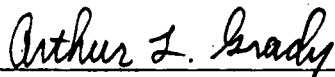
Wayne D. Lanning

PREPARED FOR:

**NATIONAL AERONAUTICS AND SPACE ADMINISTRATION
GEORGE C. MARSHALL SPACE FLIGHT CENTER
AERO-ASTRODYNAMICS LABORATORY**

Under Contract NAS8-26268

REVIEWED AND APPROVED BY:



A. L. Grady, Director
Advanced Engineer Analysis Section

FOREWORD

Northrop-Huntsville, in support of Marshall Space Center contract NAS8-26268, Shuttle Ascent and Shock Impingement Aerodynamic Heating Test, has co-sponsored with von Karman Institute an investigation of leeward heating on delta wings. This study, which is partially funded under Northrop purchase order 510-41036, Delta Wing Leeward Heating, is being conducted by Wayne D. Lanning, a Northrop employee currently on leave to attend the von Karman Institute at Rhode-Saint-Genese, Belgium.

ACKNOWLEDGMENTS

I would like to acknowledge my indebtedness and gratitude to Professor B. E. Richards for the continuous help and guidance he provided during the course of this research.

I should also like to thank the Longshot Technical Staff, Messrs. Jean Hugé and F. Vanderbroeche, for making this research a practical success.

This research was conducted while the author was on leave from the Northrop Corporation. The support of the Company is gratefully appreciated.

ABSTRACT

Results are presented of a study of the pressure and heat transfer distributions on a 75-degree sweep slab delta wing. The wing had cylindrical leading edges with a tangent sphere nose. The hypersonic flowfield study was performed in the von Karman Institute's piston-driven wind tunnel at nominal Mach numbers of 15 and 20 at Reynolds numbers per meter of 1.8×10^7 and 8.7×10^6 , respectively. The maximum angle-of-attack investigated was 25 degrees. Nitrogen was used as the test gas. Oil-flow visualization studies were included in the program.

The results indicated that the leeward surface flowfield was not conical for the range of test conditions investigated. For angles-of-attack greater than 5 degrees, boundary layer separation occurred at the junction of the leading edge and expansion surface. The resulting vortex reattached near the centerline inducing a region of high pressure and heat transfer. The peak heating rate occurred a short distance aft of the nose and tended to move forward with increasing angle-of-attack. The strength of the vortex appeared greater on the aft part of the model. The effect of increasing the Mach number was to increase the relative lee-side flowfield properties.

Based on the experimental results obtained during the investigation, the dominant flowfield characteristics for the leeward surface flowfield over a blunt delta wing were postulated.

TABLE OF CONTENTS

<u>Section</u>	<u>Title</u>	<u>Page</u>
	FOREWORD	ii
	ACKNOWLEDGMENTS	ii
	ABSTRACT	iii
	LIST OF ILLUSTRATIONS	v
	NOMENCLATURE	vi
I	INTRODUCTION	1-1
II	APPARATUS AND TESTS.	2-1
	2.1 LONGSHOT FREE-PISTON TUNNEL	2-1
	2.2 MODEL DESCRIPTION AND INSTRUMENTATION	2-1
	2.3 RANGE OF TEST CONDITIONS	2-4
	2.4 FLOWFIELD VISUALIZATION TECHNIQUE	2-4
	2.5 DATA REDUCTION	2-4
III	RESULTS AND DISCUSSION	3-1
	3.1 PRESSURE DISTRIBUTION	3-1
	3.2 HEAT TRANSFER DISTRIBUTION	3-8
	3.3 VISUAL STUDIES.	3-26
IV	FLOWFIELD DESCRIPTION	4-1
V	CONCLUSIONS	5-1
VI	REFERENCES	6-1

LIST OF ILLUSTRATIONS

<u>Figure</u>	<u>Title</u>	<u>Page</u>
1-1	LEEWARD SURFACE FLOWFIELD	1-2
2-1	DELTA WING MODEL.	2-2
2-2	LONGSHOT TEST SECTION	2-3
3-1	CENTERLINE PRESSURE VARIATION WITH ANGLE-OF-ATTACK FOR MACH NUMBERS OF 15 AND 20	3-2
3-2	SPANWISE PRESSURE DISTRIBUTION AT VARIOUS CHORDWISE STATIONS AS A FUNCTION OF ANGLE-OF- ATTACK AND MACH NUMBER	3-5
3-3	CENTERLINE STANTON NUMBER DISTRIBUTION AS A FUNCTION OF ANGLE-OF-ATTACK AND MACH NUMBER	3-9
3-4	SPANWISE STANTON NUMBER DISTRIBUTION AS A FUNCTION OF ANGLES-OF-ATTACK AND MACH NUMBERS	3-17
3-5	VORTEX REATTACHMENT REGION	3-24
3-6	OIL-FLOW PATTERNS	3-27
3-7	SCHLIEREN PHOTOGRAPHS	3-31
4-1	LEE-SIDE FLOWFIELD	4-2

NOMENCLATURE

<u>Symbols</u>	<u>Definition</u>
c	One-half the span of the wing at each (L/t) station
C_p	Coefficient of specific heat at constant pressure
h	Heat transfer coefficient
L	Longitudinal distance measured from the geocentric stagnation point of the nose along the centerline
M	Mach number
p	Static pressure
r	Recovery factor
Re_t	Reynolds number
S	Spanwise distance measured perpendicularly from the geometric stagnation point of the leading edge to the centerline
S_o	Spanwise distance measured perpendicularly from the centerline to the geometric stagnation point of the leading edge
St	Stanton number
t	Model thickness
T	Static temperature
T_{aw}	Adiabatic wall temperature
T_o	Stagnation temperature
U	Freestream velocity
γ	Ratio of specific heats
ρ	Density
μ	Dynamic viscosity

Subscripts

l	Refers to local value
w	Refers to wall value
∞	Freestream quantity

Section I

INTRODUCTION

Reusable space vehicle systems are now nearer reality with the completion of preliminary design studies on the Space Shuttle vehicle. Mission requirements suggest that the combined weight of the vehicle structure and thermal protection system will largely influence the useful payload. In minimizing the thermal protection system, the location and magnitude of the maximum heating rates encountered during reentry must be known within some acceptable degree of accuracy and confidence. The thermal protection system requirements for the windward surfaces have successfully been defined due to extensive heat transfer investigations.

The same conclusion is not, however, true for leeward or expansion surface. In fact, these surfaces had not really been examined in detail until packaging of instrumentation on the leeward surface was recently suggested during the design of reusable systems. Consequently, there is a dearth of experimental data on leeward surface flowfield properties, especially for conditions approximating hypersonic flight. Available experimental data are inconclusive and do not provide sufficient insight for the development of either analytical or even empirical prediction methods. The purpose of this investigation is to perform a much needed experimental study on a blunt delta wing at hypersonic conditions in an effort to fill the existing void of experimental data.

A description of the flowfield phenomena on the lee surface of a delta wing at angle-of-attack, as illustrated in Figure 1-1, can be found in references 1 through 4. Although these descriptions pertain mostly to sharp leading-edge wings at various flow regimes, the flowfield is essentially the same for blunt leading-edge delta wings at hypersonic speeds although additional entropy gradients exist. The similarities and differences will be substantiated a posteriori. The flow is characterized by a bow shock which envelopes the entire wing, twin vortices, and embedded shocks. Flow separation occurs either inboard of or at the leading edges depending on the leading-edge geometry, sweep angle, and freestream conditions. After separation,

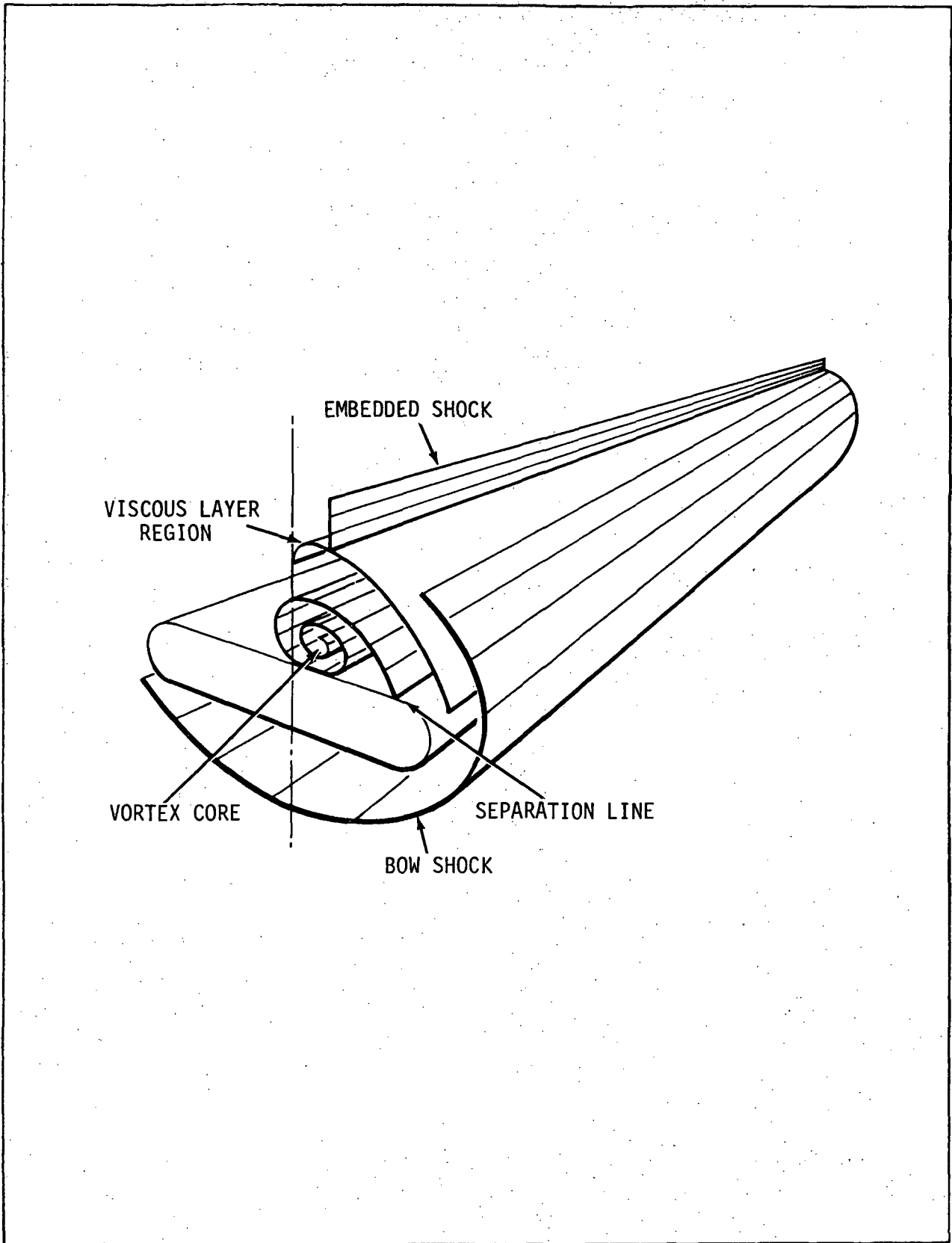


Figure 1-1. LEEWARD SURFACE FLOWFIELD

vortices are formed in the flowfield above the leeward surface which attaches near the centerline producing an appreciable increase in the pressure and heat transfer. An embedded shock wave is located in the inviscid flowfield above the wing contributing to the already significant viscous-inviscid interactions.

Cross (ref. 2) was able to obtain an excellent description of the complex three-dimensional flowfield by interpreting both qualitative and quantitative experimental data. His investigation contributes significantly to the basic understanding of the leeward surface flowfield. His experimental analysis included the measurement of the static pressures, wall temperature, and impact pressures in the flowfield around a sharp leading-edge 75-degree swept delta wing in Mach 10 flow. More emphasis was placed on the measurement of surface pressure than on measurement of the surface temperature. The measured wall pressures were always less than the freestream pressures for angles-of-attack greater than five degrees. Since the bow shock and viscous boundary were located along radial lines from the apex, Cross assumed that the flowfield was essentially conical. Using this and other assumptions, he was able to correlate the impact pressures and viscous region thickness rather successfully.

Whitehead and Keyes (ref. 3) studied the leeward surface flowfield over a sharp delta wing at Mach 6. Both leading-edge and off-leading-edge separations were studied by analyzing heat transfer and pressure data and from the results of flow visualization studies. Although the model had trailing-edge flaps, it was demonstrated that flap deflection was not sensed by the upstream flow. Contrary to references 1 and 5, Whitehead and Keyes concluded that with a detached shock wave at the leading edge, the Mach number normal to the leading edge and the sweep angle determine if the flow separates at the leading edge or at some position between the leading edge and surface centerline. The experimental flowfield obtained by Cross (ref. 2) also supports Whitehead and Keyes' conclusion. An interesting comparison is that for the latter investigation, separation occurred at the leading edge for a sweep angle of 78 degrees. In Cross' study, separation at the leading edge did not occur for a sweep angle of 75 degrees but did occur for a sweep angle of 70 degrees although the test conditions were similar. Reference 3 supported Cross' assumption of a

conical flow insomuch as the experimental flowfield did not exhibit nonconical flow behavior. Similarly, only slight variation in the spanwise pressure, even though separated regions, was noted for angles-of-attack of five degrees or smaller.

In reference 4, Whitehead again reported on the effect of vortices on the delta wing at Mach 6 but with separation occurring at the leading edge. It should be noted that both Whitehead and Cross (ref. 2) used 75-degree swept wings but separation occurred inboard of the leading-edge in Cross' investigation. The centerline heating rates at Reynolds numbers of 2.4×10^6 were found to be almost double the values at the same axial location for the smaller Reynolds number. This investigation is characteristic of leading-edge separation data. For higher Reynolds number flow, the data could be correlated in conical coordinates. It was noted that the centerline Stanton numbers at zero degree angle-of-attack were ten to fifteen percent lower than the Stanton numbers at five degrees incidence for the same unit Reynolds number. For Reynolds numbers exceeding 6×10^6 , the centerline Stanton numbers were correlated with a modified Spalding-Chi turbulent strip method.

Bertram and Everhart (ref. 6) performed an extensive experimental study of the pressure and heat-transfer distribution on a 70-degree swept slab delta wing in hypersonic flow. Although the primary consideration in this study was the windward surface, the data for the leeward surface were also presented but without any significant discussion. The majority of the data was obtained at Mach 6.8 and 9.6 in air for a wide range of angles-of-attack for both sharp and blunt prow wings. Wall pressure data were presented for incidence angles of five and ten degrees at Mach 18.4 in helium. A significant observation can be made concerning the comparison of the relative magnitudes of the local pressure and heat transfer data for the two nose geometries. The general trends for the blunt prow wing are slightly higher than the values for the sharp prow wing at the same location and flow conditions. A comparison of this data with the present investigation is performed subsequently with further discussion pertaining to Bertram and Everhart's experimental study.

Another NASA/Langley team, Stallings et al. (ref. 7) presented leeward surface flowfield data in the form of pressure and heat-transfer coefficients on a 70-degree swept delta wing at Mach numbers of 3.5 and 4.65. Leeward surface data were presented for models having dihedral angles of 0 and 24 degrees. The majority of the instrumentation were located on the nose region and along the leading edges. Both sharp and blunt nose geometries were investigated. The pressure and heat transfer trends were affected at stations downstream for a distance of 4.5 nose radii. The local pressure coefficient was larger for the sharp nose than for the blunt nose along the leading edge and windward centerline. The trend was reversed for the heat transfer data. The heat transfer coefficients were larger for the blunt nose.

The problems encountered when trying to analyze lee-surface heating rate distribution using simple theories on axisymmetric models are described in refernece 8. A multipurpose reusable spacecraft was also tested in Mach 10 flow and the data were attempted to be predicted using tangent-cone theory, strip theory, and shock expansion theory. In all cases the comparisons were poor. The authors suggested an empirical formulation in view of the extremely complexity of the flowfield. An interesting comparison between this configuration and the slab delta wing models is that the data trends are similar at appreciable angles-of-attack which positions the spacecraft leeward surface entirely in the expanded flow.

Section II

APPARATUS AND TESTS

2.1 LONGSHOT FREE-PISTON TUNNEL

This investigation was performed in the von Karman Institute's Longshot free-piston hypersonic tunnel. A description of its operating characteristics and performance may be found in reference 9. This tunnel is a form of gun tunnel designed specifically for simulating very high Reynolds number flows. Mach numbers from 15 to 20 are produced with a conical nozzle using different sizes of throat inserts. Reynolds numbers per meter ranging from 1.8×10^7 at Mach 15 to 9×10^6 at Mach 20 using nitrogen as the test gas are obtainable. These conditions are high enough to simulate turbulent heating on reentry configurations at full scale Reynolds numbers. The tunnel has previously been used to study boundary layer separation, heat transfer to flat plates and cones, and free-flight stability of cones. Theoretical performance of the tunnel is described in references 9 and 10.

2.2 MODEL DESCRIPTION AND INSTRUMENTATION

Figure 2-1 shows photographs of the slab delta wing which has a 75-degree sweep angle and cylindrical leading edges. The model is assembled from three pieces of aluminum; a base with the instrumentation, a cover plate, and a sting attachment fixture. The length and thickness is 26.67 and 2.54 centimeters, respectively. The apex is formed by a sphere and tangential cylinders having the same diameter as the slab thickness.

The instrumentation is shown fitted into the base of the model in Figure 2-1b. The pressure and thin film gauges alternate along the centerline and along 6- and 12-degree rays emanating from the model apex. The gauges lay along a line perpendicular to the leading edge in the spanwise direction. This particular arrangement was chosen such that boundary layer separation and vortex reattachment could be measured.

The orientation of the model within the dump tank test section is shown in Figure 2-2. The model was positioned as near as possible to the centerline of the nozzle and slightly downstream of the nozzle exit within a cylindrical

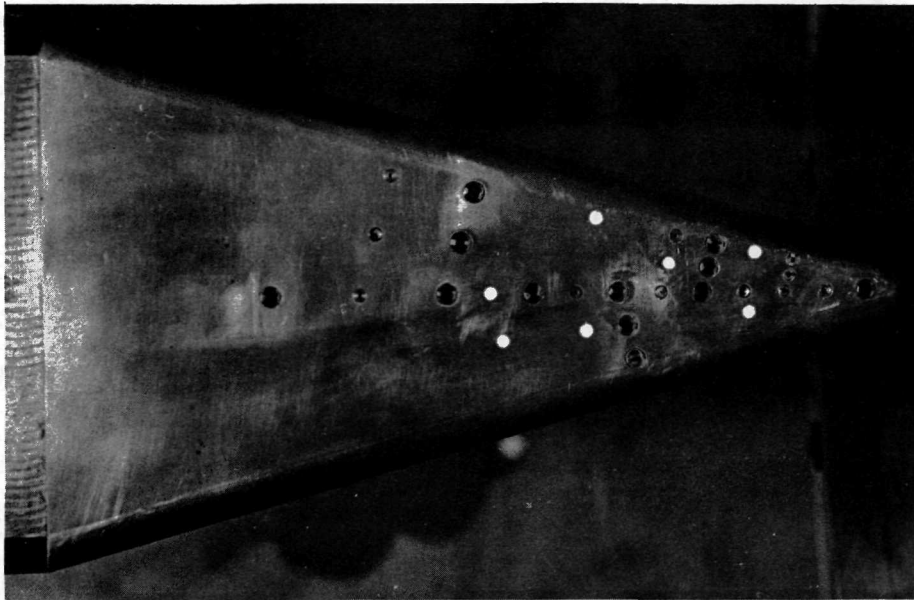


Figure 2-1a. DELTA WING MODEL (WINDWARD SURFACE)

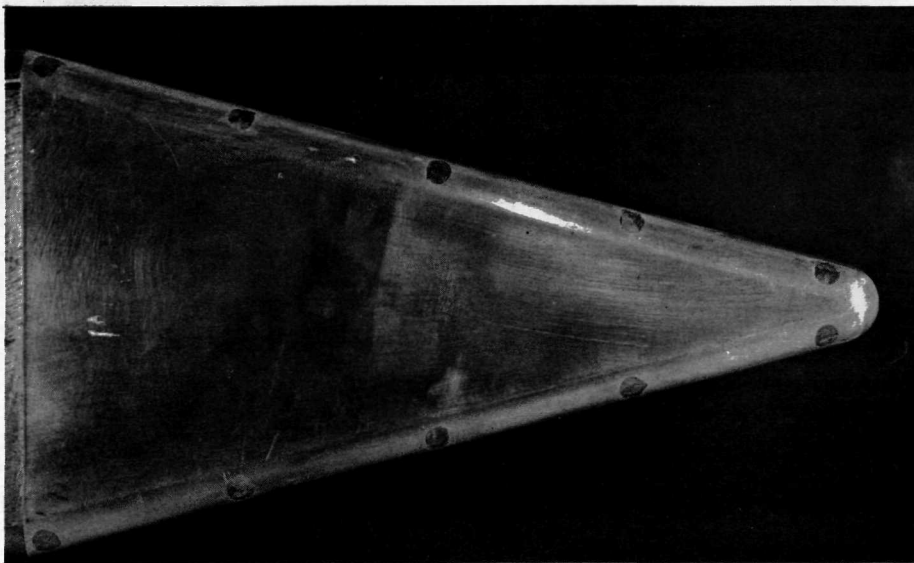


Figure 2-1b. DELTA WING MODEL (LEEWARD SURFACE)

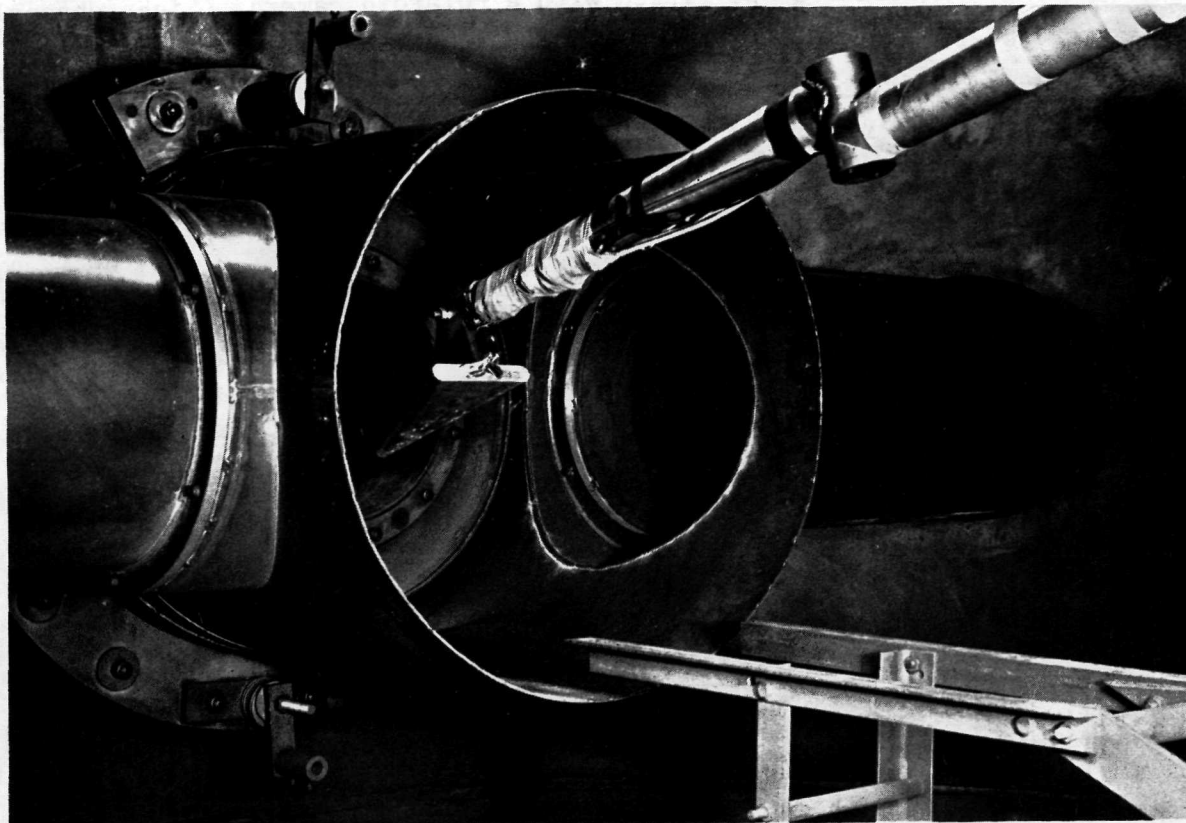


Figure 2-2. LONGSHOT TEST SECTION

baffle for each test run. The baffle was used to prevent disturbances from shock reflections within the dump tank to seriously affect the flow. The channel located on each side of the baffle leads to a viewing window for the schlieren system.

The surface pressures were measured using commercially available Hydyne type W and HR variable reluctance diaphragm pressure transducers. The signals are processed and recorded using a C.E.C. type 5-124 recording oscillograph and type 7-361 galvanometers. Eight channels of data were recorded on photographic paper at a speed of 254 centimeters per second.

The heat transfer on the leeward surface of the model was measured using thin-film platinum resistance thermometers. These gauges were manufactured and calibrated in the von Karman Institute Hypervelocity Laboratory. The transient surface temperature signal gauge was passed through an analogue circuit giving a direct reading of heat transfer rate. This trace was recorded

on a Tektronix oscilloscope fitted with a Polaroid camera. Eight channels of heat transfer data were obtained for each test run. At least two runs were required at every test condition to monitor all thirty pieces of instrumentation in the model.

2.3 RANGE OF TEST CONDITIONS

Heat transfer and static pressure measurements were obtained on the lee-surface of the delta wing at nominal Mach numbers of 15 and 20 in nitrogen. The overall angle-of-attack range of the Mach 15 investigation was 0 degree and 25 degrees in increments of five degrees excluding an angle-of-attack of 20 degrees. Angles-of-attack of 5 degrees and 10 degrees were studied at Mach 20. Table 2-1 summarizes the test conditions.

Table 2-1. TEST CONDITIONS

M_{∞}	α (deg)	N_{Re} (per m)	P_o (n/m ²)	T_o (°K)	T_w (°K)
15	0-25	1.8×10^7	3.9×10^8	2400.	295.
20	5, 10	8.7×10^6	4.0×10^8	2500.	295.

2.4 FLOWFIELD VISUALIZATION TECHNIQUE

A surface-oil-flow technique was used to examine the leeward surface flowfield qualitatively. A mixture of silicone oil and black dye was applied to the model surface in rows of dots of reasonably constant sizes. A photograph of the final oil pattern was taken after each test run to study the location of maximum surface shear.

Schlieren photographs were taken at each test condition to observe the bow shock configuration. The schlieren system utilized an argon-jet single spark light source with a horizontal knife edge.

2.5 DATA REDUCTION

The heat transfer at each thin film gauge location was obtained by applying the change-of-voltage signal from a Wheatstone bridge into an analog

network as described in reference 10. This network solves the thermal diffusion equation of the gauge to give the heat transfer as a function of time.

The heating rate data were presented in non-dimensional form as the product of the Stanton numbers based on local undistributed freestream properties and the square root of the Reynolds numbers based on thickness of the model. The recovery temperatures were calculated from the relation:

$$\frac{T_{aw}}{T_o} = \frac{1 + r \frac{\gamma - 1}{2} M_1^2}{1 + \frac{\gamma - 1}{2} M_1^2}$$

The recovery factor was chosen as 0.896 for turbulent flow. The Mach number was obtained using the ratio of the local measured pressure on the model surface to an assumed impact pressure behind the bow shock. The impact pressure was taken to be equal to 90 percent of the freestream total pressure at that station. This simplification was based on experimental results of references 2 and 11. Cross (ref. 2) measured the impact pressure at various locations above the delta wing centerline. The variation of the impact pressure with angle-of-attack was found to be one to eight-tenths of the corresponding free-stream impact pressure for angles-of-attack from zero to fifteen degrees. Creager (ref. 11) measured the impact pressure on the lee-side of a blunt leading-edge flat plate and found that the total pressure was approximately nine-tenths of the freestream value for 75-degree swept flat plate.

The assumption is also considered adequate because a thirty percent variation in the Mach number produces less than one-half of one percent error in the recovery temperature. Reference 12 also agrees with this fact that the recovery temperature and Stanton number are very weak functions of the Mach number.

The pressure data were non-dimensionalized by the undisturbed freestream pressure corresponding to the field position of the gauge in the conical flow-field. In this manner, the conicity of the flow was eliminated in both the pressure and heat transfer non-dimensional values.

Section III

RESULTS AND DISCUSSION

The purpose of this section is to present the experimental results in a manner which will contribute to determining the nature of the flowfield of a slab delta wing in hypersonic flow. An assessment of the flow pattern is made in Section IV. In attempting to explain the trends of the data, comparisons of the present data with other data are made to emphasize dominant flowfield characteristics. First, surface pressure and local heat transfer data are examined and analyzed in some detail. Secondly, qualitative data obtained from schlieren and oil-flow studies supplement the above quantitative results to determine more accurately the locations of boundary layer separation and vortex reattachment. Throughout this section, noteworthy differences and similarities between blunt and sharp leading-edge delta wings, the effect of nose geometry, Reynolds number effect, Mach number effect, and angle-of-attack effect are discussed.

3.1 PRESSURE DISTRIBUTION

The variation of the measured wall pressure along the model centerline with angle-of-attack is shown in Figure 3-1 for nominal Mach numbers of 15 and 20. The pressure is nondimensionalized by the freestream static pressure that corresponds to the undisturbed value at the same location in the test section as the sensing gauge. The pressures are plotted against the nondimensional distance S/t measured perpendicularly from the geometric stagnation point, defined at zero incidence, of the cylindrical leading edges to the model centerline. The model thickness is denoted by t . The juncture between the curved leading edge and plane leeward surface is at $S/t = 0.785$. The angle-of-attack range is 0 to 15 degrees in increments of five degrees. The solid line connects the data points. No useful pressure data were obtained for 25 degrees angle-of-attack. The wall pressure at this incidence angle was of the order of 0.1 psi and the electronic noise suppressed the gauge signal.

For all angles-of-attack and Mach numbers the centerline pressure decreases with increasing angle-of-attack. At 15 degrees incidence the pressure decreases significantly, particularly for the aft section of the model. This

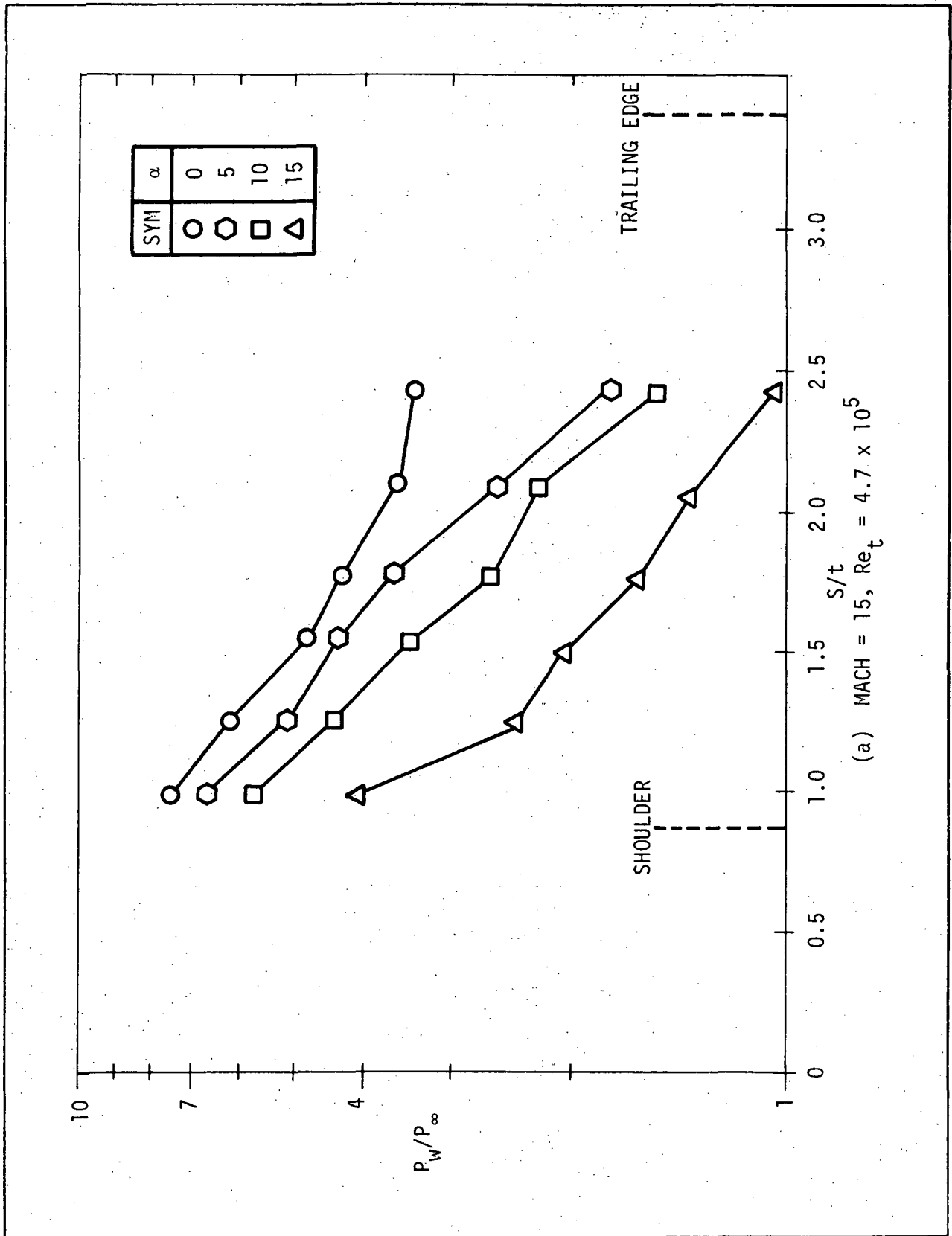
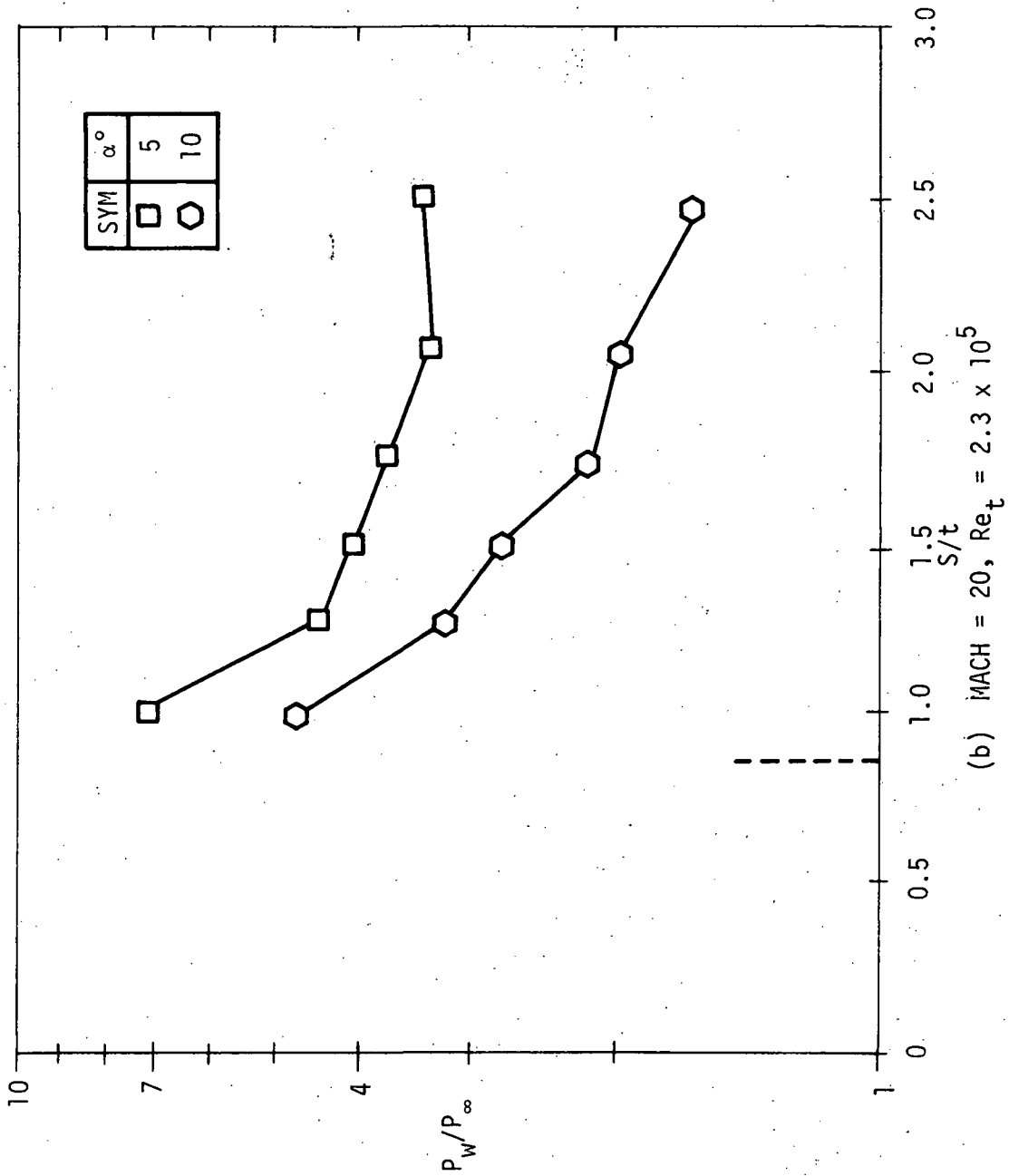


Figure 3-1. CENTERLINE PRESSURE VARIATION WITH ANGLE-OF-ATTACK FOR MACH NUMBERS OF 15 AND 20



(b) MACH = 20, $Re_t = 2.3 \times 10^5$

Figure 3-1. CENTERLINE PRESSURE VARIATION WITH ANGLE-OF-ATTACK FOR MACH NUMBERS OF 15 AND 20 (Concluded)

pressure behavior agrees with other data and signifies the decreasing effect of the blunt leading edge with increasing distance along the model.

An empirical power law variation of the pressure could be formulated in a manner similar to reference 11, but the usefulness of such a curve fit is questionable since the results cannot be readily used to predict the heat transfer variation. Simplified theories were not applied to the present data because the theories do not account for vortical flowfield. Reference 13 emphasizes the limitations of linear theories applied to complicated flowfields.

The pressure distributions in the spanwise direction are shown in Figure 3-2. The nondimensional pressure is plotted against the parameter S_0/c where S_0 is defined as S above but the origin is now taken at the lee-surface centerline. The variable c is the total distance from the centerline to the geometrical leading-edge stagnation point or one-half the span at each L/t station. The distance L is measured along the centerline from the geometric tip of the nose of the model. The pressure data were plotted in this manner in an attempt to locate vortex impingement and possibly boundary layer separation.

For 0 and 5 degrees incidence, the flow seems to be attached to the leeward surface and without any vortices since the pressures are nearly constant in the spanwise direction as shown in Figures 3-2a and 3-2b. An increase in the centerline pressure at 10 and 15 degrees of incidence is evident in Figure 3-2c and 3-2d. The pressure is nearly constant along the span near the leading edge where separation is probably occurring and the vortex is being generated. This is a low pressure region typical of vortex development (ref. 14). The vortex reattaches either on or near the centerline creating the high pressures as shown in the above figures. The reattachment point cannot be accurately located without more dense pressure instrumentation near the centerline region. The heat transfer data will be combined with the pressure data in locating the reattachment region in the next section.

A noteworthy difference between the flowfields of sharp and blunt leading-edges delta wings is that for the sharp models the wall pressure along the centerline was less than the ambient pressure for angles-of-incidence of

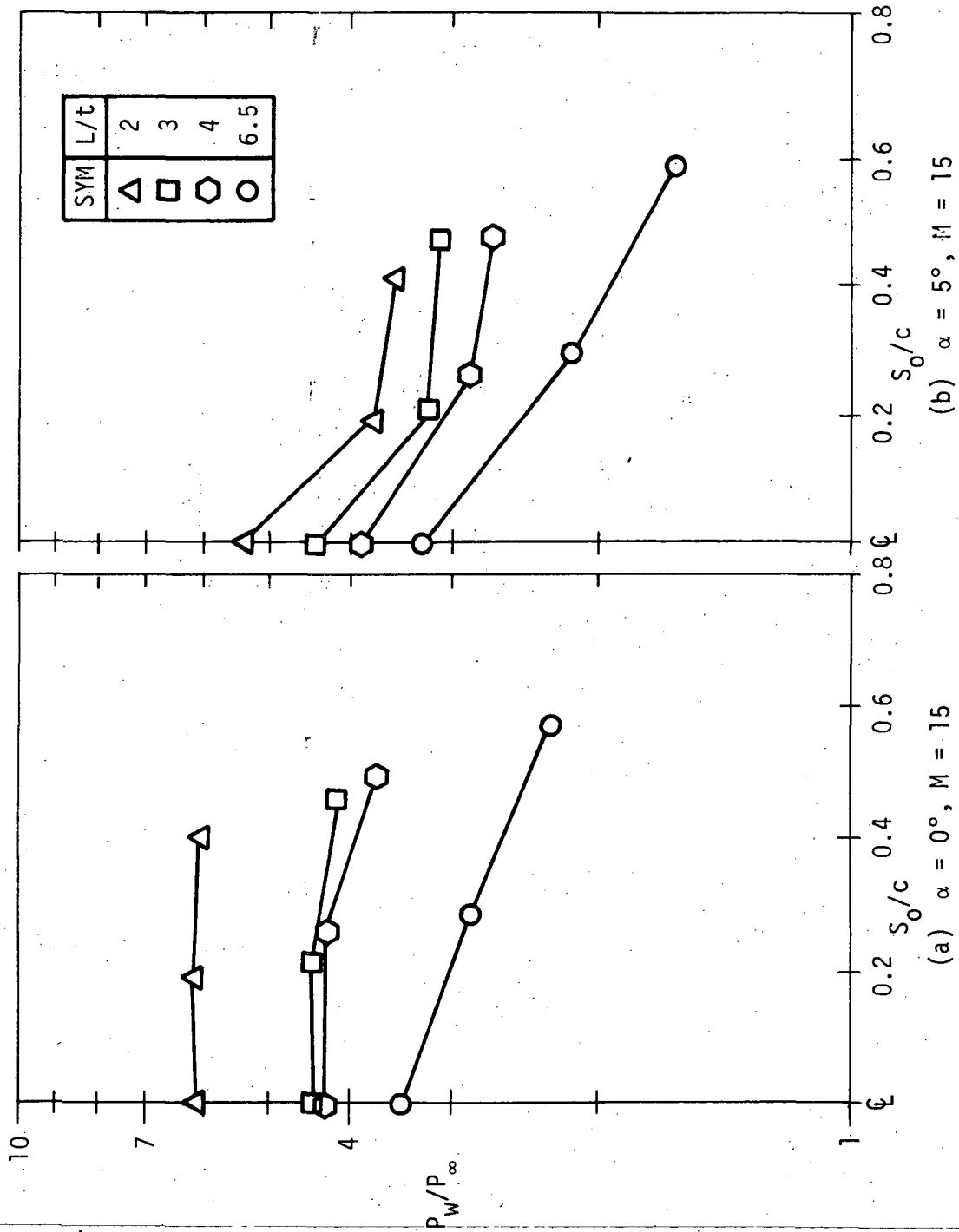


Figure 3-2. SPANWISE PRESSURE DISTRIBUTION AT VARIOUS CHORDWISE STATIONS AS A FUNCTION OF ANGLE-OF-ATTACK AND MACH NUMBER

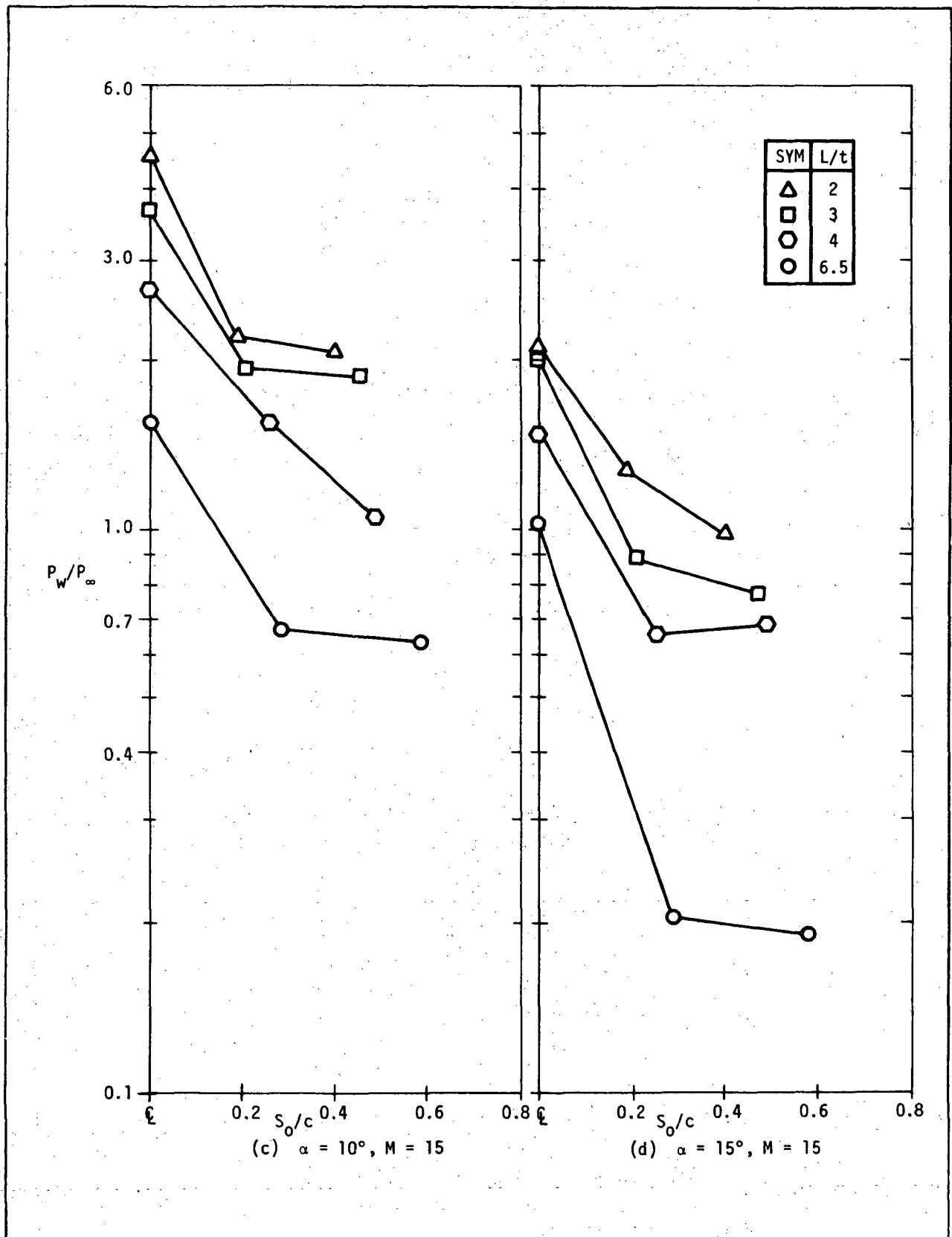


Figure 3-2. SPANWISE PRESSURE DISTRIBUTION AT VARIOUS CHORDWISE STATIONS AS A FUNCTION OF ANGLE-OF-ATTACK AND MACH NUMBER (Continued)

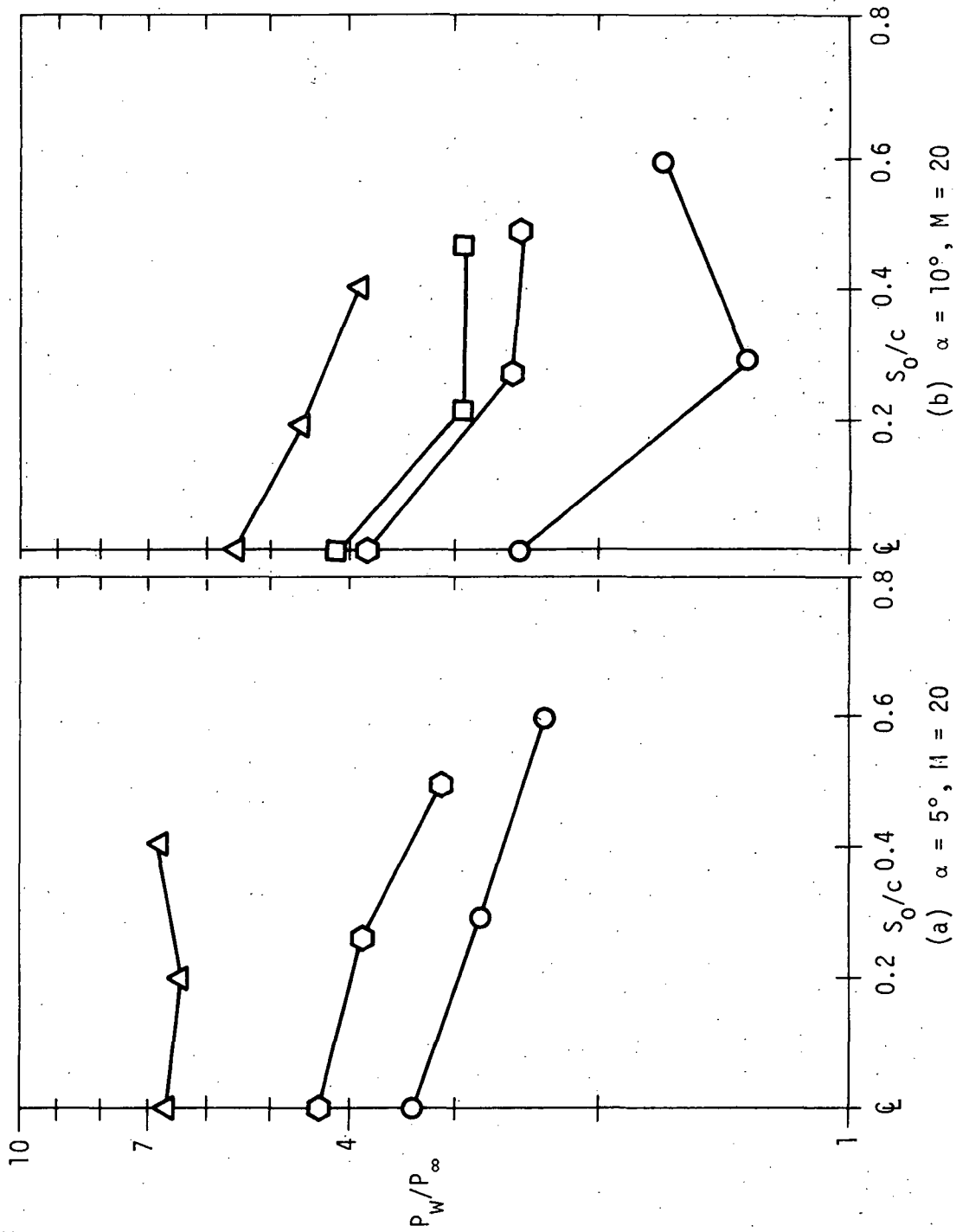


Figure 3-2. SPANWISE PRESSURE DISTRIBUTION AT VARIOUS CHORDWISE STATIONS AS A FUNCTION OF ANGLE-OF-ATTACK AND MACH NUMBER (Concluded)

5 degrees or larger. Cross (ref. 2) found that the wall pressure was approximately equal to the freestream pressure at 5 degrees incidence and decreased for larger angles-of-attack for a sharp leading-edge wing. Similarly, Whitehead's data (ref. 4) showed that the maximum wall pressure was approximately seven-tenths of the freestream value for 5 degrees incidence. Both investigators compared their pressure data to Prandtl-Meyer expansion theory and found the theory to underpredict the data by approximately 40 to 85 percent.

Supporting the observation of the present investigation that the wall pressure exceeds the freestream value for blunt leading edges, Bertram and Everhart (ref. 6) consistently found this observation to be true for both sharp and blunt prow wings. This increase is probably the result of leading-edge bluntness and viscous effects. The flow has passed through a blunt detached shock inducing higher pressures than the oblique shock for the sharp wing. The effect on the heat transfer data was more significant producing extremely large variations as illustrated in the next section.

3.2 HEAT TRANSFER DISTRIBUTION

Centerline Stanton number distributions for the angle-of-attack range for the two Mach numbers are shown in Figure 3-3. The Stanton number and Reynolds number are based on the freestream conditions using the local heat transfer coefficient and model thickness in the respective definition. The heating rate parameters are plotted against the same parameters as were the centerline pressure data in Figure 3-1. This parameter $St\sqrt{Re}$ is used to give a basis for comparison with other experimental data.

A smooth variation in the data is noted for 0 and 5 degrees angle-of-attack. Figure 3-3b shows a comparison of the data with crossflow and strip turbulent theories. The Spalding-Chi turbulent method was applied in these theories using the charts of reference 15. The normal component of the Mach number was used to compute the crossflow curve shown in the figure. The leading-edge juncture was assumed to be the virtual origin for the turbulent boundary layer. As evident from the figure, the comparison is poor as would be expected when one applies simple flat plate theory to an extremely complicated vortical flowfield. The purpose of this correlation is to allow comparison

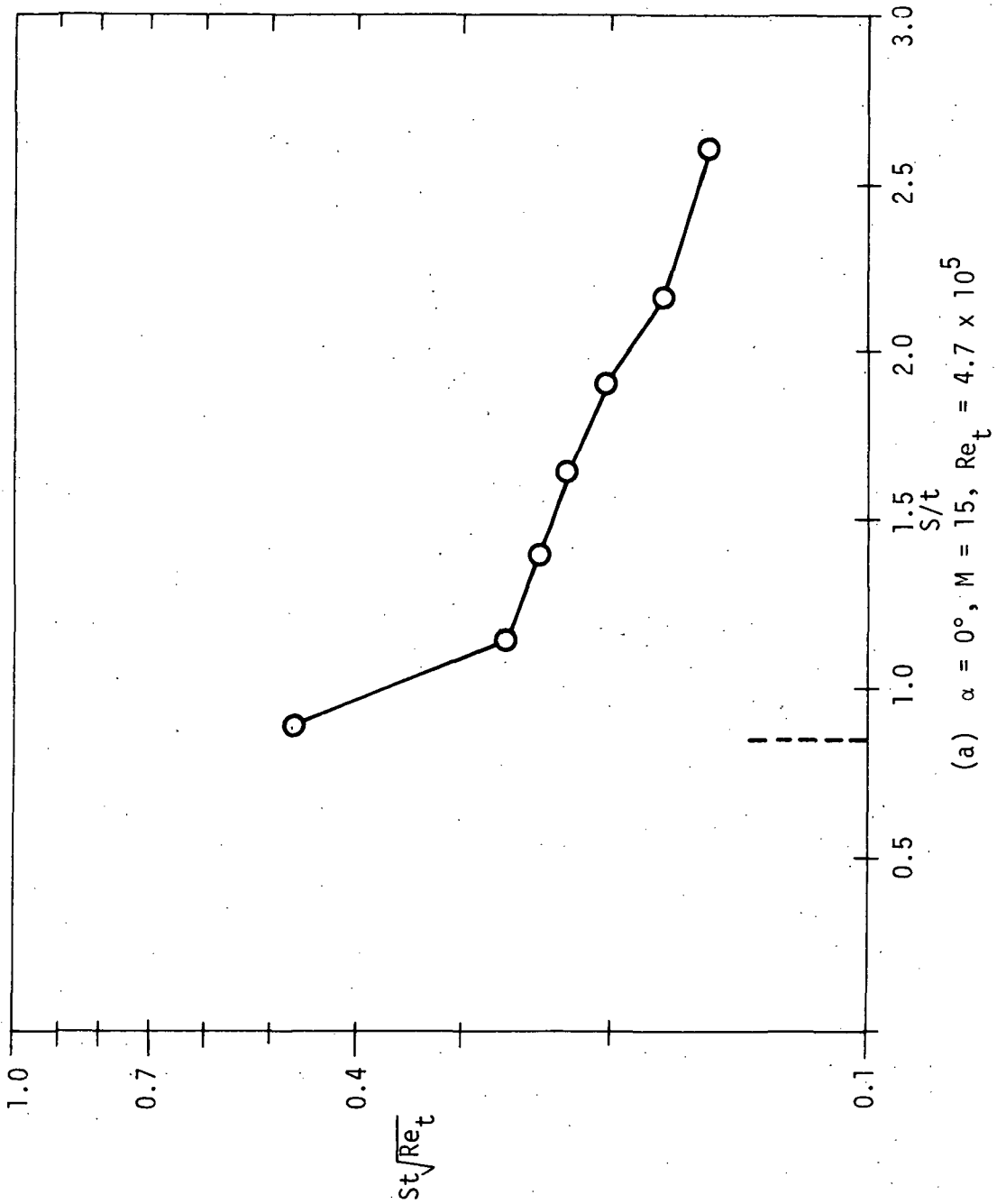


Figure 3-3. CENTERLINE STANTON NUMBER DISTRIBUTION AS A FUNCTION OF ANGLE-OF-ATTACK AND MACH NUMBER

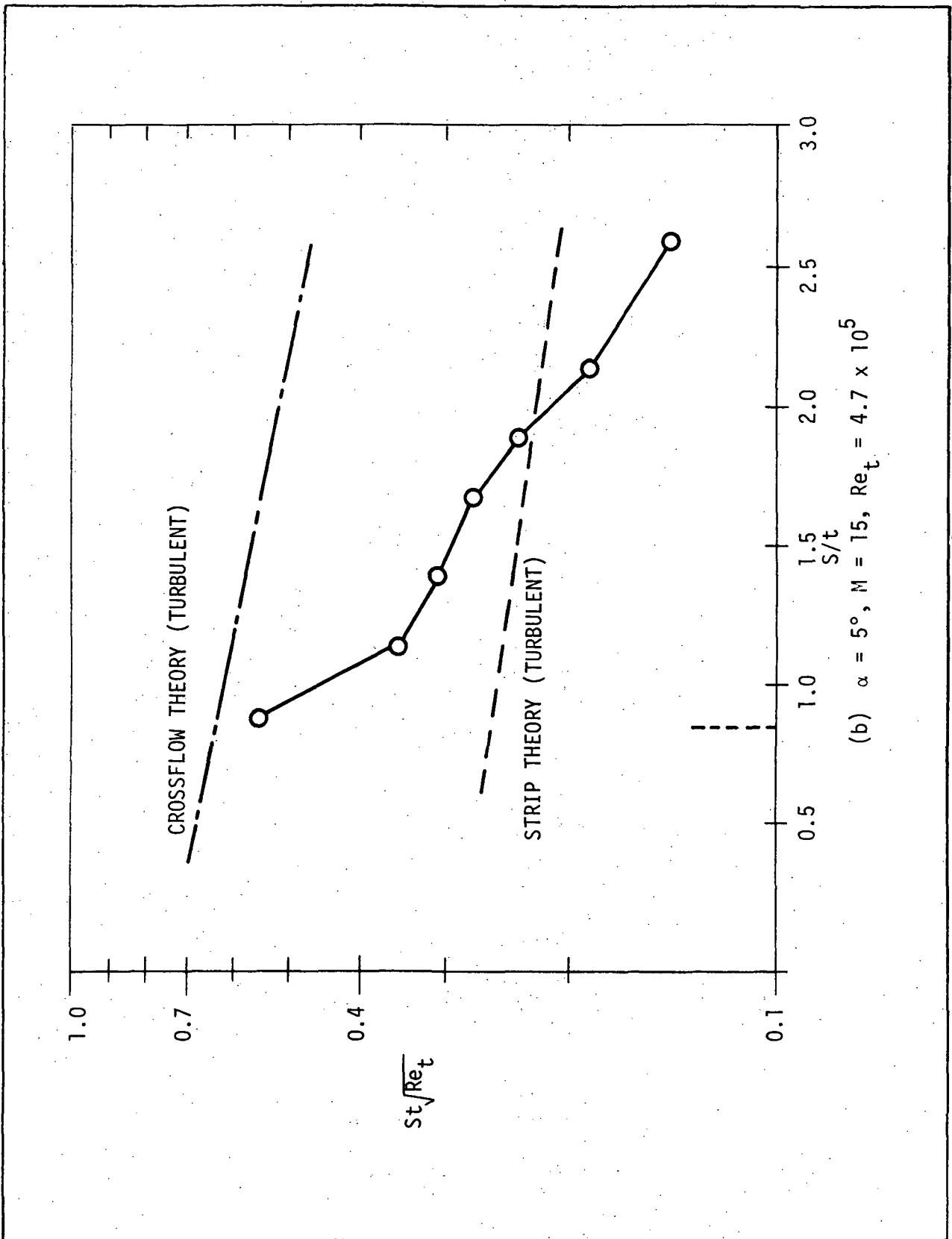


Figure 3-3. CENTERLINE STANTON NUMBER DISTRIBUTION AS A FUNCTION OF ANGLE-OF-ATTACK AND MACH NUMBER (Continued)

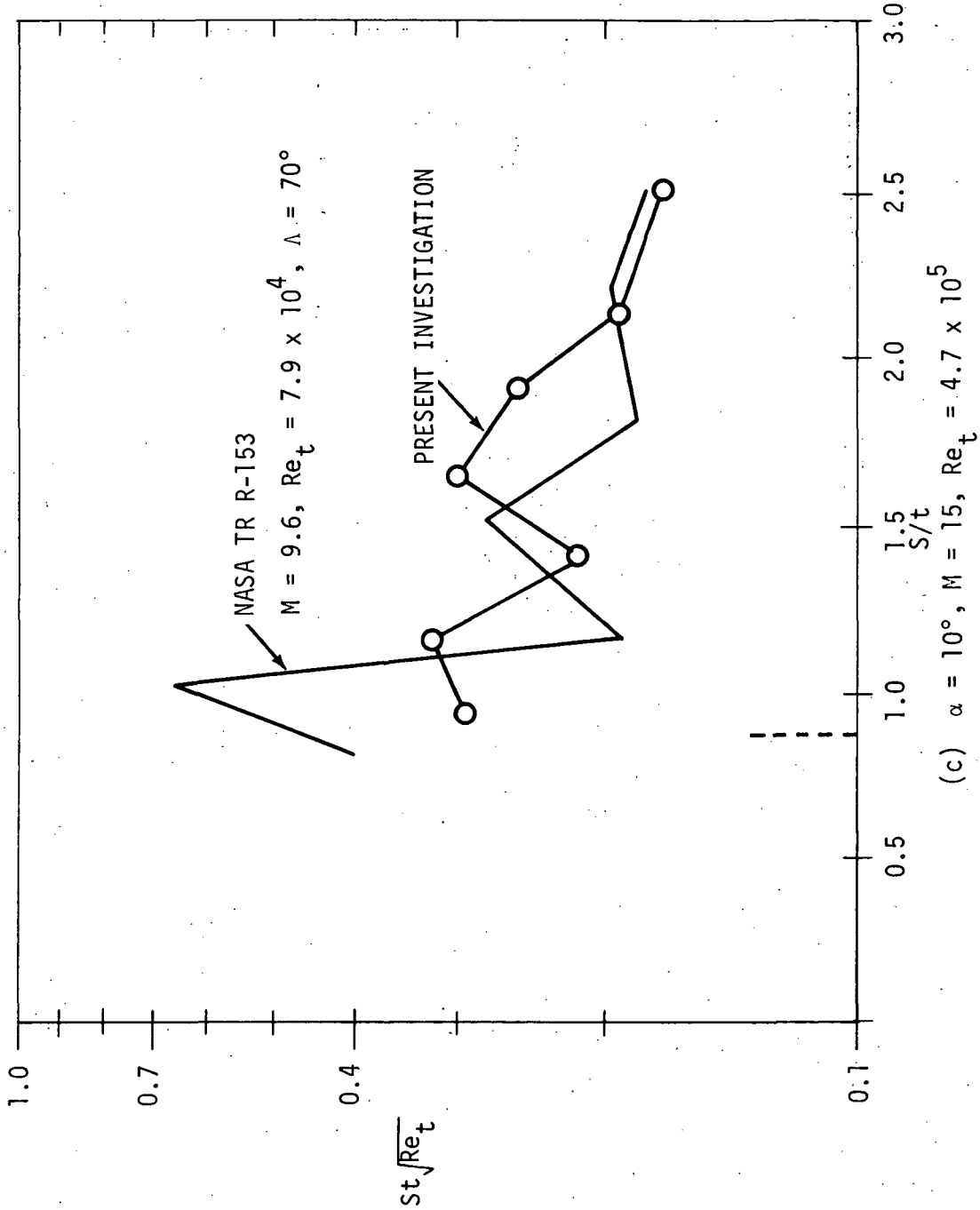


Figure 3-3. CENTERLINE STANTON NUMBER DISTRIBUTION AS A FUNCTION OF ANGLE-OF-ATTACK AND MACH NUMBER (Continued)

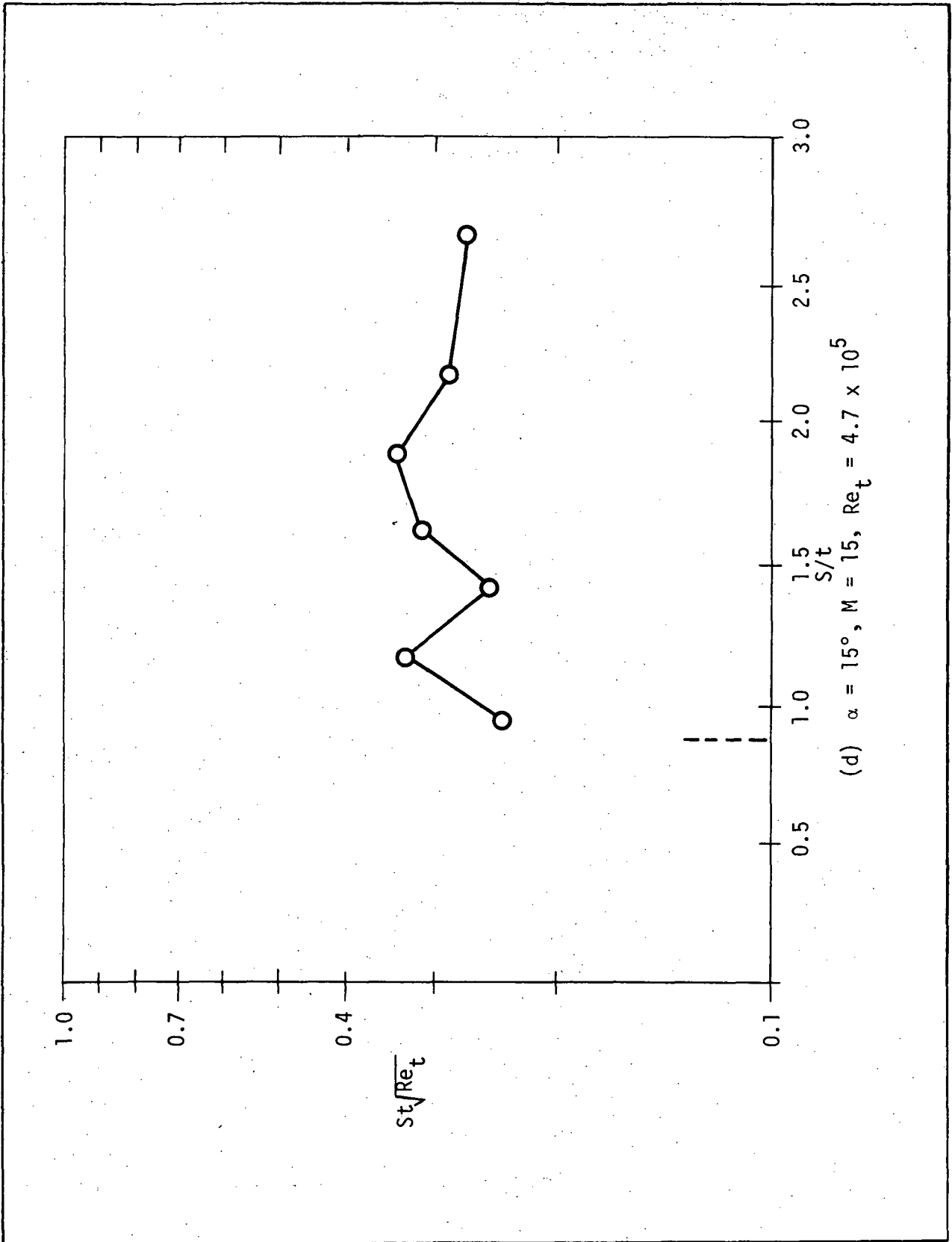


Figure 3-3. CENTERLINE STANTON NUMBER DISTRIBUTION AS A FUNCTION OF ANGLE-OF-ATTACK AND MACH NUMBER (Continued)

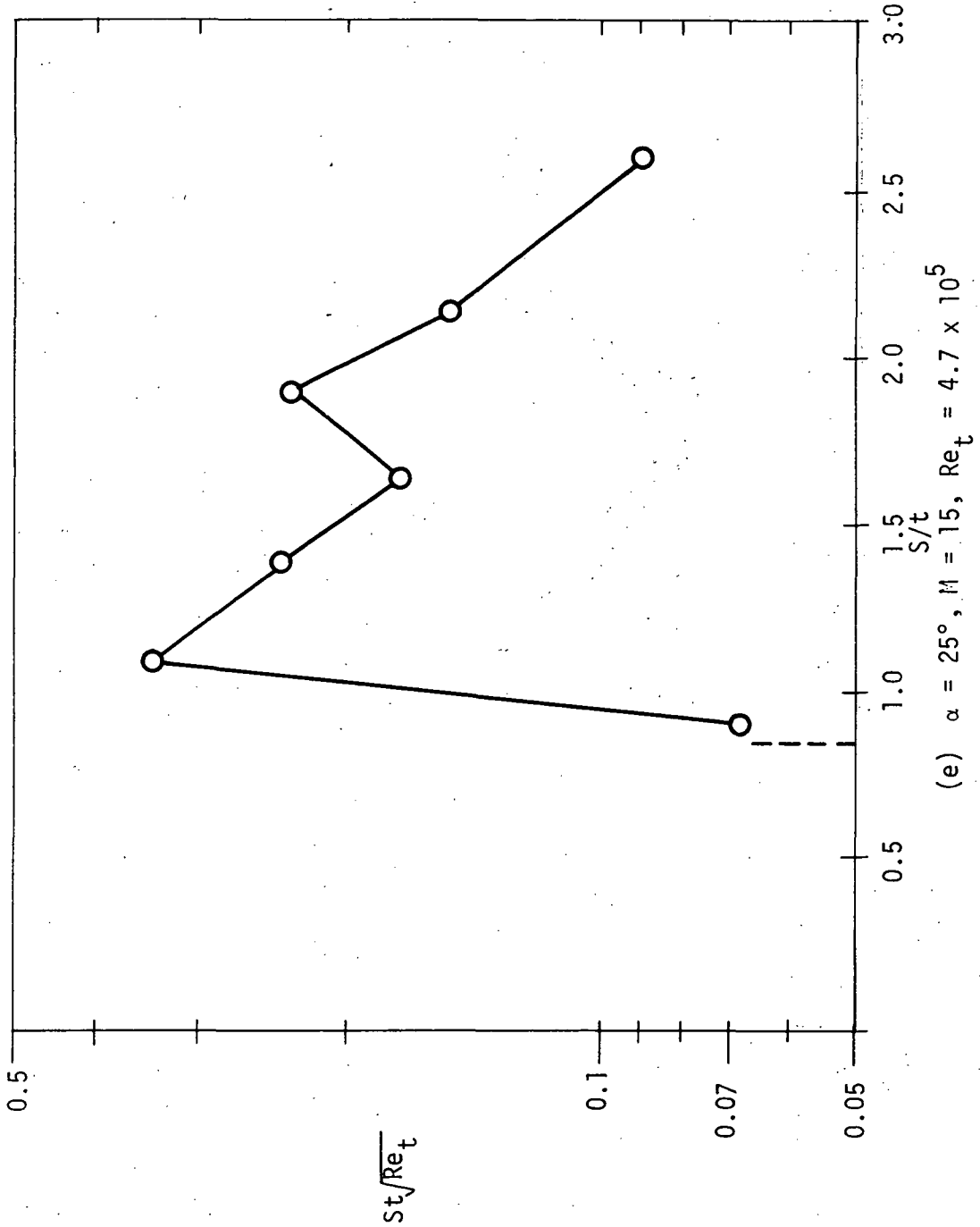


Figure 3-3. CENTERLINE STANTON NUMBER DISTRIBUTION AS A FUNCTION OF ANGLE-OF-ATTACK AND MACH NUMBER (Continued)

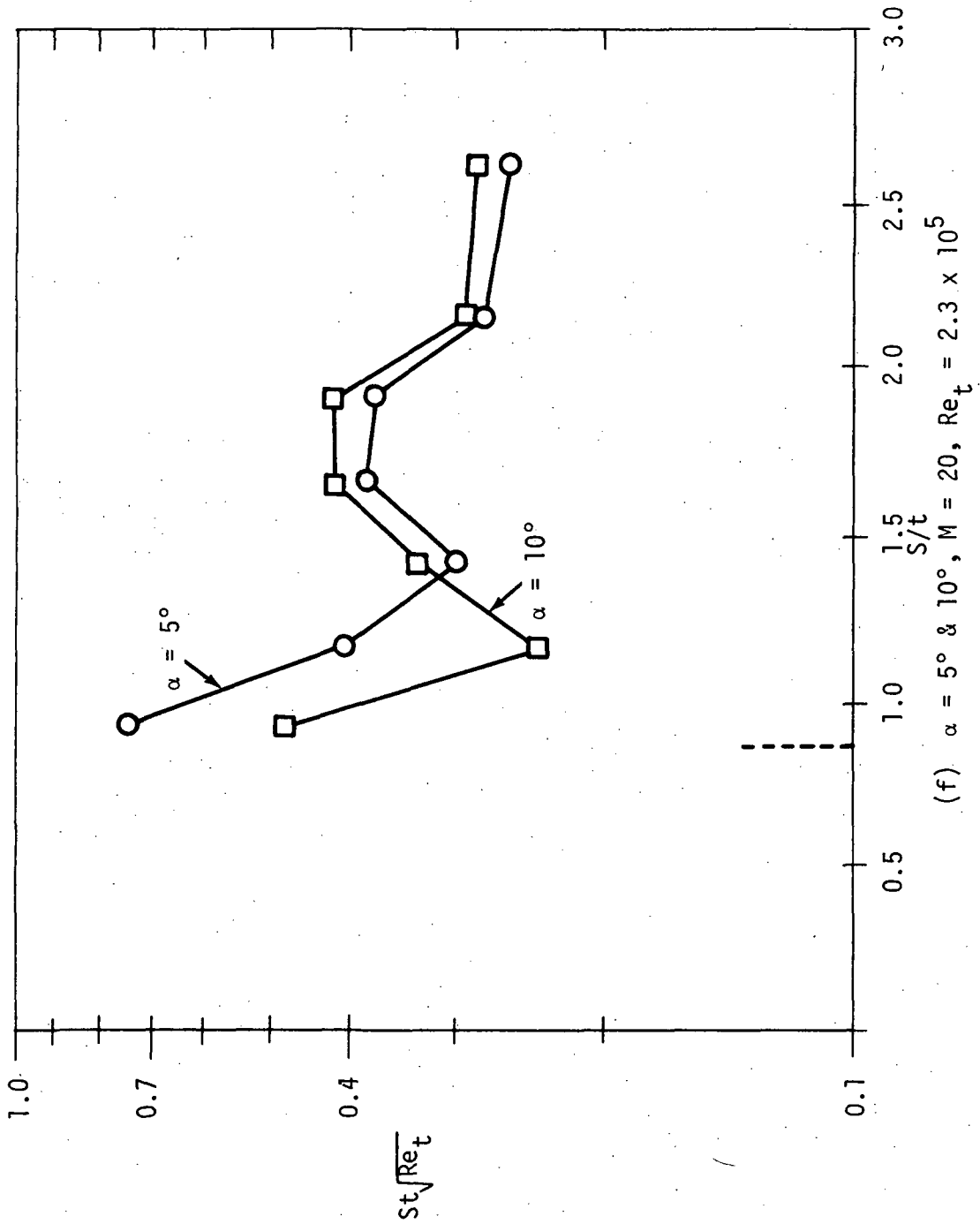


Figure 3-3. CENTERLINE STANTON NUMBER DISTRIBUTION AS A FUNCTION OF ANGLE-OF-ATTACK AND MACH NUMBER (Concluded)

with other experiments. The lack of agreement merely re-emphasizes the need for a more elaborate prediction method. Whitehead (refs. 3 and 4) similarly obtained poor comparisons in applying the Spalding-Chi theory to his experiments.

Figure 3-3c shows a comparison of the present data with that of reference 6 for 10 degrees incidence at $M = 9.6$ and $Re_t = 7.9 \times 10^4$. The trends are the same except where the peaks occur. This could be the result of different instrumentation locations. The solid lines connect data points and the peaks shown in the figure do not necessarily coincide with the position of maximum heat transfer. The peak heating rate at any station could occur between the gauges. More dense instrumentation is required to accurately locate the maximum heat-transfer location.

Several peaks were also noted along the centerline on tests on space shuttle configurations as reported in reference 16. These heating rate peaks exceeded the heating rate distribution occurring over the same model at zero degree incidence. These peaks were also found to be more sensitive to Reynolds number than to angle-of-attack. The present investigation reveals that the peaks move slightly closer to the nose as the angle-of-attack is increased. This is the same conclusion as reference 14 made for angles-of-attack exceeding 20 degrees. The magnitude of the Stanton number occurring at the first peak was relatively unaffected. Only at the higher angles-of-attack did the heating rate values near the aft section show any appreciable decrease. The lowest heating rate was found to be in the region of the nose as was the case in reference 16.

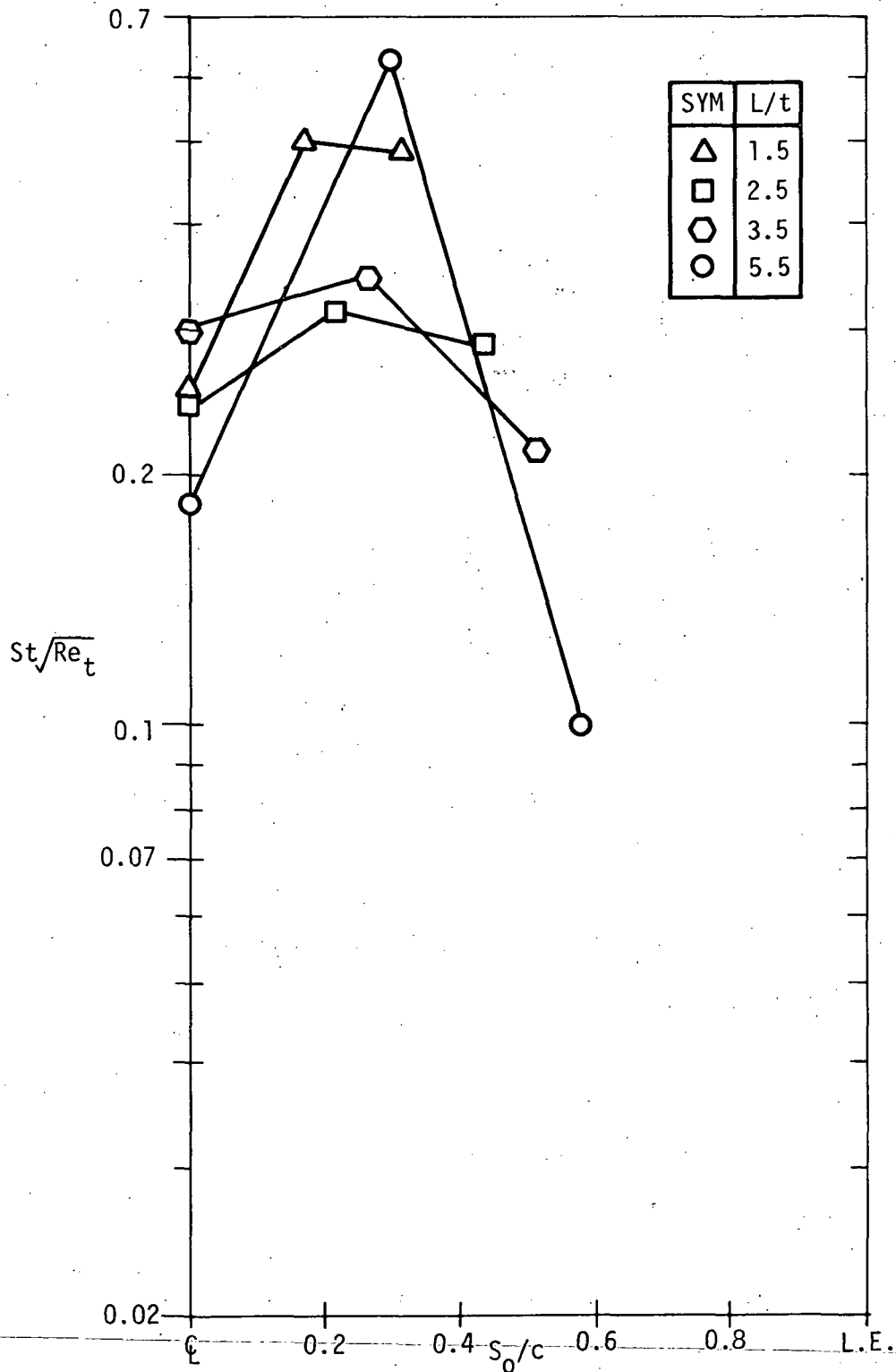
The Mach number also influences the occurrence of peaks along the centerline. Figure 3-3f shows the Stanton number distribution for Mach number 20 flow at 5 and 10 degrees angle-of-attack. The peaks appearing in the Mach 20 tests at 5 degrees incidence did not occur for the Mach 15 flow shown in Figure 3-3b. The peaks occur near the 50 percent chord which are indicative of transition flow from laminar to turbulent flow. However, transitional flows would be more likely to occur at the higher Reynolds number at Mach 15. The development of the primary vortex could also produce a similar result.

The strength of the vortex seems to increase with increasing Mach number. The magnitudes of the Stanton number parameters are increased with increasing Mach number. A comparison of Figures 3-3b and 3-3f for 5 degrees incidence reveals that the level of $St \sqrt{Re}$ is higher for the Mach 20 data. A similar comparison of reference 6 data for Mach numbers of 6.8 and 9.6 will yield the same conclusion.

The variation of the Stanton number in the spanwise direction is shown in Figure 3-4. Ideally, the point of vortex reattachment would be located as an abrupt rise in the Stanton number distribution. In order to accurately locate the reattachment point, the heat transfer gauges would have to be densely populated. Unfortunately in the present investigation limitations in the number of instrument channels prevented such a dense distribution. Hence, only the approximate location of reattachment can be determined. The data points in Figure 3-4 are joined by a solid line to aid in selecting the Stanton number peak location at each station. But due to the sparsely located instrumentation, a gauge may not be in the reattachment region and the results may be confusing. Therefore, the heat transfer results must be combined with the flow visualization studies to locate the reattachment region.

The spanwise variation for 0 and 5 degrees incidence indicate that there are no vortices or that they are extremely weak ones. At 10 degrees angle-of-attack there are more pronounced peaks in the data indicating vortex impingement. For the remaining two angles-of-attack, the peaks can be easily extrapolated using the data. The oil-flow results, which are discussed in the next article, are very useful in locating the reattachment region. The reattachment band obtained by using both heat transfer data and oil-flow results is shown in Figure 3-5 for all angles-of-attack. The accuracy of the method was not precise enough to reveal any significant variation with angle-of-attack. All the data obtained by extrapolating the spanwise data to find the peaks lay within the band shown in the Figure. The broken lines indicate an extension of the results along the model where instrumentation were not present.

The spanwise Stanton number behavior is further discussed in subsection 3.3.1 after examining surface oil-flow results.



(a) $\alpha = 0^\circ, M = 15$

Figure 3-4. SPANWISE STANTON NUMBER DISTRIBUTION FOR VARIOUS ANGLES-OF-ATTACK AND MACH NUMBERS

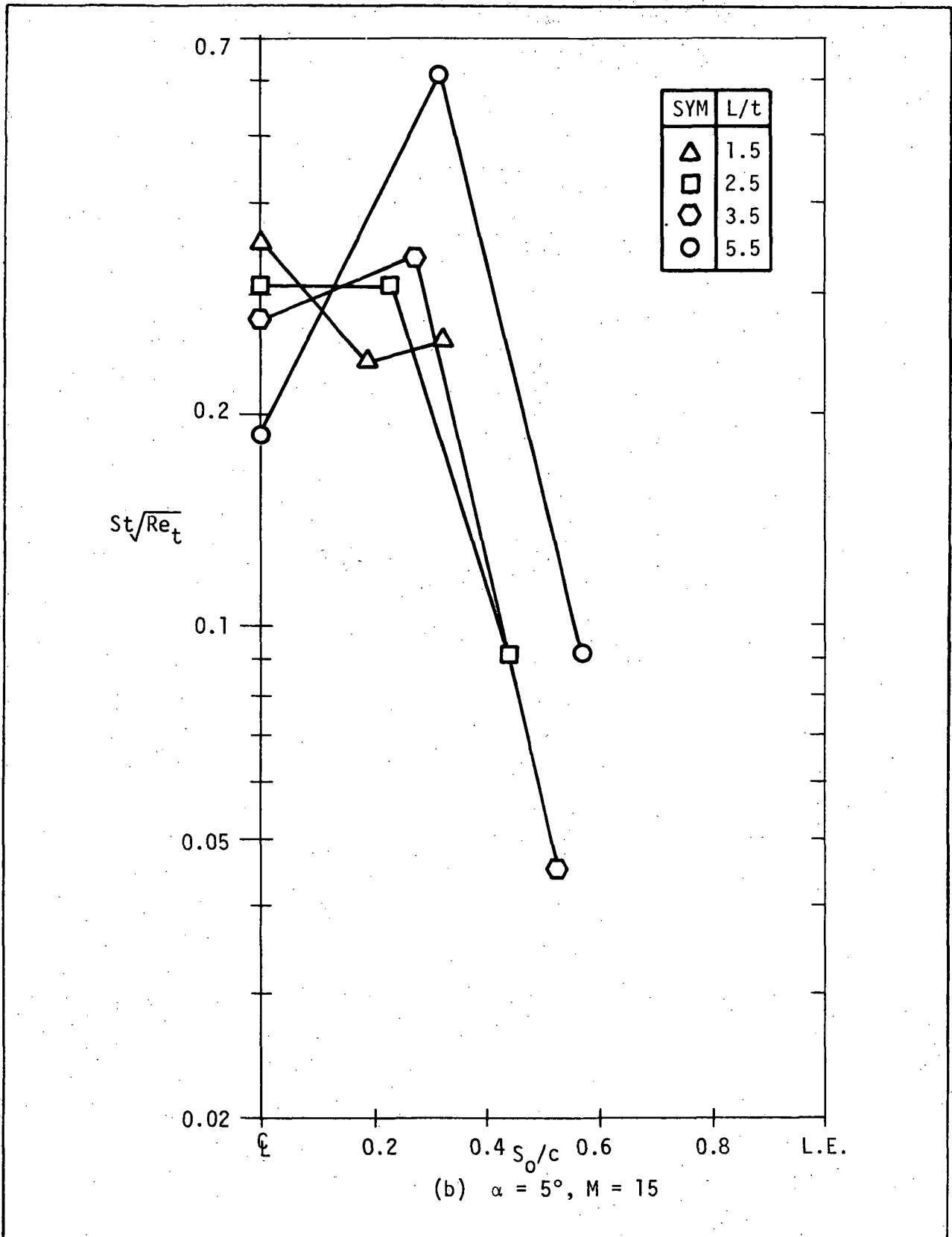


Figure 3-4. SPANWISE STANTON NUMBER DISTRIBUTION FOR VARIOUS ANGLES-OF-ATTACK AND MACH NUMBERS (Continued)

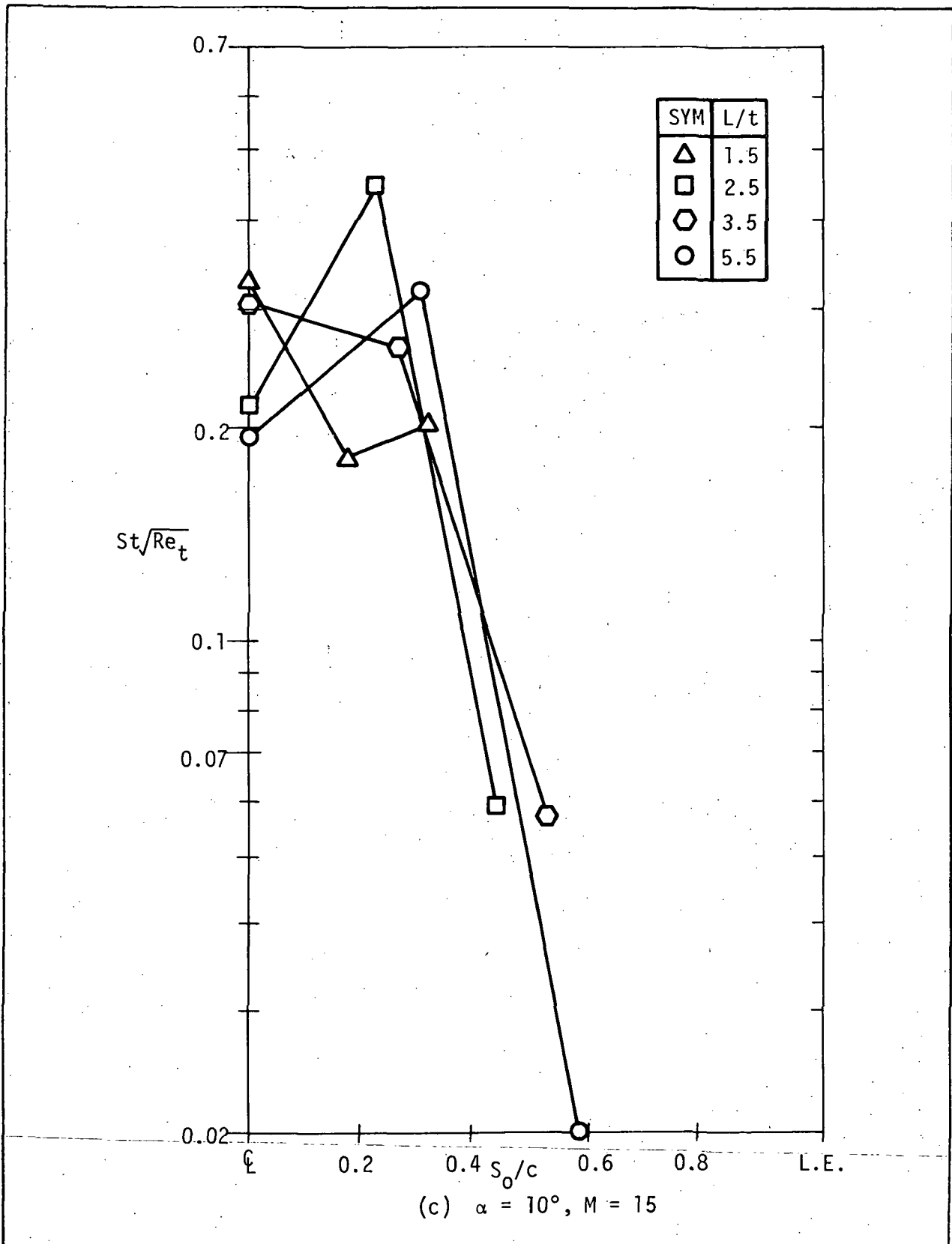


Figure 3-4. SPANWISE STANTON NUMBER DISTRIBUTION FOR VARIOUS ANGLES-OF-ATTACK AND MACH NUMBERS (Continued)

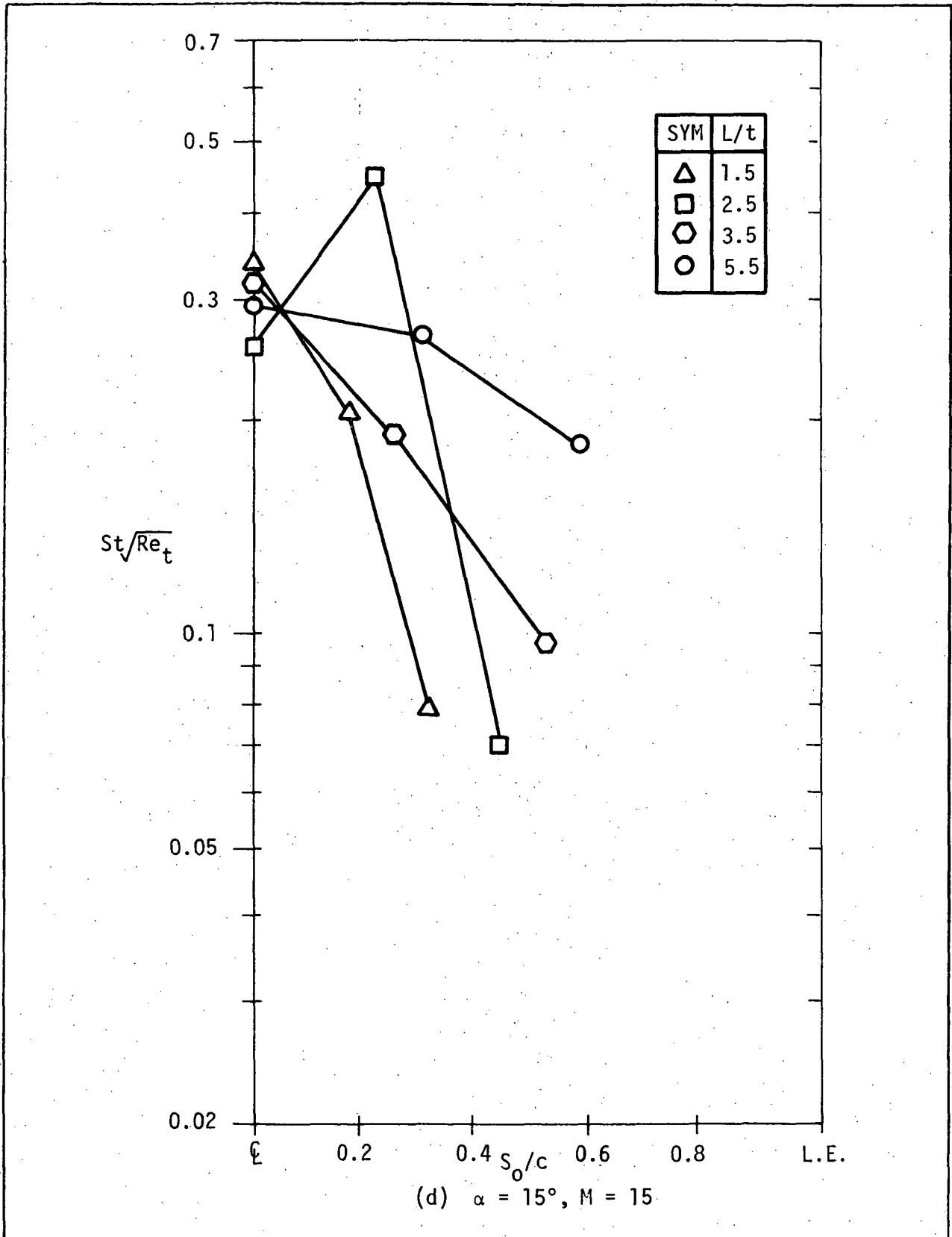


Figure 3-4. SPANWISE STANTON NUMBER DISTRIBUTION FOR VARIOUS ANGLES-OF-ATTACK AND MACH NUMBERS (Continued)

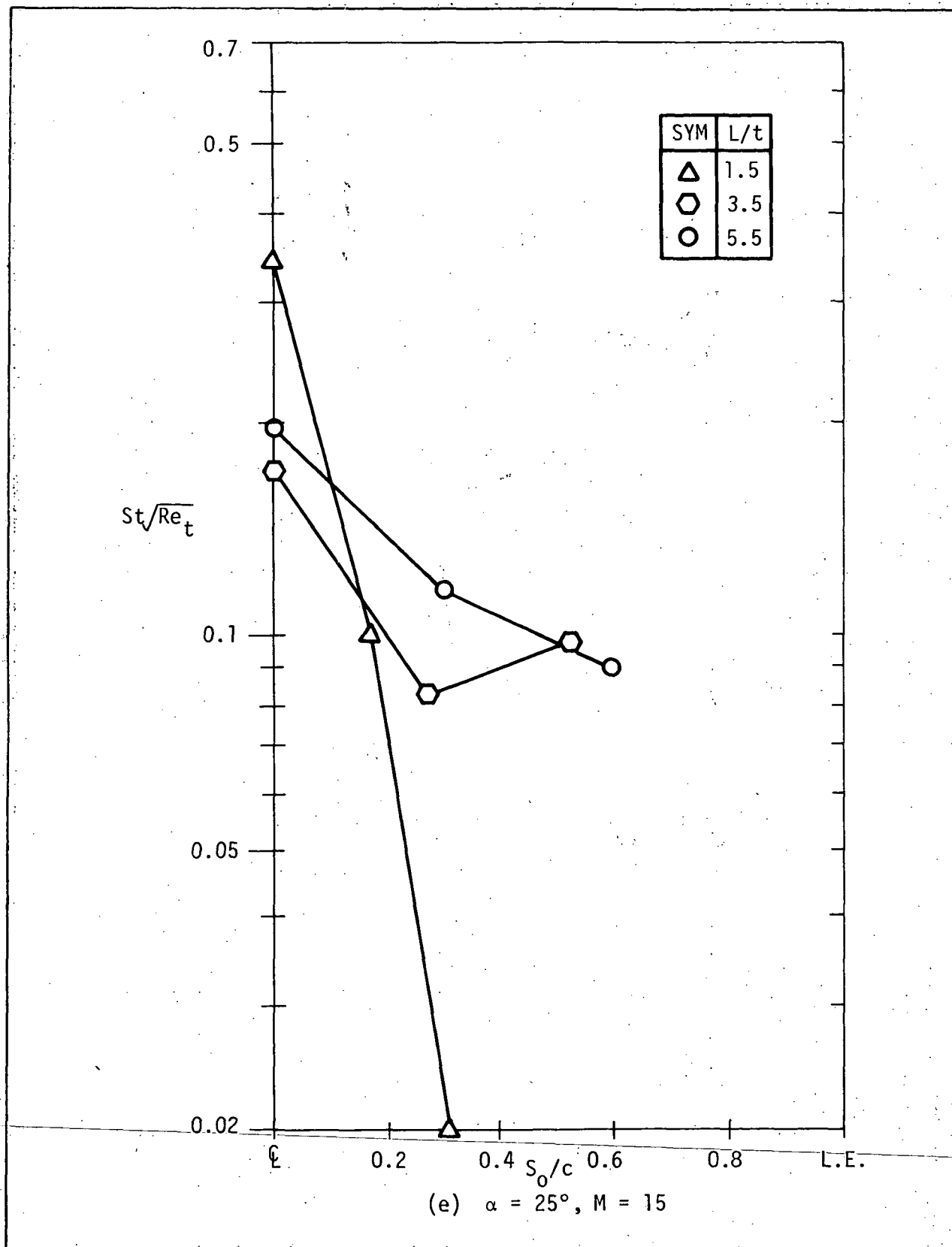


Figure 3-4. SPANWISE STANTON NUMBER DISTRIBUTION FOR VARIOUS ANGLES-OF-ATTACK AND MACH NUMBERS (Continued)

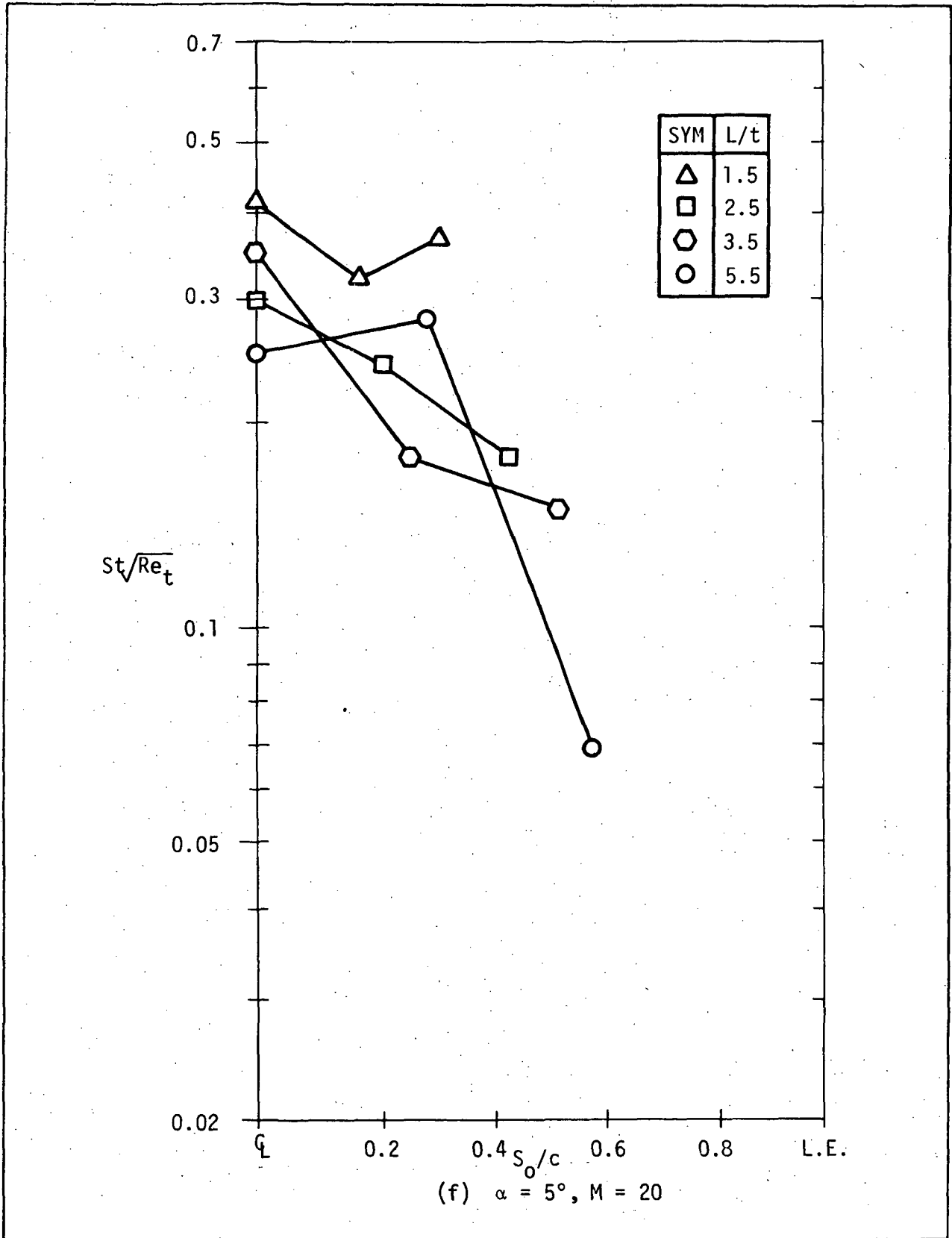


Figure 3-4. SPANWISE STANTON NUMBER DISTRIBUTION FOR VARIOUS ANGLES-OF-ATTACK AND MACH NUMBERS (Continued)

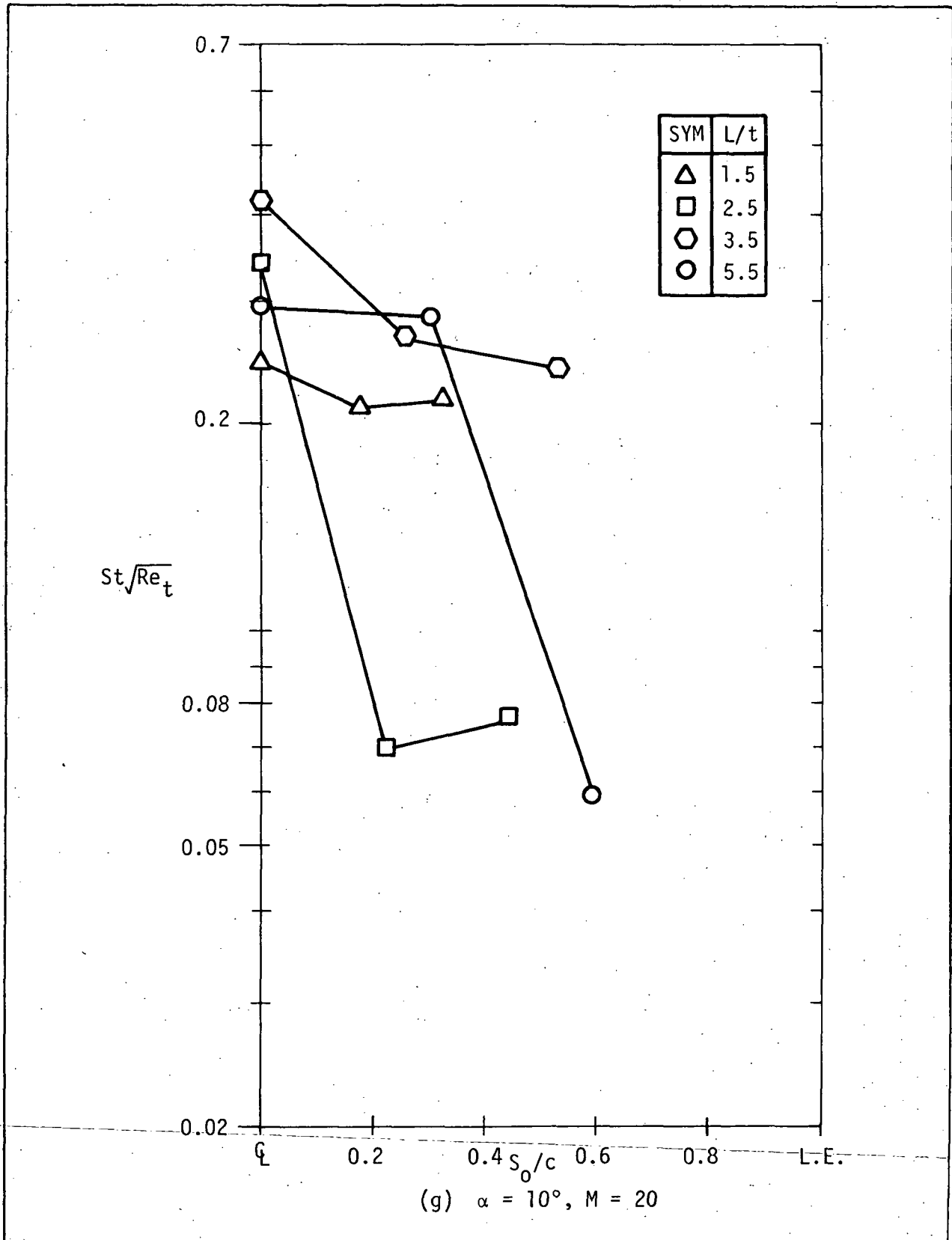


Figure 3-4. SPANWISE STANTON NUMBER DISTRIBUTION FOR VARIOUS ANGLES-OF-ATTACK AND MACH NUMBERS (Concluded)

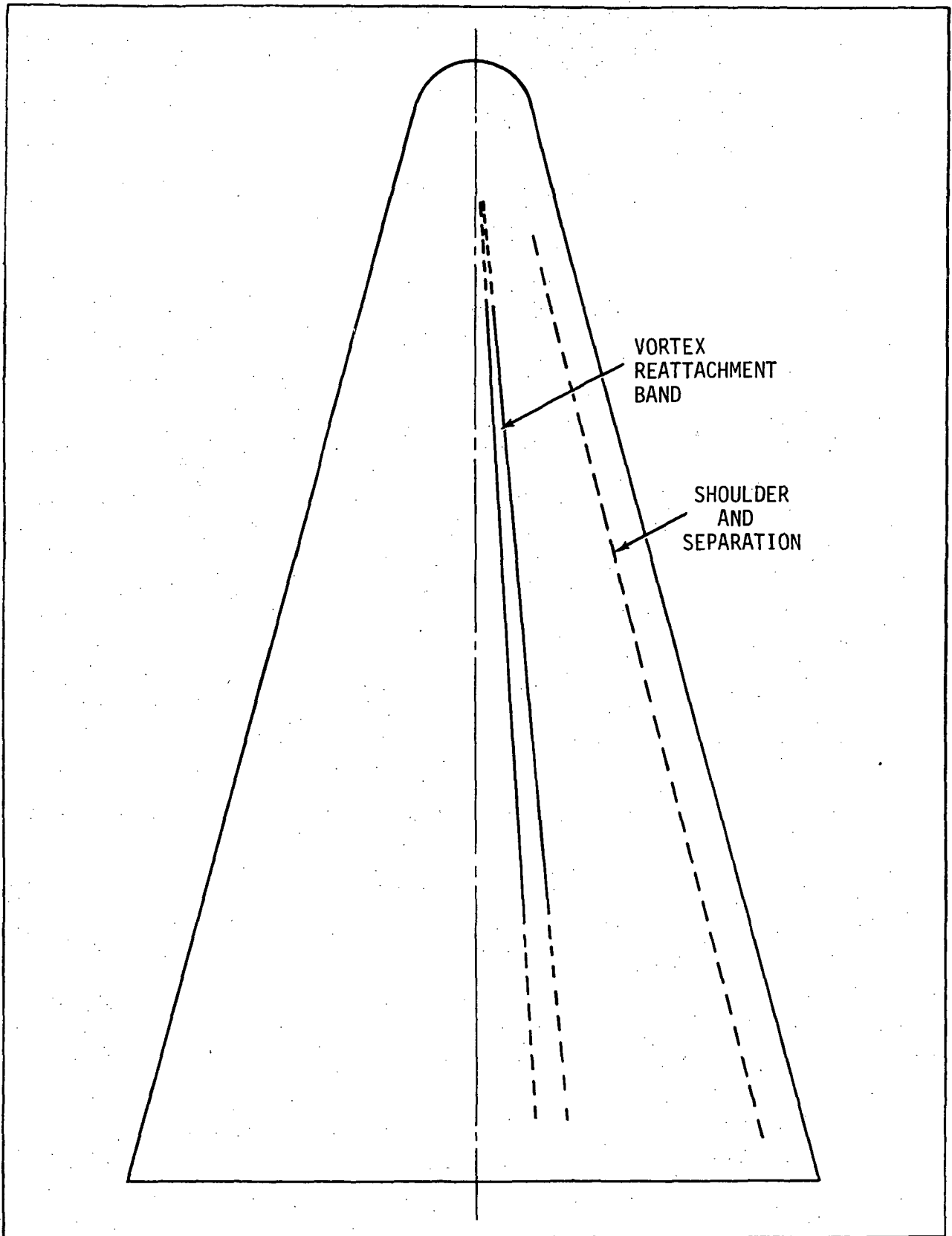


Figure 3-5. VORTEX REATTACHMENT REGION

The instrumentation was located along rays centered at the model tip of 6 and 12 degrees from the centerline to determine if the flow was conical for a blunt wing. Cross (ref. 2) and Whitehead (ref. 3) had individually concluded that the flow was conical for a sharp leading-edge delta wing at high Reynolds number and low incidence angles. After careful examination of the present data, it was concluded that no conical flow existed for any combination of test conditions and model angle-of-attack for the blunt leading-edge model. The data from the present study was nondimensionalized in the same manner as was performed in obtaining Figure 2 of reference 4. The spanwise Stanton numbers were nondimensionalized at each station by the centerline value and plotted against the ray angle measured from the centerline. The present data displayed a very erratic pattern and are not presented herein. A plot of the local Stanton numbers along the rays yielded in similar result. Hence, the flowfield for a blunt delta wing at incidence is not conical in any manner for the range of conditions tested.

The effect of Reynolds number was not investigated in the present study. Although the effect of Reynolds number on the heat transfer to the body is catastrophic (ref. 4), more emphasis was placed on obtaining a Mach number and Reynolds number combination which was representative of actual flight trajectories for the Space Shuttle vehicle. A combination was chosen to insure the initiation of the vortex system and separated flow on the leeward surface. Reference 16 found that by increasing the Reynolds number, the peak heating near the nose was increased and the heating on the aft section of the model was decreased. There are not enough experimental data available at this time to precisely determine the effect of Reynolds number on the leeward surface heating.

The effect of nose shape on the heating rate distribution can be realized from reference 6. The magnitudes of the Stanton numbers for a blunt nose are generally larger than those for a sharp nose for the same test conditions. Intuitively, the heating rate level of a blunt leading-edge delta wing would be larger than the corresponding sharp leading-edge wing. This trend was true for the pressure variation previously discussed. The induced vortex from the blunt leading-edge is apparently stronger than the vortices generated by

sharp leading edges. The differences can be attributed to the different fluid energies of the two shocked configurations

3.3 VISUAL STUDIES

Surface oil-flow and schlieren photographs were taken at each test condition and configuration to study the leeward surface flowfield. The results of these tests are described in this section.

3.3.1 Surface Oil-Flow Patterns

Figure 3-6 displays the results for the surface oil-flow tests for all angles-of-attack for Mach numbers of 15 and 20. The flowfield at 5 degrees incidence appears attached and without vortices. The flow is parallel to the centerline along the central region for all angles-of-attack. At 10 degrees angle-of-attack, vortices have been generated creating the outflow from the centerline region of the model. The highest shear is along the centerline of the model for the fore section shifting off the centerline on the aft section of the model. This phenomena can possibly explain the peaks in the spanwise Stanton number distribution for the aft stations shown in Figure 3-4. The flow immediately turns in the longitudinal direction at the juncture of the cylindrical leading-edge and the slab leeward surface. Hence, separation occurs at the shoulder. The lowest shear region occurs just after separation. Similar results occur at an angle-of-attack of 15 degrees.

There does not seem to be as well defined vortical flowfield for 25 degrees incidence as was in the previous cases. Although the highest shear is still along the centerline in Figure 3-6d, the surface shear appears approximately equal over the remainder of the model.

Figure 3-6 indicates that vortices are present at 5 degrees angle-of-attack for a Mach number of 20. The largest shear region is off the centerline as previously described for the 10 degree and Mach 15 case. An interesting difference is that the flow turns in the longitudinal direction before the juncture of the leading edge and slab surface. This phenomenon is easily seen in Figure 3-6 (Mach = 20, $\alpha = 5$ degrees). This flowfield pattern could be induced by the oil dots placed on the leading edge.

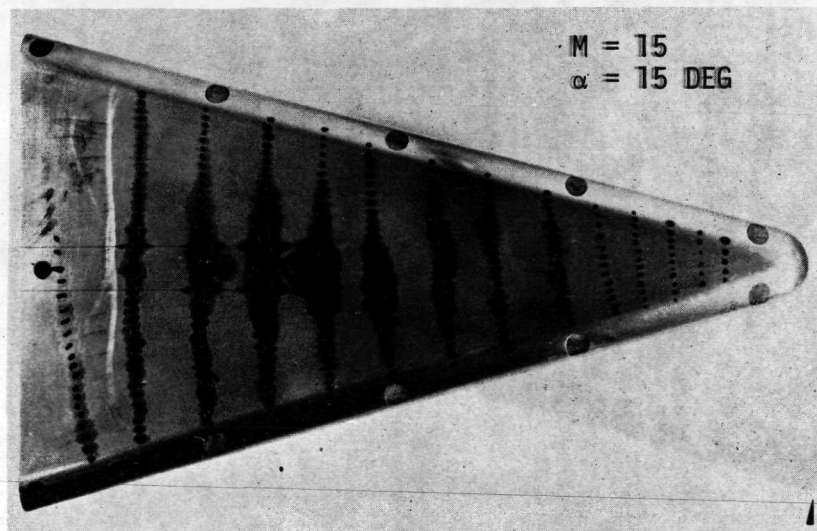
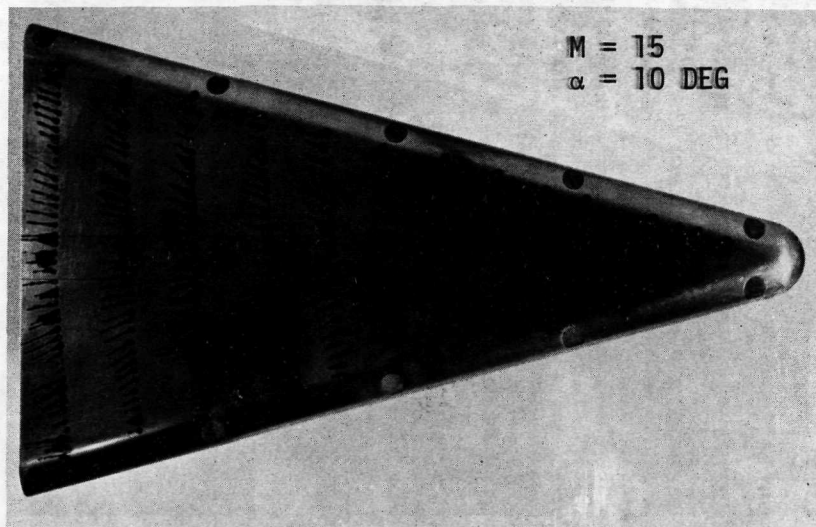
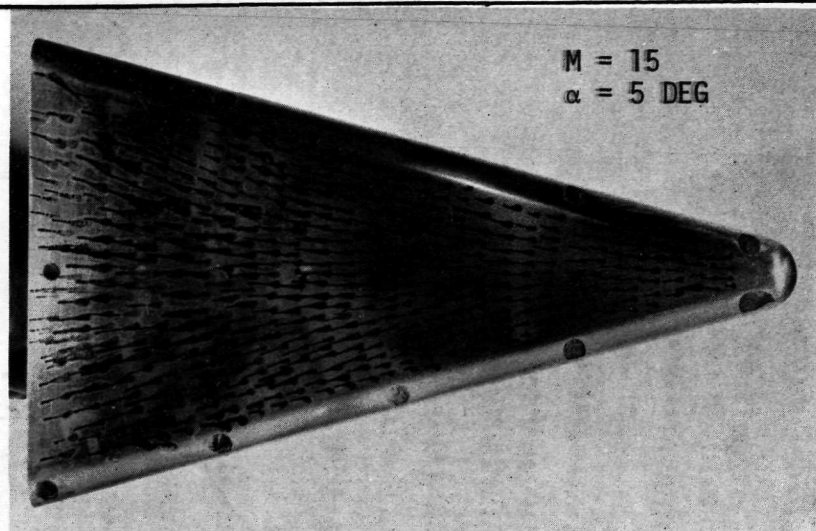


Figure 3-6. OIL FLOW PATTERNS

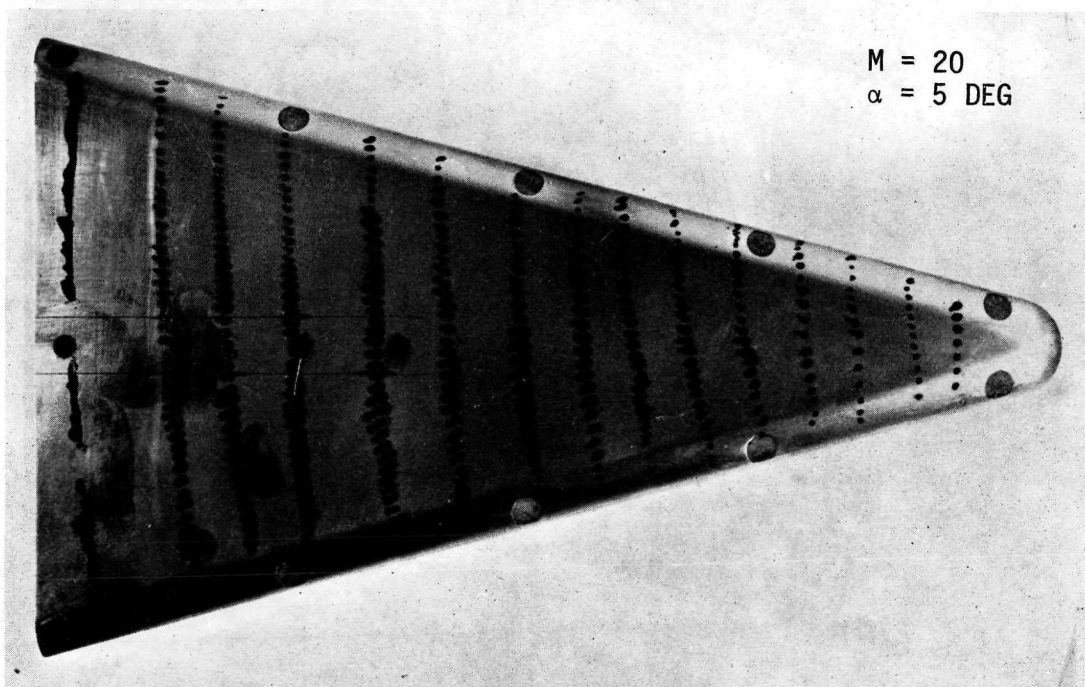
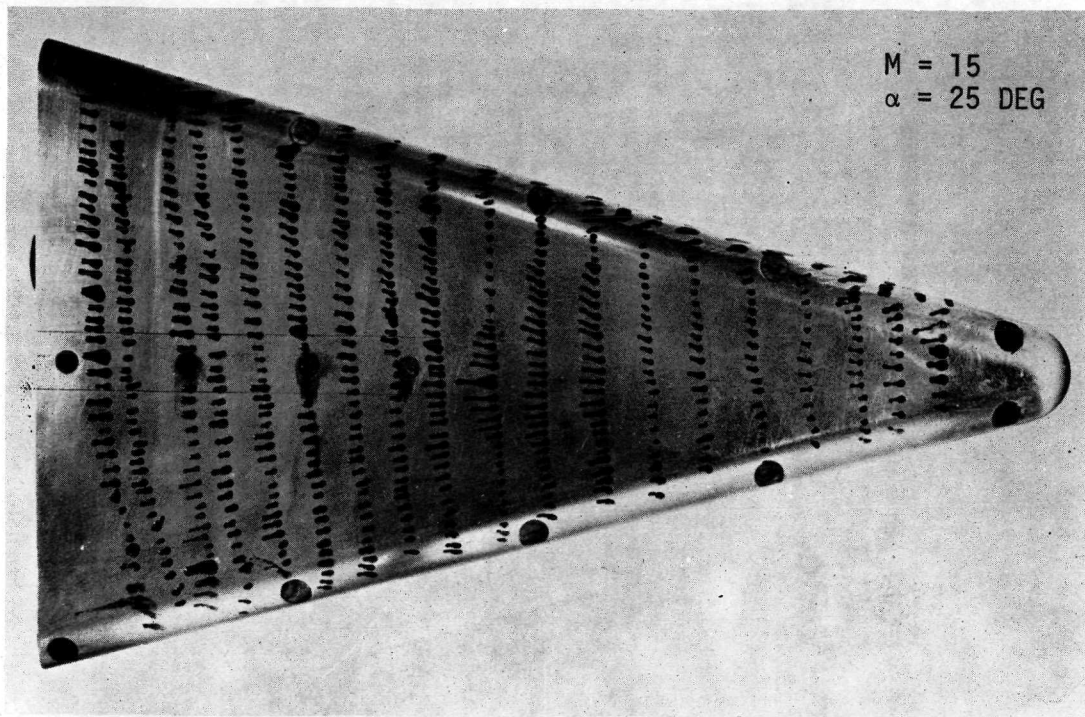


Figure 3-6. OIL FLOW PATTERNS (Continued)

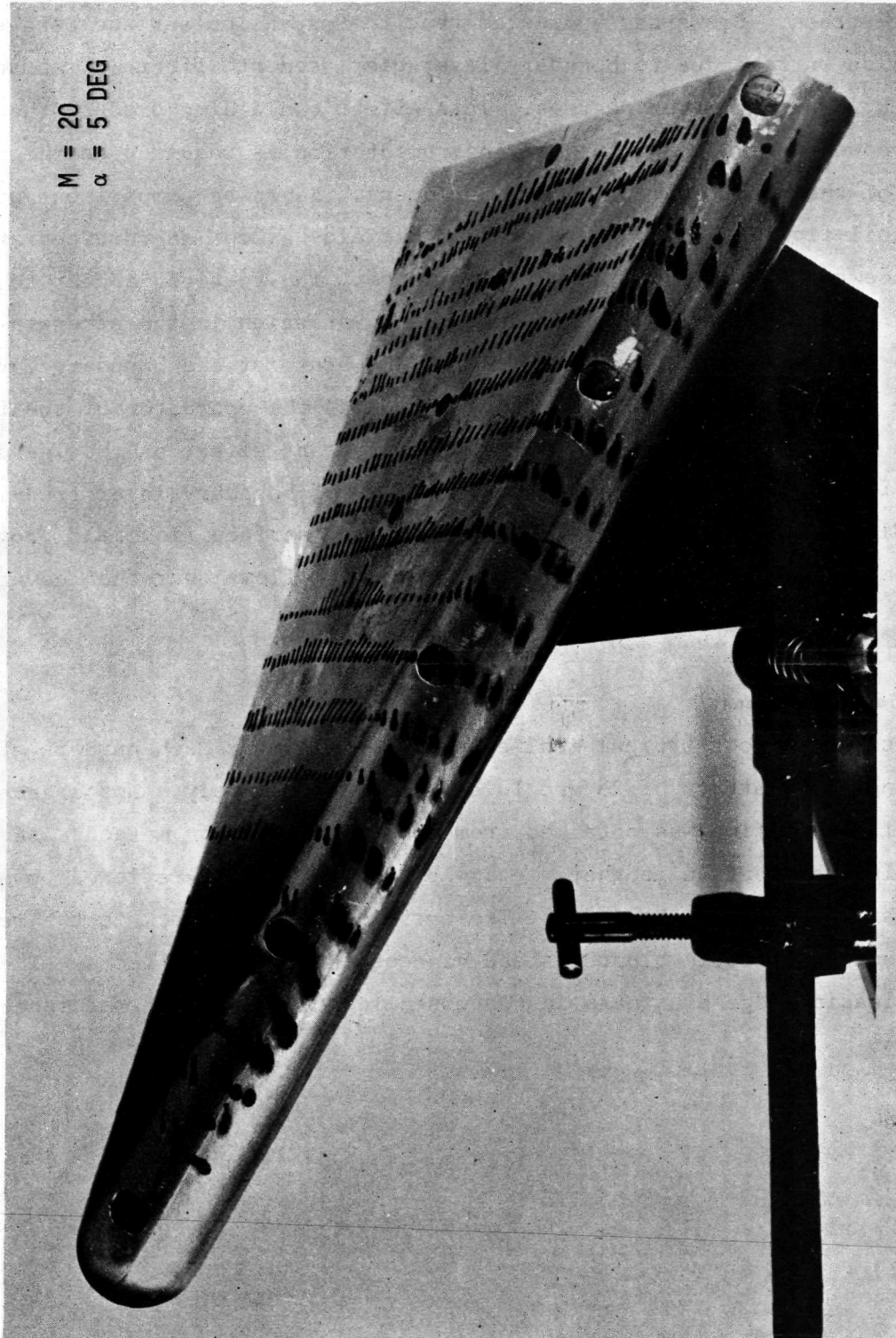
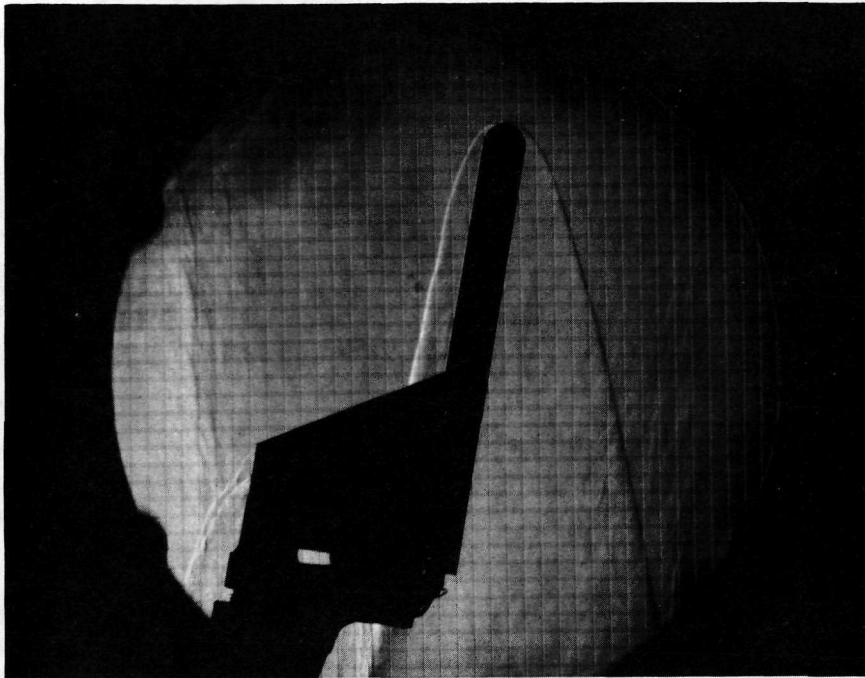


Figure 3-6. OIL FLOW PATTERNS (Concluded)

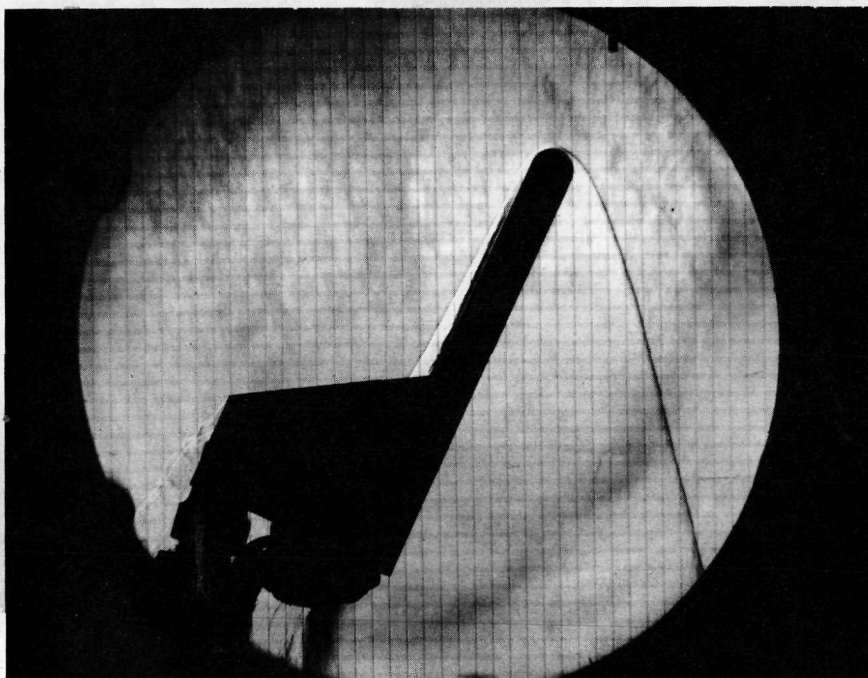
The heat transfer data in Figure 3-4f supports the existence of a high shear region on the aft section of the model at Mach 20. This seems to imply that the vortical flowfield has a stronger dependence on Mach number than on angle-of-attack. Cross has suggested that the expansion surface behaves as a compression surface due to boundary layer displacement effects at an angle-of-attack less than seven degrees. This effect could also produce the outflow effect shown in Figure 3-5e. More instrumentation is required on the aft section of the model to clarify the phenomena. Based on comparisons with the Mach 15 oil-flow patterns, the Mach 20 flowfield has coiled vortices attaching to the leeward surface at 5 degrees incidence. The vortices appear to be stronger on the aft part of the model. This variation in the strength of the vortices is probably a strong function of the state of the boundary layer on both the leeward and windward surface. In fact, the character of the flowfield on the windward surface may have an important effect on the leeward surface flowfield. For instance, the location of boundary layer transition on the windward surface could affect the leeward surface flowfield properties since some of the fluid from the windward surface flows over the leeward surface.

3.3.2 Schlieren Photographs

Figure 3-7 shows typical schlieren photographs for Mach numbers of 15 and 20 for angles-of-attack of 25 and 10 degrees, respectively. Not a great deal of useful information was obtained from this visualization method. An interesting observation is that the bow shock is slightly reflexed toward the model near the nose of the model. The curvature of the shock is the result of leading-edge hypersonic bluntness and viscous interaction effects. The phenomenon of leading-edge bluntness is discussed in some detail in reference 13.



M = 20
 α = 10 DEG



M = 15
 α = 25 DEG

Figure 3-7. SCHLIEREN PHOTOGRAPHS

Section IV

FLOWFIELD DESCRIPTION

Before an analytical description of the leeward surface flowfield can be realized, a detailed understanding of the flowfield phenomena is essential. Until recently, the lack of experimental data had prevented a qualified interpretation of the flowfield. The experimental investigations which did contribute to describing the lee-side flowfield were performed for sharp leading-edge wings. The most noteworthy flowfield description was postulated by Cross (ref. 2).

The purpose of this section is to systematically describe, in the author's opinion, the principal aspects of the leeward surface flowfield over a blunt leading-edge delta wing at incidence in hypersonic flow. The postulated flowfield is obtained by analyzing the experimental data obtained in the present investigation and by comparisons of the data with other sharp leading-edge data. Another objective of this section is to resolve the principal lee-side flowfield differences between sharp and blunt leading-edge delta wings.

A description of the lee-side flowfield of a delta wing at incidence is difficult due to the highly three-dimensional and viscous nature of the problem. The flow initially senses the spherical nose of the model and the detached bow shock is developed accordingly. The flow behind the stagnation point of the model expands around the nose remaining attached to the surface. Figure 4-1 displays a schematic of the principal flow characteristics that are described in this section.

Away from the nose where the planform of the leading edge becomes cylindrical, the flow initially traveling towards the wing leading edge is first accelerated instantaneously outwards and upwards away from the wing. The flow is then gradually turned inwards and downstream along the centerline by means of the expansion waves around and parallel to the leading edges. Due to symmetry, the flow must finish parallel to the centerline. Two flow aligning shocks, which are often referred to as embedded shocks because they are located between the bow shock and viscous region, are the mechanisms for

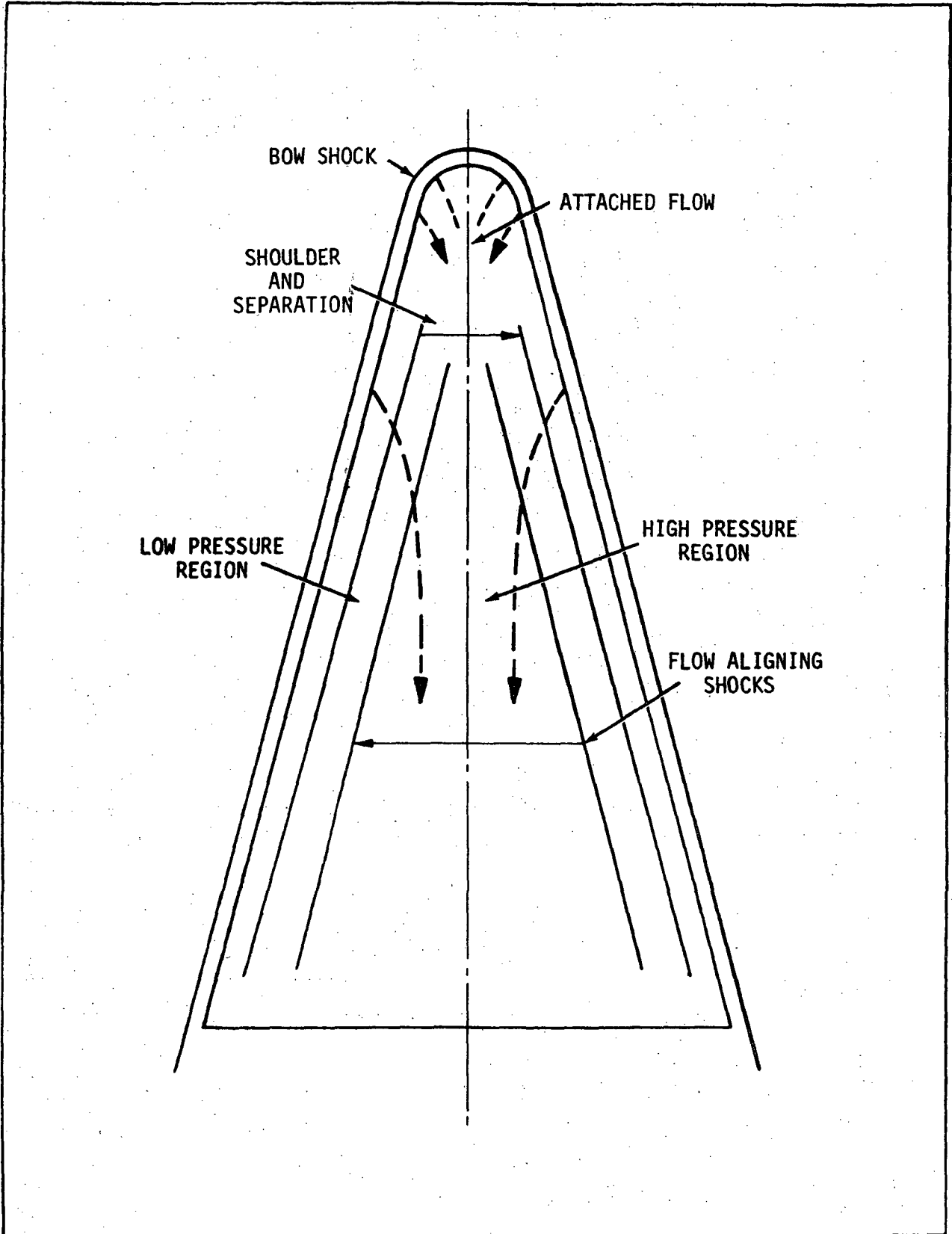


Figure 4-1. LEE-SIDE FLOWFIELD

turning the flow along the centerline. Thus, in the outer inviscid region below the bow shock, there exists a region near the centerline which will have a much higher pressure level than in the region outboard of the flow-aligning shocks (see Figure 4-1). The boundary layer will not be able to cope with this sudden pressure gradient and the flow will separate outboard of the embedded shock. This separation phenomena possesses some similarities which are characteristic of the two-dimensional flat plate with a ramp configuration except for the strong cross-stream convection component causing the separated stream to be swept helically along the surface toward the trailing edge. Entrainment causes the separated region to increase forming the vortex type flow. Evidence for this flow description lies in the measurement of the embedded shock for a sharp leading-edge wing by Cross (ref. 2), in the surface pressure measurements given in Figure 3-2, and in the surface flow visualization results in Figure 3-6.

The above description also suggests the differences in the flowfields between blunt and sharp leading-edge wings. In the blunt case, the development of the vortex flow will probably begin several nose diameters downstream of the attached flow region near the nose. For the sharp case, the vortex will occur near the tip of the nose. The relative strengths of the bow and embedded shocks could help to explain the reason for the local flowfield properties to be larger for the blunt leading-edge delta wing than for the sharp wing. The flow behind the blunt detached shock wave has passed through a stronger shock wave producing higher pressures and temperatures than would exist for the fluid behind an oblique shock associated with the sharp delta wing.

For continuity reasons the flow aligning shocks will probably begin close together and grow further apart with increasing distance along the model. For the fore section of the wing, vortex reattachment will occur very close to the centerline and the maximum flow properties may appear to be on the centerline. The reattachment line will not occur on the centerline because of symmetry and continuity requirements. The streamlines just outside of the dividing streamline sheet cannot pass through the surface of the wing and must turn parallel to it. The reattachment region also occurs at an increasing distance from the centerline as illustrated in Figure 3-5.

The boundary layer appears to remain attached in the streamline direction along the centerline as seen in the oil-flow photographs of Figure 3-6. The flow probably becomes turbulent on the aft section of the model. Reference 4 predicted turbulent flow for Reynolds numbers exceeding 6×10^6 . The thickness of the boundary layer has probably been reduced as a result of the outflow caused by the vortices. The thinning of the boundary layer can also help explain the increased heat transfer rates on the aft section of the model as shown in Figure 3-3. The flowfield properties associated with the reattachment of the vortex are not appreciably dissipated by the boundary layer and the effect is transferred directly to the surface.

The location of vortex separation occurs either inboard of or at the leading edge. Reference 2 indicated that for an attached leading-edge shock wave, separation will occur inboard of the leading edge. In the shock detached case, the main parameters which determine the position of separation is thought to be a function of the model half-angle and angle-of-attack. For example, the high pressure region along the centerline produces a strong adverse gradient in the spanwise direction. If the half-angle is small, this gradient is sensed at the leading edge and separation occurs. For separated flow, the zone of influence of a pressure disturbance is increased by increasing the strength of the disturbance. If the wing has a low aspect ratio, the disturbance caused by the embedded shocks can influence the leading-edge region. If the incidence is decreased the relative strength of the disturbance is likely to be decreased reducing the separation region. There is probably a limiting angle-of-attack at which the effects of the vortical system are sensed on the leeward surface. In the present study, the effect appeared significantly reduced at 25 degrees incidence. Boundary layer separation is an extremely complex phenomenon and is apparently a function of more than one variable. Cross (ref. 2) and Whitehead (ref. 4) obtained different separation locations for sharp leading-edge delta wings having the same sweep angle.

Section V CONCLUSIONS

The purpose of this investigation was to obtain experimental flowfield data on the leeward surface of a delta wing with blunt leading edges in hypersonic flow. This objective has been accomplished quite successfully by obtaining both quantitative and qualitative data on the leeward surface for an angle-of-attack range of 0 to 25 degrees at Mach 15 and 5 to 10 degrees at Mach 20. Based on the results of this experimental investigation and comparisons of the data with other investigations, the following conclusions are made:

- The leeward surface flowfield is not conical for Mach numbers of 15 and 20 for angles-of-attack of 25 degrees and less.
- Coiled vortices were generated at the juncture of the cylindrical leading edges and leeward slab surface and reattached near the centerline for angles-of-attack larger than 5 degrees at Mach number 15.
- Both the local pressure and Stanton numbers are larger for the blunt leading delta wing than for the sharp leading-edge counterpart.
- As the Mach number is increased, the magnitude of the expansion surface local flowfield properties are increased at the same angle-of-attack.
- Flat plate strip and crossflow turbulent boundary layer theories under and overpredict the heat transfer to the lee-side of a delta wing in a vortical flowfield.
- The peak heating rate occurred off the centerline and on the aft section of the model for a given angle-of-attack. The peak heating rate on the centerline occurred slightly downstream of the nose and moved forward with increasing angle-of-attack.

Section VI
REFERENCES

1. Stanbrook, A. and Squire, L. C., "Possible Types of Flow at Swept Leading Edges", The Aeronautical Quarterly, Vol. XV, Part I, February 1964.
2. Cross, E. J., Jr., "Experimental and Analytical Investigation of the Expansion Flow Field Over a Delta Wing at Hypersonic Speeds", Aerospace Research Laboratories, ARL 68-0027, February 1968.
3. Whitehead, A. H., Jr. and Keyes, J. W., "Flow Phenomena and Separation over Delta Wings with Trailing-Edge Flaps at Mach 6", AIAA J., Vol 6, No. 12, December 1968, pp. 2380-2387.
4. Whitehead, A. H., Jr., "Effect of Vortices on Delta Wing Lee-Side Heating at Mach 6", AIAA J., Vol. 8, No. 3, March 1970, pp. 599-600.
5. Rein, J. A., "Flow Over the Suction Surface of Sharp Edge Delta Wings with Detached Leading Edge Shock Waves", Dept. of Supply, Australian Defense Scientific Service, Weapons Research Establishment, Technical Note HSA 102.
6. Bertram, M. H. and Everhart, P. E., "An Experimental Study of the Pressure and Heat-Transfer Distribution on a 70° Sweep Slab Delta Wing in Hypersonic Flow", NASA TR R-153, December 1963.
7. Stallings, R. L. et al., "Heat Transfer and Pressure Measurement on Delta Wings at Mach Numbers of 3.51 and 4.65 and Angles-of-Attack from -45° to 45°", NASA TN D-2387, August 1964.
8. Young, C. H. et al., "Aerothermodynamic Analyses of a Lifting Entry Vehicle at Mach 10", General Dynamics, Convair Division, GDC-ERR-1415, March 1970.
9. Richards, B. E. and Enkenhus, K. R., "Hypersonic Testing in the V.K.I. Longshot Free-Piston Tunnel", AIAA Paper No. 69-333, April 1969.
10. Richards, B. E., "Data Reduction Program for the Longshot Free-Piston Tunnel", VKI report to be published.
11. Creager, M. O., "The Effect of Leading-Edge Sweep and Surface Inclination on the Hypersonic Flow Field Over a Blunt Flat Plate", NASA Memo 12-26-58A, January 1959.
12. Holloway, P. F. et al., "An Investigation of Heat Transfer Within Regions of Separated Flow at a Mach Number of 6.0", NASA TN D-3074, November 1965.
13. Barber, E. A., "Some Experiments on Delta Wings in Hypersonic Flow", AIAA J., Vol. 4, No. 1, January 1966, pp. 72-83.
14. Ghorai, S. C., "Leading-Edge Vortices and Shock-Detachment Flow Over Delta Wings", J. AIRCRAFT, Vol. 6, No. 3, May 1969, pp. 228-232.

15. Neal, Jr., Luther and Bertram, M. H., "Turbulent-Skin Friction and Heat-Transfer Charts Adapted From the Spalding and Chi Method", NASA TN D-3969, May 1967.
16. Hefner, J. H. and Whitehead, Jr., A. H., "Lee Side Heating Investigations, Part I: Experimental Lee Side Heating Study of a Delta Wing Orbiter", NASA Space Shuttle Conference, Hampton, Virginia, March 1971.

Appendix D

EFFECTS OF ROUGHNESS ON COMPRESSIBLE FLOWS

EFFECTS OF ROUGHNESS ON COMPRESSIBLE FLOWS

By

**Kynric M. Pell and Daljit Singh
Auburn University**

**Final Report
Northrop Contract 714-41060**

June 1971

ABSTRACT

This report treats the results of a six-month program to investigate roughness effects on the location of boundary layer transition as well as the variations in local aerodynamic heating caused by roughness. The program was restricted to two-dimensional roughness, in particular, sinusoidal roughness. A literature survey was made. Experimental transition data obtained from the surveyed material is presented. In an attempt to develop an improved correlation for heat transfer to a sinusoidal wall with a turbulent boundary layer, a finite difference computer program of the Spalding-Patankar type was modified to treat the flow over a sinusoidal wall. Preliminary runs with this program yield encouraging results and indicate that a parametric investigation is feasible. Results for several different H/w ratios are presented and areas for future study are outlined.

TABLE OF CONTENTS

Nomenclature

I. Introduction.

II. Previous Studies.

 A. Theoretical Studies - Laminar Boundary Layer.

 B. Theoretical Studies - Turbulent Boundary Layer.

 C. Experimental Studies.

III. Current Study

 A. Turbulent Compressible Boundary Layers on Sinusoidal
 Walls - A Model

 B. The Computer Program.

IV. Computer Studies.

V. Summary

VI. References.

 Appendix I -Computer Program.

 a) Input Data.

 b) Program Listing

 Appendix II -Elliptic Integral

 Appendix III-The Effect of Roughness on Transition Location. .

NOMENCLATURE

a,b,c,d	General groups of symbols
A,B,C	General coefficients in difference equation
A*	Damping constant in van Driest's hypothesis
h	Specific total enthalpy
H	Height of wave
k	Mixing length constant
L	Wave length of sinusoidal element
ℓ	Mixing length
M	Mach number
\dot{m}''	Mass flux
Pr	Laminar (molecular) Prandtl number
Pr _{eff}	Effective Prandtl number
Pr _T	Turbulent Prandtl number
\dot{q}	Heat flux
Re	Reynolds number
r	Radius from axis of symmetry
T	Temperature
u,U	Velocity in x direction
v	Velocity in y direction
W	Width of wave = H_2
x	Coordinate along body surface
y	Coordinate normal to body surface
y_ℓ	Characteristic thickness of boundary layer
<hr/>	
λ	Mixing-length constant
μ	Laminar (molecular) viscosity
μ_{eff}	Effective viscosity

ρ	Mass density
σ	Zero for two-dimensional flow; one for axisymmetric flow
τ	Shear stress
ϕ	Generalized dependent variable
ψ	Stream function
ω	Normalized stream function

Superscripts

'	Fluctuation quantity
—	Average with respect to time

Subscripts

<i>AW</i>	Adiabatic wall
<i>E</i>	Outer edge of boundary layer
<i>I</i>	Inner edge of boundary layer
<i>w</i>	Body surface or wall
∞	Free stream

I. INTRODUCTION

Compressible flow over rough surfaces is a significant aerodynamic problem associated with all high speed flight. At some viewing level all surfaces may be considered rough. One need not go to the microscopic level to observe roughness in most engineering surfaces, in particular, the skin of high speed flight vehicles is generally macroscopically rough in the atmospheric flight environment. The roughness which is referred to is not the roughness associated with fasteners and joints, but rather the buckling which occurs due to use of stressed skin structures as well as the buckling which occurs due to thermal stresses.

This type of roughness may be idealized in the form of sinusoidal roughness within a reasonable degree of approximation. The work which follows will treat sinusoidal roughness in two-dimensions.

Introduction

The purpose of this document is to provide a comprehensive overview of the project's objectives, scope, and timeline. It is intended for all stakeholders involved in the project, including team members, management, and external partners.

The project aims to develop a new software application that will streamline our internal processes and improve efficiency. The scope of the project includes the design, development, testing, and deployment of the application.

The project is scheduled to begin in January 2024 and is expected to be completed by June 2024. The timeline is subject to change based on the progress of the project and any unforeseen circumstances.

The project team consists of a project manager, a team of developers, a quality assurance team, and a user acceptance testing team. Each team member has specific responsibilities and is working towards the common goal of a successful project completion.

The project budget is estimated to be \$500,000. This budget includes the costs of software licenses, hardware, personnel, and other resources required for the project. The budget is subject to review and approval by the project sponsor.

The project risks are identified and categorized into high, medium, and low risk. The project manager will monitor these risks throughout the project and take appropriate actions to mitigate them.

The project communication plan outlines the frequency and methods of communication between the project team and stakeholders. This includes regular status meetings, email updates, and a project website.

The project success criteria are defined as the completion of the application on time, within budget, and to the satisfaction of the user requirements. The project manager will track these criteria throughout the project.

The project is a complex and challenging task, but with the support of the project sponsor and the dedication of the project team, we are confident that we will achieve our goals and deliver a high-quality software application.

II. PREVIOUS STUDIES

A. Theoretical Studies - Laminar Boundary Layer

The first theoretical studies of the boundary layer flow over a sinusoidal wall appear to be the work of *Quick and Schröder*¹. These investigators treated laminar incompressible flow using small perturbation theory for the external flow and a numerical technique (finite difference) to solve the boundary layer equations. It is interesting to note that they limited the amplitude to the waves of the wall to that value which caused a one percent variation (or less) in the free stream velocity. They found velocity profiles characteristic of flow separation for this case as well as in the limit of infinitesimal amplitude waves. It was concluded that sinusoidal disturbances of laminar incompressible flow always leads to separation and in addition, it was conjectured that this led to transition to turbulence. A restricted case of small amplitude waves where the wavelength of the waves is much smaller than the overall length of the wall was treated by *Görtler*^{2,3}, who found that separation depended on the geometry. Further research on the laminar incompressible problem was reported by *Soprunenko*⁴, who showed that for a given wave (of the wall) there is an amplitude, A^* (of that wave) such that for all $A < A^*$, no separation occurs, while for $A > A^*$, the boundary layer will separate at this ridge. A finite difference program was used by *Pashonov and Soprunenko*⁵ to determine A^* for the first and second waves of a sinusoidal wall. It is interesting to note that their results apparently agreed with the results of a separation prediction technique reported by *Ban-Zelikovich*⁶.

Both the compressible and incompressible laminar boundary layers were investigated by *Fannelöp and Flügge-Lotz*⁷ using the Flügge-Lotz-Blottner finite difference technique. Their solutions for the incompressible case were essentially in agreement with the results of *Quick and Schröder*¹; however, they take issue with the solution for the flow in separated region and the conjecture that this

separation leads to transition to turbulence. This investigation also led to the result that a laminar, compressible flow would result in separation sufficiently far down the wall. A finite difference program which includes real gas effects was developed by *Savage and Nagel* ⁸ to treat sinusoidal roughness. The program treats laminar compressible flows in a straightforward manner and is applied to turbulent flows using an integral correlation technique. The correlation for heat transfer to walls with sinusoidal roughness and laminar flow presented in Reference [10] is based primarily on empirical work.

$$\frac{\dot{q}_{max}}{\dot{q}_{smooth}} = 1 + \frac{1}{36} [M_L / \delta_L^* / H]^{1.9} \quad (1')$$

where

- \dot{q}_{max} = maximum laminar heating to wave
- \dot{q}_{smooth} = laminar heating to flat plate at equivalent distance
- M_L = local Mach number at first wave
- δ_L^* = local displacement of boundary layer
- H = maximum height of surface protuberance

B. Theoretical Studies - Turbulent Boundary Layer

The only attempt at a theoretical study for a turbulent boundary layer over sinusoidal roughness appears to be the empirical correlation by *Jaeck*⁸ based on the laminar theory of Savage and Nagel. Based on this work, *Jaeck*⁸ suggests the following correlation for heat transfer to a sinusoidally rough wall with a turbulent boundary layer.

$$\frac{\Delta \dot{q}}{\dot{q}} = \frac{1}{2} \left[\frac{H/W}{F} \left(1 - \frac{\delta_T^*}{H} \right) - 2.5 + \left\{ 6.25 + \frac{5H}{FW} \times \left(1 + \frac{\delta_T^*}{H} \right) + \left[\frac{H/W}{F} \left(1 - \frac{\delta_T^*}{H} \right) \right]^2 \right\}^{1/2} \right] \quad (2')$$

where

$$F = \beta_1 / (\gamma \pi M_L^2)$$

δ_T^* = turbulent boundary layer thickness on an equivalent flat plate.

C. Experimental Studies

Experimental studies of compressible boundary layers over sinusoidal roughness appear to be limited to rather high Mach numbers. With the exception of one study [9] of three-dimensional sinusoidal protuberances conducted at a free stream Mach number of 3.0, all of the experiments treat flows with free-stream Mach numbers in excess of 6.0. The five studies [8,10,11,12,13] which explicitly treat two-dimensional sinusoidal roughness are characterized in Table I. It should be noted that only the results for sharp leading edge plates will be presented and discussed. Typical experimental results are presented in Figures 1, 2 and 3 which are taken from *Cary and Morrissette*¹⁰ since this study involved tests at the lowest free-stream Mach numbers. Figure (1b) illustrates the results for the pressure variations over the sinusoidal roughness as well as for a flat plate at zero angle of attack.

The pressure rise upstream of the first wave typified by the rise to a plateau followed by a subsequent rise to a peak value is characteristic of the pressure in the neighborhood of a compression corner in separated supersonic laminar or transitional flow. It should be noted that the pressure variation in the neighborhood of the first wave in Figure (2e) is typical of a compression corner in supersonic turbulent flow.

In Figure (3), again taken from Reference 10, the heat transfer to both flat and sinusoidally rough plates with both initially laminar and initially turbulent flow are presented.

Based on these previous studies one may conclude:

1. The maximum laminar heating on multiple waves may be correlated with equation (1'). Succeeding waves of a train may be treated as a single wave standing alone.

Table 1. EXPERIMENTAL STUDIES OF SINUSOIDAL ROUGHNESS

MODEL	DATA	B.L. TRIP	α	M_w	R_w/cm	T_w/T_t	Ref.
MW	Press.	No	-5	6.0	0.21×10^6	0.89	Cary and Morrisette [10]
MW	Press.	No	0	6.8	0.21×10^6	0.89	
MW	Press.	No	5	6.0	0.21×10^6	0.89	
MW	Press.	No	10	5.3	0.21×10^6	0.89	
MW	Press.	No	15	4.6	0.21×10^6	0.89	
MW	H.T.	No	-5	6.8	0.26, 0.165	0.6	Same as above
			0	6.0	0.087×10^6	0.6	
			5	5.3	"	0.6	
			10	4.6	"	0.6	
			15	4.0	"	0.6	
MW	H.T.	Yes	0	6.0	0.26, 0.165	0.6	Same as above
			5	5.3	0.087×10^6		
			10	4.6			
			15	4.0			
SW	H.T.	Yes	0	6.0	0.27, 0.14	0.6	
			15	4.0	0.063×10^6		
MW	H.T. and Press.	No	0	19.8	0.067×10^6	0.62	[13]
			5	21.6	0.157		
			10	22.2	0.216		
MW	H.T. and Press.	No	-5	8.0	$0.0097 \text{ to } 0.29 \times 10^6$	0.4	[12]
			0				
			5				
			10				
			15				

2. For a given local Mach number, the effect of local unit Reynolds number on the maximum turbulent heating for the first wave, or single waves, was similar to the Reynolds number effect on smooth flat-plate turbulent heating. The turbulent maximum heating for a series of waves succeeding a particular first wave decreased almost linearly with increasing local Reynolds number.

3. Tests on single waves and the first wave of the multiple-wave model indicated that in turbulent flow the maximum heating on the waves increased almost linearly with decreasing geometric width-height ratio of waves.

4. The correlation for turbulent flow is not satisfactory when separation occurs.

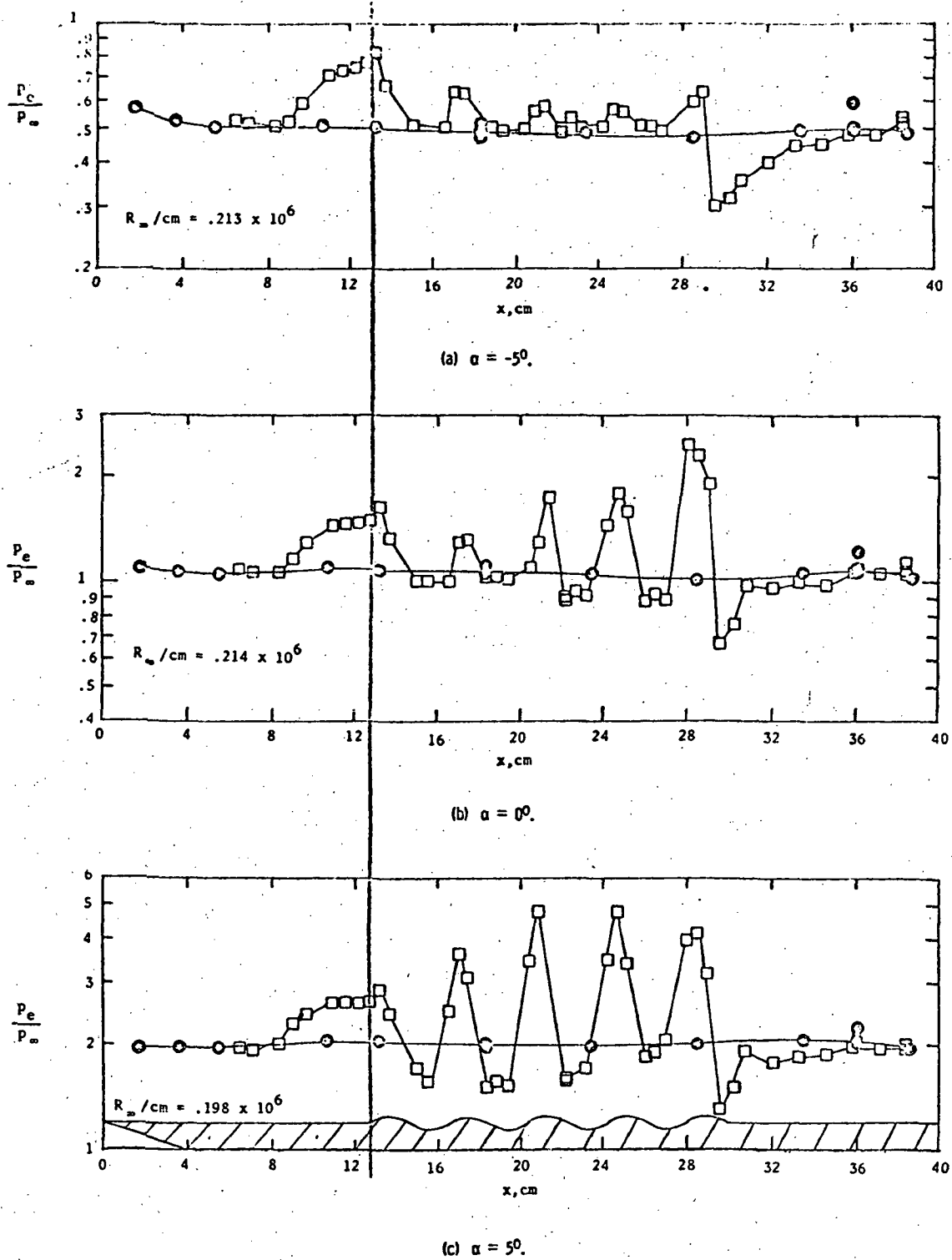
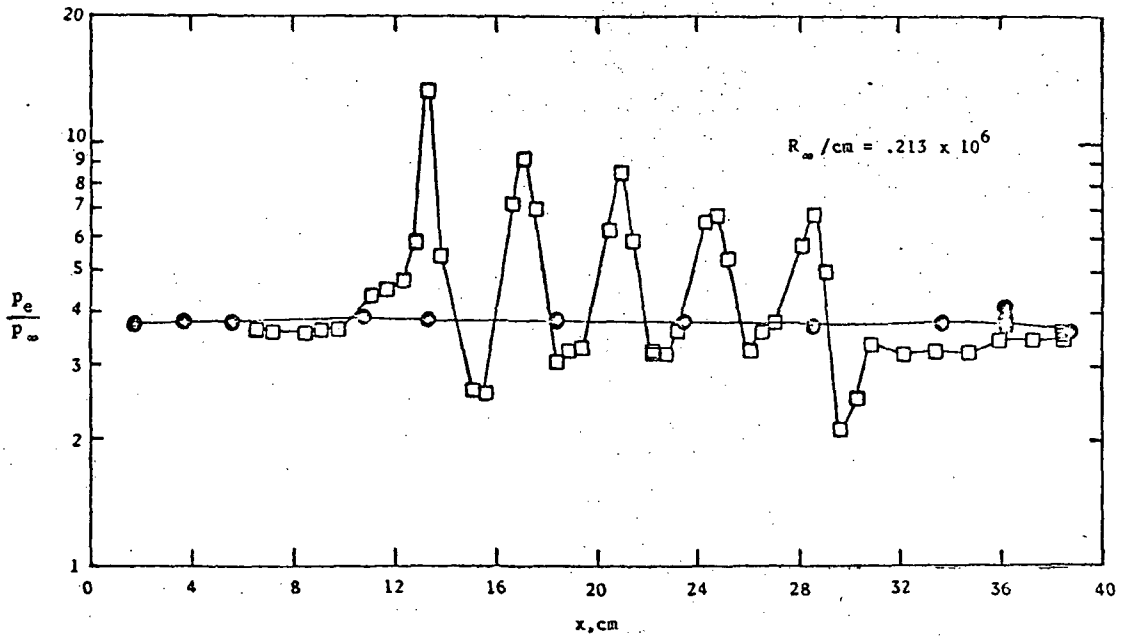
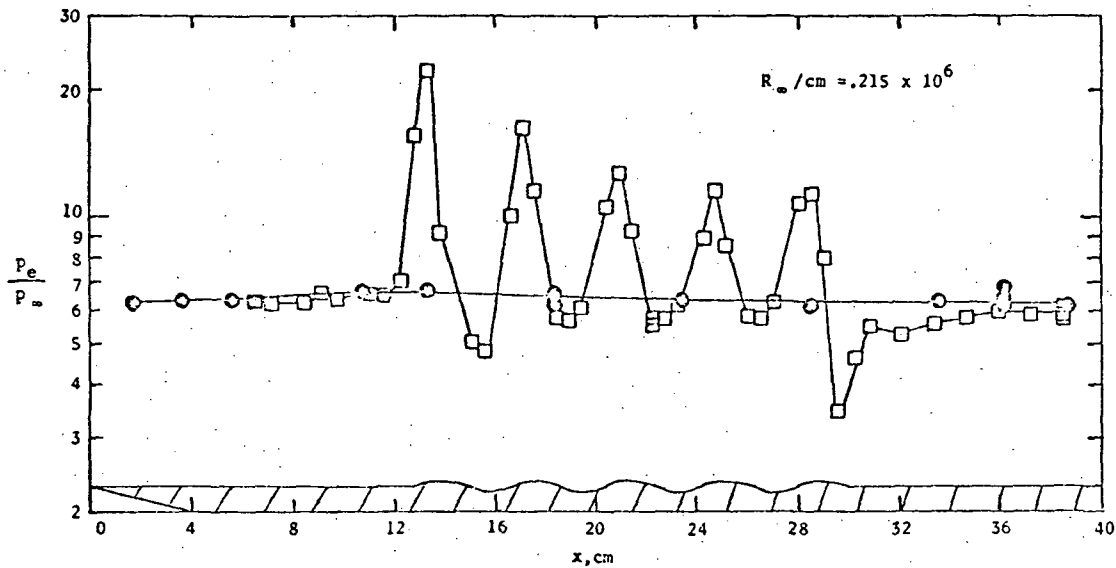


Figure 1

Effect of multiple-sinc-wave protuberances on the surface pressure for the sharp-leading-edge model. $M_\infty = 6$. Open symbols, multiple-wave surface; solid symbols, flat surface. (From Reference [10]).



(d) $\alpha = 10^\circ$.



(e) $\alpha = 15^\circ$.

Figure 2

Effect of multiple-sine-wave protuberances on the surface pressure for the sharp-leading edge model. $M_{\infty} = 6$. Open symbols, multiple-wave surface; solid symbols, flat surface. (From Reference [10]).

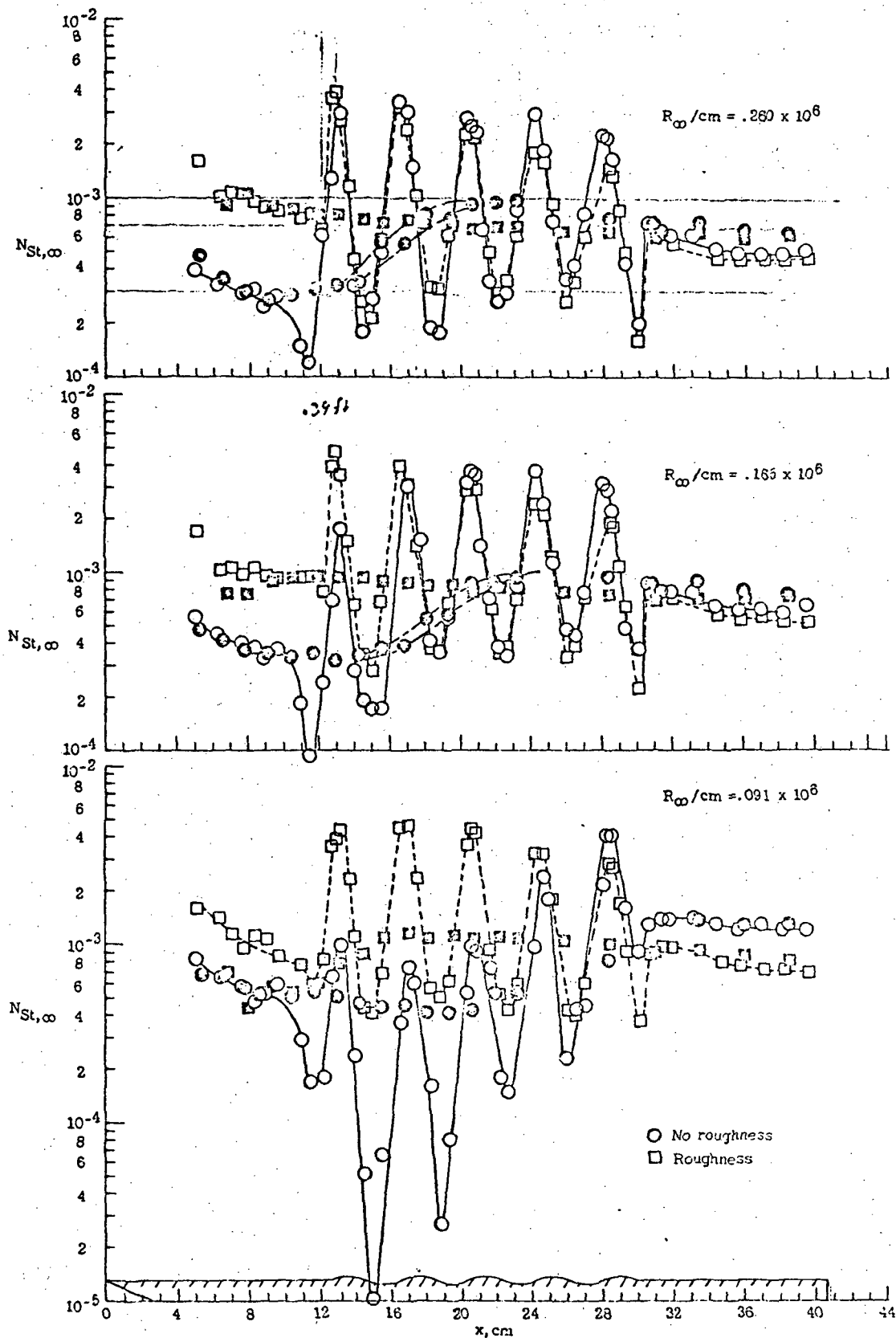


Figure 3

Effect of multiple-sine-wave protuberances on surface heating for the sharp-leading-edge model. $M_\infty = 6$. Open symbols, multiple-wave surface; solid symbols, flat surface. (From Reference [10]).

III. CURRENT STUDY

A. Turbulent Compressible Boundary Layers on Sinusoidal Walls - A Model

From the point of view of the Shuttle designer, the most significant flow regime would be the turbulent compressible boundary layer by virtue of the fact that this will be the environment of most of the vehicle in the atmospheric portion of flight. Considering the Theoretical Studies Section of this report, it may be noted that the correlation in this regime is based on the empirical modification of the laminar flow computer model. Considering the Experimental Studies Section it may be noted that this is also the regime of poorest correlation. In an attempt to provide an alternate correlation for the turbulent boundary layer case, a computer technique which treated the turbulent boundary layer in a more direct manner was sought. It should be noted that the attack on the problem was still modelled on previous studies inasmuch as a more or less classical approach to solving the boundary layer problem was initiated. The potential flow solution over the wall was assumed to be given by small perturbation theory which is consistent with all previous studies [1-8]. A computer program which could treat turbulent boundary layers and could be modified to take both the sinusoidal wall geometry and the sinusoidally varying potential flow conditions at the boundary layer edge was made available by Dr. David Dyer. The basic Spalding-Patankar program which was modified for this study has been used successfully for predicting heat transfer to smooth flat plates and cone/cylinder combinations by other investigators [14,15]. The program was modified for this study by:

1. Modification of the external boundary specification to allow the variation in properties determined from small perturbation theory.
2. Fixing the streamwise step size.
3. Specification of the sinusoidal wall geometry.

For completeness a description of the program given by *Dyer* and *Mayne*¹⁴ is adapted and follows here.

B. The Computer Program

The purpose of this section is to describe an analytical model which has been developed for application to turbulent boundary layers on sinusoidal-walled two-dimensional bodies. The theoretical model is based on the mixing-length treatment of the eddy-viscosity hypothesis, which has been shown to be of rather wide applicability. The present work is based on that of *Patankar* and *Spalding*^{16,17}, although a number of modifications and extensions have been made to their technique by *Dyer* and *Mayne*¹⁴. The computer program used in this study has the capability of treating both laminar and turbulent boundary layers, with an instantaneous transition from laminar to turbulent flow. The gas under consideration is treated as both thermally and calorically perfect. Comparisons with experiment are made where these assumptions are reasonable.

The boundary-layer equations expressing the conservation of mass, momentum, and energy are transformed into a normalized von Mises coordinate system and solved using a marching, implicit finite-difference procedure. The transport terms in the equations for a turbulent boundary layer are treated by employing a two-layer effective viscosity model based on Prandtl's mixing length and a modification of van Driest's analysis for the near-wall region.

Basic Equations

The normalized von Mises coordinate system is shown in Figure 4; the cross-stream variable ω defined by

$$\omega = \frac{\psi - \psi_I}{\psi_E - \psi_I} \quad (1)$$

is introduced. $\partial\psi/\partial y = r^\sigma \rho u$ and $\partial\psi/\partial x = -r^\sigma (\rho v + \overline{\rho'v'})$. ρ, u, v , etc. will refer to time-averaged values of variables unless otherwise noted. In the von Mises system the boundary layer equations are:

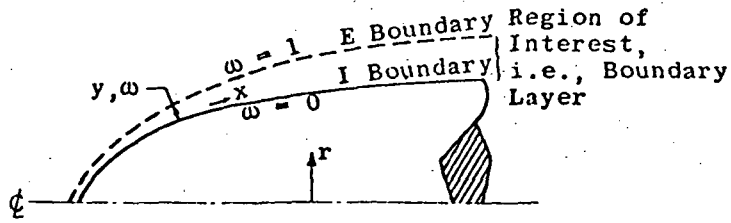


Figure 4

x- ω Coordinate System

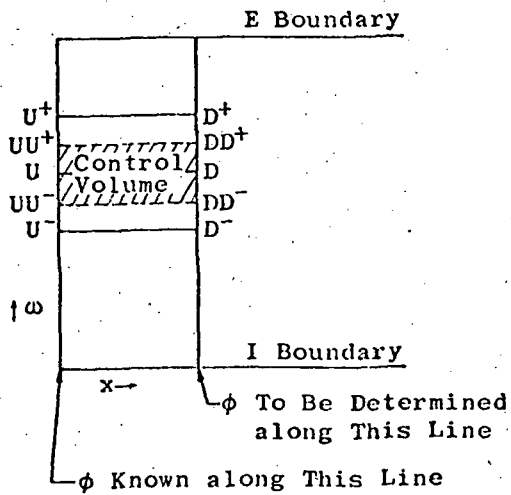


Figure 5

Finite-Difference Network

Momentum

$$\begin{aligned} \frac{\partial u}{\partial x} + \left\{ \frac{r_I^\sigma \dot{m}_I'' + \omega(r_E^\sigma \dot{m}_E'' - r_I^\sigma \dot{m}_I'')}{\psi_E - \psi_I} \right\} \frac{\partial u}{\partial \omega} \\ = \frac{\partial}{\partial \omega} \left\{ \frac{\rho u r^{2\sigma} \mu_{eff}}{(\psi_E - \psi_I)^2} \frac{\partial u}{\partial \omega} \right\} - \frac{1}{\rho u} \frac{dp}{dx} \end{aligned} \quad (2)$$

Energy

$$\begin{aligned} \frac{\partial h}{\partial x} + \left\{ \frac{r_I^\sigma \dot{m}_I'' + \omega(r_E^\sigma \dot{m}_E'' - r_I^\sigma \dot{m}_I'')}{\psi_E - \psi_I} \right\} \frac{\partial h}{\partial \omega} \\ = \frac{\partial}{\partial \omega} \left\{ \frac{\rho u r^{2\sigma} \mu_{eff}}{Pr_{eff} (\psi_E - \psi_I)^2} \frac{\partial h}{\partial \omega} \right\} \\ + \frac{\partial}{\partial \omega} \left\{ \frac{\rho u r^{2\sigma} \mu_{eff}}{(\psi_E - \psi_I)^2} \left(1 - \frac{1}{Pr_{eff}} \right) \frac{\partial u^2/2}{\partial \omega} \right\} \end{aligned} \quad (3)$$

where $\zeta = 0$ for two-dimensional flow and $\zeta = 1$ for axisymmetric flow. (In this study $\zeta = 0$.) In (2) and (3) the eddy transport coefficients have been incorporated into the effective viscosity and effective Prandtl number.

Equations (2) and (3) are equivalent to the classical boundary-layer equations with the exception that the effects of transverse curvature are included. These effects are significant for the case of an axisymmetric body on which the boundary-layer thickness at a given point is of the same order of magnitude as the body radius at that point. Equations (1) and (2) possess the common form

$$\frac{\partial \phi}{\partial x} + (a + b\omega) \frac{\partial \phi}{\partial \omega} = \frac{\partial}{\partial \omega} \left(c \frac{\partial \phi}{\partial \omega} \right) + d \quad (4)$$

where ϕ represents either u or h .

Transport Laws

The shear stress in a turbulent boundary layer is treated herein by the use of a two-layer model using Prandtl's mixing-length hypothesis and a modification of van Driest's analysis for the region near the wall. This results in a continuous distribution of the shear stress from the laminar value at the wall, through the fully turbulent region, reaching zero at the outer edge of the boundary layer. The energy transport in a turbulent boundary layer is treated by incorporation of the eddy conductivity into an effective Prandtl number which includes the effect of the molecular conductivity near the wall and goes to a constant turbulent Prandtl number in the outer region of the boundary layer.

The effective shear stress may be written:

$$\tau = \mu \frac{\partial u}{\partial y} - \rho \overline{u'v'} \quad (5)$$

where the term $-\rho \overline{u'v'}$ is the Reynolds' stress and represents the shear stress introduced by the turbulence. Using Prandtl's mixing-length hypothesis one has

$$-\rho \overline{u'v'} = \rho \ell^2 \left| \frac{\partial u}{\partial y} \right|^2 \quad (6)$$

where ℓ is the mixing length. Combining this with (5) yields

$$\tau = \left(\mu + \rho \ell^2 \left| \frac{\partial u}{\partial y} \right| \right) \frac{\partial u}{\partial y} = \mu_{eff} \frac{\partial u}{\partial y} \quad (7)$$

Assuming the turbulent contributions to the shear stress are much greater than the laminar contributions,

$$\mu_{eff} \sim \rho \ell^2 \left| \frac{\partial u}{\partial y} \right| \quad (8)$$

After Escudier¹⁸, Patankar and Spalding¹⁶ recommend the following variation

of ℓ

$$\begin{aligned} \ell &= ky, \text{ for } 0 < y \leq \lambda y_\ell/k & (a) \\ \ell &= \lambda y_\ell, \text{ for } \lambda y_\ell/k < y & (b) \end{aligned} \tag{9}$$

By analogy with Stokes' solution for an infinite flat plate undergoing simple harmonic motion parallel to itself in an infinite fluid, *van Driest*¹⁹ has concluded that in the vicinity of a wall the shear stress in a turbulent flow should be of the form

$$\tau = \mu \frac{\partial u}{\partial y} + \rho k^2 y^2 \left[1 - \exp \left(- \frac{y \sqrt{\tau_w \rho}}{\mu A^*} \right) \right]^2 \left(\frac{\partial u}{\partial y} \right)^2 \tag{10}$$

This results in an exponential damping of the turbulent part of the shear as the wall is approached, and yields the laminar shear stress form, $\tau = \mu \partial u / \partial y$, at the wall. Although (10) was originally developed for incompressible flow, it is applied to compressible flow with the additional modification, suggested by *Patankar and Spalding*⁸, that the local value of shear stress be used rather than the wall value. The effective viscosity which has been used in this work is a combination of (8), (9), and (10);

$$\mu_{eff} = \mu + \rho k^2 y^2 \left[1 - \exp \left(- \frac{y \sqrt{\tau \rho}}{\mu A^*} \right) \right]^2 \left| \frac{\partial u}{\partial y} \right| \tag{a}$$

$$\text{for } 0 \leq y \leq \lambda y_\ell/k$$

and

$$\mu_{eff} = \rho \lambda^2 y_\ell^2 \left| \frac{\partial u}{\partial y} \right| \tag{b}$$

$$\text{for } \lambda y_\ell/k < y$$

(11)

The values used for the various constants were $k = 0.435$, $\lambda = 0.09$, and $A^* = 26.0$. The value of y at the point where the velocity in the boundary layer was equal to 0.99 of the velocity at the boundary layer outer edge was used for y_ℓ . These values follow *Patankar and Spalding*, except that the damping constant A^* is that

originally determined by van Driest. It may be noted that if the laminar contribution to the effective viscosity becomes small as $y = \lambda y_\ell/k$ is approached from below, and the exponential term in (11a) becomes small at the same time, then the effective viscosity given by (11a) will smoothly approach that of (11b) and a continuous distribution of μ_{eff} from the near-wall region through the outer region will result.

The effective Prandtl number used in obtaining the results presented herein was determined from

$$\frac{\mu_{eff}}{\Pr_{eff}} = \frac{\mu}{\Pr} + \frac{\rho k^2 y^2}{\Pr_T} [1 - \exp(-\frac{y \sqrt{\tau \rho}}{\mu A^*})]^2 \left| \frac{\partial u}{\partial y} \right| \quad (a)$$

$$\text{for } 0 \leq y \leq \lambda y_\ell/k$$

and (12)

$$\Pr_{eff} = \Pr_T \quad (b)$$

$$\text{for } \lambda y_\ell/k < y$$

A constant value of 0.7 was used for the laminar Prandtl number, whereas a constant value of 0.9 was used for the turbulent Prandtl number. The laminar viscosity of the gas was computed using Sutherland's Law in Reference 20.

Finite Difference Technique

The solution of the simultaneous, nonlinear, parabolic partial differential equations (2) and (3) was performed by obtaining linear finite-difference equivalents of the equations and solving these using a marching, tridiagonal matrix method. A brief description of the solution technique will be given in terms of the general form presented in Equation (4).

In order to solve an equation of the type of (4) it is necessary to know the variation of ϕ along the inner (x) and the external (z) boundaries, together with the variation of ϕ across the layer at some x location. The solution can then proceed downstream from the given x location. Referring to Fig. 5, if it is assumed that the boundary conditions on ϕ and the values of ϕ at a given value of x and a discrete set of values of ω are known, then the following procedure, devised by Patankar and Spalding, may be applied. Let U , U^+ , and U^- be typical upstream points where ϕ is known, and D , D^+ , and D^- be downstream points where ϕ is to be determined. With UU^+ , DD^+ , DD^- , and UU^- lying midway between the indicated points, consider the control volume of which they are the corners. Rather than truncating a Taylor series expansion, as is usually done, each term in (4) may be replaced by a finite-difference form obtained by expressing that term as an integrated average over the indicated control volume. In order to obtain more tractable results, certain restrictions are placed on the quantities involved: ϕ is assumed to vary linearly between ω points, and to vary stepwise in the x direction, having the upstream value ϕ_U from x_U to x_D , and taking on the value ϕ_D at x_D . In order to insure that the resulting equations will be linear in ϕ at the downstream location, the values used for a , b , and c are those at the upstream location. Because of accuracy and stability considerations, Patankar and Spalding recommend evaluating the $\partial/\partial\omega$ terms using the values of ϕ at the downstream location. Finally, because it is sometimes quite complicated, the source

term d is treated as

$$d)_D = d)_U + \frac{\partial d}{\partial \phi})_U (\phi_D - \phi_U) \quad (13)$$

After this treatment is applied to Equation (4), the resulting algebraic expression may be rearranged as

$$\phi_D = A \phi_{D^+} + B \phi_{D^-} + C \quad (14)$$

where A , B , and C are known quantities. There will be one equation of this form for each interior ω point where the value of ϕ is to be determined, and at the two extreme interior points either ϕ_{D^+} or ϕ_{D^-} will be known from the boundary condition. This set of N linear equations in N unknowns is of tridiagonal form and can be solved efficiently and easily by standard means.

Modifications and Observations

The x step size was fixed at a specific value. Experience has shown that any choice of initial u and h profiles which is not entirely unreasonable can be used with a negligible effect on the downstream results if the computations are begun near the leading edge or stagnation point.

The cross-stream step size used was computed by taking at the initial x location a step distribution based on a geometric progression in the y step size and computing from this the corresponding ω intervals. Typical values of the ratio of successive y steps ranged from 1.17 to 1.19, and typically 175 points were employed across the layer. This procedure yields a small step size near the wall where the gradients are large, and gives larger steps in the outer region where the variables change more slowly. It should be noted that ω always varies from zero to unity, regardless of the x location, and that the discrete values of ω chosen at the initial x location are used along the whole body.

The original technique of Patankar and Spalding achieved computational efficiency and still maintained accuracy in the region near the wall by applying a Couette flow analysis to the flow very near the wall. This procedure has certain shortcomings, however, such as not being easily applicable to flows with simultaneous surface mass transfer and longitudinal pressure gradients. In addition, some of the assumptions made in the Couette flow analysis seem unjustifiable; in particular, the density was assumed uniform near the wall where tremendous temperature gradients are experienced under many practical conditions. In view of these problems, the Couette flow technique has been abandoned in favor of applying the basic finite-difference scheme across the entire boundary layer. The use of the variable cross-stream step size yields accurate results near the body surface while still permitting computation to proceed efficiently. It might be noted that the so-called "slip-value" scheme employed by Patankar and Spalding has also been discarded.

The computation of the rate of mass entrainment into the boundary layer is essential to calculations in the $x-\omega$ system. Because there was no mass transfer through the body surface in the cases considered herein, the quantities \dot{m}_I'' and ψ_I are both zero for these calculations. At the outer edge of the boundary layer the definition of the stream function gives

$$\frac{d\psi_E}{dx} = -r^\sigma \dot{m}_E'' \quad (15)$$

and the variation of ψ_E with x is determined by integrating (15) with respect to x . It is necessary, therefore, to determine the variation of \dot{m}_E'' with respect to x . The entrainment rate may be determined by applying the momentum equation at or near the boundary layer edge, where $\omega \sim 1.0$ and $\partial u / \partial x \sim 1/\rho u \, dp/dx$. This results in,

$$\dot{m}_E'' \sim \frac{1}{r^\sigma} \frac{\partial}{\partial \omega} \left\{ \frac{r^{2\sigma} \rho u \mu_{eff}}{\psi_E - \psi_I} \frac{\partial u}{\partial \omega} \right\} / \frac{\partial u}{\partial \omega} \quad (16)$$

where it must be remembered that (16) is to be applied only at or near the boundary-layer edge. At this point it should be noted that the entrainment rate does not have a unique value; rather, it is sufficient that it be large enough that the resulting region over which the boundary layer equations are solved does indeed enclose the entire region over which the dependent variables change significantly. If an entrainment rate which is too small is used, the resulting solutions will suppress the boundary layer artificially and yield erroneous results. In view of this, the present solutions were obtained using an entrainment rate which was twice that determined by equation (16); this yielded solutions in which, for instance, the profiles had a much more asymptotic character at the outer edge than did solutions obtained by a direct application of (16). On some reflection this procedure can be seen to be valid, since the entrainment is "self-correcting". If an overly large quantity is added to the boundary layer at a given step, this will tend to

reduce the amount entrained at the next step. Treatment of the entrainment in this manner resulted in quite satisfactory results in all cases considered.

In the supersonic flow regime, potential flow over a sinusoidal wall is described using small perturbation theory by:

$$u = U + u'$$

$$v = v'$$

where the primed quantities represent perturbations on the free stream values and are given by:

$$u' = - \frac{U\epsilon\alpha}{\sqrt{M_\infty^2-1}} \cos \alpha[X_1 - X_2 \sqrt{M_\infty^2-1}]$$

$$v' = U\epsilon\alpha \cos \alpha[X_1 - X_2 \sqrt{M_\infty^2-1}]$$

when the wall is described by

$$X_2 = \epsilon \sin\alpha X_1 \quad \text{and} \quad \alpha = \frac{2\pi}{L}.$$

This results in a pressure coefficient

$$C_p = \frac{2\epsilon\alpha}{\sqrt{M_\infty^2-1}} \cos \alpha[X_1 - X_2 \sqrt{M_\infty^2-1}]$$

These conditions were used as the edge conditions to be matched by the boundary layer finite difference program. The conditions at the wall were, of course, the usual boundary-layer boundary conditions--that is, the velocity at the wall is zero. The geometry of the wall is shown in Fig. 6.

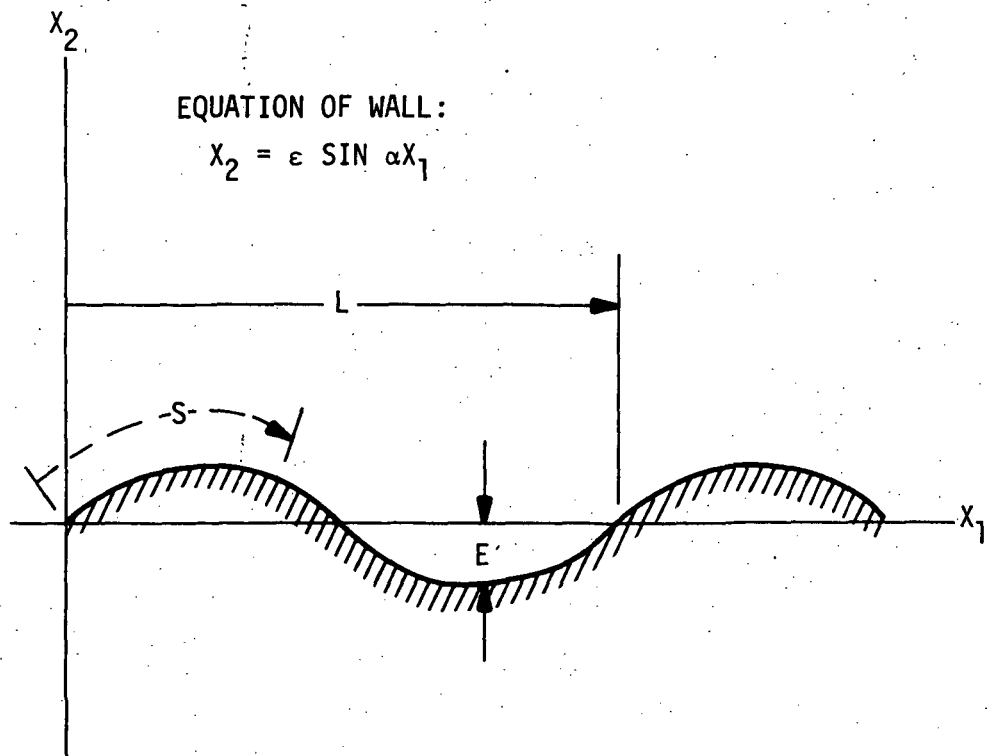


Figure 6. WAVY WALL GEOMETRY

IV. COMPUTER STUDIES

A series of initial studies treated a sharp leading edge plate with an initial flat section 9.3 ft. long followed by a section of two-dimensional sinusoidal roughness. The wavelength of the sinusoids was held at one foot whereas their amplitude was varied in the three increments: 0.033, 0.050 and 0.067 ft.

The geometry is typified by Figure 7. Free stream flow conditions were:

$$M_{\infty} = 3.0$$

$$P_{\infty} = 628.5 \text{ lb/ft}^2$$

$$T_{\infty} = 532.2^{\circ}\text{R}$$

For convenience, let us label this series of tests as I(a), I(b), and I(c) for the respective geometries.

In order to start the computer solution, an initial guess as to the velocity profile at some point on the plate is required. Integration was initiated at a point 8.5 feet from the leading edge of the plate where a 1/7th power law was assumed for the velocity distribution. It was assumed that the boundary layer thickness at this point was given by

$$\delta = x \cdot (128.0 \mu / (3.0 \rho \cdot V_{\infty} \cdot x))^{\frac{1}{2}}$$

Computer results for case I(a) are presented in Figures 8 - 10.

Velocity profiles for eight stations along the wavy segment of the wall are plotted in Figure 8. A definite retarding effect may be noted by comparing the profiles for stations 1 and 8. It is conceivable that for a sufficient number of waves (distance down the plate) this would result in separation; however, this was not examined due to the limited computer time available for this study.

Temperature profiles for the same stations are plotted in Figure 9. A strong conduction effect can be noted at the wall. Heat transfer to the wall, as well as other parameters of interest, are plotted as a function of distance along the wall in Figure 10. The heat transfer rate is seen to vary more or less periodically

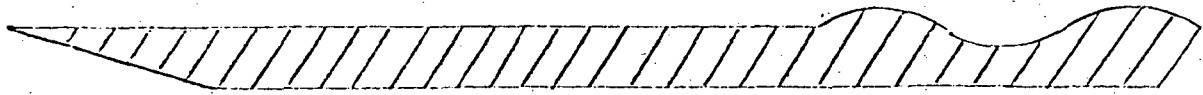


Figure 7

Geometry of the wall used in computer studies.

after an initial oscillation which is due to the mismatch in the two external flow solutions. Heating rate appears to be correlated with the velocity in as much as the peaks in both of these parameters occurs at the wall inflection point. It should be noted that all of the results presented represent a single computer run at each test condition. No attempt was made to converge on a solution taking into account the displacement thickness or an "effective wall". Qualitative comparisons to be made with the experiments of Cary and Morrissette¹⁰ will involve only discussion of case I(a) since the essential features of computer runs I(a), I(b), and I(c) are qualitatively similar. The effect of increasing amplitude of the waves of heat transfer is shown in Figure 10b.

Velocity and temperature profiles cannot be compared with experimental data since none are available. The fact that the flow is accelerated as it expands over the wave following the shock at the leading edge of the first wave is intuitively reasonable and the shapes of the profiles are again intuitively reasonable. The temperature profiles are also reasonable.

A qualitative comparison of the calculated pressure distribution, Figure 11c, and heat transfer distribution, Figure 10, may be made with results of Cary and Morrissette¹⁰ shown in Figure 2e, and Figure 3a. At an angle of attack of zero, a Reynolds number of $.260 \times 10^6$, with roughness elements, it appears that the boundary layer ahead of the waves was turbulent based on the heat transfer results. The peak heat transfer on the first and each succeeding wave occurs slightly ahead of the wave peak in the experimental situation whereas the computer results indicate peak heating at the inflection point on the aft side of the wave.

Considering the calculated pressure distribution, Figure 11c, one notes that small-perturbation theory indicates a peak pressure immediately following a discontinuity at the leading edge of the first wave followed by a decrease back to the inflection point on the aft of the wave where a recompression commences. This is in general agreement with an inviscid shock-Prandtl-Meyer expansion calculation

VELOCITY PROFILES FOR TURBULENT B. L.

$M_\alpha = 3.0$, $T_\alpha = 532.2^\circ R$, $T_W = 532.2^\circ R$

WAVE AMPLITUDE = 0.033 ft

WAVE LENGTH = 1.0 ft

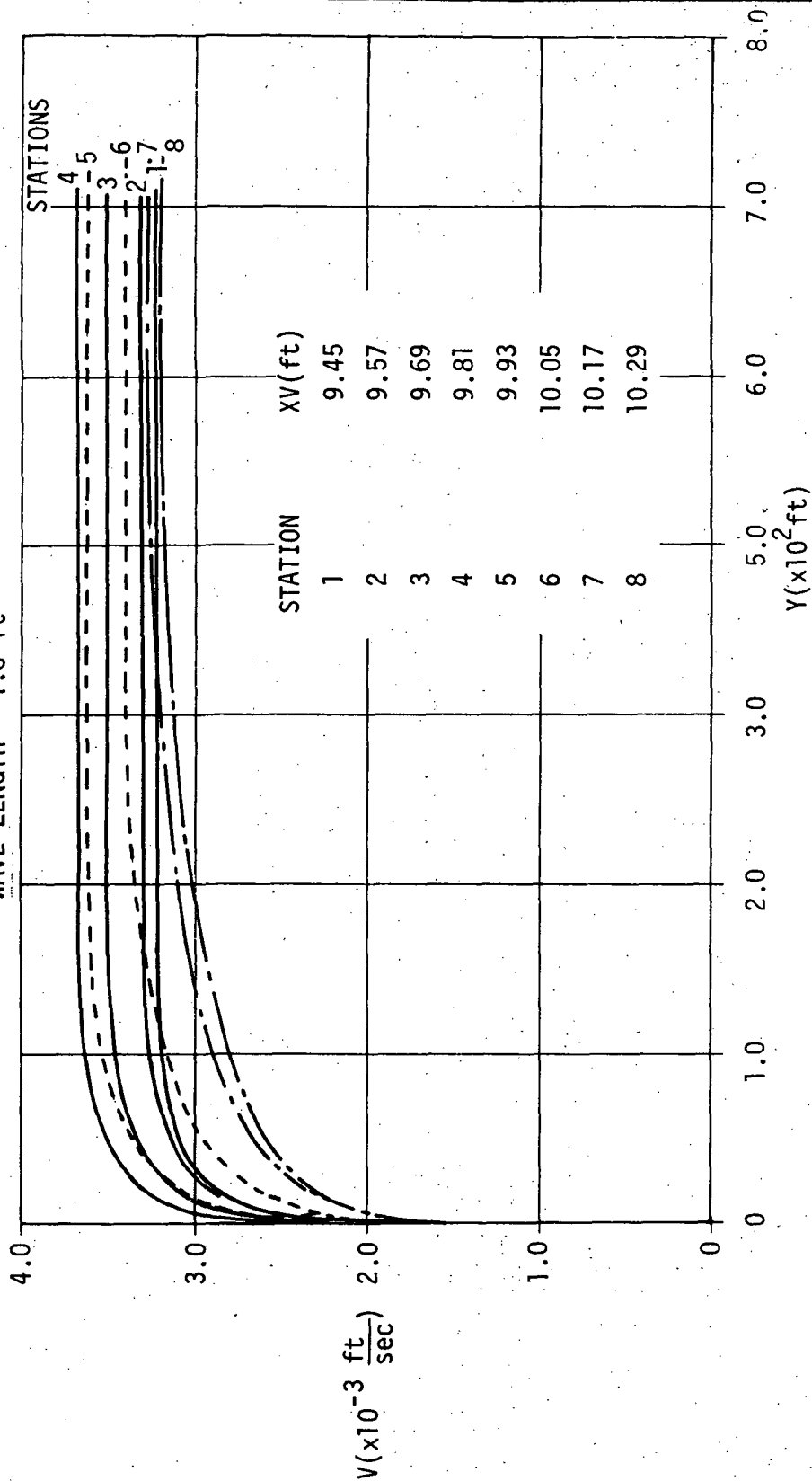


Figure 8. VELOCITY PROFILES FOR TURBULENT BOUNDARY LAYER

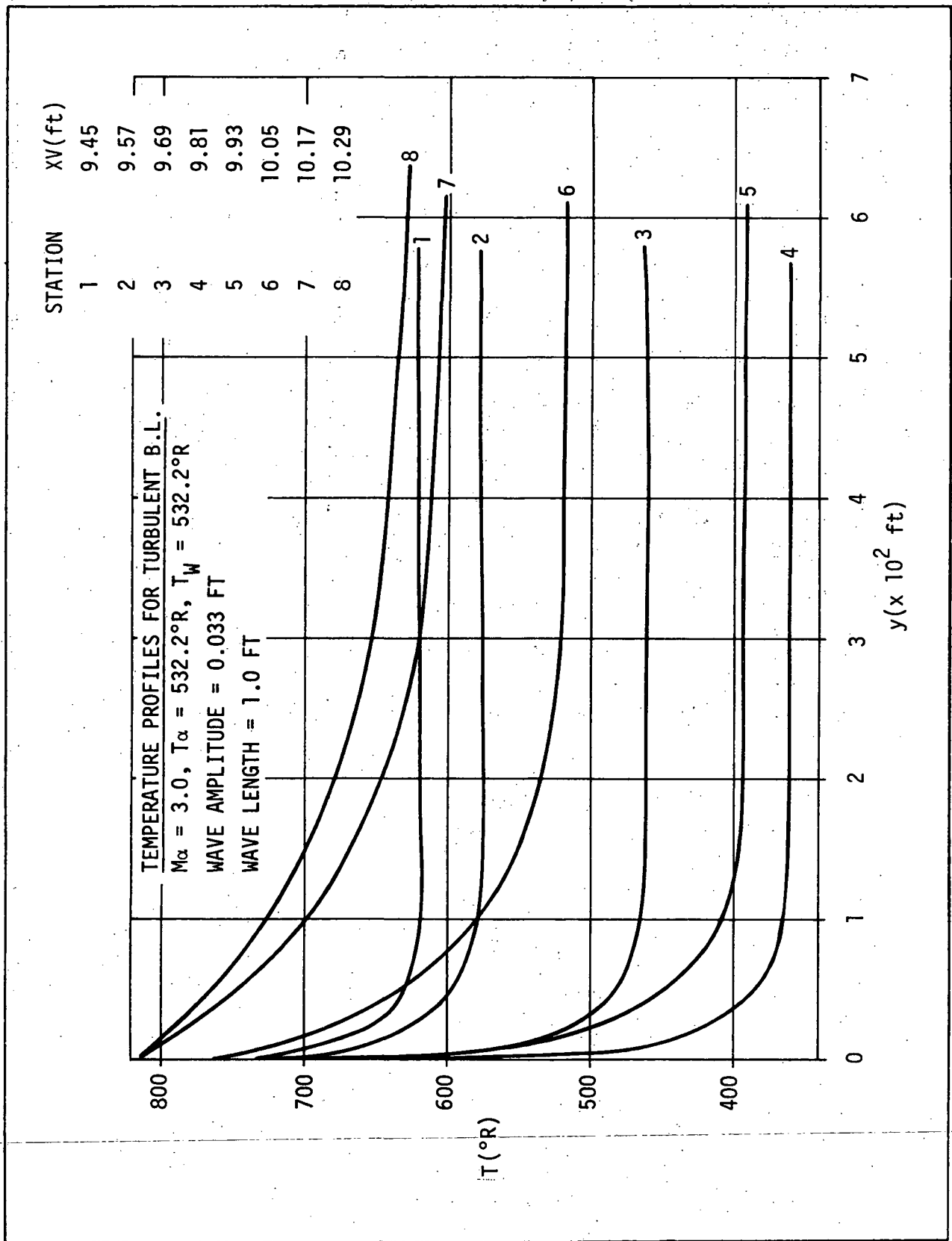


Figure 9. TEMPERATURE PROFILES FOR TURBULENT BOUNDARY LAYER

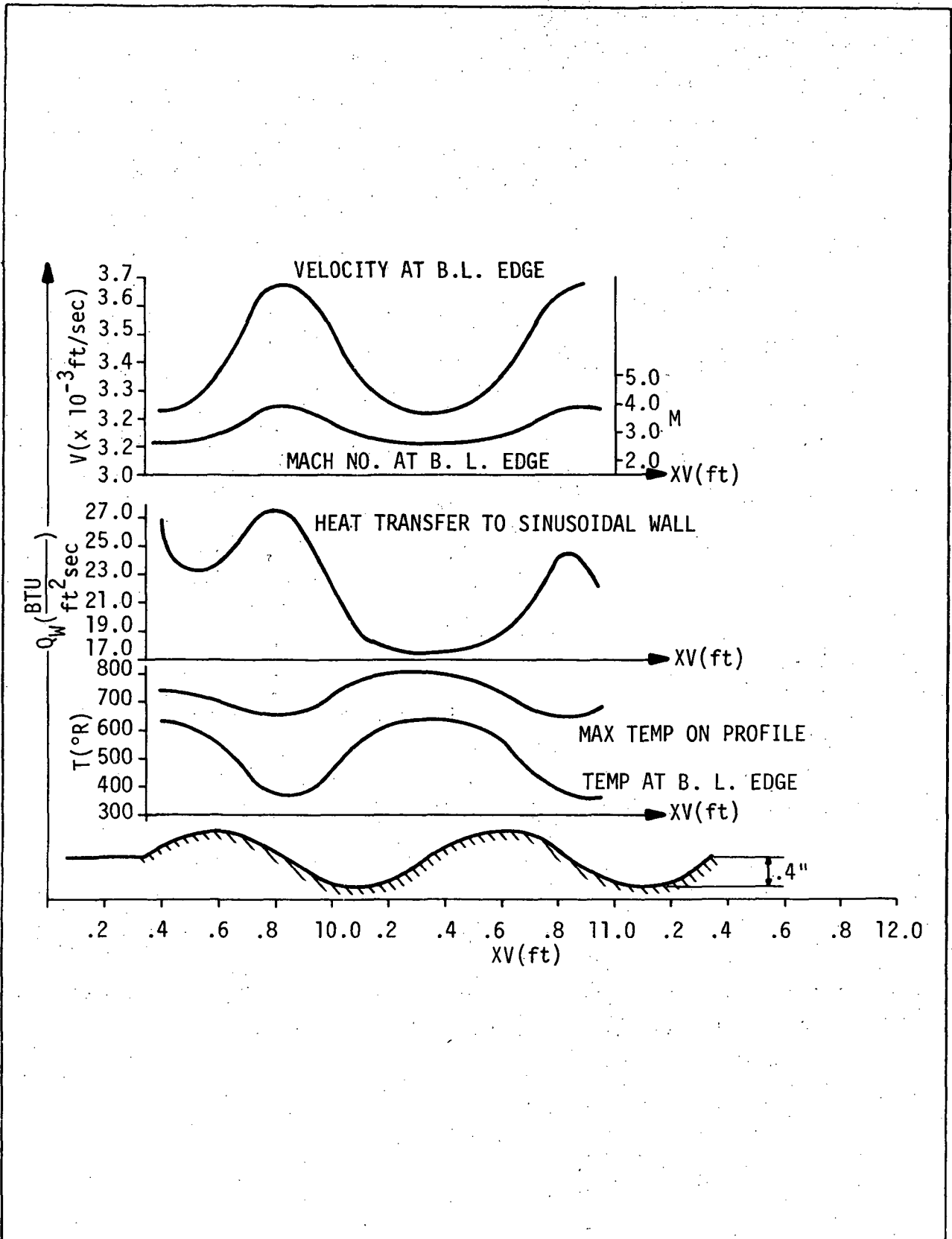


Figure 10. BOUNDARY LAYER PARAMETERS FOR TURBULENT BOUNDARY LAYER

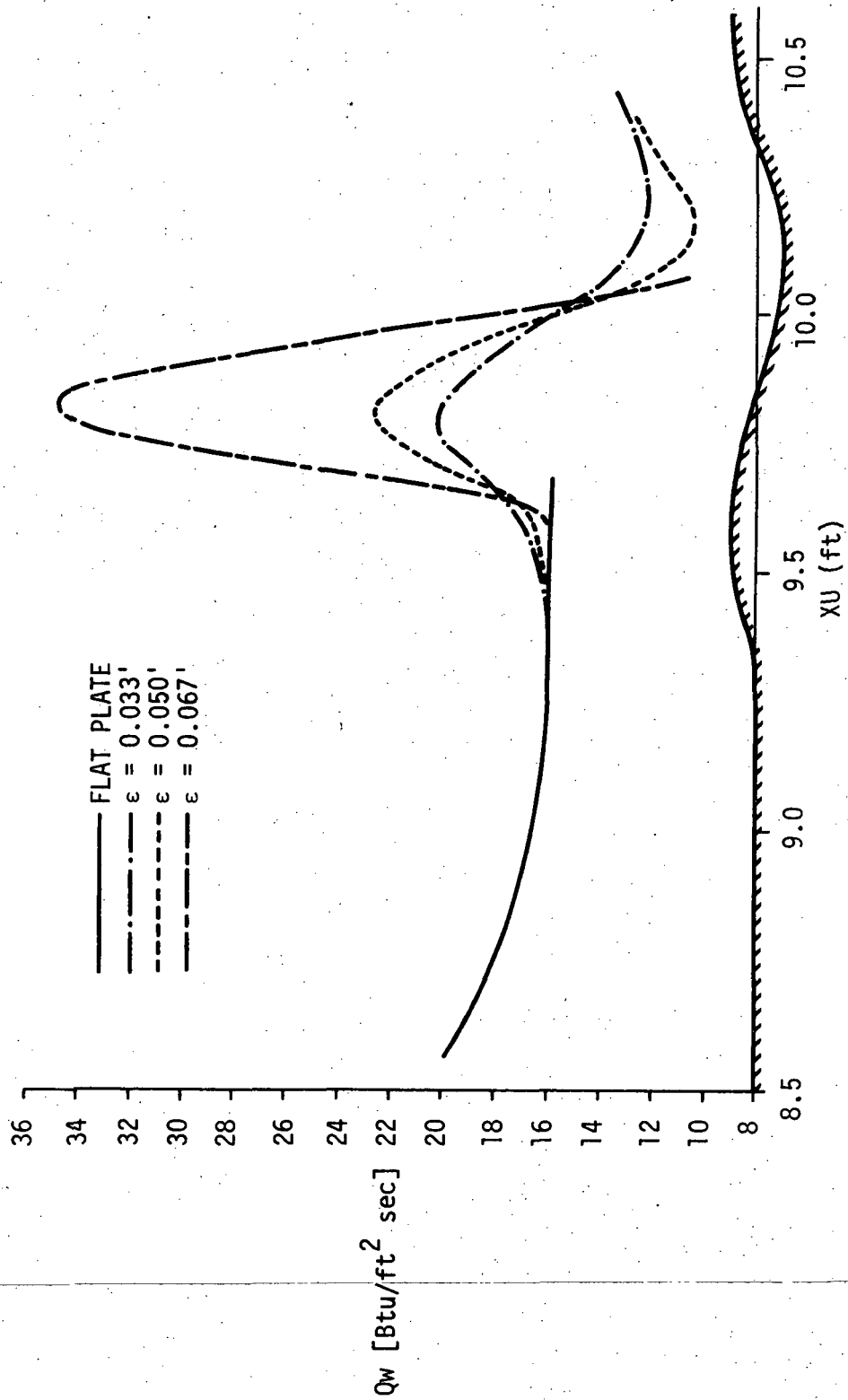


Figure 10(b). HEAT TRANSFER RATE

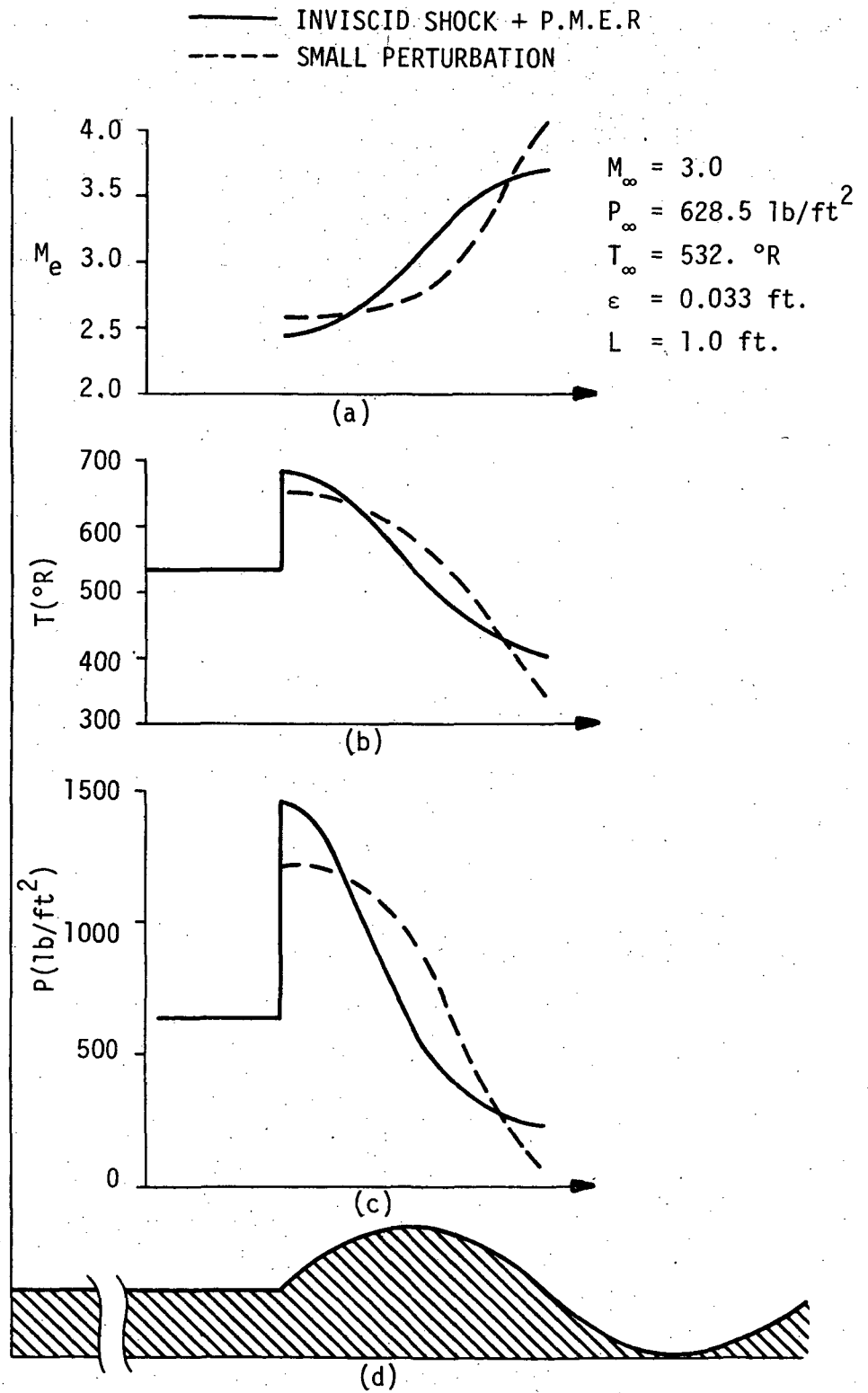


Figure 11. MACH NUMBER, TEMPERATURE, AND PRESSURE DISTRIBUTION ALONG SINUSOIDAL WALL

which is also shown in Figure 11c. This behaviour is also at odds with the experimental result shown in Figure 2e, where the peak pressure is found to occur slightly ahead of the wave peak.

The sinusoidal geometry and flow conditions for these initial studies were chosen because they were thought to be representative of a Shuttle configuration. Unfortunately, no experimental data exists against which a direct comparison can be made. In view of this difficulty further studies were initiated.

The experimental data of Cary and Morrisette¹⁰ appears to be most nearly representative of the required flow and geometry. For this reason the computer program was modified to attempt to duplicate the conditions of this experimental study. Unfortunately, some difficulty was experienced in attempting to define the freestream temperature and pressure which prevailed during the experiments. Estimated conditions corresponding to the zero angle-of-attack, Mach 6.0, $.26 \times 10^6$. Reynolds number conditions tested by Cary and Morrisette are:

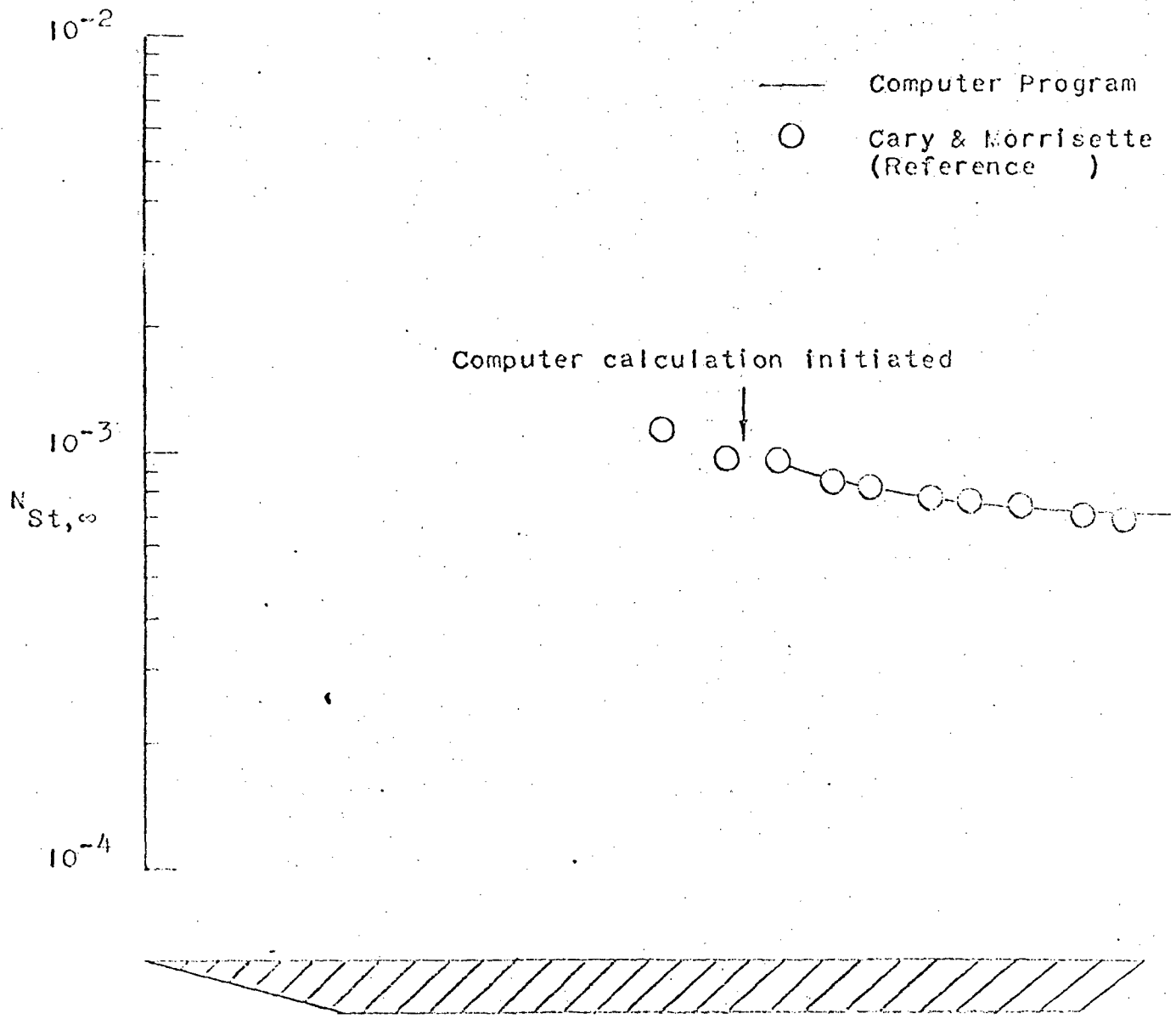
$$M_{\infty} = 6.0$$

$$P_{\infty} = 60 \text{ lb/ft}^2$$

$$T_{\infty} = 180^{\circ}\text{R}$$

The geometry of the wall was duplicated with no difficulty. A computation of the heat transfer to a flat plate under these flow conditions was also made. The experimental results of Cary and Morrisette for a flat plate and the computer study (11a) are presented on Figure 12. The results for the sinusoidal wall (11b) follow in Figure 13. The flat plate results are seen to agree to a remarkable extent. This could be a fortuitous result since the actual flow conditions of the experiment were not known but rather estimated.

The results for the heat transfer to the sinusoidal wall are not in the excellent agreement found for the flat plate situation. The pertinent question at this point is "does this technique for solving problems turbulent boundary layer over sinusoidal roughness work at all in view of this poor agreement?"



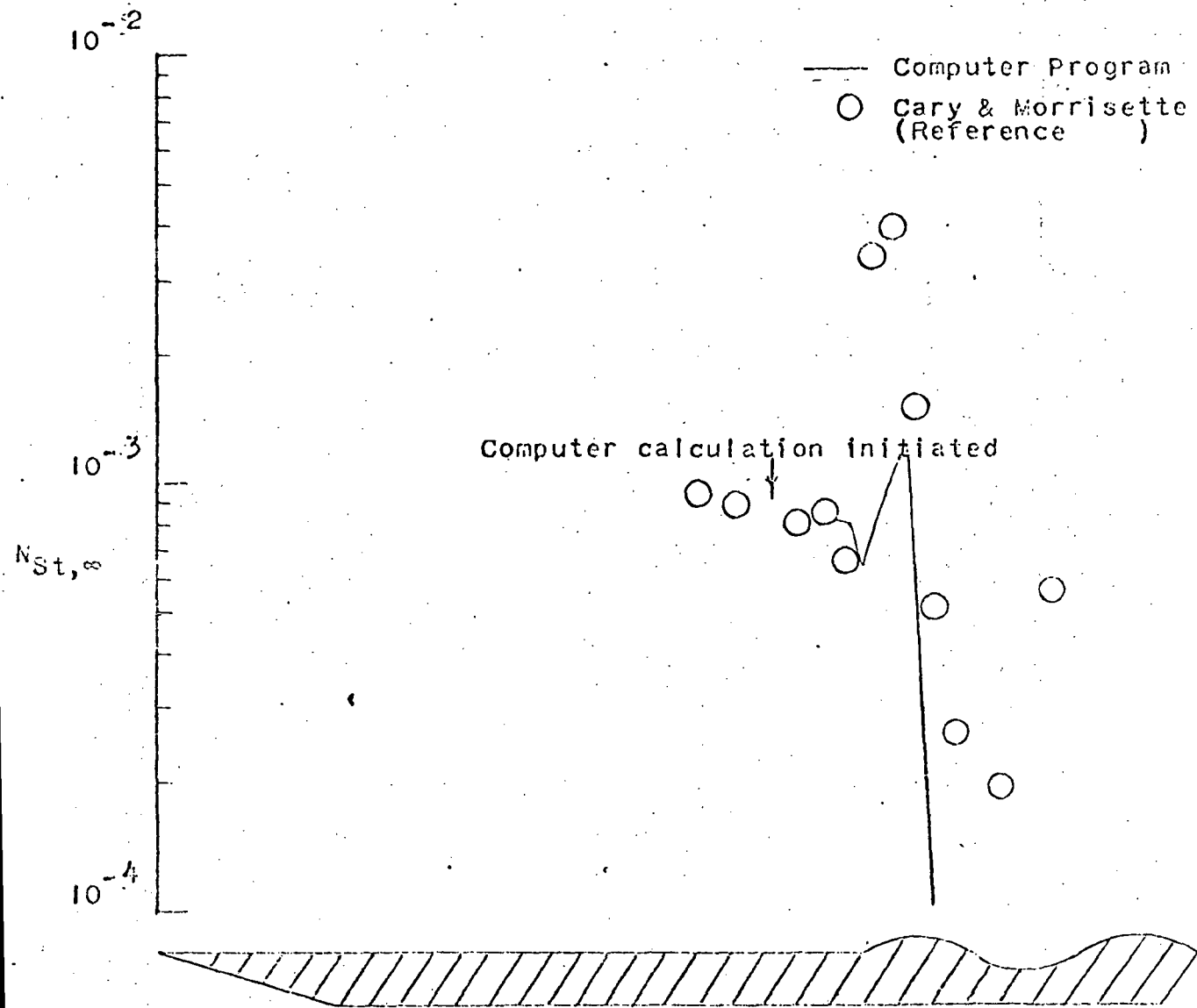


Figure 13 - Heat transfer to a sharp-leading-edge sinusoidal plate. Zero angle of attack. $M_{\infty} = 6.0$.

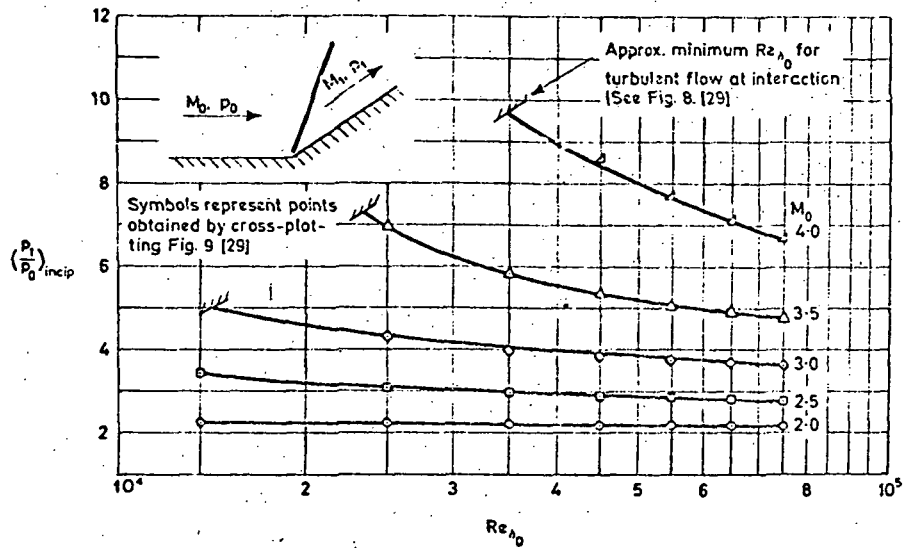
First consider the problem of possible flow separation ahead of the first wave. Assuming a turbulent boundary layer the data presented in Figure 14(b) may be used to determine whether one would anticipate separated flow. A wedge deflection angle for the sinusoidal wall may be determined using:

$$\textcircled{H} = \left. \frac{dx_2}{dx_1} \right|_{x_1 = 0} = \epsilon \alpha \cos \alpha x_1 \Big|_{x_1 = 0}$$

For the geometries of tests I(a), I(b) and I(c), one obtains $\textcircled{H} = 11.88, 18.0, 24.12$ degrees respectively. A calculation of Re_{δ_0} for these test conditions yields 3.6×10^3 . Obviously for these cases one would not anticipate flow separation.

Calculation of Re_{δ_0} for the experimental conditions corresponding to 11(b) does not appear possible because of an uncertainty in δ_0 . It may be noted that Re_{δ_0} would have to be in excess of 8×10^4 before one would anticipate separation.

The discrepancy between the heat transfer and the pressure distributions does not appear, therefore, to be due to separation at the beginning of the first wave. The variation between the calculated pressure distribution and the experimental distribution in the neighborhood of the beginning of the first wave must be due to viscous interaction. For a compression corner the pressure distribution for several flow conditions and deflection angles has been measured by *Kuehn*²¹. The first curve of Figure 15 gives a typical distribution in attacked, turbulent flow. It is easy to see how this behaviour coupled with the decrease in pressure due to the expansion over the wave could result in the experimentally observed distribution. That is, with the pressure peak located some distance up the front face of the wave. This is particularly true for the relatively short wavelength sinusoids used in the experimental program [10]. Intuitively, one would expect the peak pressure for the situation in computer studies I(a,b,c) to be located much closer to the beginning of the wave in terms of percent of the period α . Thus, for the longer wavelengths, the small perturbation theory probably gives a better represent-



(a)

Effect of Reynolds number on the pressure rise for incipient separation for compression corners in turbulent flow [21]

$$Re_{\delta_0} = \frac{u \delta}{12\nu_0}, \text{ where } u \text{ is velocity, } \delta \text{ is boundary layer thickness, and}$$

the subscript \circ refers to the condition near the beginning of the interaction.

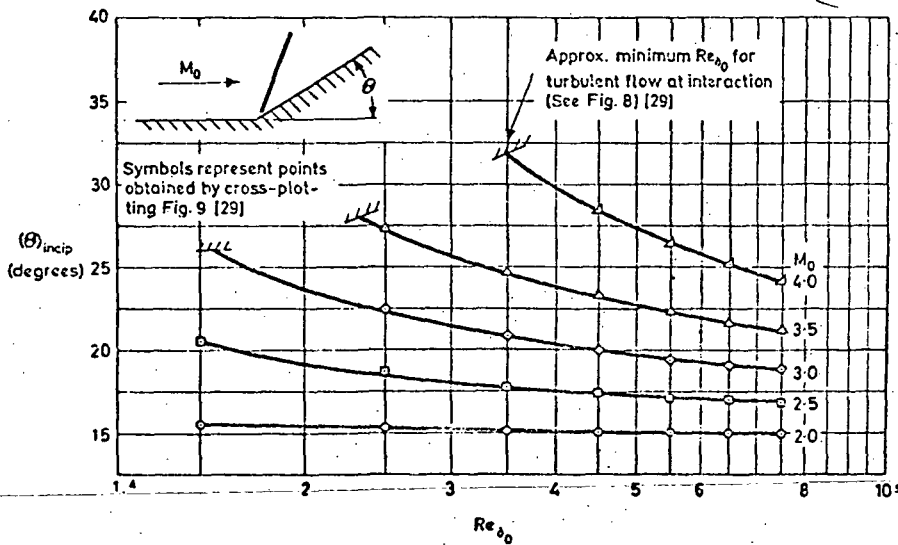


Figure 14

Effect of the Reynolds number on the flow deflection angle for incipient separation for compression corners in turbulent flow [21].

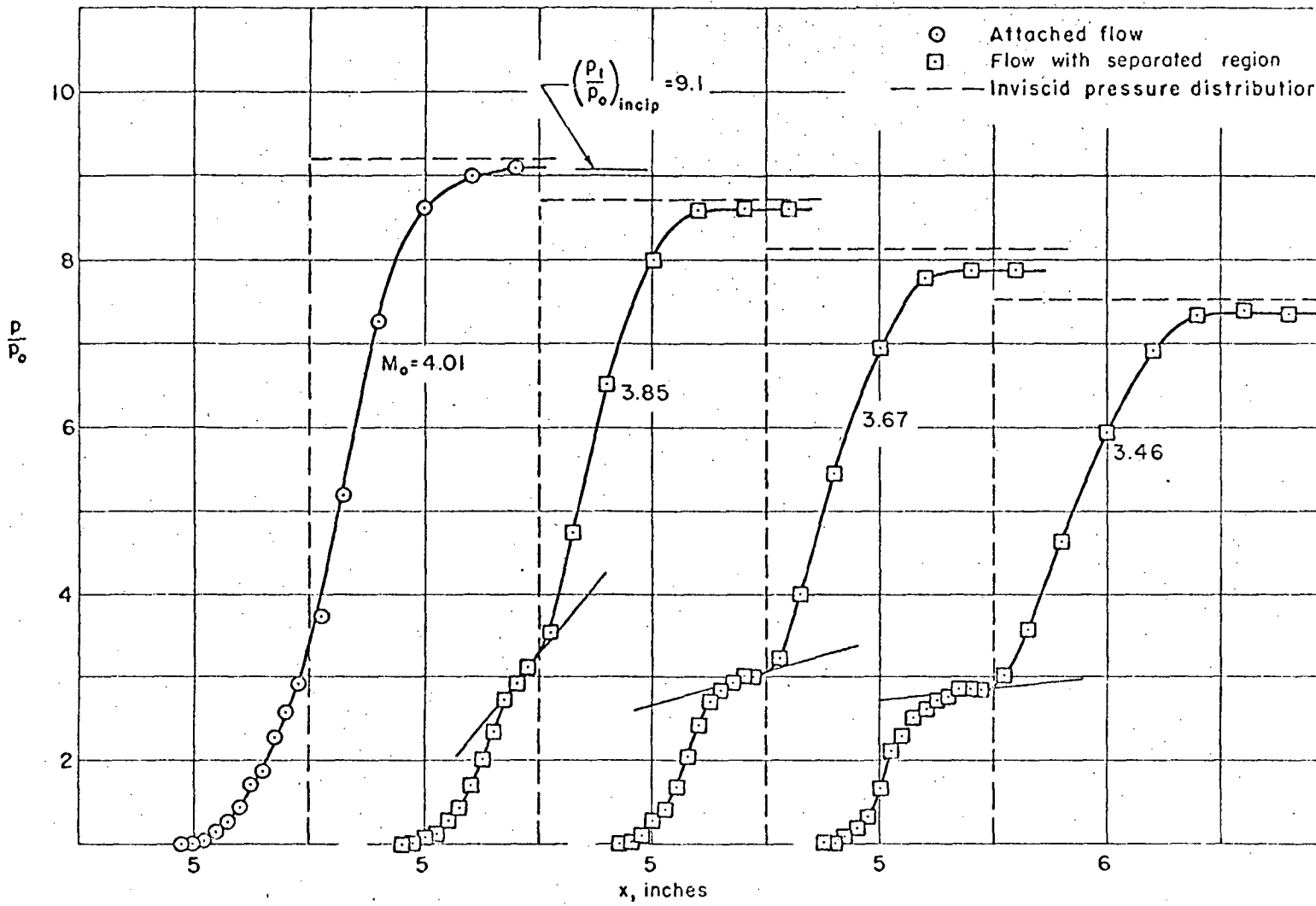


Figure 15

Pressure distributions illustrating the occurrence of separation with a change in Mach number for a compression corner; $CC30^\circ$, $R_{\delta_0} = 4.4 \times 10^4$. (From Reference [21]).

ation of the pressure distribution than found for conditions II.

Although small perturbation theory seems to be in reasonable agreement with the inviscid shock-Prandtl-Meyer expansion calculation for the small W/H ratio, it does not agree for the larger W/H ratios typical of the experimental situation of reference [10]. It should be noted that the peak pressure on the first wave found in these experiments can be predicted using inviscid shock-Prandtl-Meyer expansion calculations although the location of the peak does not agree with the experiments.

V. SUMMARY

To summarize the results of this study:

1. Viscous interaction significantly affects the flow in the region of the origin of the first wave.
2. This interaction dominates the pressure distribution for large W/H ratios.
3. The small perturbation theory appears to be in reasonable agreement with the inviscid shock-Prandtl-Meyer calculations only for the smallest W/H ratio considered.
4. The results of computer study I(a) should be in the best agreement with the physical situation of all the studies conducted.

Further studies should include an interaction on the "effective wall" which should result in better agreement. The larger H/W ratios will require a better solution for the exterior flow than small perturbation theory affords. A simple technique for including the effect of viscous interaction at the first wave needs to be incorporated in the analytical technique. Extension of the method to handle separation on the aft side of the waves seems possible.

REFERENCES

1. Quick, A.W. and Schröder, K., Math. Nachr. 8 (1952) p 217
2. Görtler, H., Z. angew Math. Mech. 25/27 (1947) p 233
3. Görtler, H., Z. angew Math. Mech. 25/27 (1948) p 13
4. Soprunenko, I.P. "Pogranichnyi sloi na volnistoi stenke" (Boundary Layer on Wavy Wall) - Izvestiya AN SSSR, seriya mekhanikai mashinostroeniya, No. 2, 1962
5. Paskonov, V.M. and Soprunenko, I.P. "Boundary Layer on a Slightly Wavy Wall", Numerical Methods in Gas Dynamics, ed. G.S. Roslyakov and L.A. Chudov, Translated by Z. Lerman NASA TT F 360 NASA TT 65-50138
6. Bam-Zelikovich, G.M. "Raschet otryva pogranichnogo sloya" (Calculation of Boundary Layer Separation) - Izvestiya AN SSSR, otdelenie tekhnicheskikh nauk, No. 12, 1954
7. Fannelöp, T. and Flügge-Lotz, I. "Laminar Compressible Boundary Layer Along a Wave-Shaped Wall", Ingenieur-Archiv 33, (1963) p 24
8. Jaeck, C.L. "Analysis of Pressure and Heat Transfer Tests on Surface Roughness Elements with Laminar and Turbulent Boundary Layers", NASA CR-537 (1966)
9. Shore, C.P.; Dixon, S.C. and Griffith, G.E. "Experimental Turbulent Heat Transfer Coefficient Associated with Sinusoidal Protuberances on a Flat Plate", NASA TN D-1626 (1963)
10. Carey, Aubrey M. Jr. and Morrisette, E. Leon "Effect of Two-Dimensional Multiple Sine-Wave Protrusions on the Pressure and Heat-Transfer Distributions for a Flat Plate at Mach 6", NASA TN D-4437 (1968)
11. Bertram, M.H.; Weinstein, L.M.; Carey, A.M. Jr. and Arrington, J.P. "Heat Transfer to Wavy Wall in Hypersonic Flow", AIAA J., Vol. 5, No. 10, October, 1967
12. Weinstein, Leonard M. "Effects of Two-Dimensional Sinusoidal Waves on Heat Transfer and Pressure over a Plate at Mach 8.0", NASA TN D-5937 (1970)
13. Arrington, James P. "Heat-Transfer and Pressure Distributions Due to Sinusoidal Distortions on a Flat Plate at Mach 20 in Helium", NASA TN D-4907 (1968)
- ~~14. Mayne, A.W. Jr. and Dyer, D.F. "Comparisons of Theory and Experiment for Turbulent Boundary Layers on Simple Shapes at Hypersonic Conditions", Proc. of the Heat Trans. and Fluid Mech. Institute~~
15. Powell, T.E. and Strong, A.B. "Calculation of the Two-Dimensional Turbulent Boundary Layer with Mass Addition and Heat Transfer", Proc. of the Heat Transfer and Fluid Mech. Institute

16. Patankar, S.V. and Spalding, D.B. "A Finite-Difference Procedure for Solving the Equations of the Two-Dimensional Boundary Layer", Int. J. of Heat and Mass Transfer, Vol. 10, pp. 1389-1411 (1967)
17. Patankar, S.V. and Spalding, D.B., Heat and Mass Transfer in Boundary Layers, CRC Press, Cleveland, 1968
18. Escudier, M.P. "The Distribution of Mixing Length in Turbulent Flow near Walls", Mechanical Engineering Dept. Rep. TWF/TN/1, Imperial College, 1965
19. van Driest, E.R. "On Turbulent Flows near a Wall", J. Aero. Sci., Vol. 23, pp. 1007-1011, 1036, (1956)
20. Tables of Thermal Properties of Gases, NBS Circular 564, U.S. Dept. of Commerce, 1955
21. Kuehn, D.M. "Experimental Investigation of the Pressure Rise Required for Incipient Separation of Turbulent Boundary Layers in Two-Dimensional Supersonic Flow", NASA Memo 1-21-59A (February, 1959)

6.2 BIBLIOGRAPHY IN THE GENERAL AREA OF ROUGHNESS EFFECTS ON BOUNDARY LAYER TRANSITION AND WALL FLUXES

NOTE: † - unavailable due to confidential status

* - Unable to obtain copies during the contract period.

1. A. W. Quick and K. Schröder, Math. Nachr. 8 (1952) p. 217.
2. H. Görtler, Z. angew Math. Mech 25/27 (1947) p. 233.
3. H. Görtler, Z. angew Math. Mech 25/27 (1948) p. 13.
4. I. P. Soprunenko, "Pogranichnyi sloi na volnistoi stenke", (Boundary layer on Wavy Wall) - Izvestiya AN SSSR, Seriya mekhanikai mashinostroeniya, No. 2, 1962.
5. V. M. Paskonov and I. P. Soprunenko, "Boundary Layer on Slightly Wavy Wall", Numerical Methods in Gas Dynamics, e.d. G. S. Roslyakov and L. A. Chudov. Translated from Russian by Z. Lerman NASA TT F 360, TT 65-50138.
6. G. M. BAM-Zelikovich, "Raschet otryva pogranichnogo sloya" (Calculation of Boundary - Layer Separation) - Izvestiya AN SSSR, otdelenie tehnickheskikh nauk, No. 12, 1954.
7. T. Fannelöp and I. Flügge - Lotz, "Laminar Compressible Boundary Layer Along a Wave - Shaped Wall", Ingenieur - Archiv 33, (1963) p. 24.
8. James P. Arrington, "Heat-Transfer and Pressure Distributions Due to Sinusoidal Distortions on a Flat Plate at Mach 20 in Helium", NASA TN D-4907 (1968)
9. Aubrey M. Carey, Jr., and E. Leon Morrisette, "Effect of Two-Dimensional Multiple Sine-Wave Protrusions on the Pressure and Heat-Transfer Distributions for a Flat Plate at Mach 6", NASA TN D-4437 (1968).
10. Leonard M. Weinstein, "Effects of Two-Dimensional Sinusoidal Waves on Heat Transfer and Pressure over a Plate at Mach 8.0", NASA TN D-5937 (1970).
11. C. L. Jaeck, "Analysis of Pressure and Heat Transfer Tests on Surface Roughness Elements with Laminar and Turbulent Boundary Layers", NASA CR-537 (1966).
12. Shore, C. P., Dixon, S. C., and Griffith, G. E, "Experimental Turbulent Heat Transfer Coefficient Associated with Sinusoidal Proturberances on a Flat Plate," NASA TN D-1626 (1963).
13. Abbott, Ira H.; Some factors contributing to scale effect at supersonic speeds. AGARD-AG8/M4 (67 28P).
14. Braslow, Albert L., Review of the effect of distributed surface roughness on Boundary - layer transition AGARD 254 (1960, 17p).
15. Devikis, William D. and Walker, Robert W., "Local aerodynamic heat transfer and Boundary layer transition on roughened-sphere-ellipsoid bodies at Mach number 30", NASA TN D-907.
16. Howard, Paul W. and Czarnecki, K. R., "Effect of Fabrication-type Surface Roughness on Transition on Ogive Cylinder Models at Mach Numbers of 1.61 and 2.01", NASA TN D-1933 (July, 1963 49 p.).

17. Potter, J. L. and Whitfield, J. D., "Coment on Effects of Controlled Roughness on Boundary-layer Transition at a Mach Number of 6.0", AIAA Journal, Vol. 2, (Feb. 1964 p. 407-8).
18. Dunn, M. G., "Effects of three dimensional roughness elements on Boundary Layer Transition and Aerodynamics Heating", Journal of Spacecraft and Rockets, Vol. 1 (Jan. - Feb. 1964) p. 68-72, 20 refs.) AF 04/647/673.
19. Holloway, P. F. and Sterrett, J. R., "Effects of Controlled Roughness on Boundary Layer Transition at a Number of 60", AIAA J., V., No. 8 (Aug. 1963).
20. Holloway, P. F. and Sterrett, J. R., "Effect of Controlled Surface Roughness On Boundary Layer Transition and Heat Transfer at Mach Numbers of 4.8 and 6.0", NASA TN D-2054 (Apr. 1966 47 p.).
21. Harris, R. V. Jr., "Effects of Distributed Roughness Height on Aerodynamic Characteristics and Boundary - Layer Transition of a Wing-Body-Tail Configuration at a Mach Number of 1.61", NASA TN D-2334 (Jun. 1964, 22 p.).
22. Van Driest, E. R., "Recent Studies in Boundary Layer Transition", Society of Engineering Science, Founders Meeting, Purdue V. No. V. 4, 1963. International Journal of Engineering Science, Vol. 3. (Aug. 1965, p: 341-353) AF49/638/-250 AF 49/638/-1178.
23. Holloway, P. F. and Morrisette, E. L., "Roughness effects on Boundary Layer Transition for Blunt-Leading-Edge Plates at Mach 6", NASA TN D-3517 (Aug. 1966, 42 p).
24. Owen, P. R. and Thomson, W. R., "Heat Transfer Across Rough Surfaces", Journal of Fluid Mechanics, Vol. 15, Pt. (March 3, 1963, 321-334 p.)
25. Evvard, J. C., Tucker, M. and Burgess, W. C., "Statistical Study of Transition Point Fluctuations in Supersonic Flow", NACA TN 3100 (1954).
26. Lees, L., The Stability of the Laminar Boundary Layer in a Compressible Flow", NACA TN 1360 (1947) and NACA Rep. 876 (1947).
27. P. F. Brinich, Boundary Layer Transition at Mach 3.12 With and Without Single Roughness Element. NACA TN 3267 (1954).
28. Czarnecki, K. R., Robinson, R. B., and Hilton, J. H. Jr., "Investigation of Distributed Surface Roughness on a Body of Revolution at a Mach Number of 1.61", NACA TN 3230 (1954).
29. Braslaw, Albert L. and Harris, Roy V. Jr., "Use of Grit-type Boundary-Layer-Transition Trips on Wind Tunnel Models" NASA TN D-3579 September 1966.
30. Braslow, Albert L., "A Review of Factors Affecting Boundary-Layer Transition", NASA TN D-3384, August 1966.
31. Howell, Ronald H., and Korst, Helmut H., "Drag Associated With Separated Flow Over Two-dimensional V-shaped Notches Under Transonic and Supersonic Conditions", NASA CR-1132, September 1968.

32. Czarnecki, K. R. and Monta, W. J., "Pressure Distributions and Wave Drag Due To Two-Dimensional Fabrication-Type Surface Roughness on an Ogive Cylinder at Mach Numbers of 1.61 and 2.01", NASA TN D-835 (1961).
- *33. Coats, Jack D., Rudy, R. W., and Edmunds, E. W., "Effects of Surface Gaps and Steeps on Laminar Heat-Transfer Rates at Local Mach Numbers From 3 to 10", AEDC-TR-70-17 (Feb. 70 57P) Contract: F406-69-C-0001, Proj: AF-136 AR)-VT0041.
- +34. McCauley, William D., "Boundary Layer Transition Study Group Meeting", Aerospace Corporation, San Bernardino, California, San Bernardino Operations, TR-0158 (S3816-63)-1-Vol-2 (Aug. 67 234P) Contract: F04695-67-C-0185, Monitor: BSD TR-67-213-Vol-2.
- *35. Markovin, Mark V., "Critical Evaluation of Transition From Laminar to Turbulent Shera Layers With Emphasis on Hypersonically Travelling Bodies", Martin Marietta Corp. Baltimore, Maryland, Research Institute For Advanced Studies, (10 APR 67-30 AUG 68, M MAR 69 154P) RIAS-TR-68-13C. Contract: F33651-67-C-1662, Proj: AF-1366, Task: 136606, Monitor: AFFDL TR-68-149.
36. Van Driest, E. R., and Blumer, C. B., "Boundary-Layers Transition at Supersonic Speeds; Roughness Effects With Heat Transfer", North American Rockwell Corporation, Anaheim, California, Ocean Systems Operations. (Oct. 67 7P). Contract: AF 49(638)-1442, Proj: AF-9781, Task: 978102. Monitor: AFOSR 69-0507TR.
- *37. Van Driest, E. R., Blumer, C. B., and Wells, C. S. Jr., "Boundary-Layer Transition On Blunt Bodies--Effect and Roughness", North American Aviation Inc. Anaheim, California, (June 67 5P) Contract: AF49(638)-1442, Proj: AF-9871, Task: 987102, Monitor: AFOSR 68-0092.
38. Van Driest, E. R. and Blumer, C. B., "Boundary Layer Transition On Cones and Spheres at Supersonic Speeds--Effects of Roughness and Cooling", (V). North American Rockwell Corp. Anaheim Ocean Systems Operations, C7-2007/020 (JUL 67 39P) Contract: AF 49 (638)-1442. Proj: AF-978102, Monitor: AFOSR 67-2048.
- *39. Michel, R., "Examination of the Factors Affecting the Transition of Turbulence in Boundary Layers", Foreign Technology Division Wright-Patterson AFB, Ohio, FTD-77-65-1115, (Dec 65 16P).
40. Van Driest, E. R. and Blumer, C. B., "Effect of Roughness on Transition in Supersonic Flow", North American Aviation Inc., Downey, Calif. SID 61-285-17-26 (Jan 61 10P) Contract: AF 49 638 250, Monitor: IDEP 347.00.00.00-F1-01.
- ~~41. Mabey, D. G., "Boundary Layer Transition Measurements Using a Surface Hot Film Down Stream of Distributed Roughness in Wind Tunnels at Mach Numbers From 1.3 to 4.0", RAE TN AERO2941, (Dec. 63 30P).~~
42. Kleleanoff, P. S., Spangenberg, W., and Schubauer, G. B., "Investigation of Boundary Layer Transition", NBS REPT. 7194 (Aug. 1, 1901 3P). NASA Proj. 0603-11-06430.

43. Klebanoff, P. S., Spangenberg, W., and Schubauer, G. B., "Investigation of Boundary Layer Transition", NBS Rept. 7428 (Feb. 8, 1962, 6P), NASA Order R-51, NBS Proj. 0603-11-06430.OTS.
44. Klebanoff, P. S., Spangenberg, W., and Schubauer, G. B., "Investigation of Boundary Layer Transition. NBS REPT. 7497 (May 4, 1962. 4; Jan. 1, 1962 to Mar. 31, 1962) NASA orders R-51, NBS Proj. 0603-11-06430.
45. Rable, Leonard and Krasnican, Milan J., "Effects of Surface Roughness and Extreme Cooling on Boundary-Layer Transition For 15 Degree Cone-Cylinder at Mach Numbers to 7.6", NACA RM E57K19 (Mar. 1958, 61P).
46. Strass, H. Kurt and Tyner, Thomas W., "Some Effects of Roughness on Stagnation Point heat Transfer at a Mach Number of 2, A Stagnation Temperature of 3,530 Deg F, and a Reynolds Number of 2.5X10 Super 6 Per Foot", NACA RM L 58C10 (May 1958, 31P).
- *47. Komoda, Hinoyuki, and Komatsu, Yasuo, "Boundary-Layer Transition By Isolated Roughness", University of Tokyo, Aeronautical Research Institute, Vol. 28, No. 7, Report No. 375 (Nov. 1962, 129-143 P).
48. Lyons, W. C., Jr. and Levensteins, Z. J., "Determination of Critical Surface Height for Boundary Layer Transition", NOLTR-61-87, Ballistic Res. Rept.-49 (Dec. 1962 58 P. 11 Refs).
49. Fenter, Felix W., "The Turbulent Boundary Layer on Uniformly Rough Surfaces at Supersonic Speeds", Texas U. Defense Research Lab., Austin. Contract Nord-16498. DRL-437, CM-941. (Jan. 1960, 217 P, 78 Refs).
- +50. Tetrvin, Neal, "Transition, Minimum Critical; Minimum Transition, and Roughness Reynolds Numbers, for Seven Blunt Bodies of Revolution in Flight Between Mach Numbers of 1.72 and 15.1", NOLTR-62-65, Aerodynamics Res. Rept.-173. (Aug. 16, 1962, 106 P., 31 Refs).
- *51. Harwell, Berks, England, Myers, J. E., Purdue U, Myers, J. E., and Savage, D. W., "The Effect of Artificial Surface Roughness on Heat and Momentum Transfer", American Institute of Chemical Engineers, Journal NSF G-6318 (Vol. 9, Sept. 1963. P. 694-702, 18 Refs.).
52. Akiyama, S. and Komatsu, Y., "Experimental Investigation on The Laminar Boundary Layer Transition By an Isolated Roughness", Nihon U. Research Institute of Technology, Journal (Oct. 1963, 196-208 P., 14 Refs.).
53. Van Driest, E. R., "Recent Studies In Boundary-Layer Transition", AF49/638/-250, AF 49/638/-1178 SID-64-546, AFOSR-64-0589, AD-437283.
54. Blumer, C. B. and Van Driest, E. T., "Boundary Layer Transition Roughness and Free Stream Turbulence Effects", Presented at the 4th Intern-Symp. on Space Technol. and Sci., Tokyo, (Oct. 1962, 10 p) SID-62-1308.
55. Klebanoff, P. S. and Spangenberg, W., "Investigation of Boundary-Layer Transition Progress Report", NASA Order R-51, NASA CR-56197, NBS-8350.

56. Mabey, D. G., "Boundary Layer Transition Measurements Using a Surface Hot Film Down-Stream of Disturbed Roughness at Mach Numbers From 1.3-4.0", Royal Aeronautical Society, Journal, Vol. 69. (Feb. 1965, P. 96-100).
57. Ayling, D. L., "AEDC Tunnel C, Boeing Test No. 010, Surface Roughness, Heat Transfer and Pressure Test on Model AD-633 M-2. AF 33/657/-7132, D2-80912, AD-425543 (Dec. 4, 1963. 464 P).
58. Advisory Group For Aeronautical Research and Development, Paris, "Recent Developments in Boundary Layer Research", Part III. AGARDOGRAPH-97, Pt. IV (May, 1965. 122 p).
59. Cook, T. A., "Some Supersonic Wind Tunnel Tests on the Firing of Boundary-Layer Transition Using Distributed Roughness Bands", RAEOTN-AERO-2772. (July 1961. 20 p).
- +60. Gumley, P. and Sheriff, N., "Heat Transfer and Friction Properties of Surfaces With Discrete Roughness", United Kingdom Atomic Energy Authority, Risley, England. TRG-929/R/. (1965, 39 P).
- *61. Goertler, Hencry, Berlin, Klebanoff, P. S., "The Effect of a Two-Dimensional Roughness Element on Boundary Layer Transition", Springer-Verlag, 1966. p 803-805. Applied Mechanics, Proceedings of the Eleventh International Congress of Applied Mechanics, Munich, West Germany.
- *62. Young, F. L., "Experimental Investigation of the Effects of Surface Roughness on Compressible Turbulent Boundary Layer Skin Friction and Heat Transfer", NORD-16498, DRL-532, CR-21, AD-621085. (May 1965, 166 p).
- +63. Wilkie, D., "Heat Transfer From Surfaces Roughened by Square Riles at a Pitch to Height Ratio of 7.2", United Kingdom Atomic Energy Authority, Windscale, England. TRG-987/W/, (1965, 22 p).
64. Braslow, A. L., "Analysis of Boundary-Layer Transition on X-152-2 Research Airplane", NASA TN D-3487 (July 1966. 18 P).
- +65. Wilkie, D., "Heat Transfer From Surfaces Roughened by Square Ribs at Pitch to Height Ratios of 5, 7.2, 9.4, and 15", United Kingdom Atomic Energy Authority, Risley, England. TRG-1127/W/, (8 Mar. 1966. 22 p).
66. Hicks, J. G., "Boundary Layer Transition", SEE X67-11930-06-12, Lockheed-Georgia Co., Marietta. Aerospace Sciences Lab. In Its Aerospace Sci. Boundary Layer Symp. at the Lockheed Georgia Res. Lab. (1965. 81-99 p).
- *67. Blumer, C. B. and Van Driest, E. R., "Boundary Layer Transition Study Group Meeting", Vol. II. SEE X67-23560 24-12/AF 49/638/-1442 (Aug. 1967. 31 p).
- *68. Arrington, J. P., Bertram, M. H., Cary, A. M., Jr., and Weinstein, L. M., "Effect of Two Dimensional Multiple Wave Distortions on the Heat Transfer to a Wall at Mach Numbers of 6 to 20", NASA TM X-59597 (1966. 48 p).

- *69. Komoda, Hiroyuki and Komatsu, Basuo, "Boundary-Layer Transition by Isolated Roughness", Nihon V., Iitiro Tani, and Matsusaburo Iuchi. I.I.S. Rept. 375, Vol. 28, No. 7. (November 1962. 18 p).
70. Brinich, P. F., "Boundary Layer Transition at Mach 3.12 With and Without Single Roughness Element", NACA TN 3267 (1954).
71. Czarnecki, K. R., Robinson, R. B., and Hilton, J. H., Jr., "Investigation of Distribution Surface Roughness on a Body of Revolution at a Mach Number of 1.61", NACA TN 3230 (1954).
72. Czarnecki, K. R. and Sevier, J. R., "Investigation of Effects of Roughness, Surface Cooling and Shock Impingement on Boundary Layer Transition on a Two-Dimensional Wing", NASA TN D-147, 1--41 (1960).
73. van Driest, E. R. and Blumer, C. B., "Boundary Layer Transition at Supersonic Speeds--Three-Dimensional Roughness Effects (Spheres)", JASS 29, 909--916 (1962).
74. Dryden, H. L., "Review of Published Data On the Effect of Roughness on Transition from Laminar to Turbulent Flow", JAS 20, 477--482 (1953).
75. Dryden, H. L., "Effects of Roughness and Suction on Transition from Laminar to Turbulent Flow", Publications Scientifiques et Techn. de Ministere de l' Air Paris (SDJT) 49--60 (1954).
76. Gregory, N. and Walker, S., "The Effect on Transition of Isolated Surface Excrescences in the Boundary Layer", ARC RM 13,436 (1950).
77. Liepmann, H. W. and Fila, G. H., "Investigations of Effects of Surface Temperature and Single Roughness Elements on Boundary Layer Transition", NACA TN 1196 (1947) and NACA Rep. 890 (1947).
78. Potter, J. L. and Whitfield, J. D., "Effects of Slight Nose Bluntness and Roughness on Boundary Layer Transition in Supersonic Flows", JFM. 12, 501--535 (1962).
79. Tani, I., Hama, R., and Mituisi, S., "On the Permissible Roughness in the Laminar Boundary Layer", Aero. Res. Inst. Tokyo, Imp. Univ. Rep. 199 (1940).
80. Tani, I. and Hama, R., "Some Experiments on the Effects of a Single Roughness Element on Boundary Layer Transition", JAS 20, 289--290 (1953).
81. Tani, I., Juchi, M., and Yammamoto, K., "Further Experiments on the Effect of a Single Roughness Element on Boundary Layer Transition", Rep. Inst. Sci. Technol. Tokyo Univ. 8, (Aug. 1954).
82. Demetriades, A., An Experiment on the Stability of Hypersonic Laminar Boundary Layers. JFM 7, 385--396 (1960).
83. van Driest, E. R. and Boison, J. C., "Experiments on Boundary Layer Transition at Supersonic Speeds", JAS 24, 885-899 (1957).

84. Dryden, H. L., Recent Advances in the Mechanics of Boundary Layer Flow, Ed. by R. V. Mises and Th. v. Karman, Advances in Appl. Mech. I, 1--40, New York (1948).
85. Dryden, H. L., "Transition from Laminar to Turbulent Flow at Subsonic and Supersonic Speeds, Proc. Conference on High-Speed Aeronautics", Polytechnic Institute of Brooklyn, NY 1955, 41--74.
86. Dryden, H. L., "Recent Investigations on the Problem of Transition", SFW 4, 89-95 (1956).
87. Dunn, D. W. and Lin, C. C., "On the Stability of the Laminar Boundary Layer in a Compressible Fluid", JAS 22, 455--477 (1955); see also: JAS 20, 577 (1953 and 19, 491 (1952).
88. Evvard, J. C., Tucker, M., and Burgess, W. C., "Transition Point Fluctuations in Supersonic Flow", JAS 21, 731--738 (1954).
89. Evvard, J. C., Tucker, M., and Burgess, W. C., "Statistical Study of Transition Point Fluctuations in Supersonic Flow", NACA TN 3100 (1954).
90. Fage, A. and Preston, J. H., "On Transition from Laminar to Turbulent Flow in the Boundary Layer", Proc. Roy. Soc. A 178, 201--227 (1941).
91. van Ingen, J. L., "A Suggested Semi-Empirical Method for the Calculation of the Boundary Layer Transition Region", Techn. University, Sept. of Aeronautics, Delft, Report V. T. H. 74(1956).
92. Jones, B. M., "Flight Experiments on the Boundary Layer (Wright Brothers Lecture)", Jas 5, 81-101 (1938); also, Aircraft Eng. 10, 135-141 (1938).
93. Korkegi, R. H., "Transition Studies and Skin-Friction Measurements on an Insulated Flat Plate at a Mach Number of 5.8", Jas 23, 970102 (1956).
94. Lange, A. H. and Lee, R. E., "Note on Boundary Layer Transition in Supersonic Flow", JAS 21, 1, 58 (1954) and 22, 282 (1955).
95. Laufer, J. and Vrebalovich, Th., "Stability and Transition of a Supersonic Laminar Boundary Layer on a Flat Plate", JFM. 9, 257-299 (1960).
96. Lees, L. and Lin, C. C., "Investigation of the Stability of the Laminar Boundary Layer in a Compressible Fluid", NACA TN 1115 (1946).
- *97. Schnell, W. C. and Ginoux, J. J., "Effect of Surface Roughness on Axisymmetric Laminar Separated Flows at $M = 5.4$." VKI-TN-41, Jan. 1968, AD-674003.
- *98. van Driest, Edward R. and Blumer, Charles B., "~~Boundary Layer Transition on Cones and Spheres at Supersonic Speeds - Effects of Roughness and Cooling~~", AFOSR-67-2048, July 1967, AD-66131.
99. Vaucheret, Xavier, "Artificial Initiation of the Supersonic Transition", (Declenchment Artificiel de la Transition en Supersonic) Rech. Aero-spatiale, No. 120. NASA TT F 11558.

- *100. Benson, Bruce W., "Cavitation Inception on Three-Dimensional Roughness Elements", DTMB 2104, May 1966, AD-634319.
- 101. Mattioli, Ennoi, "Experimental Research on the Effect of Pressure Gradient and Free Stream Turbulence on the Boundary Layer of a Rough Flat Plate," Report No. 9, Politecnico di Troino (Italy) Institute de Meccanica Applicata. AFOSR, 66-0339, Nov. 1965, AD 630799.
- *102. Scottron, Victor E. and Power, John L., "The Influence of Pressure Gradient on the Turbulent Boundary Layer Over a Rough Surface", DTMB 2115, Dec. 1965, AD-626086.
- *103. Cook, T. A., "Some Supersonic Wind Tunnel Tests on the Fixing of Boundary Layer Transition Using Distributed Roughness Bands", RAE-TN-AERO 2772 July 1961.

6.3 SINUSOIDAL WALL BIBLIOGRAPHY

- 1. Quick, A. W. and Schröder, K., Math. Nachr. 8 (1952) p. 217.
- 2. Görtler, H., Z. Angew Math. Mech 25/27 (1947) P. 233.
- 3. Görtler, H., Z. Angew Math. Mech . 25/27(1948) P. 13.
- 4. Soprunenko, I. P., "Pogranichnyi sloi na volnistoi Stenke", (Boundary Layer on Wavy Wall) - Izvestiya AN SSSR, seriya mekhanikai mashinostroeniya, No. 2, 1962.
- 5. Paskanov, V. M. and Soprunenko, I. P., "Boundary Layer on Slightly Wavy Wall", Numerical Methods in Gas Dynamics, ed. G. S. Roslyakov and L. A. Chudov. Translated from Russian by Z. Lerman. NASA TT F 360, TT 65-50138.
- 6. Bam-Zelikovich, G. M., "Raschet otnyua progranichnoyo sloya", (Calculation of Boundary-Layer Separation) - Izvestiya AN SSSR, otdelenie tekhnicheskikh nauk, No. 12, 1954.
- 7. Fannelöp, T and Flügge-Lotz, I., "Laminar Compressible Boundary Layer Along a Wave-Shaped Wall", Ingenieur-Archiv 33, (1963) P. 24.
- 8. Arrington, James P., "Heat-Transfer and Pressure Distributions Due to Sinusoidal Distortions on a Flat Plate at Mach 20 in Helium", NASA TN D-4907 (1968).
- 9. Carey, Aubrey M., Jr., and Morrisette, E. Leon, "Effect of Two-Dimensional Multiple Sine-Wave Protrusions on the Pressure and Heat-Transfer Distributions for a Flat Plate at Mach 6", NASA TN D-4437 (1968).
- 10. Weinstein, Leonard M., "Effects of Two-Dimensional Sinusoidal Waves on Heat Transfer and Pressure Over a Plate at Mach 8.0", NASA TN D-5937 (1970).

11. Jaeck, C. L., "Analysis of Pressure and Heat Transfer Tests on Surface Roughness Elements with Laminar and Turbulent Boundary Layers", NASA CR-537 (1966).
12. Shore, C. P., Sixon, S. C., and Griffith, G. E., "Experimental Turbulent Heat Transfer Coefficient Associated with Sinusoidal Protuberances on a Flat Plate", NASA TN D-1626 (1963).
13. Czarnecki, K. R., and Monta, W. J., "Pressure Distributions and Wave Drag Due to Two-Dimensional Fabrication-Type Surface Roughness on an Ogive Cylinder at Mach Numbers of 1.61 and 2.01", NASA TN D-835 1961.
14. Bertram, M. H., Weinstein, L. M., Cary, A. M., Jr., and Arrington, J. P., "Heat Transfer to Wavy Wall in Hypersonic Flow", AIAA J., Vol. 5, No. 10, Oct. 1967.

6.4 BIBLIOGRAPHY ON HIGH SPEED SEPARATED FLOWS

Collected by L. C. Chow

The University of Tennessee Space Institute

Abbott, D. E., Holt, M., and Nielsen, J. N. "Investigation of Hypersonic Flow Separation and Its Effects on Aerodynamic Control Characteristics." ASD-TDR-62-963, November 1962.

AGARD Conference Proceedings No. 4, North Atlantic Treaty Organization, Separated Flows, Parts I and II, May 1966.

Alber, I. E., "Integral Theory for Turbulent Base Flows at Subsonic and Supersonic Speeds," Calif. Inst. of Technology, Pasadena, California, Ph.D. Thesis (1967).

Alber, I. E. and Lees, L., "Integral Theory for Supersonic Turbulent Base Flows," AIAA J., 6, 1343-1351, 1968.

Allen, H. J., Heaslet, M. A. and Nitzberg, G. E., The Interaction of Boundary-Layer and Compression Shock and Its Effect Upon Airfoil Pressure Distributions, N.A.C.A. RM.A7A02, 1947.

Amick, J. L., "A Semi-Empirical Relation for Laminar for Laminar Separation." J. Aerospace Sci. 26, p. 603, 1959.

Arens, M. and Spiegler, E., "Shock-Induced Boundary Layer Separation in Over-Expanded Conical Exhaust Nozzles," AIAA J. 1, 578-581, March 1963.

Bardsley, O. and Mair, W. A., "The Interaction Between an Oblique Shock-Wave and a Turbulent Boundary-Layer," Phil. Mag., 1951, 42, 29.

Barry, F. W., Shapiro, A. H. and Neumann, E. P., "The Interaction of Shock Waves with Boundary-Layers on a Flat Surface." J. Aero. Sci., 18, 229, 1951.

Barry, F. W., "A Review of Experimental Results on Boundary Layer-Shock Wave Interaction," North American Aviation, AL-1599, 15 December 1952.

Beastall, D. and Eggink, H., "Some Experiments on Break-away in Supersonic Flow." Part I. R.A.E. Tech. Note Aero. 2041, 1950; Part II, R.A.E. Tech. Note Aero. 2061, 1950.

Bernsteine, H. and Brunk, W. E. "Exploratory Investigation of Flow in the Separated Region Ahead of Two Blunt Bodies at Mach Number 2," NACA RM E55D07b, June 1955.

Bloom, M. H., "On Moderately Separated Viscous Flows," J. Aerospace Sci., Vol. 28, No. 4, pp. 339-340, 1961.

Bray, K. N. C., et al, "Some Calculations by the Crocco-Lees and Other Methods of Interaction Between Shock Waves and Laminar Boundary Layers, Including Effects of Heat Transfer and Suction." Aeronautical Research Council A.R.C., 21, 834, F.M.2937, (ASTIA no. AD 241490), April 5, 1960.

Bogdonoff, S. M., Kepler, C. E. and Sanlorenzo, E., "A Study of Shock Wave Turbulent Boundary-Layer Interaction at $M = 3$." Princeton University Aeronautical Engineering Laboratory, Report No. 222, 1953.

Bogdonoff, S. M., "Some Experimental Studies of the Separation of Supersonic Turbulent Boundary Layers," Princeton Univ. Report 336, June 1955.

Buchanan, T. D., "Study of Flow Separation on Missile by Jet Plume"; M.S. Thesis, Univ. of Tenn. Space Institute, Tullahoma, Tenn., 1967.

Burbank, P. B., Newlander, R. A., and Collins, I. K., "Heat Transfer and Pressure Measurements on a Flat Plate Surface and Heat Transfer Measurements on Attached Protuberances in a Supersonic Turbulent Boundary Layer at Mach Numbers of 2.65, 3.41, and 4.44," NASA TN D-1372, December 1962.

Bursnall, W. J., and Loftin, L. K., "Experimental Investigation of Localized Regions of Laminar-Boundary-Layer Separation, NACA TN 2338, 1951.

Carriere, P., "Recherches Recentes Effectuees a L'O.N.E.R.A. sur les Problemes de Recollment," Communication Presented at the Seventh Fluid Dynamics Symposium, Jurata September, 1965.

- Carlson, W. O., "Heat Transfer in Laminar Separated and Wake Flow Regions," Heat Transfer and Fluid Mechanics Institute, Stanford University Press, June 1959.
- Chapman, D. R., Kuehn, D. M., and Larson, H. K., "Investigation of Separated Flows in Supersonic and Subsonic Streams with Emphasis on the Effect of Transition." NACA Report, 1356, 1958.
- Cheng, S. I., Bray, K. N. C., "On the Mixing Theory of Crocco and Lees and Its Application of the Interaction of Shock Wave and Laminar Boundary Layer, Part I, General and Formulation," Princeton University, Dept. of Aeronautical Engineering, Report 376, AFOSR TN 57-283, May 1957.
- Cheng, S. I., Chang, I. D., "On the Mixing Theory of Crocco and Lees and Its Application to the Interaction of Shock Wave and Laminar Boundary Layer, Part II, Results and Discussion," Princeton Univ., Dept. of Aeronautical Engineering, Report 376, AFOSR TN 58-3, November 1957.
- Childs, M. E., Paynter, G. C., and Redeker, E., "The Prediction of Separation and Reattachment Flow Characteristics for Two-Dimensional Supersonic and Hypersonic Turbulent Boundary Layers," AGARD Symposium CP#4, May 1966.
- Chow, W. L., and H. H. Korst. "On the Structure Within a Constant Pressure Compressible Turbulent Jet Mixing Region," Univ. of Illinois, ME TN 393-1, 1962.
- Clauser, F. H., "Turbulent Boundary Layers in Adverse Pressure Gradients," J. Aero. Sci. 21, 91-108, 1954.
- Crossen, J. W. and O'Brien, R. L., "Investigation of the Diffusion Characteristics of Supersonic Streams Composed Mainly of Boundary Layers," AIAA J. Aircraft, Vol. 2, No. 6, Nov-Dec., 1965, pp. 485-492.
- Cohen, C. B., and Reshotko, E., "The Compressible Laminar Boundary Layer with Heat Transfer and Arbitrary Pressure Gradient," NACA TR T294, 1956.
- Coles, D., "The Law of the Wake in Turbulent Boundary Layers," Journal of Fluid Mechanics, Vol. 1, 1958, p.191.
- Coles, P., "The Turbulent Boundary Layer in a Compressible Fluid," Phys. of Fluids, Sept., 1964, p. 1403.

- Cooke, J. C. "Separated Supersonic Flow." RAE Tech Note Aero, 2879, March 1963.
- Cope, W. F. "The Measurement of Skin Friction in a Turbulent Boundary-Layer at a Mach Number of 2.5, Including the Effect of a Shock Wave." Proc. Roy. Soc. (A), 1952, 215, 84.
- Crawford, D. R. "Supersonic Separated Flow Downstream of a Backward Facing Step." Aeronautical Sciences Div., Univ. of Calif. Berkeley, Rep. AS-65-9, May 1967.
- Crocco, L. "Considerations on the Shock Wave Boundary Layer Interaction." Proc. of the Centenary Meeting of Brooklyn Polytechnic Institute, p. 75, December 1954.
- Crocco, L. and Lees, L. "A Mixing Theory for the Interaction between Dissipative Flows and Nearly Isentropic Streams." Journal of Aeronautical Sciences, Vol. 19, No. 10, October 1952.
- Crocco, L. and Probst, R. F., "The Peak Pressure Rise across an Oblique Shock Emerging from a Turbulent Boundary Layer over a Plane Surface." Princeton Univ. Report No. 254, March 1954.
- Curle, N. "Accurate Solutions of the Laminar Boundary Layer Equations for Flow Having a Stagnation Point and Separation. ARCR and M No. 3164, 1958.
- Curle, N. "A Two Parameter Method for Calculating the Two-Dimensional Incompressible Laminar Boundary Layer," Jour. Roy. Aeronautical Soc., Vol. 71, p. 117, 1967.
- Curle, N., and Skan, S. W. "Approximate Methods for Predicting Separation Properties of Laminar Boundary Layers," Aeronautical Quarterly, Vol. VIII, p. 257, 1957.
- Czarnecki, K. R., Sinclair, A. R., "A Note on the Effect of Heat Transfer on Peak Pressure Rise Associated with Separation of Turbulent Boundary Layer on a Body of Revolution (NACA RM-10) at a Mach Number of 1.61," NACA TN 3997, April 1957.
- Donaldson, C. du P. "Effects of Interaction between Normal Shock and Boundary-Layer." NACA CB-4A27, 1944.
- Donaldson, C. du P., Lange, R. H., "Study of the Pressure Rise across Shock Waves Required to Separate Laminar and Turbulent Boundary Layers," NACA TN No. 2770, 1952.

- Drougge, G., "Experimental Investigation of the Influence of Strong Adverse Pressure Gradients on Turbulent Boundary-Layers at Supersonic Speeds." Paper read at the 8th Int. Congr. on Theoretical and Applied Mechanics, Istanbul, 1952.
- Erdos, J., and A. Pallone. "Shock Boundary Layer Interaction and Flow Separation," Proc., Heat Transfer Fluid Mech. Inst., 1962.
- Fage, A., and Sargent, R. F., "Shock wave and Boundary Layer Phenomena Near a Flat Surface", Proc. Roy. Soc. A, Vol. 190, p. 1, 1947.
- Falkner, V. M. and Skan, S. N., "Some Approximate Solutions of the Boundary Layer Equations," R&M No. 1314, British A.R.C., 1930.
- Ferguson, H. and Schaefer, J. W., "Heat Transfer and Pressure Distribution on Cone-Cylinder-Flare Configuration with Boundary Layer Separation." NASA TN D-1436, October 1962.
- Gadd, G. E., "A Theoretical Investigation of Laminar Separation in Supersonic Flow." J. Aero. Sci., Vol. 24, p. 759, 1957.
- Gadd, G. E. "A Simple Theory for Interactions Between Shock Waves and Entirely Laminar Boundary-Layers," A.R.C. 16, 416, 1953.
- Gadd, G. E. "Interactions between Wholly Laminar and Wholly Turbulent Boundary Layers and Shock Waves Strong Enough to Cause Separation." Journal of Aeronautical Sciences, Vol. 20, No. 11, Nov. 1953.
- Gadd, G. E. "A Theoretical Investigation of the Effects of Mach No., Reynolds No., Wall Temperature and Surface Curvature on Laminar Separation in Supersonic Flow" Rep. No. FM 2415, British A.R.C., June 1956.
- Gadd, G. E., "The Interaction between a Weak Normal Shock Wave and a Turbulent Boundary Layer." British A.R.C., C.P. No. 424, 1959.
- Gadd, G. E., "Boundary Layer Separation in the Presence of Heat Transfer," AGARD Report 280, 1960.
- Gadd, G. E., Cope, W. F., and Attridge, J. L., "Heat Transfer and Skin Friction Measurements at a Mach number of 2.44 for a Turbulent Boundary Layer on a Flat Surface and in Regions of Separated Flow." British A.R.C. 20,472, October 1958.

- Gadd, G. E. and Holder, D. W., "The Behavior of Supersonic Boundary Layers in the Presence of Shock Waves," IAS, Paper No. 59-138, Presented at 7th Anglo-American Aeronautics Conf., Oct. 5-7, 1959.
- Gadd, G. E., Holder, D. W. and Regan, J. D., "The Interaction of an Oblique Shock Wave with the Boundary-Layer on a Flat Plate." Part II. Interim note on the results for $M = 1.5, 2, 3$ and 4 . A.R.C 15, 591 - F.M.1855, Jan. 30, 1953.
- Gadd, G. E., Holder, D. W., and Regan, J. D. "An Experimental Investigation of the Interaction between Shock Waves and Boundary Layers." Proc. of Roy. Soc. of London, A, 1954.
- Gault, D. E., "An Experimental Investigation of Regions of Separated Laminar Flow," NACA TN3505, 1955.
- Ginoux, J. J., "Laminar Separation in Supersonic Flow," Final Report Contract AF EOAR 64-7, October 1964.
- Ginoux, J. J., "Investigation of Flow Separation over Ramps at $M_{\infty} = 3$." AEDC-TR-65-273 (AD475242), Dec. 1965.
- Glick, H. S., "Modified Crocco-Lees Mixing Theory for Supersonic Separated and Reattaching Flows." GALCIT, Hypersonic Research Project Memo. No. 53, (AD239560), May 2, 1960.
- Glick, H. S. "Modified Crocco-Lees Mixing Theory for Supersonic Separated and Reattaching Flows." J. of the Aerospace Sciences, Vol. 29, No. 10, October 1962.
- Goldstein, S., "On Laminar Boundary Layer Flow Near a Point of Separation." Quart. J. Mech. Appl. Math. 1, 43, 1948.
- Golik, R. J., Webb, W. H. and Lees, L., "Further Results of Viscous Interaction Theory for the Laminar Supersonic Near Wake," AIAA Preprint 67-61, Jan. 1967.
- Goodwin, F. K., and Lynes, L. L., "Inhibition of Flow Separation at High Speed. Vol. IV - Calculation of Non-adiabatic Laminar Boundary Layers on Conical Compression Surfaces." Air Force Flight Dynamics Lab. Tech. Rep. AFFDL-TR-68-119, Vol. IV, Nov. 1968.
- Goodwin, F. K., and Lynes, L. L., "Computer Program for Calculating Laminar Flow Separation at Supersonic Speeds on Conical Compression Surfaces." NEAR TR 12, Jan. 1969.

- Goodwin, F. K., Nielsen, J. N., and Lynes, L. L., "Calculation of Laminar Boundary Layer-Shock Wave Interaction on Cooled Walls by the Method of Integral Relations." NEAR Rep. TR 2, July 1967.
- Goodwin, F. K., Nielsen, J. N., and Lynes, L. L., "Inhibition of Flow Separation at High Speed. Vol. II - Calculation of Nonadiabatic Laminar Boundary Layers." Air Force Flight Dynamics Lab. Tech. Rep. AFFDL-TR-68-119, Vol. II, Oct. 1968.
- Gray, J. D., "A Correlation of Axisymmetric Laminar Flow Separation Characteristics." AIAA Paper No. 64-475, 1964.
- Gray, J. D., "Laminar Boundary-Layer Separation on Flared Bodies at Supersonic and Hypersonic Speeds." AEDC-TDR-64-277 (AD609341), January 1965.
- Gray, J. D., "On the Existence of a Pressure Plateau in Pure Laminar Separated Flows." AIAA Journal, Vol. 4, August 1966.
- Gray, J. Don, "Investigation of the Effect of Flare and Ramp Angle on the Upstream Influence of Laminar and Transitional Reattaching Flows from Mach 3 to 7," AEDC-TR-66-190, January 1967.
- Grange, J. M., Klineberg, J. M., and Lees, L., "Laminar Boundary Layer Separation and Near-Wake Flow for a Smooth Blunt Body at Supersonic and Hypersonic Speeds," AIAA J., 5, 1089-1096, 1967.
- Greber, I., Hakkinen, R. J. and Trilling, L., "Some Problems of Laminar Boundary Layer Shock Wave Interaction Heat Transfer and Fluid Mechanics Institute, CIT, June 1957, pp. 138-158.
- Green, J. E., "Two-Dimensional Turbulent Reattachment as a Boundary Layer Problem." Proc. Roy. Soc., London, A237, 543-559, 1956.
- Griggs, C. F. and Goldsmith, E. L., "Shock Oscillation Ahead of Centre-Body Intakes at Supersonic Speeds," R.A.E. Report Aero. 2477, A.R.C. 15634, Sept. 1952.
- Gortler, H., "A New Series of the Calculation of Steady Laminar Boundary-Layer Flow," Jour. Math. and Mech. Vol. 6, 1957.
- Guman, W. J., "On the Plateau and Peak Pressure of Regions of Pure Laminar and Fully Turbulent Separation in Two Dimensional Supersonic Flow," J.A.S., 26, 1(Jan, 1959) 56.

- Hakkinen, R. J., Greber, I., Trilling, L., and Abarbanel, S. S., "The Interaction of an Oblique Shock Wave with a Laminar Boundary Layer." NASA TM 2-18-59W, March 1959.
- Hammit, A. C., "The Interaction of Shock Waves and Turbulent Boundary Layers," J.A.S., 25, 6, June 1958.
- Hammit, A. G., Vas, I. E., and Hight, S., "An Analysis of the Effect of Shock Waves on Turbulent Boundary Layers," Princeton Univ. Report No. 396, AFOSR TN 57-297, July 1957.
- Head, M. R., and Hayasi, N., "Approximate Calculation of the Incompressible Laminar Boundary Layer." Aero. Quarterly, August 1967.
- Hewson, C. T., "Growth and Separation of a Turbulent Boundary Layer." ASME Symposium on Stall, 1958.
- Heyser, A. and Maurer, F., "Experimental Investigations on Solid Spoilers and Jet Spoilers at Mach Numbers of 0.6 to 2.8," Jet Propulsion Lab. Transl. 32, Feb. 21, 1964.
- Hill, W. G., "Initial Development of Compressible Turbulent Free Shear Layers," Ph.D. Thesis, Rutgers - The State Univ., 1966.
- Holden, M., "An Analytical Study of Separated Flows Induced by Shock Wave-Boundary Layer Interaction." CAL R-AI-1972-A-3, Dec., 1965.
- Holder, D. W., Chinneck, A. and Gadd, G. E., "An Experimental Investigation of the Interaction of a Shock Wave with a Subsonic Stream Bounded by a Wall." Phil. Mag., 1954, 45, 992.
- Holder, D. W., North, R. J. and Chinneck, A., "Experiments with Static Tubes in a Supersonic Airstream." Part I and II., R&M.2782., July 1950.
- Holder, D. W., Pearcey, H. H., and Gadd, G. E., "The Interaction between Shock Waves and Boundary Layers," British A.R.C. CP 180, 1955.
- Holden, M. S., "Heat Transfer in Separated Flow," Ph.D. Thesis, Univ. of London, 1964.
- Holden, M. S., "An Analytical Study of Separated Flows Induced by Shock Wave-Boundary Layer Interaction," CAL Report No. AI-1972-A-3, 1965.

- Holt, M., "Separation of Laminar Boundary Layer Flow Past a Concave Corner," AGARD Conf. Proc., No. 4, Rhode-Saint-Genese, Belgium, May 1966.
- Holt, M., "Separation of Laminar Boundary Layers on Cooled Reentry Bodies," Reprint from the Proc. of the XVIIth International Astronautical Cong., Madrid Spain, Oct. 1966.
- Holt, M., "Laminar Boundary Layer Separation and Reattachment Near a Concave Corner." Proc. of the XVIIIth Cong. of the International Astronautics Federation, Belgrade, Yugoslavia, 1967.
- Honda, M., "A Theoretical Investigation of the Interaction Between Shock Waves and Boundary Layers," Journal of Aeron. Sci., Nov. 1958, p. 667.
- Howarth, L., "The Propagation of Steady Disturbances in a Supersonic Stream Bounded on One Side by a Parallel Subsonic Stream," Proc. Camb. Phil. Soc. 1947, 44, Part 3.
- Johannesen, N. H., "Experiments on Two-Dimensional Supersonic Flow in Corners and Over Concave Surfaces," Communicated by P.D.S.R.(A), Ministry of Supply, A.R.C. 14,607-F.M.1669, Jan. 29, 1952.
- Kaufman, L. G., S. A. Hartofilis, W. J. Evans, R. A. Oman, L. H. Meckler, and D. Weiss. "A Review of Hypersonic Flow Separation and Control Characteristics," ASD TDR 62-168, March 1962.
- Kaufman, L. G., II, Meckler, L., Hartofilllis, S. A., and Weiss, D., "An Investigation of Hypersonic Flow Separation and Control Characteristics," AFFDL-TR-64-174, Jan. 1965.
- Kepler, C. E., and Bogdonoff, S. M., "Interaction of a Turbulent Boundary Layer with a Step at $M = 3$." Princeton Univ. Aero. Eng. Report 238, Sept., 1953.
- Kepler, C. E., and O'Brien, R. L., "Supersonic Turbulent Boundary Layer Growth over Cooled Walls in Adverse Pressure Gradients." ASD-TDR-62-87, October 1962.
- Kessler, T. J., "Supersonic Turbulent Boundary Layer Separation Ahead of a Wedge," Ph.D. Thesis, Rutgers - The State Univ., 1965.

Kessler, T. J., "Comment on the Effect of Sudden Compressions on the Turbulent Boundary Layer," AIAA J. Nov. 1967, p. 2109.

Kirk, F. N., "An Approximate Theory of Base Pressure in Two-Dimensional Flow at Supersonic Speeds," R.A.E. Tech. Note Aero 2377, Dec. 1959.

Kistler, A. L., "Fluctuating Wall Pressure Under a Separated Flow," J. Acoust. Soc. Am. 36, 543-550, March 1964.

Kline, S. J., "Some New Conceptions of the Mechanism of Stall in the Turbulent Boundary Layer, Jour. Aero. Sci., Vol. 24, pp. 470-471, 1957. Also on the Nature of Stall, Jour. of Basic Engr. Trans. ASME, Series D, Vol. 81, p. 305, 1959.

Klineberg, J. M., "Theory of Laminar Viscous-Inviscid Interactions in Supersonic Flow," Calif. Institute of Tech., Pasadena, Calif, Ph.D. Thesis, 1968.

Ko, D. R. S. and Kubota, T., "Supersonic Laminar Boundary Layer Along a Two-Dimensional Adiabatic Curved Ramp," Preprint No. 68-109, AIAA 6th Aerospace Sci. Meeting New York, N. Y., Jan. 22-24, 1968.

Korkegi, R. H., "The Intermittent Hypersonic Wind Tunnel H-1," TCEA TM-15, von Karman Institute for Fluid Dynamics, 1963.

Korst, H. H., "A Theory for Base Pressures in Transonic and Supersonic Flow," J. Appl. Mech., 593-600, 1956.

Korst, H. H., R. H. Page, and M. E. Childs. "Compressible Two-Dimensional Jet Mixing at Constant Pressure," TN 392-1, Eng. Exp. Sta., Mechanical Eng. Dept., Univ. of Illinois, 1954.

Korst, H. H., Page, R. H. and Childs, M. E., "A Theory for Base Pressure in Transonic and Supersonic Flow," Univ. of Illinois, Rept. METN 392-2, March 1955.

Kubota, T. and Fernandez, F. L., "Boundary Layer Flows with Large Injection and Heat Transfer," AIAA J. 6:1, 22-28, 1968.

Kubota, T. and Ko, D. R. S., "A Second Order Weak Interaction Expansion for Moderately Hypersonic Flow Past a Flat Plate," AIAA J., 5:10, 1915-1917, 1967.

- Kuehn, D. M., "Experimental Investigation of the Pressure Rise Required for the Incipient Separation of Turbulent Boundary Layers in Two-Dimensional Supersonic Flow," NASA Memo 1-21-59A, February 1959.
- Kuehn, D. M., "Turbulent Boundary Layer Separation Induced by Flares on Cylinders at Zero Angle of Attack," NASA TR R-117, 1961.
- Kuehn, D. M., "Laminar Boundary-Layer Separation Induced by Flares on Cylinders at Zero Angle of Attack." NASA TR-R-146, June 1962.
- Kuethé, A. M., McKee, P. B., and Curry, W. H., "Measurements in the Boundary Layer of a Yawed Wing," NACA TN 1946, 1949.
- Kutalcladze, S. and Leont'ev, A., "Turbulent Boundary Layers in Compressible Gases," Academic Press, 1964, p. 36.
- Kutschenreuter, P. H., Jr., "Investigation of Hypersonic Inlet Shock-Wave Boundary Layer Interaction," Air Force Flight Development Lab. AFFDL-TR-65-36, March 1965.
- Kutschenreuter, P. H., Jr., Brown, D. L., and Hoelmer, W., "Investigation of Hypersonic Inlet Shock-Wave Boundary Layer Interaction, Part II," Air Force Flight Development Lab., AFFDL-TR-65-36, July 1966.
- Lamb, J. P., "The Development of Free Turbulent Shear Layers" AEDC-TR-65-184, Nov. 1965.
- Lange, R. H., "Present Status of Information Relative to the Prediction of Shock Induced Boundary Layer Separation," NACA TN 3065, 1954.
- Larson, H. K., "Heat Transfer in Separated Flows," Paper presented at the IAS 27th Annual Meeting, New York, January 1959, IAS Report No. 59-37.
- Larson, R. E., C. J. Scott, D. R. Elgin, and R. E. Seiver. "Turbulent Base Flow Investigations at Mach Number 3.0" Rosemont Aero. Lab. Res. Rep. No. 183, Univ. of Minnesota, Inst. of Tech.
- Lee, J. D., "The Influence of High Adverse Pressure Gradients on Boundary Layers in Supersonic Flow." UTIA Report 21, October 1952.
- Lees, L., "Interaction Between the Laminar Boundary-Layer over a Plane Surface and an Incident Oblique Shock Wave." Princeton Univ. Aero. Eng. Lab. Rept. 143, 1949.

- Lees, L., "On the Boundary Layer Equations in Hypersonic Flow and Their Approximate Solutions," J. Aero. Sci., 20, 143-145, 1953.
- Lees, L., "Viscous-Inviscid Flow Interactions at Supersonic Speeds," First Annual Dena's Lecture, Univ. of Notre Dame, April 10-11, 1967.
- Lees, L. and Reeves, B. L., "Supersonic Separated and Re-attaching Laminar Flows: I. General Theory and Application to Adiabatic Boundary Layer-Shock-Wave Interactions." AIAA J., November 1964.
- Levin, V., and T. J. Fabish. "Thermal Effects of Shock Wave Turbulent Boundary Layer Interaction at Mach Numbers 3 and 5," North American, NA 62H-795, 1962.
- Lewis, J. E., Kubota, T. and Lees, L., "Experimental Investigation of Supersonic Laminar, Two-Dimensional Boundary-Layer Separation on a Compression Corner with and without Cooling," AIAA J., 6:1, 7-14, 1968.
- Libby, P. A., Baronti, P. O., and Napolitano, L., "Study of the Incompressible Turbulent Boundary Layer with Pressure Gradient," AIAA J., 2, 445-452, 1964.
- Libby, P. A. and Visich, M., Jr., "Laminar Heat Transfer in Two-Dimensional Subsonic Effusers." J. Aeronaut. Sci., Vol. 22, No. 6, pp. 425-431, June 1955.
- Liepmann, H. W., "The Interaction between Boundary Layer and Shock Waves in Transonic Flow," J.A.S., 13, 12, Dec. 1946, pp. 623-638.
- Liepmann, H. W., Roshko, A. and Dhawan, S., "On the Reflection of Shock Waves from Boundary-Layer," Galcitt Report.
- Lighthill, M. J., "Reflection at a Laminar Boundary-Layer of a Weak Steady Disturbance to a Supersonic Stream Neglecting Viscosity and Heat Conduction." Quart. J. Mech. and Appl. Maths, 1950, 3, 303.
- Lighthill, M. J., "On Boundary Layers and Upstream Influences, Part I. A Comparison Between Subsonic and Supersonic Flows.", Proceedings of Roy. Soc., London (A), 1953, p. 344, Part II. Supersonic Flow without Separation. *ibid*, 1953, p. 478.
- Lighthill, M. J., "The Response of Laminar Skin Friction and Heat Transfer to Fluctuations in the Stream Velocity," Proc. Roy. Soc. A, Vol. 224, p. 1, 1954.

Ludwig, G. R. "An Experimental Investigation of Laminar Separation from a Moving Wall," AIAA Preprint 64-6 (January 1964).

- Liu, C. Y., "Boundary Layer Separation, Ph.D. Dissertation, Colorado State Univ., 1967.
- Liu, C. Y., and Sandborn, V. A., "Laminar Velocity Profiles in Adverse Pressure Gradients." *Journal of Aircraft*, Vol. 5, p. 93, 1968.
- Liu, C. Y., and Sandborn, V. A., "Evaluation of the Separation Properties of Laminar Boundary Layers, *Aeron. Quarterly*, Vol. XIX, p. 235, 1968.
- Love, E. S., "Pressure Rise Associated with Shock Induced Boundary Layer Separation," NACA TN 3601, 1955.
- Lukasiewicz, J., "Conical Flow as a Result of Shock and Boundary-Layer Interaction on a Probe." R&M.2669, September 1948.
- Lynés, L. L., Nielsen, J. N., and Goodwin, F. K., "Inhibition of Flow Separation at High Speed. Vol. I - Supersonic Turbulent Boundary Layers." Air Force Flight Dynamics Lab. Tech. Rep. AFFDL-TR-68-119, Vol. I, Sept. 1968.
- Lynes, L. L., Nielsen, J. N., and Kuhn, G. D., "Calculation of Compressible Turbulent Boundary Layers with Pressure Gradients and Heat Transfer." NEAR TR 6, Aug. 1968.
- Mafkofski, R. A., "A Two Parameter Method for Shock Wave-Laminar Boundary Layer Interaction and Flow Separation," *Proceedings 1963 Heat Transfer Fluid Mech. Inst.*, pp. 112-127.
- Mager, A., "Prediction of Shock Induced Turbulent Boundary Separation," *J.A.S.*, 22, 3 pp. 201-202, March 1955.
- Mager, A., "On the Model of the Free Shock-Separated Turbulent Boundary Layer," *J. Aeronaut. Sci.* 23, 181-184, 1956.
- Mager, A., "Transformation of the Compressible Turbulent Boundary Layer," *J. Aero. Sci.* 23, 305-311, 1958.
- Martellucci, A. and Libby, P. A., "Heat Transfer Due to the Interaction Between a Swept Planar Shock and a Laminar Boundary Layer," ASD-TR-61-727, Vol. I, Feb. 1962.
- Maskell, E. C., "Flow Separation in Three Dimensions, Report Aero. 2565, British RAE, 1955.
- Maurer, F., "Interaction Effects of Lateral Control Jets Expanding into a Supersonic Flow," Deutsche Versuchsanstalt für Luft- und Raumfahrt, Munich, Germany Report 65-04, 1965.

- Maydew, R. C., and Reed, J. F., "Turbulence Mixing in Axisymmetric Compressible Jets (in the $\frac{1}{2}$ Jet Region) with Quiescent Air", Sandia Corp. Research Report, SC 4764 (RR), March 1963.
- Mellor, G. L., and Gibson, D. M., "Equilibrium Turbulent Boundary Layers," Journal of Fluid Mechanics, Vol. 24, p. 225, 1966.
- Mendenhall, M. R., Goodwin, F. K., and Nielsen, J. N., "Preliminary Investigation of a Separated Laminar Boundary Layer in a Two-Dimensional Cavity." NEAR TR 13, October 1968.
- Miller, L. D., "Predicting Turbulent Compressible Boundary Layers in Strong Adverse Pressure" AIAA Paper No. 67-196, 1967.
- Miller, D. S., Hijman, R., and Childs, M. E., "Mach 8 to 22 Studies of Flow Separations Due to Deflected Control Surfaces." AIAA J. Vol. 2, Feb. 1964.
- Monaghan, R. J., "Comparison Between Experimental Measurements and a Suggested Formula for the Variation of Turbulent Skin Friction in Compressible Flow." A.R.C.C.P. No. 45, 1950.
- Monaghan, R. J. and Johnson, J. E., "The Measurement of Heat Transfer and Skin Friction at Supersonic Speeds. Part II. Boundary-Layer Measurements on a Flat Plate at $M = 2.5$ and Zero Heat Transfer." A.R.C.C.P. 64, 1949.
- Moore, F. K., "Boundary Layer Research", Ed. H. Gortler, Springer-Verlag, Berlin, 1958.
- Moore, F. K., "On the Separation of the Unsteady Laminar Boundary Layer, Boundary Layer Research," Ed. H. Gortler, Springer-Verlag, Berlin, p. 296, 1958.
- Moses, H. L., "The Behavior of Turbulent Boundary Layers in Adverse Pressure Gradients," Gas Turbine Lab. Rept. No. 73, M.I.T., 1964.
- Mueller, T. J., "An Experimental Investigation of the Re-attachment of Compressible Two-Dimensional Jets," Proc. of A.S.M.E. Symposium on Separated Flows, 1964.
- Mueller, T. J., Korst, H. H., and Chow, W. L., Jour. Basic Engr. Vol. 86, p. 221, 1964.

- Murphy, J. S., "The Separation of Axially Symmetric Turbulent Boundary Layers" Part I, Douglas Aircraft Co., Report No. E.S.17513, 1955.
- McDonald, H., "Turbulent Shear Layer Reattachment with Special Emphasis on the Base Pressure Problem," Aero. Quart., Vol. XV, 247-280, 1964.
- McDonald, H., "A Study of the Turbulent Separated-Flow Region Occurring at a Compression Corner in Supersonic Flow," J. Fluid Mech. V. 22, pp. 481-505, 1965.
- McLafferty, G. H., and Barber, R. E., "The Effect of Adverse Pressure Gradients on the Characteristics of Turbulent Boundary Layers in the Supersonic Streams" J. Aero. Sci., 29, 1-11, 1962.
- Nash, J. F., "An Analysis of Two Dimensional Turbulent Base Flow, Including the Effect of the Approaching Boundary Layer," R&M No. 3344, Aero. Res. Council, July 1962.
- Nash, J. F., "Discussion on 'Review of Recent Development in Turbulent Supersonic Base Flow'". AIAA J., March 1966, p. 574.
- Needham, D. A., "Progress Report on the Imperial College Hypersonic Gun Tunnel," Imperial College Dept. of Aeronautics Rep. 118, 1963.
- Needham, D. A. "Laminar Separation in Hypersonic Flow." Ph.D. Thesis, Univ. of London, August 1965.
- Needham, D. A. and Stallery, J. L., "Boundary Layer Separation in Hypersonic Flow," AIAA Paper 66-455, 1966.
- Newman, B. G., "Some Contributions to the Study of Turbulent Boundary-Layer Near Separation." Report ACA-53, Aero. Res. Consultative Comm., Australia, 1951.
- Newton, E. M. H., "An Experimental Investigation of Supersonic Flow in the Neighborhood of a Forward Facing Step," Master's Thesis in Mech. Eng., Univ. of Washington, Seattle, Wash., 1964.
- Nielsen, J. N., Lynes, L. L., Goodwin, F. K., and Holt, M. "Calculation of Laminar Separation with Free Interaction by the Method of Integral Relations." Presented to AIAA 2nd Aerospace Sci. Meeting, 25-27 Jan. 1965, New York City, AIAA Paper No. 65-50.

- Nielsen, J. N., Lynes, L. L., and Goodwin, F. K., "Calculation of Laminar Separation with Free Interaction by the Method of Integral Relations." Part I - Two-Dimensional Supersonic Adiabatic Flows. Air Force Flight Dynamics Lab. Rep. AFFDL-TR-65-107, Oct. 1965.
- Nielsen, J. N., Lynes, L. L., and Goodwin, F. K., "Calculation of Laminar Separation with Free Interaction by the Method of Integral Relations." Part II- Two-Dimensional Supersonic Nonadiabatic Flow and Axisymmetric Supersonic Adiabatic and Nonadiabatic Flows. Air Force Flight Dynamics Lab. Rep. AFFDL-TR-65-107, Jan. 1966.
- Nielsen, J. N., Lynes, L. L., and Goodwin, F. K., "Theory of Laminar Separated Flows on Flared Surfaces Including Supersonic Flow with Heating and Cooling." AGARD Conf. Proc., No. 4, Part 1, Proceedings of AGARD Fluid Dynamics Panel held in Rhode-Saint-Genese, Belgium, 10-13 May 1966.
- Nielsen, J. N., Lynes, L. L., and Goodwin, F. K., "Inhibition of Flow Separation at High Speed," Vol. III- Experimental Results for Laminar Boundary Layers. Air Force Flight Dynamics Lab. Tech. Rep. AFFDL-TR-68-119, Vol. III, Sept. 1968.
- Nishikawa, J. J., "An Investigation of Two-Dimensional Supersonic Jet Mixing," Master's Thesis in Mechanical Engineering, Univ. of Washington, Seattle, Wash, 1963.
- Oswatitsch, K. and Wieghardt, K., "Theoretical Analysis of Stationary Potential Flows and Boundary-Layers at High Speed." German Wartime Report, 1941. Translated as NACA TM.1189.
- Page, R. H., Kessler, T. J., and Hill, W. G., "Reattachment of Two-Dimensional Supersonic Turbulent Flows." ASME Paper No. 67-FE-20.
- Panov, Y. A., and Schnets, A. I., Prikladnaye Mekhanika, Vol. 2, No. 1, pp. 99-105, 1966.
- Pate, S. R., "Investigation of Flow Separation on a Two-Dimensional Flat Plate Having a Variable-Span Trailing Edge Flap at $M_\infty = 3$ and 5." AEDC-TDR-64-14, March 1964.
- Paynter, G. C., "On the Prediction of Separation and Reattachment Flow Characteristics for Two-Dimensional Supersonic Turbulent Boundary Layers," Ph.D. Thesis, Univ. of Wash., 1965.

- Pearcey, H. H., "Some Effects of Shock-Induced Separation of Turbulent Boundary-Layers in Transonic Flow Past Aerofoils." Proc. of the Symposium on Boundary-Layer Effects in Aerodynamics, N.P.L., March-April, 1955.
- Pearcey, H., "A Method for the Prediction of the Onset of Buffeting and Other Separation Effects from Wind-Tunnel Tests on Rigid Models," ARC 20,631, Dec. 1958.
- Pearcey, H. H., Sinnott, C. S., and Osborne, J., "Some Effects of Wind Tunnel Influence Observed in Tests on Two-Dimensional Aerofoils at High Subsonic and Transonic Speeds." NPL-373.
- Pickney, S. Z., "Semiempirical Method for Predicting Effects of Incident-Reflecting Shocks on the Turbulent Boundary Layer," NASA TN D-3029, October 1965.
- Pickney, S. Z., "Data on Effects of Incident-Reflecting Shocks on the Turbulent Boundary Layer," NASA TM X-1221, March 1966.
- Plate, E. J., and Lin, C. W., Colo. State Univ. Rept. CER65EJP14, 1965.
- Prandtl, L., "The Mechanics of Viscous Fluids, Aerodynamic Theory," Div. G., pp. 34-208, W. F. Durand, ed., Durand Reprinting Committee, Pasadena, Calif.
- Putnam, L. E., "Investigation of Effects of Ramp Span and Deflection Angle on Laminar Boundary Layer Separation at $M = 10.03$." NASA TN D-2833, 1965.
- Ramm, H. J., "Transonic Flow" - Lecture Notes von Karman Institute, Rhode-Saint-Genese, Belgium, Aug. 1968.
- Ray, A. K., "Estimation of the Critical Pressure Rise for Separation in Two-Dimensional Shock Boundary Layer Interaction Problems," Z. Flugwiss.
- Reeves, B. L., "The Compressible Boundary Layer in Separated Flow Past a Compression Corner," Space General Corp. Rept. May 3, 1963.
- Reeves, B. L., and Lees, L. "Theory of the Laminar Near Wake of Blunt Bodies in Hypersonic Flow," AIAA J. 3, 2061-2074, 1965.
- Reshotko, E. and Tucker, M., "Effect of a Discontinuity on Turbulent Boundary-Layer Thickness Parameters with Application to Shock-Induced Separation," NACA TN 3454, 1955.

- Ribner, H. S. and Arnoff, E. L., "Interaction between a Supersonic Stream and a Parallel Subsonic Stream Bounded by Fluid at Rest." NACA TN 2860, 1952.
- Ritter, A. and Kuo, Y. H., "Reflection of a Weak Shock Wave from a Boundary-Layer Along a Flat Plate. I. Interaction of Weak Shock Waves with Laminar and Turbulent Boundary-Layers Analyzed by Momentum-Integral Method." NACA TN 2868, 1953.
- Robertson, J. M., and Holl, J. W., "Effects of Adverse Pressure Gradients on Turbulent Boundary Layers in Axisymmetric Conduits, Jour. Appl. Mech., Vol. 24, Trans. ASME, Vol. 79, 1957.
- Robinson, A., "Wave Reflection Near a Wall," College of Aeronautics Report No. 37, A.R.C. 13,252 - F.M. 1459, May 1950.
- Roshko, A. and Thomke, G. J., "Flow Separation and Re-attachment Behind a Downstream Facing Step," Douglas Aircraft Co., Rept. SM-43056-1, Jan. 1964.
- Rott, N., and Crabtree, L. F., "Simplified Laminar Boundary Layer Calculations for Bodies of Revolution and for Yawed Wings." J. of Aeron. Sci., Vol. 19, No. 8, Aug 1952.
- Sandborn, V. A., "Preliminary Experimental Investigation of Low-Speed Turbulent Boundary Layers in Adverse Pressure Gradients." NACA TN 3031, 1953.
- Sandborn, V. A., "An Equation for the Mean Velocity Distribution of Boundary Layers," NASA Memo 2-5-59E, 1959.
- Sandborn, V. A., and Kline, S. J., "Flow Models in Boundary Layer Stall Inception, Jour. of Basic Eng., Trans. ASME, Series D, Vol. 83, p. 317, 1961.
- Sandborn, V. A. and Liu, C. Y., "On Turbulent Boundary Layer Separation, Jour. Fluid Mech., Vol. 23, p. 293, 1968.
- Sanders, F., and Crabtree, L. F., "A Preliminary Study of Large Regions of Separated Flow in a Compression Corner." British A.R.C. 23, 006, FM 3106.
- Sasman, P. K. and Cresci, R. J., "Compressible Turbulent Boundary Layer with Pressure Gradient and Heat Transfer." AIAA J. 1, 19-25, 1966.
- Sayano, S., "Heat Transfer in Shock Wave-Turbulent Boundary Layer Interaction Regions," Douglas Aircraft Co. Rept. SM-42567, November 19, 1962.

- Schlichting, H., "Boundary Layer Theory," McGraw-Hill Book Co., New York (4th Edition), 1960, p. 523.
- Schubauer, G. B., and Klebanoff, P. S., "Investigation of Separation of the Turbulent Boundary Layer," NACA Report 1030, 1951.
- Schubauer, G. B., and Klebanoff, P. S., "Contributions on the Mechanics of Boundary-Layer Transition." NACA Report 1289, 1956.
- Schubauer, G. B. and C. M. Tchen, "Turbulent Flow," Princeton Aero. Paperbacks, No. 9.
- Seddon, J., "Boundary-Layer Interaction Effects in Intakes with Particular Reference to those Designed for Dual Subsonic and Supersonic Performance." R.A.E. Tech. Report No. 66099 - A.R.C. 28368, March 1966.
- Seddon, J. and L. Haverty. "Experiments at Mach numbers from 0.5 to 1.8 on Side Intakes of Normal-Shoack Type without Boundary Layer Control (Part I)" R.A.E. Tech. Note Aero. 2329, A.R.C. 17398, October 1954.
- Sichel, M. and Yiu, Y. K., "Axisymmetric Similarity Solution for Viscous Transonic Flow" Journal of Fluid Mechanics, Vol. 28, Part 3, 1967.
- Silverstein, A., and Becker, J. V., "Determination of Boundary-Layer Transition on Three Symmetrical Airfoils in the NACA Full Scale Wind Tunnel." NACA Report 637, 1939.
- Simon, W. E., "A First Order Non-Affine Integral Solution for the Two-Dimensional Incompressible Laminar Boundary Layer," Ph.D. Dissertation, Univ. of Colo. June 1967.
- Sinnott, C. S., "On the Prediction of Mixed Subsonic-Supersonic Pressure Distributions Over Aerofoils." Part I. Introduction and Qualitative Analysis. British A.R.C. 20,459, October 1958.
- Spaid, F. W. and Zukoski, E. E., "A Study of the Interaction of Gaseous Jets from Transverse Slots with Supersonic External Flows," Douglas Aircraft Co., Paper 4480, April 1967.
- Speaker, W. V. and Ailman, C. M., "Spectra and Space-Time Correlations of the Fluctuating Pressures at a Wall Beneath a Supersonic Turbulent Boundary Layer Perturbed by Steps and Shock Waves," NASA CR-486, May 1966.

- Spence, D. A., "The Development of Turbulent Boundary Layers,"
Journal of the Aeronautical Sciences, Vol. 23, No. 1,
January 1956.
- Stalker, R. J., "The Pressure Rise at Shock-Induced Tur-
bulent Boundary-Layer Separation in Three-Dimensional
Supersonic Flow," J. Aero. Sci., Vol. 24, p. 547, 1957.
- Sterret, J. R., and J. C. Emery, "Extension of Boundary
Layer Separation Criteria to a Mach Number of 6.5 by
Utilizing Flat Plates with Forward Facing Steps,"
NASA TN D-618, December 1960.
- Sterrett, J. R. and Emery, J. C., "Experimental Separation
Studies for Two-Dimensional Wedges and Curved Surfaces
at Mach Numbers of 4.8 to 6.2." NASA TN D-1014,
February 1962.
- Sterrett, J. P., and Holloway, P. F., "On the Effects of
Transition on Parameters within a Separation Region at
Hypersonic Speeds; with Emphasis on Heat Transfer,"
Symposium on Fully Separated Flows, ASME, New York,
1964.
- Stewartson, K., "Correlated Incompressible and Compressible
Boundary Layers," Proc. Roy. Soc. (London). Ser. A,
Vol. 200, No. A1060, 84-100, 1949.
- Stewartson, K., "On the Interaction Between Shock Waves and
Boundary-Layers." Proc. Camb. Phil. Soc., 1951, 47, 545.
- Stewartson, K., "Further Solutions of the Falkner-Skan
Equation," Proc. Camb. Phil. Soc. 50, 454-465, 1954.
- Stollery, J. L., Maull, D. J. and Belcher, B. JI, "The
Imperial College Hypersonic Gun Tunnel, August 1958-
July 1959." J. Roy. Aero. Soc. 64, 24-32, 1960.
- Strahle, W. C., "Mass Transfer Perturbations about Stewartson's
Reversed Flow Profiles," AIAA J. 5:1, 181-183, 1967.
- Stratford, B. S., "Flow in the Laminar Boundary Layer Near
Separation," ARC R&M 3002, 1957.
- Stratford, B. S., "An Experimental Flow with Zero Skin
Friction Throughout Its Region of Pressure Rise." Jour.
Fluid Mech. Vol. 5, p. 17, 1958
- Stratford, B. S., "The Prediction of Separation of the
Turbulent Boundary Layer," J. Fluid Mech. 5, p. 1, 1959.

- Strike, W. T. and Rippey, J., "Influence of Suction on the Interaction of an Oblique Shock with a Turbulent Boundary Layer at Mach Number 3," AEDC-TN-61-129, October 1961.
- Strike, W. T., Jr., "A Study at Mach 10 of the Aerodynamic Disturbances Generated over a Flat Plate Containing Lateral Jet Nozzles," AEDC-TR-66-48, April 1966.
- Sutton, W. G. L., "An Approximate Solution of the Boundary Layer Equations for a Flat Plate," Phil. Mag. 23, 1146-1152, 1937.
- Tani, I., "On the Solution of the Laminar Boundary Layer Equations," Journal Physical Soc. of Japan, Vol. IV, p. 149, 1949.
- Tani, I., "On the Approximate Solution of the Laminar Boundary Equations," J. Aeronaut. Sci. 21, 487-504, 1954.
- Tani, I., Iuchi, M., Komoda, "Experimental Investigation of Flow Separation Associated with a Step or a Groove," Rep. Aero. Res. Inst., Univ. of Tokyo, 364, April 1961.
- Terrill, B. L., "Flow Near Separation with and without Suction," Trans. Roy. Soc. Series A, Vol. 253, p. 55, 1961.
- Thomann, H., "Measurements of Heat Transfer and Recovery Temperature in Regions of Separated Flow at a Mach Number of 1.8" Aeronautical Research Institute of Sweden, Report 82, 1959.
- Thomke, G. J., "Separation and Reattachment of Supersonic Turbulent Boundary Layer Behind Downstream Facing Steps and over Cavities," Douglas R SM 43062, March 1964.
- Thompson, B. G., "A Critical Review of Existing Methods of Calculating the Turbulent Boundary Layer," Aeronautical Research Council (Grit. Brit.) R&M 3447.
- Thwaites, B., "Approximate Calculations of the Laminar Boundary Layer, Aeronautical Quarterly, Vol. I, p. 245, 1949.
- Townsend, A. A., "The Structure of Turbulent Shear Flow," Cambridge Univ. Press, 1956, p. 281.
- Townsend, A. A., "Self Preserving Development within Turbulent Boundary Layers in Strong Adverse Pressure Gradients." J. of Fluid Mech., Part IV, p. 767, 1965.

- Townsend, J. C., "Effects of Leading Edge Bluntness and Ramp Deflection Angle on Laminar Boundary-Layer Separation in Hypersonic Flow," NASA TN D-3290, November 1965.
- Tsien, H. S. and Finston, M., "Interaction between Parallel Streams of Subsonic and Supersonic Velocities," J. Aero. Sci., 1949, 16, 515.
- Tucker, M., "Approximate Turbulent Boundary Layer Development in Plane Compressible Flow Along Thermally Insulated Surfaces with Application to Supersonic-Tunnel Contour Correction," NACA TN 2045, March 1950.
- Tyler, R. D. and Shapiro, A. H., "Pressure Rise Required for Separation in Interaction between Turbulent Boundary Layer and Shock Wave." J. Aero. Sci., Vol. 20, No. 12, December 1953.
- Tyson, T. J., "Laminar Boundary Layers in the Neighborhood of Abrupt Spatial Disturbances," Calif. Inst. of Technology, Pasadena, Calif. Ph.D. Thesis, 1967.
- Van Driest, E. R., "Investigation of Laminar Boundary Layer in Compressible Fluids Using the Crocco Method," NACA TN 2597, January 1962.
- Van Le, N., "Transformation Between Compressible and Incompressible Boundary Layer Equations," Journal of Aeronautical Sciences, August 1953, p. 583.
- Vas, I., and S. M. Bogdonoff, "Interaction of a Shock Wave with a Turbulent Boundary Layer at $M = 3.85$," D.A.E. Rep. 294, Princeton Univ., April 1955.
- Vasiliu, J., "Pressure Distribution in Regions of Step Induced Turbulent Separation," J.A.S., 29, 5, May 1962, p. 596.
- von Doenhoff, A. E. and Tetervin, N., "Determination of General Relations for the Behavior of Turbulent Boundary Layers," NACA Report 772, 1943.
- Walz, A., "Anwendung des Energiesatzes von Wieghardt auf einparametrische Geschwindigkeitsprofile in laminaren Grenzschichten," Ing.-Arch. 16, 243-248, 1948.
- White, R. A., "Turbulent Boundary Layer Separation from Smooth Convex Surfaces in Supersonic Two-Dimensional Flow," Ph.D., Thesis, Univ. of Illinois, 1963.

White, R. A., "Effects of Sudden Expansions or Compressions on the Turbulent Boundary Layer," AIAA J. December 1966, p. 2232.

Wilson, R. E., "An Experimental Investigation of Separated Turbulent Supersonic Flow at $M = 3.0$ " M.S. Thesis, Univ. of Tenn. Space Institute, Tullahoma, Tenn. 1966.

Wooten, G. G., S. Hight, and I. Vas. "Interaction of a Turbulent Boundary Layer with a Step at $M = 2.3$," D.A.E., Rep. 297, Princeton University.

Wu, J. M., Hahn, T. S., and Wilson, R. E., "Turbulent Boundary Layer Separation Induced by Forward-Facing High Steps," Unpublished paper, 1969.

Young, A. D., "Skin Friction in the Laminar Boundary Layer in Compressible Flow," Aeronautical Quarterly, 1949, I, 137.

Zukoski, E. E., "Review of Data Concerning Turbulent Boundary Layer Separation in Front of a Forward Facing Step," Guggenheim Jet Propulsion Center, California Institute of Technology, Pasadena, Calif., Rept. 66-8-15-1, August 1966.

Zukoski, E. E., "Turbulent Boundary-Layer Separation in Front of a Forward-Facing Step," AIAA Journal, October 1967, p. 1746.

APPENDIX I

Computer Program

a) Input Data

"WALLGEO"

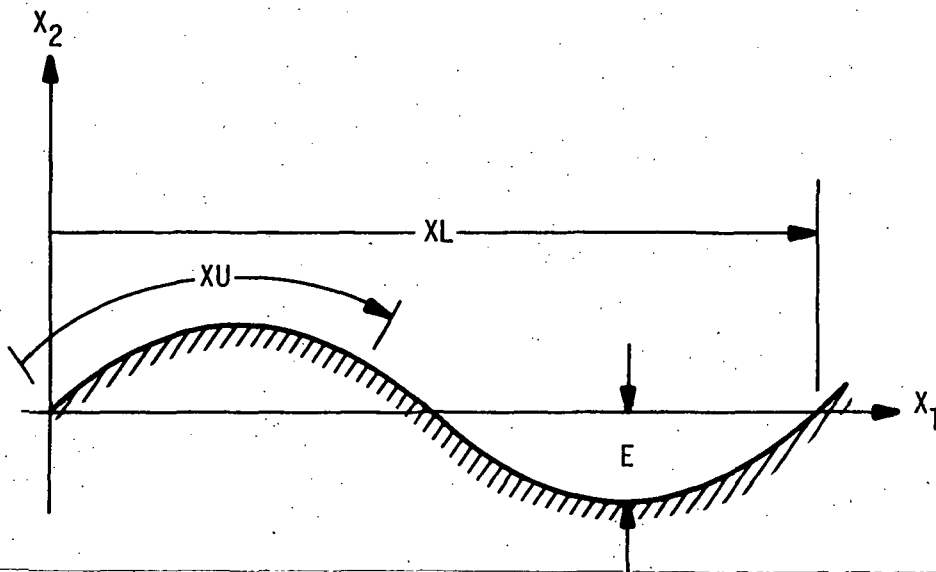
The listing which follows is a program which uses the incomplete elliptic integral scientific subroutine and a least squares curve fit to obtain a tenth order polynomial expression for the value of x_1 as a function of x_u . For a sinusoidal wall described by the equation

$$x_2 = E * \sin (\alpha * x_1),$$

where

$$\alpha = \frac{2\pi}{XL}$$

the required input is E (amplitude) and XL (wavelength). This information is input on cards 3 and 4 of the main program (units are feet). The output consists of a list of the 11 coefficients of a tenth order polynomial listed in ascending order. Following this list is a check of the value of x_1 , x_1 generated by the polynomial and x_u .



Input data for the computer program is contained on nine data cards. The first card is a test description card which may contain any title for the

output which the programmer desires. Variables associated with the wave geometry are input on the second card which contains (in order):

- EPSILO - wave amplitude
- WLENG - wavelength
- WSTART - distance from leading edge to the beginning of the wavy wall.
- WEND - distance from the leading edge to the end of the waves.
- COMPIN2 - twice the value of the complete elliptic integral for the geometry under consideration.

On the third and fourth data cards, the coefficients from the tenth order polynomial for x_1 are input. The fifth card contains output data parameters. In the first five column field is the value of IFLUX, which indicates the number of steps along the wall for each printing of the fluxes in the output data. IPROF appears in the next five column field and indicates the number of printings of the fluxes desired for each printing of the profiles. With IFLUX = IPROF = 1, fluxes and profiles are printed every step. With IFLUX = 3 and IPROF = 1, the fluxes are printed every third step and the profiles are printed at every third step.

The sixth card contains the problem boundary conditions in the following order:

- TINF - temperature of free stream
- TW - temperature of the wall
- PINF - pressure in the free stream
- MACH - free-stream Mach number
- XU - distance from the leading edge at which you desire to start the solution.
- XL - total length of the plate you wish to integrate over.
- KASE - wall index
- ALFAD - cone half-angle (zero for plate).

Input on the seventh card consists of the constants for fluid specifications:

- CP - specific heat
- EDK - E/K
- SIG - sigma
- ECON - gas constant
- AMW - atomic weight.

On the eighth card we find

KRAD - 0 for two-dimensional, 1 for axisymmetric

NEQ - number of equations to be solved (2-momentum and energy)

N - number of stations normal to the wall

KR - dummy = 1 (neglects radiation).

The ninth card has the value of YKK - a normal spacing parameter (not equal to one).

SPALDING-PATANKAR COMPUTER PROGRAM

PILEP OPTIONS - NAME= MAIN,OPT=02,LINCNT=59,SIZE=0000K,
SOURCE,ERCDIC,NOLIST,NODECK,LOAD,MAP,NOFDT,NOID,NOXREF

REAL MACH
COMMON/GEN/PEI,AMI,AME,D PDX,PREF(251),PR(1),DEN,AMU,XU,XD,XL,DX, 00000002

1 CSALFA,PRT,INTG 00000003

COMMON/CWRIT/IFLUX,I PROF,IWRIT 00000004

COMMON/CFLUX/DRAGC,STNO,TAUIW,OW 00000005

COMMON/COC/SC(551),AU(551),BU(551),CU(551),A(1,551),B(1,551), 00000006

1 C(1,551) 00000007

COMMON/COT/N,NP1,NEQ,NPH,KRAD,NH,KASE 00000008

COMMON/COL/AK,ALMG 00000009

COMMON/COPR/UGU,UGO 00000010

COMMON/CPROP/HE(1),CP,TR,HW,TK 00000011

COMMON/DATA/VINE,DELTA,TW,TINF,OS,MACH,KR 00000012

COMMON/V/U(251),F(1,251),R(251),RHO(251),OM(251),Y(251),TEMP(251) 00000013

COMMON/CTOT/QWT,FDR 00000014

COMMON/CNDM/ YND(50),JND(50),HND(50),YT(251) 00000015

COMMON/NDATA/PHOINF 00000016

COMMON/CWGED/EPSILO,ALPHA,XONE,WLENG, WSTART,WEND,COMPIN2,COE(11) 00000017

COMMON/RAD/AMUINF 00000018

REAL*8 TIME 00000018

FNTH(TC)=25051.6*(-1.45201+(248.25212+(-21.57262+(00000019

1 19.56195-3.80043*TC)*TC)*TC)*TC) 00000020

DIMENSION TODAY(8) 00000021

CALL DATE(TODAY) 00000022

WRITE(6,99999)(TODAY(I),I=1,8) 00000023

000000 FORMAT(1X,PA4) 00000024

CALL SPEXIT 00000025

2000 FORMAT(2E20.6) 00000026

10 CONTINUE 00000027

X = 0.0 00000028

FDR = 0.0 00000029

QWT = 0.0 00000030

16 CONTINUE 00000031

INTG=0 00000032

CALL CONST 00000033

CALL BEGIN 00000034

AMI=0. 00000035

AME=0. 00000036

GO TO 25 00000037

15 CALL READY 00000038

25 CONTINUE 00000039

IWRIT = IWRIT + 1 00000040

INTG=INTG+1 00000041

C *****START LENGTH***** 00000042

C *****YL = Y(NP1) NOW IN VEFF ***** 00000043

CALL ENTRN 00000044

C CHOICE OF FORWARD STEP 00000045

FRA = 0.05 00000046

DX=Y(NP1)*0.5 00000047

DX=0.25*Y(NP1) 00000048

DX=0.002 00000049

XD=XU+DX 00000050

IF(XD.LT.XL)GO TO 77 00000051

DX=XL-XU 00000052

IF(XU.EQ.XL) IWRIT = IFLUX 00000053

IF(DX.EQ.0.0)DX=Y(NP1) 00000054

XD=XU+DX 00000054

```

77 CONTINUE
C SPECIFIES FORM OF FREE STREAM VELOCITY
C EPSILO=0.4/12. FT,
C L=1.0 FT.
UGU=UGD
UGD = VINF
IF(XD.LT.WSTART) GO TO 8
E=EPSILO
ALPHA=(2.0*3.1415929)/WLENG
AMINF=VINF/(SQRT(1.4*53.3*32.2*TINF))
APP=(AMINF**2-1.0)**0.5
NIC=(XD-WSTART)/COMPIN2
XPART=NIC*WLENG/2.0
XY=(XD-WSTART)-NIC*COMPIN2
XONE=XPART+COE(1)+COE(2)*XY+COE(3)*XY*XY+COE(4)*XY**3
1+COE(5)*XY**4+COE(6)*XY**5+COE(7)*XY**6+COE(8)*XY**7
2+COE(9)*XY**8+COE(10)*XY**9+COE(11)*XY**10
XTWO=E*SIN(ALPHA*XONE)
AARG=ALPHA*(XONE-XTWO*APP)
UFRE=VINF-(VINF*E*ALPHA*COS(AARG))/APP
VFRE=VINF*E*ALPHA*COS(AARG)
UGD=SQRT(UFRE**2+VFRE**2)
9 CONTINUE
C *****SUBROUTINE DPF *****
DPDX=0.0
IF(XD.LT.WSTART) GO TO 9
DPDX0=-RHOINF*VINF*VINF*ALPHA**2.0*E*SIN(ALPHA*(XONE-E*SIN(ALPHA
1*XONE)*APP))*(1.0-E*ALPHA*COS(ALPHA*XONE)*APP)/APP
DXODX=1.0/SQRT(1.0+E*ALPHA*COS(ALPHA*XONE))
DPDX=DPDX0*DXODX
9 CONTINUE
C *****SUBROUTINE MASS, SPECIFY AMI IF NON ZERO *****
CALL WALL
26 IF(IWRIT.EQ.1FLUX) CALL OUTPUT
CALL COEFF
U(NP1) = UGD
CALL SOLVE(AU,BU,CU,U)
IF(NEQ.EQ.1) GO TO 30
DO 45 J=1,NPH
DO 46 I=2,NP1
AU(I)=A(J,I)
BU(I)=B(J,I)
46 CU(I)=C(J,I)
DO 47 I=1,NP1
47 SC(I)=F(J,I)
HI = 0.01*(F(NH,NP1)-0.5*U(NP1)*U(NP1))/25051.6
HI=0.1*HI
TEMP(NP1)=-20.84374+4513.25491*HI-1294.53738*HI*HI+627.65683
1*HI*HI*HI+119.73469*HI*HI*HI
CALL SOLVE(AU,BU,CU,SC)
DO 48 I=1,N
48 F(J,I)=SC(I)
45 CONTINUE
C THIS PROGRAM DOES NOT ACCEPT FLUXES AT WALL--ADD HERE
C CALCULATION OF AUXILLARY PARAMETERS
DO 100 I=2,N
HI=0.01*(F(NH,I)-0.5*U(I)*U(I))/25051.6

```

	HI = 1*HI	00000096
	TEMP(I) = -20.84374 + 4513.25491*HI - 1294.53738*HI*HI + 627.65683*HI*HI*HI	00000097
	11 + 119.73469*HI*HI*HI*HI	00000098
100	CONTINUE	00000099
	CALL DENSTY	00000100
20	CONTINUE	00000101
	XL = XD	00000102
	PEI = PEI + DX*(P(1)*AMI - R(NP1)*AME)	00000103
C	THE TERMINATION CONDITION	00000104
	IF(XII, LE, XL) GO TO 15	00000105
	GOTO 10	00000106
85	STOP	00000107
	END	00000108

PILER OPTIONS - NAME= MAIN,OPT=02,LINFCNT=59,SIZE=0000K,
SOURCE,ERCOIC,NOLIST,NODECK,LOAD,MAP,NOEDIT,NOID,NOXREF

C	SUBROUTINE DENSITY	00000109
C		00000110
	SLRROUTINE DENSITY	00000111
	COMMON/COI/N,NP1,NEQ,NPH,KRAD,NH,KASE	00000112
	COMMON/CPROP/HF(3),CP,TR,HW,TK	00000113
	COMMON/GEN/PFI,AMI,AME,DPDX,PREF(251),PR(1),DEN,AMU,XU,XD,XL,DX,	00000114
1	CSALEA,PRT,INTG	00000115
	COMMON/V/U(251),F(1,251),R(251),RHO(251),DM(251),V(251),TEMP(251)	00000116
	DO 45 I=1,NP1	00000117
	RHO(I) = DEN*(TR/TEMP(I))	00000118
45	CONTINUE	00000119
	RETURN	00000120
	END	00000121

```

ILRR OPTIONS - NAME= MAIN,OPT=02,LINECNT=59,SIZE=0000K,
SOURCE,EBDCIC,NOLIST,NODECK,LOAD,MAP,NOEDIT,NOID,NOXREF
C      SUBROUTINE OUTPUT                                00000122
C      SUBROUTINE OUTPUT                                00000123
      SUBROUTINE OUTPUT                                00000124
      REAL MACH                                        00000125
      COMMON/CWRIT/IFLUX,I PROF,IWRIT                 00000126
COMMON/CTOT/QWT,FDP                                  00000127
COMMON/CFLUX/DPAGC,STNO,TAUIW,QW                    00000128
COMMON/CROW/QW2                                       00000129
      COMMON/CGEO/ALFA                                 00000130
COMMON/COC/SC(551),AU(551),BU(551),CU(551),A(1,551),B(1,551),
1 C(1,551)                                             00000131
COMMON/COI/N,NP1,NEQ,NPH,KRAD,NH,KASE                00000132
COMMON/CPPDP/HF(1),CP,TR,HW,TK                       00000133
      COMMON/CSHE/SHE(551)                             00000135
COMMON/DATA/VINF,DELTA,TW,TINF,OS,MACH,KR            00000136
COMMON/GEN/PEI,AMI,AME,DPDX,PRFF(251),PR(1),DEN,AMU,XU,XD,XL,DX,
1 CSALFA,PRT,INTG                                     00000137
      COMMON/INPCON/PINF,EDK,SIG,GCON,AMW             00000139
COMMON/V/U(251),F(1,251),R(251),RHO(251),OM(251),Y(251),TEMP(251) 00000140
      COMMON/CSEMU/SEMU(551)                           00000141
COMMON/CNW/ONEW                                       00000142
COMMON/NDATA/RHOINF                                  00000143
COMMON/RAD/AMUINF                                    00000144
IF(INTG.NE.1) GO TO 15                                00000143
      IPRF = IPRF - 1                                   00000144
WRITE(6,50)KRAD,KASE,NEQ,N,KR,I PROF,IFLUX           00000145
ALFAD = ALFA*180.0/3.14159                            00000146
WRITE(6,150)TINF,TW,PINF,MACH,XU,XL,ALFAD            00000147
WRITE(6,250)EDK,SIG,GCON,AMW                          00000148
CPO = CP/25051.6                                       00000149
WRITE(6,350)CPO,DEN,AMU,TK                            00000150
50  FORMAT(3X,'INDICES- KRAD=',I4,5X,'KASE=',I4,5X,'NEQ=',I4,5X,'N=',
1 I5,5X,'KR=',I4,5X,'I PROF =',I4,5X,'IFLUX =',I4/) 00000152
150  FORMAT(3X,'BOUNDARY CONDITIONS- TINF=',F8.2,' R',4X,'TW=',F6.1,' R
1 ',4X,'PINF=',F8.1,' PSF',4X,'MACH NUMBER=',F6.2/24X,'XU=',F5.2,
2 ' FT',4X,'XL=',F5.1,' ET',4X,'ALFA=',F5.1,' DEGREE CONE HALF-ANGLE
3 '/) 00000155
250  FORMAT(3X,'GAS CONSTANTS- E/K=',F6.2,' K',4X,'SIGMA=',F7.3,
1 ' ANGSTROM',4X,'GCON=',F7.2,' FT-LBM/LBF-R',4X,'AMW=',F7.2/) 00000158
350  FORMAT(3X,'GAS PROPERTIES- CP=',F7.3,' BTU/LBM-R',4X,'DEN=',F7.4,
1 ' LBM/CIU-FT',4X,'AMU=',F12.4,' LBM/FT-SEC',4X,'TK=',F7.4,
3 ' BTU/HR-FT-F') 00000161
WRITE(6,40) (OM(I),I=1,NP1)                             00000162
40  FORMAT(24H)THE VALUES OF OMEGA ARE/(1X,11(1X,E10.5)) 00000163
15  CONTINUE                                           00000164
      IPRF = IPRF + 1                                   00000165
C      IPRIF IS PROFILE WRITE INDEX, IWRIT IS HEADING INDEX 00000166
      IWRIT = 0                                         00000167
DRAGC=64.4*TAUIW/(RHO(NP1)*U(NP1)**2)                 00000168
C      THIS STANTON NUMBER IS BASED ON ADIABATIC WALL ENTHALPY + R= 915 00000169
      RECF = .915                                       00000170
      DELH = F(NH,NP1)+(RECF-1.0)*(U(NP1)**2)/2.0-F(NH,1) 00000171
      STNO = QW*778.0*32.2/(RHO(NP1)*U(NP1)*DELH)      00000172
PEX=(RHOINF*VINF*XU)/(AMUINF)

```

```

WRITE(6,51) XU,REX,PEI,INTG
51  FORMAT(//,5X,'XU =',2PE11.2,4H FT,4X,'REX =',E11.2,4X,
1  'PEI =',E12.4,4X,'INTG =',I4)
WRITE(6,55) DRAGC,STNO,TAUIW,QW
WRITE(6,80) QW2
80  FORMAT(10X,'QW2 =',E12.2,'RTU/FT2 SEC')
1909  FORMAT(1X,'QNEW=',E20.6)
WRITE(6,1909) QNEW
55  FORMAT(10H DRAGC =2PE13.4,10H STNO =2PE13.4,11H TAUIW =
1  2PE13.4,9H LRF/SO-FT,9H QW =2PE13.4,15H RTU/(SO-FT SEC))
WRITE(6,9876) QWT,FDR,DX,AME
9876  FORMAT(3X,4HQWT=,E16.6,10X,4HFDR=,E16.6,10X,'DX =',E14.5,10X,
1  'AME =',E12.4,///)
IF(IPRF.LT.IPROF) RETURN
IPRF = 0
WRITE(6,52)
52  FORMAT(8X,'Y',11X,'U',11X,'HS',10X,'T',11X,'PR',10X,'M',
1  10X,3HRHO,8X,5HSHEAR,8X,3HEMU,9X,'HCP',/)
WRITE(6,60)
60  FORMAT(6X,4H(FT),7X,8H(FT/SEC),3X,10H(FT2/SEC2),4X,7H(DEG-R),3X,
1  24X,'(LRM/FT2)',3X,'(LRF/FT2)',/)
63  FORMAT(1X,1PE12.3)
NP1M = NP1 - 20
DO 10 J1=1,NP1
J2=NP1-J1+1
HCP=F(NH,J2)-0.5*U(J2)**2
HCP=HCP/25051.6
AMACH = U(J2)/SQRT(2402.764*TEMP(J2))
WRITE(6,53)Y(J2),U(J2),F(1,J2),TEMP(J2),
1  IPRF(J2),AMACH,RHO(J2),SHE(J2),SEMU(J2),HCP
10  CONTINUE
GO TO 1
DO 11 J1=NP1M,NP1
J2=NP1-J1+1
HCP=F(NH,J2)-0.5*U(J2)**2
HCP = HCP/25051.6
AMACH = U(J2)/SQRT(2402.764*TEMP(J2))
WRITE(6,53)Y(J2),U(J2),F(1,J2),TEMP(J2),
1  IPRF(J2),AMACH,RHO(J2),SHE(J2),SEMU(J2),HCP
11  CONTINUE
IF (KP.EQ.1) WRITE(6,62)
62  FORMAT(6X,26HRADIATION EFFECTS INCLUDED)
IF (KP.NE.1) WRITE(6,63)
63  FORMAT(6X,12HNO RADIATION,/)
C *****NON-DIMENSIONAL PROFILES CALCULATED HERE*****
1  RETURN
END

```

```

00000174
00000175
00000176
00000177
00000178
00000179
00000180
00000181
00000182
00000183
00000184
00000185
00000186
00000187
00000188
00000189
00000190
00000191
00000192
00000193
00000194
00000195
00000196
00000197
00000198
00000199
00000200
00000201
00000202
00000203
00000204
00000205
00000206
00000207
00000208
00000209
00000210
00000211
00000212
00000213
00000214
00000215
00000216
00000217
00000218
00000219
00000220

```

```

FILE OPTIONS - NAME= MAIN,OPT=02,LINECNT=59,SIZE=0000K,
SOURCE,EBCDIC,NOLIST,NODECK,LOAD,MAP,NOEDIT,NOID,NOXREF
C SUBROUTINE SOURCE 00000221
C 00000222
SUBROUTINE SOURCE(J,I,CS,DS) 00000223
C FOR CONSERVATION OF STAGNATION ENTHALPY 00000224
C CAUTION- USE CONSISTENT UNITS 00000225
REAL MACH 00000226
COMMON/COC/SC(551),AU(551),BU(551),CU(551),A(1,551),B(1,551),
1 C(1,551) 00000227
COMMON/GEN/PEI,AMI,AME,DPDX,PREF(251),PR(1),DEN,AMU,XU,XD,XL,DX, 00000229
1 CSALFA,PPT,INTG 00000230
COMMON/V/U(251),F(1,251),P(251),RHO(251),OM(251),Y(251),TEMP(251) 00000231
C*** **IF(J,NE,1) GO TO 2 ADD HERE FOR OTHER THAN ENERGY***** 00000232
CS=SC(I)*(U(I+1)*U(I+1)-U(I)*U(I))/(OM(I+1)-OM(I)) 00000233
CS=CS-SC(I-1)*(U(I)*U(I)-U(I-1)*U(I-1))/(OM(I)-OM(I-1)) 00000234
CS=(1.-1./PREF(I))*CS/(OM(I+1)-OM(I-1)) 00000235
DS=0.0 00000236
C *****ADD OTHER SOURCE TERMS HERE***** 00000237
RETURN 00000238
END 00000239

```

```

C ILER OPTIONS - NAME= MAIN,OPT=02,LINCCNT=59,SIZE=0000K,
SOURCE,FBCDIC,NOLIST,NODECK,LOAD,MAP,NOEDIT,NOID,NOXREF
C SUBROUTINE BEGIN 00000240
C 00000241
SUBROUTINE BEGIN 00000242
REAL MACH 00000243
COMMON/COT/N,NP1,NEQ,NPH,KRAD,NH,KASE 00000244
COMMON/CPROP/HF(1),CP,TR,HW,TK 00000245
COMMON/CSHF/SHE(551) 00000246
COMMON/DATA/VINF,DELTA,TW,TINF,OS,MACH,KR 00000247
COMMON/GEN/PET,AMT,AME,DPDX,PREF(251),PR(1),DEN,AMU,XU,XD,XL,DX, 00000248
1 CSALFA,PRT,INTG 00000249
COMMON/V/U(251),F(1,251),R(251),PHO(251),OM(251),Y(251),TEMP(251) 00000250
COMMON/CFEMJ/SEMU(551) 00000251
COMMON/CFAC/YM 00000252
ENTH(TC)= 1*(85.34116+2112.45358*TC+233.25733*TC*TC-26.63394*TC*TC 00000253
1*TC+1.24827*TC*TC*TC*TC)*25051.6 00000254
NPH=NEQ-1 00000255
C PROBLEM SPECIFICATION 00000256
NP1=N+1 00000257
C Y SVER SIZE ACCORDING TO DY(I)=YKK*DY(I-1) (YKK NOT EQUAL TO 1) 00000258
YM = 0.0 00000259
READ(5,50) YKK 00000260
50 FORMAT(F10.0) 00000261
WRITE(6,100) YKK 00000262
100 FORMAT(1X/3X,'YKK =',F6.4/) 00000263
DY1=(1.-YKK)/(1.-YKK**((FLOAT(NP1)-1.)))*DELTA 00000264
Y(1)=0.0 00000265
DO 5 I=2,NP1 00000266
5 Y(I)=DY1*(1.-YKK**((FLOAT(I-1))))/(1.-YKK) 00000267
IF(NEQ.EQ.1) GO TO 45 00000268
C INITIAL VELOCITY PROFILE 00000269
TEMP(1) = TW 00000270
TEMP(NP1)=TINF 00000271
U(1) = 0.0 00000272
HW=ENTH(0.001*TW) 00000273
HE=ENTH(0.001*TINF) 00000274
F(NH,1)=HW 00000275
F(NH,NP1)=HE+0.5*VINF*VINF 00000276
DF=F(NH,NP1)-F(NH,1) 00000277
U(1) = 0.0 00000278
U(NP1)=VINF 00000279
C INITIAL PROFILES OF OTHER DEPENDENT VARIABLES 00000280
DO 201 I=1,NP1 00000281
TFM=(Y(I)/V(NP1))**0.14285714 00000282
U(I)=VINF*TFM 00000283
F(NH,I)=TFM*DF+F(NH,1) 00000284
201 CONTINUE 00000285
45 CONTINUE 00000286
C INITIAL VALUES OF AUXILIARY PARAMETERS 00000287
DO 300 I=2,N 00000288
HI=0.01*(F(NH,I)-0.5*U(I)*U(I))/25051.6 00000289
HI=,1*HI 00000290
TEMP(I)=-20.84374+4513.25491*HI-1294.53738*HI*HI+627.65683*HI*HI*HI 00000291
1 I+119.73469*HI*HI*HI 00000292
300 CONTINUE 00000293

```


	CALL DENSTY	00000294
C	INITIAL DISTRIBUTION OF EFFECTIVE VISCOSITY	00000295
	GAM=.05	00000296
	DEL = Y(NP1)	00000297
	TAUW = VISCO(1) * U(2)/Y(2)	00000298
	SEMU(1) = VISCO(1)	00000299
	DO 500 I = 2, NP1	00000300
	ETA = Y(I)/Y(NP1)	00000301
	DELP = (Y(NP1)/VISCO(I)) * SQRT(RHO(I) * TAUW)	00000302
	DU = (U(I)-U(I-1))/(Y(I)-Y(I-1))	00000303
500	SEMU(I) = VISCO(I) + PHO(I) * (DEL * (0.4 * ETA - 0.5 * ETA	00000304
	1 **2 + 0.2 * ETA **3) * (1.0 - EXP(-GAM * DELP * ETA	00000305
	2 **2 * ABS(DU	00000306
	DO 505 I=1, N	00000307
505	SHE(I)=SEMU(I)*ABS((U(I+1)-U(I))/(Y(I+1)-Y(I)))	00000308
	SHE(NP1)=SHE(N)	00000309
C	CALCULATION OF RADII	00000310
	CALL PAD(XU,R(1),CSALFA)	00000311
	IF(CSALFA.EQ.0.0.OR.KRAD.EQ.0) YM=0.0	00000312
	DO 28 I=2, NP1	00000313
	28 R(I)=R(1)+YM*CSALFA*Y(I)	00000314
	CALL PREFE	00000315
C	CALCULATION OF OMEGA VALUES	00000316
	OM(1)=0.0	00000317
	DO 49 I=2, NP1	00000318
	BB=(U(I)-U(I-1))/(Y(I)-Y(I-1))	00000319
	AA=U(I-1)-BB*Y(I-1)	00000320
	RHOA=(RHO(I)+RHO(I-1))*0.5	00000321
	DI=PHOA*(R(1)*AA*(Y(I)-Y(I-1))+(YM*CSALFA*AA+R(1)*BB)*	00000322
	1 (Y(I)*Y(I)-Y(I-1)*Y(I-1))*0.5+	00000323
	2 YM*CSALFA*BB*(Y(I)*Y(I)*Y(I)-Y(I-1)*Y(I-1)*Y(I-1))/3.0)	00000324
49	OM(I)=OM(I-1)+DI	00000325
	PEI=OM(NP1)	00000326
	DO 59 I=2, NP1	00000327
59	OM(I)=OM(I)/PEI	00000328
C	SEE MAIN IF INDI IS CHANGED	00000329
	RETURN	00000330
	END	00000331

PILER OPTIONS - NAME= MAIN,OPT=02,LINECNT=59,SIZE=0003K,
SOURCE,FBCDIC,NOLIST,NODECK,LOAD,MAP,NOEDIT,NOID,NOXREF

C	SUBROUTINE COEFF	0000033
C	SURROUTINE COEFF	0000033
	COMMON/COC/SC(551),AU(551),RU(551),CU(551),A(1,551),R(1,551),	0000033
	1 C(1,551)	0000033
	COMMON/COI/N,NP1,NEQ,NPH,KRAD,NH,KASE	0000033
	COMMON/COI/AK,ALMG	0000033
	COMMON/GEN/PEI,AMI,AMF,DPDX,PREF(251),PR(1),DEN,AMU,XU,XD,XI,DX,	0000033
	1 CSAIFA,PRT,INTG	0000034
	COMMON/V/U(251),F(1,251),R(251),RHO(251),QM(251),Y(251),TEMP(251)	0000034
	COMMON/CSFMU/SEMU(551)	0000034
	DIMENSION G1(251),G2(251),G3(251),D(1,251),S1(251),S2(251),S3(251)	0000034
C	CALCULATION OF SMALL C S	0000034
	DO 98 I=1,N	0000034
	RA=.5*(R(I+1)+R(I))	0000034
	RH=.5*(RHO(I+1)+RHO(I))	0000034
	UM=.5*(U(I+1)+U(I))	0000034
	CALL VEFF(I,I+1,EMU)	0000034
	SEMU(I)=EMU	0000035
	98 SC(I)=RA*RA*RH*UM*FMU/(PEI*PEI)	0000035
C	THE CONVECTION TERM	0000035
	SEMU(NP1)=SEMU(N)	0000035
	CALL PREF	0000035
	SA=R(1)*AMI/PEI	0000035
	SR=(R(NP1)*AMF-R(1)*AMI)/PEI	0000035
	DX=XD-XI	0000035
	P2=-SR*.25	0000035
	S3(2)=0.0	0000035
	DO 71 I=2,N	0000036
	QMD=QM(I+1)-QM(I-1)	0000036
	P2=.25/DX	0000036
	P3=P2/QMD	0000036
	P1=(QM(I+1)-QM(I))*P3	0000036
	P3=(QM(I)-QM(I-1))*P3	0000036
	P2=3.*P2	0000036
	Q=SA/QMD	0000036
	P2=R2/QMD	0000036
	R1=-(QM(I+1)+3.*QM(I))*R3	0000036
	R3=(QM(I-1)+3.*QM(I))*R3	0000037
	G1(I)=P1+Q+R1	0000037
	G2(I)=P2+P2	0000037
	G3(I)=P3-Q+R3	0000037
	CU(I)=-P1*U(I+1)-P2*U(I)-P3*U(I-1)	0000037
C	THE DIFFUSION TERM	0000037
	AU(I)=2./QMD	0000037
	RU(I)=SC(I-1)*AU(I)/(QM(I)-QM(I-1))	0000037
	AU(I)=SC(I)*AU(I)/(QM(I+1)-QM(I))	0000037
	IF(NEQ,EQ,1) GO TO 33	0000037
	DO 34 J=1,NPH	0000038
	C(J,I)=-P1*F(J,I+1)-P2*F(J,I)-P3*F(J,I-1)	0000038
	CALL SOURCE(J,I,CS,D(J,I))	0000038
	C(J,I)=-C(J,I)+CS-F(J,I)*D(J,I)	0000038
	A(J,I)=AU(I)/PREF(I)	0000038
	B(J,I)=RU(I)/PREF(I)	0000038

	34 CONTINUE	00000386
C	SOURCE TERM FOR VELOCITY EQUATION	00000387
33	S1(I)=DPDX*DX	00000388
	S2(I)=P2*S1(I)/(RHO(I)*U(I))	00000389
	IF(I.EQ.2) GO TO 999	00000390
	S3(I)=P3*S1(I)/(RHO(I-1)*U(I-1))	00000391
999	CONTINUE	00000392
	S1(I)=P1*S1(I)/(RHO(I+1)*U(I+1))	00000393
	CU(I)=-CU(I)-2.*(S1(I)+S2(I)+S3(I))	00000394
	S1(I)=S1(I)/U(I+1)	00000395
	S2(I)=S2(I)/U(I)	00000396
	IF(I.EQ.2) GO TO 200	00000397
	S3(I)=S3(I)/U(I-1)	00000398
	GO TO 71	00000399
200	S3(I)=0.0	00000400
	S1(I)=0.0	00000401
	S2(I)=1.0/(RHO(2)*U(2)*U(2))*DPDX	00000402
71	CONTINUE	00000403
C	COEFFICIENTS IN THE FINAL FORM	00000404
	DO 91 I=2,N	00000405
	RL=1./(G2(I)+AU(I)+BU(I)-S2(I))	00000406
	AU(I)=(AU(I)+S1(I)-G1(I))*RL	00000407
	BU(I)=(BU(I)+S3(I)-G3(I))*RL	00000408
91	CU(I)=CU(I)*RL	00000409
	IF(NEQ.EQ.1) GO TO 76	00000410
	DO 92 J=1,NPH	00000411
	DO 92 I=2,N	00000412
	RL=1./(G2(I)+A(J,I)+B(J,I)-D(J,I))	00000413
	A(J,I)=(A(J,I)-G1(I))*RL	00000414
	B(J,I)=(B(J,I)-G3(I))*RL	00000415
	C(J,I)=C(J,I)*RL	00000416
92	CONTINUE	00000417
76	CONTINUE	00000418
	RETURN	00000419
	END	00000420

FILE OPTIONS - NAME= MAIN,OPT=C2,LINFCNT=59,SIZE=0000K,
SOURCE,ERCDIC,NOLIST,NODECK,LOAD,MAP,NOEDIT,NOID,NOXREF

C	SUBROUTINE SOLVE	00000421
C		00000422
	SUBROUTINE SOLVE(A,R,C,F)	00000423
C	THIS SOLVES EQUATIONS OF THE FORM	00000424
C	$F(I) = A(I)*F(I+1) + B(I)*F(I-1) + C(I)$	00000425
C	FOR I=2,NP2	00000426
	COMMON/CRT/N,NP1,NEQ,NPH,KRAD,NH,KASE	00000427
	DIMENSION A(NP1),B(NP1),C(NP1),F(NP1)	00000428
	$R(2) = R(2)*F(1) + C(2)$	00000429
	DO 48 I=3,N	00000430
	$T = 1. / (1. - B(I)*A(I-1))$	00000431
	$A(I) = A(I)*T$	00000432
48	$R(I) = (R(I)*R(I-1) + C(I))*T$	00000433
	DO 50 I=2,N	00000434
	J=NP1-I+1	00000435
50	$F(J) = A(J)*F(J+1) + R(J)$	00000436
	RETURN	00000437
	END	00000438

FILE OPTIONS - NAME= MAIN,OPT=02,LINFCNT=59,SIZE=0000K,
SOURCE,ERCNIC,NOLIST,NODECK,LOAD,MAP,NOEDIT,NOID,NOXREF

C	SUBROUTINE READY	00000430
C	SUBROUTINE READY	00000440
	COMMON/CFAC/ YM	00000441
	COMMON/COI/N,NP1,NEQ,NPH,KRAD,NH,KASE	00000442
	COMMON/GEN/PEI,AMI,AME,DPOX,PREF(251),PR(1),DEN,AMU,XU,XD,XL,DX,	00000443
1	CSALFA,PRT,INTG	00000445
	COMMON/V/U(251),F(1,251),P(251),RHO(251),QM(251),Y(251),TEMP(251)	00000446
	CALL DENSTY	00000447
	CALL RAD(XU,R(1),CSALFA)	00000448
	IF(KRAD.NE.0) GO TO 15	00000449
5	Y(2)=2.0*PEI*QM(2)/(RHO(2)*U(2))	00000450
	DO 10 I=2,NP1	00000451
1	Y(I)=Y(I-1)+.5*PEI*(1.0/(RHO(I-1)*U(I-1)*P(I-1))	00000452
	+ 1.0/(RHO(I)*U(I)*R(I)))*(QM(I)-QM(I-1))	00000453
	GO TO 25	00000454
15	CONTINUE	00000455
	RHOA=.5*(RHO(1)+RHO(2))	00000456
	RAV=.5*(R(1)+R(2))	00000457
	Y(2)= SORT(2.0*PEI*QM(2)*Y(2)/(RHOA*RAV*U(2)))	00000458
	A=R(1)*Y(2)+.5*Y(2)*Y(2)*CSALFA*YM	00000459
	DI=0.0	00000460
	DO 20 I=3,NP1	00000461
	RR=(U(I)-U(I-1))/(QM(I)-QM(I-1))	00000462
	AA=U(I-1)-RR*QM(I-1)	00000463
	DI=PEI* ALOG((AA+RR*QM(I))/(AA+RR*QM(I-1)))	00000464
	RHOA=.5*(RHO(I-1)+RHO(I))	00000465
	DI=DI/(RR*RHOA)+DI	00000466
	C=A+DI	00000467
	IF(YM.EQ.0.0) GO TO 30	00000468
	Y(I)=(-R(1)+(P(1)*R(1)+2.0*YM*CSALFA*C)**0.5)/(CSALFA*YM)	00000469
	GO TO 20	00000470
30	Y(I) = C/R(1)	00000471
20	CONTINUE	00000472
25	DO 40 I=2,NP1	00000473
40	P(I)=P(1)+YM*Y(I)*CSALFA	00000474
	RETURN	00000475
	END	00000476

FILEP OPTIONS - NAME= MAIN,OPT=02,LINECNT=59,SIZE=0000K,
SOURCE,EBODIC,NOLIST,NODECK,LOAD,MAP,NOEDIT,NOID,NOXREF

C SUBROUTINE VEFF

00000477

C

00000478

SUBROUTINE VEFF(I,IP1,EMU)

00000479

COMMON/COI/N,NP1,NEQ,NPH,KRAD,NH,KASE

00000480

COMMON/COI/AK,ALMG

00000481

COMMON/CSHE/SHE(551)

00000482

COMMON/V/U(251),F(1,251),R(251),RHO(251),OM(251),Y(251),TEMP(251)

00000483

C THIS SUBROUTINE USES THE MIXING-LENGTH HYPOTHESIS

00000484

YL = Y(NP1)

00000485

AL=ALMG*YL

00000486

BRB=SHE(I)*RHO(I)

00000487

EXP2=EXP(-Y(I)*SORT(BRB)/(VISCO(I)*27.5))

00000488

DAMP=1.0-EXP2

00000489

IF(Y(I).LE.AL/AK) AL=AK*Y(I)*DAMP

00000490

64 EMU=.5*(RHO(I)+RHO(IP1))*AL*AL*ABS((U(I)-U(IP1))/(Y(I)-Y(IP1)))

00000491

EMU=EMU+(VISCO(I)+VISCO(IP1))*0.5

00000492

IF(I.EQ.NP1) GO TO 1

00000493

SHE(I)=EMU*(U(I+1)-U(I-1))/(Y(I+1)-Y(I-1))

00000494

SHE(I)=ABS(SHE(I))

00000495

GO TO 2

00000496

1 SHE(NP1)=SHE(N)

00000497

2 CONTINUE

00000498

RETURN

00000499

END

00000500

```

LFER OPTIONS - NAME= MAIN,OPT=02,L INECNT=59,SIZE=0000K,
SOURCE,EBRDIC,NOLIST,NODECK,LOAD,MAP,NOEDIT,NOID,NOXREF
C
C
SUBROUTINE ENTRN 00000501
C 00000502
SUBROUTINE ENTRN 00000503
COMMON/COI/N,NP1,NEO,NPH,KRAD,NH,KASE 00000504
COMMON/GEN/PET,AMI,AME,DPDX,PREF(251),PR(1),DEN,AMU,XU,XD,XL,DX, 00000505
1 CSALFA,PRT,INTG 00000506
COMMON/V/U(251),F(1,251),R(251),RHO(251),OM(251),Y(251),TEMP(251) 00000507
COMMON/C SEMU/SEMU(551) 00000508
NM1=N-1 00000509
TERM1=1.0/(R(N)**KPAD*PET) 00000510
TERM2=R(NP1)**(2*KRAD)*RHO(NP1)*SEMU(NP1) 00000511
TERM2=TERM2+R(N)**(2*KRAD)*RHO(N)*SEMU(N) 00000512
TERM2=TERM2*(U(NP1)**2-U(N)**2)/(2.0*(OM(NP1)-OM(N))) 00000513
TERM4=R(N)**(2*KRAD)*RHO(N)*SEMU(N) 00000514
TERM4=TERM4+R(NM1)**(2*KRAD)*RHO(NM1)*SEMU(NM1) 00000515
TERM4=TERM4*(U(N)**2-U(NM1)**2)/(2.0*(OM(N)-OM(NM1))) 00000516
TERM2=(TERM2-TERM4)/(OM(NP1)-OM(NM1)) 00000517
TERM3=(U(NP1)-U(NM1))/(OM(NP1)-OM(NM1)) 00000518
IF(INTG,EO,1) AME=-0.8 00000519
AMEOLD=AME 00000520
K=NP1-15 00000521
RATIO=(F(1,K)-F(1,1))/(F(1,NP1)-F(1,1)) 00000522
IF(RATIO,GE,.999) AME=AMEOLD/100. 00000523
IF(RATIO,GE,.999) GO TO 10 00000524
IF(TERM3,LT,1.0E-30) AME=1.5*AMEOLD 00000525
IF(TERM3,LT,1.0E-30) GO TO 10 00000526
AME=TERM1*TERM2/TERM3 00000527
AME=(AME+AMEOLD)*.5 00000528
IF(AME,GE,0.0) AME=AMEOLD 00000529
IF(ABS(AME),GE,1.5*ABS(AMEOLD)) AME=1.5*AMEOLD 00000530
CONTINUE 00000531
RETURN 00000532
END 00000533

```

FILED OPTIONS - NAME= MAIN,OPT=02,LINECNT=59,SIZE=0000K,
SOURCE,ERCDIC,NOIIST,NODECK,LOAD,MAP,NOEDIT,NOID,NOXREF

```

C      SUBROUTINE WALL                                00000530
C                                                    00000531
      SUBROUTINE WALL                                00000532
      COMMON/CELIIX/DRAGC,STNO,TAUIW,QW            00000533
      COMMON/CROW/QW2                                00000534
      COMMON/GEN/PEI,AMI,AME,OPDX,PREF(251),PR(1),DEN,AMU,XU,XD,XL,DX, 00000535
1     CSALFA,PPT,INTG                                00000540
      COMMON/V/U(251),F(1,251),R(251),RHO(251),OM(251),Y(251),TEMP(251) 00000541
      COMMON/CSEMU/SEMU(551)                          00000542
      COMMON/CPRDP/HF(1),CP,TR,HW,TK                00000543
      COMMON/CTOT/QWT,FDP                             00000544
      COMMON/CNW/QNEW                                  00000545
      DATA NC,CN/60,60.0/                             00000546
      SUMY=0.0                                          00000547
      SUMT=0.0                                          00000548
      SUMYY=0.0                                         00000549
      SUMYT=0.0                                         00000550
      DO 10 I=1,NC                                     00000551
      SUMYT=SUMYT+Y(I)*TEMP(I)                         00000552
      SUMT=SUMT+TEMP(I)                                00000553
      SUMY=SUMY+Y(I)                                   00000554
10     SUMYY=SUMYY+Y(I)*Y(I)                           00000555
      A=(CN*SUMYT-SUMY*SUMT)/(CN*SUMYY-SUMY*SUMY)     00000556
      QNEW=TK*A/3600.0                                 00000557
C      ASSUMES LEWIS NO=1 AND NO BLOWING              00000558
      TAUIW = SEMU(1)*U(2)/(32.2*Y(2))                 00000559
      FDP=FDP+6.28*R(1)*DX*TAUIW                      00000560
      QW=TK*(TEMP(10)-TEMP(2))/(Y(10)-Y(2))           00000562
      QW=QW/3600.0                                     00000563
      QW2=TK*((TEMP(3)-TEMP(1))*Y(2)**2-(TEMP(2)-TEMP(1))*Y(3)**2)/ 00000564
1     (Y(2)*Y(3)*(Y(2)-Y(3))*3600.0)                 00000565
      QWT=QWT+6.28*R(1)*DX*QW                         00000566
      RETURN                                           00000567
      END                                             00000567

```


COMPILER OPTIONS - NAME = MAIN, OPT = 02, LINECNT = 59, SIZE = 0000K,
SOURCE, ERCDIC, NOLIST, NODECK, LOAD, MAP, NOEDIT, NOID, NOXREF

SUBROUTINE VISCO

00000568

00000569

FUNCTION VISCO(I)

00000570

COMMON/INPCON/PINE, EDK, SIG, GCON, AMW

00000571

COMMON/V/U(251), F(1,251), R(251), RHO(251), OM(251), Y(251), TEMP(251)

00000572

TSTAR = TEMP(I) / (1.8 * EDK)

00000573

OMEG = 0.62464 + 1.4593 / TSTAR - 0.97121 / TSTAR**2 + 0.67836 / TSTAR**3

00000574

1 - 0.231 / TSTAR**4 + 0.027865 / TSTAR**5

00000575

VISCO = (1.79396E-6) * SQRT(AMW * TEMP(I) / 1.8) / (OMEG * SIG**2)

00000576

RETURN

00000577

END

00000578

COMPILER OPTIONS - NAME= MAIN,OPT=02,I INECNT=59,SIZE=0000K,
SOURCE,ERCDDIC,NOLIST,NODECK,LOAD,MAP,NOEDIT,NOID,NOXREF

```

C      SUBROUTINE CONST
C
SUBROUTINE CONST
REAL MACH
COMMON/V/U(251),F(1,251),R(251),RHO(251),DM(251),Y(251),TEMP(251)
COMMON/CGFO/ALFA
COMMON/COL/AK,ALMG
COMMON/COPR/UGU,UGD
COMMON/CPRCP/HF(1),CP,TR,HW,TK
COMMON/DATA/VINF,DELTA,TW,TINF,OS,MACH,KR
COMMON/GEN/PEI,AMI,AME,DPDX,PREF(251),PR(1),DEN,AMU,XU,XD,XL,DX,
1  CSALFA,PRT,INTG
COMMON/CWRIT/IFLUX,IPOFF,IWRIT
COMMON/COI/N,NP1,NEQ,NPH,KRAD,NH,KASE
COMMON/INPCON/PINF,EDK,SIG,GCON,AMW
COMMON/NOATA/RHOINF
COMMON/CWGFO/EPSILO,ALPHA,XONE,WLENG,WSTART,WEND,COMPIN2,COE(11)
COMMON/PAD/AMJINF
DIMENSION TITLE(25)
C UNITS-TEMP(R),DEN(LBM/FT3),AMU(LBM/FT-SEC),CP(FT2/SEC2-R)
C IF KR=1 RADIATION EFFECTS INCLUDED, OTHERWISE THEY ARE NOT
C THERMAL AND VELOCITY BOUNDARY CONDITIONS
READ(5,20) (TITLE(I),I=1,20)
20  FORMAT(20A4)
WRITE(6,30) (TITLE(I),I=1,20)
30  FORMAT(1HC,20X,20A4///)
READ(5,2020) EPSILO,WLENG,WSTART,WEND,COMPIN2
2020 FORMAT(5F10.0)
READ(5,2021)(COE(I),I=1,11)
2021 FORMAT(6F10.4)
WRITE(6,2022)EPSILO,WLENG,WSTART,WEND,COMPIN2
2022 FORMAT(3X,'WAVE GEOMETRY- EPSILO=',F10.5,'FT',4X,'WLENG=',F10.5,
1 'FT',4X,'WSTART=',F10.5,'FT'/19X,'WEND=',F10.5,'FT',
2 'COMPIN2=',F10.5)
WRITE(6,2023)(COE(I),I=1,11)
2023 FORMAT(22H0THE VALUES OF COE ARE/(1X,11(1X,E10.4)))
READ(5,100) IFLUX,IPOFF
100  FORMAT(2I5)
IWRIT = IFLUX - 1
READ(5,900)TINF,TW,PINF,MACH,XU,XL,KASE,ALFAD
900  FORMAT(6F10.0,I3,F10.0)
C  CONSTANTS FOR FLUID SPECIFICATION
READ(5,908) CP,EDK,SIG,GCON,AMW
908  FORMAT(5F10.0)
READ(5,1010)KRAD,NEQ,N,KR
1010 FORMAT(4I5)
C  DENSITY AND VISCOSITY REFERENCE VALUES IF REQUIRED.
C  INITIAL BOUNDARY LAYER HEIGHT
ALFA=ALFAD*3.14159/1.80
NP1=N+1
TR = 537.0
DEN=PINF/(GCON*TR)
VINF=MACH*SQRT(1.4*53.3*32.2*TINF)
UGD = VINF
    
```

RHOINF=PINF/(GCON*TINF)	00000621
TEMP(NP1)=TINF	00000622
AMUINF=VISCO(NP1)	00000623
AMU=AMUINF	00000624
DELTA=128.C*AMUINF/(3.0*RHOINF*VINF*XU)	00000625
DELTA = XU*SQRT(DELTA)	00000626
NH = 1	00000627
AK=-.435	00000628
ALMG=-.09	00000629
DPT=0.0	00000630
PR(1)=-7	00000631
TK=0.0147	00000632
RETURN	00000633
END	00000634

```
MPILER OPTIONS - NAME= MAIN,OPT=02,LINECNT=59,SIZE=0000K,  
SOURCE,EBCDIC,NOLIST,NODECK,LOAD,MAP,NOEDIT,NOID,NOXREF  
C SUBROUTINE RAD 000006  
C 000006  
SUBROUTINE RAD(XU,R1,CSALFA) 000006  
C APPLICABLE TO PLANE FLOWS 000006  
COMMON/CGEO/ALFA 000006  
COMMON/CWGeo/EPSILO,ALPHA,XONE,WLENG,WSTART,WEND,COMPIN2,CDE(11) 000006  
R1=10.0 000006  
IF(XU.LT.WSTART) GO TO 10  
R1=10.0+EPSILO*SIN(ALPHA*(XONE))  
10 CONTINUE 000006  
CSALFA=1.0 000006  
RETURN 000006  
END 000006
```

```

PILEE OPTIONS - NAME= MAIN,OPT=02,LINECNT=59,SIZE=0000K,
SOURCE,ERCDIC,NOLIST,NODECK,LOAD,MAP,NOEDIT,NOID,NOXREF
SUBROUTINE PREF 00000648
COMMON/COI/AK,ALMG 00000649
COMMON/V/U(251),F(1,251),P(251),RHO(251),QM(251),Y(251),TFMP(251) 00000650
COMMON/GEN/PEI,AMI,AME,DPOX,PREF(251),PR(1),DEN,AMU,XU,XD,XL,DX, 00000651
1 CSALFA,PRT,INTG 00000652
COMMON/CSHE/SHE(551) 00000653
COMMON/CSEMU/SEMU(551) 00000654
COMMON/COT/N,NP1,NEQ,NPH,KRAD,NH,KASE 00000655
30 PREF(I)=PR(I) 00000656
DO 60 I=2,NP1 00000657
IF( .NOT.(Y(I).GT.Y(NP1)*ALMG/AK)) GO TO 50 00000658
40 PREF(I)=PRT 00000659
GO TO 60 00000660
50 P1=VISCO(I)/DP(I) 00000661
P2=RHO(I)*AK*AK*Y(I)*Y(I)/PRT*ABS((U(I+1)-U(I-1))/(Y(I+1)-Y(I-1))) 00000662
P3=Y(I)*SQRT(SHE(I)*RHO(I))/(VISCO(I)*27.5) 00000663
P3=1.-EXP(-P3) 00000664
P3=P3*P3 00000665
PREF(I)=SEMU(I)/(P1+P2*P3) 00000666
60 CONTINUE 00000667
C 00000668
RETURN 00000669
END 00000670

```

-FRIDAY, JUNE 04, 1971
 MEMORANDUM CASE 1 MEM Y(11) AND DX=0.5 * Y(INB1) 000000A71
 NAME GEOMETRY- EPSILO= 0.93330FT WLENG= 1.00000FT MSTART= 9.34000FT
 WEND= 12.00000FTCOMPING= 0 90544
 THE VALUES OF COE ARE
 0.4440E-03 0.9921E-01 0.2929E-01 0.1174E-02 0.1410E-03 0.5289E-04 0.1076E-04 0.7885E-06 0.1074E-07
 YNR =1.1200
 INDICES- KRAD= 0 KASE= 10 NEO= 2 N= 100 NR= 2 IPRF= 1 IFLUX= 3
 BOUNDARY CONDITIONS- YINF= 532.20 R TN= 532.2 P PTF= 628.5 PSF MACH NUMBER= 3.00
 KUB= 9.33 FT XL= 12.0 FT ALFA= 0 O DEGREE COME HALF-ANGLE
 GAS CONSTANTS- FKA= 97.00 K SIGMA= 3.617 ANGSTROM GCOM= 53.34 FT-LBM/LBF-R AMW= 28.96
 GAS PROPERTIES- CP= 0.000 BTU/LBM-R DEN= 0.9219 LBM/CU-FT AMJ= 0.1232E-04 LBM/FT-SEC TR= 0.0147 BTU/MR-FT-F
 THE VALUES OF OMEGA ARE
 0.8073E-08 0.2604E-07 0.4834E-07 0.7534E-07 1.0769E-06 1.4617E-06 2.1567E-06 3.0923E-06 3.8408E-06
 0.4721E-06 0.5755E-06 0.6969E-06 0.8393E-06 1.0064E-05 1.2022E-05 1.4317E-05 1.7004E-05 2.0191E-05 2.3856E-05 2.8149E-05
 0.3119E-05 0.3910E-05 0.4601E-05 0.5410E-05 0.6356E-05 0.7463E-05 0.8757E-05 1.0272E-04 1.2043E-04 1.4114E-04 1.6537E-04
 0.1937E-04 0.2268E-04 0.2656E-04 0.3109E-04 0.3639E-04 0.4259E-04 0.4984E-04 0.5828E-04 0.6824E-04 0.7985E-04 0.9342E-04
 0.1093E-03 0.1278E-03 0.1496E-03 0.1750E-03 0.2048E-03 0.2396E-03 0.2803E-03 0.3288E-03 0.3838E-03 0.4472E-03 0.5212E-03
 0.6059E-03 0.7012E-03 0.8096E-03 0.9430E-03 1.1025E-02 1.2885E-02 1.5045E-02 1.7538E-02 2.1399E-02 2.5669E-02 3.0343E-02
 0.3473E-02 0.4099E-02 0.4806E-02 0.5636E-02 0.6610E-02 0.7759E-02 0.9100E-02 1.0682E-01 1.2542E-01 1.4730E-01 1.7309E-01
 0.2033E-01 0.2390E-01 0.2812E-01 0.3308E-01 0.3894E-01 0.4586E-01 0.5403E-01 0.6370E-01 0.7514E-01 0.8869E-01 1.0479E-01
 0.1238E-00 0.1444E-00 0.1733E-00 0.2053E-00 0.2436E-00 0.2892E-00 0.3437E-00 0.4090E-00 0.4875E-00 0.5818E-00 0.6935E-00
 0.8207E-00 1.0000E-01
 RU = 93.30E-01 FT REX = 56.90E-06 PET = 46.0961E-01 INTG = 1
 BRAGG = 32.9089E-00 SIND = 57.8524E-02 TAUIV = 13.0204E-04 LBF/SO-FT OM = 91.3263E-02 RTU/(SO-FT SEC)
 ORZ = 0.51E-06 BTU/FT2 SEC
 ORW = 0.201001E-02 FDR = 0.163536E-05 DX = 0.20000E-02 AME = -0.4125E-00
 0.114706E-04

Y	U	MS	T	PR	M	AMD	SHEAR	EMU	MCP
(FT)	(FT/SEC)	(FT2/SEC2)	(DEG-R)			(LBM/FT3)	(LBF/FT2)		
0.079E-03	3.32E-03	8.94E-06	5.32E-02	9.00E-01	3.00E-00	2.214E-02	6.60E-01	9.32E-04	1.27E-02
7.07E-03	3.32E-03	8.927E-06	5.523E-02	9.00E-01	2.887E-00	2.194E-02	6.60E-01	1.037E-03	1.316E-02
6.104E-03	3.260E-03	8.715E-06	5.699E-02	9.00E-01	2.786E-00	2.068E-02	6.40E-01	1.172E-03	1.358E-02
5.213E-03	3.195E-03	8.606E-06	5.864E-02	9.00E-01	2.692E-00	2.009E-02	1.050E-02	1.299E-03	1.398E-02
4.419E-03	3.132E-03	8.494E-06	6.019E-02	9.00E-01	2.605E-00	1.928E-02	1.273E-02	1.397E-03	1.435E-02
3.611E-03	3.070E-03	8.384E-06	6.164E-02	9.00E-01	2.522E-00	1.912E-02	1.495E-02	1.458E-03	1.469E-02
2.803E-03	3.009E-03	8.291E-06	6.299E-02	9.00E-01	2.446E-00	1.870E-02	1.708E-02	1.472E-03	1.502E-02
2.017E-03	2.900E-03	8.190E-06	6.426E-02	9.00E-01	2.374E-00	1.834E-02	1.996E-02	1.452E-03	1.532E-02
1.241E-03	2.822E-03	8.091E-06	6.545E-02	9.00E-01	2.300E-00	1.800E-02	2.207E-02	1.401E-03	1.561E-02
0.477E-03	2.844E-03	7.994E-06	6.656E-02	9.00E-01	2.241E-00	1.770E-02	2.361E-02	1.324E-03	1.597E-02
1.647E-03	2.778E-03	7.899E-06	6.759E-02	9.00E-01	2.180E-00	1.743E-02	2.312E-02	1.236E-03	1.612E-02
1.737E-03	2.724E-03	7.806E-06	6.854E-02	9.00E-01	2.122E-00	1.719E-02	2.398E-02	1.137E-03	1.635E-02



1-510E-03	2-670E-03	7-714E-06	6-943E-02	5-004E-01	2-067E-00	1-697E-02	2-459E-02	1-034E-03	1-657E-02
1-313E-03	2-617E-03	7-625E-06	7-026E-02	5-354E-01	2-014E-00	1-677E-02	2-498E-02	9-328E-04	1-677E-02
1-142E-03	2-655E-03	7-537E-06	7-102E-02	6-692E-01	1-964E-00	1-694E-02	2-518E-02	8-348E-04	1-695E-02
9-929E-04	2-514E-03	7-517E-06	7-173E-02	6-033E-01	1-914E-00	1-643E-02	2-522E-02	7-408E-04	1-712E-02
8-634E-04	2-645E-03	7-367E-06	7-738E-02	6-399E-01	1-860E-00	1-628E-02	2-513E-02	6-547E-04	1-728E-02
6-508E-04	2-414E-03	7-284E-06	7-297E-02	6-818E-01	1-825E-00	1-615E-02	2-492E-02	5-761E-04	1-743E-02
6-529E-04	2-348E-03	7-203E-06	7-352E-02	7-325E-01	1-782E-00	1-603E-02	2-463E-02	5-051E-04	1-756E-02
5-677E-04	2-321E-03	7-124E-06	7-402E-02	7-957E-01	1-741E-00	1-592E-02	2-428E-02	4-416E-04	1-768E-02
4-936E-04	2-276E-03	7-046E-06	7-447E-02	8-755E-01	1-701E-00	1-582E-02	2-388E-02	3-853E-04	1-779E-02
4-293E-04	2-231E-03	6-969E-06	7-489E-02	9-761E-01	1-663E-00	1-573E-02	2-344E-02	3-354E-04	1-789E-02
3-733E-04	2-186E-03	6-805E-06	7-524E-02	1-101E-00	1-626E-00	1-566E-02	2-299E-02	2-027E-04	1-798E-02
3-244E-04	2-141E-03	6-621E-06	7-558E-02	1-255E-00	1-590E-00	1-559E-02	2-254E-02	2-530E-04	1-804E-02
2-822E-04	2-101E-03	6-450E-06	7-589E-02	1-438E-00	1-556E-00	1-553E-02	2-210E-02	2-708E-04	1-813E-02
2-454E-04	2-056E-03	6-279E-06	7-615E-02	1-647E-00	1-522E-00	1-547E-02	2-167E-02	1-921E-04	1-820E-02
2-134E-04	2-010E-03	6-107E-06	7-638E-02	1-874E-00	1-490E-00	1-543E-02	2-127E-02	1-672E-04	1-825E-02
1-850E-04	1-979E-03	6-542E-06	7-657E-02	2-102E-00	1-459E-00	1-538E-02	2-090E-02	1-458E-04	1-830E-02
1-614E-04	1-940E-03	6-474E-06	7-676E-02	2-308E-00	1-428E-00	1-535E-02	2-058E-02	1-273E-04	1-834E-02
1-403E-04	1-901E-03	6-411E-06	7-688E-02	2-605E-00	1-399E-00	1-533E-02	2-030E-02	1-144E-04	1-838E-02
1-229E-04	1-864E-03	6-347E-06	7-705E-02	2-554E-00	1-370E-00	1-530E-02	2-008E-02	9-778E-05	1-840E-02
2-061E-04	1-827E-03	6-285E-06	7-709E-02	2-565E-00	1-342E-00	1-529E-02	1-902E-02	8-607E-05	1-843E-02
2-226E-04	1-791E-03	6-223E-06	7-715E-02	2-566E-00	1-315E-00	1-527E-02	1-884E-02	7-602E-05	1-844E-02
8-023E-05	1-755E-03	6-163E-06	7-720E-02	2-305E-00	1-289E-00	1-526E-02	1-863E-02	6-741E-05	1-845E-02
6-974E-05	1-721E-03	6-105E-06	7-722E-02	2-257E-00	1-263E-00	1-526E-02	1-846E-02	6-004E-05	1-846E-02
6-066E-05	1-687E-03	6-047E-06	7-724E-02	2-001E-00	1-238E-00	1-526E-02	2-008E-02	5-372E-05	1-846E-02
5-275E-05	1-653E-03	5-990E-06	7-721E-02	1-930E-00	1-214E-00	1-525E-02	2-074E-02	4-832E-05	1-846E-02
4-587E-05	1-621E-03	5-925E-06	7-718E-02	1-778E-00	1-190E-00	1-527E-02	2-076E-02	4-374E-05	1-845E-02
3-988E-05	1-589E-03	5-860E-06	7-713E-02	1-647E-00	1-167E-00	1-528E-02	2-128E-02	3-974E-05	1-844E-02
3-468E-05	1-557E-03	5-827E-06	7-707E-02	1-513E-00	1-144E-00	1-529E-02	2-195E-02	3-636E-05	1-842E-02
3-016E-05	1-527E-03	5-775E-06	7-699E-02	1-399E-00	1-122E-00	1-530E-02	2-277E-02	3-366E-05	1-840E-02
2-622E-05	1-496E-03	5-724E-06	7-690E-02	1-302E-00	1-101E-00	1-532E-02	2-376E-02	3-098E-05	1-838E-02
2-280E-05	1-467E-03	5-674E-06	7-680E-02	1-217E-00	1-080E-00	1-534E-02	2-495E-02	2-866E-05	1-835E-02
1-983E-05	1-438E-03	5-624E-06	7-668E-02	1-144E-00	1-059E-00	1-537E-02	2-636E-02	2-704E-05	1-833E-02
1-724E-05	1-409E-03	5-576E-06	7-655E-02	1-081E-00	1-039E-00	1-539E-02	2-800E-02	2-549E-05	1-830E-02
1-499E-05	1-381E-03	5-520E-06	7-641E-02	1-026E-00	1-019E-00	1-542E-02	2-901E-02	2-415E-05	1-826E-02
1-305E-05	1-354E-03	5-483E-06	7-627E-02	9-704E-01	1-000E-00	1-545E-02	3-212E-02	2-300E-05	1-823E-02
1-133E-05	1-327E-03	5-437E-06	7-611E-02	9-304E-01	9-814E-01	1-548E-02	3-466E-02	2-201E-05	1-819E-02
9-853E-06	1-301E-03	5-393E-06	7-598E-02	9-040E-01	9-639E-01	1-551E-02	3-757E-02	2-117E-05	1-815E-02
8-567E-06	1-275E-03	5-340E-06	7-577E-02	8-752E-01	9-451E-01	1-555E-02	4-088E-02	2-043E-05	1-811E-02
7-449E-06	1-250E-03	5-306E-06	7-561E-02	8-496E-01	9-275E-01	1-559E-02	4-465E-02	1-970E-05	1-806E-02
6-474E-06	1-225E-03	5-264E-06	7-541E-02	8-273E-01	9-102E-01	1-563E-02	4-892E-02	1-924E-05	1-802E-02
5-631E-06	1-201E-03	5-223E-06	7-522E-02	8-078E-01	8-934E-01	1-567E-02	5-375E-02	1-874E-05	1-797E-02
4-895E-06	1-177E-03	5-183E-06	7-502E-02	7-907E-01	8-768E-01	1-571E-02	5-919E-02	1-831E-05	1-792E-02
4-254E-06	1-154E-03	5-143E-06	7-482E-02	7-756E-01	8-607E-01	1-575E-02	6-532E-02	1-792E-05	1-787E-02
3-700E-06	1-131E-03	5-104E-06	7-461E-02	7-623E-01	8-449E-01	1-579E-02	7-222E-02	1-758E-05	1-782E-02
3-216E-06	1-109E-03	5-066E-06	7-440E-02	7-507E-01	8-292E-01	1-584E-02	8-002E-02	1-727E-05	1-777E-02
2-796E-06	1-087E-03	5-029E-06	7-418E-02	7-407E-01	8-140E-01	1-588E-02	8-882E-02	1-700E-05	1-772E-02
2-430E-06	1-065E-03	4-993E-06	7-396E-02	7-322E-01	7-990E-01	1-593E-02	9-477E-02	1-677E-05	1-767E-02
2-113E-06	1-044E-03	4-957E-06	7-374E-02	7-251E-01	7-844E-01	1-598E-02	1-100E-03	1-656E-05	1-761E-02
1-836E-06	1-023E-03	4-922E-06	7-351E-02	7-192E-01	7-700E-01	1-603E-02	1-228E-03	1-630E-05	1-756E-02
1-596E-06	1-003E-03	4-887E-06	7-328E-02	7-145E-01	7-569E-01	1-608E-02	1-372E-03	1-624E-05	1-750E-02
1-387E-06	9-831E-04	4-853E-06	7-305E-02	7-104E-01	7-420E-01	1-613E-02	1-536E-03	1-612E-05	1-744E-02
1-205E-06	9-634E-04	4-820E-06	7-282E-02	7-080E-01	7-284E-01	1-618E-02	1-721E-03	1-602E-05	1-730E-02
1-047E-06	9-444E-04	4-788E-06	7-259E-02	7-068E-01	7-151E-01	1-623E-02	1-931E-03	1-595E-05	1-733E-02
9-094E-07	9-256E-04	4-756E-06	7-235E-02	7-061E-01	7-020E-01	1-629E-02	2-168E-03	1-585E-05	1-727E-02
7-899E-07	9-072E-04	4-725E-06	7-211E-02	7-029E-01	6-892E-01	1-634E-02	2-435E-03	1-578E-05	1-722E-02
6-860E-07	8-891E-04	4-694E-06	7-188E-02	7-021E-01	6-765E-01	1-639E-02	2-738E-03	1-572E-05	1-716E-02
5-945E-07	8-713E-04	4-664E-06	7-164E-02	7-014E-01	6-641E-01	1-645E-02	3-079E-03	1-567E-05	1-710E-02
5-170E-07	8-539E-04	4-634E-06	7-140E-02	7-010E-01	6-519E-01	1-650E-02	3-464E-03	1-561E-05	1-704E-02
4-487E-07	8-374E-04	4-605E-06	7-116E-02	7-007E-01	6-399E-01	1-656E-02	3-900E-03	1-554E-05	1-699E-02
3-853E-07	8-199E-04	4-577E-06	7-092E-02	7-005E-01	6-281E-01	1-661E-02	4-391E-03	1-549E-05	1-693E-02



Y	U	HS	T	DR	M	RHO	SHEAR	EMII	HCB
(FT)	(FT/SEC)	(FT/SEC2)	(DEG-P)			(LRM/FT3)	(LRF/FT2)		
2.374E-07	8.034E-02	4.540E-06	7.038E-02	7.002E-01	4.145E-01	1.647E-02	4.046E-02	1.548E-05	1.687E-02
2.027E-07	7.972E-02	4.521E-06	7.024E-02	7.002E-01	4.051E-01	1.678E-02	5.531E-02	1.543E-05	1.681E-02
2.534E-07	7.912E-02	4.494E-06	7.010E-02	7.001E-01	5.030E-01	1.670E-02	6.291E-02	1.539E-05	1.675E-02
1.001E-07	7.554E-02	4.448E-06	6.901E-02	7.001E-01	5.828E-01	1.684E-02	7.086E-02	1.515E-05	1.664E-02
1.001E-07	7.451E-02	4.441E-06	6.971E-02	7.001E-01	5.710E-01	1.695E-02	7.994E-02	1.530E-05	1.664E-02
1.644E-07	7.200E-02	4.416E-06	6.947E-02	7.000E-01	5.611E-01	1.694E-02	8.037E-02	1.524E-05	1.658E-02
1.427E-07	7.177E-02	4.409E-06	6.923E-02	7.000E-01	5.600E-01	1.702E-02	1.020E-02	1.522E-05	1.652E-02
1.224E-07	7.062E-02	4.385E-06	6.898E-02	7.000E-01	5.400E-01	1.708E-02	1.153E-02	1.518E-05	1.646E-02
1.057E-07	6.976E-02	4.360E-06	6.876E-02	7.000E-01	5.205E-01	1.714E-02	1.305E-02	1.514E-05	1.640E-02
9.010E-08	6.862E-02	4.316E-06	6.855E-02	7.000E-01	5.103E-01	1.725E-02	1.470E-02	1.509E-05	1.634E-02
7.827E-08	6.576E-02	4.302E-06	6.828E-02	7.000E-01	5.001E-01	1.724E-02	1.677E-02	1.505E-05	1.628E-02
6.711E-08	6.370E-02	4.268E-06	6.801E-02	7.000E-01	4.900E-01	1.733E-02	1.945E-02	1.501E-05	1.622E-02
5.755E-08	6.200E-02	4.244E-06	6.776E-02	7.000E-01	4.800E-01	1.730E-02	2.184E-02	1.496E-05	1.616E-02
4.010E-08	6.170E-02	4.221E-06	6.751E-02	7.000E-01	4.700E-01	1.730E-02	2.472E-02	1.492E-05	1.611E-02
4.188E-08	6.041E-02	4.197E-06	6.724E-02	7.000E-01	4.600E-01	1.752E-02	2.826E-02	1.488E-05	1.604E-02
3.544E-08	5.823E-02	4.174E-06	6.701E-02	7.000E-01	4.500E-01	1.758E-02	3.249E-02	1.483E-05	1.598E-02
2.003E-08	5.694E-02	4.150E-06	6.678E-02	7.000E-01	4.400E-01	1.765E-02	3.744E-02	1.479E-05	1.592E-02
2.513E-08	5.543E-02	4.126E-06	6.644E-02	7.000E-01	4.300E-01	1.772E-02	4.305E-02	1.474E-05	1.586E-02
2.095E-08	5.411E-02	4.102E-06	6.622E-02	7.000E-01	4.200E-01	1.770E-02	4.930E-02	1.469E-05	1.579E-02
1.732E-08	5.266E-02	4.078E-06	6.598E-02	7.000E-01	4.100E-01	1.797E-02	5.842E-02	1.464E-05	1.573E-02
1.417E-08	5.174E-02	4.052E-06	6.554E-02	7.000E-01	4.000E-01	1.795E-02	6.884E-02	1.459E-05	1.566E-02
1.142E-08	4.034E-02	4.028E-06	6.534E-02	7.000E-01	3.900E-01	1.803E-02	8.197E-02	1.454E-05	1.558E-02
0.034E-08	4.795E-02	3.998E-06	6.501E-02	7.000E-01	3.832E-01	1.812E-02	9.806E-02	1.448E-05	1.550E-02
0.958E-08	4.614E-02	3.968E-06	6.466E-02	7.000E-01	3.762E-01	1.822E-02	1.218E-02	1.442E-05	1.542E-02
5.153E-08	4.421E-02	3.946E-06	6.428E-02	7.000E-01	3.688E-01	1.834E-02	1.460E-02	1.435E-05	1.535E-02
3.584E-08	4.107E-02	3.908E-06	6.380E-02	7.000E-01	3.600E-01	1.847E-02	2.041E-02	1.426E-05	1.527E-02
2.210E-08	3.810E-02	3.851E-06	6.310E-02	7.000E-01	3.491E-01	1.865E-02	2.981E-02	1.416E-05	1.520E-02
1.032E-08	3.513E-02	3.782E-06	6.220E-02	7.000E-01	3.350E-01	1.892E-02	4.787E-02	1.406E-05	1.485E-02
0.0	0.0	3.186E-06	5.322E-02	7.000E-01	0.0	2.214E-02	4.102E-02	1.232E-05	1.272E-02

XU = 93.34E-01 FT DEX = 56.03E-06 DEI = 4A.2430E-03 INTR = 4
 DRAG = 25.6345E-01 STND = 25.6732E-05 TAILW = 1A.1176E-04LBF/SO-FT OH = 4C.4248E-01P.TIIV(40-ET SEC)
 QNFWE = 0.310377E-01
 QMT = 0.611377E-04 FDFE = 0.160480E-05 DX = 0.2207E-02 AMF = 0.4300E-01

Y	U	HS	T	DR	M	RHO	SHEAR	EMII	HCB
(FT)	(FT/SEC)	(FT/SEC2)	(DEG-P)			(LRM/FT3)	(LRF/FT2)		
8.412E-03	3.302E-03	8.040E-06	5.335E-02	9.000E-01	2.006E-01	2.709E-02	6.600E-01	7.508E-04	1.272E-02
7.454E-03	3.224E-03	9.927E-06	5.522E-02	9.000E-01	2.087E-01	2.734E-02	5.040E-01	7.508E-04	1.316E-02
6.433E-03	3.205E-03	9.715E-06	5.705E-02	9.000E-01	2.178E-01	2.767E-02	6.317E-01	8.284E-04	1.358E-02
5.433E-03	3.104E-03	8.604E-06	5.867E-02	9.000E-01	2.260E-01	2.808E-02	7.821E-01	9.071E-04	1.398E-02
4.937E-03	3.130E-03	8.205E-06	6.025E-02	9.000E-01	2.340E-01	1.954E-02	9.746E-01	9.976E-04	1.436E-02
4.330E-03	3.066E-03	8.347E-06	6.174E-02	9.000E-01	2.417E-01	1.908E-02	1.224E-02	1.022E-03	1.472E-02
3.802E-03	3.002E-03	9.279E-06	6.317E-02	9.000E-01	2.490E-01	1.865E-02	1.553E-02	1.226E-03	1.506E-02
3.342E-03	2.930E-03	8.172E-06	6.452E-02	9.000E-01	2.560E-01	1.824E-02	1.971E-02	1.368E-03	1.538E-02
2.941E-03	2.877E-03	9.067E-06	6.577E-02	9.000E-01	2.628E-01	1.701E-02	2.451E-02	1.518E-03	1.569E-02
2.592E-03	2.817E-03	7.066E-06	6.691E-02	9.000E-01	2.722E-01	1.741E-02	2.910E-02	1.650E-03	1.594E-02
2.288E-03	2.752E-03	7.872E-06	6.879E-02	9.000E-01	2.816E-01	1.735E-02	3.416E-02	1.765E-03	1.620E-02
1.024E-03	2.714E-03	7.790E-06	6.971E-02	9.000E-01	2.912E-01	1.714E-02	3.941E-02	1.878E-03	1.648E-02
1.794E-03	2.645E-03	7.708E-06	6.956E-02	9.000E-01	3.004E-01	1.694E-02	4.474E-02	1.921E-03	1.666E-02
1.509E-03	2.616E-03	7.420E-06	7.034E-02	8.374E-01	2.912E-01	1.675E-02	3.763E-02	1.442E-03	1.670E-02
1.424E-03	2.560E-03	7.551E-06	7.111E-02	8.431E-01	1.965E-01	1.652E-02	3.867E-02	1.275E-03	1.670E-02
1.274E-03	2.521E-03	7.477E-06	7.189E-02	8.469E-01	1.918E-01	1.630E-02	3.889E-02	1.114E-03	1.716E-02
1.144E-03	2.474E-03	7.406E-06	7.264E-02	8.504E-01	1.872E-01	1.622E-02	3.947E-02	0.688E-04	1.735E-02



1.033E-03	2.627E-03	7.130E-04	7.384E-02	8.540E-01	1.824E-00	3.823E-02	1.404E-02	3.770E-02	9.382E-04	1.754E-02
9.245E-04	2.280E-03	7.277E-06	7.420E-02	8.515E-01	1.781E-00	3.770E-02	1.587E-02	3.770E-02	7.227E-04	1.774E-02
8.483E-04	2.333E-04	7.221E-04	7.516E-02	8.714E-01	1.734E-00	3.714E-02	1.549E-02	3.714E-02	4.296E-04	1.794E-02
7.731E-04	2.287E-03	7.169E-06	7.607E-02	8.851E-01	1.692E-00	3.649E-02	1.540E-02	3.649E-02	5.313E-04	1.819E-02
7.072E-04	2.241E-03	7.123E-06	7.703E-02	8.932E-01	1.647E-00	3.619E-02	1.530E-02	3.619E-02	4.521E-04	1.841E-02
6.484E-04	2.105E-03	7.032E-06	7.803E-02	9.026E-01	1.603E-00	3.568E-02	1.519E-02	3.568E-02	3.825E-04	1.865E-02
5.897E-04	2.149E-03	7.044E-06	7.907E-02	9.124E-01	1.559E-00	3.495E-02	1.499E-02	3.495E-02	3.274E-04	1.891E-02
5.541E-04	2.312E-03	7.013E-06	8.017E-02	9.202E-01	1.514E-00	3.398E-02	1.479E-02	3.398E-02	2.849E-04	1.918E-02
5.188E-04	2.064E-03	6.983E-06	8.131E-02	9.265E-01	1.469E-00	3.291E-02	1.459E-02	3.291E-02	2.454E-04	1.944E-02
4.801E-04	2.044E-03	6.953E-06	8.250E-02	9.316E-01	1.423E-00	3.174E-02	1.439E-02	3.174E-02	2.095E-04	1.975E-02
4.404E-04	1.957E-03	6.926E-06	8.371E-02	9.354E-01	1.374E-00	3.048E-02	1.419E-02	3.048E-02	1.765E-04	2.005E-02
4.022E-04	1.892E-03	6.891E-06	8.486E-02	9.382E-01	1.324E-00	2.914E-02	1.399E-02	2.914E-02	1.461E-04	2.033E-02
3.641E-04	1.838E-03	6.841E-06	8.584E-02	9.400E-01	1.280E-00	2.782E-02	1.379E-02	2.782E-02	1.185E-04	2.057E-02
3.275E-04	1.785E-03	6.765E-06	8.684E-02	9.409E-01	1.231E-00	2.652E-02	1.359E-02	2.652E-02	9.227E-05	2.079E-02
3.576E-04	1.735E-03	6.662E-06	8.785E-02	9.418E-01	1.187E-00	2.524E-02	1.339E-02	2.524E-02	6.802E-05	2.079E-02
3.478E-04	1.685E-03	6.528E-06	8.864E-02	9.416E-01	1.143E-00	2.397E-02	1.319E-02	2.397E-02	4.925E-05	2.072E-02
3.257E-04	1.633E-03	6.398E-06	8.930E-02	9.403E-01	1.100E-00	2.271E-02	1.299E-02	2.271E-02	3.755E-05	2.057E-02
3.124E-04	1.565E-03	6.358E-06	8.985E-02	9.377E-01	1.057E-00	2.146E-02	1.279E-02	2.146E-02	2.778E-05	2.033E-02
3.004E-04	1.511E-03	6.304E-06	9.030E-02	9.340E-01	1.014E-00	2.022E-02	1.259E-02	2.022E-02	2.022E-05	2.004E-02
2.896E-04	1.457E-03	6.246E-06	9.066E-02	9.293E-01	9.707E-00	1.900E-02	1.239E-02	1.900E-02	1.511E-05	1.971E-02
2.799E-04	1.405E-03	6.184E-06	9.093E-02	9.237E-01	9.267E-00	1.777E-02	1.219E-02	1.777E-02	1.093E-05	1.936E-02
2.695E-04	1.354E-03	6.119E-06	9.112E-02	9.172E-01	8.824E-00	1.654E-02	1.199E-02	1.654E-02	8.093E-05	1.899E-02
2.585E-04	1.303E-03	6.052E-06	9.122E-02	9.098E-01	8.378E-00	1.531E-02	1.179E-02	1.531E-02	5.925E-05	1.861E-02
2.477E-04	1.252E-03	5.983E-06	9.122E-02	9.014E-01	7.930E-00	1.408E-02	1.159E-02	1.408E-02	4.224E-05	1.824E-02
2.409E-04	1.201E-03	5.912E-06	9.112E-02	8.920E-01	7.479E-00	1.285E-02	1.139E-02	1.285E-02	2.924E-05	1.787E-02
2.345E-04	1.150E-03	5.840E-06	9.093E-02	8.817E-01	7.026E-00	1.162E-02	1.119E-02	1.162E-02	1.924E-05	1.751E-02
2.285E-04	1.100E-03	5.768E-06	9.066E-02	8.705E-01	6.572E-00	1.039E-02	1.099E-02	1.039E-02	1.324E-05	1.717E-02
2.229E-04	1.050E-03	5.696E-06	9.030E-02	8.585E-01	6.119E-00	9.16E-03	1.079E-02	9.16E-03	8.24E-05	1.685E-02
2.171E-04	1.000E-03	5.624E-06	9.085E-02	8.457E-01	5.666E-00	7.93E-03	1.059E-02	7.93E-03	5.85E-05	1.653E-02
2.119E-04	9.50E-04	5.552E-06	9.122E-02	8.322E-01	5.213E-00	6.70E-03	1.039E-02	6.70E-03	4.24E-05	1.621E-02
2.066E-04	9.00E-04	5.480E-06	9.141E-02	8.178E-01	4.760E-00	5.47E-03	1.019E-02	5.47E-03	2.92E-05	1.589E-02
2.014E-04	8.50E-04	5.408E-06	9.158E-02	8.025E-01	4.307E-00	4.24E-03	9.99E-03	4.24E-03	1.66E-05	1.557E-02
1.961E-04	8.00E-04	5.336E-06	9.175E-02	7.863E-01	3.854E-00	3.01E-03	9.79E-03	3.01E-03	8.24E-05	1.524E-02
1.909E-04	7.50E-04	5.264E-06	9.192E-02	7.690E-01	3.401E-00	1.78E-03	9.59E-03	1.78E-03	4.58E-05	1.504E-02
1.857E-04	7.00E-04	5.192E-06	9.209E-02	7.507E-01	2.948E-00	5.57E-04	9.39E-03	5.57E-04	2.49E-05	1.482E-02
1.805E-04	6.50E-04	5.120E-06	9.226E-02	7.315E-01	2.495E-00	3.34E-04	9.19E-03	3.34E-04	1.36E-05	1.460E-02
1.753E-04	6.00E-04	5.048E-06	9.243E-02	7.115E-01	2.042E-00	1.12E-04	8.99E-03	1.12E-04	6.24E-05	1.438E-02
1.701E-04	5.50E-04	4.976E-06	9.260E-02	6.907E-01	1.589E-00	5.06E-05	8.79E-03	5.06E-05	3.36E-05	1.416E-02
1.649E-04	5.00E-04	4.904E-06	9.277E-02	6.692E-01	1.136E-00	2.81E-05	8.59E-03	2.81E-05	1.76E-05	1.394E-02
1.597E-04	4.50E-04	4.832E-06	9.294E-02	6.468E-01	6.84E-00	1.55E-05	8.39E-03	1.55E-05	8.24E-05	1.372E-02
1.545E-04	4.00E-04	4.760E-06	9.311E-02	6.235E-01	2.39E-00	7.28E-05	8.19E-03	7.28E-05	4.36E-05	1.350E-02
1.493E-04	3.50E-04	4.688E-06	9.328E-02	6.002E-01	1.93E-00	4.01E-05	7.99E-03	4.01E-05	2.28E-05	1.328E-02
1.441E-04	3.00E-04	4.616E-06	9.345E-02	5.769E-01	1.47E-00	2.49E-05	7.79E-03	2.49E-05	1.16E-05	1.306E-02
1.389E-04	2.50E-04	4.544E-06	9.362E-02	5.536E-01	1.01E-00	1.49E-05	7.59E-03	1.49E-05	5.57E-05	1.284E-02
1.337E-04	2.00E-04	4.472E-06	9.379E-02	5.303E-01	5.55E-00	8.16E-05	7.39E-03	8.16E-05	2.92E-05	1.262E-02
1.285E-04	1.50E-04	4.400E-06	9.396E-02	5.070E-01	1.00E-00	4.64E-05	7.19E-03	4.64E-05	1.56E-05	1.240E-02
1.233E-04	1.00E-04	4.328E-06	9.413E-02	4.837E-01	4.47E-00	2.72E-05	6.99E-03	2.72E-05	8.24E-05	1.218E-02
1.181E-04	5.00E-05	4.256E-06	9.430E-02	4.604E-01	3.01E-00	1.55E-05	6.79E-03	1.55E-05	4.36E-05	1.196E-02
1.129E-04	4.00E-05	4.184E-06	9.447E-02	4.371E-01	2.55E-00	8.79E-05	6.59E-03	8.79E-05	2.28E-05	1.174E-02
1.077E-04	3.00E-05	4.112E-06	9.464E-02	4.138E-01	2.09E-00	5.11E-05	6.39E-03	5.11E-05	1.27E-05	1.152E-02
1.025E-04	2.00E-05	4.040E-06	9.481E-02	3.905E-01	1.63E-00	2.92E-05	6.19E-03	2.92E-05	6.54E-05	1.130E-02
1.072E-04	1.50E-05	4.000E-06	9.498E-02	3.672E-01	1.17E-00	1.74E-05	5.99E-03	1.74E-05	3.57E-05	1.108E-02
1.019E-04	1.00E-05	3.960E-06	9.515E-02	3.439E-01	7.11E-00	9.24E-05	5.79E-03	9.24E-05	1.99E-05	1.086E-02
1.066E-04	8.00E-05	3.920E-06	9.532E-02	3.206E-01	2.65E-00	5.06E-05	5.59E-03	5.06E-05	1.05E-05	1.064E-02
1.013E-04	7.00E-05	3.880E-06	9.549E-02	2.973E-01	2.19E-00	2.87E-05	5.39E-03	2.87E-05	5.57E-05	1.042E-02
1.060E-04	6.00E-05	3.840E-06	9.566E-02	2.740E-01	1.73E-00	1.69E-05	5.19E-03	1.69E-05	2.92E-05	1.020E-02
1.007E-04	5.00E-05	3.800E-06	9.583E-02	2.507E-01	1.27E-00	9.64E-05	4.99E-03	9.64E-05	1.56E-05	9.98E-03
1.054E-04	4.00E-05	3.760E-06	9.600E-02	2.274E-01	8.11E-00	5.91E-05	4.79E-03	5.91E-05	8.24E-05	9.76E-03
1.001E-04	3.00E-05	3.720E-06	9.617E-02	2.041E-01	3.55E-00	3.34E-05	4.59E-03	3.34E-05	4.36E-05	9.54E-03
1.048E-04	2.00E-05	3.680E-06	9.634E-02	1.808E-01	2.09E-00	1.76E-05	4.39E-03	1.76E-05	2.28E-05	9.32E-03
1.095E-04	1.50E-05	3.640E-06	9.651E-02	1.575E-01	1.63E-00	1.00E-05	4.19E-03	1.00E-05	1.27E-05	9.10E-03
1.042E-04	1.00E-05	3.600E-06	9.668E-02	1.342E-01	1.17E-00	5.92E-05	3.99E-03	5.92E-05	6.54E-05	8.88E-03
1.089E-04	8.00E-05	3.560E-06	9.685E-02	1.109E-01	7.11E-00	3.34E-05	3.79E-03	3.34E-05	3.57E-05	8.66E-03
1.036E-04	7.00E-05	3.520E-06	9.702E-02	9.86E-02	6.65E-00	1.76E-05	3.59E-03	1.76E-05	1.99E-05	8.44E-03
1.083E-04	6.00E-05	3.480E-06	9.719E-02	8.61E-02	6.19E-00	9.24E-05	3.39E-03	9.24E-05	1.05E-05	8.22E-03
1.030E-04	5.00E-05	3.440E-06	9.736E-02	7.36E-02	5.73E-00	5.06E-05	3.19E-03	5.06E-05	5.57E-05	8.00E-03
1.077E-04	4.00E-05	3.400E-06	9.753E-02	6.11E-02	5.27E-00	2.87E-05	2.99E-03	2.87E-05	2.92E-05	7.78E-03
1.024E-04	3.00E-05	3.360E-06	9.770E-02	4.86E-02	4.81E-00	1.69E-05	2.79E-03	1.69E-05	1.56E-05	7.56E-03
1.071E-04	2.00E-05	3.320E-06	9.787E-02	3.61E-02	4.35E-00	9.24E-05	2.59E-03	9.24E-05	8.24E-05	7.34E-03
1.018E-04	1.50E-05	3.280E-06	9.804E-02	2.36E-02	3.89E-00	5.06E-05	2.39E-03	5.06E-05	4.36E-05	7.12E-03
1.065E-04	1.00E-05	3.240E-06	9.821E-02	1.11E-02	3.43E-00	2.87E-05	2.19E-03	2.87E-05	2.28E-05	6.90E-03
1.012E-04	8.00E-05	3.200E-06	9.838E-02	9.86E-03	2.97E-00	1.69E-05	1.99E-03	1.69E-05	1.27E-05	6.68E-03
1.059E-04	7.00E-05	3.160E-06	9.855E-02	8.61E-03	2.51E-00	9.24E-05	1.79E-03	9.24E-05	6.54E-05	6.46E-03
1.006E-04	6.00E-05	3.120E-06	9.872E-02	7.36E-03	2.05E-00	5.06E-05	1.59E-03	5.06E-05	3.57E-05	6.24E-03
1.053E-04	5.00E-05	3.080E-06	9.889E-02	6.11E-03	1.59E-00	2.87E-05	1.39E-03	2.87E-05	1.99E-05	6.02E-03
1.000E-04	4.00E-05	3.040E-06	9.906E-02	4.86E-03	1.13E-00	1.69E-05	1.19E-03	1.69E-05	1.05E-05	5.80E-03
1.047E-04	3.00E-05	3.000E-06	9.923E-02	3.61E-03	6.65E-00	9.24E-05	9.79E-03	9.24E-05	5.57E-05	5.58E-03
1.094E-04	2.00E-05	2.960E-06	9.940E-02	2.36E-03	6.19E-00	5.06E-05	7.59E-03	5.06E-05	2.92E-05	5.36E-03
1.041E-04	1.50E-05	2.920E-06	9.957E-02	1.11E-03	5.73E-00	2.87E-05	5.39E-03	2.87E-05	1.56E-05	5.14E-03
1.088E-04	1.00E-05	2.880E-06	9.974E-02	9.86E-04	5.27E-00	1.69E-05	3.19E-03	1.69E-05		

Y	II	MS	T	DR	M	RHM	SHEAR	FWI	MCD
9.066E-05	4.646E-03	3.457E-06	5.700E-02	7.706E-01	3.931E-03	2.35E-02	2.10E-02	1.44E-05	1.390E-02
9.788E-05	4.072E-03	3.648E-06	5.775E-02	7.706E-01	3.457E-03	2.40E-02	2.75E-02	1.44E-05	1.376E-02
9.457E-05	3.561E-03	3.430E-06	5.740E-02	7.706E-01	3.27E-03	2.46E-02	2.44E-02	1.420E-05	1.373E-02
8.164E-05	3.17E-03	3.420E-06	5.744E-02	7.706E-01	2.653E-03	2.51E-02	2.20E-02	1.476E-05	1.26E-02
7.870E-05	2.73E-03	3.410E-06	5.737E-02	7.706E-01	2.037E-03	2.658E-02	5.31E-02	1.633E-05	1.245E-02
7.402E-05	2.30E-03	3.400E-06	5.730E-02	7.706E-01	2.043E-03	2.64E-02	6.54E-02	1.430E-05	1.361E-02
7.072E-05	1.86E-03	3.386E-06	5.671E-02	7.710E-01	1.578E-03	2.78E-02	8.76E-02	1.421E-05	1.352E-02
6.819E-05	1.43E-03	3.376E-06	5.651E-02	7.710E-01	1.384E-03	2.8E-02	1.18E-02	1.414E-05	1.347E-02
6.574E-05	1.01E-03	3.362E-06	5.631E-02	7.710E-01	1.214E-03	2.82E-02	1.42E-02	1.41E-05	1.342E-02
6.338E-05	7.23E-04	3.350E-06	5.611E-02	7.710E-01	1.067E-03	2.84E-02	1.71E-02	1.404E-05	1.337E-02
6.106E-05	5.19E-04	3.337E-06	5.590E-02	7.710E-01	9.26E-04	2.86E-02	2.05E-02	1.397E-05	1.332E-02
5.881E-05	3.45E-04	3.325E-06	5.568E-02	7.710E-01	8.17E-04	2.88E-02	2.44E-02	1.390E-05	1.327E-02
5.663E-05	2.21E-04	3.312E-06	5.547E-02	7.710E-01	7.13E-04	2.90E-02	2.80E-02	1.383E-05	1.322E-02
5.455E-05	1.33E-04	3.300E-06	5.525E-02	7.710E-01	6.10E-04	2.92E-02	3.15E-02	1.376E-05	1.317E-02
5.247E-05	6.15E-05	3.288E-06	5.503E-02	7.710E-01	5.16E-04	2.94E-02	3.50E-02	1.369E-05	1.312E-02
5.038E-05	3.17E-05	3.276E-06	5.482E-02	7.710E-01	4.30E-04	2.96E-02	3.84E-02	1.362E-05	1.307E-02
4.838E-05	1.60E-05	3.264E-06	5.460E-02	7.710E-01	3.50E-04	2.98E-02	4.18E-02	1.355E-05	1.302E-02
4.633E-05	3.72E-06	3.252E-06	5.438E-02	7.710E-01	2.75E-04	2.99E-02	4.52E-02	1.348E-05	1.297E-02
4.427E-05	3.02E-06	3.240E-06	5.416E-02	7.710E-01	2.15E-04	2.99E-02	4.86E-02	1.341E-05	1.292E-02
4.211E-05	2.36E-06	3.228E-06	5.393E-02	7.710E-01	1.60E-04	2.99E-02	5.20E-02	1.334E-05	1.287E-02
3.995E-05	1.80E-06	3.216E-06	5.370E-02	7.710E-01	1.10E-04	2.99E-02	5.54E-02	1.327E-05	1.282E-02
3.779E-05	1.24E-06	3.204E-06	5.348E-02	7.710E-01	6.50E-05	2.99E-02	5.88E-02	1.320E-05	1.277E-02
3.563E-05	6.8E-07	3.192E-06	5.326E-02	7.710E-01	2.50E-05	2.99E-02	6.22E-02	1.313E-05	1.272E-02
3.347E-05	2.2E-07	3.180E-06	5.304E-02	7.710E-01	8.0E-06	2.99E-02	6.56E-02	1.306E-05	1.267E-02
3.131E-05	5.6E-08	3.168E-06	5.282E-02	7.710E-01	2.0E-06	2.99E-02	6.90E-02	1.299E-05	1.262E-02
2.915E-05	1.0E-08	3.156E-06	5.260E-02	7.710E-01	5.0E-07	2.99E-02	7.24E-02	1.292E-05	1.257E-02
2.700E-05	2.0E-09	3.144E-06	5.238E-02	7.710E-01	1.0E-07	2.99E-02	7.58E-02	1.285E-05	1.252E-02
2.484E-05	4.0E-10	3.132E-06	5.216E-02	7.710E-01	2.0E-08	2.99E-02	7.92E-02	1.278E-05	1.247E-02
2.269E-05	8.0E-11	3.120E-06	5.194E-02	7.710E-01	4.0E-09	2.99E-02	8.26E-02	1.271E-05	1.242E-02
2.053E-05	1.6E-11	3.108E-06	5.172E-02	7.710E-01	8.0E-10	2.99E-02	8.60E-02	1.264E-05	1.237E-02
1.838E-05	3.2E-12	3.096E-06	5.150E-02	7.710E-01	1.6E-10	2.99E-02	8.94E-02	1.257E-05	1.232E-02
1.622E-05	6.4E-13	3.084E-06	5.128E-02	7.710E-01	3.2E-11	2.99E-02	9.28E-02	1.250E-05	1.227E-02
1.407E-05	1.3E-13	3.072E-06	5.106E-02	7.710E-01	6.4E-12	2.99E-02	9.62E-02	1.243E-05	1.222E-02
1.191E-05	2.6E-14	3.060E-06	5.084E-02	7.710E-01	1.3E-12	2.99E-02	9.96E-02	1.236E-05	1.217E-02
9.76E-06	5.2E-15	3.048E-06	5.062E-02	7.710E-01	2.6E-13	2.99E-02	1.030E-01	1.229E-05	1.212E-02
7.61E-06	1.0E-15	3.036E-06	5.040E-02	7.710E-01	5.2E-14	2.99E-02	1.064E-01	1.222E-05	1.207E-02
5.46E-06	2.0E-16	3.024E-06	5.018E-02	7.710E-01	1.0E-14	2.99E-02	1.098E-01	1.215E-05	1.202E-02
3.31E-06	4.0E-17	3.012E-06	5.000E-02	7.710E-01	2.0E-15	2.99E-02	1.132E-01	1.208E-05	1.197E-02
1.16E-06	8.0E-18	3.000E-06	4.982E-02	7.710E-01	4.0E-16	2.99E-02	1.166E-01	1.201E-05	1.192E-02
9.0E-07	1.6E-18	2.988E-06	4.964E-02	7.710E-01	8.0E-17	2.99E-02	1.200E-01	1.194E-05	1.187E-02

XII = 93.42E-01 ET RCX = 56.97E-06 DEL = 46.2764E-01 INTG = 7
 DRACC = 24.4747E-03 SPNO = 48.3680E-03 TAUHM = 74.500E-01 RE/SO-FT OM = 11.3137E-02 RTM/ISO-FT SFC1
 OM2 = -0.74E-02 CBRTU/ET2 SEC
 ONEN = 0.115601E-02
 ONT = 0.70046E-04 FDR = 0.1723E-05 DV = 0.2000E-02 AVE = -0.8861E-01



AUBURN UNIVERSITY COMPUTER CENTER

APPENDIX II
Elliptic Integral

The output of this program is eleven coefficients which are used to characterize the wall geometry in the main program.

The input to the program requires specifying the amplitude of the waves in feet in statement 4. That is:

4 E = ~~XXX~~

Also required is the wavelength in feet in statement 5.

5 XL = XXX

```

1  C    CALCULATES XU(WAVY DISTANCE) AND POLYNOMIAL COEFFICIENTS
2      DIMENSION RES(99),XX(99),Y(99),CX(11)
3      PI=3.141592965
4      E=0.050
5      XL=1.0
6      CALL COMPLETE (XL,E,XLC)
7      ALFA=2.*PI/XL
8      EA=E*E*ALFA**2
9      D=((1.+EA)**.5)/ALFA
10     A=1.0
11     B=1.0-EA/(1.0+EA)
12     CMOD=B**.5
13     DO 10 I=1,49
14     XX(I)=(XL/200.0)*FLOAT(I)
15     PHI=ALFA*XX(I)
16     ARG=TAN(PHI)
17     CALL ELI2(RES(I),ARG,CMOD,A,B)
18     RES(I)=D*RES(I)
19     10 CONTINUE
20     DO 11 I=50,99
21     XX(I)=(XL/200.0)*FLOAT(I)
22     IF(I.EQ.50) GO TO 12
23     RES(I)=XLC/2.-RES(100-I)
24     GO TO 11
25     12 RES(I)=XLC/4
26     11 CONTINUE
27     MX=10
28     NX=99
29     NNX=11
30     CALL CURFIT(RES,XX,MX,NX,CX,NNX)
31     DO 16 I=1,99
32     F1=CX(1)
33     F2=CX(2)*RES(I)
34     F3=CX(3)*RES(I)**2
35     F4=CX(4)*RES(I)**3
36     F5=CX(5)*RES(I)**4
37     F6=CX(6)*RES(I)**5
38     F7=CX(7)*RES(I)**6
39     F8=CX(8)*RES(I)**7
40     F9=CX(9)*RES(I)**8
41     F10=CX(10)*RES(I)**9
42     F11=CX(11)*RES(I)**10
43     Y(I)=F1+F2+F3+F4+F5+F6+F7+F8+F9+F10+F11
44     16 CONTINUE
45     WRITE(6,607)
46     607 FORMAT('1',1X,'POLYNOMIAL COEFFICIENTS ARE GIVEN BELOW')
47     WRITE(6,604)(CX(J),J,J=1,NNX)
48     604 FORMAT(' ',E14.7,5X,I2)
49     WRITE(6,606)
50     606 FORMAT(1X,'X1',9X,'X1P',12X,'XU')
51     WRITE(6,605)(XX(I),Y(I),RES(I),I,I=1,99)
52     605 FORMAT(' ',F14.7,1X,F14.7,1X,F14.7,1X,I3)
53     STOP
54     END

```

```

1      SUBROUTINE CURFIT(X,Y,M,N,C,NN)
2      DIMENSION X(N),Y(N),A(11,11),B(11),C(NN),P(20)
3      DO 5 I=1,NN
4          5 C(I)=0.0
5          MX2=M*2
6          DO 13 I=1,MX2,1
7              P(I)=0.0
8              DO 13 J=1,N,1
9                  13 P(I)=P(I)+X(J)**I
10             L=M+1
11             DO 30 I=1,L,1
12             DO 30 J=1,L,1
13             K=I+J-2
14             IF (K) 29,29,28
15             28 A(I,J)=P(K)
16             GO TO 30
17             29 A(1,1)=N
18             30 CONTINUE
19             B(1)=0.0
20             DO 21 J=1,N,1
21             21 B(1)=B(1)+Y(J)
22             DO 22 I=2,L,1
23             B(I)=0.0
24             DO 22 J=1,N,1
25             22 B(I)=B(I)+Y(J)*X(J)**(I-1)
26             NM1=L-1
27             DO 300 K=1,NM1,1
28             KP1=K+1
29             MX2=K
30             DO 400 I=KP1,L,1
31             IF (ABS(A(I,K))-ABS(A(MX2,K))) 400,400,401
32             401 MX2=I
33             400 CONTINUE
34             IF (MX2-K) 500,500,405
35             405 DO 410 J=K,L,1
36                 TEMP=A(K,J)
37                 A(K,J)=A(MX2,J)
38             410 A(MX2,J)=TEMP
39                 TEMP=B(K)
40                 B(K)=B(MX2)
41                 B(MX2)=TEMP
42             500 DO 300 I=KP1,L,1
43                 FACTOR=A(I,K)/A(K,K)
44                 A(I,K)=0.0
45                 DO 301 J=KP1,L,1
46             301 A(I,J)=A(I,J)-FACTOR*A(K,J)
47             300 B(I)=B(I)-FACTOR*B(K)
48                 C(L)=B(L)/A(L,L)
49                 I=NM1
50             710 IP1=I+1
51                 SUM=0.0
52                 DO 700 J=IP1,L,1
53             700 SUM=SUM+A(I,J)*C(J)

```

```
54      C(I)=(B(I)-SUM)/A(I,I)
55      I=I-1
56      IF(I) 800,800,710
57 800  RETURN
58      END
```

```

1      SUBROUTINE COMPLETE (XL,E,XLC)
2  C    COMPLETE ELLIPTIC INTEGRALS
3      WRITE(6,300)
4      300 FORMAT('1','COMPLETE WAVE LENGTH(FT.)',3X,'EPSILON(FT.)')
5      PI=3.141592965
6      ALFA=2.*PI/XL
7      EA=E*E*ALFA**2
8      D=((1.+EA)**.5)/ALFA
9      A=1.
10     B=1.-EA/(1.+EA)
11     AK=(EA/(1.+EA))**.5
12     IER=C
13     CALL CEL2(RES,AK,A,B,IER)
14     RES=RES*D*4.0
15     XLC=RES
16     WRITE (6,400) RES,E
17     400 FORMAT(' ',7X,F10.8,14X,F6.4)
18     RETURN
19     END

```


PCLYNCMIAL COEFFICIENTS ARE GIVEN BELOW

-0.7113060E-03	1
C.1005421E 01	2
-C.1292982E 00	2
-C.1195782E 01	4
0.1445790E 02	5
-C.5429271E 02	6
C.1352269E 03	7
-C.3080117E 03	8
C.3749993E 03	9
C.9191301E 02	10
-C.3531654E 03	11

X1	X1P	XU	
0.005	0.0044213	0.0051084	1
C.010	C.0095461	C.0102167	2
0.015	0.0146623	C.0153245	3
C.020	0.0197693	C.0204317	4
0.025	0.0248664	0.0255380	5
0.030	0.0299536	C.0306433	6
0.035	0.0350306	C.0357473	7
C.040	0.0400975	C.0408500	8
0.045	0.0451542	0.0459509	9
C.050	0.0502010	C.0510501	10
0.055	0.0552382	0.0561473	11
C.060	0.0602662	0.0612424	12
0.065	0.0652852	0.0663350	13
C.070	0.0702962	C.0714253	14
0.075	0.0752996	0.0765130	15
C.080	0.0802959	C.0815980	16
0.085	0.0852859	0.0866801	17
C.090	0.0902699	0.0917591	18
0.095	0.0952491	0.0968351	19
C.100	0.1002238	C.1019080	20
0.105	0.1051947	C.1069776	21
C.110	0.1101632	C.1120440	22
0.115	0.1151291	C.1171069	23
C.120	C.1200936	0.1221666	24
0.125	0.1250571	0.1272228	25
C.130	0.1300205	0.1322756	26
0.135	0.1349841	0.1373250	27
C.140	0.1399490	C.1423710	28
0.145	0.1449152	0.1474137	29
C.150	0.1498836	0.1524531	30
0.155	0.1548544	0.1574892	31
C.160	0.1598281	0.1625222	32
0.165	0.1648050	0.1675521	33
C.170	0.1697853	C.1725787	34
0.175	0.1747697	0.1776026	35
C.180	0.1797580	0.1826238	36
0.185	0.1847505	0.1876424	37
C.190	0.1897470	0.1926583	38
0.195	0.1947479	0.1976720	39
C.200	0.1997530	C.2026836	40
0.205	0.2047622	C.2076932	41
C.210	0.2097751	0.2127007	42
0.215	0.2147919	C.2177066	43
C.220	0.2198120	0.2227113	44
0.225	0.2248352	C.2277144	45
C.230	0.2298611	0.2327166	46
0.235	0.2348894	C.2377179	47

C. 240	0.2399195	0.2427186	48
C. 245	0.2449510	0.2477188	49
C. 250	0.2499838	0.2527193	50
C. 255	0.2550170	0.2577199	51
C. 260	0.2600494	0.2627201	52
C. 265	0.2650811	0.2677208	53
C. 270	0.2701113	0.2727221	54
C. 275	0.2751396	0.2777243	55
C. 280	0.2801654	0.2827274	56
C. 285	0.2851883	0.2877321	57
C. 290	0.2902075	0.2927380	58
C. 295	0.2952229	0.2977455	59
C. 300	0.3002342	0.3027551	60
C. 305	0.3052407	0.3077667	61
C. 310	0.3102422	0.3127804	62
C. 315	0.3152385	0.3177963	63
C. 320	0.3202299	0.3228149	64
C. 325	0.3252159	0.3278360	65
C. 330	0.3301972	0.3328600	66
C. 335	0.3351732	0.3378866	67
C. 340	0.3401450	0.3429165	68
C. 345	0.3451129	0.3479494	69
C. 350	0.3500775	0.3529856	70
C. 355	0.3550392	0.3580250	71
C. 360	0.3599993	0.3630677	72
C. 365	0.3649586	0.3681137	73
C. 370	0.3699180	0.3731631	74
C. 375	0.3748789	0.3782159	75
C. 380	0.3798424	0.3832721	76
C. 385	0.3848097	0.3883318	77
C. 390	0.3897822	0.3933947	78
C. 395	0.3947608	0.3984611	79
C. 400	0.3997474	0.4035307	80
C. 405	0.4047430	0.4086035	81
C. 410	0.4097481	0.4136796	82
C. 415	0.4147643	0.4187586	83
C. 420	0.4197907	0.4238407	84
C. 425	0.4248286	0.4289257	85
C. 430	0.4298770	0.4340134	86
C. 435	0.4349352	0.4391037	87
C. 440	0.4399990	0.4441963	88
C. 445	0.4450703	0.4492913	89
C. 450	0.4501428	0.4543886	90
C. 455	0.4552087	0.4594877	91
C. 460	0.4602668	0.4645887	92
C. 465	0.4653056	0.4696913	93
C. 470	0.4703167	0.4747953	94
C. 475	0.4752883	0.4799007	95
C. 480	0.4802085	0.4850070	96
C. 485	0.4850541	0.4901142	97
C. 490	0.4898095	0.4952220	98
C. 495	0.4944543	0.5003302	99

APPENDIX III

The Effect of Roughness on Transition Location

Heat transfer data on sharp leading edge flat plates at zero angle of attack from two investigations [11, 12] was used to determine the location of boundary layer transition for smooth flat plates and smooth flat plate leading sections followed by sinusoidal roughness for a limited range of Mach numbers and Reynolds numbers. The heat transfer data was fit with three straight lines using a least squares fit. Several approaches to fitting the data over the region of sinusoidal roughness were used.

Two locations related to transition location were determined. These have been termed "the transition onset" and "fully developed turbulent" locations (see Figure 16).

Heat transfer data were input to a least squares fit computer program which treated the data in two distinct ways. First, all of the data were used to obtain the three straight lines shown in Figure 16. The data were then treated using only the extreme points. Results for both of these studies are presented in Figure 17. Here it seems that transition onset is delayed while the fully developed turbulent location is either unaffected or moved slightly forward. The apparent delay of transition onset is probably a result of the separation which occurs upstream of the first wave if the flow is laminar. Based on the limited data available and recognizing that it is all for relatively high Mach number flows, it may be concluded that transition location is not significantly affected by sinusoidal roughness in the case of sharp leading edge flat plates at zero angle of attack.

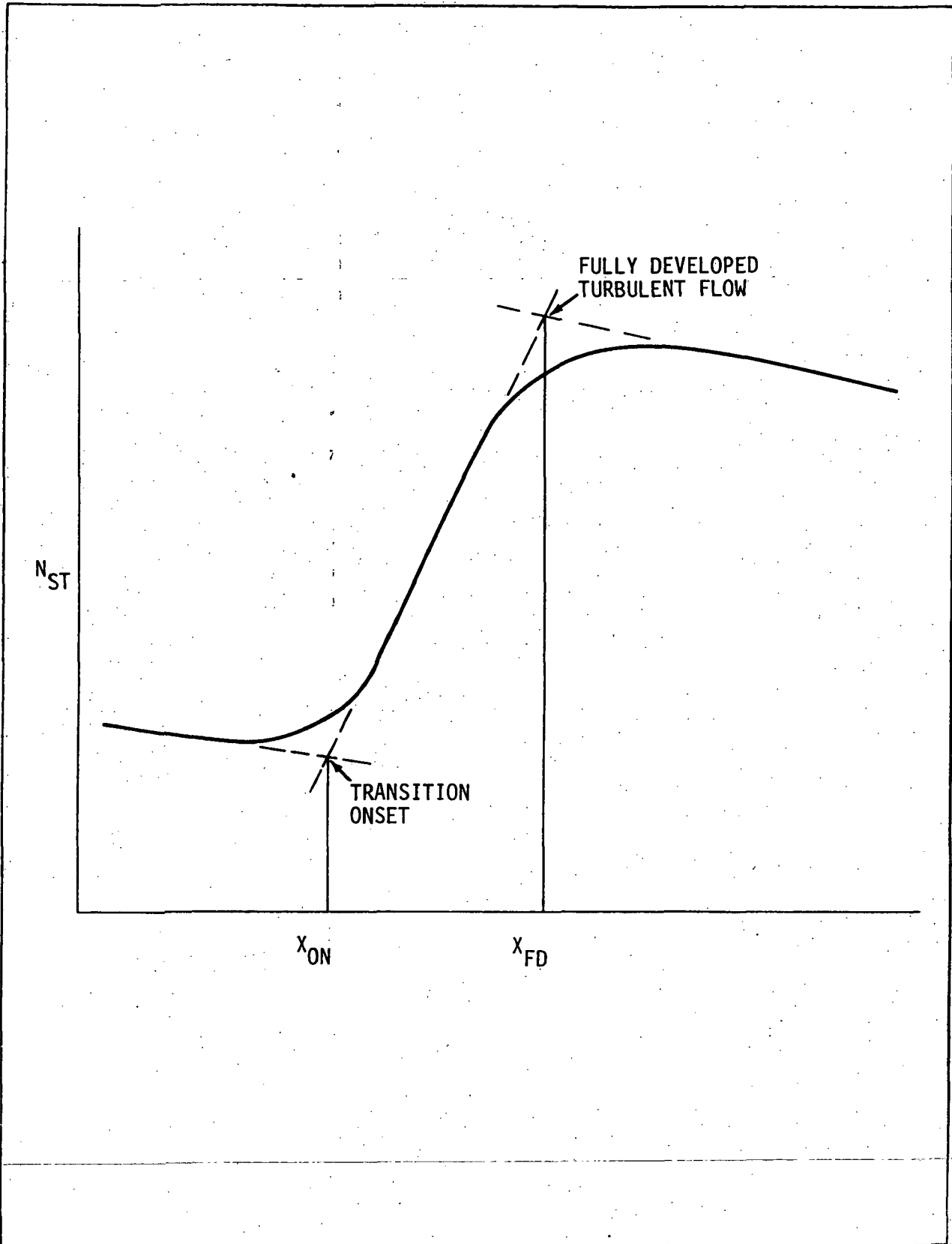


Figure 16. DETERMINATION OF TRANSITION LOCATION

Table II. TRANSITION AT 0° ANGLE-OF-ATTACK FOR SHARP LEADING EDGE
 VARIATION OF R_T WITH $R\alpha/C_m$

Point	$R\alpha/C_m$	x	R_T	Wall	Remark	Transition	M_α
○ ₁	.11 X 10 ⁶	25 Cm.	2.75 X 10 ⁶	Wavy	NASA-TN D-5937	On Set	8.0
□ ₁	.11 X 10 ⁶	22 Cm.	2.42 X 10 ⁶	Flat	NASA TN D-5937	On Set	8.0
○ ₂	.13 X 10 ⁶	22 Cm.	2.86 X 10 ⁶	Wavy	NASA TN D-5937	On Set	8.0
□ ₂	.13 X 10 ⁶	14 Cm.	1.82 X 10 ⁶	Flat	NASA TN D-5937	On Set	8.0
○ ₃	.29 X 10 ⁶	11 Cm.	3.19 X 10 ⁶	Wavy	NASA TN D-5937	On Set	8.0
□ ₃	.29 X 10 ⁶	10 Cm.	2.9 X 10 ⁶	Flat	NASA TN D-5937	On Set	8.0
○ ₁	.11 X 10 ⁶			Wavy	NASA TN D-5937	Fully Developed	8.0
△ ₁	.11 X 10 ⁶			Flat	NASA TN D-5937	Fully Developed	8.0
○ ₂	.13 X 10 ⁶	39 Cms	5.07 X 10 ⁶	Wavy	NASA TN D-5937	Fully Developed	8.0
△ ₂	.13 X 10 ⁶	35 Cms	4.55 X 10 ⁶	Flat	NASA TN D-5937	Fully Developed	8.0
○ ₃	.29 X 10 ⁶	27 Cms	7.84 X 10 ⁶	Wavy	NASA TN D-5937	Fully Developed	8.0
△ ₃	.29 X 10 ⁶	26 Cms	7.54 X 10 ⁶	Flat	NASA TN D-5937	Fully Developed	8.0
□ ₄	.137 X 10 ⁶	26 Cms	3.56 X 10 ⁶	Flat	AIAA Oct. 1967,p.1766	On Set	6.0
△ ₄	.137 X 10 ⁶			Flat	AIAA Oct. 1967,p.1766	Fully Developed	6.0
○ ₄	.137 X 10 ⁶	25 Cms	3.42 X 10 ⁶	Wavy	AIAA Oct. 1967,p.1766	On Set	6.0
○ ₄	.137 X 10 ⁶			Wavy	AIAA Oct. 1967,p.1766	Fully Developed	6.0
○ ₅	.264 X 10 ⁶	10.2 Cm	2.7 X 10 ⁶	Wavy	AIAA Oct. 1967,p.1763	On Set	6.0
○ ₅	.264 X 10 ⁶	25 Cms	6.6 X 10 ⁶	Wavy	AIAA Oct. 1967,p.1763	Fully Developed	6.0
□ ₅	.264 X 10 ⁶	9.5 Cm	2.51 X 10 ⁶	Flat	AIAA Oct. 1967,p.1763	On Set	6.0
△ ₅	.264 X 10 ⁶	20 Cms	5.3 X 10 ⁶	Flat	AIAA Oct. 1967,p.1763	Fully Developed	6.0
○ ₆	.083 X 10 ⁶	20 Cms	1.6 X 10 ⁶	Wavy	AIAA Oct. 1967,p.1763	On Set	6.0
○ ₆	.083 X 10 ⁶	25 Cms	2.1 X 10 ⁶	Wavy	AIAA Oct. 1967,p.1763	Fully Developed	6.0
□ ₆	.083 X 10 ⁶	20 Cms	1.6 X 10 ⁶	Flat	AIAA Oct. 1967,p.1763	On Set	6.0
△ ₆	.083 X 10 ⁶	28 Cms	2.32 X 10 ⁶	Flat	AIAA Oct. 1967,p.1763	Fully Developed	6.0
○ ₇	.13 X 10 ⁶	22.9 Cm	2.98 X 10 ⁶	Wavy	AIAA Oct. 1967,p.1763	On Set	8.0
○ ₇	.13 X 10 ⁶			Wavy	AIAA Oct. 1967,p.1763	Fully Turbulent	8.0

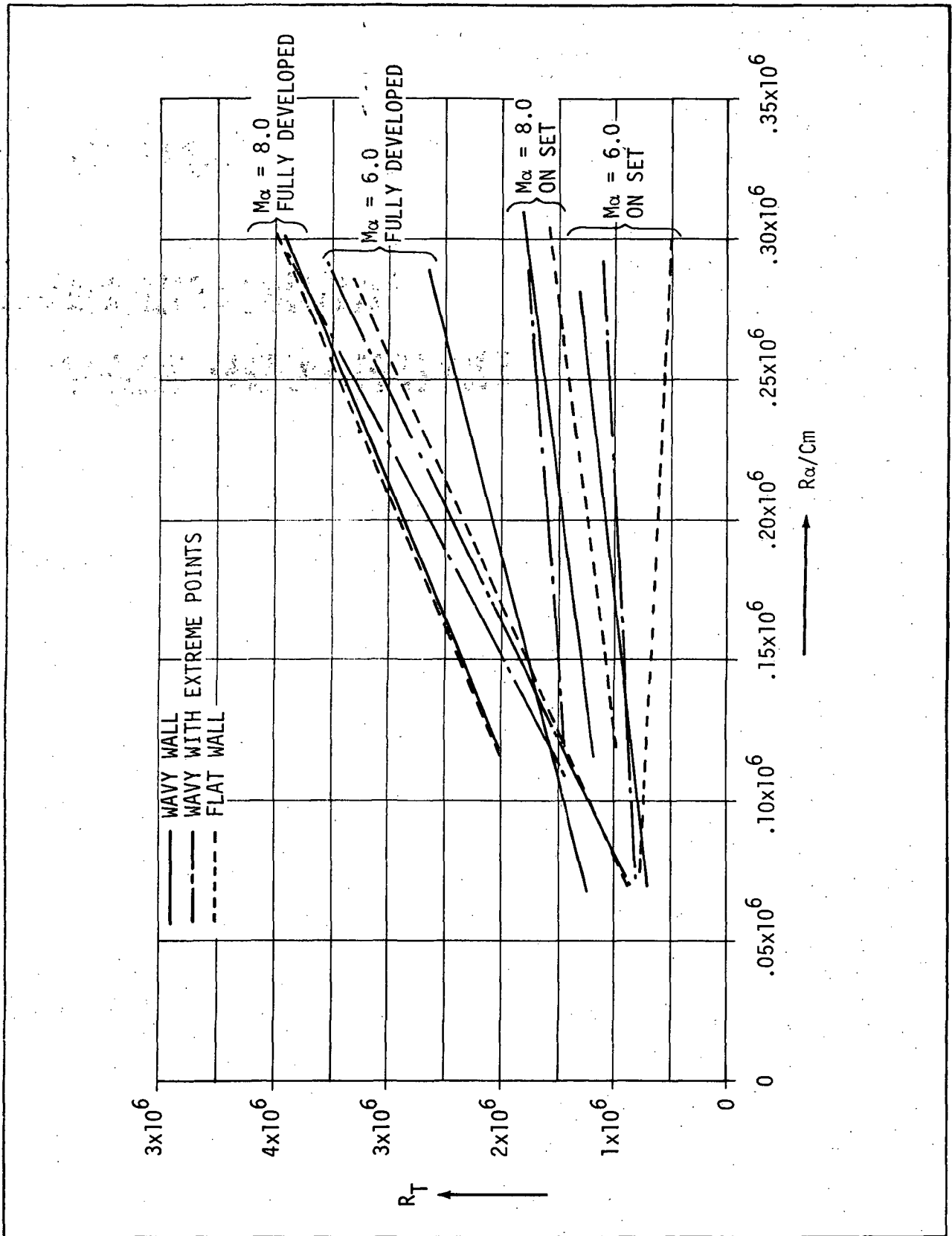


Figure 17. VARIATION OF TRANSITION REYNOLDS NUMBER AS A FUNCTION OF EXTREME POINTS

Appendix E

**SATURN S-II BASE
ENVIRNOMENT REVIEW**

REMTECH Inc.
1744 Oxmoor Road
Birmingham, Alabama 35209

RTR 003-2

D R A F T C O P Y

SATURN S-II
BASE ENVIRONMENT REVIEW

Final Report
on
Subcontract 510-41028

1 December 1971

Prepared for
Northrop Services Inc.
6025 Technology Drive
Huntsville, Alabama 35805

Prepared by
John E. Reardon

6.0 SATURN S-II BASE ENVIRONMENT REVIEW

TABLE OF CONTENTS

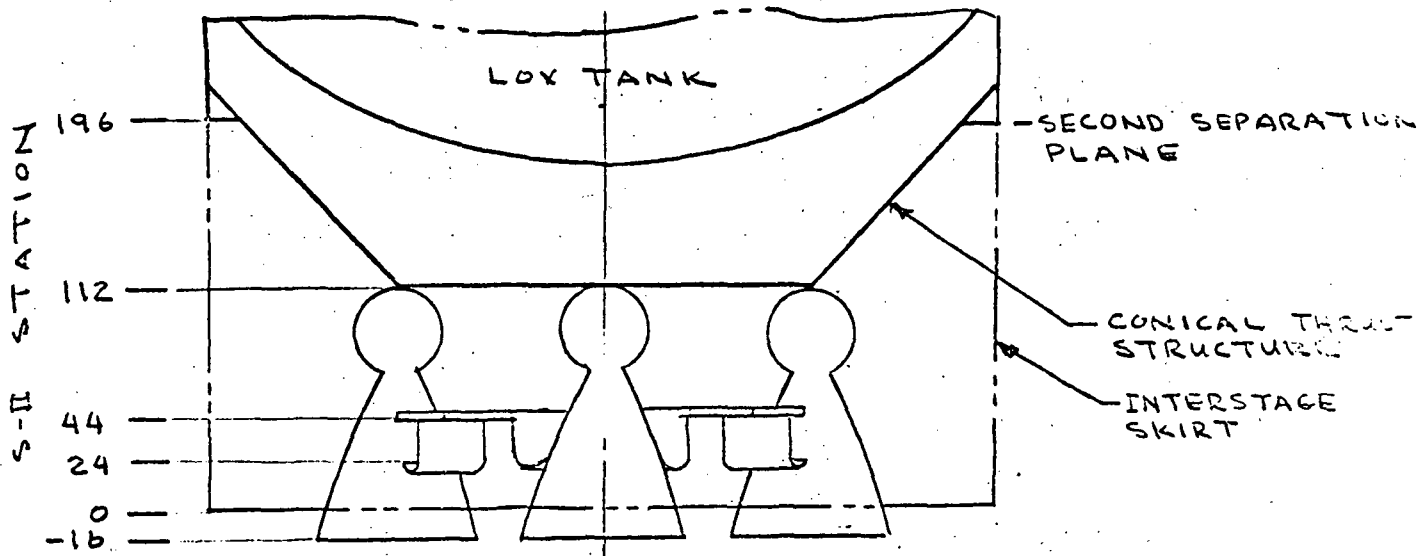
6.1	S-II CONFIGURATION
6.2	J-2 ENGINE CHARACTERISTICS
6.3	PREDICTION METHODS
6.4	MODEL TEST AND PARAMETRIC DATA
6.5	FLIGHT TEST AND PARAMETRIC DATA
6.6	COMPARISON OF MODEL AND FLIGHT TEST RESULTS
6.7	REFERENCES

6.0 SATURN S-II STAGE

6.1 S-II CONFIGURATION

The S-II stage is the second stage of the Saturn V vehicle. Separation from the S-IC stage is accomplished using a dual-plane method. The first separation plane is at station 0 (16 inches forward of the engine exit plane) and separation at this point may occur at altitudes as low as 53.4 km. Approximately 30 seconds after first plane separation, when dynamic pressure has dropped to a negligible value, the interstage skirt is separated at station 196 and falls away without any mechanical guidance.

Propulsion for the S-II stage is provided by a cluster of five rocketdyne J-2 engines arranged as shown in Figure 6.1-1. A heat shield located at station 44 (aft face) protects the components and structure in the base region from the recirculating exhaust gases of the engine cluster. Flexible curtains between the engines and the heat shield permit engine movement, and the outboard engines are gimballed for control. Extreme engine movements from null (including overshoot) are limited to 7.5° in both pitch and yaw or 10.6° resultant toward or away from the center engine (or in the plane normal to this movement). Because of engine and stage misalignments and deflection (compliance) of the thrust structure under load, the exact alignment of the engines is difficult to define. In order to assure that the thrust structure compliance does not cause engine deflections which increase the severity of the base environment, the outboard engines are precanted outboard under no load so that they will not be canted toward the center engine when thrust is applied. The initial precant angle was 1.8 degrees directly away from the center engine, but this has been changed to account for changes in the thrust structure flexibility. The precant angle was increased to 2.3 degrees on the 504 vehicle to compensate for the new thrust structure which was expected to be more flexible. Subsequent evaluation of the thrust structure compliance led to the reduction of the precant angle to 1.3 degrees on AS 505, and a further reduction to 0.6 degrees was required on AS 510 to prevent possible interstage collision.



ENGINE GIMBAL PLANE AT STATION 100

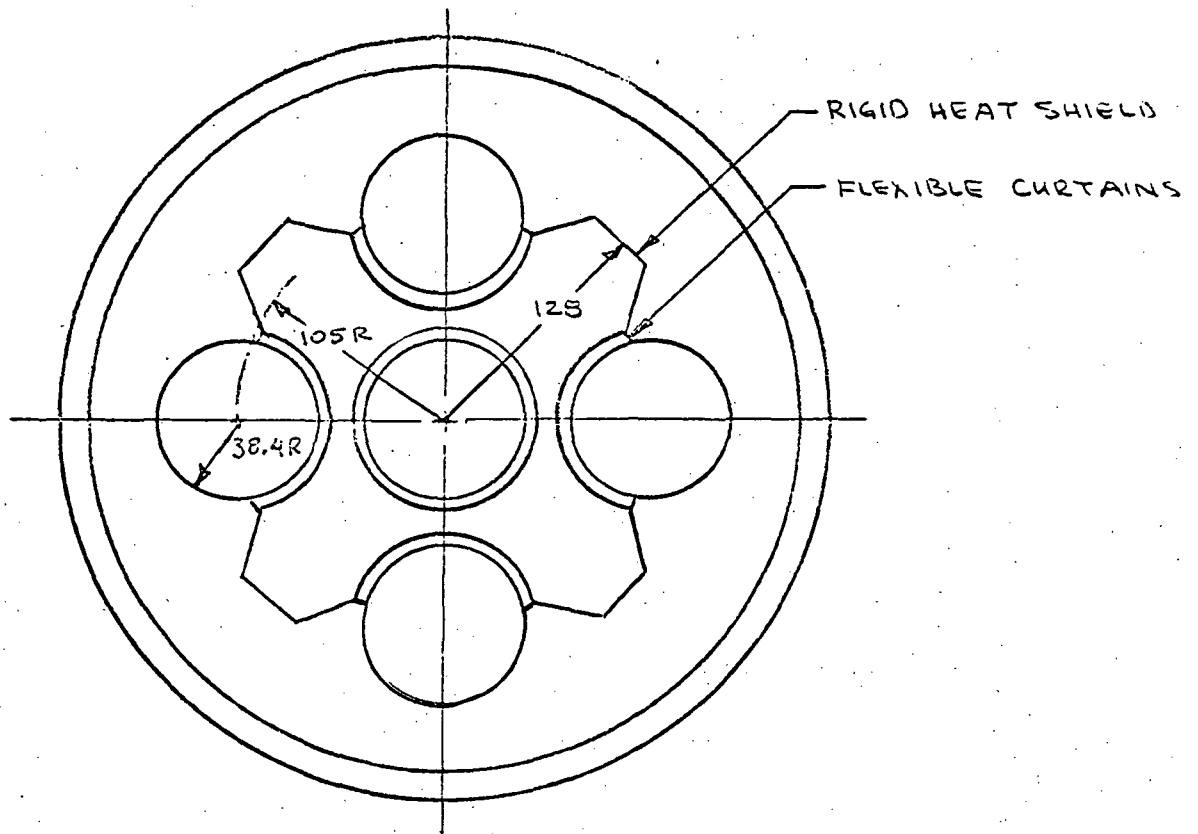


FIGURE 6.1-1 S-II BASE GEOMETRY

6.2 J-2 ENGINE CHARACTERISTICS

The J-2 engine used on the S-II stage was uprated during development by increasing chamber pressure and propellant flow rate. The final flight version produces 230,000 lbf. at altitude with a nozzle stagnation pressure of 718 psia and an overall mixture ratio (oxygen/hydrogen) of 5.5. Although this mixture ratio is maintained for most of the stage operation, the engines are started at a propellant mixture (PMR) of 5.0 then switched to 5.5 with a later shift to 4.7 near the end of the flight. Another propulsion system variable which has been added in later flights is the center engine cutoff (CECO) to reduce the vehicle acceleration. The operation of the propulsion system can be varied to suit particular flight objectives, and some representative values of flight timing are outlined in Table 6.2-1.

TABLE 6.2-1

Representative Flight Schedules

<u>Condition</u>	Time (Seconds) from Ignition				
	Shift to PMR=5.5	Interstage Separation	CECO	Shift to PMR=4.7	Shut- Down
Design Nominal - Case 1	2.5	30	-	280	374
Case 2	2.5	30	-	295	351
Design Engine-out Case 1	2.5	30	-	350	467
Case 2	2.5	30	-	367	437
504 Flight	N/A	28.3	-	287.3	371.0
505 Flight	N/A	28.2	295.5	324.4	388.5

The J-2 has a regeneratively (hydrogen) cooled nozzle with an area ratio of 27.15. Turbine exhaust gases are introduced through 180 orifices between the tubes which form the nozzle wall in a plane approximately 48 inches forward of the exit (area ratio = 13.2). Typical data which illustrate the mixture ratio effect and mass flow of the turbine exhaust are given in Table 6.2-2.

TABLE 6.2-2

Nominal J-2 Engine Propellant Flow Rates

	Combustion Chamber	Turbine Exhaust	Overall Engine
Oxidizer flow (lbm/sec)	454.39	3.49	457.88
Fuel flow (lbm/sec)	79.54	3.71	83.25
Total flow (lbm/sec)	533.93	7.20	541.13
Mixture ratio (O/F)	5.71	0.94	5.50

Exhaust plume characteristics vary with mixture ratio and chamber pressure. Typical gas property variations for an overall mixture ratio of 5 are presented in Table 6.2-3, with corresponding plume isomachs shown in Figure 6.2-1. These data from reference 6.8 were obtained using the last right running characteristic as a start line with smoothing of the flow directions near the nozzle centerline to eliminate negative flow angles. The Mach Number along the start line varies from 3.39 at the lip to 4.1 on the axis.

TABLE 6.2-3

Thermodynamic Properties - J-2 Engine Plume

<u>Mach Number</u>	<u>Pressure (PSF)</u>	<u>Temperature (°R)</u>	<u>Specific Heat Ratio</u>
5	63.4	1654	1.2937
6	16.7	1207.	1.3184
7	5.5	915.	1.3342
8	2.3	721.	1.3438
9	0.97	579.	1.3503
10	0.40	466.	1.3551
12	0.05	331.	1.3603
15	0.002	214.	1.3642
20	0.0002	121.	1.3670

Mixture Ratio = 5.17 Chamber Pressure = 680 psia Chamber Temperature = 5958°R

Molecular Weight = 12.423

Propellant analysis based on equilibrium composition during expansion.

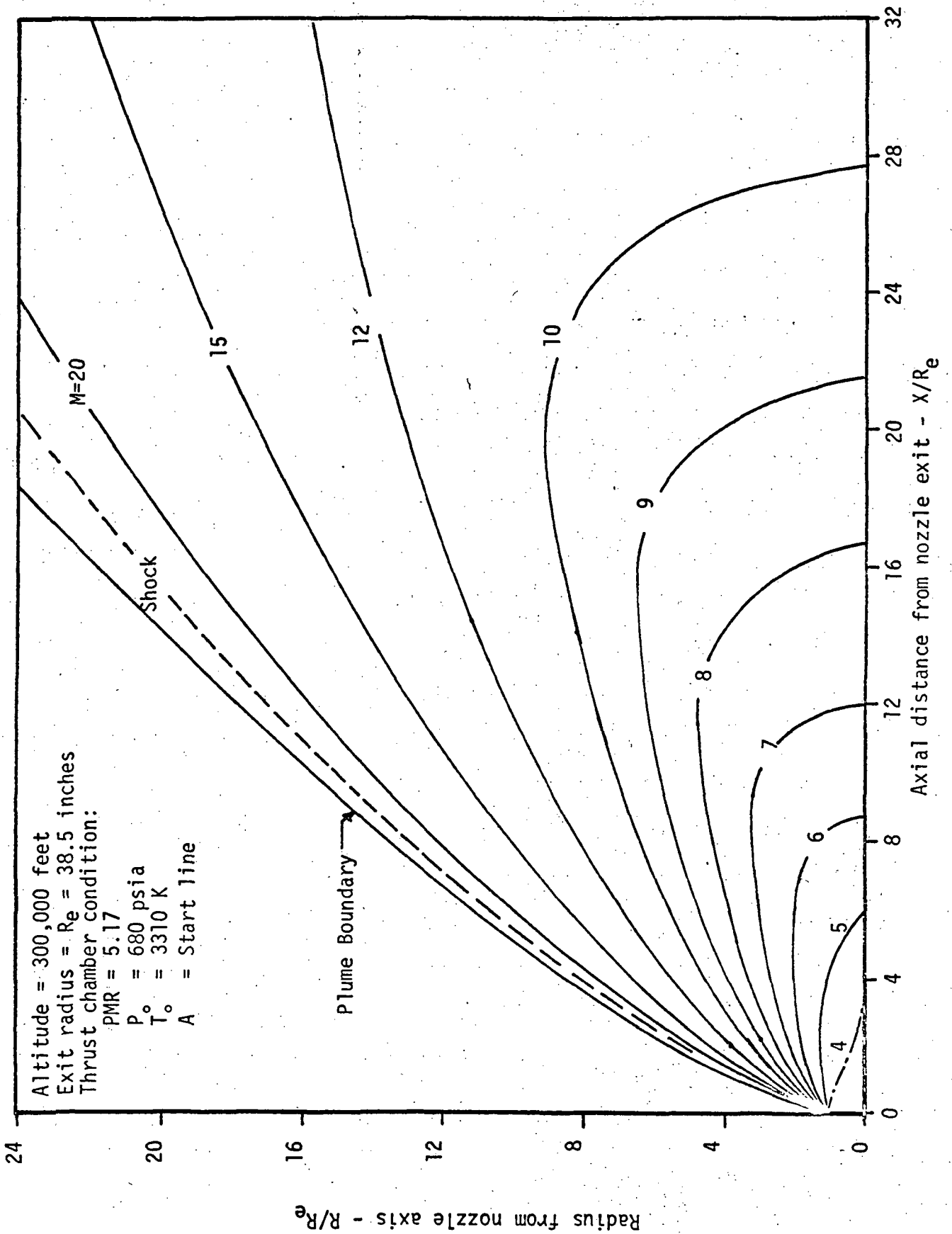


Figure 6.2-1 Typical J-2 engine plume.

6.3 PREDICTION METHODS

Pre-flight base heating predictions for the S-II stage were based on model test results for convection and analytical predictions of radiation. Since the S-II stage operates at altitudes which cannot be conveniently duplicated in continuous flow test facilities, the short duration base heating test technique developed by Cornell Aeronautical Laboratory was used. This technique had been applied successfully to the six-engine S-IV configuration which operated under similar altitude conditions. Experience with the S-IV indicated that flight measurements were in reasonably good agreement with unscaled results from the 0.1 scale short duration model, so the same technique of using unscaled model data was chosen to define convective heating on the S-II. Although an increase in scale normally leads to a decrease in the heat transfer coefficient, there has been experimental and analytical evidence (ref. 6.9) to indicate the recovery temperature will increase with scale (without turbine exhaust injection in the nozzle). The opposing effects of scale on the heat transfer coefficient and recovery temperature produces characteristics similar to those depicted in Figure 6.3-1 in which use of the model results would produce a conservative heat shield design. Because of problems with the turbine exhaust simulation on the model and the apparent predominate effect of the turbine exhaust in cooling the reversed flow, the prediction method proved to be too conservative.

During the model test program it was found that any inboard deflection of an outboard engine would cause an increase in convective heating in the base region. A full actuator movement (in one plane) of 7.5 degrees combined with the corresponding trim deflections from other engines caused the heat shield convective heating to increase approximately 400 percent. Even moderate deflections of less than 1 degree indicated significant increases in heating. Due to the sensitivity of the heating to gimbelling and the inability to characterize the deflection effects so that they could be systematically investigated, it was necessary to

test failure cases and the resulting trim deflections for each failure mode likely to be of interest. Initially, generous 3σ control movements were included with trim and failure effects in the test patterns, but the high heating encountered caused a change to more realistic conditions. These included the failure condition to be tested with 3σ engine misalignments added along with the resultant trim deflections. After a time, the sensitivity to deflection caused a more thorough investigation of engine deflections, and it was found that structural compliance of the thrust cone caused significant inboard deflections which were added to the misalignment and trim deflections. The resulting high heating rates for the nominal and outboard-engine-out conditions caused concern that the heat shield design might be marginal, so the engines were precanted outboard as described in the previous section (6.1).

Because of the significant scale effects anticipated in the water vapor radiation from the exhaust plume, it was necessary to rely on analytical techniques to estimate the radiance to the heat shield. Two independent radiance estimates were made using different techniques. The design environment (ref. 6.6) was calculated by NAR using total emissivity data of Hottel, and later spot checks were made using a band model representative of the water vapor radiation with data averaged over 25 cm^{-1} spectral intervals. In spite of the differences in the two methods and the approximations required in predicting the plume properties, good agreement was obtained between both prediction methods and measured flight data.

In the estimate for the design environment, Hottel's approximate method of total emissivity gradients was used in a computer program to evaluate the radiant intensity along lines of sight passing through the plume predicted for the 5 engine cluster (ref. 6.11). The incident radiative flux at a point of interest was obtained by integrating results from various lines of sight over the solid angle

representing the field of view subtended by the plumes. This program used a table of emissivity data taken from Hottel's data (ref. 6.10) for a total pressure of one atmosphere and a water vapor particle pressure of zero.

Exhaust plume properties required for use with the radiation program were predicted using a method-of-characteristics program for the free plume with estimates of the properties in the interaction regions between plumes. The pressure and temperature in the interaction regions was assumed to be uniform normal to the impingement plane with variations in the axial direction. These variations were estimated by using the values which would be produced by an oblique shock which would turn the undisturbed streamline into the impingement plane. The boundaries of the impingement region in a plane normal to the impingement plane were estimated to be approximately elliptical in shape. The major axis was equivalent to the cord formed between intersecting points on the circular plumes and the minor axis was estimated from photographs of model plumes.

The later verification of the design radiation environment (ref. 6.7) was made using an analysis based band model representation of the water vapor radiation and a different method of approximating the exhaust plume.

The radiation program integrated radiation along various lines of sight over the field of view visible at any particular point of interest. It used a method of calculating the gas transmissivity based on random (or statistical) band models with a modified Curtiss-Godson approximation to account for property variations along the lines of sight. Although the data and computer program used provided for integration using spectral intervals of 25 cm^{-1} and spatial intervals along the lines of sight of 3 inches, larger intervals were used to reduce computation time. Spectral intervals of 100 cm^{-1} were used with an indicated error of less than one percent based on the typical line of sight

illustrated in Figure 6.3-2. Spatial integration was carried out by averaging property values taken at 3 inch intervals along the line of sight as long as the temperature change was less than 200 R. This procedure essentially transformed the line of sight into a series of isothermal slabs of varying thickness. The slabs were terminated whenever the temperature variation exceeded 200 R or the slope of the temperature curve (dT/ds) changed sign. This spatial integration procedure reduced the computation time 75 percent for the typical line of sight (Fig. 6.3-2) compared with a constant 3 inch integration interval. The indicated error was less than one percent.

The exhaust plume for the five-engine cluster was approximated by using an axisymmetric method-of-characteristics program with the flow configuration shown in Figure 6.3-3. The flow was expanded into a cone at the nozzle exit then turned into a cylinder with a radius equal to the distance from the nozzle axis to the impingement plane. It was necessary to use a 45° angle cone rather than one approximating the free boundary so that an oblique shock could exist at the cone/cylinder corner. The arrangement of radial planes used in the flow field approximation is shown by Figure 6.3-4, and a typical section of the exhaust plume is illustrated in Figure 6.3-2.

The points in the base region at which the radiant flux was calculated are illustrated in Figure 6.3-5 and a comparison of the results with the previous calculation (ref. 6.6) is presented in Table 6.3-1. In general, the predictions of the two methods are in good agreement.

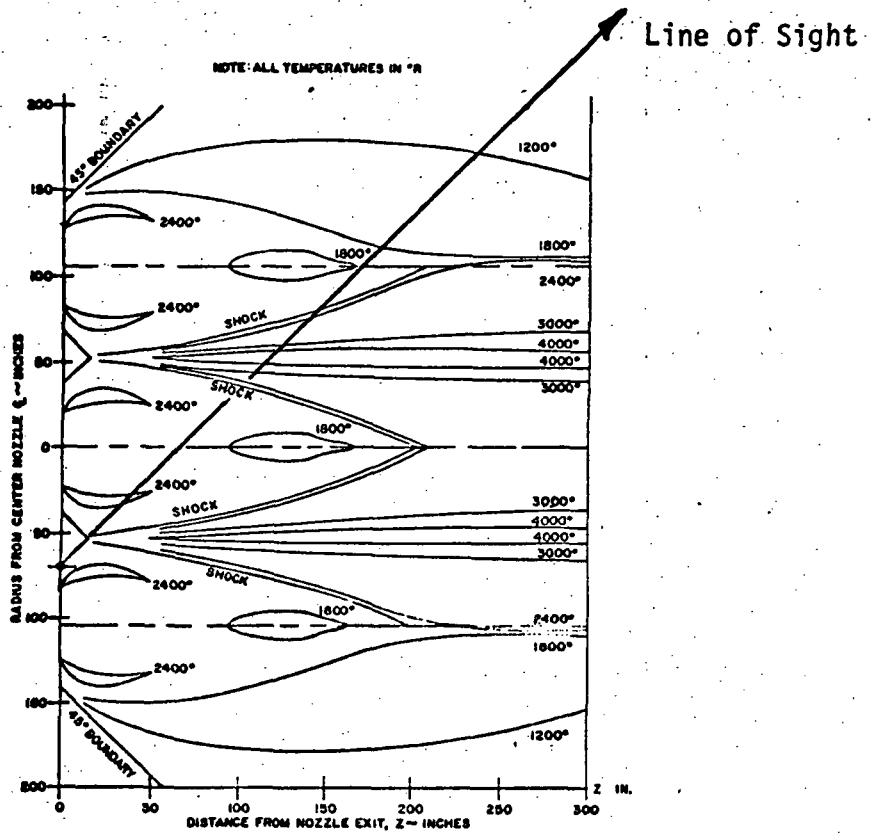
TABLE 6.3-1

Results or Radiation Predictions

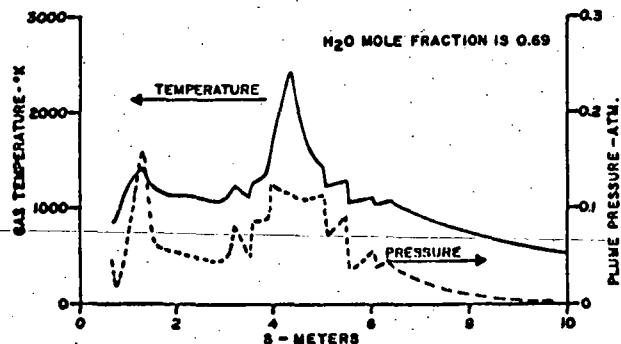
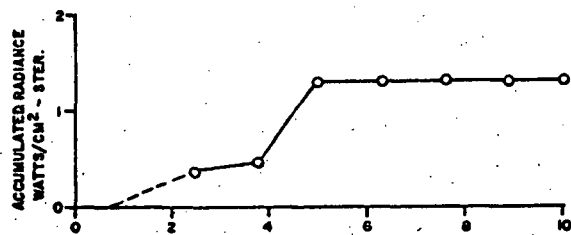
Point	Coordinates ¹ - inches			Radiative Flux - watts/cm ²	
	X	Y	Z	Total Emissivity Ref. 6.6	Band Model Ref. 6.7
Heat Shield - HS-1	52.5	0	-60	0.90	1.11
	HS-2	70.7	-70.7	-60	1.18
Nozzle Exit ² - NE-1	66.6	0	0	4.20	4.41
	NE-2	66.6	0	0	2.04
Thrust Structure ³ - TS-1	140.0	-140.0	-212	0.17	0.15
	TS-2	124.5	-124.5	-212	0.07
Interstage - IS-1	140.0	-140.0	-16	0.73	0.79
	IS-2	140.0	-140.0	-16	1.25

Notes:

1. See Figure 6.3-5
2. Surface at NE-1 faces aft at the nozzle exit, while NE-2 faces laterally inboard.
3. Without the interstage skirt in place.



(b) Typical flow field section across three nozzle exits.



(a) Properties and Accumulated Flux

Figure 6.3-2 Typical line of sight for S-II radiation prediction.

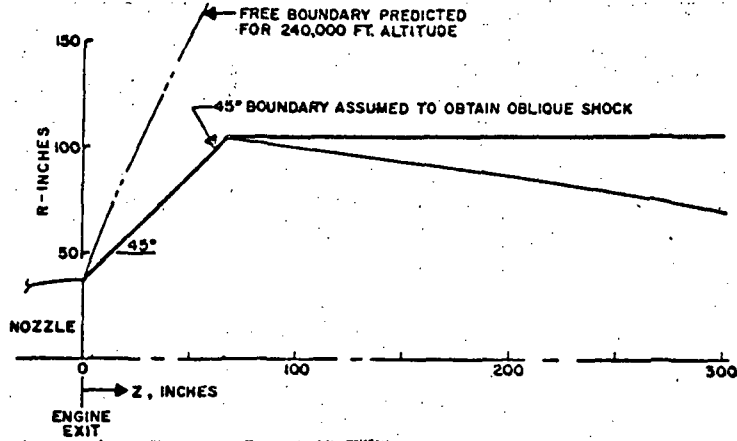


Figure 6.3-3 Configuration for axisymmetric flow field approximation.

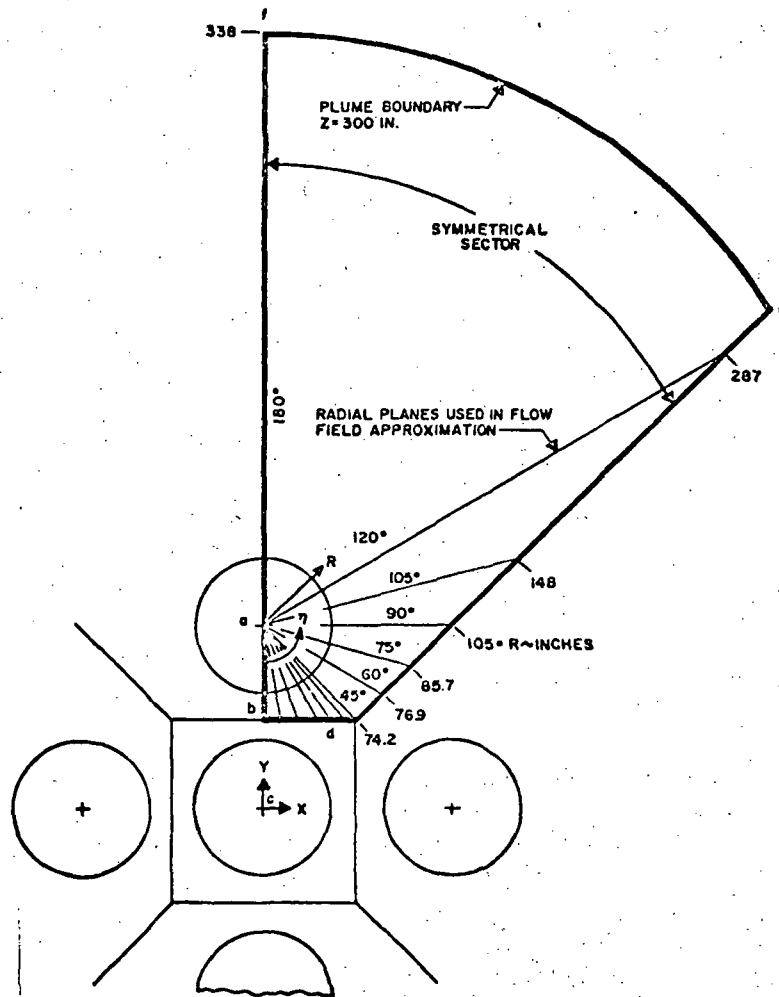


Figure 6.3-4 Location of planes used in approximating the S-II flow field.

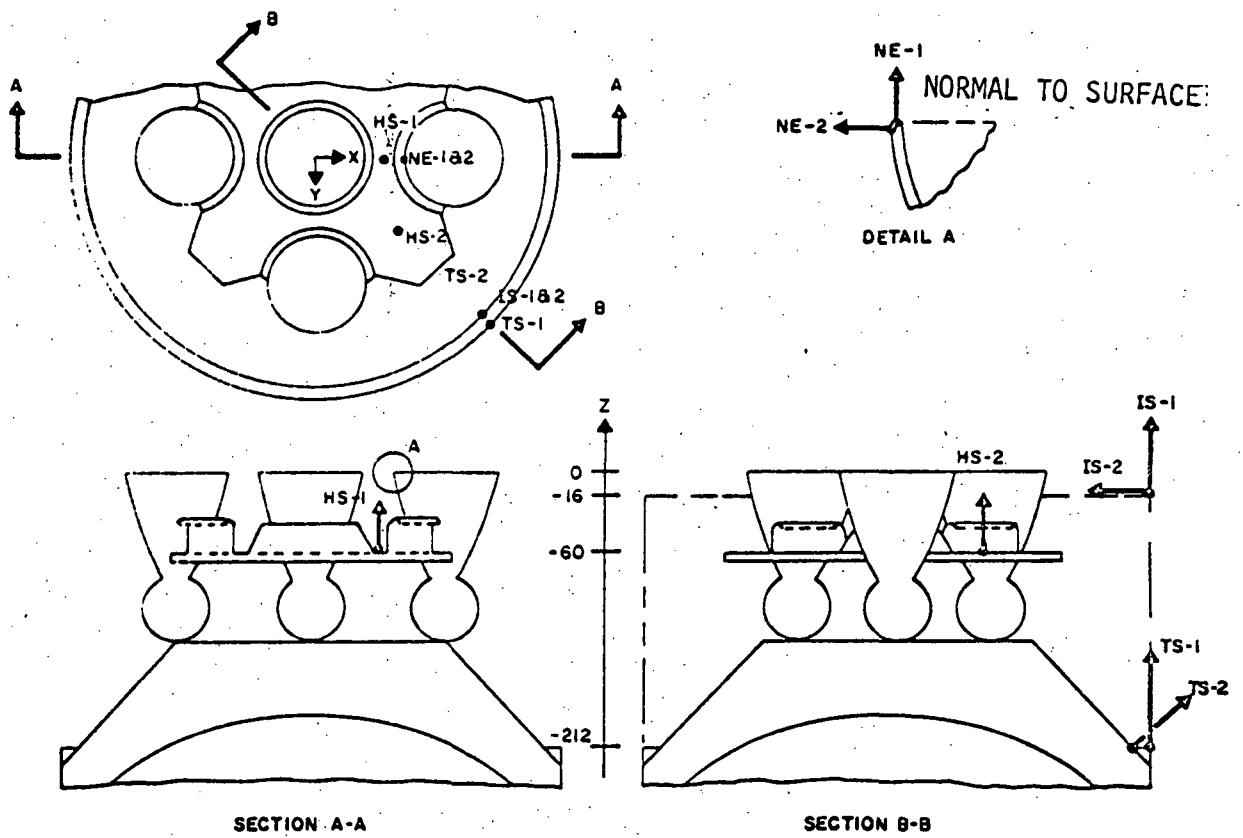


Figure 6.3-5 Location of points in the base region at which band model calculations were made.

6.4 MODEL TESTS AND PARAMETRIC DATA

All base heating tests on the Saturn S-II were conducted using short-duration tests with no simulated external flow. Two models were used. First, a model in which the base geometry could be varied was tested in 1962 (ref. 6.1) to evaluate the effects of the number and spacing of the engines. Subsequent testing was performed using a model of the prototype base region. Tests of this model were conducted first at Cornell Aeronautical Laboratory during 1963 and 1964 (ref. 6.2) and then at the Impulse Base Flow Facility at MSFC in 1964 and 1965. Both of the test models were 0.04 scale and used scaled J-2 nozzle contours (area ratio of 27.5 and exit diameter of 3.08 in.).

Data from the two tests will be presented along with brief descriptions of the models. In presenting the data, effects of parametric variations will be emphasized rather than distributions of heating rates in the base region.

Parametric Model Tests

The parametric test model, Figure 6.4-1, was designed so that the engine and base spacing could be varied. There was a movable cylindrical skirt to simulate the interstage structure and a flame deflector to simulate the type heat shield under consideration for the S-II stage. In addition to the parametric variations available in the five engine configuration, the center J-2 model nozzle could be removed for 4-engine tests. Due to the large number of variations tested, much of the data available comes from a single run with no repeat runs to check the validity of the data. Since repeat runs of a given model configuration often exhibit data scatter of ± 20 percent about the mean, caution should be used in evaluating the data as being an absolute indication of the parametric variation under consideration.

Model data were recorded by photographing oscilloscopes and was usually limited to about 20 measurements per test firing. Instrumentation on the model

base consisted of 36 calorimeters and 41 surface pressures. In addition, a contoured strip was available for attachment to the exterior of the nozzles which had 27 calorimeters arranged in three rows. Calorimeters were the thin film type with a platinum resistance element deposited on a Pyrex substrate. Pressure measurements were made using piezoelectric transducers mounted to minimize acceleration effects from the model firing.

Parametric variations during the test included engine spacing, base location, interstage length, flame deflector position, ambient pressure, and combustion chamber pressure. Results of these variations taken from reference 6.1 are presented in Figures 6.4-2 through 6.4-15. Brief comments on the results of each variation are presented below.

Engine Spacing - Results of varying the engine mounting circle diameter presented in Figures 6.4-2 and 6.4-3 illustrate the different characteristic distributions of heating and pressure and show a marked reduction of heating with increasing engine spacing on the four engine configuration. The trend in heating rate on the five engine configuration is not well defined due to lack of data, but the trend in base pressures indicate that the heat rates should be expected to decrease with increasing engine spacing.

Base Location - Effects of varying the position of the base forward of the nozzle exits are shown in Figure 6.4-4 for the five-engine configuration. This illustrates the increasing base pressure and heating rates which occur as vent areas between the engines are reduced by moving the base toward the nozzle exit plane. Results of the four-engine configuration, Figure 6.4-5, follow the same trend except for the case where the base is located at the nozzle exits. The shift in pressure distribution at this point and the slight reduction in heating rate may indicate a significant change in the base flow pattern, but since the data represent only one test run and the heating and pressure trends do not agree, no conclusion seems justified.

Interstage Length - As the interstage length is increased from flush with the base to a position in the plane of the nozzle exits an increase in base pressure would be expected particularly in the outer portions of the base. This general trend is evident in the five-engine results, Figure 6.4-6, but in the outer areas of the four-engine base, Figure 6.4-7, insufficient pressure data are available and the trends in heating are not consistent. Much of the variation in the inner region of the base is likely to have resulted from run-to-run variations rather than the effect of the interstage.

Flame Deflector Position - In this configuration the flame deflector is sealed around the nozzles and represents a heat shield while the model base can be considered to represent the vehicle thrust structure. The important effects are the variation in base heating rates near the edge of the base and the effect of the interstage in increasing both base pressure and heating rates. These effects are illustrated in Figure 6.4-8 for the 5-engine configuration, but since data on the 4-engine configuration in Figure 6.4-9 are limited to the inner region of the base, the trend near the edge of the base was not documented.

Ambient Pressure - Base pressures and heating rates are presented in Figures 6.4-10 through 6.4-13, but no effects of pressure are apparent except in the outer base regions. This result is not unexpected since the range of altitudes for S-II operation did not go low enough for the ambient pressure to have a significant influence.

Combustion Chamber Pressure - Simulated model combustor pressure was varied from approximately 300 to 700 psia with representative effects on base pressure and heat transfer rate as shown in Figure 6.4-14. The indicated variation of base recovery temperature with chamber pressure and typical data taken for recovery temperature are illustrated in Figure 6.4-15. The variation in heating rate at each base temperature is an indication of the uncertainty in a particular measurement. Because of the uncertainty in recovery temperature on this test,

results of the chamber pressure effects are not considered to be as accurate as those obtained later in the research test program reported in reference 6.9.

Prototype Model Test

The prototype test model, Figure 6.4-16, was designed to simulate the flight configuration as closely as possible. Several components were simulated on the conical thrust structure and a removable interstage skirt was provided to simulate the base configuration during the time between first and second plane separations. The model was initially intended to operate at a propellant mixture ratio (PMR) of 5 with a nozzle stagnation pressure of 632 psia, but during the tests, mixture ratio of the model was varied from 4.5 to 5.5 with nozzle pressures of 546 to 715 psia to cover the range of PMR planned for the prototype.

Flexible rubber boots were used on the model to simulate the flexible heat shield curtains on the prototype and allow engine gimbaling to study various misalignment and malfunction control patterns. Preliminary tests were conducted with round heat shields representing full scale diameters of 210, 228, and 246 inches before the final 256 inch configuration shown in Figure 6.4-16 was chosen.

The prototype model was first tested at Cornell Aeronautical Laboratory (reference 6.2) in a program consisting of approximately 350 runs and then it was transferred to MSFC for a test of approximately 700 runs. (MSFC results were used for design, but have not been published for other use.) Tests were primarily for heat transfer with comparatively little base pressure data taken. The large number of runs were required by the great number of configuration variables and the policy of making several repeat runs in tests at MSFC in an attempt to assure the data was representative. The regions of interest for heat transfer data were the nozzle walls, heat shield, engine components forward of the heat shield, and the thrust structure. Tests with the interstage skirt

indicated that its presence had a large effect on the thrust structure and region forward of the heat shield, but effects on the heat shield and nozzle walls were not significant and often difficult to define. The parametric variation which had the greatest effect on heating rates on the nozzles and heat shield aft surface was engine deflection. Approximately 30 deflection patterns were tested which represented engine and gimbal actuator failures as well as normal engine misalignments.

Since most of the engine deflection patterns represented assumed misalignments and actual control responses, there was generally no step by step variation of a single gimbal angle to evaluate its effect, so the results are difficult to characterize for general application. Considering this problem, the results to be presented are intended to demonstrate the general effect that was observed without going into details of specific deflection patterns. The parametric variations to be reviewed include the effect of heat shield size, interstage structure, turbo-pump exhaust simulation, out-board engine failure, single gimbal actuator failure, dual gimbal actuator failure, and variations in mixture ratio.

Heat Shield Size - Heat shield size was increased in an attempt to reduce heating rates in the thrust cone (structure) area since no thermal protection was planned for the structure and components mounted on the structure had relatively low temperature limits. Initial experiments used heat shield diameters of 210, 228 and 256 inches (full scale) with both flat and turned edges as shown in Figure 6.4-16. Based on the results of these tests, the 256 inch trapezoidal heat shield was chosen for the prototype and was used on almost all of the model tests at MSFC. During tests at CAL it was doubtful that steady flow was achieved on the thrust structure and the results of heat shield size on heating rate, shown in Figure 6.4-17, did not present a consistent trend. However, there was a general indication of a reduction in heating with increasing heat shield size, and tests indicated that heating with the smaller heat shield was more likely

to increase with increasing altitude while the large heat shield did not indicate this trend. Later tests of longer duration at MSFC gave more confidence of steady flow being attained on the thrust cone and the measured heating rates were slightly higher, but there was no indication of a better definition of heat shield size effects.

Interstage Skirt - The interstage structure extends from the first separation plane, Station 0, to the second separation plane, Station 196, as indicated in Figure 6.4-16. Although there sometimes appear to be effects of the interstage on the heat shield aft side heating distribution, there was no consistent indication that the peak heating increased. The primary effect of the interstage is on the thrust cone heating rates as illustrated in Figure 6.2-18. It is apparent that the interstage traps the flow off of the heat shield and directs it toward the thrust cone. The data shown is on a radial line between outboard engines where the heating is the highest. Lowest heating on the thrust cone is on a radial line through an outboard engine, but heating in this location is also increased significantly by the interstage.

Turbo-Pump Exhaust - The turbo-pump exhaust injection into the J-2 nozzle described in Section 6.2 was simulated on the nozzle by fifty 0.067 inch diameter holes drilled normal to the nozzle wall. Hydrogen heated to the estimated turbine exhaust gas temperature (1140°R) was used in the model simulation. The mass flow rate was simulated assuming an orifice discharge coefficient of 0.88 with sonic flow and a 16 psia stagnation pressure. Simulation of the mass flow rate with the lower molecular weight hydrogen causes an increase in the injection velocity and momentum and increases the relative volume in the base region. Simulation was also doubtful because of the probable different effects the injection would have on the nozzle and full scale boundary layer and possible separation and reattachment. In addition to these theoretical inaccuracies in simu-

lation, it was also difficult to time the flow of heated hydrogen to correspond to the short test event. If the hydrogen arrived too soon, it flowed into the base region causing instrumentation problems and required more time for the initiation of steady flow when the combustor fired. This is particularly important in regard to the thrust cone heating. Because of the piping the gas passed through on the way to the manifold around the model nozzle, there was a tendency for the gas to cool, but three turbine exhaust qualification runs indicated the desired temperature could be maintained by using a supply reservoir temperature of 1460R. The effects of the simulated turbine exhaust in lowering the peak heating rates are illustrated in Figures 6.4-19 through 6.4-22, but possible increases in some regions are also indicated in Figures 6.4-21 and 6.4-22. Although turbine exhaust injection is expected to lower the base recovery temperature since it cools the plume boundary, it was decided to base the S-II thermal environment on testing without the simulated injection because of the difficult and questionable simulation and the expected increase in recovery temperature with scale due to boundary layer effects.

Outboard Engine Failure - The significant effects resulting from an outboard engine failure are due to the engine deflections required for trim rather than the absence of the outboard exhaust plume. Experimental outboard engine failure patterns and the resulting increase in peak heat shield heating are illustrated in Figure 6.4-23. As the engines deflect, the location of the peak heating on the heat shield moves in the direction of the inboard deflection component and occurs at a smaller radius from the base center.

Single Actuator Failure - Deflection patterns which were tested as being representative of a single actuator failure at 7.5, 5, and 3 degrees are shown in Figure 6.4-24 as cases 3C, 5, 6 and 6A. In addition, three variations of combined engine misalignment and thrust structure compliance patterns (Cases 9,

9A and 9B) are considered as being representative of the type of flow pattern resulting from single actuator failures. As the gimbal angle increases, the peak heating moves across the heat shield (towards the outboard engine at which the maximum deflection component is pointed) and finally occurs on the flexible curtain attachment flange at the nozzle for the maximum angle tested. To illustrate this effect, results are presented in Figure 6.4-24 for both the rigid heat shield and the flexible curtain attachment flange. The results presented for the heat shield illustrate the most significant effect of a single actuator failure, but other effects have been observed. Heat rates on the nozzle wall increase for failures which direct the engine inboard, and increases in thrust cone heating have been noted when the failure directs the engines outboard.

Dual Actuator Failure - Movement of both actuators in an inboard direction causes significant increases in heating on the heat shield and center nozzle. In the extreme case of 7.5° deflection in pitch and yaw, plume impingement on the center nozzle was evident on the model, and good correlation was obtained between the peak measured heating and predictions using stagnation point heat transfer analysis. The effects of dual actuator deflection on the heat shield are illustrated in Figure 6.4-25. As in the case of a single actuator failure, the point of peak heating moves from the rigid portion of the heat shield to the flexible curtain at large deflection angles. Effects of dual actuator movement on the environment of the center nozzle are illustrated in Figure 6.4-26. The extremely high heating rates near the nozzle lip rapidly decrease as the distance from the plume impingement point increases, so there is no appreciable increase in heating on the forward portion of the nozzle.

Mixture Ratio - As the mixture ratio is increased on the J-2 engine, the total propellant flow rate also increases, so the chamber pressure varies with

mixture ratio as indicated in Table 6.4-1. The resulting heating rate variations

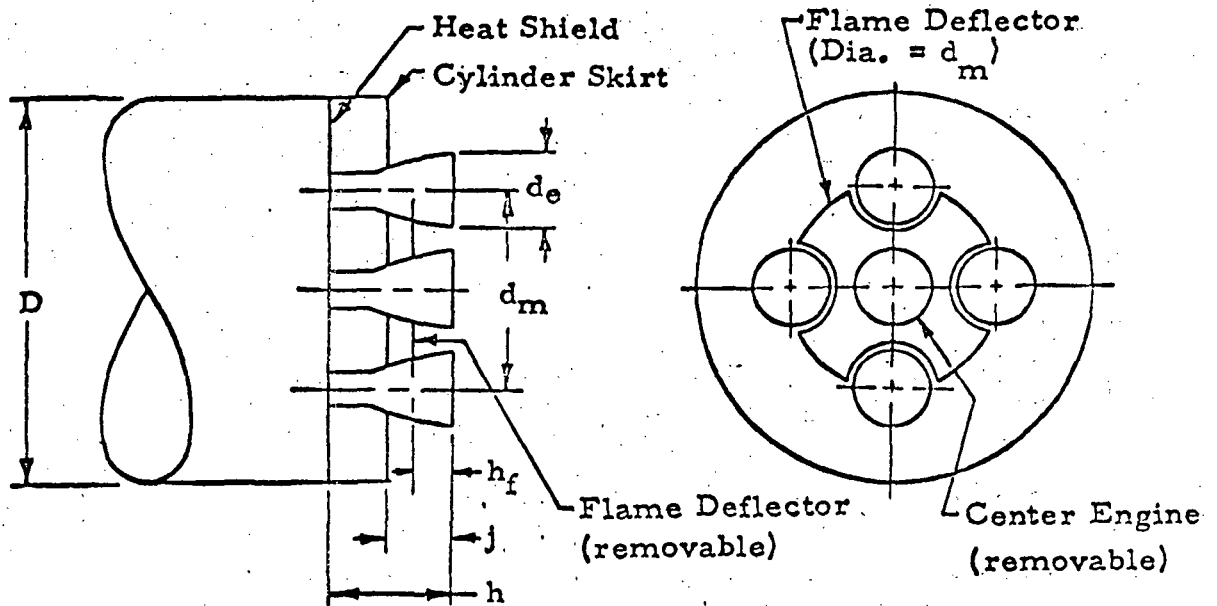
Table 6.4-1

<u>PMR</u>	<u>Predicted Nozzle Pressure-P_o-psia</u>	<u>Stagnation Temperature-T_o °R</u>	<u>P_o/P_o(5.0)</u>	<u>T_o/T_o(5.0)</u>
4.5	546	5626	0.865	0.947
4.7	584	5717	0.924	0.970
5.0	632	5891	1.0	1.0
5.5	715	6101	1.131	1.042

will be affected by both the pressure and temperature change. Test results were conclusive from a qualitative standpoint that the heating rates and base pressure increase with mixture ratio, but quantitative results were not significant since test-to-test variations in heating are comparable to a significant portion of the anticipated variation in heating.

FIGURE 6.4-1

SATURN S-II PARAMETRIC MODEL ARRANGEMENT



Nominal Configuration

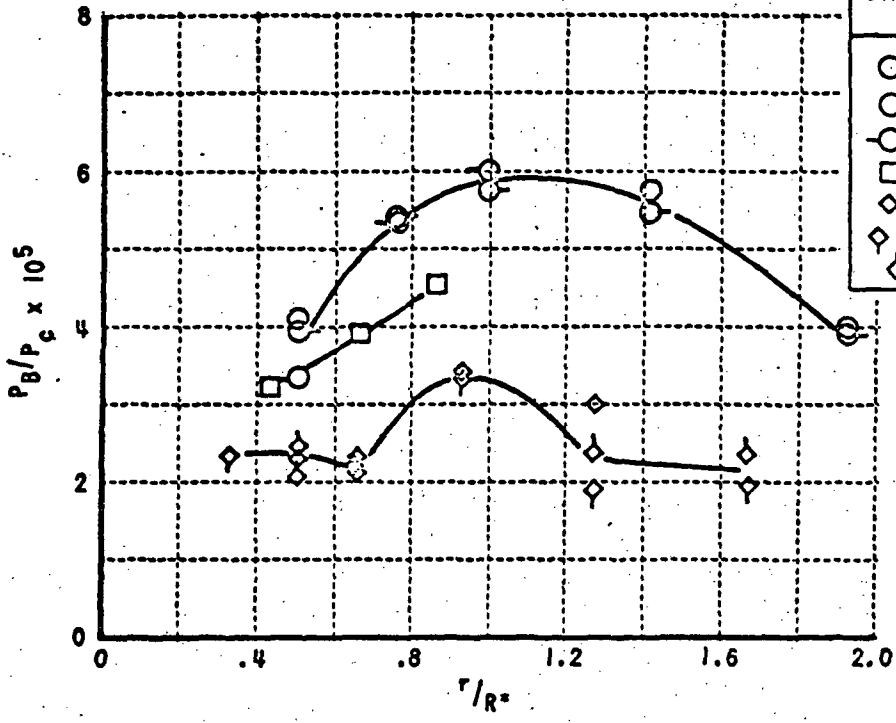
Dimension	Model Scale Inches	Full Scale Inches	Dimensionless Ratio
D	15.64	396	
d_e (I.D.)	3.08	77	$d_e/D = 0.1944$
d_m	8.40	210	$d_m/D = 0.5303$
h	1.72	43	$h/D = 0.1086$
j	1.72	43	$j/D = 0.1086$

Chamber pressure = $P_R = 632$ psia

No Flame Deflector

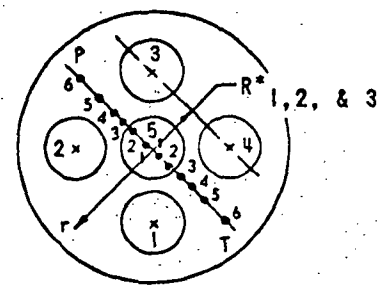
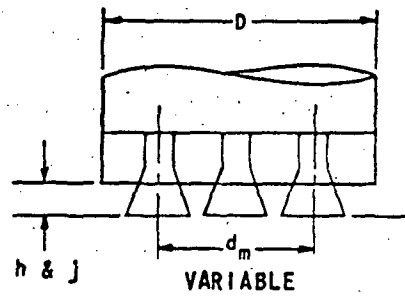
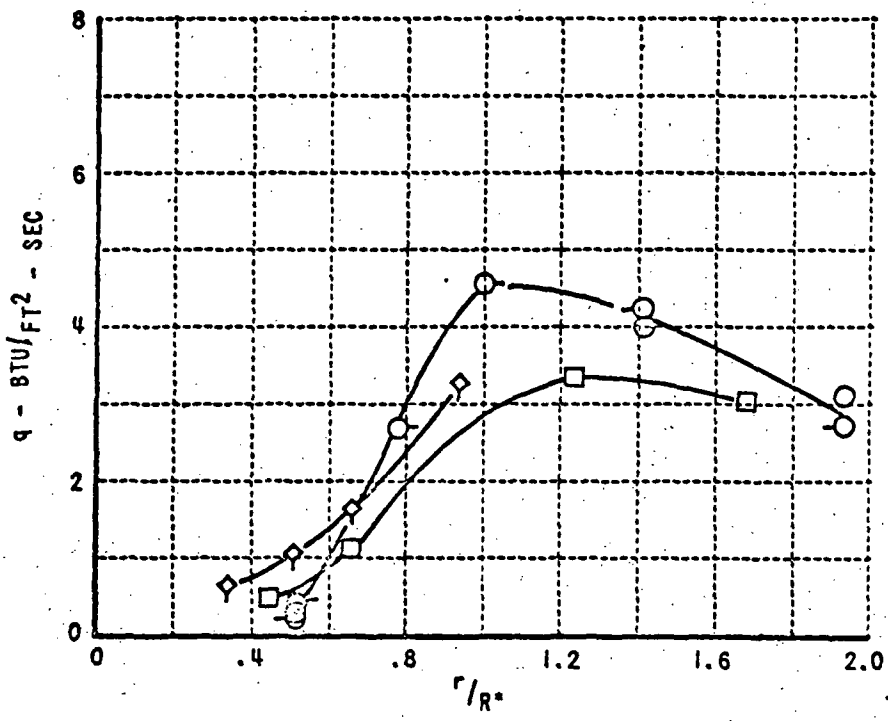
Five Engines

5 ENGINE CONFIGURATION



SYM	RUN	CONFIGURATION			
		d_m/D	j/D	h/D	h_f/D
○	3	.5303	.1086	.1086	-
○	21	↓	↓	↓	-
○	22	↓	↓	↓	-
□	208	.6060	↓	↓	-
◇	224	.7980	↓	↓	-
◇	237	↓	↓	↓	-
◇	238	↓	↓	↓	-

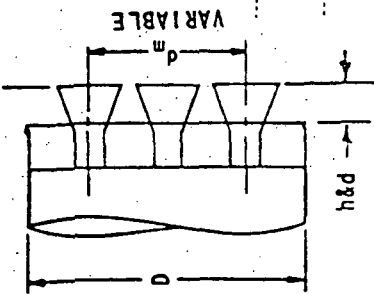
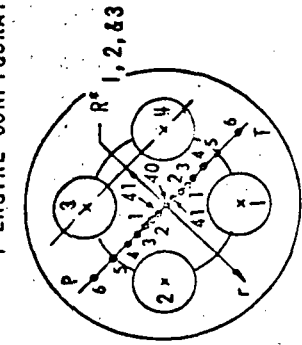
$P_C = 632$ PSIA NOMINAL
 ALT - 240,000 FT
 $P_{\infty}/P_C = .08 \times 10^{-5}$



EFFECT OF ENGINE MOUNTING CIRCLE DIAMETER ON BASE PRESSURE AND HEAT TRANSFER (5 ENGINE)

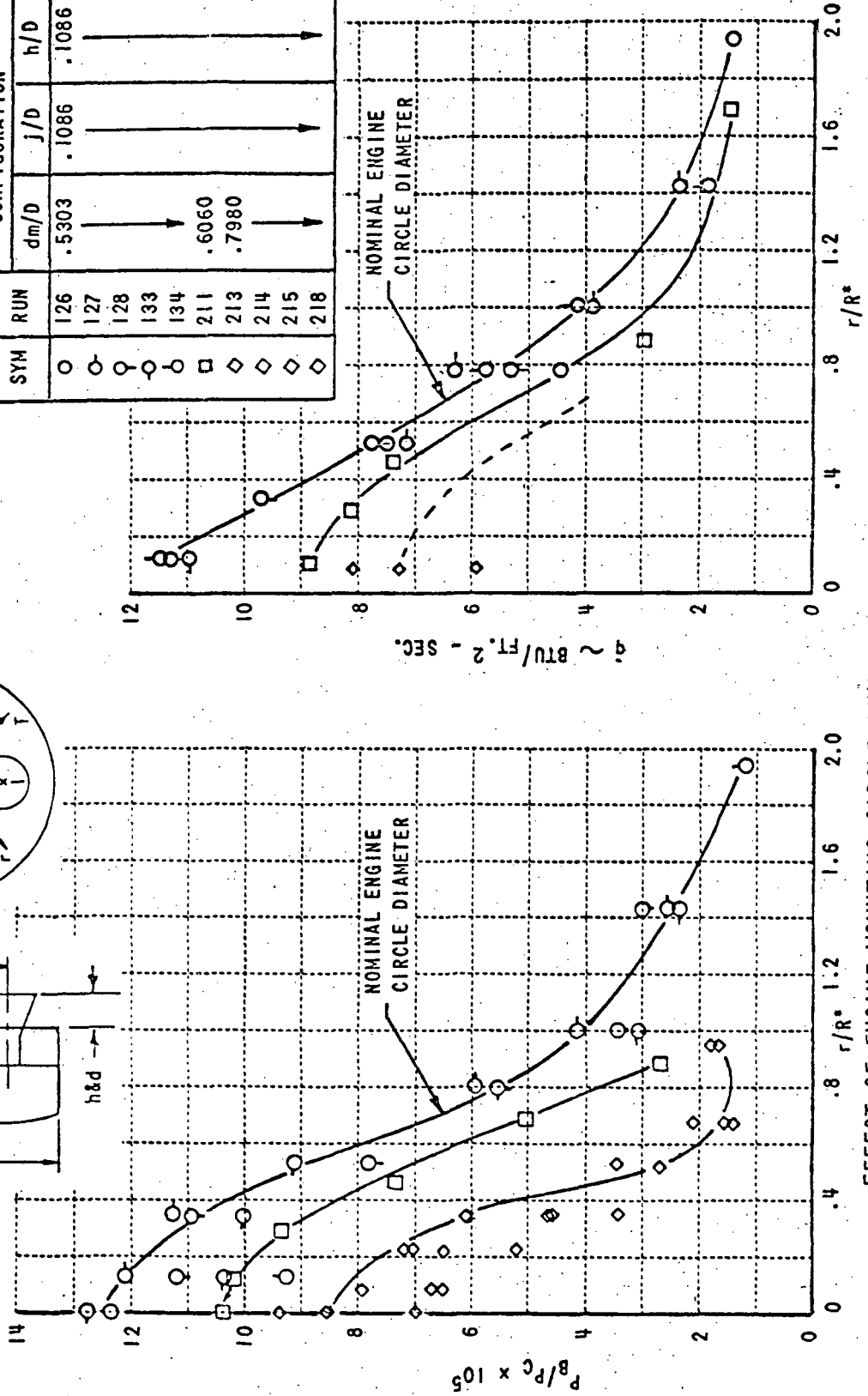
Figure 6.4-2

4-ENGINE CONFIGURATION



P_c - 632 PSIA NOMINAL
 ALT - 240,000 FT.
 P_{∞}/P_c - .08 x 10⁻⁵

SYM	RUN	CONFIGURATION			
		dm/D	J/D	h/D	hf/D
○	126	.5303	.1086	.1086	—
○	127	→	→	→	→
○	128	→	→	→	→
○	133	→	→	→	→
○	134	→	→	→	→
□	211	.6060	→	→	→
◇	213	.7980	→	→	→
◇	214	→	→	→	→
◇	215	→	→	→	→
◇	218	→	→	→	→

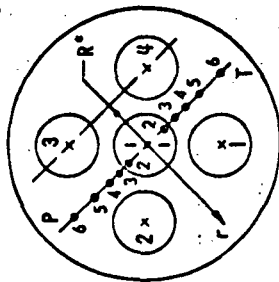
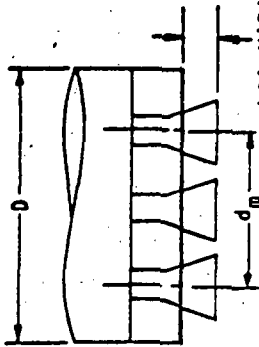


EFFECT OF ENGINE MOUNTING CIRCLE DIAMETER ON BASE PRESSURE AND HEAT TRANSFER (4 ENGINE)

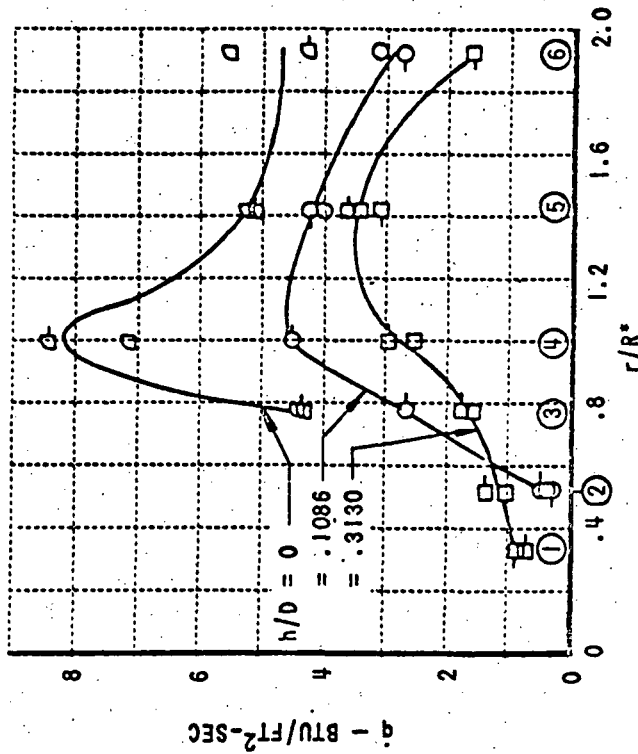
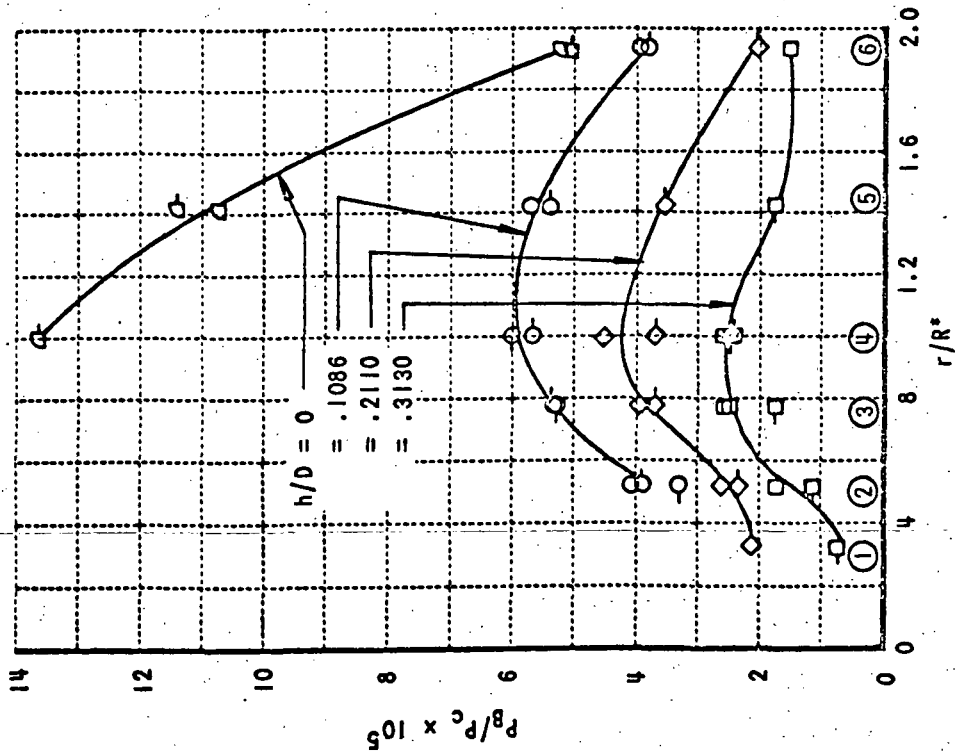
Figure 6.4-3

5 ENGINE
CONFIGURATION

P_c - 632 PSIA NOMINAL
ALT - 240,000 FT
 P_{∞}/P_c - $.08 \times 10^{-5}$



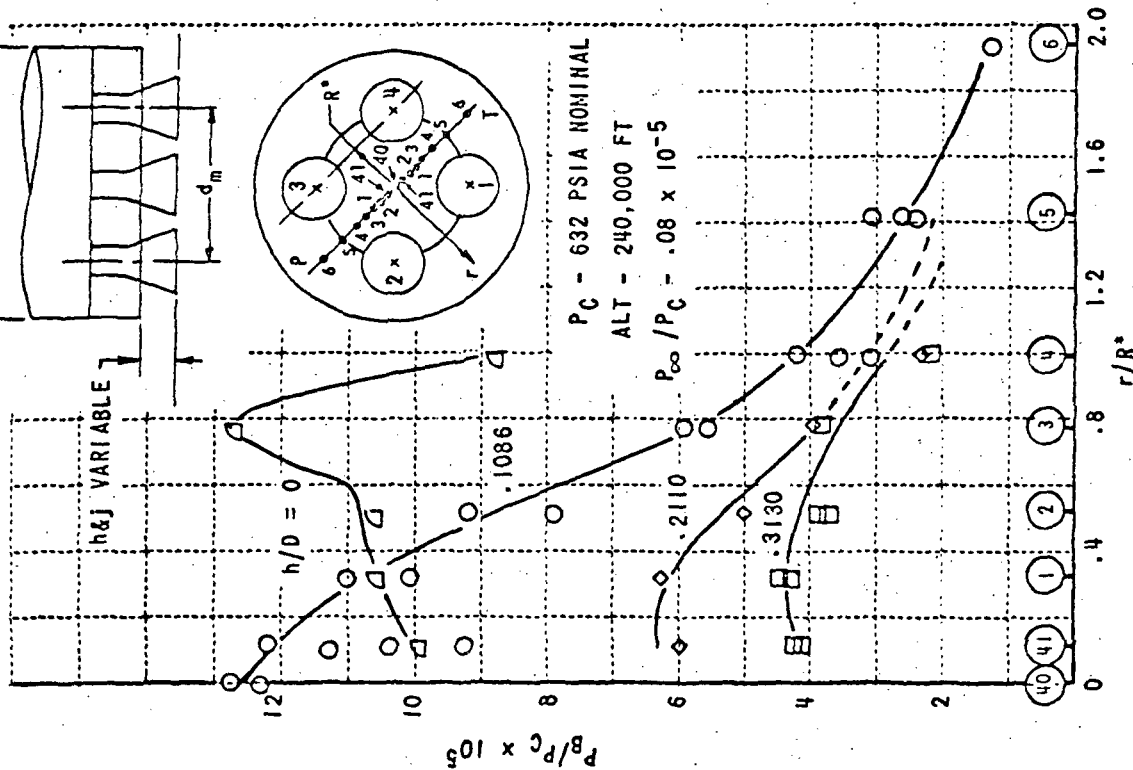
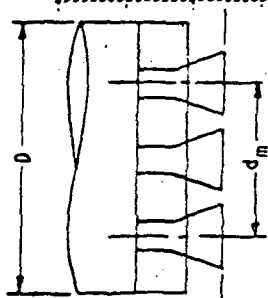
SYM	CONFIGURATION			
	d_m/D	J/D	h/D	h_f/D
□	.5303	.3130	.3130	—
▣	—	—	—	—
▢	—	.2110	.2110	—
◇	—	.1086	.1086	—
○	—	—	—	—
◊	—	—	—	—
◌	—	—	—	—
◐	—	—	—	—
◑	—	—	—	—



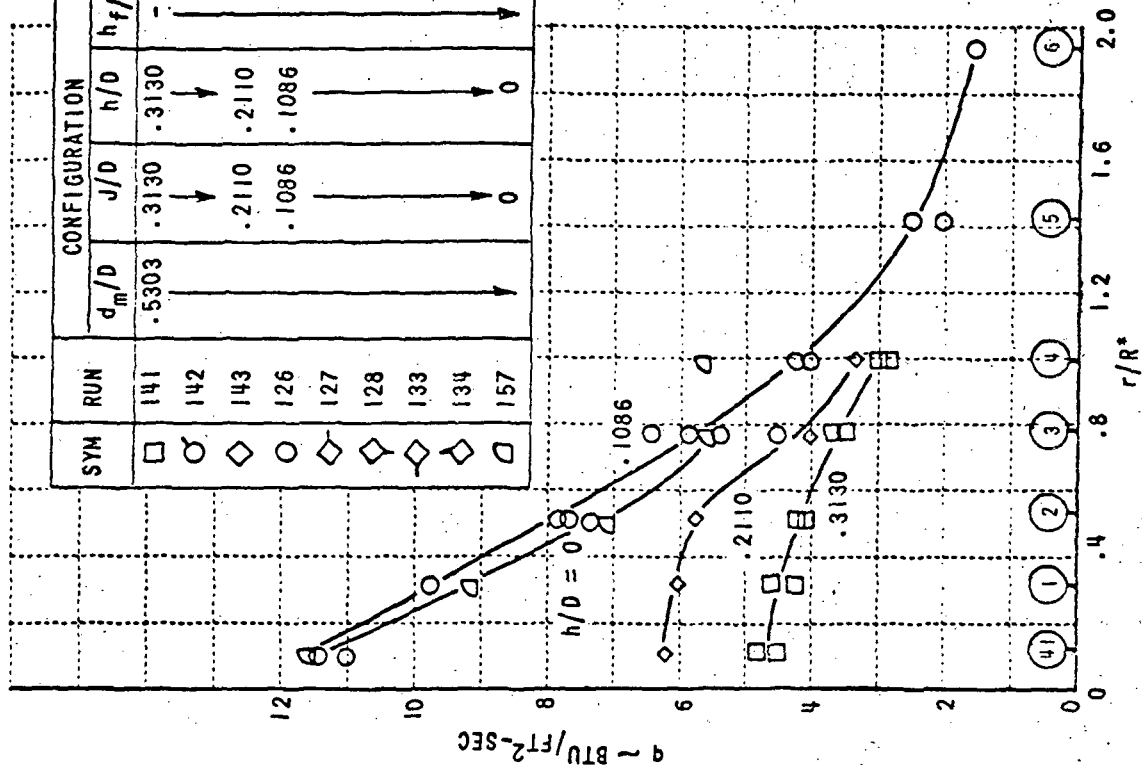
EFFECT OF BASE LOCATION ON BASE PRESSURE AND HEAT TRANSFER (5 ENGINE)

Figure 6.4-4

4-ENGINE CONFIGURATION

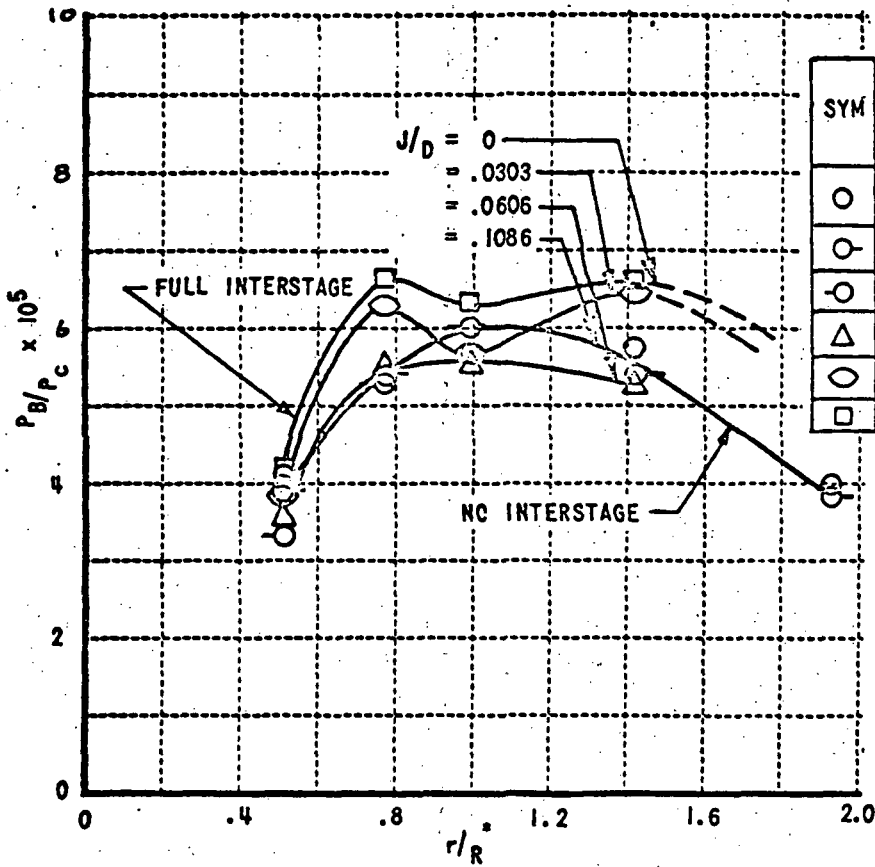


SYM	RUN	CONFIGURATION		
		d_m/D	J/D	h_f/D
□	141	.5303	.3130	-
○	142	→	→	→
◇	143	→	.2110	→
○	126	→	.1086	→
◇	127	→	→	→
◇	128	→	→	→
◇	133	→	→	→
◇	134	→	→	→
□	157	→	→	→



EFFECT OF BASE LOCATION ON BASE PRESSURE AND HEAT TRANSFER (4 ENGINE)

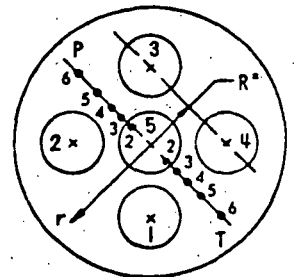
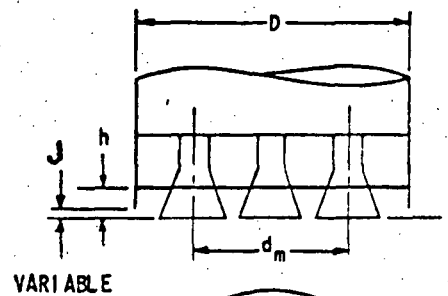
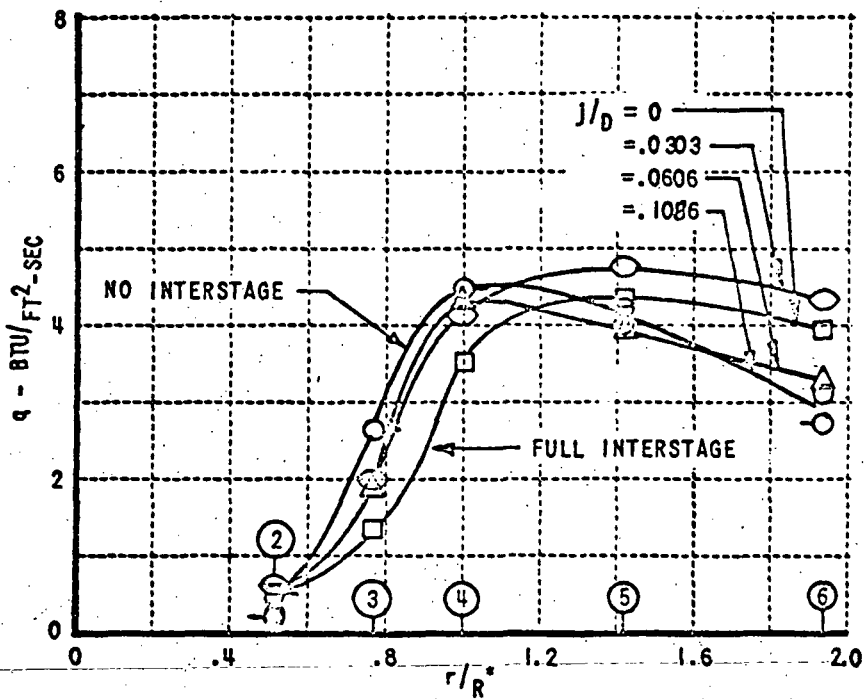
Figure 6.4-5



SYM	RUN	CONFIGURATION			
		dm/D	J/D	h/D	hf/D
○	3	.5303	.1086	.1086	-
○	21				-
○	22				-
△	25		.0606		-
○	24		.0303		-
□	23	▽	0	▽	

5 ENGINE CONFIGURATION

$P_c = 632$ PSIA NOMINAL
 ALT. - 240,000 FT
 $P_\infty/P_c = .08 \times 10^{-5}$



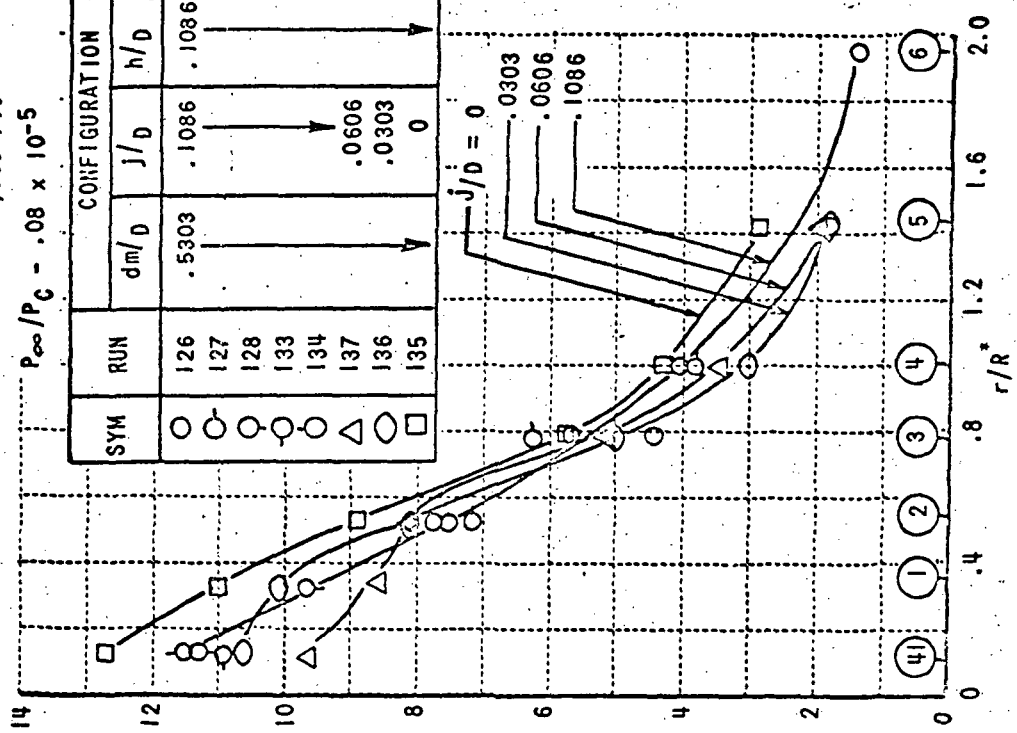
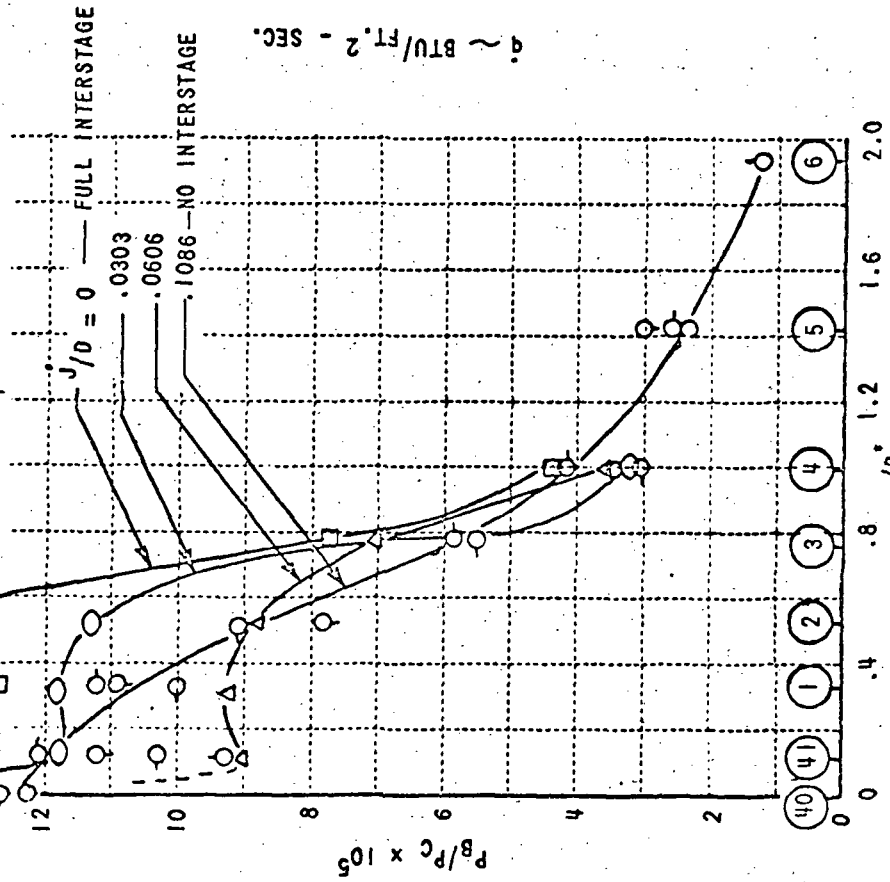
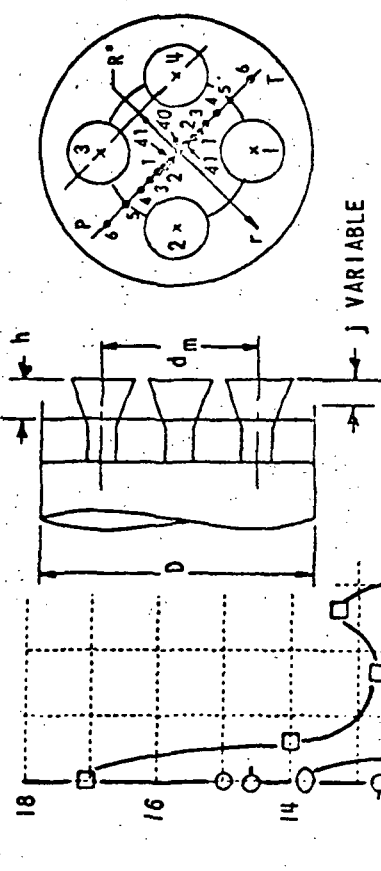
EFFECT OF INTERSTAGE LENGTH ON BASE PRESSURE AND HEAT TRANSFER (5 ENG.)

Figure 6.4-6

4-ENGINE CONFIGURATION

P_C - 632 PSIA NOMINAL
 ALT. - 240,000 FT.
 P_{∞}/P_C - $.08 \times 10^{-5}$

		CONFIGURATION			
SYM	RUN	d_m/D	J/D	h/D	hf/D
○	126	.5303	.1086	.1086	→
○	127				→
○	128		→		
○	133				→
○	134				→
△	137		.0606		
◇	136		.0303		
□	135		0		

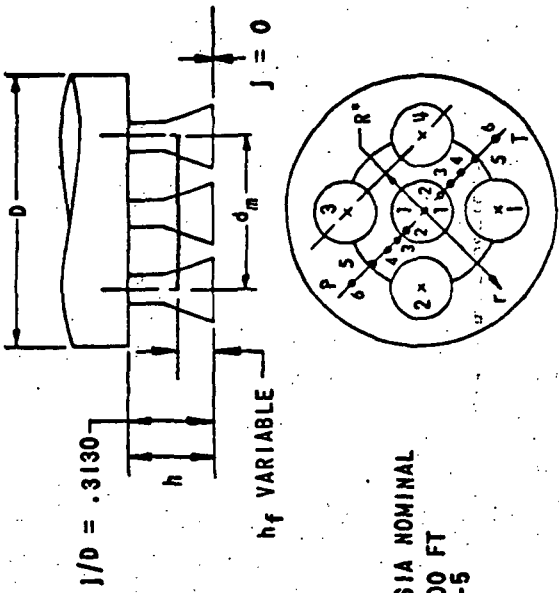


EFFECT OF INTERSTAGE LENGTH ON HEAT TRANSFER q BASE PRESSURE (4 ENGINE)

Figure 6.4-7

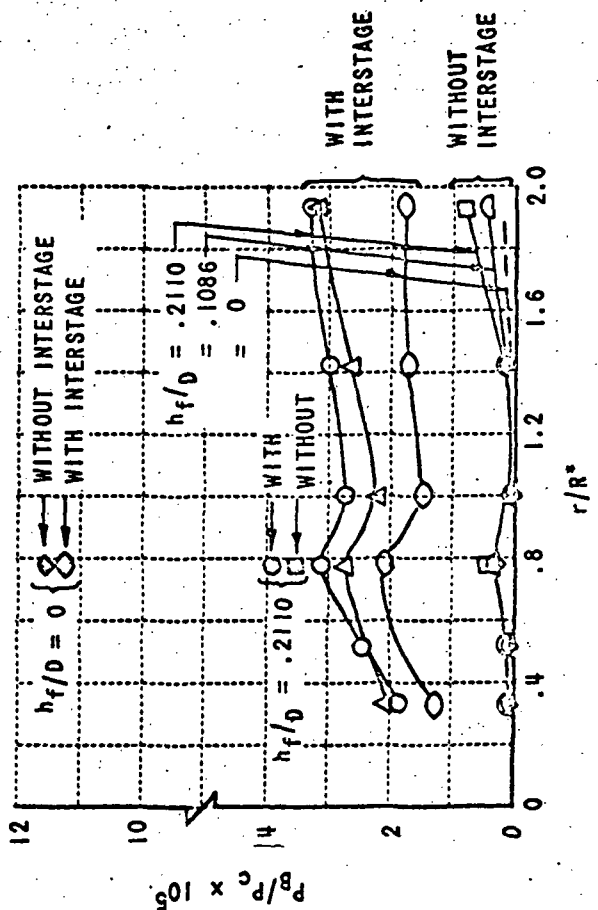
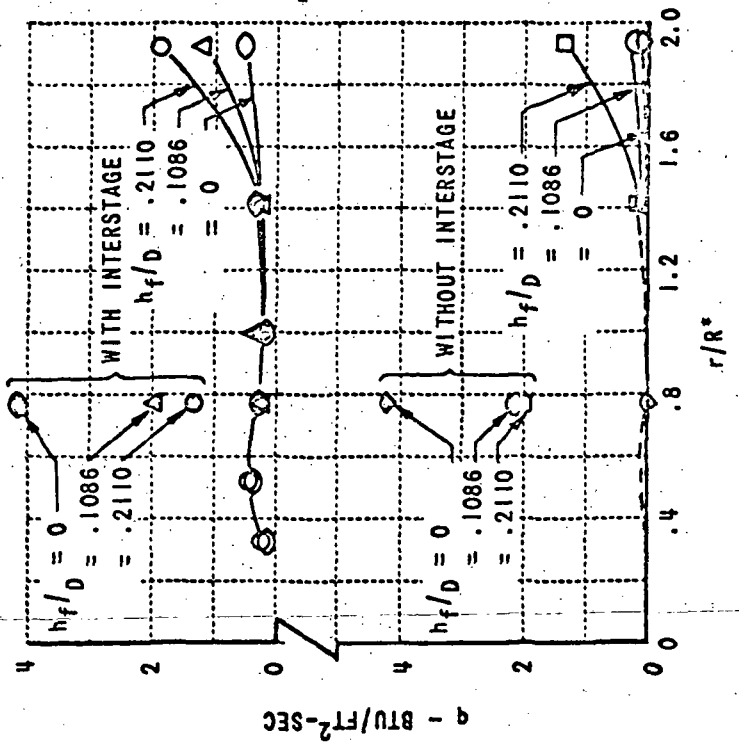
SYM (AVE)	RUNS	CONFIGURATION			
		d_m/D	J/D	h/D	h_f/D
○	55, 56, 58, 86, 100	.5303	0	.3130	.2110
△	59, 91, 94	↓	↓	↓	.1086
◇	95, 99	↓	.3130	↓	0
□	57, 61, 87, 88	↓	↓	↓	.2110
▽	90, 92, 93, 108, 109	↓	↓	↓	.1086
◇	98	↓	↓	↓	0

5 ENGINE
CONFIGURATION



P_c - 632 PSIA NOMINAL
 ALT - 240,000 FT
 P_∞ / P_c - $.08 \times 10^{-5}$

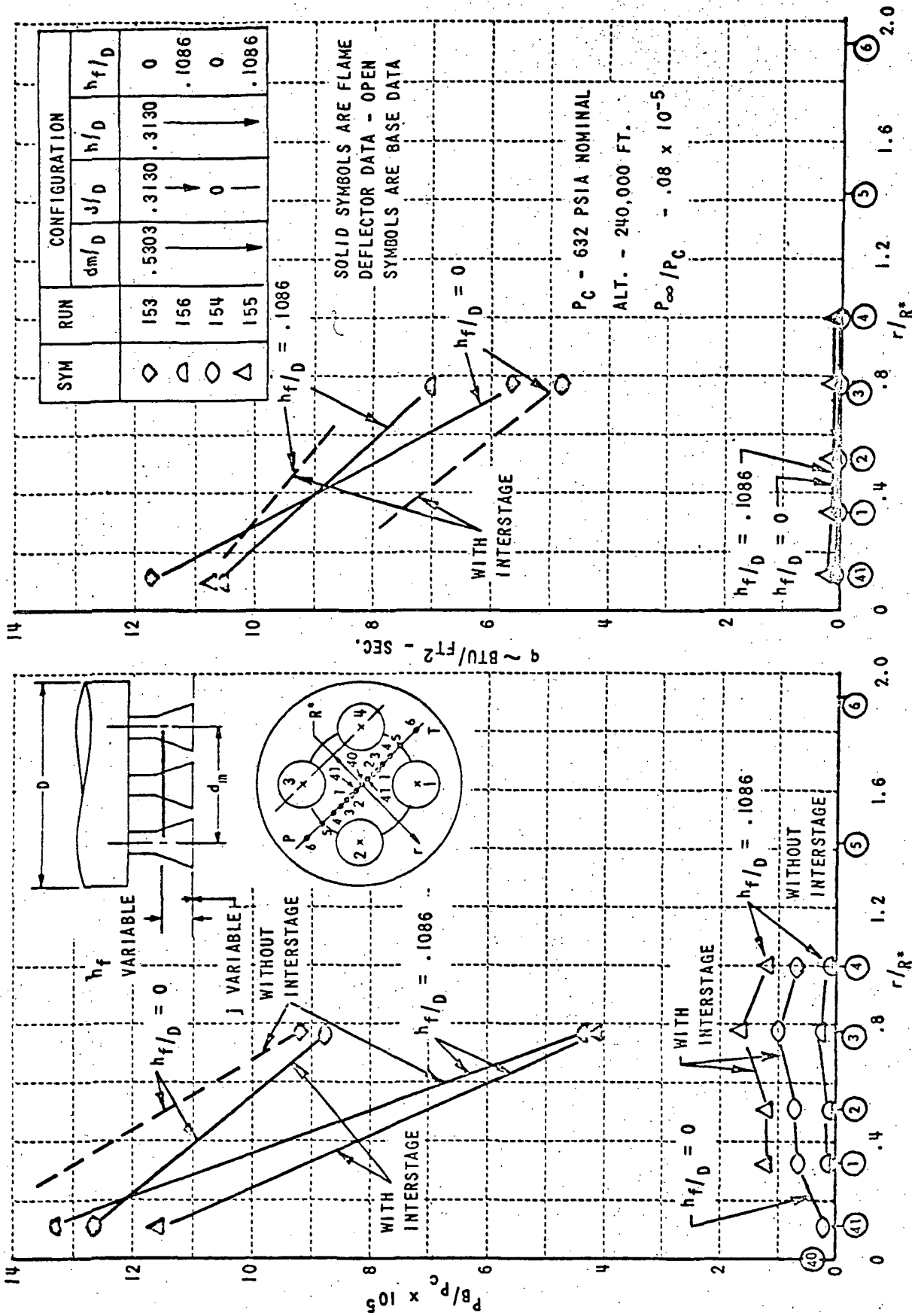
SOLID SYMBOLS ARE FLAME
DEFLECTOR DATA



EFFECT OF FLAME DEFLECTOR (NO GAP) POSITION ON BASE PRESSURE AND HEAT TRANSFER (5 ENGINE)

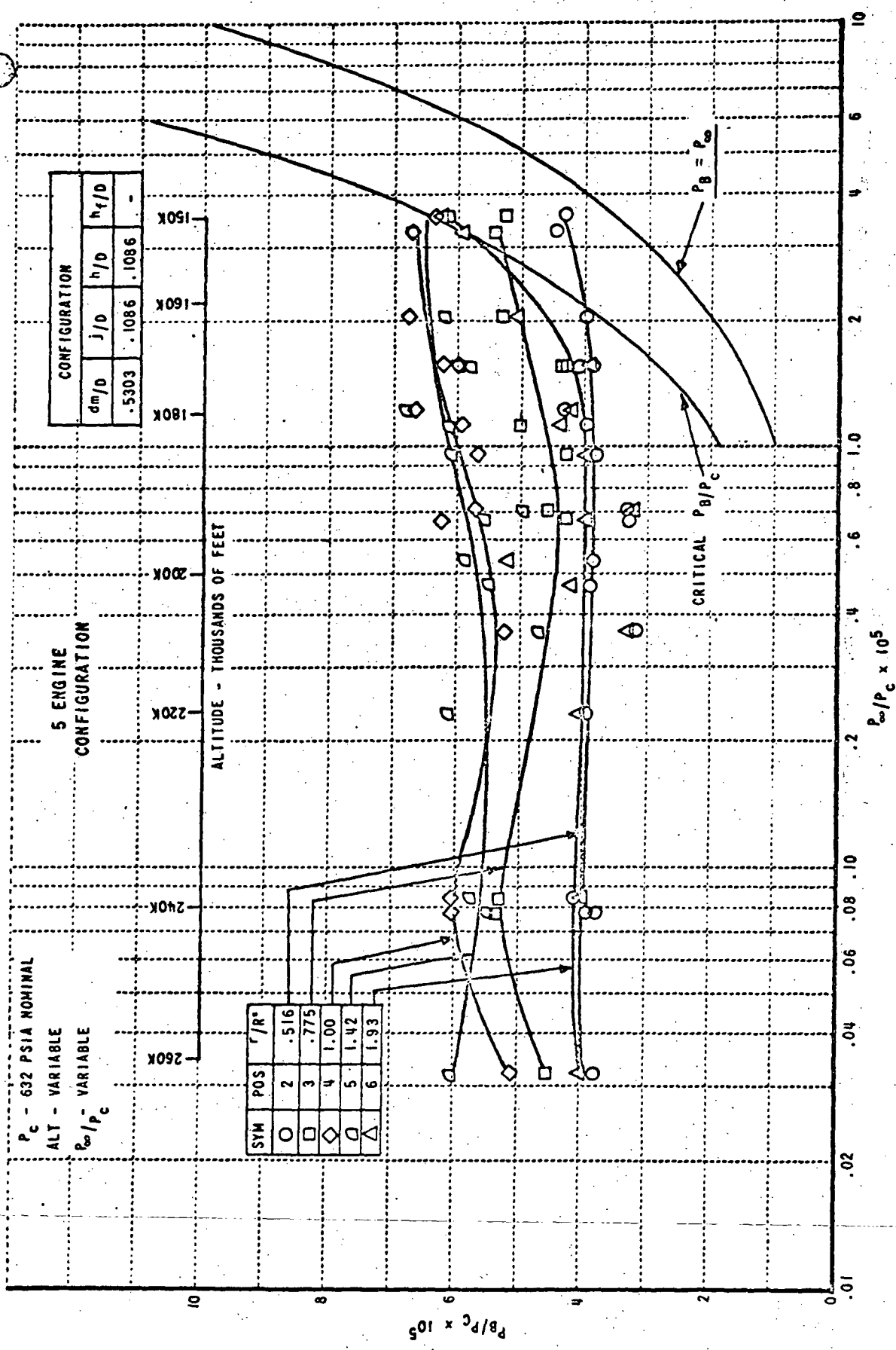
Figure 6.4-8

4-ENGINE CONFIGURATION



EFFECT OF FLAME DEFLECTOR (NO GAP) POSITION ON BASE PRESSURE AND HEAT TRANSFER (4 ENGINE)

Figure 6.4-9



EFFECT OF AMBIENT PRESSURE ON BASE PRESSURE (5 ENGINE)

Figure 6.4-10

5 ENGINE
CONFIGURATION

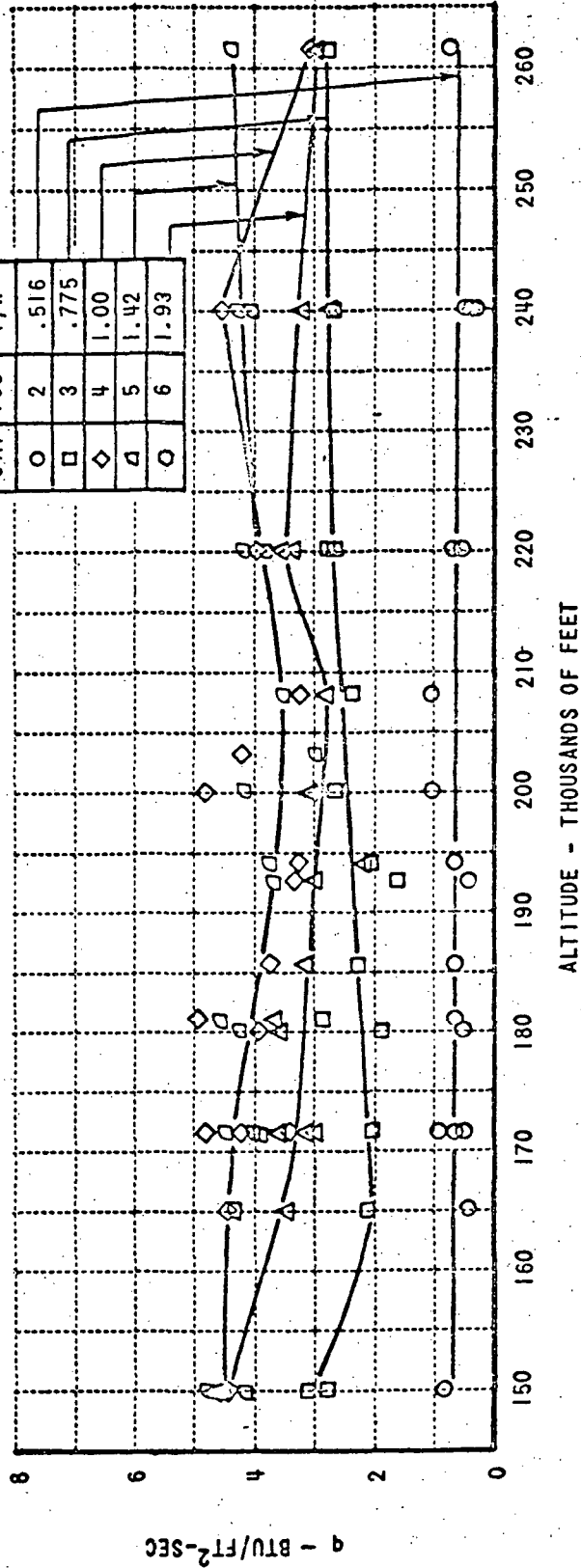
P_c - 632 PSIA (NOMINAL)

ALT - VARIABLE

P_∞/P_R - VARIABLE

CONFIGURATION			
d_m/D	J/D	h/D	h_r/D
.5303	.1086	.1086	-

SYM	POS	r/R^*
○	2	.516
□	3	.775
◇	4	1.00
△	5	1.42
○	6	1.93



EFFECT OF ALTITUDE ON BASE HEAT TRANSFER RATES (5 ENGINE)

Figure 6.4-11

4-ENGINE CONFIGURATION

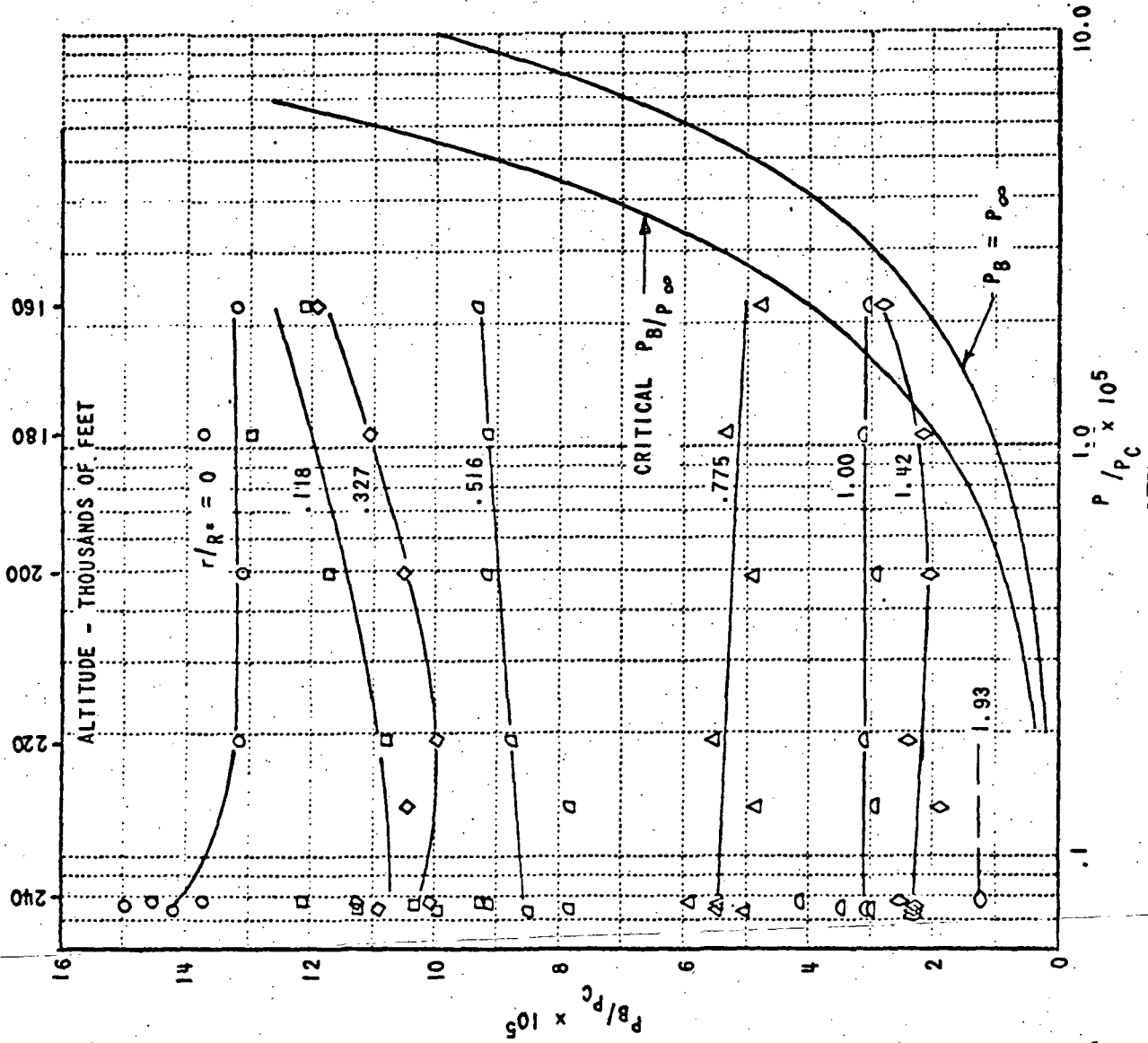
CONFIGURATION			
d_m/D	b/D	h/D	h_f/D
.5303	.1086	.1086	—

P_c - 632 PSIA NOMINAL

ALT. - VARIABLE

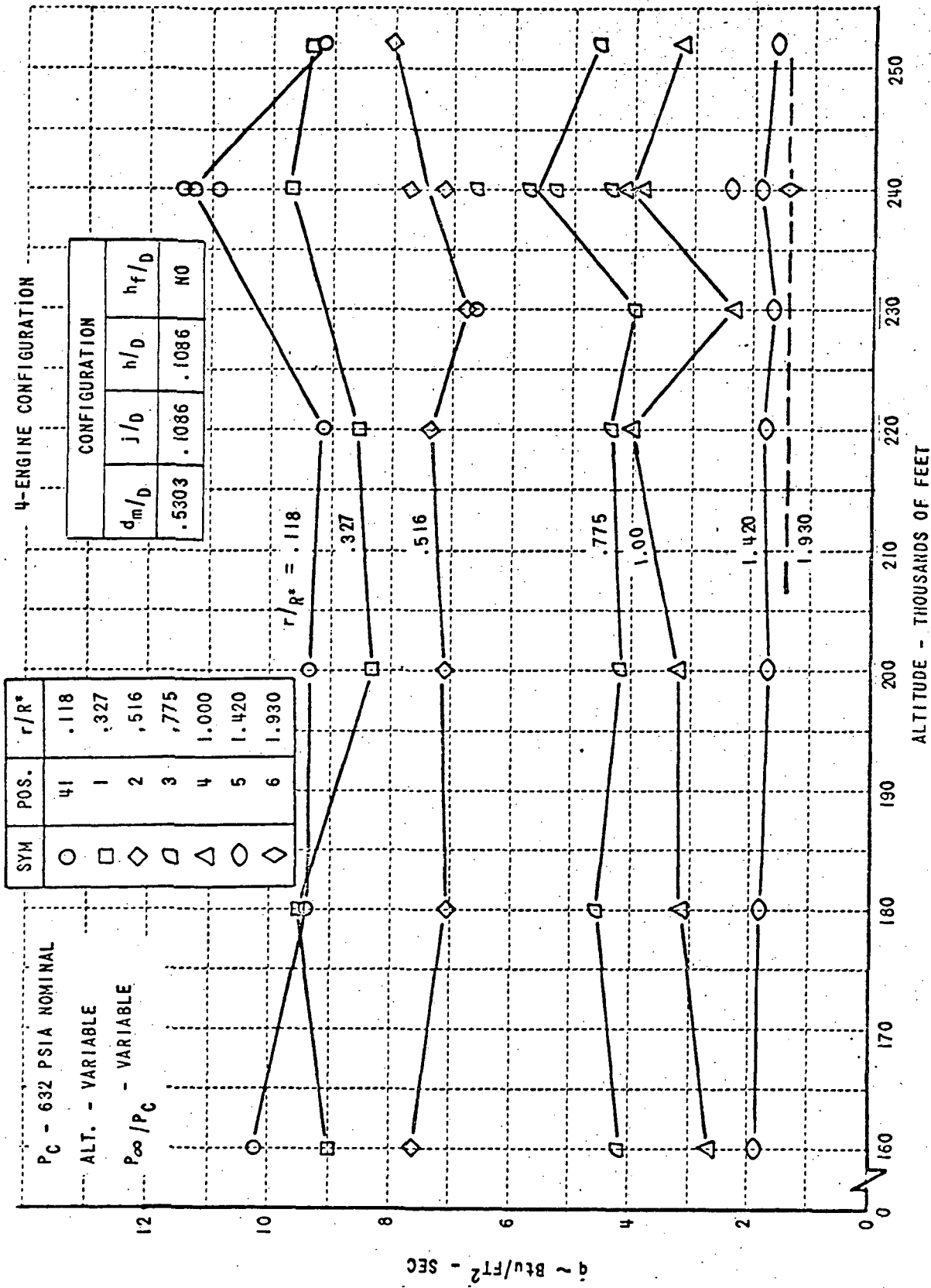
P_∞/P_c - VARIABLE

SYM	POS.	r/R^*
○	40	0
□	41	.118
◇	1	.327
▷	2	.516
△	3	.775
◐	4	1.000
◑	5	1.420
◒	6	1.980



EFFECT OF ALTITUDE ON BASE PRESSURE (4 ENGINE)

Figure 6.4-12



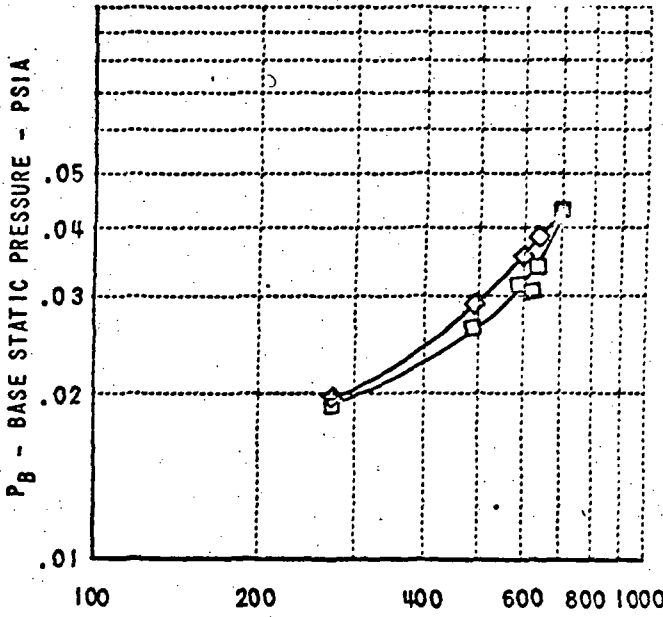
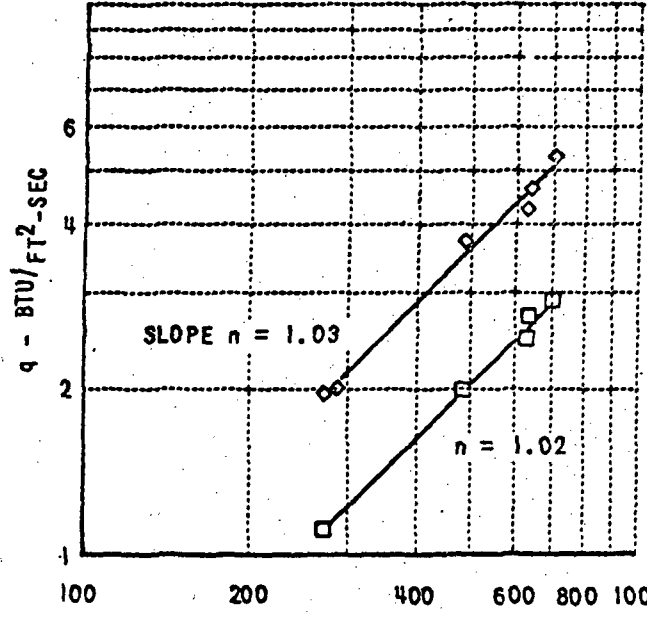
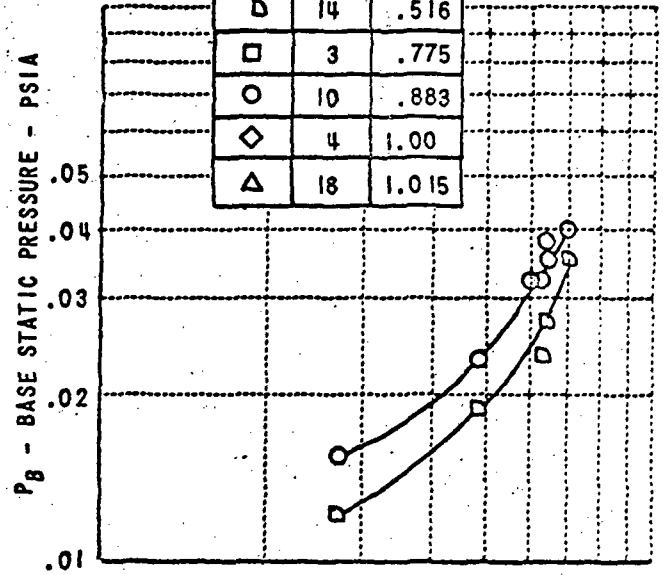
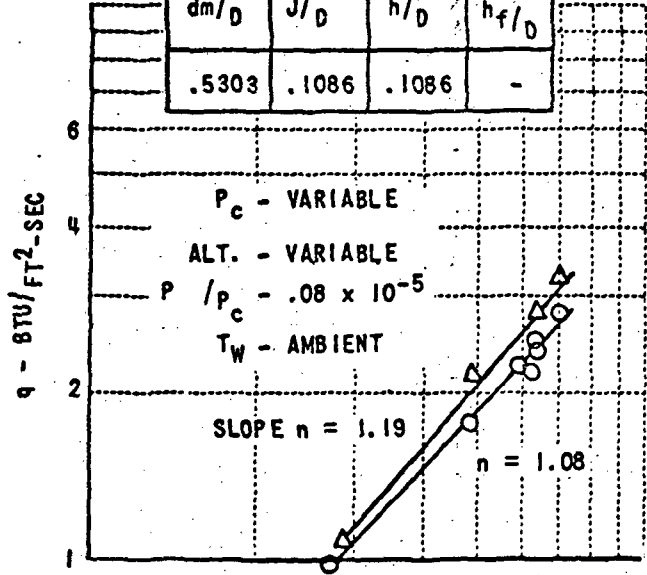
EFFECT OF ALTITUDE ON BASE HEAT TRANSFER. (4 ENGINE)

Figure 6.4-13

5 ENGINE CONFIGURATION

CONFIGURATION			
dm/D	J/D	h/D	h _f /D
.5303	.1086	.1086	-

SYM	POS	r/R*
◻	14	.516
◻	3	.775
○	10	.883
◇	4	1.00
△	18	1.015



COMBUSTION CHAMBER PRESSURE - PSIA.

EFFECT OF COMBUSTION CHAMBER PRESSURE ON
 BASE HEAT TRANSFER & PRESSURE
 (5 ENGINE)

Figure 6.4-14

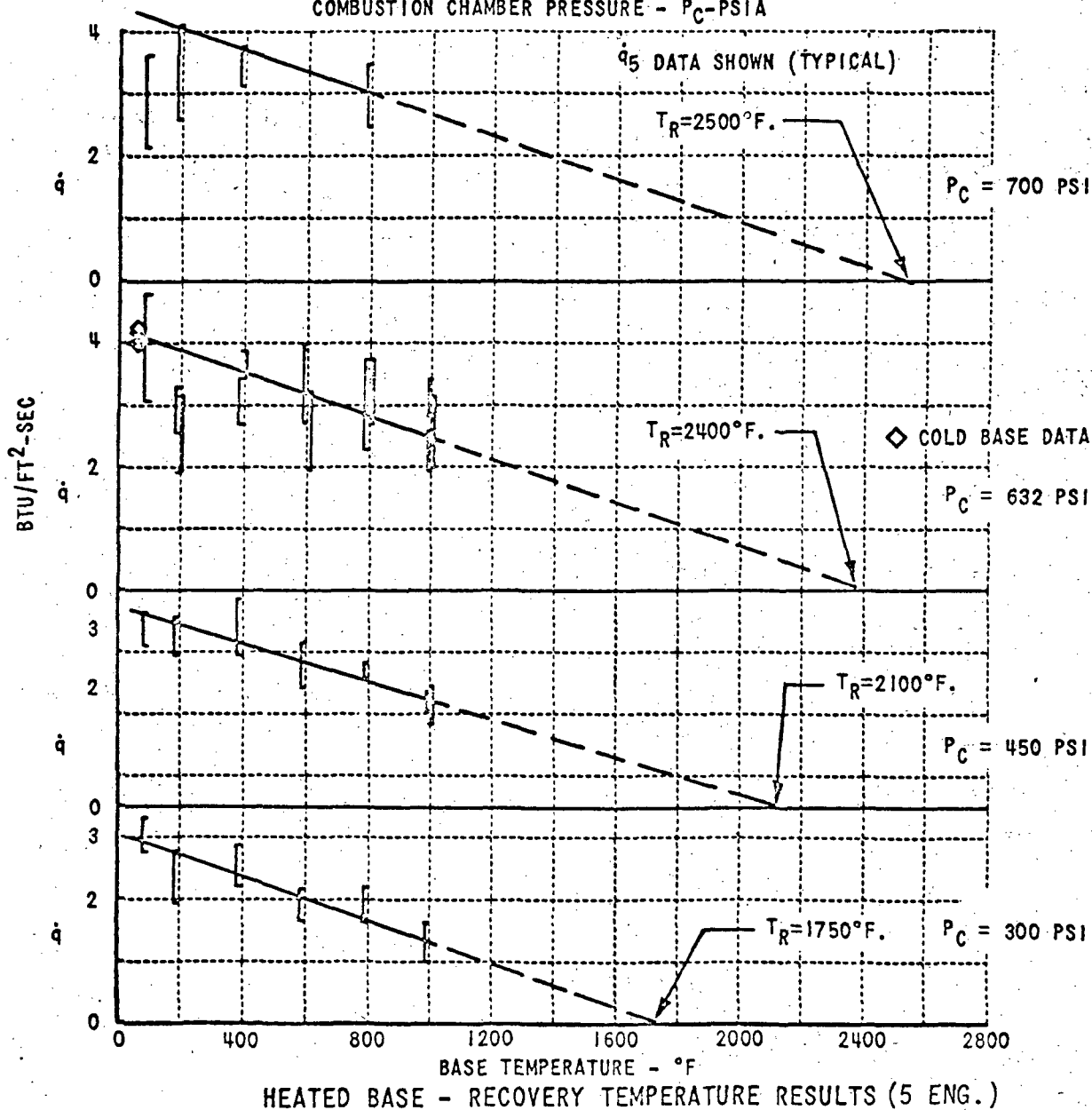
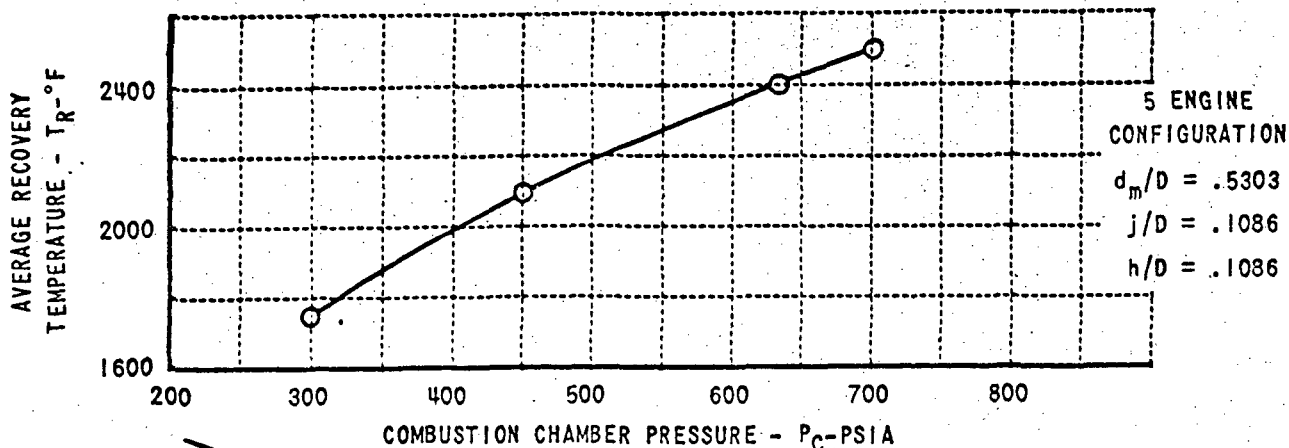


Figure 6.4-15

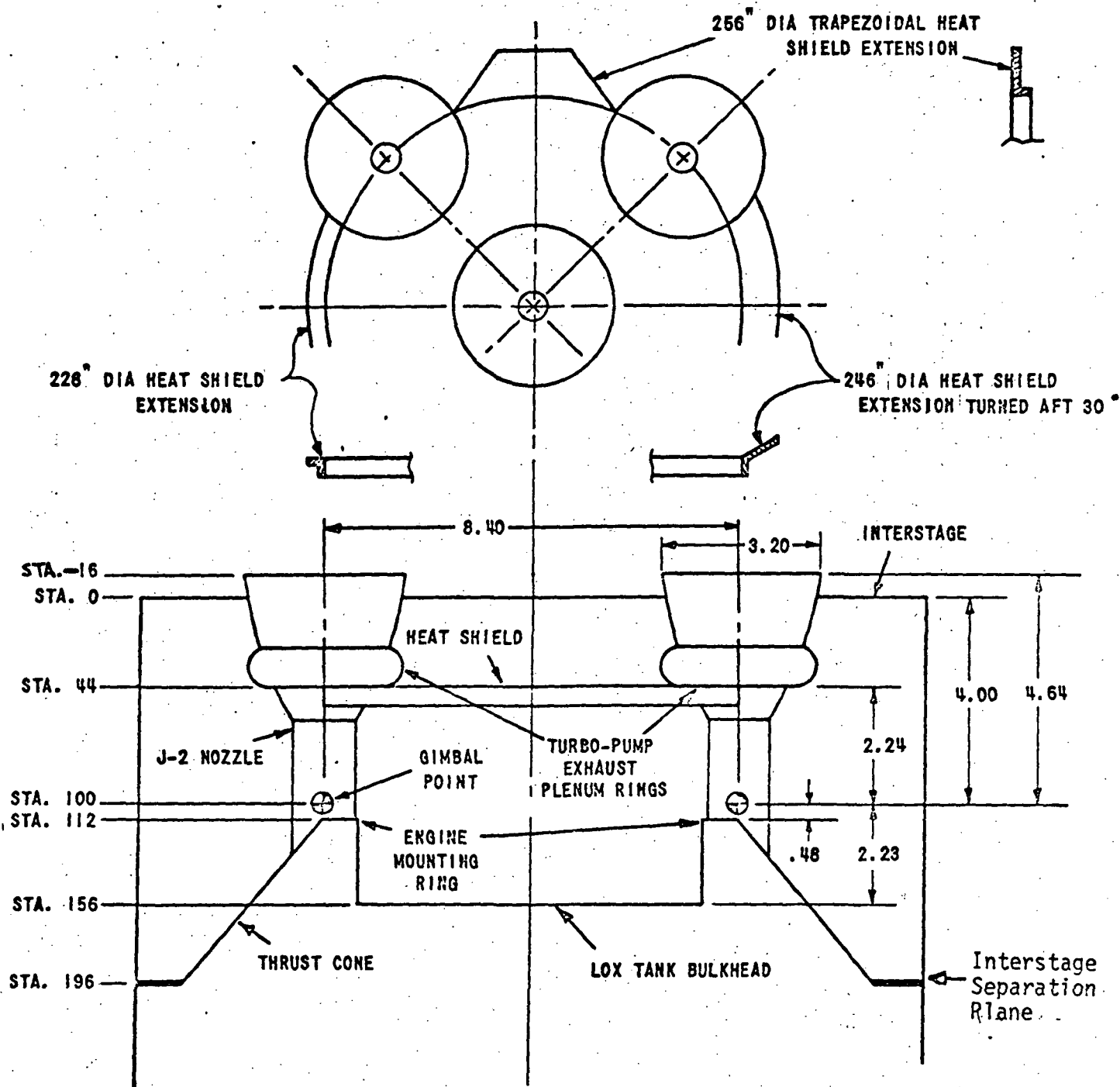
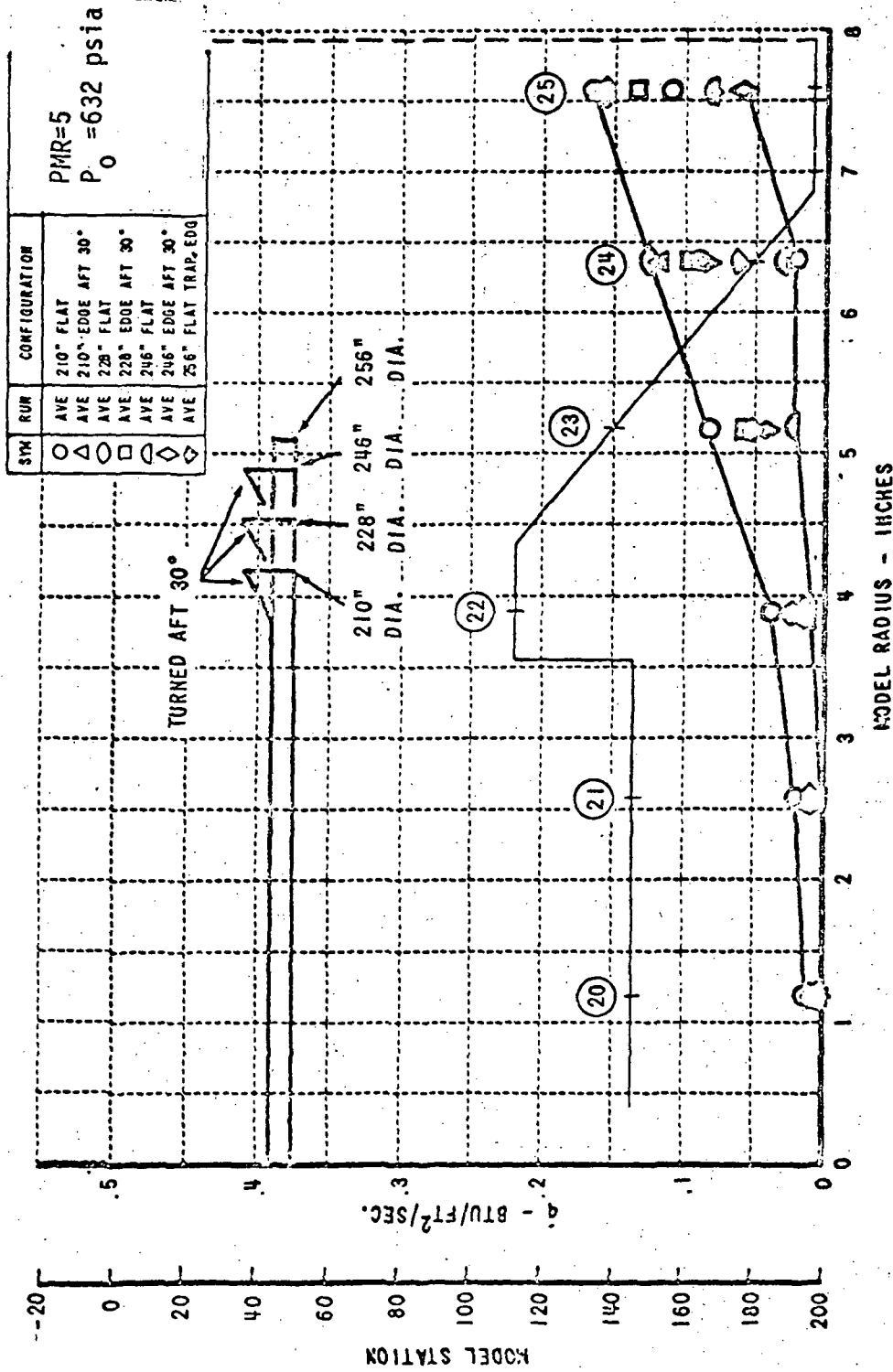


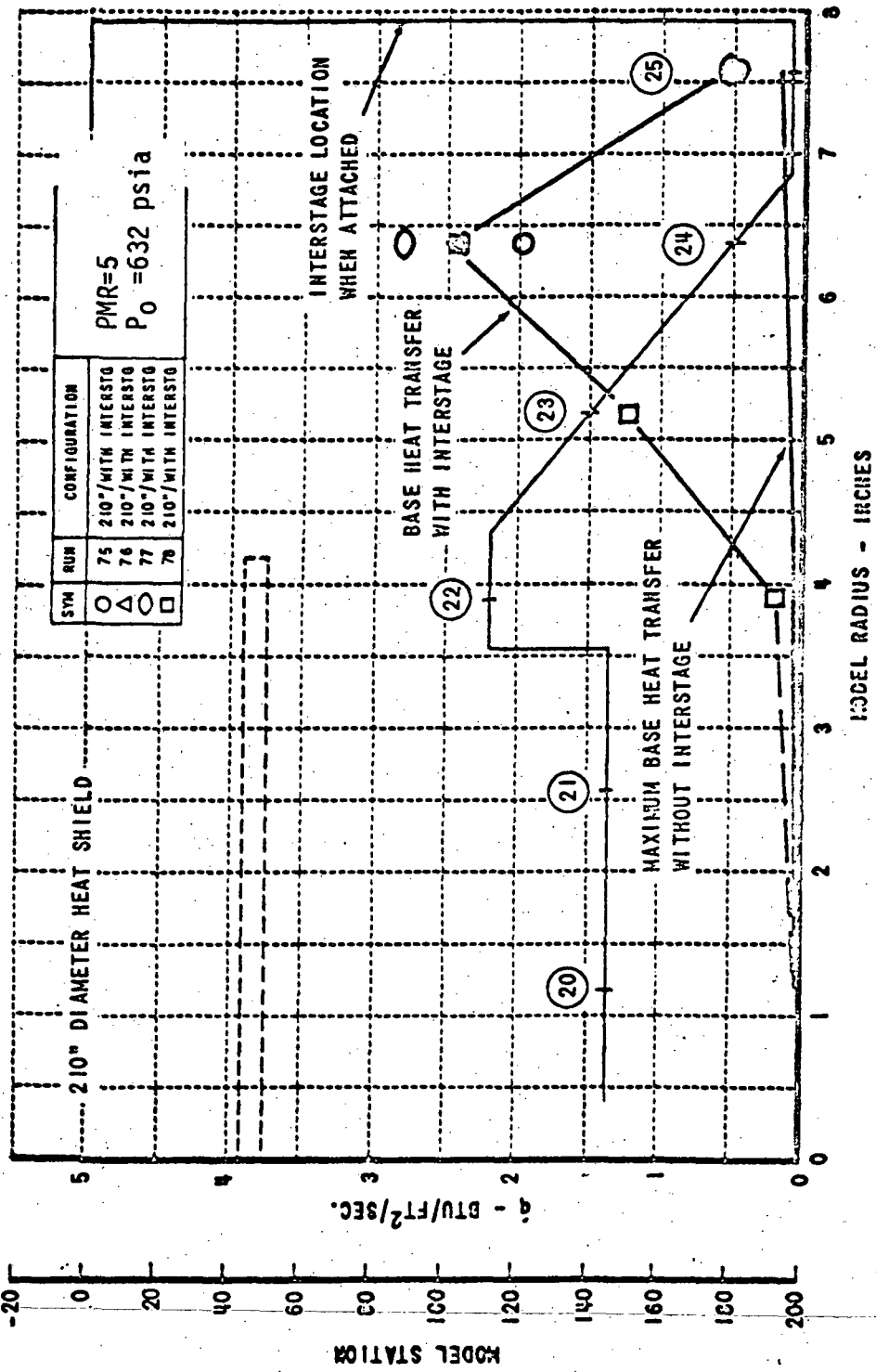
Figure 6.4-16 S-II PROTOTYPE MODEL SCHEMATIC



EFFECT OF HEAT SHIELD EDGE CONFIGURATION ON BASE REGION HEAT FLUX

Figure 6.4-17

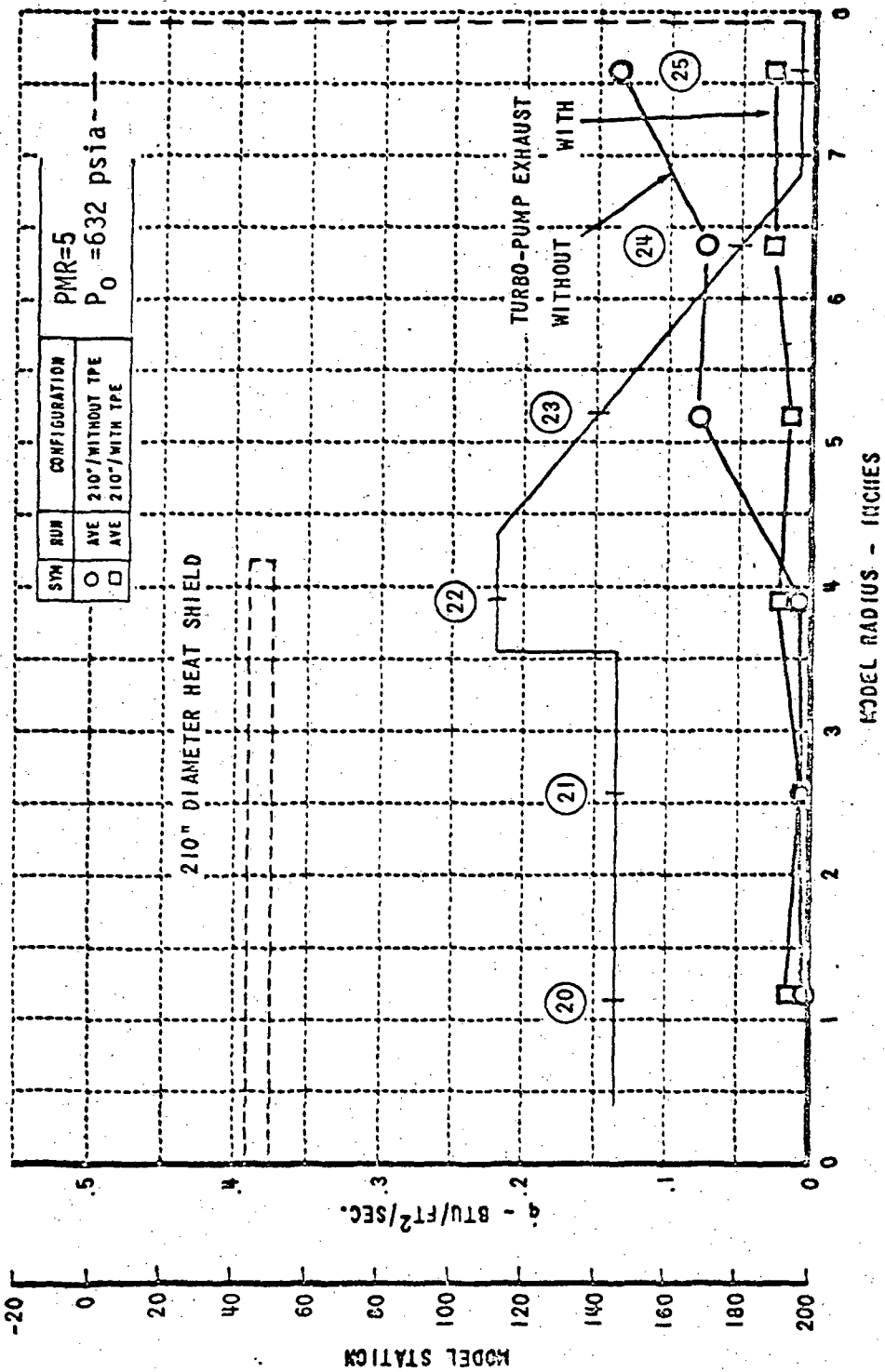
Section shown with gages 20 thru 25 is in a plane between outboard engines.



EFFECT OF INTERSTAGE ON BASE HEAT TRANSFER RATES

Figure 6.4-18

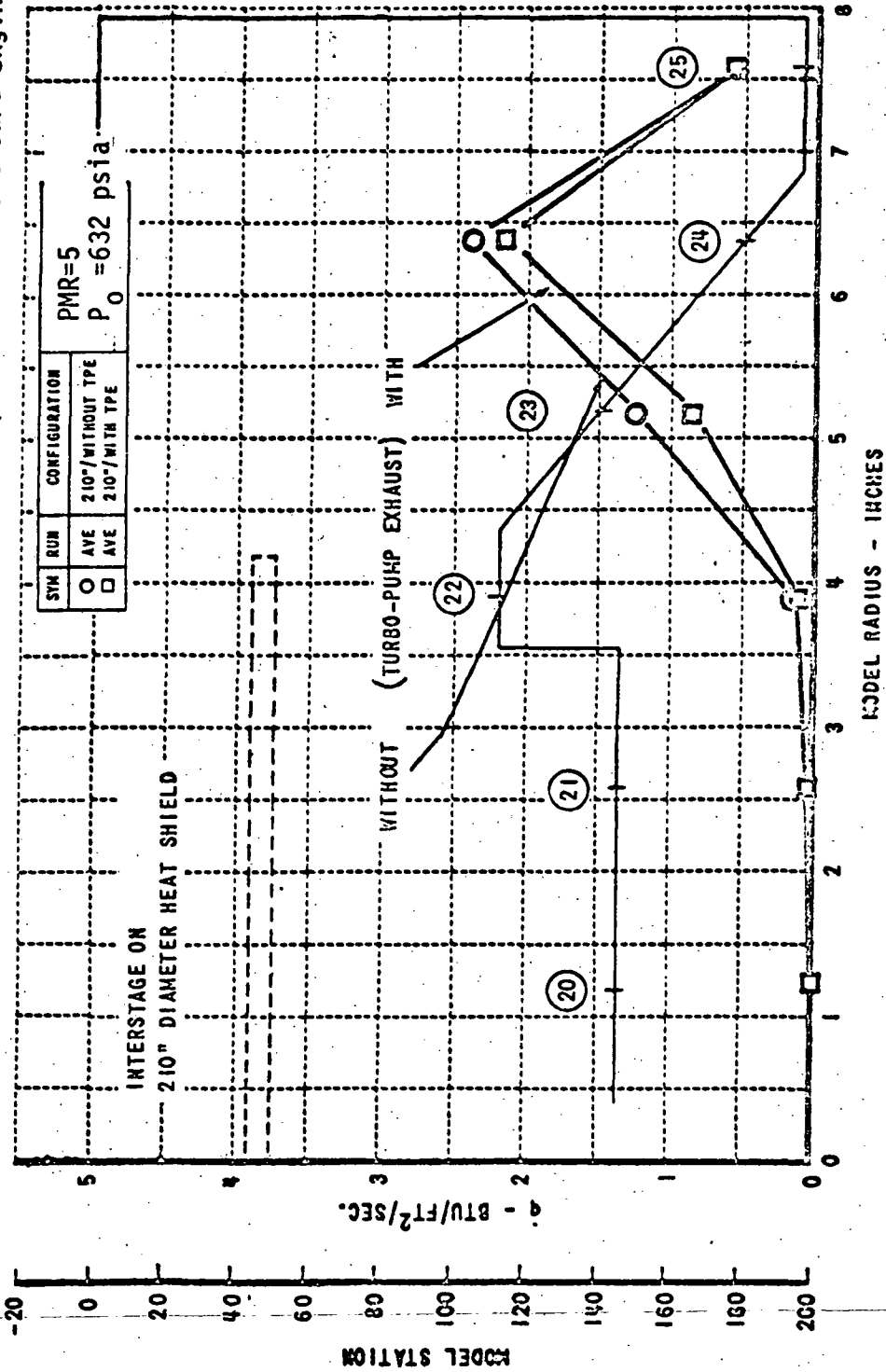
Section shown with gages 20 thru 25 is in a radial plane between outboard engines.



EFFECT OF TURBO-PUMP EXHAUST (TPE) ON BASE REGION HEAT FLUX

Figure 6.4-19

Section shown with gages 20 thru 25 is in a radial plane between outboard engines.

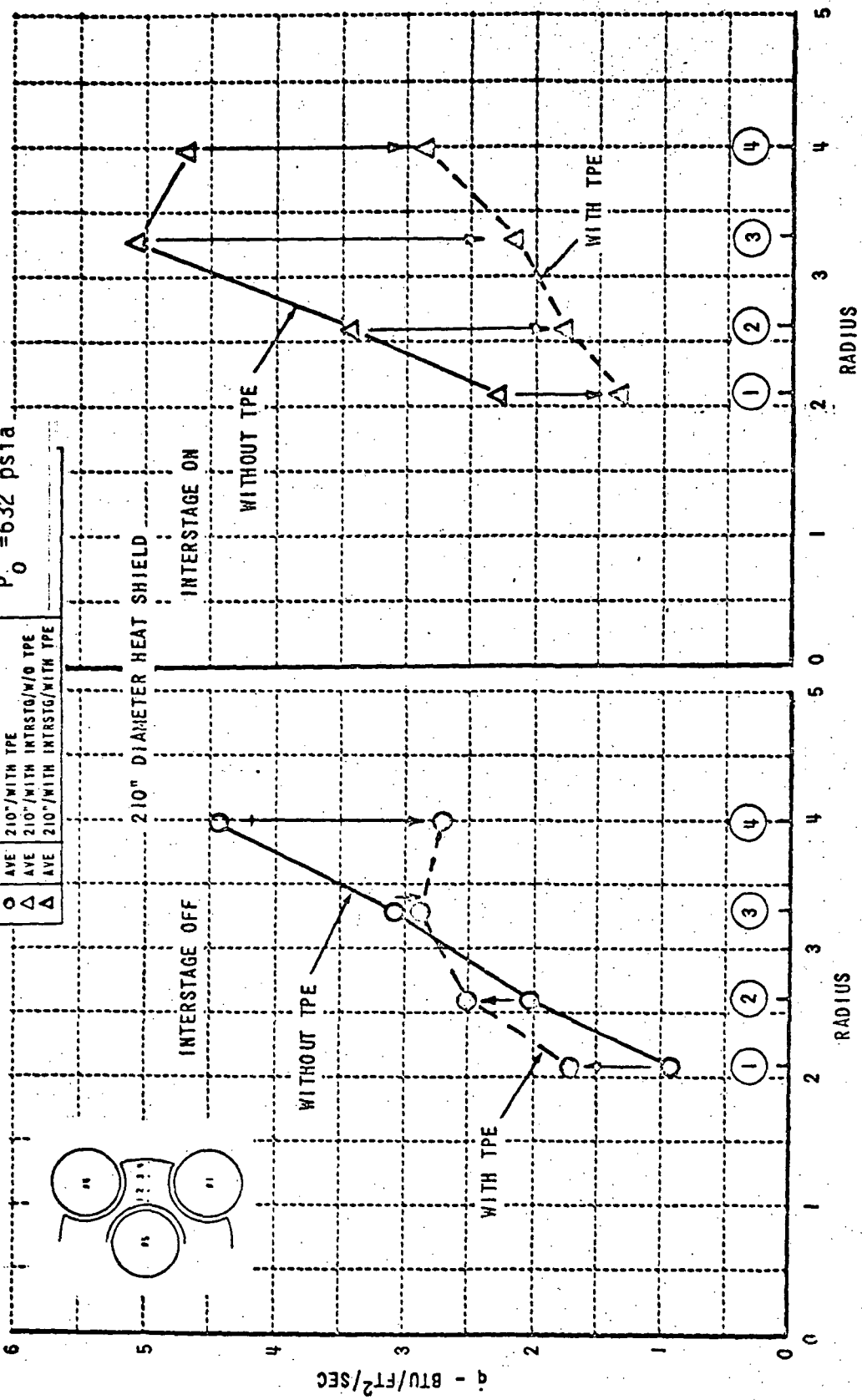


EFFECT OF TURBO-PUMP EXHAUST (TPE) ON BASE REGION HEAT FLUX

Figure 6.4-20

PMR=5
 $P_0 = 632 \text{ psfa}$

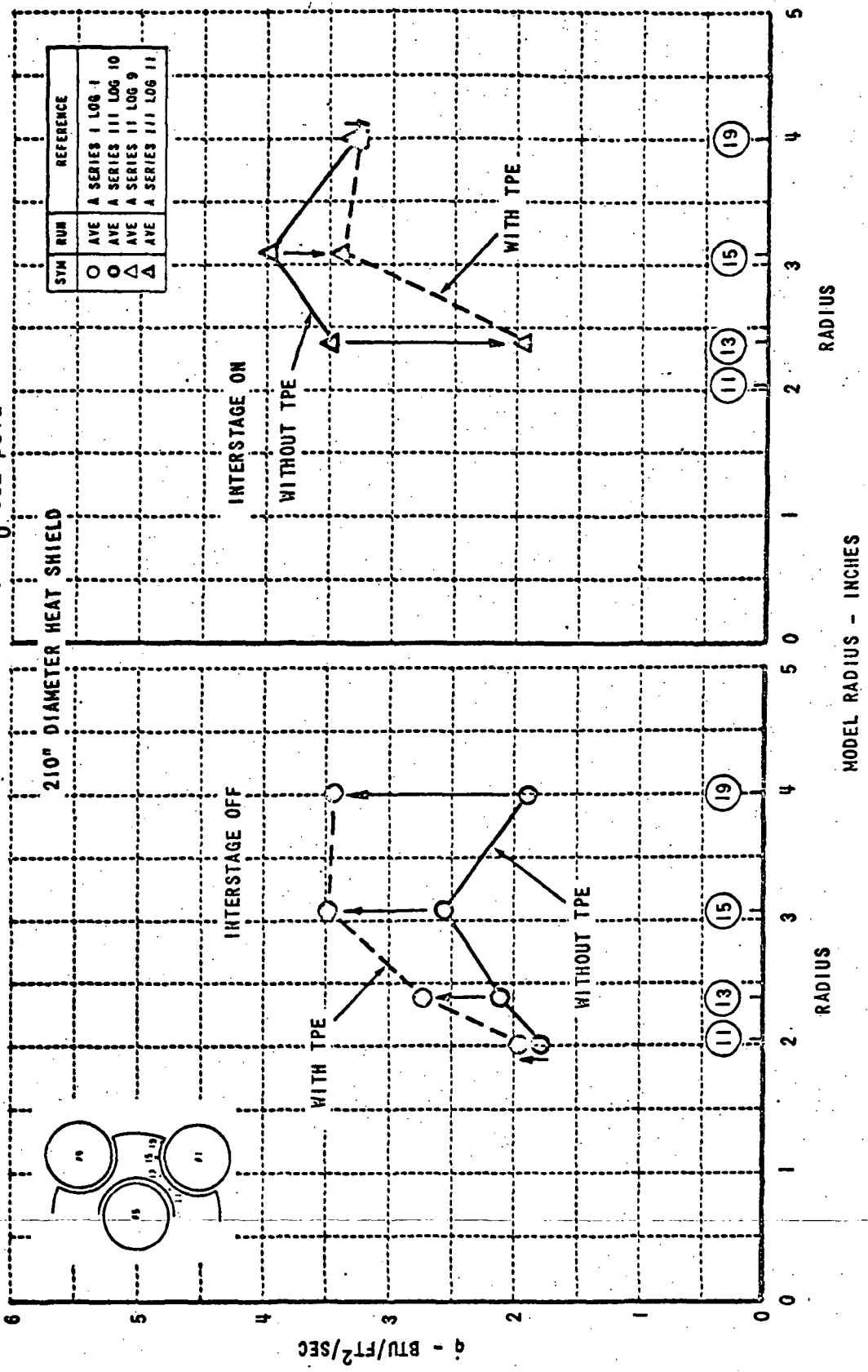
SYM	RUN	CONFIGURATION
○	AVE	210"/WITHOUT TPE
○	AVE	210"/WITH TPE
△	AVE	210"/WITH INTRSTG/W/O TPE
△	AVE	210"/WITH INTRSTG/WITH TPE



EFFECT OF TURBO-PUMP EXHAUST (TPE) ON HEAT SHIELD HEAT FLUX

Figure 6.4.21

PMR=5 P₀=632 psia



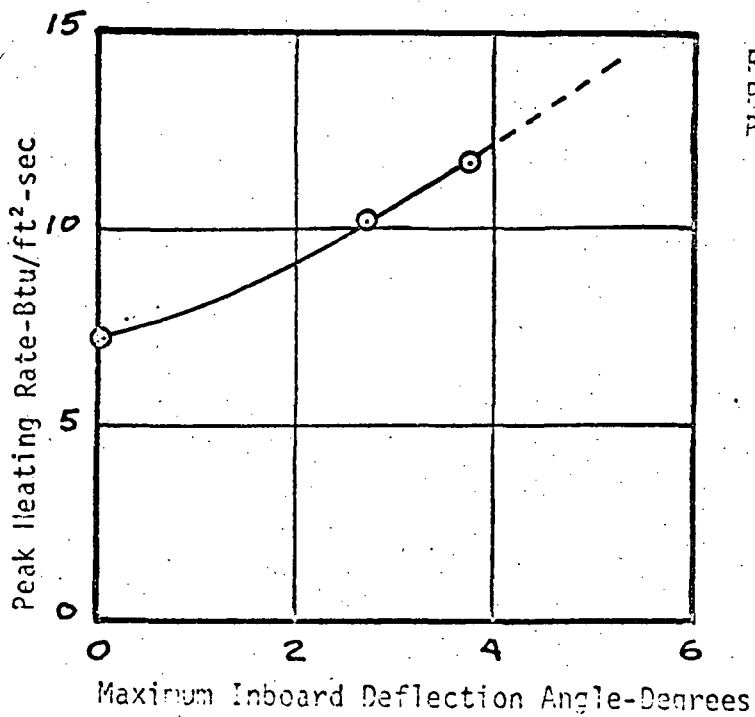
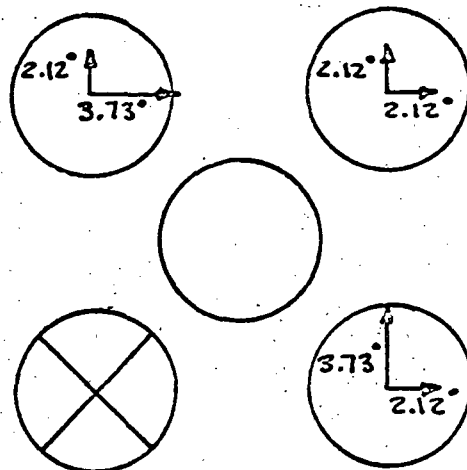
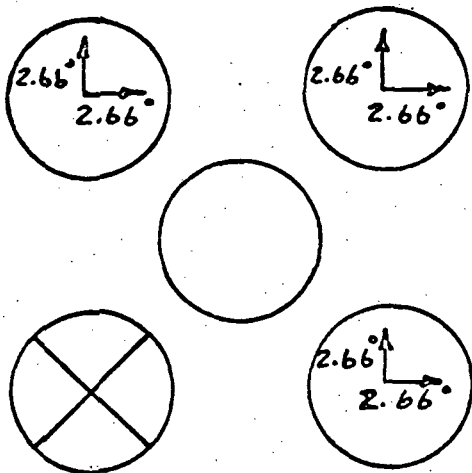
EFFECT OF TURBO-PUMP EXHAUST (TPE) ON HEAT SHIELD HEAT FLUX

Figure 6.4-22

Model Engine-Out Deflection Patterns

Case 2

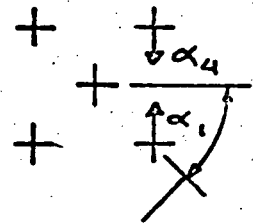
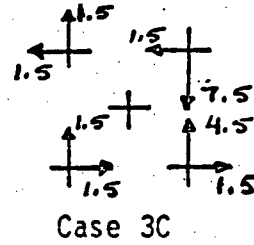
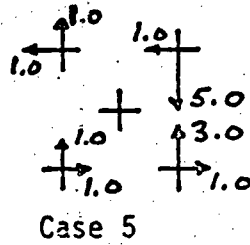
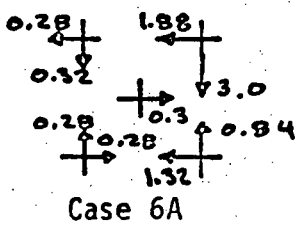
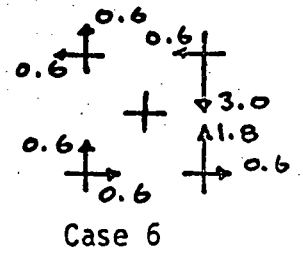
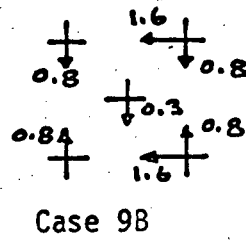
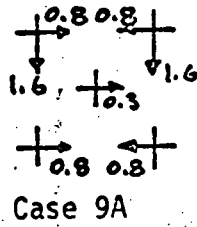
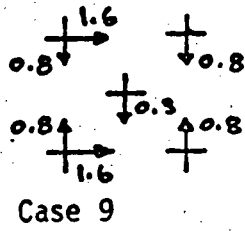
Case 2B



Results for
 PMR = 5.5
 $P_o = 715$ psia

Figure 6.4-23 Effects of outboard engine failure on the maximum heat shield heating rate.

Model Deflection Patterns



Instrumentation
in this octant.

40 Data adjusted to PMR=5.5, $P_0=715$ psia

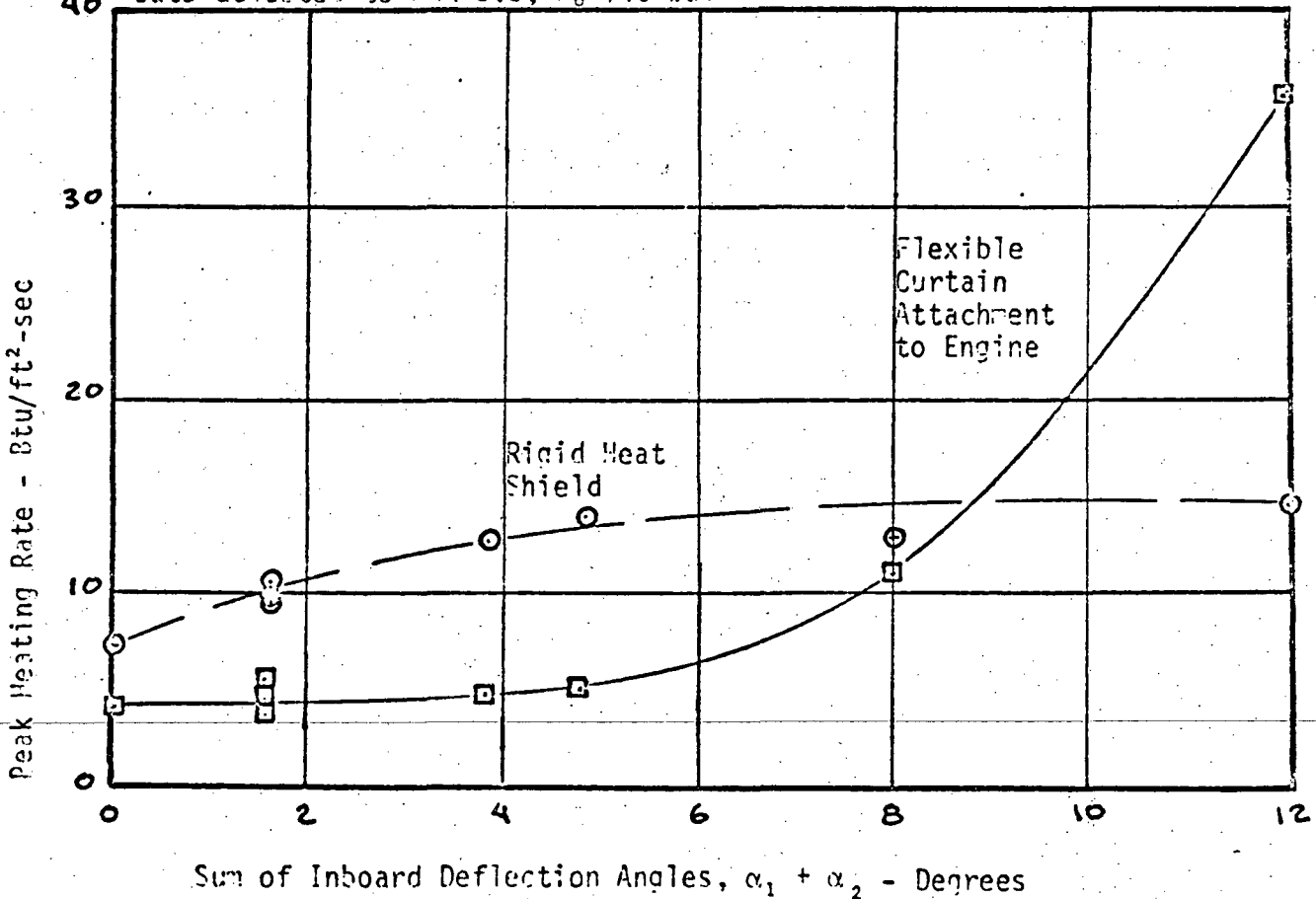


Figure 6.4-24 Effects of single actuator failure inboard on heat shield heating rates.

Symbol	$\beta_p = \beta_y$
○	7.5
◇	6
□	5

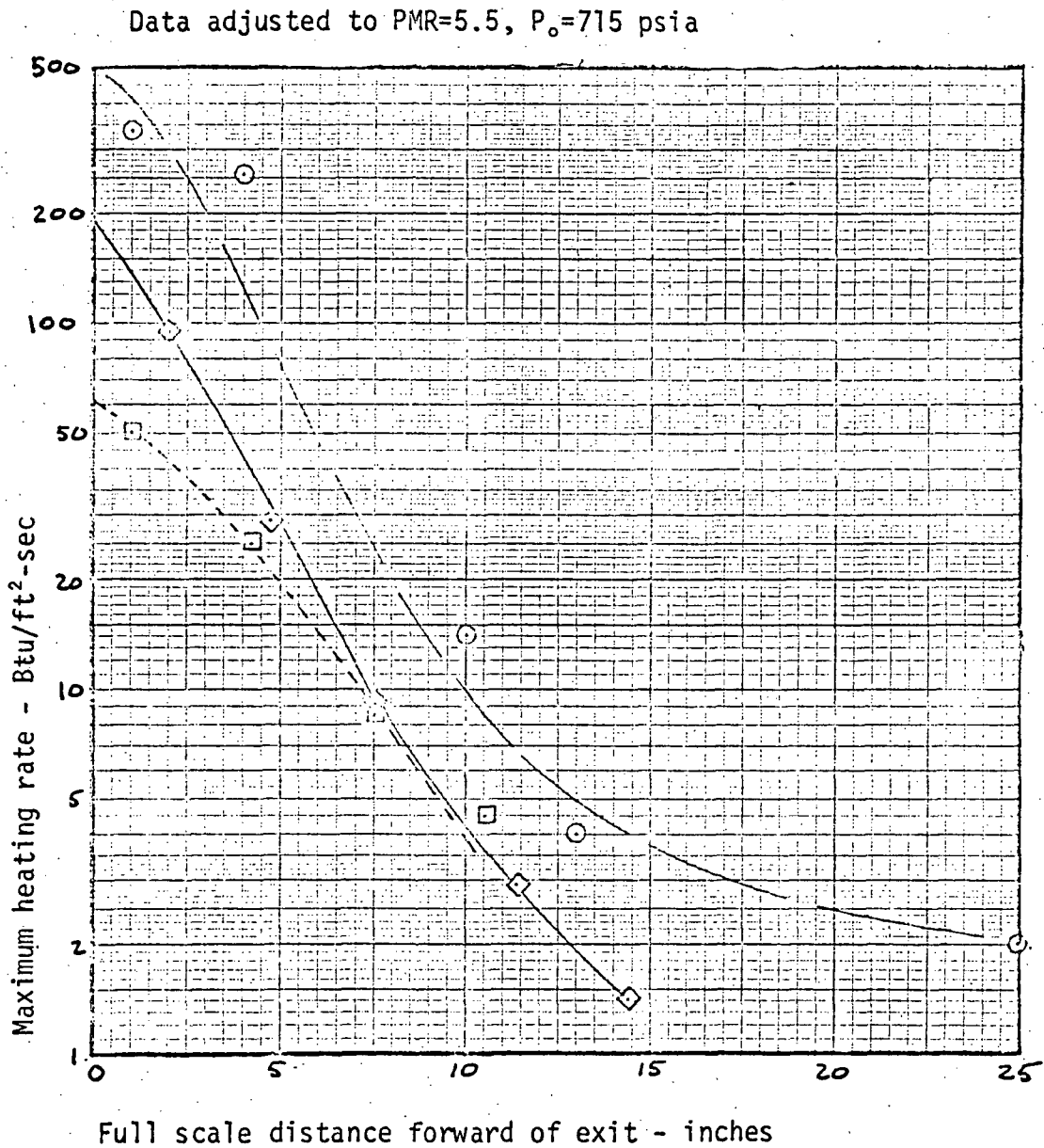
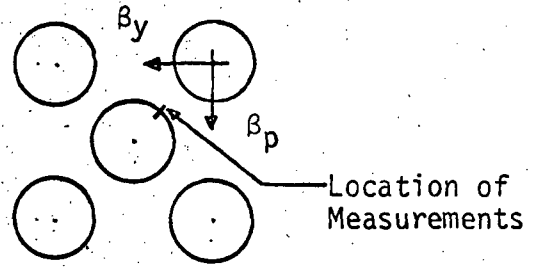


Figure 6.4-26 Effects of dual actuator failure on center nozzle heating.

Model Deflection Patterns

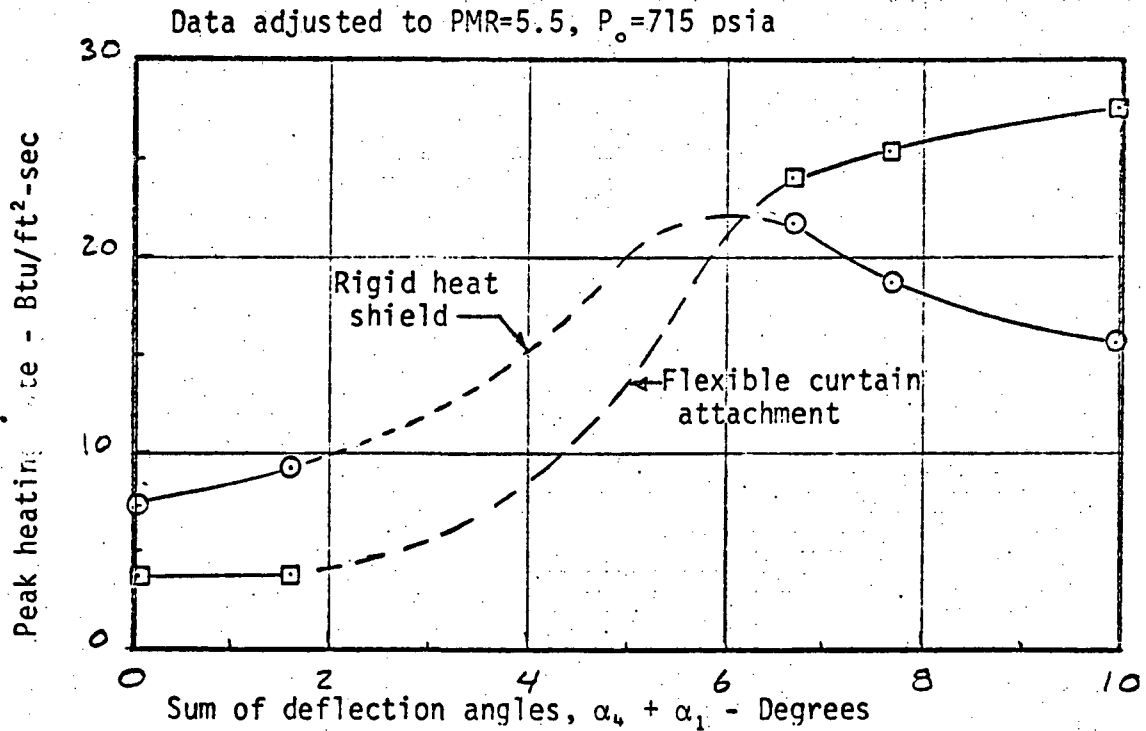
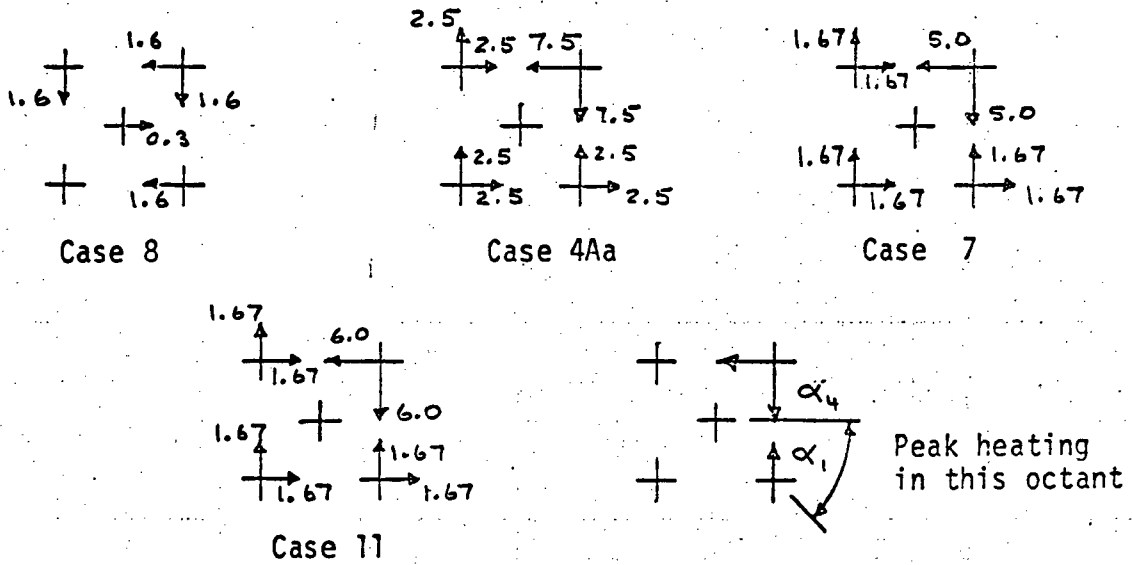


Figure 6.4-25 Effects of dual actuator failure on heat shield heating rates.

6.5 FLIGHT TEST AND PARAMETRIC DATA

S-II base environment instrumentation consisted of pressure transducers, total and radiation calorimeters, gas temperature probes, and structural temperature sensors. The first five vehicles (AS 501 thru AS 505) had extensive instrumentation, but the instrumentation was very limited on subsequent flights. The quality of the flight data was generally good. The design of the gas temperature probes did not permit a direct gas temperature measurement, but the correction procedures used to estimate gas temperatures from the probe temperature appear to give results which are consistent with other heating measurements.

In presenting the flight results, the pressure, interstage effect, and gas temperature results will be reviewed first, then the radiation and total heating results for the heat shield and thrust structure will be reviewed. The results presented are taken primarily from the first five vehicles, (references 6.3 and 6.4) but experience in later flights is summarized where significant differences have been noted.

Pressure

The pressures on the aft face of the heat shield shown in Figure 6.5-1 are constant to slightly decreasing thru most of the flight following the transient caused by interstage separation approximately 30 seconds after ignition. The PMR shift and consequent chamber pressure reduction produce a marked drop in the 450 to 500 second range. On AS 505, the PMR shift was preceded by CECO at about 460 seconds which also caused an appreciable drop.

The interstage separation can cause opposite effects as illustrated on instrument D95 (Figure 6.5-1). On AS 505 there is a pronounced rise which is counter to most interstage separation results, but this effect was also noted on total heating rates on other flights. This apparent anomaly may be caused by changes in the pressure distribution since most evidence points to a general pressure drop in the base region after interstage separation. The drop in

pressure after the second separation is most pronounced forward of the heat shield as illustrated in Figure 6.5-2.

Interstage Separation

More detailed records of the base environment during interstage separation are presented in Figure 6.5-3. In these data the separation process is shown to have a pronounced transient effect which is particularly noticeable in the pressure. The slower response of the calorimeters and gas temperature probe tend to attenuate the rapid changes, but the more sensitive radiation calorimeter shows a marked change.

Gas Temperature

Gas temperature on the aft face of the heat shield is measured with unshielded probes extending approximately 2 inches from the heat shield. The probes have a high heat capacity and emissivity, so a large discrepancy exists between the probe indicated temperature and the gas recovery temperature. To correct the probe indication to the gas recovery temperature, assumptions must be made to evaluate the convective and radiative heat gain and the radiation and conduction heat losses. Since heating rates and recovery temperatures vary in the base region, each probe must be corrected differently. The procedure used in making the corrections is outlined in reference 6.5, and typical results are shown in Figure 6.5-4.

There is a definite increase in recovery temperature caused by CECO as illustrated on AS 505 (Figure 6.5-4) and a decrease in recovery temperature due to the lower mixture ratio after PMR shift. On AS 507 the engine precoat was reduced from 2.3 to 1.3 degrees to bring the engines to a more nearly null position during firing and a definite increase (to 856K) was noted in the recovery temperature during 5-engine operation. On AS 508 it appeared that a steady state engine deflection caused a more severe thermal environment and CECO occurred

prematurely at 330 sec. so the flight was longer than nominal. The maximum temperatures recorded on AS 508 were as follows:

<u>Condition</u>	<u>Predicted Recovery Temperature</u>
Before CECO	910K (1180F)
After CECO	1045K (1420F)
After PMR Shift	940K (1230F)

These are the highest temperatures recorded to date.

Heat Shield Heating Rates

Since the incident radiation on the heat shield was expected to be fairly uniform, only two radiation calorimeters were installed on the heat shield for the first five flights. The measured incident radiation (corrected for instrument view factor) shown in Figure 6.5-5 indicates little variation in the peak heating rates. The radiation calorimeters generally show rather a gradual response. This characteristic is particularly apparent in the slow initial rise, and has not been satisfactorily explained. NAR is investigating possible contribution of the quartz window radiation to the indicated flux.

Variations in radiation are caused by the PMR shift and by engine shutdown on Flights AS 502 and 505. On AS 502, engines 2 and 3 shut down at approximately 413 seconds causing a large drop on instrument C665 (by engine 2) and a small dip followed by a rise on instrument C692. The rise on C692 must be attributed to deflection of engines 1 and 4, but the long duration of the rise would not be expected.

The center engine cut-off on AS 505 caused a definite drop on both radiation instruments followed by a further drop at PMR shift. This is in contrast to a general rise in total heating at CECO.

Representative total heating rates for AS 501 thru AS 505 are presented in Figures 6.5-6 thru 6.5-9. These data have not been corrected to cold wall conditions, but the calorimeters remain relatively cool, so the correction would be small. The results indicate much more variation than the radiation. This could be caused by variations in engine performance and alignment which would affect both the overall heating and the distribution of heating rates.

The divergence in trends caused by interstage separation noted earlier in the heat shield aft face pressures is also apparent in the total heating rates.

The reduction of heating resulting from the PMR shift is apparent in all total heating rates, but an increase in heating as a result of CECO on AS 505 is not consistently indicated. Although there is no pronounced decrease in total heating due to CECO, some instruments do not show an increase. For example the maximum increase is indicated on C687 (Figure 6.5-8) while C720 (also Figure 6.5-8) in the same area, shows a very slight declining trend. This indicates a definite shift in distribution, but there is no evidence of an increase in peak heating.

Shutdown of engines 2 and 3 on AS 503 causes both increases and decreases in heating depending upon position. Instruments C721 and C858 are between engines 2 and 3 so they (Figure 6.5-7) indicate a drastic drop in heating, while instruments C687 and C720 between engines 1 and 4 indicate an increase in heating (Figure 6.5-8).

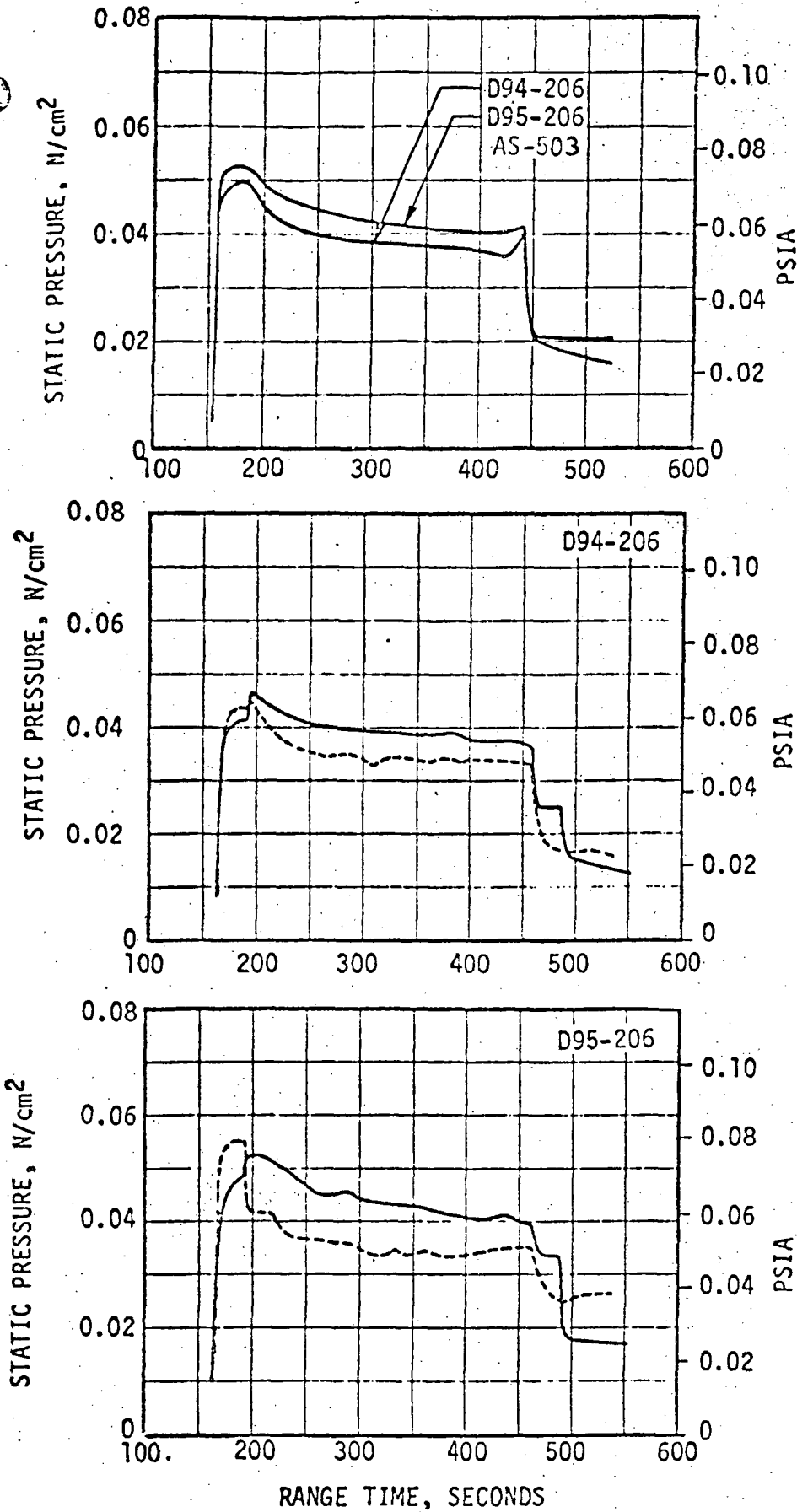
The only total heating calorimeter on AS 506 thru AS 509 (C722) indicated somewhat higher heating rates than the maximum of 3 watts/cm² noted on AS 503 (Figure 6.5-6). When precant was reduced on AS 507 the C722 heating rate reached a peak of 3 watts/cm² compared to approximately 2.7 watts/cm² on flights AS 504 and AS 505 which had a similar thrust structure and the higher precant (precant was increased to 2.3° with the new thrust structure on AS 504 and was reduced to 1.3° on AS 507). On AS 509, C722 indicated a peak of 3.22 watts/cm² was recorded after the premature CECO.

The heating rate on the forward face of the heat shield was measured on AS 504 and AS 505 (Calorimeter C723, Figure 6.5-9). The results indicated the expected significant effect of the interstage skirt, but a large increase was also noted after interstage separation on AS 504. It is suspected that this

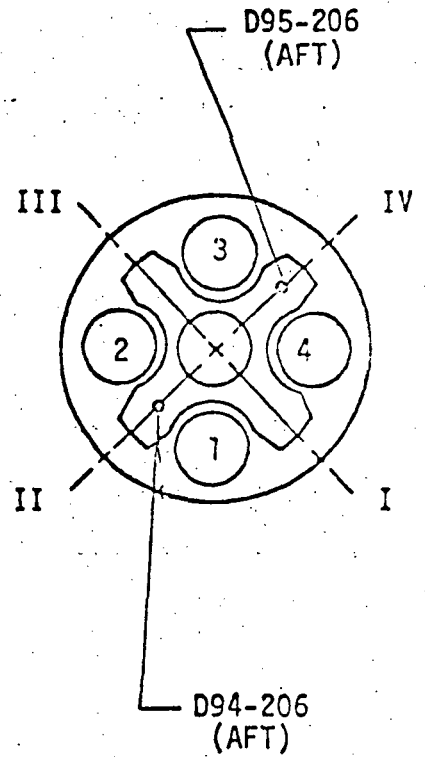
peak was caused by leakage at the flexible curtain around engine 4 because of improper lacing of the curtain to the heat shield. This would allow leakage which could be modulated by small engine gimbal movements.

Thrust Cone Heating Rates

The thrust cone total and radiation heating rates are presented in Figure 6.5-10. They indicate significant convective heating with the interstage in place, particularly near the middle of the thrust cone (C666 and C821). After interstage separation the total heating rates are so low that it is difficult to evaluate the relative effects of convective and radiant heating. The results indicate a reduction in heating at the PMR shift and a transient increase on C688 for AS 502. This increase was associated with hot gas leakage forward of the heat shield from the failure of engine 2.



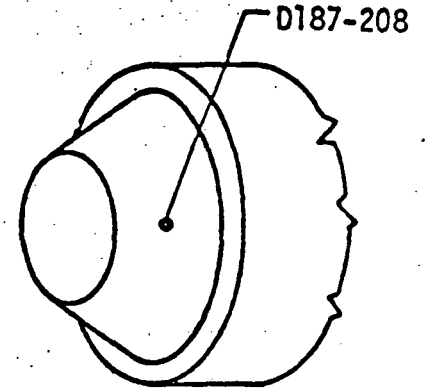
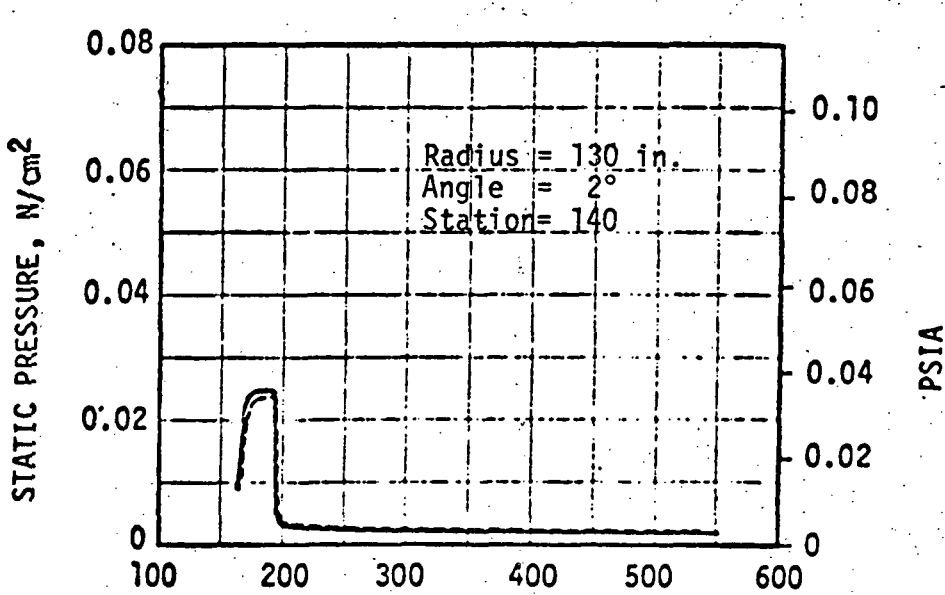
Inst.	Radius Inches	Angle Degrees
D95	85	270
D94	85	90



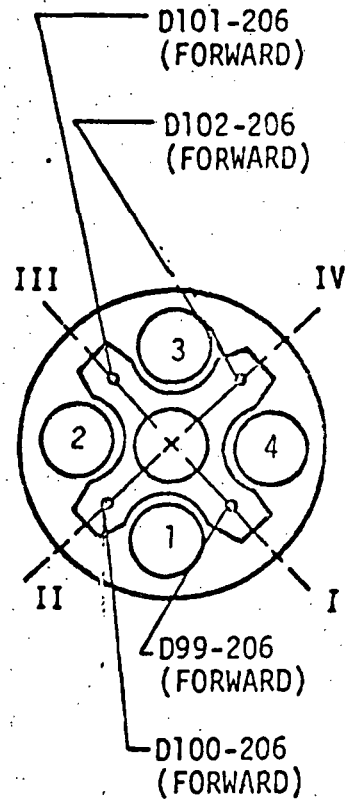
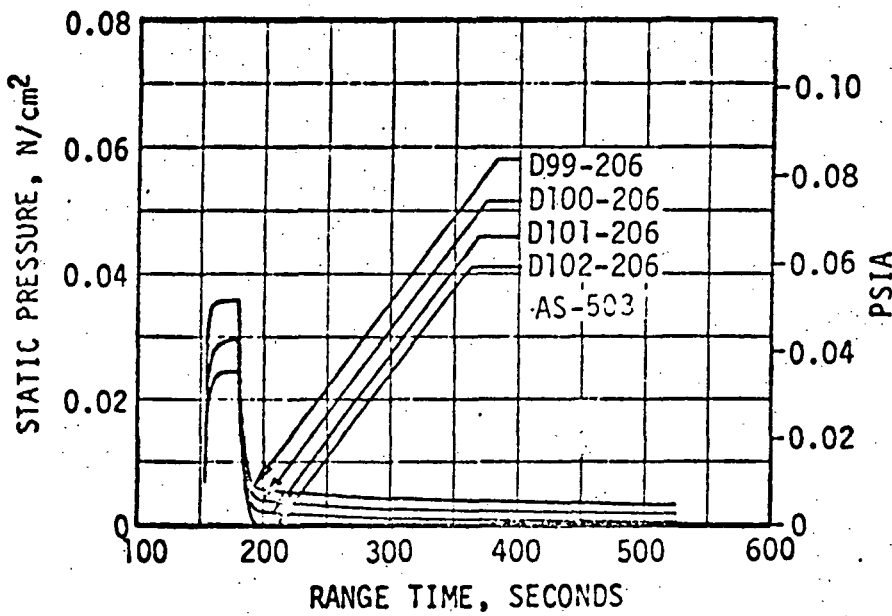
FLIGHT DATA

----- AS-504
 ————— AS-505

FIGURE 6.5-1 STATIC PRESSURES ON THE HEAT SHIELD AFT FACE.



FLIGHT DATA
 --- AS-504
 — AS-505



R = 85 inches on D99 thru D102

FIGURE 6.5-2 STATIC PRESSURES FORWARD OF THE HEAT SHIELD.

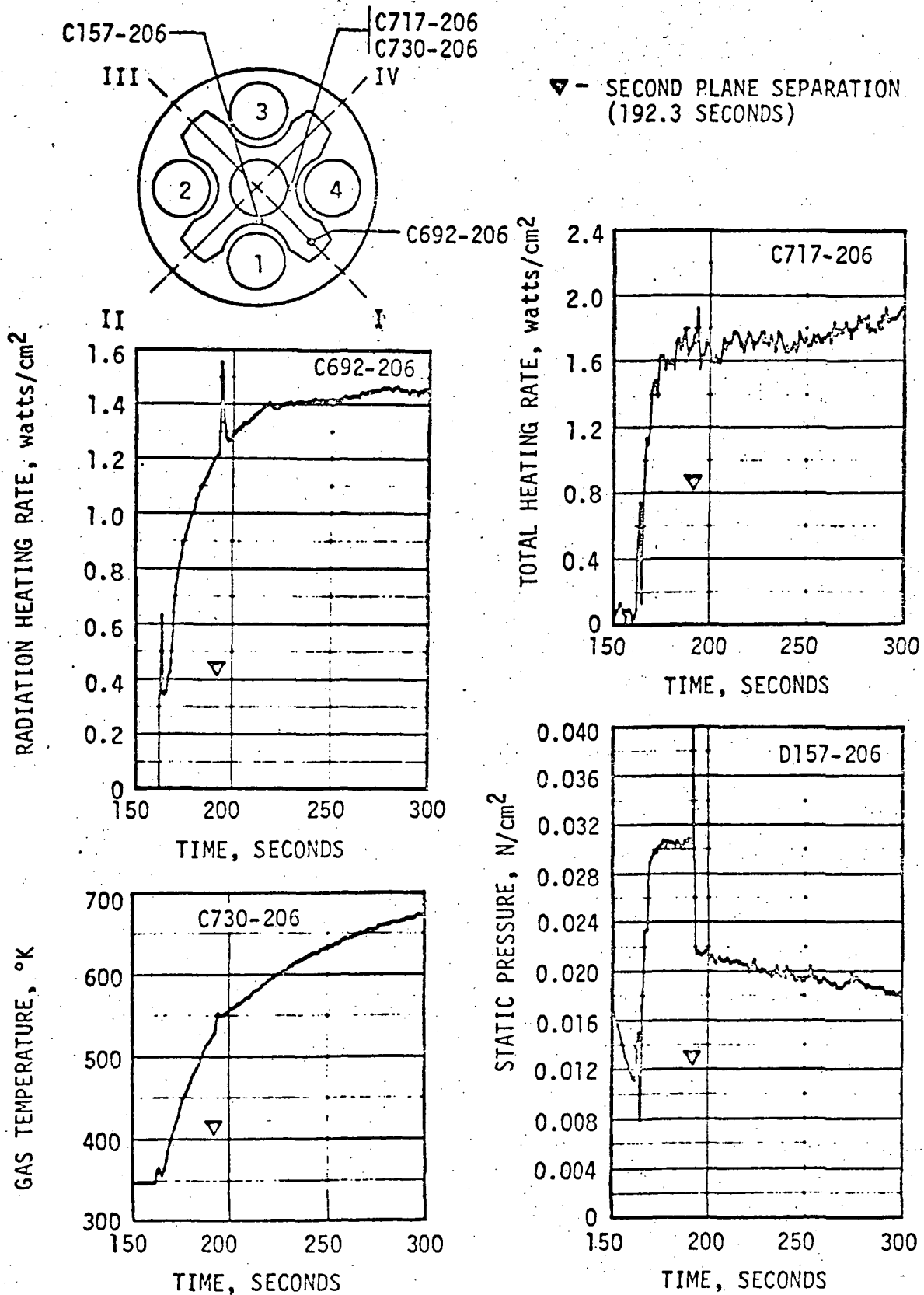


FIGURE 6.5-3 TYPICAL BASE REGION ENVIRONMENT DURING INTERSTAGE SEPARATION (AS-505)

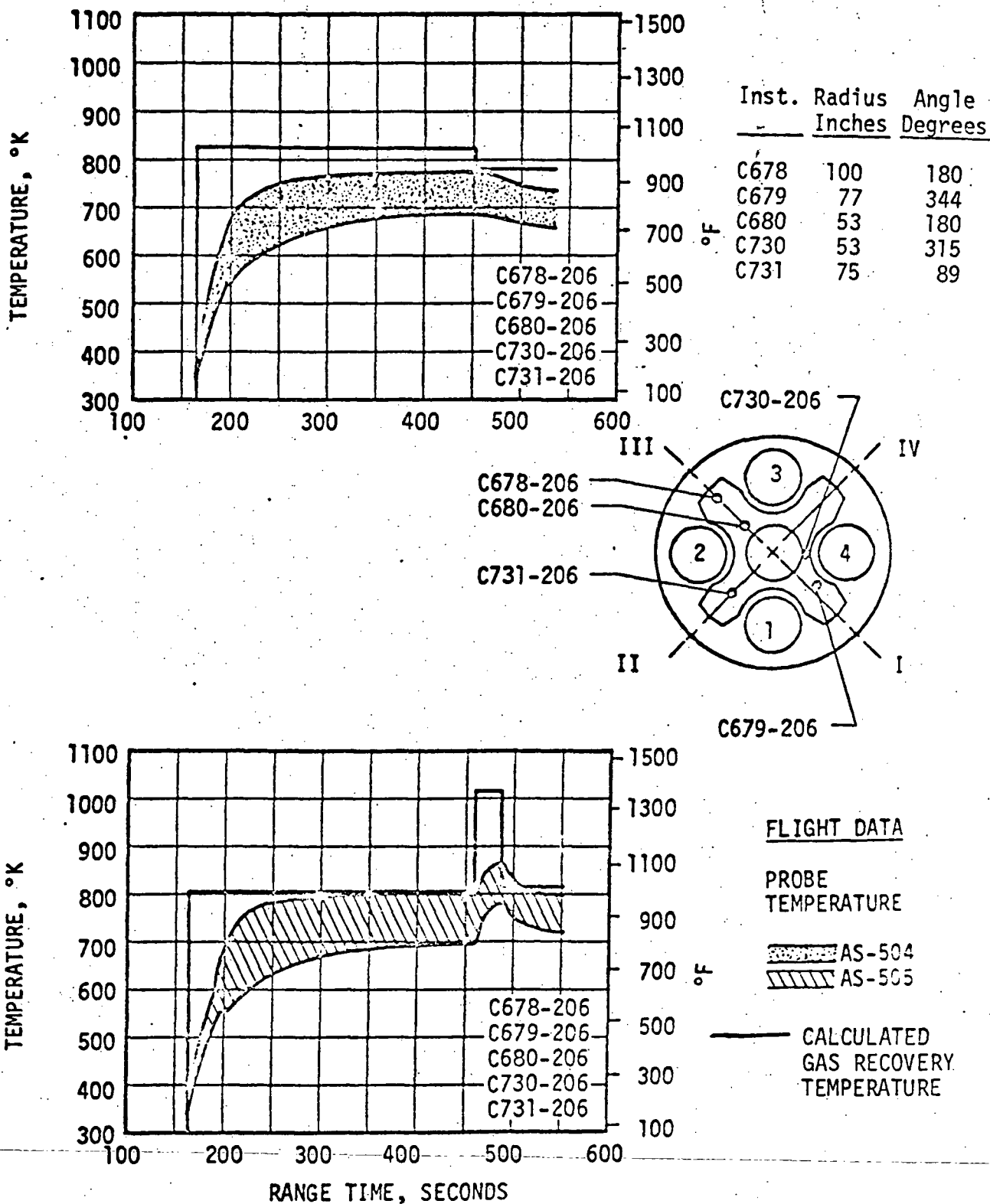
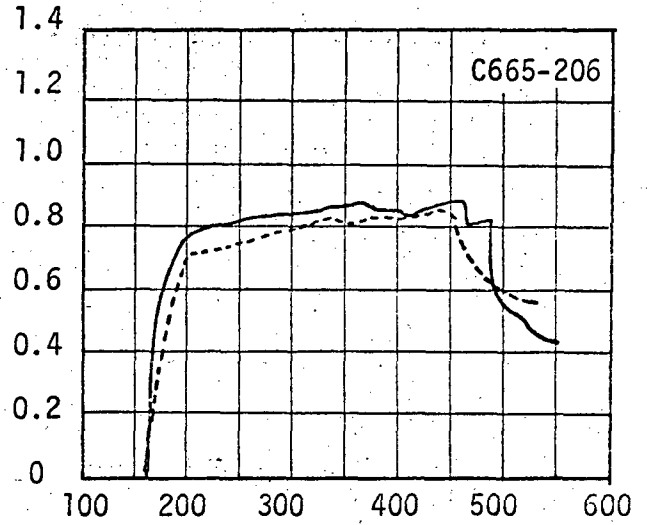
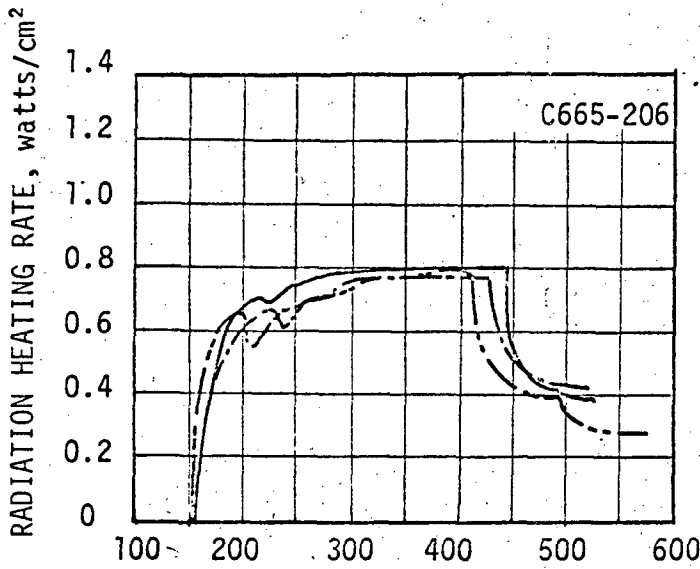
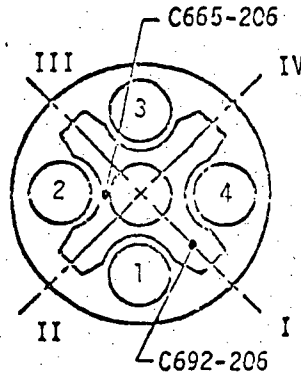


FIGURE 6.5-4 TYPICAL HEAT SHIELD GAS RECOVERY TEMPERATURES ON AS 504 and AS 505.



FLIGHT DATA
 - - - AS-501
 - · - AS-502
 — AS-503

Inst.	Radius Inches	Angle Degrees
C665	53	135
C692	100	0



FLIGHT DATA
 - - - AS-504
 — AS-505

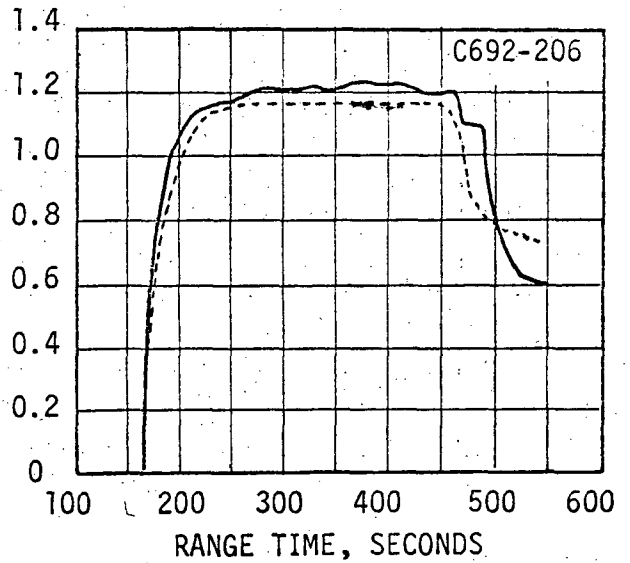
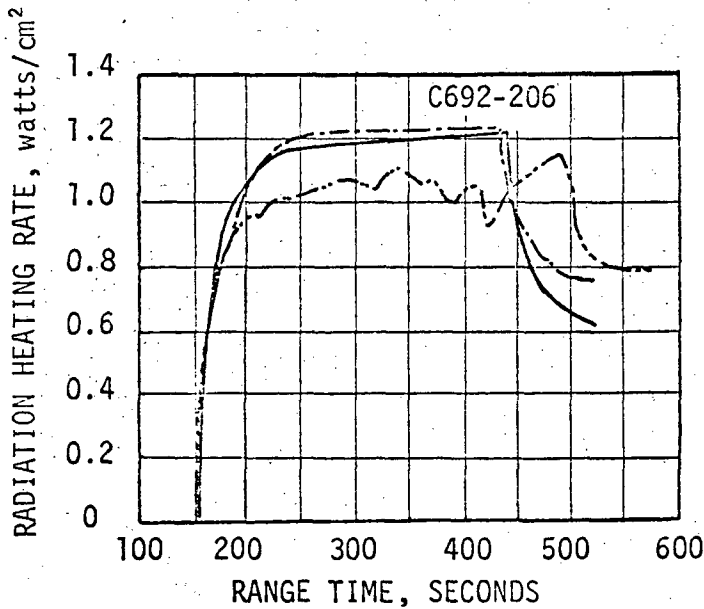


FIGURE 6.5-5 HEAT SHIELD AFT FACE RADIATION HEATING RATES ON AS-501 THRU AS-505.

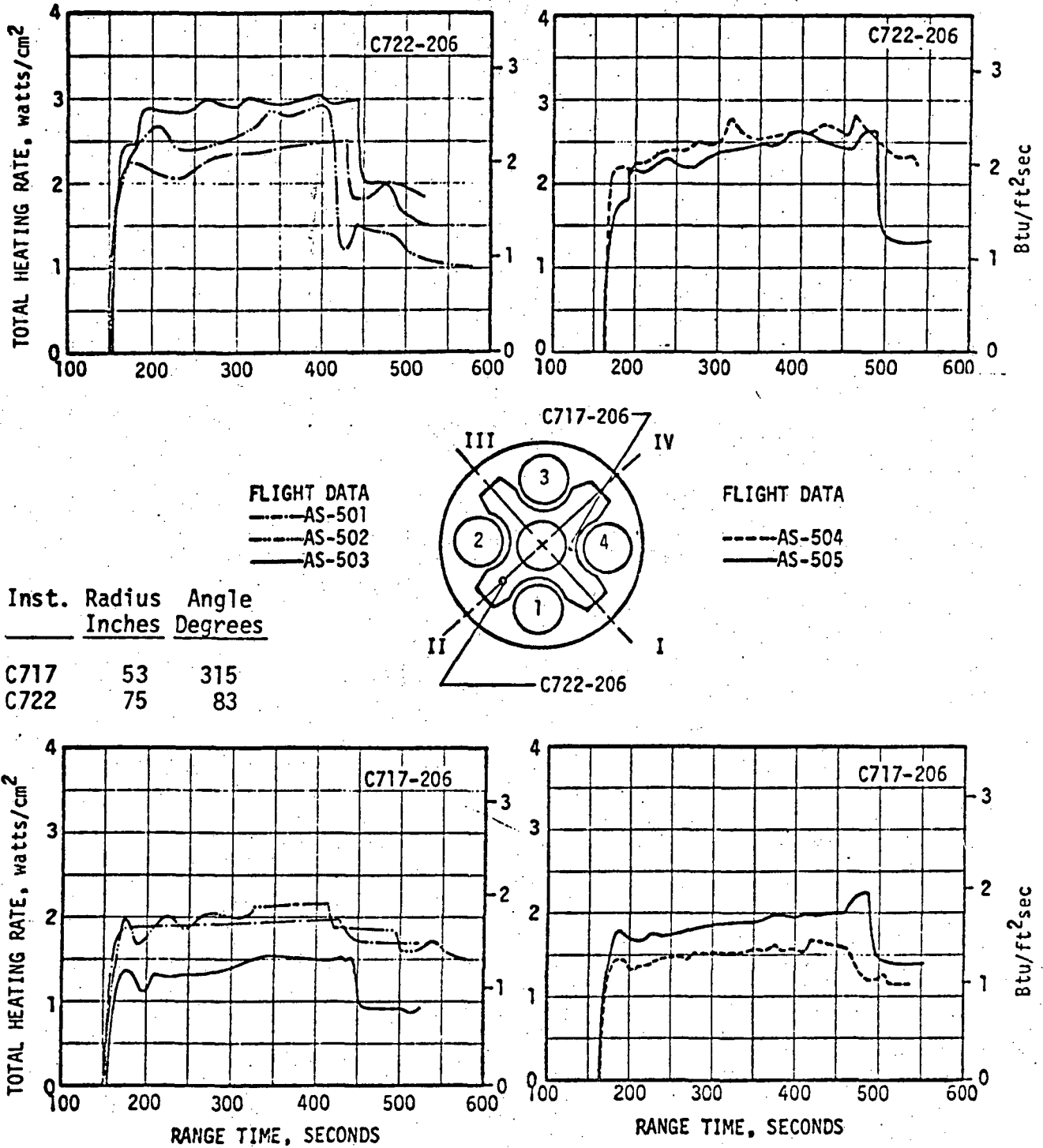
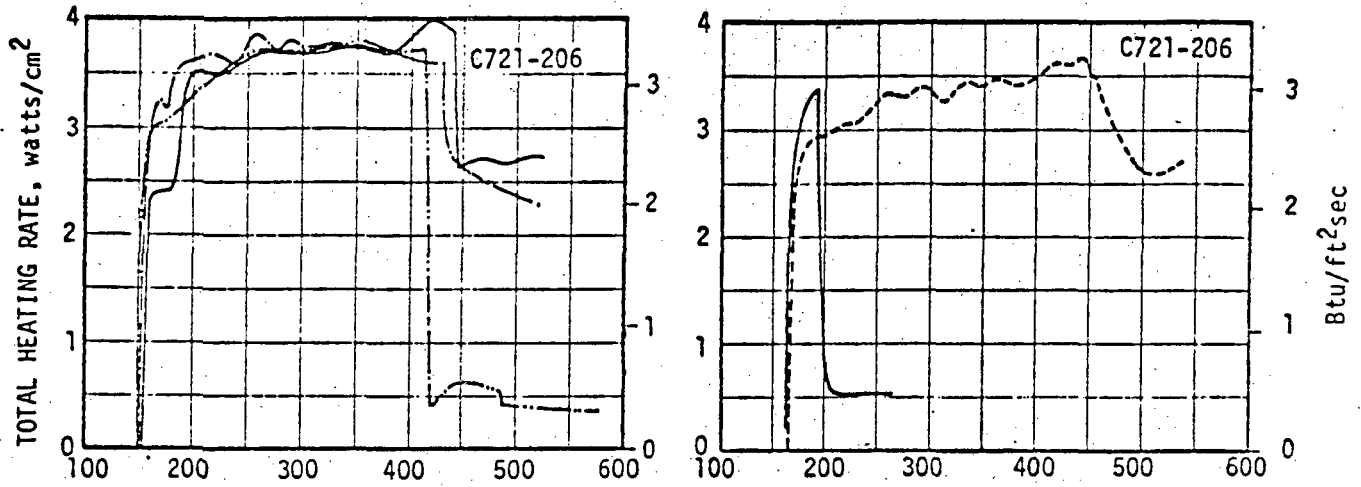
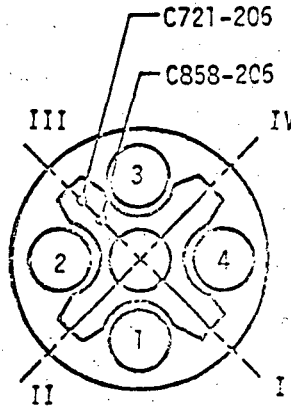


FIGURE 6.5-6 HEAT SHIELD AFT FACE TOTAL HEATING RATES ON AS-501 thru AS-505.



FLIGHT DATA
 - - - AS-501
 - · - AS-502
 — AS-503

FLIGHT DATA
 - - - AS-504
 — AS-505



Inst.	Radius Inches	Angle Degrees
-------	------------------	------------------

C721	100	180
C858	53	180

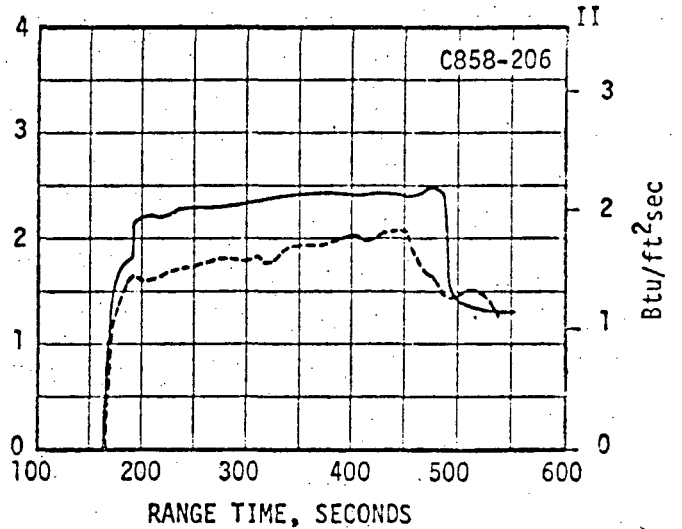
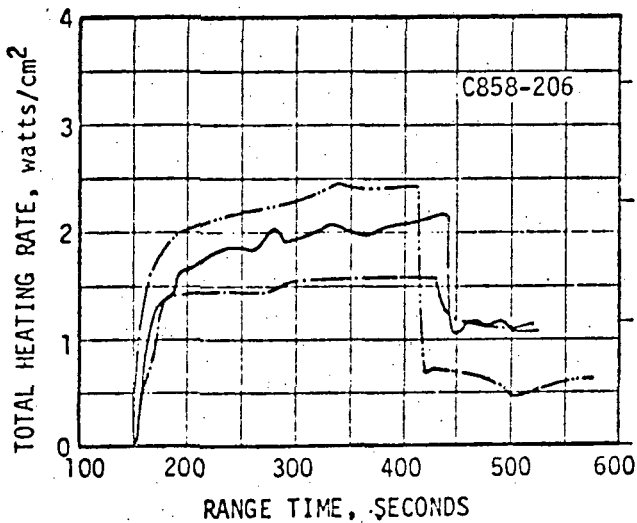
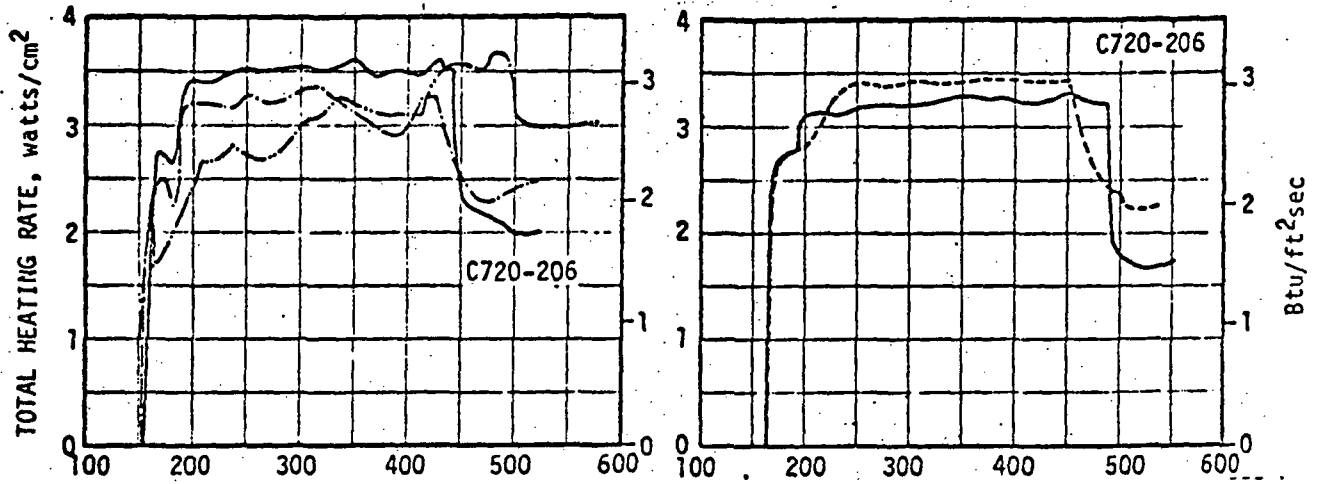


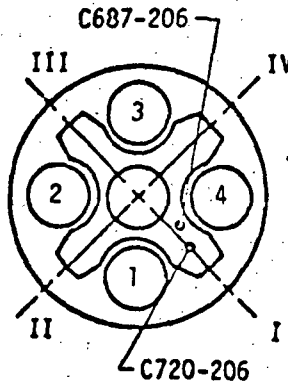
FIGURE 6.5-7 HEAT SHIELD AFT FACE TOTAL HEATING RATES ON AS-501 thru AS-505.



FLIGHT DATA

--- AS-501
 -.- AS-502
 — AS-503

Inst.	Radius Inches	Angle Degrees
C687	77	344
C720	83	0



FLIGHT DATA

--- AS-504
 — AS-505

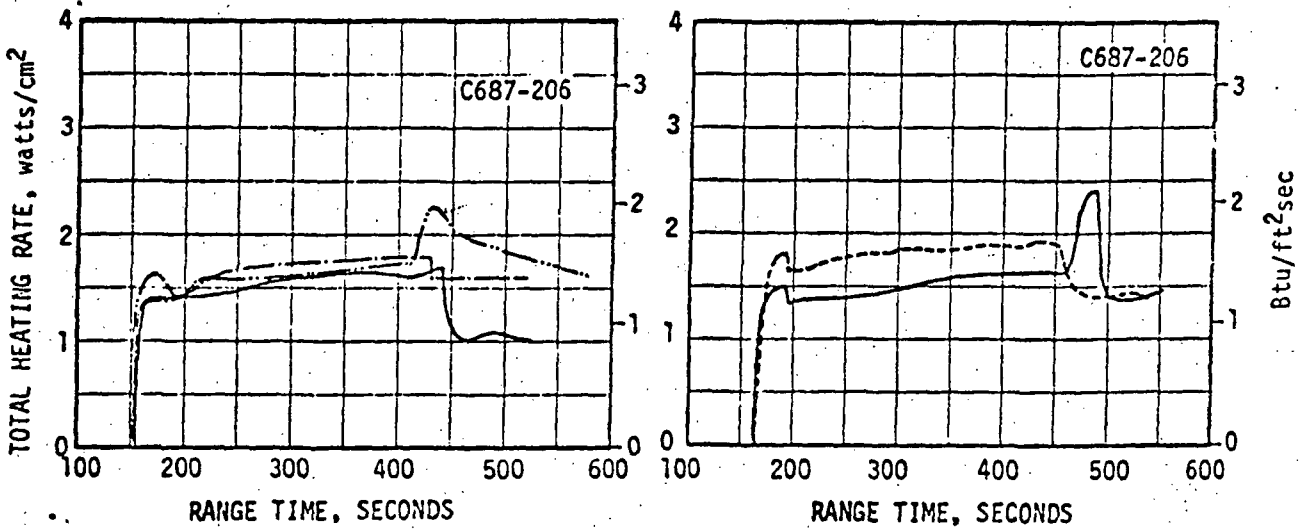
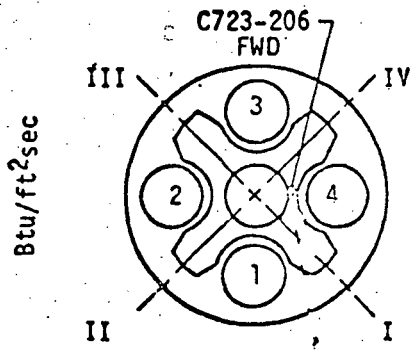
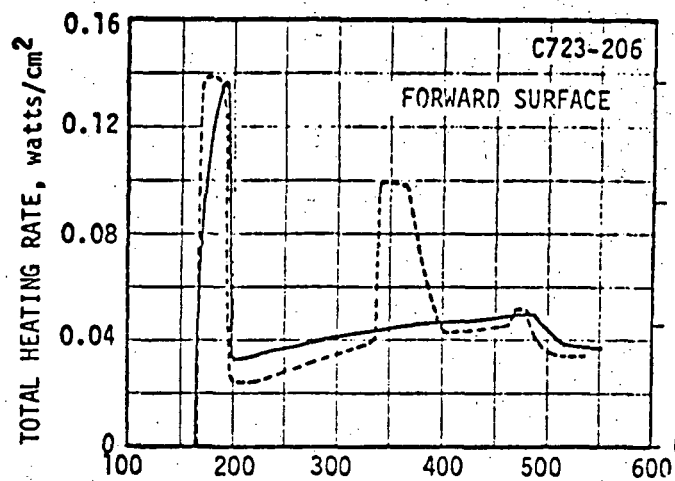
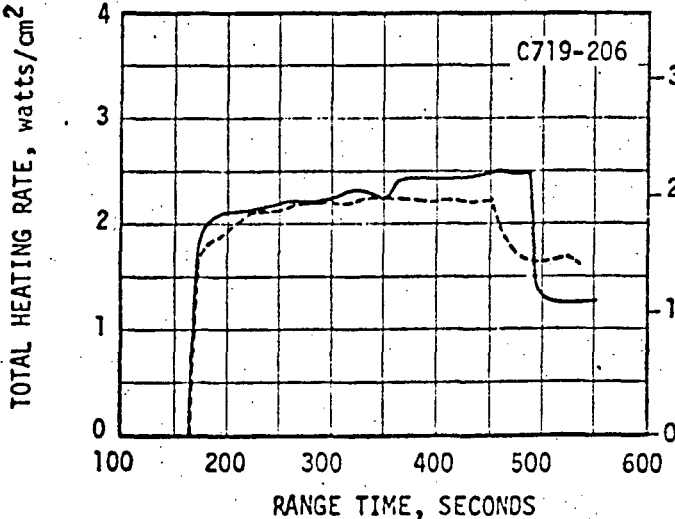
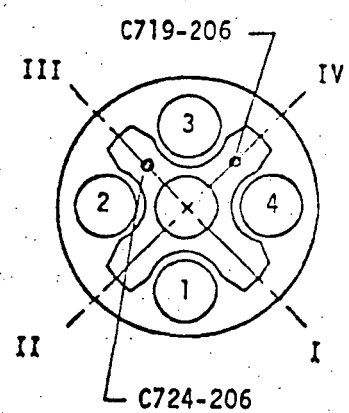
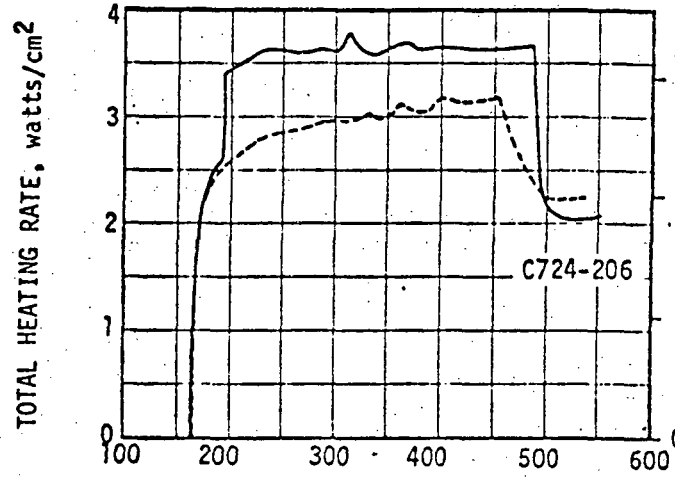


FIGURE 6.5-8 HEAT SHIELD AFT FACE TOTAL HEATING RATES ON AS-501 thru AS-505.



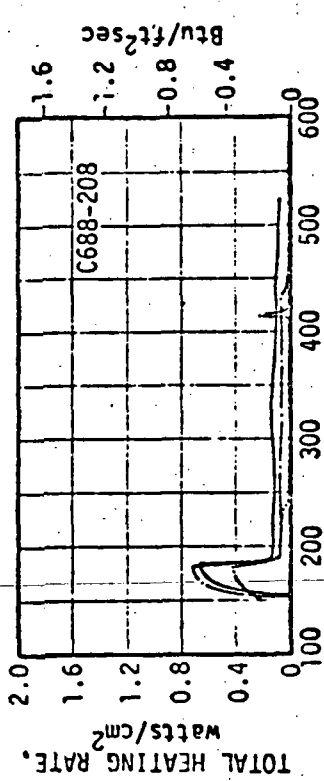
Inst.	Radius Inches	Angle Degrees
-------	------------------	------------------

C719	65	270
C723	52	315
C724	75	180

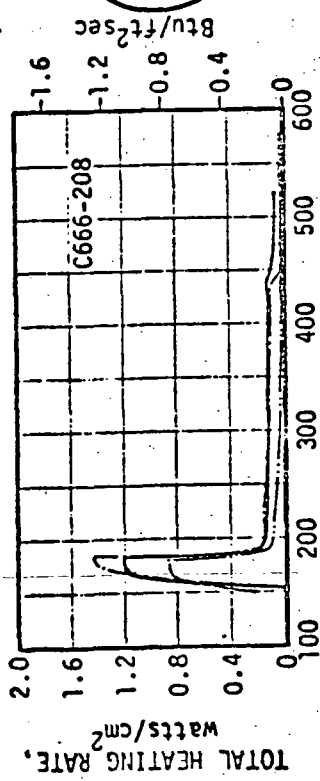


FLIGHT DATA
 -----AS-504
 _____AS-505

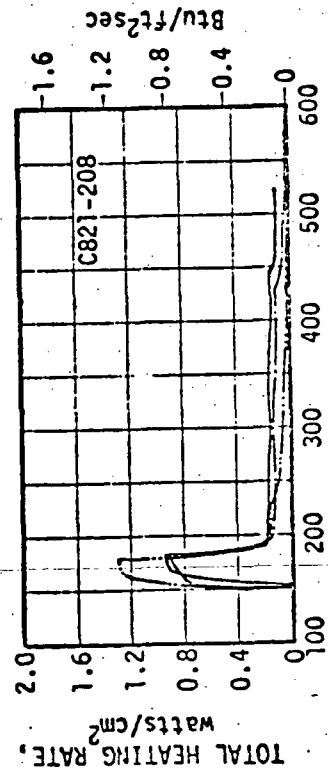
FIGURE 6.5-9 TOTAL HEATING RATES ON HEAT SHIELD FORWARD AND AFT SURFACES ON AS-504 and AS 505.



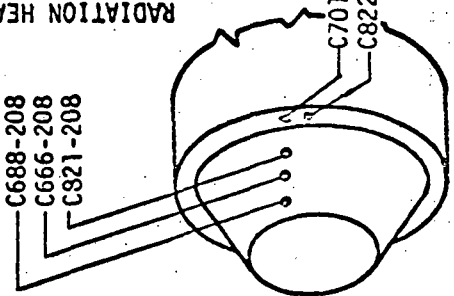
C688-208
C666-208
C821-208



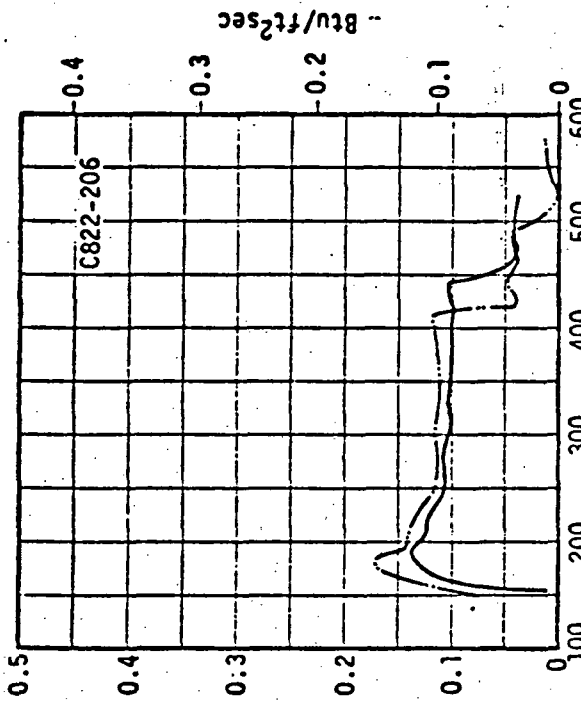
Btu/ft²sec



Btu/ft²sec



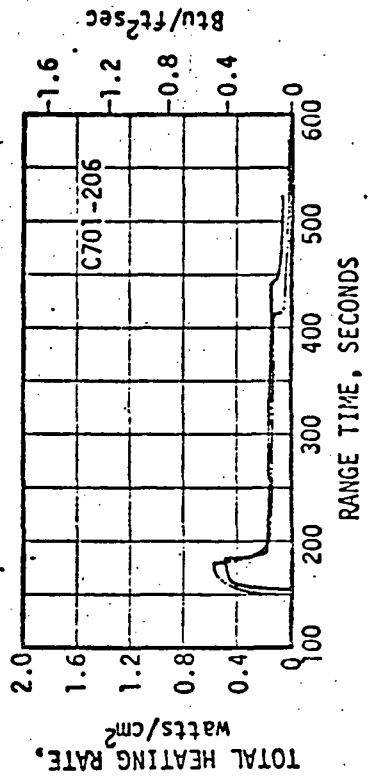
FLIGHT DATA
 - - - AS-501
 - - - AS-502
 — AS-503



Btu/ft²sec

Inst. Radius Inches Angle Degrees Station

C666	144	275	140
C688	180	275	115
C701	180	270	196
C821	184	275	170
C822	184	270	196



Btu/ft²sec

RANGE TIME, SECONDS

RANGE TIME, SECONDS

FIGURE 6.5-10 THRUST CONE TOTAL AND RADIATION HEATING RATES ON AS-501 thru AS-503.

6.6 COMPARISON OF MODEL AND FLIGHT TEST RESULTS

A precise comparison of model and flight results is almost impossible because of variations in both model and flight data which make it difficult to define a basis for comparison. During the process of model testing, a large range of configurations are tested and the data for each configuration exhibit considerable scatter. The vehicle design environment is selected from a conservative evaluation of the model results because of the large uncertainties involved in model simulation and operation. Because of this, flight deviations from the resulting design values are not necessarily representative of poor model simulation accuracy, but rather a combination of uncertainties in model simulation and in the important factors which affect the base environment. Because of these uncertainties, the model results can be evaluated based on different criteria to indicate agreement with the flight test results or large discrepancies depending upon the perspective chosen. Based on the conservative evaluation of model results which represents the design environment, the convective heating on the flight vehicle was significantly overpredicted by the model results. But evaluation of the model results based on flight experience with adjustments for the cooling effects of the turbine exhaust injection into the rocket nozzle wall can show reasonably good agreement with the measured convection heating.

The comparisons to be presented for convective heating will illustrate the range of model and flight results with comments on the effect of reduced recovery temperature. Comparisons will be made using the analytical predictions of radiation since scale effects limited the model radiation to approximately 4 percent of the values measured in flight. Before reviewing the comparison of radiative and convective heating, the base pressure results will be compared.

Pressure

Since base pressure was not a critical factor in the S-II base design, a conservative estimate of the base pressure was used for design and relatively few measurements of pressure were made during the model test program. Based on the measurements which were made, heat shield aft face pressures in the range of 0.02 to 0.035 psia would have been predicted from prototype model tests with engines near the null position. Parametric model tests with the heat shield closer to the nozzle exit (43 rather than 60 inches) indicated an average pressure of 0.045 psia at the maximum pressure location. This would increase to 0.051 psia if corrected for the increase in nozzle stagnation pressure from 632 to 715 psia for the PMR shift from 5.0 to 5.5.

Flight test results indicate good agreement with the model results on the inner portion of the heat shield while they are much higher in the outer regions. The general behavior and range of data are illustrated in Figure 6.6-1. The flight results shown illustrate pressures (averaged over the indicated flights) for three flight conditions: (1) interstage on, (2) just after second plane separation, and (3) at high altitude just before the PMR step (or CECO on AS 505). Model data should be expected to agree with the lowest flight results since external flow was not simulated in the model tests, but the flight results at the peak location are 60 to 70 percent above the model results. This is probably due to the increase in the reversed mass flow from the turbine exhaust injection into the nozzle boundary layer. Comparative model results with and without turbine exhaust are limited, but at two comparable locations (both at a full scale radius of 83 inches) the model turbine exhaust simulation caused an increase in heat shield pressure of 30 to 56 percent.

Pressures on the thrust cone with the interstage skirt removed are so low on both model and flight tests that measurement is difficult and comparisons

would be more representative of instrumentation problems than scale differences. With the interstage in place the pressure measured on the model (≈ 0.024 psia) is slightly lower than the range of 0.029 to 0.035 psia recorded in flight, but the measurements were in slightly different positions. Considering the difficulties in achieving steady flow in the interstage during a short duration test, the agreement is considered very good.

Radiation Heating

Two methods of predicting radiation described in Section 6.3 were used to define the base environment since model radiation is greatly different from full scale values. In the comparison with flight results, the radiation predictions used as the design environment (reference 6.6) will be referred to as "design prediction", while the later analysis using a band model description of the gaseous radiation (reference 6.7) will be referred to as "band model".

Comparison of the flight data and predicted radiation on the heat shield is shown in Figure 6.6-2. Flight measurements are in good agreement with the predictions on a radial line between outboard engines ($\theta=0^\circ$), but the band model prediction is slightly high between the outboard and center engines ($\theta=45^\circ$). Both predictions were based on plume properties for a propellant mixture ratio of 5.5 which is nominal for the overall engine. If the thrust chamber nominal mixture ratio of 5.71 had been used, the predictions would have been slightly higher.

Peak values of radiation heating measured on the thrust cone close-out (typical data in Figure 6.5-10) are approximately equal to the predicted values. Comparisons both with and without the interstage shown in Table 6.6-1 indicate the range of flight results and predictions.

TABLE 6.6-1

Comparison of Thrust Cone Radiation

	Heating rate - watts/cm ²	
	<u>Interstage On</u>	<u>Interstage Off</u>
Flight	0.13 - 0.25	0.10 - 0.15
Design Prediction	0.29	0.15
Band Model	-	0.15

Although the radiation comparisons appear to be very good, additional analysis of the radiation calorimeter used in flight would be required to assure that the comparison presented is valid. No adjustments have been made for the limited long wavelength transmissivity of the quartz window on the calorimeter or the possible convective heating and subsequent radiation from the window to the calorimeter.

Convective Heating

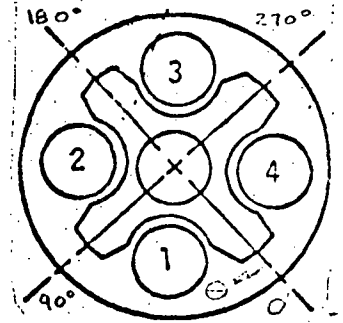
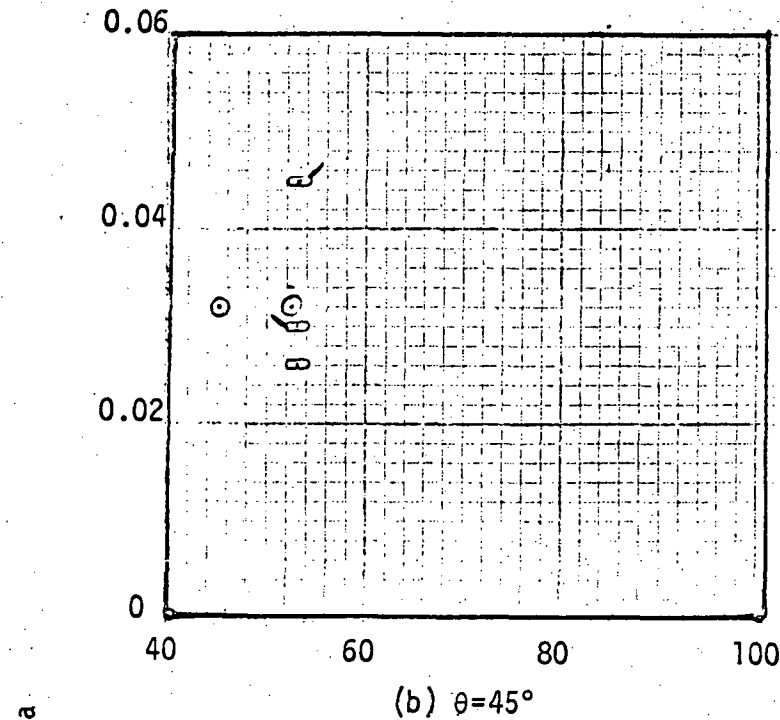
Due to interest in various engine deflection arrangements, model tests with a true null engine arrangement at a mixture ratio of 5.5 were limited, and no tests were run with slight outboard deflections representative of the engine positions resulting from precant on the first five flight vehicles. However, the probable effect of the slight outboard deflection would be to reduce the heating rate by less than 20 percent which is small in comparison to the spread between flight and model data.

The comparison of flight and model convective heating on the heat shield in Figure 6.6-3 shows good agreement near the center nozzle on a line between outboard engines with the model results becoming much greater at larger radii and between center and outboard engines. The differences in the results are attributed to the higher recovery temperature on the model because of the absence of turbopump exhaust injection into the nozzle.

A possible explanation of the good agreement near the center nozzles is that heating at this location is caused by recirculation of gas from the

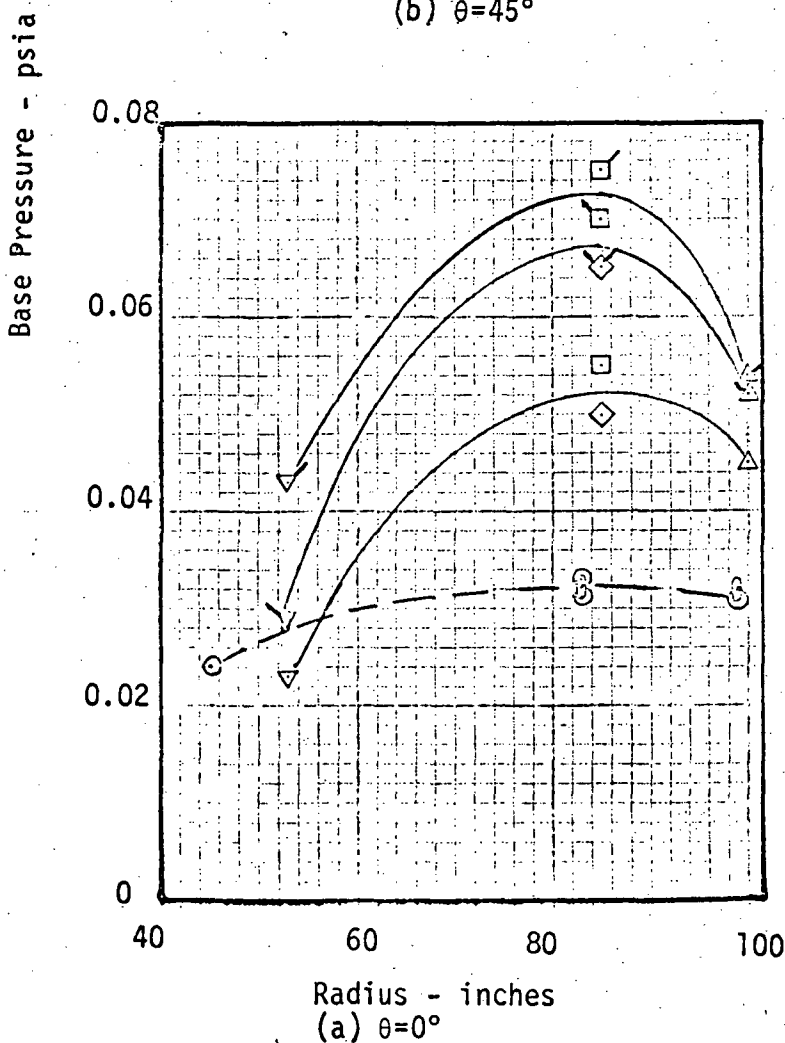
reversed flow impingement regions farther out on the heat shield. Because of this, the model flow is cooled more than the flight vehicle by the cooler heat shield surface so the temperature difference between model and flight conditions is reduced and better data agreement results.

Adjustments for recovery temperature are difficult since the recovery temperature varies with position on the heat shield and no direct measurement of recovery temperature could be made on the model. Based on temperature measurements made on the model it is expected that the recovery to surface temperature difference is nominally about twice the flight value in regions of maximum heating and increases to almost three times the flight value for model measurements used in the design criteria. If the model heating rates could be adjusted to flight conditions based on the correct temperature difference for flight conditions with turbine exhaust injection into the nozzles, the flight and model heating would probably agree within the uncertainties in the measurements and engine misalignment effects. This would indicate that there is no large scale effect on the heat transfer coefficient.



Average Flight Data

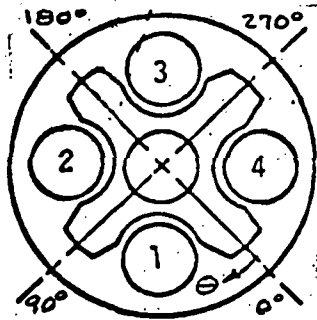
Symbol	Flights	Instrument
\triangle	5	D162
\diamond	3	D94
\square	3	D95
∇	2	D161
\circ	5	D157



Flags

- ∇ Interstage on
Just after interstage separation
- None Just before PMR step or CECO
- \circ Average Prototype Model data from MSFC tests for $O/F = 5.5$
- \circ Average Prototype Model data from CAL corrected to $O/F=5.5$

Figure 6.6-1 Comparison of model and flight measurements of heat shield aft face pressures.



- Flight
- 501
 - △ 502
 - 503
 - ◇ 504
 - ▽ 505
 - Band model prediction
 - Design prediction for all θ

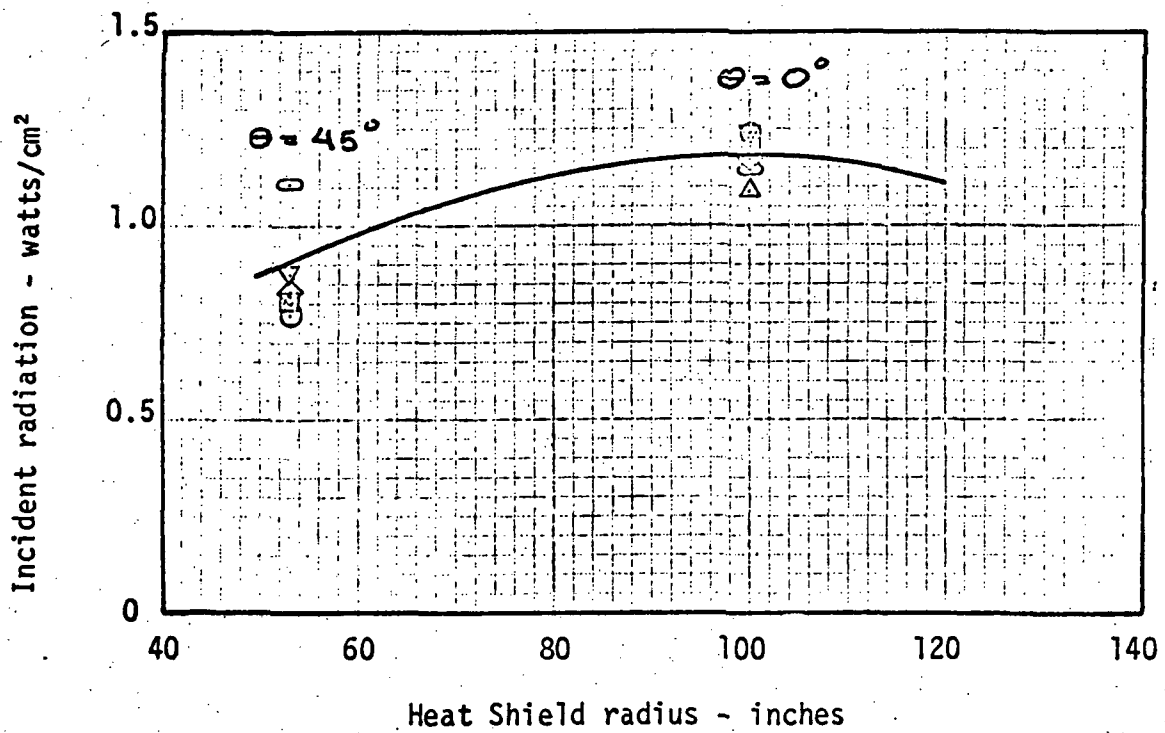
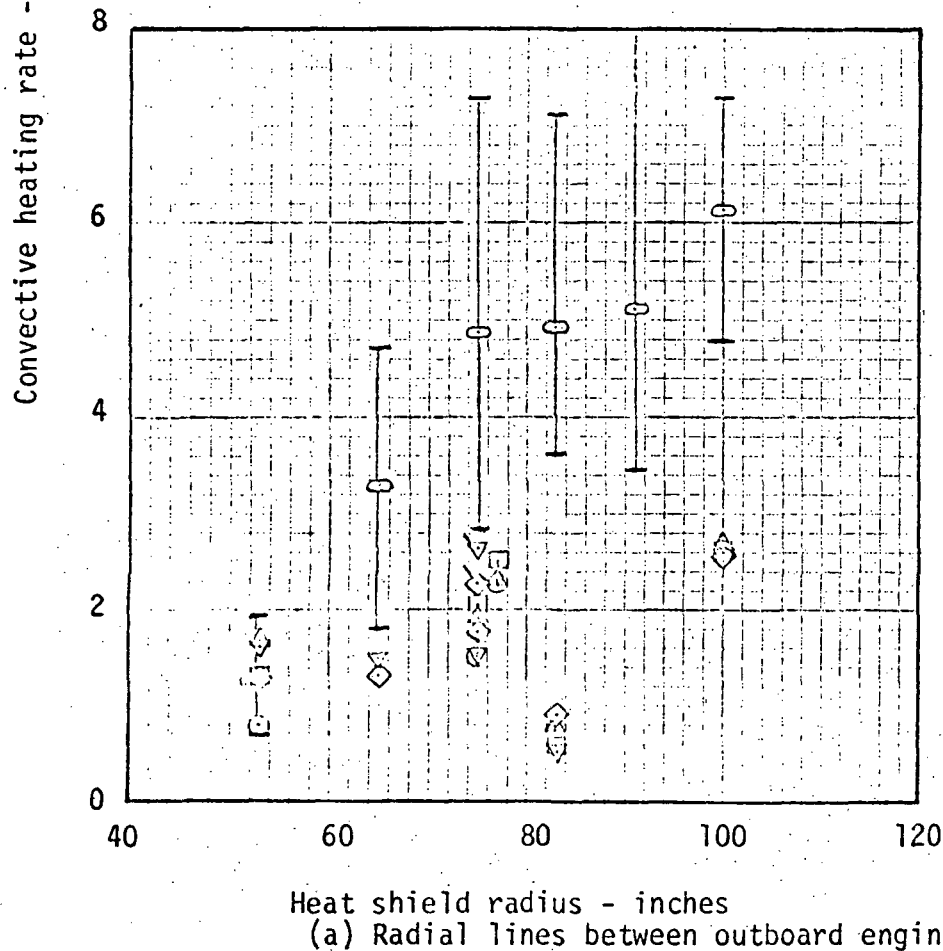
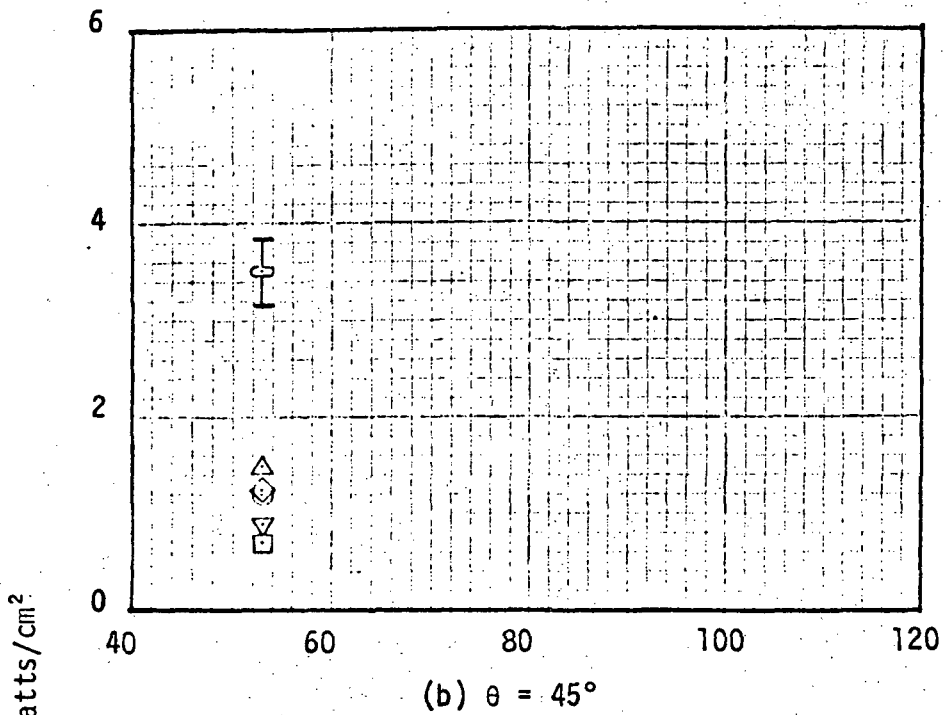
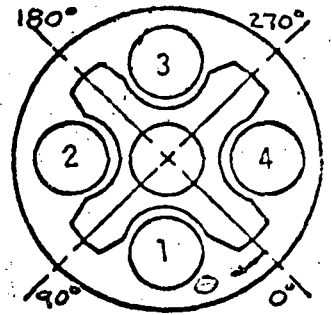


Figure 6.6-2 Comparison of heat shield radiation heating rates for 5 engine operation with PMR = 5.5.



- Flight
- 501
 - △ 502
 - 503
 - ◇ 504
 - ▽ 505
 - Average model data from MSFC tests at PMR=5.5
 - I Range of model data
 - 、 Inst. C724 - other data at 75 in. is C722

Figure 6.6-3 Comparison of model and flight convective heating

6.7 REFERENCES

- 6.1 Rickard, W. D., "High Altitude Investigations on the Saturn S-II Stage Using Short-Duration Techniques. Part I - Parameter Studies," Cornell Aeronautical Laboratory HM-1510-Y-17 (I), April 1965.
- 6.2 Rickard, W. D., "High Altitude Investigations on the Saturn S-II Stage Using Short-Duration Techniques. Part II - Prototype Base Environment," Cornell Aeronautical Laboratory HM-1510-Y-17 (II), April 1965.
- 6.3 "Saturn V Aerothermodynamics Flight Evaluation Summary - AS 501 thru AS 503," Boeing Report D-15796-1, June 19, 1969.
- 6.4 "Saturn V Aerothermodynamics Flight Evaluation Summary - AS 504 and AS 505," Boeing Report D-15796-2, Nov. 14, 1969.
- 6.5 "AS-503 S-II Base Region Gas Recovery Temperature Evaluation," NAR Internal Letter, S-II-190-700-69-21, March 7, 1969.
- 6.6 "Radiation Figures for Inclusion in S-II Final Design Base Region Thermal Environment," NAR Internal Letter, S-II/SI 65-68 Addendum I, August 9, 1965.
- 6.7 White, S. A. and Reardon, J. E., "Prediction of the Saturn S-II Base Radiation Environment," Hayes International Report 1469, August 1967.
- 6.8 "J-2 Engine Exhaust Plume Impingement Heating Rates and Pressures for Skylab ICD," NAR Internal Letter, LEVA-190-405-71/32, March 25, 1971.
- 6.9 Sergeant, R.J., "Base Heating Scaling Criteria for a Four-Engine Rocket Cluster Operating at High Altitude," AIAA Paper 65-826 presented at the Aerothermochemistry of Turbulent Flows Conference, Dec. 1965.
- 6.10 McAdams, W.H., "Heat Transmission" 3rd Ed., McGraw-Hill Book Co., Inc., New York, 1954.
- 6.11 "Methodology Used for Establishing S-II Stage Base Region Design Radiative Heat Rates," NAR Internal Letter, LEVA-190-405-71/86, July 1971.

Appendix F

BOUNDARY LAYER PROGRAM

**A SUMMARY OF THE NASA/LEWIS COMPRESSIBLE LAMINAR AND TURBULENT BOUNDARY
LAYER COMPUTER PROGRAM (BLAYER) AND NORTHROP-HUNTSVILLE MODIFICATIONS**

July 1971

by


W. W. Youngblood

PREPARED FOR:

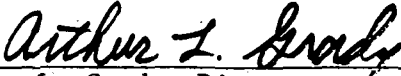
**NATIONAL AERONAUTICS AND SPACE ADMINISTRATION
GEORGE C. MARSHALL SPACE FLIGHT CENTER
AERO-ASTRODYNAMICS LABORATORY**

Under Contract NAS8-26268

REVIEWED AND APPROVED BY:



Dr. D. O. Barnett, Chief
Aerothermodynamics Branch



A. L. Grady, Director
Aerophysics Section

**NORTHROP CORPORATION
HUNTSVILLE, ALABAMA**

July 1971

TO: J. A. Forney, S&E-AERO-AT

FROM: W. W. Youngblood, Northrop-Huntsville

SUBJECT: A Summary of the NASA/Lewis Compressible Laminar and Turbulent Boundary Layer Computer Program (BLAYER) and Northrop-Huntsville Modifications

Copies: See Distribution

Section I. INTRODUCTION

This memorandum will provide a brief summary of a relatively powerful computer program (Program BLAYER) formulated for compressible laminar and turbulent boundary layers in arbitrary pressure gradients (ref. 1). Northrop-Huntsville placed the program in operation on the IBM 7094 in an effort to determine its usefulness in the overall definition of the NASA space shuttle thermal environment.

Since the computer program was designed for arbitrary pressure gradients on arbitrary two-dimensional geometries, it appeared to lend itself readily to a variety of problems. The basic BLAYER program will be outlined in Section II.

After placing the basic Program BLAYER into operation and debugging it, Northrop found it necessary to make several fundamental modifications and corrections to the program. Some of these changes were necessary since the originators of the program had never tested it on cases involving high supersonic and hypersonic Mach number flows. An additional major modification to the program was the addition of axisymmetric options to both the laminar and turbulent subroutines. None of these options has been extensively tested to date. Thus, Northrop does not yet consider the modified BLAYER formulation to be a production program. A brief description of the modifications made by Northrop is given in Section III.

Section II. THE BASIC BOUNDARY LAYER PROGRAM (BLAYER)

Program BLAYER was prepared by the NASA/Lewis Research Center in an effort to allow the inclusion of some real flow boundary-layer effects under known conditions of pressure gradient in the analytical prediction of turbomachinery performance. BLAYER is a Fortran IV language computer program for the computation of two-dimensional, compressible laminar and turbulent boundary layers in arbitrary pressure gradients. Arbitrary selection of initial values is possible in both laminar and turbulent regions. Laminar separation is predicted and specification of reattachment is optional. Laminar-to-turbulent transition is predicted by the Schlichting-Ulrich-Granville method (ref. 2).

2.1 LAMINAR BOUNDARY LAYER

Solution of the laminar boundary layer is accomplished by Cohen and Reshotko's (ref. 3) approximate method based on Thwaites' correlation concept. The method results from the application of Stewartson's transformation to Prandtl's equations. This provides a nonlinear set of two first-order differential equations. These equations are then expressed in terms of dimensionless parameters related to the wall shear, the surface heat transfer, and the transformed freestream velocity. Subsequently, these parameters are assumed to be uniquely interdependent according to Thwaites' concept. Exact solutions allowing evaluation of these quantities was carried out earlier by Cohen and Reshotko (ref. 4). Cohen and Reshotko then derived methods for the evaluation of the two-dimensional and axially symmetric laminar boundary layer with arbitrary freestream velocity distribution, Mach number, and surface temperature. McNally (ref. 1) generated the laminar subroutine for the two-dimensional case from the methods of Cohen and Reshotko, including elaborate curve-fits of their correlations.

Following the methodology outlined above, Cohen and Reshotko were able to reduce the laminar boundary layer problem to the solution of one first-order, ordinary, nonhomogeneous differential equation in terms of a freestream velocity gradient parameter. This can be shown to have the form of equation (28) of reference 3,

$$-U_e \frac{d \left(\frac{n}{\frac{dU_e}{dX_{tr}}} \right)}{dX_{tr}} = N(n, S_w) \quad (1)$$

where:

$$\frac{dU_e}{dX_{tr}} = a'_o \frac{dM_e}{dx} \frac{1}{\frac{dX_{tr}}{dx}} = a'_o \frac{dM_e}{dx} \frac{a'_o P'_o}{k_{su} a_e P_e}$$

For isothermal, or nearly isothermal, surfaces, the solution of equation (1) is simplified since N can be expressed as a linear function of the pressure gradient parameter (correlation number) n as follows:

$$N = A + Bn \quad (2)$$

The solution of equation (1) is then equation (32) of reference 3,

$$n = -AU_e^{-B} \frac{dU_e}{dX_{tr}} \int_0^{X_{tr}} U_e^{B-1} dX_{tr} \quad (3)$$

When transformed back to physical quantities by using Stewartson's transformation, this becomes

$$n = -AM_e^{-B} \frac{dM_e}{d(x/L)} \left(1 + \frac{\gamma-1}{2} M_e^2 \right)^{(3\gamma-1)/(2\gamma-2)} \int_0^{x/L} \frac{M_e^{B-1}}{\left(1 + \frac{\gamma-1}{2} M_e^2 \right)^{(3\gamma-1)/(2\gamma-2)}} d(x/L) \quad (4)$$

Once n is obtained at each station, the other boundary-layer and heat-transfer parameters are easily obtained. Details of the evaluation of these parameters is contained in reference 3.

2.2 TURBULENT BOUNDARY LAYER

Sasman and Cresci's method (ref. 5) is used in the formulation of the turbulent-boundary-layer subroutine of Program BLAYER. It is also an integral method, and involves coupled momentum and moment-of-momentum differential equations. A Mager-type transformation is applied to Prandtl's equations to obtain the momentum equation which is integrated across the boundary layer to give the momentum integral equation. Similarly, the moment-of-momentum equation is obtained in the same way after multiplying the momentum equation by the transformed y-coordinate. The two derived integral relations which result from this procedure are presented as equations 5 and 6 of reference 5.

These derived equations are not in solvable form, however. Sasman and Cresci make use of Crocco's relation and a power-law assumption for velocity profiles to evaluate the enthalpy integrals in both the momentum and moment-of-momentum equations. The Ludwig-Tillman skin friction relation, transformed for compressible flow, is used for the shear-stress terms in both equations. Results from equilibrium turbulent boundary-layer analysis is used to evaluate the normalized shear distribution integral contained in the moment-of-momentum equation. After making these evaluations and substitutions and with the relation

$$f = \left(\frac{U_{e \theta}}{v_o'} \right)^{1.268} = \left(\frac{M a_{e \theta}}{v_o'} \right)^{1.268}$$

the momentum and moment-of-momentum equations may be put into the following form:

$$\frac{df}{dx} = 1.268 \left\{ \frac{-f}{M_e} \frac{dM_e}{dx} \left[1 + (1+S_w) H_i \right] + C \right\} \quad (5)$$

and

$$\begin{aligned} \frac{dH_i}{dx} = & \frac{-1}{2M_e} \frac{dM_e}{dx} \left[H_i (H_i + 1)^2 (H_i - 1) \right] \left[1 + S_w \frac{H_i^2 + 4H_i - 1}{(H_i + 1)(H_i + 3)} \right] \\ & + \frac{(H_i^2 - 1)}{f} C \left[H_i - \frac{0.011 (H_i + 1) (H_i - 1)^2}{H_i^2} \frac{2}{C_f} \frac{T_o'}{\bar{T}} \right] \quad (6) \end{aligned}$$

where:

$$C = 0.123e^{-1.561H_i} \left(\frac{M_e a'_o}{v'_o} \right) \frac{T_e}{\bar{T}} \left(\frac{T_e}{T'_o} \right)^{(\gamma+1)/(2\gamma-2)} \left(\frac{\bar{u}}{u'_o} \right)^{0.268}$$

$$\frac{C_f}{2} = \frac{\tau_w}{\rho_e u_e^2} = 0.123e^{-1.561H_i} f^{-0.2113} \left(\frac{T_e}{\bar{T}} \right) \left(\frac{\bar{u}}{u'_o} \right)^{0.268}$$

The above equations (5) and (6) are the required equations governing the development of the turbulent boundary layer. They are coupled, first-order, ordinary differential equations. Using initial values calculated in the laminar routine or given by the user, equations (5) and (6) are solved by a Runge-Kutta scheme. This produces the distribution of f and H_i along the surface. The usual boundary-layer parameters are then obtained from these two distributions. The power law is used in the calculation of turbulent velocity profiles.

2.3 TRANSITION

McNally (ref. 1) chose the Schlichting-Ulrich-Granville method (refs. 2, 6, and 7) for the theoretical prediction of transition from laminar-to-turbulent flow. McNally's choice was probably based on experience in predicting transition regions in the case of turbomachinery where the local Mach numbers were typically in the high subsonic and transonic regimes. Details of this transition criteria are summarized in reference 2. The Schlichting-Ulrich-Granville method will not be elaborated upon here due to its failure to predict transition at high supersonic and hypersonic Mach numbers. A modification made to circumvent this problem will be discussed in Section III.

2.4 SEPARATION

In the laminar boundary layer, separation is assumed to occur at the station where skin friction coefficient C_f or wall shear stress τ_w passes from positive to negative, indicating backflow. In the turbulent boundary layer, separation is predicted based on the magnitude of H_i (the transformed form factor for adiabatic flow, also called the incompressible form factor). Program BLAYER predicts turbulent separation at the station where H_i achieves a value

greater than 2.8. This value of H_i is relatively high and H_i grows rapidly near separation. McNally programmed BLAYER so that the values of H_i are printed at each output station and at each point where the turbulent differential equations are solved. Thus, a different separation point could be chosen from these printed values.

Section III. MODIFICATIONS AND CORRECTIONS TO PROGRAM BLAYER

Northrop-Huntsville prepared a working deck of Program BLAYER from reference 1. After making a number of small corrections to the program on the recommendation of McNally, attempts were made to test the program against selected sets of experimental tests. It was found that the transition criteria failed to predict transition on a sharp, leading-edge flat plate in supersonic flow. This led to a careful investigation of Program BLAYER's transition criteria and modification 1. discussed below. Subsequently, modification 2. was formulated to provide the option of calculating the turbulent boundary layer on axisymmetric bodies. Lastly, modification 3. was written to allow the option of calculating the laminar boundary layer on axisymmetric bodies. These three modifications are outlined briefly in the following paragraphs.

3.1 MODIFICATION 1. CORRECTION OF TRANSITION CRITERIA

As discussed earlier, McNally (ref. 1) chose the Schlichting-Ulrich-Granville method for the theoretical prediction of transition from laminar to turbulent flow. In an attempt to use this transition criteria in the case of a sharp leading-edge flat plate at a freestream Mach number of $M_\infty = 6.0$, an error was uncovered in the programmed transition criteria. This error was traced to a complex term in the calculation of the incompressible momentum thickness Reynolds number, Re_{θ_i} . The erroneous term was a sensitive function of both the boundary layer edge Mach number, M_e , and the enthalpy function, S_w . For certain combinations of S_w and M_e , the value of Re_{θ_i} would become negative. This situation was discussed in several telephone conversations with McNally and an attempt was made to correct the term. However, to date no adequate correction has been made and, thus, program BLAYER's Schlichting-Ulrich-Granville transition criteria

was deemed incorrect for use at supersonic Mach numbers at the boundary layer edge.

An extremely simple transition criteria was chosen in order to evaluate other features of Program BLAYER. The simple relation chosen was that used in the General Dynamics 3020 aerodynamic heating program (ref. 8),

$$Re_{CRIT} = 150 M_e \quad (7)$$

In this case the transition Reynolds number is based on the boundary layer edge conditions and the compressible momentum thickness, θ , rather than the incompressible momentum thickness Reynolds number based on wall conditions as is the case in the Schlichting-Ulrich-Granville criteria. No further effort is planned at this time to include a more elaborate transition criteria. Modification 1. makes use of the simple General Dynamics criteria for $M_e > 2.0$ and McNally's original Schlichting-Ulrich-Granville criteria for $M_e \leq 2.0$.

3.2 MODIFICATION 2. ADDITION OF AN AXISYMMETRIC OPTION TO TURBULENT SUBROUTINE OF PROGRAM BLAYER

Addition of the axisymmetric option to the turbulent subroutine of Program BLAYER was easily accomplished since the basic form of the first-order, ordinary differential equations were already formulated in the paper by Sasman and Cresci (ref. 5). Their equation (19) is identical with equation (5) of this memorandum except for the addition of a term involving the body radius, R. Equation (5) becomes, therefore,

$$\frac{df}{dx} = 1.268 \left\{ -\frac{f}{M_e} \frac{dM_e}{dx} \left[1 + (1+S_w)H_i \right] - \left(j f/R \right) \left(\frac{dR}{dx} \right) \right\} = C \quad (8)$$

where the terms are defined as before and j is 0 and 1 for the two-dimensional and axisymmetric case, respectively. Equation (6) of this memorandum doesn't change; therefore, it was only necessary to add the term

$$- \left(j f/R \right) \left(\frac{dR}{dx} \right)$$

to the original BLAYER program. It should be pointed out that equation (19) of reference 5 is actually incorrect. The correct form of the equation is given above in equation (8).

3.3 MODIFICATION 3. ADDITION OF AN AXISYMMETRIC OPTION TO LAMINAR SUBROUTINE OF PROGRAM BLAYER

The basic equation in program BLAYER leading to the determination of the laminar boundary layer parameters has already been introduced as equation (4) of this memorandum. Equation (4) is based on the derivation of Cohen and Reshotko (ref. 3) under the assumption of the validity of the linear approximation method for two-dimensional bodies. Cohen and Reshotko also formulated an equation based on the linear approximation method for laminar axisymmetric flow (ref. 3),

$$n = -A \left(1 + \frac{\gamma-1}{2} M_e^2 \right)^{\frac{3\gamma-1}{2\gamma-2}} M_e^{-B} \frac{dM_e}{d(x/L)} \frac{1}{R^2} \int_0^{x/L} \frac{R^2 M_e^{B-1}}{\left(1 + \frac{\gamma-1}{2} M_e^2 \right)^{\frac{3\gamma-1}{2\gamma-2}}} d(x/L) \quad (9)$$

Comparing equation (9) with equation (4) it may be noted that the only difference is in the addition of the square of the body radius. Numerically, it may be shown that the solution of equation (9) may be obtained from point to point by the following relationship:

$$(n)_{x_2/L} = \left[\frac{-AM_e^{-B}}{R^2} \frac{dM_e}{d(x/L)} \left(1 + \frac{\gamma-1}{2} M_e^2 \right)^{\frac{3\gamma-1}{2\gamma-2}} \right]_{x_2/L} \int_{x_1/L}^{x_2/L} \frac{R^2 M_e^{B-1}}{\left(1 + \frac{\gamma-1}{2} M_e^2 \right)^{\frac{3\gamma-1}{2\gamma-2}}} d(x/L) + \frac{\left[\frac{-AM_e^{-B}}{R^2} \frac{dM_e}{d(x/L)} \left(1 + \frac{\gamma-1}{2} M_e^2 \right)^{\frac{3\gamma-1}{2\gamma-2}} \right]_{x_1/L}}{\left[\frac{-AM_e^{-B}}{R^2} \frac{dM_e}{d(x/L)} \left(1 + \frac{\gamma-1}{2} M_e^2 \right)^{\frac{3\gamma-1}{2\gamma-2}} \right]_{x_1/L}} (n)_{x_1/L} \quad (10)$$

The validity and completeness of this modification to program BLAYER has not been fully investigated. There is some concern that the correlated values for the constants A and B may not be fully adequate for the axisymmetric case, especially for the initial conditions.

Section IV. SELECTED COMPARISONS WITH SOME EXPERIMENTAL BOUNDARY LAYERS

Program BLAYER was tested on several configurations before and after the modifications discussed in Section III. This section presents preliminary results of these computations without regard to total accuracy or comparison with other approximate techniques. Briefly, these sample problems include a subsonic NACA airfoil (NACA 0012); a sharp leading-edge, cooled flat plate in supersonic flow; a cone-cylinder-flare body at Mach 8.0; and a sharp half-angle cone in subsonic, laminar flow. In all cases the flow media was taken as air with the ratio of specific heats equal to 1.4.

4.1 PROBLEM 1. SUBSONIC NASA AIRFOIL 0012

The first sample problem is directly from McNally's report on BLAYER (ref. 1). It illustrates the prediction of transition in subsonic flow on a NACA airfoil (NACA 0012) at zero angle-of-attack. The transition criteria utilized in this problem is the Schlichting-Ulrich-Granville method discussed earlier. The freestream inlet Mach number is 0.284. The blade geometry, surface velocity distribution, and comparison of output with experimental results is given in Figure 1. Total stagnation pressure was 18.4 psia ($1.269 \times 10^5 \text{ N/m}^2$) and the total temperature was 600°R (333°K).

The boundary layer was assumed to begin at a stagnation point at the leading edge of the airfoil, and no initial values were used. Transition was predicted naturally by the program, and occurred within the range in which it was measured experimentally. Predicted values of δ^* and θ are shown in Figure 1 and compared with experimental values.

4.2 PROBLEM 2. SHARP LEADING-EDGE FLAT PLATE IN SUPERSONIC FLOW

This problem was an attempt to predict turbulent-boundary-layer heat-transfer on a flat plate with surface cooling at Mach 6. Experimental data were obtained

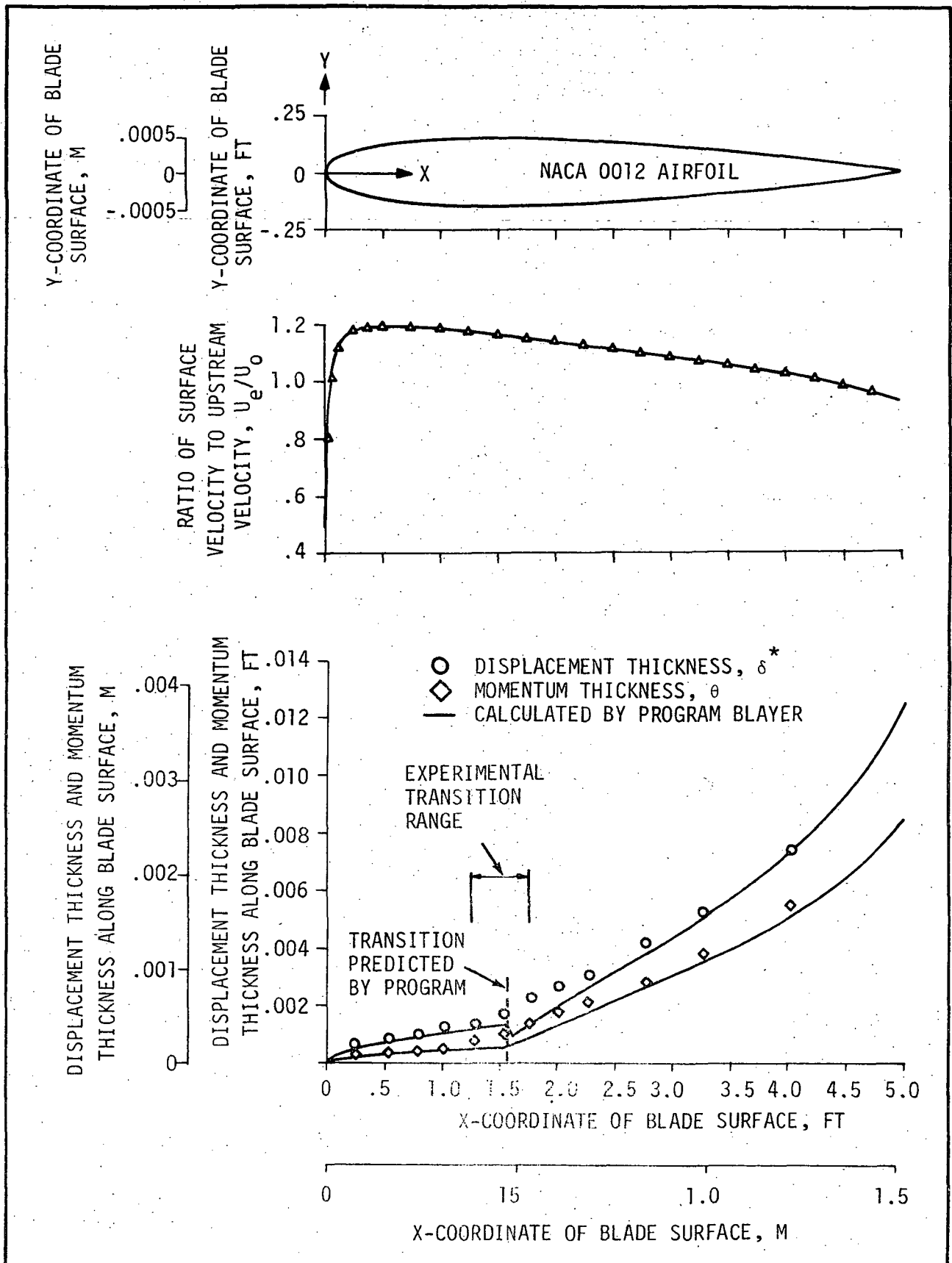


Figure 1. COMPARISON OF PROGRAM BLAYER RESULTS WITH EXPERIMENTAL DATA ON NACA 0012 AIRFOIL

from a test on a sharp-leading-edge flat plate with Reynolds numbers as high as 10^7 in the Langley 20-inch hypersonic wind tunnel (ref. 9). The configuration of the wind tunnel model is shown in Figure 2. The test conditions were a stagnation pressure of approximately 515 psia ($3.55 \times 10^6 \text{ N/m}^2$) at a stagnation temperature of about 959°R (533°K). The nominal freestream Mach number was $M_\infty = 6.0$ and the surface of the flat plate was cooled to approximately 672°R (373°K).

A comparison of the predicted Stanton number, $N_{St,\infty}$, with the experimentally determined results is shown in Figure 3. The Stanton number is defined here as

$$N_{St,\infty} = \frac{\dot{q}}{\rho_\infty u_\infty c_p (T_{aw} - T_w)} \quad (11)$$

Even though exact conditions weren't specified for a given test, the results shown are fairly commendable. The Stanton number is, for example, very sensitive to the actual wall temperature. Transition was predicted at approximately the correct station by the simple criteria discussed earlier ($Re_{CRIT} = 150 M_e$).

4.3 PROBLEM 3. AXISYMMETRIC CONE-CYLINDER-FLARE BODY AT MACH 8.0

This problem is interesting in that it was used as an example problem in the AIAA paper by Sasman and Cresci (ref. 5). As discussed earlier, it is the Sasman and Cresci formulation of the compressible turbulent boundary layer with pressure gradient and heat transfer that was used as a basis for the turbulent subroutine in Program BLAYER. In addition, it is Sasman and Cresci's formulation of the axisymmetric turbulent boundary layer used by Northrop in modification 2 to BLAYER. The original source for this sample problem is Zakkay and Callahan (ref. 10).

The model is a cone-cylinder-flare body (Figure 4) tested at Mach 8.0 in the hypersonic facility of the Polytechnic Institute of Brooklyn Aerodynamics Laboratory. Test conditions for the sample case under consideration here were as follows: freestream Mach number was 8.0; freestream stagnation pressure was 590 psia ($4.07 \times 10^6 \text{ N/m}^2$); freestream stagnation temperature was 1800°R (1000°K) and the wall temperature was 540°R (300°K). The pressure distribution on the model was given referenced to the stagnation pressure behind the conical shock.

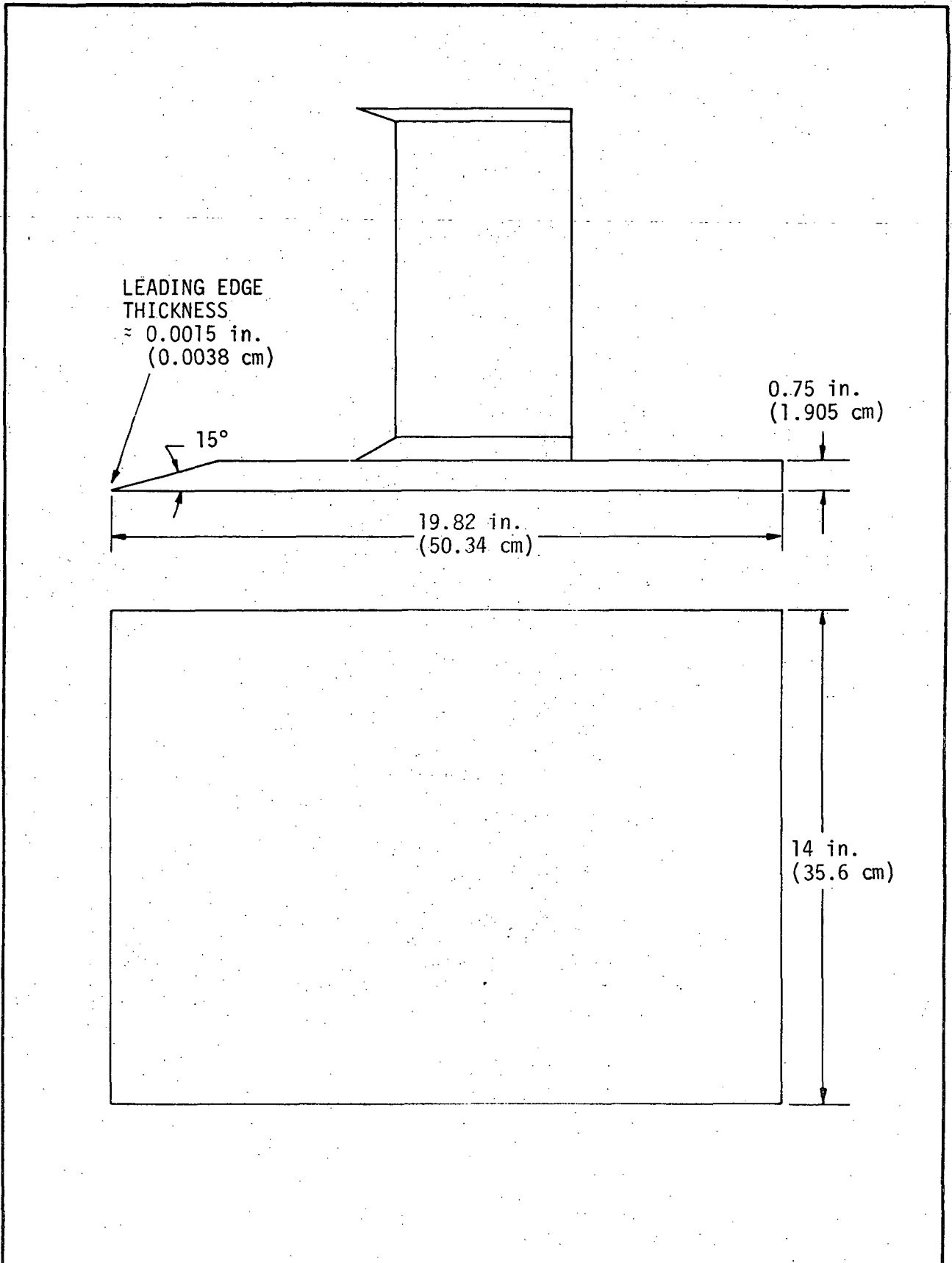


Figure 2. SHARP LEADING EDGE FLAT PLATE MODEL (Ref. 9)

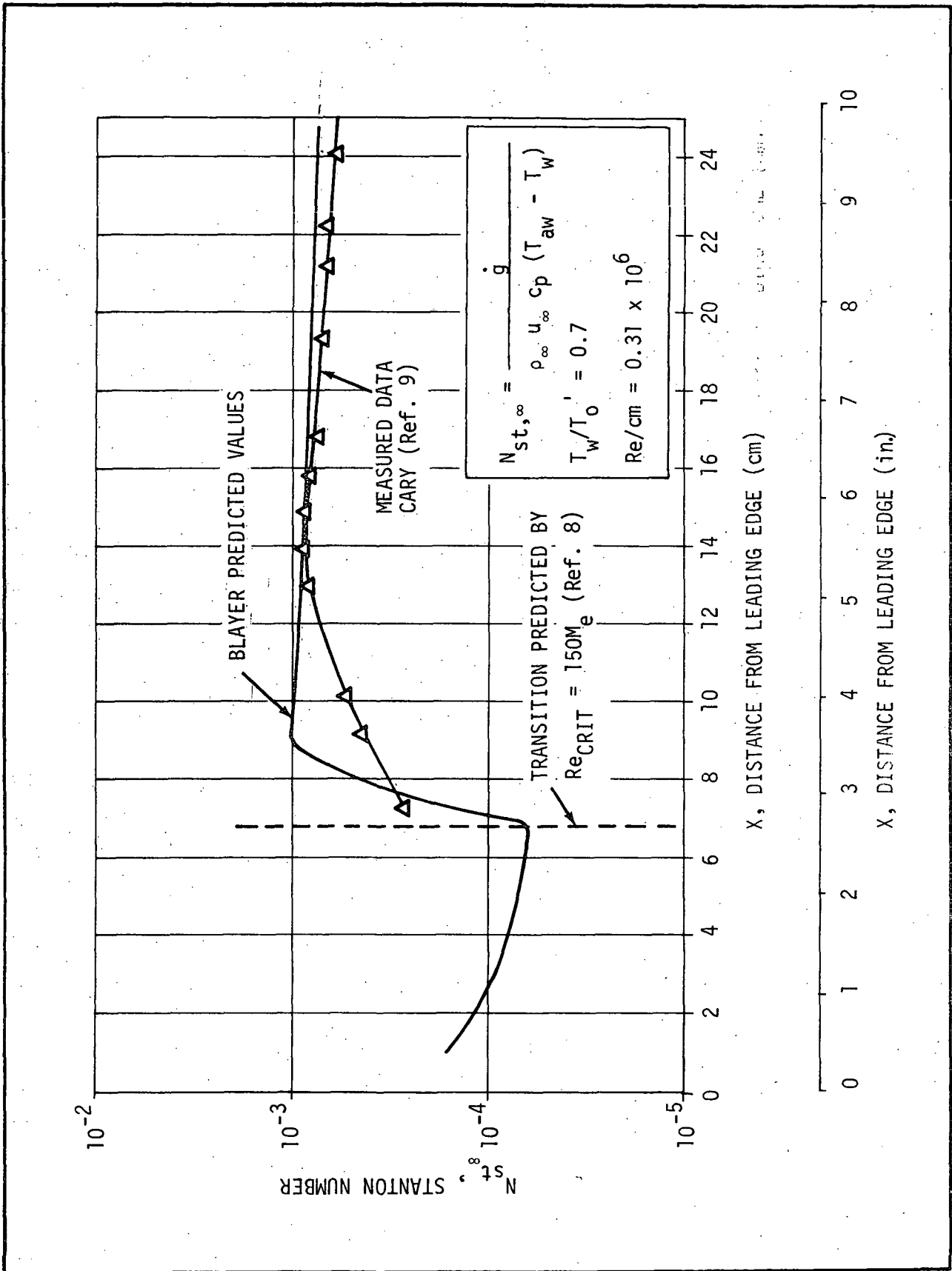


Figure 3. HEAT-TRANSFER DATA FOR COOLED FLAT PLATE AT $M_e = 6.0$

For $4.696 \text{ in.} \leq \bar{S} \leq 6.1616 \text{ in.}$
 (11.928 cm) (15.650 cm)
 $r_o = -3.563 + 5.5 \cos(68.92 - 10.42 \bar{S})$, in.

For $23.99 \text{ in.} \leq \bar{S} \leq 36.19 \text{ in.}$
 (60.935 cm) (91.9226 cm)
 $r_o = 71.854 - 69.916 \cos(19.66 - 0.82 \bar{S})$, in.

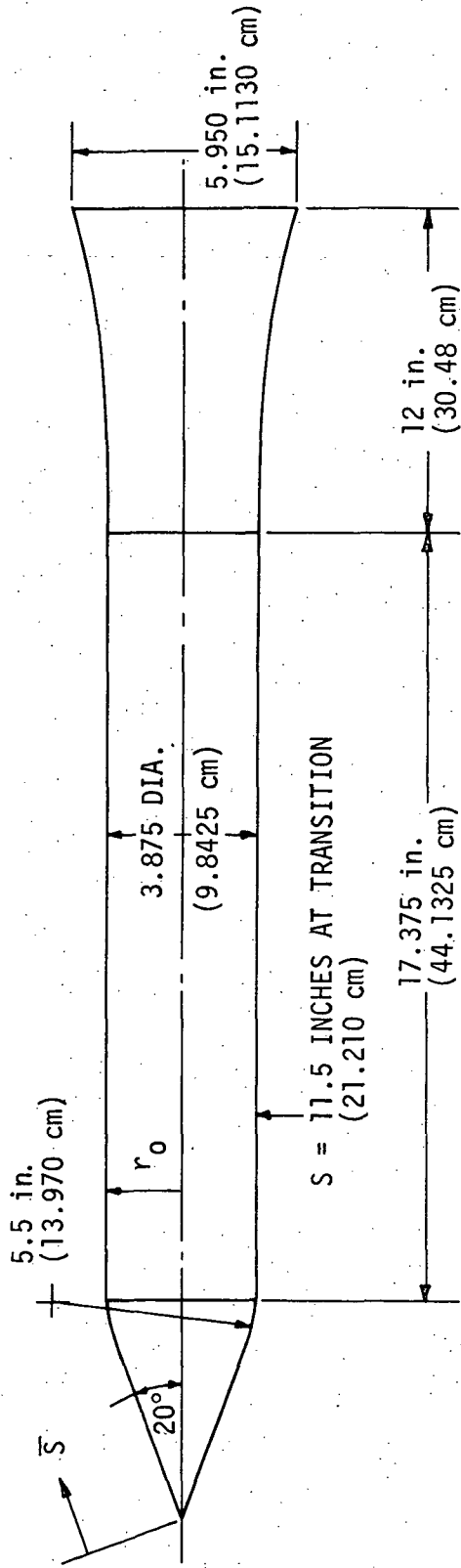


Figure 4. AXISYMMETRIC CONE-CYLINDER-FLARE BODY TESTED AT MACH 8.0 (Ref. 10)

In order to start program BLAYER in the turbulent boundary layer region, the input data were generated for conditions behind the conical shock near the region of the experimentally determined transition point. This point was taken as 11.5 inches along the surface from the point of the cone. The input data were calculated for the model and the above freestream conditions and is as follows: local freestream Mach number, 6.80; stagnation pressure, 154.5 psia (1.065×10^6 N/m²); stagnation temperature, 1800°R (1000°K); wall temperature, 540°R (300°K); momentum thickness, 0.89896×10^{-3} ft (0.0274 cm); and displacement thickness, 0.12264×10^{-1} ft (0.374 cm).

The results are plotted in Figures 5 and 6. Figure 5 is a plot of the heat transfer to the model as predicted by program BLAYER and by the Spalding-Patankar method (ref. 11). Figure 6 is a comparison of the experimental and predicted Nusselt number based on the reference enthalpy state. Again it is observed that there is reasonable agreement between program BLAYER and the experimental data.

4.4 PROBLEM 4. LAMINAR HEAT-TRANSFER ON A SHARP, 15 DEGREE HALF-ANGLE CONE AT $\alpha = 0$ DEGREE AND $M_\infty = 6.0$

This was the first and only attempt made in this study to predict laminar heat-transfer to an axisymmetric body using the modified Program BLAYER. The simple modification made to the laminar subroutine in program BLAYER was discussed earlier in this report. This sample problem was generated to match an experimental test where laminar heat-transfer and pressure measurements were made on a sharp, 15 degree half-angle cone in supersonic ($M_\infty=6.0$) flow at an angle-of-attack of zero degrees (ref. 12).

The sharp, 15 degree half-angle cone is shown in Figure 7. The test free-stream conditions where $M_\infty = 6.1 \pm 0.07$, stagnation pressure equal to 360 psia (2.48×10^6 N/m²), and stagnation temperature equal to 935°R (519°K). Local conditions were estimated behind the conical shock as follows: stagnation pressure equal to 258 psia (1.779×10^6 N/m²); static pressure for the cone surface equal to 1.01 psia (6.96×10^3 N/m²); and stagnation temperature equal to 935°R (519°K). The surface temperature was taken as approximately 540°R (300°K).

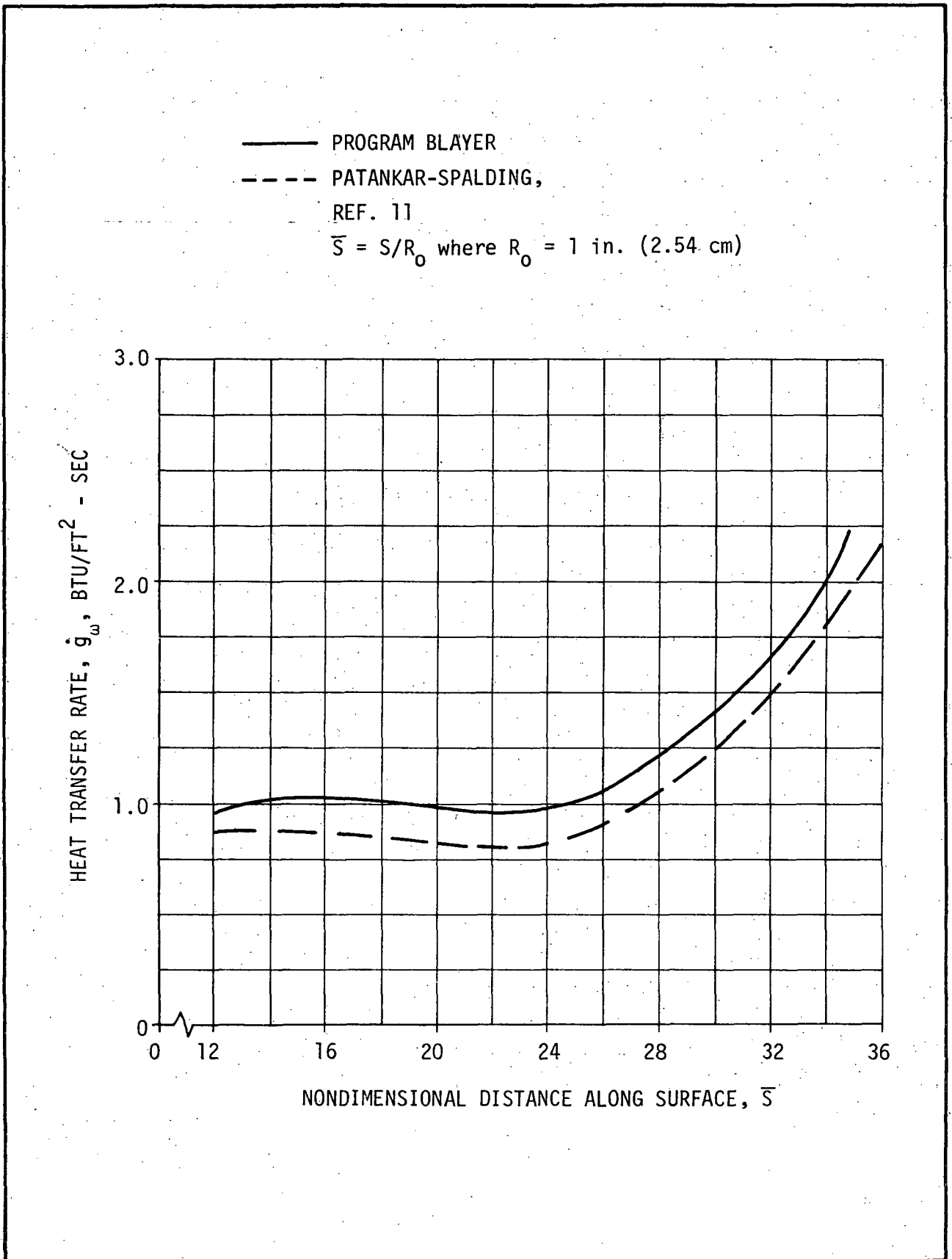


Figure 5. COMPARISON OF PREDICTED HEATING RATES ON CYLINDER - FLARE MODEL IN TURBULENT FLOW (MODEL BASED ON REF. 10)

$$\bar{S} = S/R_0 \text{ where } R_0 = 1 \text{ in. (2.54 cm)}$$

$$N_{Nu} = \text{REFERENCE ENTHALPY NUSSLETT NUMBER}$$

$$= \dot{q}_w c_p S / (h_{aw} - h_w) k$$

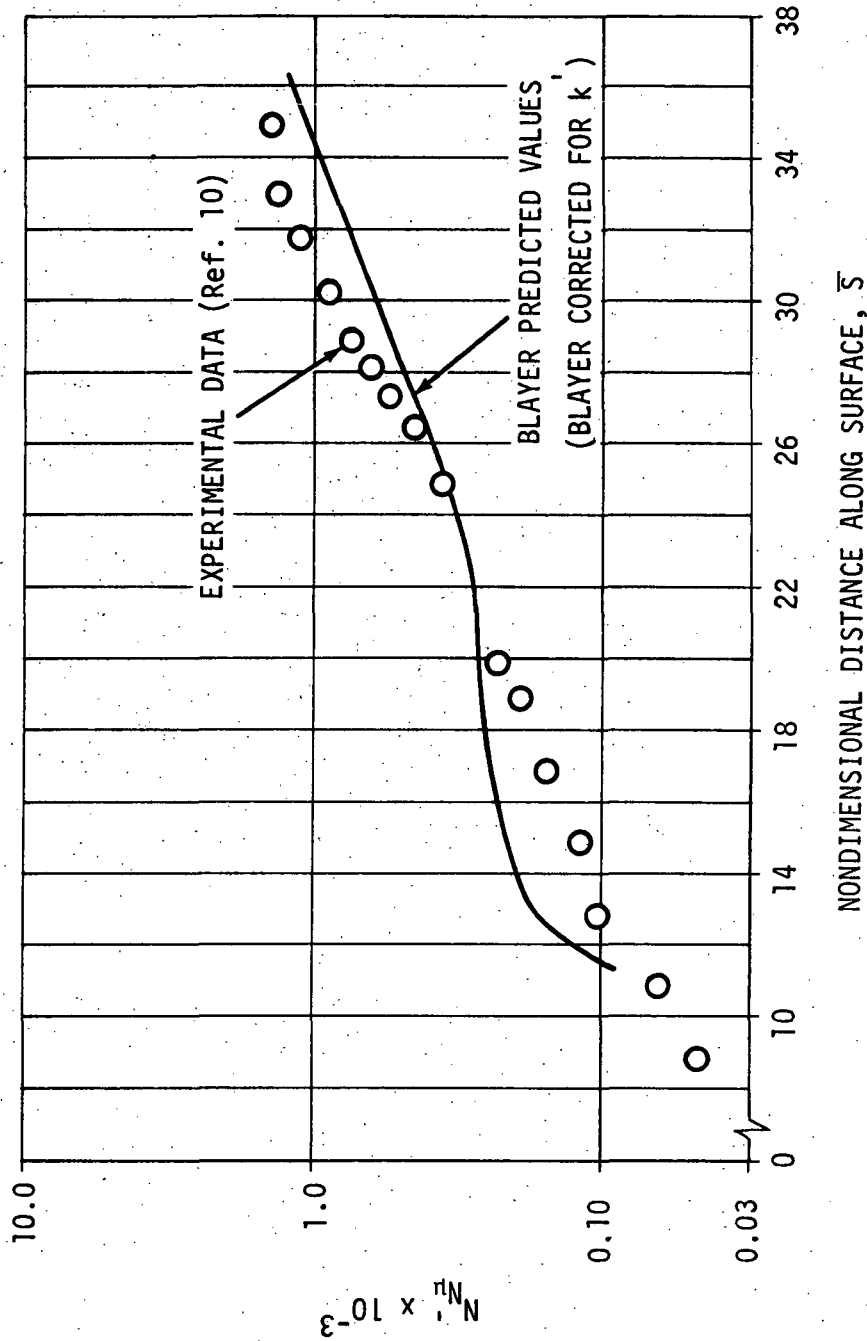
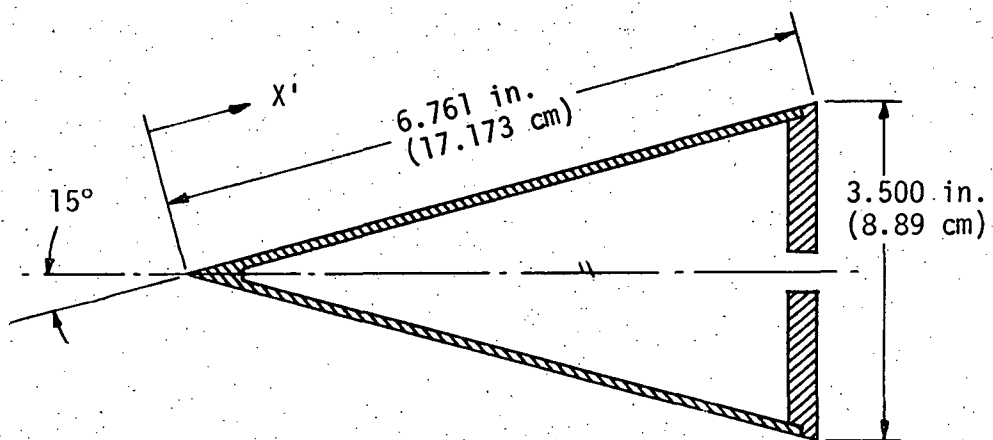


Figure 6. COMPARISON OF BLAYER HEATING RATES TO EXPERIMENTAL DATA ON CYLINDER - FLARE MODEL IN TURBULENT FLOW



WALL THICKNESS, $t = 0.030 + 0.001$ in.
(0.0762 \pm 0.0025 cm)

Figure 7. SHARP POINTED CONE MODEL (Ref. 12)

A plot of the heat transfer rate for both the experimental test and the BLAYER prediction is shown in Figure 8. The results of the BLAYER prediction are much below those of the experimental test and are very disappointing. The problem was treated as a sharp, leading-edge problem in that no initial values were given for either the momentum thickness or the displacement thickness. The constants in the linear approximation were unchanged (i.e., A and B in equation (2)) from their original values as established by McNally for the two-dimensional version of BLAYER (ref. 1).

Section V. CONCLUSIONS AND RECOMMENDATIONS

Program BLAYER, in its present form as modified by Northrop-Huntsville is an extremely versatile and powerful program for computing laminar and turbulent boundary layers on two-dimensional and axisymmetric bodies. The program can function in the presence of heat transfer and arbitrary pressure gradients. The program's major advantages are its ease of modification and its relative simplicity in input data requirements. The program can be easily modified to accept any desired transition criteria.

The major weaknesses in the program appear to be in the laminar subroutine. This subroutine is very strongly dependent on a number of curve-fitted parameters including those used in the determination of the very important pressure gradient correlation number, n . The program has not been exhaustively tested over all Mach number ranges and, therefore, the validity of the program is not fully established.

The following recommendations may be made based on experience with program BLAYER and its modified version:

1. Run program BLAYER for a series of space shuttle application problems for which there are experimental data available.
2. Modify program BLAYER to include other laminar-to-turbulent transition criteria as desired.
3. Run program BLAYER for a series of axisymmetric problems, including sharp and blunt leading-edge conditions.
4. Compare all of the above program BLAYER results with experimental data and with other prediction methods where possible.
5. Assess the need for corrections and/or modifications to be made to program BLAYER.

○ EXPERIMENTAL DATA (Ref. 12)
 --- PREDICTED BY CONE THEORY
 (REPRODUCED FROM REF. 12)
 — PROGRAM BLAYER

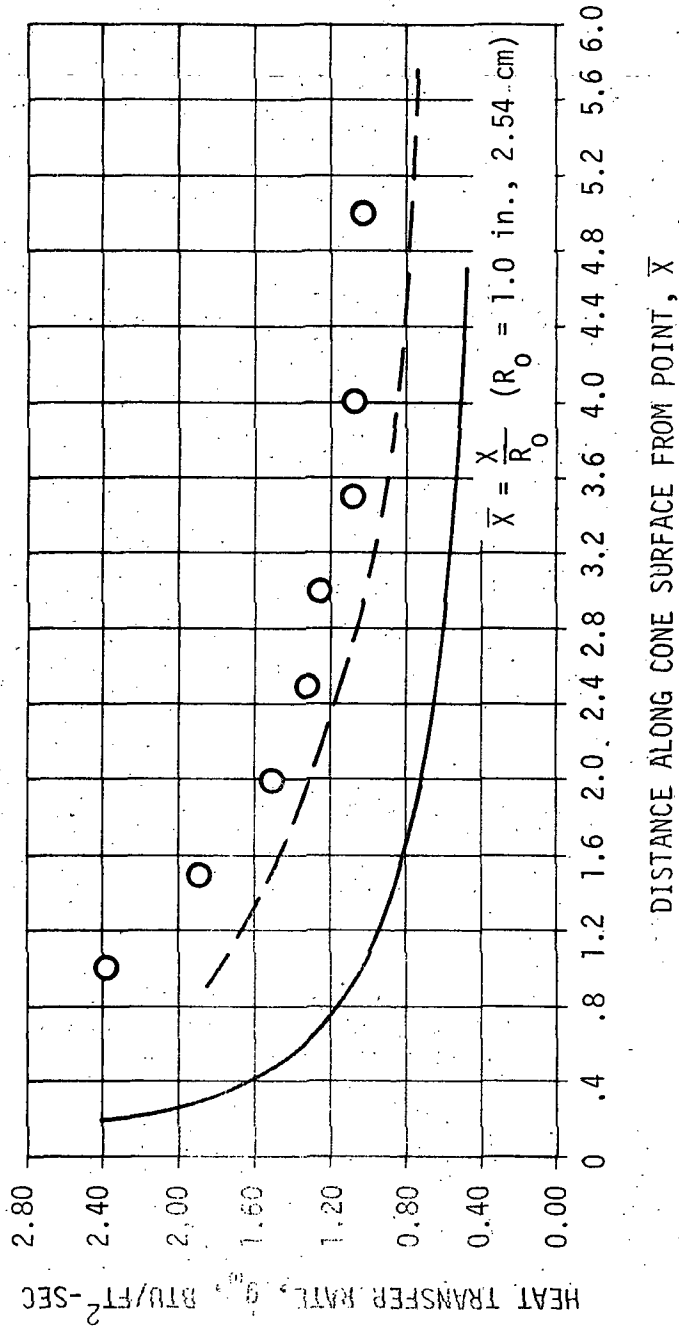


Figure 8. COMPARISON OF PROGRAM BLAYER HEAT TRANSFER RATE PREDICTIONS WITH EXPERIMENTAL DATA ON A SHARP-POINTED CONE AT MACH NUMBER 6

Section VI: REFERENCES

1. McNally, W. D., "Fortran Program for Calculating Compressible Laminar and Turbulent Boundary Layers in Arbitrary Pressure Gradients (Program BLAYER)", NASA/Lewis Research Center, NASA TN D-5681, May 1970.
2. Schlichting, H., Boundary Layer Theory, Sixth Edition, 1968, p. 471.
3. Cohen, C. B. and Reshotko, E., "The Compressible Laminar Boundary Layer with Heat Transfer and Arbitrary Pressure Gradient", NACA/Lewis Laboratory, NACA TR-1294, 1956.
4. Cohen, C. B. and Reshotko, E., "Similar Solutions for the Compressible Laminar Boundary Layer with Heat Transfer and Pressure Gradient", NACA/Lewis Laboratory, NACA TR-1293, 1956.
5. Sasman, P. K. and Cresci, R. I., "Compressible Turbulent Boundary Layer with Pressure Gradient and Heat Transfer", AIAA Journal, Vol. 4, No. 1, January 1966, pp. 19-25.
6. Schlichting, H. and Ulrich, A., "Zur Berechnung des Umschlages Laminar-Turbulent", Jahrbuch d.dt. Luftfahrtforschung, No. 1, 1942, pp. 8-35.
7. Granville, P. S., "The Calculation of the Viscous Drag of Bodies of Revolution", David Taylor Model Basin, Report 849, July 1953.
8. Pearce, B. E., "A Comparison of Simple Turbulent Heating Estimates and Boundary Layer Transition Criteria with Application to Large, Lifting Entry Vehicles", NASA TM X-52876, Vol. I, July 1970.
9. Cary, A. M., Jr., "Turbulent-Boundary-Layer Heat Transfer and Transition Measurements with Surface Cooling at Mach 6", NASA/Langley Research Center, NASA TN D-5863, June 1970.
10. Zakkay, V. and Callahan, C. J., "Laminar, Transitional and Turbulent Heat Transfer to a Cone-Cylinder-Flare Body at Mach 8.0", J. of Aerospace Sci., Vol. 29, 1962, pp. 1403-1420.
11. Patankar, S. V. and Spalding, D. B., Heat and Mass Transfer in Boundary Layers, C. R. C. Press, Cleveland, Ohio, 1968.
12. Conti, R. J., "Laminar Heat-Transfer and Pressure Measurements at a Mach Number of 6 on Sharp and BLUNT 15° Half-Angle Cones at Angles of Attack Up to 90°", NASA/Langley Research Center, NASA TN D-962, 1962.

Appendix

LIST OF SYMBOLS

A,B	constants in eqs. (2)-(4) and (9), (10)
a	speed of sound, ft/sec; m/sec
C_f	local skin friction coefficient
c_p	specific heat at constant pressure, Btu/lbm-°R; J/kg-°K
f	function of transformed momentum thickness. See definition preceding eq. (5)
H_i	transformed form factor for adiabatic flow, also called incompressible form factor
h	enthalpy, ft-lbf/slug; J/kg
k_{su}	constant in Sutherland's viscosity-temperature relation
L	total distance along boundary-layer surface, ft; m
M	Mach number
N	momentum parameter, eqs. (1) and (2)
n	correlation number (pressure gradient parameter)
P	pressure, lbf/ft ² ; N/m ²
q	heat transfer rate per unit area, Btu/ft ² -sec; watts/m ²
R	body radius of an axisymmetric body, ft; m
Re_θ	Reynolds number based on momentum thickness, $u_e \theta / \nu_w$
Re_{CRIT}	Critical Reynolds number defined by eq. (7)
S	enthalpy function, $(h'/h'_o)-1$
T	temperature, °R; °K
T_{aw}	adiabatic or recovery wall temperature, °R; °K
U	transformed longitudinal velocity, $(a'_o/a_e) u$, ft/sec; m/sec
u	longitudinal velocity parallel to boundary-layer surface in X-direction, ft/sec; m/sec

X coordinate for input of surface geometry, ft; m
X_{tr} transformed X-coordinate along body surface, ft; m
x coordinate parallel to body surface in streamwise direction, ft; m
γ ratio of specific heats
δ boundary-layer thickness, ft; m
δ* boundary-layer displacement thickness, ft; m
θ momentum thickness, ft; m
ν kinematic viscosity, ft²/sec, m²/sec
ρ density, lbf/ft³; kg/m³
τ shear stress, lbf/ft²; N/m²

Subscripts:

∞ freestream conditions away from the body
e value external to boundary layer, but adjacent to it
i incompressible quantity
tr transformed quantity
w wall or surface value
x local value based on x
o freestream value; condition external to boundary layer, usually near $x = 0$

Superscripts:

' total or stagnation condition, or quantity based on total or stagnation condition
- evaluated at reference conditions.

Distribution:

NASA - J. A. Forney (5)

Northrop - D. Barnett

J. Roux

J. Parker

W. Youngblood (3)

7946 File